Laser Spectroscopy, Energy-Transfer and Bleaching Processes in Crystalline Rare-Earth Centres

A thesis submitted in partial
fulfilment of the requirements for the
Degree of Doctor of Philosophy in Physics
in the
University of Canterbury

by

Keith Michael Murdoch

University of Canterbury
1993

Abstract

Laser selective excitation spectroscopy has been applied to investigate electronic structure, excited-state relaxation, inter-ion energy transfer and fluorescence bleaching in several species of crystalline rare-earth centres.

Group theoretical techniques have been applied to understand the polarisation behaviour of ensembles of optically-active rare-earth centres in the fluorite lattice. Polarisation experiments were conducted on the Pr^{3+} and Tb^{3+} centres in both pure and hydrogenated CaF_2 and SrF_2 crystals, to determine their site-symmetries and to identify their transitions and electronic energy levels. Model configurations and bleaching mechanisms were either proposed or confirmed for all of the known praseodymium Cs centres and Cs* photoproduct centres. These models account for the polarised-bleaching behaviour of each Cs centre.

Six new Tb^{3+} centres were found in the hydrogenated crystals and at least three of these exhibit fluorescence bleaching. One centre exhibited fluorescence enhancement, a related phenomenon reported for the first time in this study. Crystal-field calculations yielded fitted values for the crystal-field parameters of the terbium $C_{4v}F^-$ centres.

Bleaching is presented as a phonon-scattering process, involving light-induced barrier crossing in the double-well potential of two distinct ionic configurations of a RE^{3+} centre. Thermal-reverting temperatures were measured for most of the Cs centres and used to estimate their barrier potentials. The results confirm that bleaching involves barrier crossing and not quantum tunnelling.

Inter-ion energy transfer was studied in both pure and mixed praseodymium and thulium doped $CsCdBr_3$ crystals. New cross-relaxation and upconversion mechanisms were identified, including several which enable infrared to blue or ultraviolet upconversion. Some novel two-laser techniques for probing both sequential and cooperative-upconversion processes are demonstrated.

Acknowledgements

This thesis is dedicated to my parents, Noelene and Neil, whose eldest son moved to the South Island in 1986 and has been an infrequent visitor ever since. Thank you for your encouragement and support.

I would particularly like to thank my supervisor Dr Glynn Jones for his wise counsel, his gentle guidance, and for many stimulating discussions over the past four years. Glynn's enthusiasm for this project and humour while we confronted the inevitable difficulties have made my task an easier and more enjoyable one. I also wish to thank: Dr Nigel Cockroft for organising my visit to Los Alamos and suggesting an interesting project which taught me much about lanthanide spectroscopy, my acting supervisor Dr Rod Syme for carefully proof reading this thesis and providing many useful suggestion for its improvement and Mike Reid for his active interest in the work reported and for patiently answering my daily volley of questions about crystal-field theory.

I am very grateful for the prompt and capable technical support provided by Ross Ritchie (electronics and crystal growth), Wayne Smith (pumps and furnaces), Clive Rowe (storage oscilloscope and detectors), Ron Culley (plumbing and furnaces), Mark Aitchison (computers and software) and George Faulkner (Los Alamos National Laboratory). Much of the work reported was made possible by their willingness to address technical difficulties as they arose. Financial support was provided by the Department of Physics and Astronomy through a Teaching Assistantship and Research Bursary.

While working on this thesis I have enjoyed the company of the staff and other graduate students in the Department of Physics and Astronomy. In particular I wish to thank my fellow laser spectroscopists Khong Yoon Loong, Marjorie Mujaji, Nick Strickland and Jon Wells for their willing assistance with technical problems and for many helpful discussions. Jon Wells obtained the FTIR Zeeman spectra discussed in Chapter 7.

During my travels abroad to visit other scientific institutions I have enjoyed the friendly welcome and generous hospitality of a number of physicists and their families; especially Nigel Cockroft and family (Los Alamos, New Mexico), Mike Reid and family (Hong Kong), Don Hutton and family (Melbourne, Australia), Roger and Karyn Reeves (Stillwater, Oklahoma), Dr Udo Bogner (Regensburg, Germany), Prof John Wright (Madison, Wisconsin), Amanda Peet (Stanford University, California) and the late Roger Carlson (Chicago and Los Alamos). Thanks for a cool/warm bed and the interesting penny tours.

A special thank you to John, Lynn and Madeline for their interest in my endeavours, their hospitality and for many hours of interesting conversation. Finally I would like to thank Annabelle for her friendship and understanding during a time when I was often distracted by weird crystals and machines with amusing names.

Contents

IV

List of Tables

List of Figures

Chapter 1

Introduction

1.1 The Trivalent Lanthanide Ions

The rare-earth elements comprise the lanthanides, from lanthanum to lutetium, and the actinides, from actinium to lawrencium. Lanthanum has atomic number Z=57 and lutetium Z=71. The dominant oxidation state for lanthanides in ionic solids is trivalent, henceforth denoted as 'RE^{3+}'. The ground-state electronic configuration of a trivalent lanthanide ion comprises a xenon-like structure ($1s^2 2s^2 2p^6 3s^2 3p^6 3d^{10} 4s^2 4p^6 4d^{10} 5s^2 5p^6$) and N additional $4f$-electrons. N increases across the series from 0 (for La^{3+}) to 14 (for Lu^{3+}).

The $4f$-electron shell has a smaller spatial extension than the closed $5s^2 5p^6$ shells. The 'lanthanide contraction' arises from imperfect mutual shielding of the nuclear change by the $4f$-electrons. Each additional charge accentuates the effective nuclear potential and so the contraction increases across the series. Thus the $4f$-orbitals are localised and do not extend appreciably into the environment. This localisation and the shielding provided by the closed $5s^2 5p^6$ shells protects the $4f$-electrons from strong interactions with external electric or magnetic fields.

As a consequence the electronic transitions of the $4f^N$-configuration have unusually small inhomogeneously-broadened line-widths. Even in an ionic solid the electric field created by the ligand ions generates comparatively small perturbations from electronic energy levels of the free ion. For this reason RE^{3+} ions are used extensively in solid-state spectroscopy as a probe of crystalline structure. RE^{3+} centres are rich and diverse spectroscopically, while the task of interpreting their spectra remains tractable. Very good theoretical models have been developed to account for their observed energy levels and transitions.

Crystalline centres of three RE^{3+} ions were investigated in this study: Pr^{3+} (Z=59, N=2), Tb^{3+} (Z=65, N=8) and Tm^{3+} (Z=69, N=12). All three are non-Kramers ions, with an even number of $4f$-electrons. The other important properties of these ions are listed in Table 1.1. Each RE^{3+} ion has a characteristic energy level structure comprising the $^{2S+1}L_J$ quantum states, which are highly degenerate in the free ion. This structure is shown in Figure 1.1 for Pr^{3+}, Tb^{3+} and Tm^{3+}. Both the

Table 1.1: Properties of the principle ionic species included in this study. The ionic radii are in units of Å. The isotopes of the Pr^{3+}, Tb^{3+} and Tm^{3+} ions quoted here are all 100% naturally abundant. The ground-state nuclear spins of these isotopes are also listed. This data was obtained from the CRC Handbook of Chemistry and Physics.

	Pr^{3+}	Tb^{3+}	Tm^{3+}	Ca^{2+}	Sr^{2+}	Cd^{2+}	Cs^{2+}	F^-	Br^-
Atomic Weight	140.90	158.92	168.93	40.08	87.62	112.41	132.91	19.00	79.90
Ionic Radius	1.01	0.92	0.87	0.99	1.12	0.97	1.67	1.33	1.96
Isotope	141	159	169						
Nuclear Spin	$+\frac{5}{2}$	$+\frac{3}{2}$	$+\frac{1}{2}$						

$^{2S+1}L_J$ quantum labels and the spectroscopic letter notation are used to identify multiplets in this thesis. In particular, the letters 'F' and 'G' will be used to denote the $^1I_6$ and $^3P_1$ multiplets, respectively, of praseodymium.

Externally applied electric and magnetic fields will break the inherent degeneracies of the free-ion multiplets, generating a number of discrete sub-levels. These 'crystal-field' levels will be distinguished by numbers appended to the quantum labels or letter notation. For example; the n^{th} level of the $^3P_1$ multiplet of praseodymium would be labeled as either $^3P_1(n)$ or G_n respectively.

1.2 Rare-earth Centres in Alkaline-Earth Fluoride Crystals

Pure alkaline-earth fluoride crystals have the fluorite structure, shown in Figure 1.2(a). This comprises monovalent fluoride ion cubes, with the divalent alkaline-earth ions located in alternate cubes. The fluorite lattice has 0_h^5 space-group symmetry. Fluoride ions occupy sites of tetrahedral T_d point symmetry, while the alkaline-earth ions occupy sites of O_h point symmetry. The distance between neighbouring Sr^{2+} ions in the SrF_2 lattice is 5.75Å, while the distance between Ca^{2+} ions in CaF_2 is 5.45Å. The ionic radii of the lattice ions are listed in Table 1.1.

Trivalent rare-earth ions are readily accepted into the fluorite lattice and substitute for divalent alkaline-earth ions. Charge compensation is required to preserve the overall charge neutrality of the crystal. This is usually achieved by the inclusion of additional monovalent fluoride ions which occupy interstitial sites inside the lattice cubes. The affinity between the RE^{3+} ions and the interstitial F^- ions results in local charge compensation and the predominance of two types of RE^{3+} centre at low dopant concentrations.

At the beginning of the lanthanide series the tetragonal C_{4v} symmetry RE^{3+}

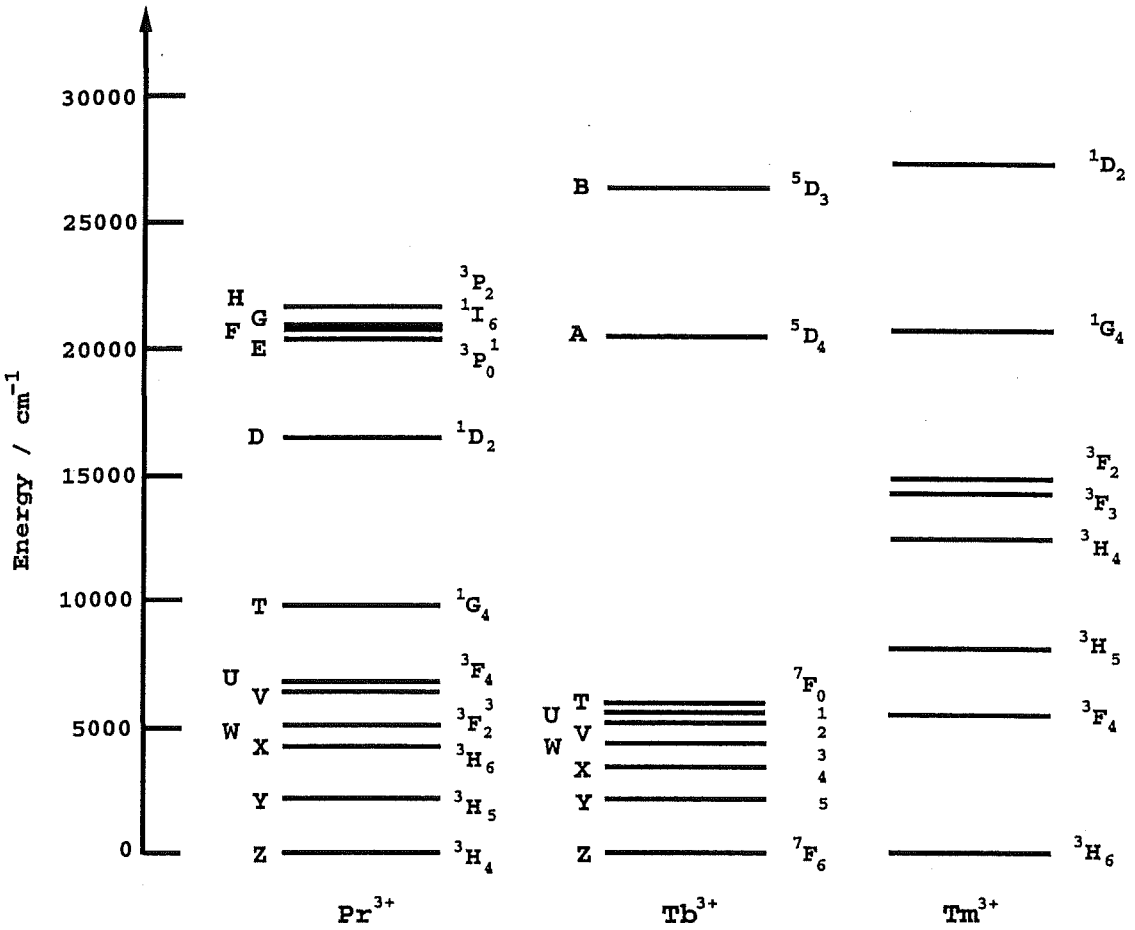

Figure 1.1: The electronic energy levels of the Pr^{3+}, Tb^{3+} and Tm^{3+} ions. There are ten terbium multiplets below 30000cm^{-1}, but higher in energy than the $^5D_3$ multiplet. These were not observed in this study and are not shown.

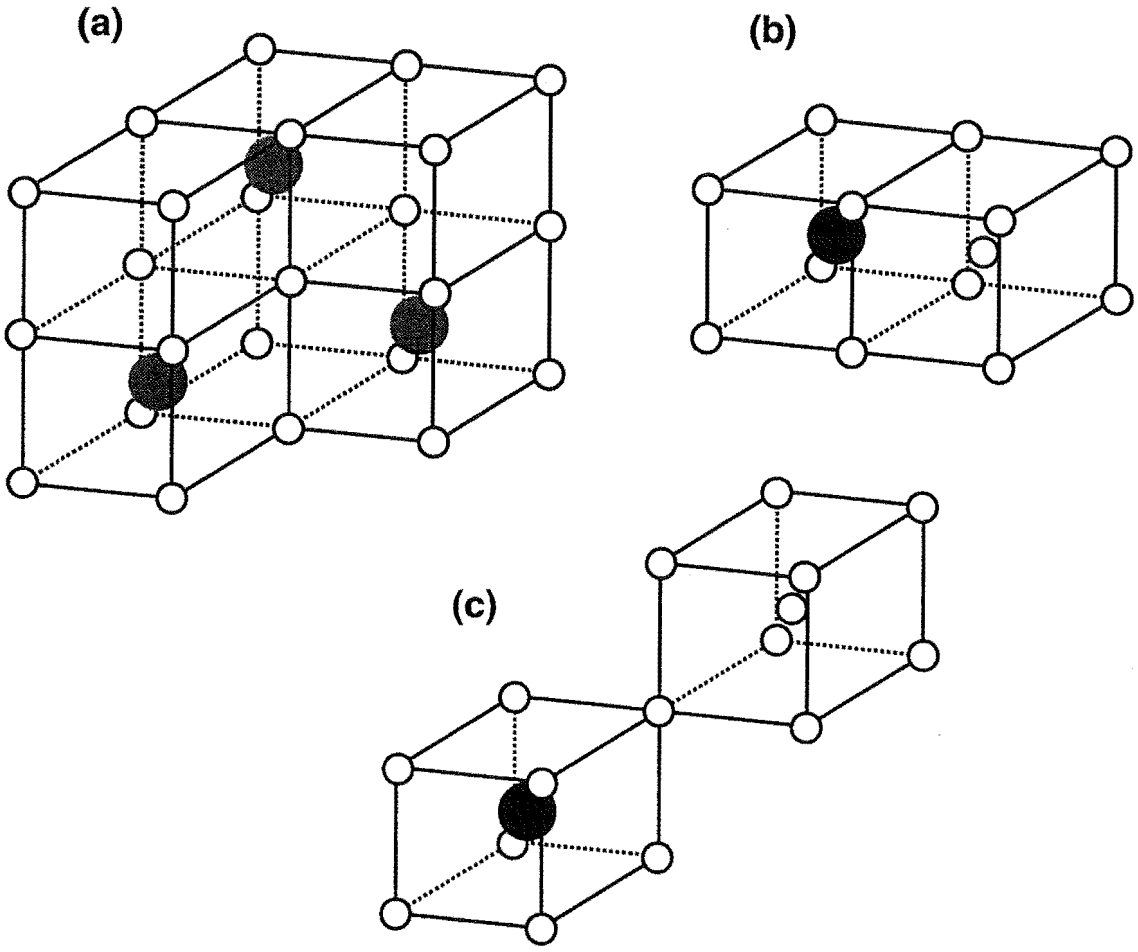

Figure 1.2: (a) The fluorite lattice structure of the alkaline-earth fluorides. (b) The tetragonal $C_{4v}F^-$ and (c) trigonal $C_{3v}F^-$ RE^{3+} centres.

centre is preferred in both CaF_2 and SrF_2 crystals, Figure 1.2(b). The charge-compensating F^- ion is located in a nearest-neighbour interstitial site, so that the RE^{3+} ion now occupies a site with C_{4v} point symmetry. At the end of the lanthanide series the trigonal C_{3v} symmetry configuration is preferred, Figure 1.2(c). The RE^{3+} ion resides in a site with C_{3v} point symmetry and the charge-compensating F^- ion is in a next-nearest-neighbour interstitial site. Whether the tetragonal or trigonal centre is dominant is determined by the radius of the dopant RE^{3+} ion relative to the crystal-lattice parameter. Both types of RE^{3+} centre act as electric dipoles. For RE^{3+} ion concentrations in excess of 1%, the proportion of cluster centres become significant [22]. These clusters are produced by the aggregation of discrete RE^{3+} centres. Particular crystal growing conditions will accentuate cluster centre formation.

New RE^{3+} centres are created through additional cation [53] [62] or anion [27] [39] [62] [77] substitutions in the vicinity of the RE^{3+} ion. In this study the substitution of H^- ions for lattice and interstitial F^- ions will be investigated. The dominant H^- site in these crystals has tetrahedral T_d symmetry and is produced by replacing lattice F^- ions, located in sites remote from any RE^{3+} centres [33]. Edgar and Newman [32] and Jones et al [47] have shown that near RE^{3+} ions the H^- ions will preferentially replace the interstitial F^- ion. This substitution leaves the point symmetry of the RE^{3+} ion unchanged and the H^- ion occupies a site with axial symmetry. Lower symmetry hydrogenic centres are produced by additional substitutions of the lattice F^- ions in the nearest coordination sphere of the RE^{3+} ion [31]. Isotopically mixed H^- and D^- ion centres are also possible [39].

Laser selective excitation studies have been performed on the multi-hydrogenic ion centres of Gd^{3+} [31], Er^{3+} [24] [26] [27], Pr^{3+} [75] [77] and Nd^{3+} [39] [40]. All of these centres were found to exhibit permanent spectral holeburning at 10K, caused by the light-induced migration of hydrogenic ions to new sites. If the resulting photoproduct centres are no longer resonant with the excitation beam there will be a permanent reduction the intensity of the observed fluorescence. This process will henceforth be called bleaching, as a sufficiently broad laser can erase the absorption transition and attenuate the fluorescence from that centre. Bleaching is generally reversible, either by selective excitation of the photoproduct centres or by heating the whole crystal. The multi-hydrogenic ion Cs centres of praseodymium, and their Cs^* photoproduct centres, will be investigated in this study. These were discovered by Roger Reeves [77], who has already elucidated much about their spectroscopic and bleaching behaviour. Reeves has proposed models for some of these centres and also a general mechanism which accounts for their diverse bleaching behaviour.

1.3 Rare-earth Centres in $CsCdBr_3$ Crystals

$CsCdBr_3$ is one of the transition metal salts of the AMX_3 type; where A^+ is a monovalent metal, M^{2+} is a divalent metal, and X^- is a halide. The physical properties of these materials were first reviewed by Ackerman et al in 1974 [1], and much initial interest was aroused by their magnetic behaviour. Specifically they presented an opportunity to study magnetic ordering in one-dimension.

$CsCdBr_3$ adopts the hexagonal $CsNiCl_3$ crystal lattice structure [58], Figure 1.3(a). This consists of linear chains of face sharing $[MX_6]^{4-}$ octahedra, separated by A^+ metal ions which are located between the chains. These chains define the crystallographic c-axis and give the AMX_3 salts their quasi one-dimensional character [1].

Rare-earth doping of $CsCdBr_3$ was first reported by McPherson and Henling in 1977 [58]. They observed that the EPR spectrum of $CsCdBr_3$:Gd^{3+} "is dominated by resonances arising from weakly coupled pairs". This was true even for gadolinium concentrations as low as 0.1atom%. From their EPR results they concluded that

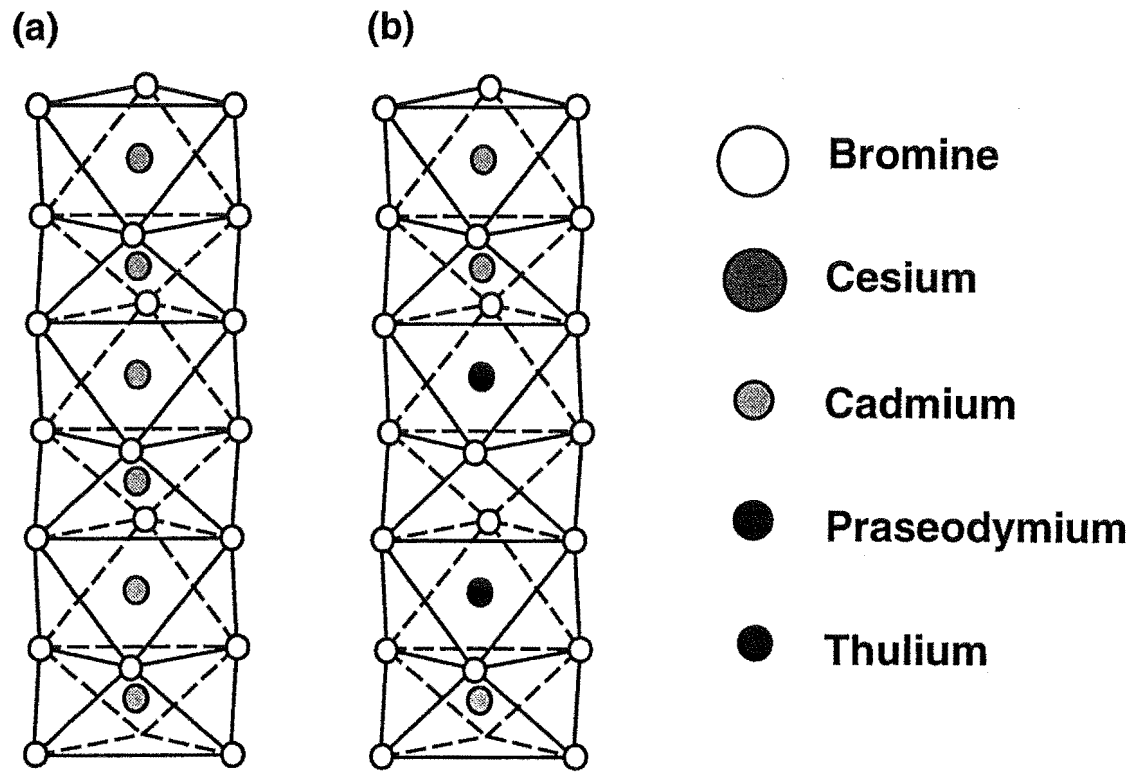

Figure 1.3: (a) The structure of the $CsCdBr_3$ lattice. (b) The dominant rare-earth pair centre in the $CsCdBr_3$:RE^{3+} crystals. These figures have been adapted from McPherson and Henling 1977. The ions in the key have been drawn to the same scale as the ion cages.

the trivalent dopant ions were readily accepted into the $CsCdBr_3$ lattice as dimer pair centres of the form RE^{3+}-Cd^{2+}vacancy-RE^{3+}, Figure 1.3(b). The RE^{3+} ions substitute for divalent metal ions, M^{2+}, in the crystal lattice. Gd^{3+} pairs occur more frequently than can be accounted for by a purely statistical distribution of the dopant ions. McPherson et al [58] [59] noted that for two trivalent ions the formation of such a pair centre would provide mutual charge compensation and so maintain the overall charge neutrality of the chain.

In a later paper Henling and McPherson [41] were able to report that this propensity for trivalent dopant ions to form pair centres was a characteristic of $CsCdBr_3$ crystals and structurally similar AMX_3 salts. Using EPR to observe pair resonances they estimated that more than 90% of the Gd^{3+} ions in $CsCdBr_3$:Gd^{3+} reside in pair centres. Each RE^{3+} ion sees a point symmetry of C_{3v}, because of the presence of the other RE^{3+} ion of the pair. They also reported calculated values for the inter-ionic spacings in the $CsCdBr_3$:Gd^{3+} lattice. These are 3.35Å for Cd^{2+}-Cd^{2+} ion pairs and 6.0Å for Gd^{3+}-Gd^{3+} ion pairs. The second result is representative of

the inter-ionic spacing for other rare-earth dopants.

McPherson et al [60] report the results of a X-ray diffraction study of a number of AMX_3 linear chain lattices, including that of $CsCdBr_3$. It was found that the $[MX_6]^{4-}$ octahedra are elongated along the crystallographic c-axis, reducing the point symmetry at each M^{2+} centre from octahedral, O_h, to trigonal, D_{3d}. They concluded that this trigonal distortion results from the mutual electrostatic repulsion between neighbouring M^{2+} ions. Such an elongation along the c-axis affects the crystal field at the site where a RE^{3+} ion resides, but not the point symmetry of the RE^{3+} centre.

In further EPR studies it was shown that divalent impurity ions in $CsMX_3$ can induce significant lattice deformations. Such a deformation will occur if there is an appreciable difference between the ionic radius of the impurity ion and that of the M^{2+} ion which it is replacing [60]. These deformations are consistent with the observation that these salts are very accommodating hosts, readily accepting most of the transition metals as ionic impurities.

Laser spectroscopic studies have shown that the RE^{3+} ions in the dominant pair centre do not always experience a crystal field of exact C_{3v} symmetry [62]. This can be observed as a broadening of the electronic transitions or even as a low symmetry splitting of degenerate levels. Ramaz et al [72] attribute this broadening to stacking disorder in the chains of bromide octahedra. They measured the angular distribution of the crystallographic c-axes using spectral holeburning and deduced a characteristic r.m.s. range of $(11\pm2)^o$.

From observations of vibronic sidebands to the electronic transitions of Nd^{3+} ions in $CsCdBr_3$:Nd^{3+}, Barthem et al [11] determined a cut-off energy for lattice phonons of $90cm^{-1}$. From Raman studies Pilla et al [67] found that there were optical-mode lattice phonons with higher energies, up to $163cm^{-1}$. Raman scattering and vibronic coupling excite different active modes, explaining the difference in the phonon cut-off energies obtained by these two methods [11]. That the phonon energies in $CsCdBr_3$ are so low, when compared to other crystal hosts, can be attributed to the heavy ions of which it is composed. The tendency for excited RE^{3+} ions to relax radiatively in $CsCdBr_3$ can be attributed to this small phonon cut-off energy [11] [12]. Alternate phonon-assisted relaxation pathways are necessarily higher order processes in host materials where the phonon energy is small.

1.4 The Objectives and Structure of this Thesis

Chapter 2 presents a theoretical introduction to the material in the rest of this thesis. Crystal-field theory has been applied successfully to determine electronic states, energy levels and transition intensities of RE^{3+} centres. This description of crystal-field theory is similar to the account given by Wybourne [93] and often his notation will be used. This chapter will also describe the hydrogen local vibrational modes observed in fluorite crystals, the electron-phonon interaction and inter-ion

energy-transfer processes.

Chapter 3 describes the experimental apparatus and techniques used to prepare crystals and to analyse them spectroscopically. RE^{3+} centres were observed by both absorption and laser selective excitation spectroscopy. Pulsed lasers were used to probe transient processes such as inter-ion energy transfer and excited-state relaxation.

Electronic transitions in crystallographic RE^{3+} centres are usually highly polarised. Aspects of their polarisation behaviour are considered in Chapter 4. A physical explanation is given to account for this polarisation dependence and group-theory is applied to predict the polarisation behaviour for specific site symmetries of non-Kramers RE^{3+} ions. Conversely the experimentally observed polarisation behaviour can be used to determine site symmetries of RE^{3+} centres and to label their energy levels. For this reason polarisation ratios have been calculated for a number of possible RE^{3+} ion site symmetries in alkaline-earth fluoride crystals. A treatment has been developed to understand the polarisation behaviour of low-symmetry RE^{3+} centres, which are derived from higher-symmetry parent centres. Its utility is demonstrated in subsequent chapters where the Cs centres of praseodymium are studied in detail. The properties of the relevant point-symmetry groups and the theoretical polarisation ratios are tabulated in Chapter 4.

Chapters 5 and 6 are concerned with the Pr^{3+} centres present in hydrogenated and deuterated SrF_2 and CaF_2 crystals. Chapter 5 presents new spectroscopic results obtained by exciting these centres selectively using a blue laser dye. These experiments complement those of several previous studies. Fluorescence polarisation ratios were measured and used to determine the site symmetries of the Cs centres and to identify some of their crystal-field energy levels. The $^1D_2$ multiplet fluorescence lifetimes were also measured and are analysed to establish the likely ionic composition of each Cs centre. The site symmetries and compositional data of the Cs(1), Cs(2) and Cs(3) centres are considered in relation to the ionic configurations proposed by Reeves et al [75] [77]. Model configurations are also proposed for the Cs(3) and Cs(5) centres.

The bleaching behaviour of the Cs and Cs* centres is analysed in Chapter 6. Specific mechanisms are proposed to account for the observed reorientational and photoproduct-formation bleaching, based on the general mechanism for light-induced ion migration suggested by Reeves et al. Model configurations for the Cs* centres and the bleaching pathways between different centre orientations are deduced from these mechanisms. The polarised bleaching behaviour of each centre can then be predicted by including the transition polarisation dependencies tabulated in Chapter 4. To test the bleaching mechanisms proposed for each centre, polarised bleaching sequences were recorded and compared with the predictions of these models.

The energetics of the bleaching process is also considered in Chapter 6. A model is presented for bleaching, which is considered in terms of the double-well potentials of the initial and photoproduct configurations. Thermal restoration of

fluorescence experiments were performed to measure barrier potentials and so estimate the excitation energies required for anion migration.

Chapter 7 reports the first laser selective excitation study of Tb^{3+} centres in CaF_2 and SrF_2 crystals. The terbium $C_{4v}F^-$ and $C_{3v}F^-$ centres were identified spectroscopically in both crystals. Irrep labels were assigned to the empirical energy levels of the $C_{4v}F^-$ centre and a crystal-field calculation was performed to fit the crystal-field parameters for the Tb^{3+} ion site. A variety of new centres were observed in the hydrogenated and deuterated crystals, some of which exhibit fluorescence bleaching. Their spectroscopy and bleaching behaviour is investigated. The $^5D_4$ multiplet fluorescence lifetimes of most of these Tb^{3+} centres were measured and are compared.

Chapter 8 presents the results from a study of inter-ion energy transfer in both pure thulium and mixed praseodymium:thulium doped $CsCdBr_3$ crystals. The Pr^{3+} and Tm^{3+} ions were expected to be particularly amenable to upconversion processes, as both ions have energy level structures comprising thirteen well distributed multiplets. There should be sufficient levels to enable a few small energy mismatches between the RE^{3+} ion pairs, without their excited states being quenched entirely by non-radiative relaxation and cross-relaxation processes.

The primary objective of these experiments was to determine the most efficient energy-transfer mechanisms between these two ions, involving visible wavelength electronic transitions. $CsCdBr_3$ was chosen as the host crystal as the predominant presence of one species of RE^{3+} centre, in which the spatial relationship between the donor and acceptor ions is invariant, simplifies the interpretation of spectroscopic and temporal observations. The tendency for trivalent impurities to form pair centres in the crystal lattice will also enhance the overall efficiency of any energy-transfer processes.

This study was first suggested by Dr Nigel Cockcroft, of the Los Alamos National Laboratory in Los Alamos, New Mexico. From May until September 1991 I visited LANL and worked in the Upconversion Laser Laboratory of the Laser and Chemical Sciences Division, with Dr Nigel Cockroft, Dr Dinh Nguyen, and Mr George Faulkner. The energy levels of the homogeneous and heterogeneous ion pairs were identified spectroscopically. A number of significant cross-relaxation mechanisms were found by exciting these ions selectively with blue or infrared excitation beams. Infrared to visible upconversion processes in both homogeneous and heterogeneous ion pairs were then investigated. Specific mechanisms are proposed to explain the energy-transfer processes observed.

Chapter 2

Theoretical Considerations

2.1 Crystal-Field Theory

Crystal-field theory has been reviewed extensively by several authors, particularly Dieke [29], Hüfner [43], Weissbluth [90] and Wybourne [93]. In this study only RE^{3+} ion transitions between electronic states of the lowest energy, $4f^N$, configuration will be investigated. The Hamiltonian H of a RE^{3+} ion in a crystallographic centre can be separated into two terms:

$$H = H_{FI} + V_{CF}\,, \tag{2.1}$$

where H_{FI} is the Hamiltonian of the free ion and V_{CF} is the potential produced by the ligand ions surrounding the RE^{3+} ion site. The electric field produced by these ligand ions is called the 'crystal field'. As the $4f$-electrons of the RE^{3+} ion are partially shielded by the closed $5s^2$ and $5p^6$ shells, V_{CF} can be treated as a perturbation of H_{FI}. So before calculating the electronic wavefunctions and energies for a RE^{3+} ion in a crystal field, it is necessary to solve the Schrödinger equation of the free ion.

2.1.1 The Free RE^{3+} Ion

The Hamiltonian of the free ion has two main contributions arising from the Coulomb interaction H_C and the spin-orbit interaction H_{SO}:

$$\begin{aligned} H_{FI} &= H_C + H_{SO} \\ &= \left[\frac{-\hbar^2}{2m}\sum_{i=1}^{N}\nabla_i^2 - \sum_{i=1}^{N}\frac{Ze^2}{r_i} + \sum_{i<j}^{N}\frac{e^2}{r_{ij}}\right] + \sum_{i=1}^{N}\zeta(r_i)l_i{\cdot}s_i\,. \end{aligned} \tag{2.2}$$

The first term in Equation 2.2 is the total kinetic energy of all N electrons, the second is their total potential in the electric field of the nucleus and the third term arises from their mutual electro-static repulsion. To find an approximate solution to the Schrödinger equation of H_C, the 'central-field approximation' is applied. This

approximation has each electron moving independently in a spherically symmetric potential $U(r_i)$ produced by the nucleus and all the other electrons. Now H_C can be expressed as the sum of a central-field term H_{cf} and a perturbation term H_p:

$$\begin{aligned} H_C &= H_{cf} + H_p \\ &= \sum_{i=1}^{N}\left[\frac{-\hbar^2}{2m}\nabla_i^2 + U(r_i)\right] + \left[-\sum_{i=1}^{N}\frac{Ze^2}{r_i} - \sum_{i=1}^{N}U(r_i) + \sum_{i<j}^{N}\frac{e^2}{r_{ij}}\right]. \end{aligned} \quad (2.3)$$

The central-field Schrödinger equation is readily solved as H_{cf} is the sum of N single-electron terms. A spin component is then included in the basis functions, which are antisymmeterised to solve for the wavefunctions of all the accessible electronic configurations. The eigenvalues are the energies of those configurations. The first two terms of H_p are purely radial and shift all the energy states within a configuration equally. In the last term, only those electrons which occupy incomplete shells will contribute to the breaking of the configurational degeneracy, thus separating the different LS states within each configuration.

In the $4f^N$-configuration of the RE^{3+} ions this residual perturbation, due to the repulsive Coulomb interaction between the $4f$-electrons themselves, is comparable to the spin-orbit interaction H_{SO}. When solving the free-ion Schrödinger equation these should be considered together and usually an 'intermediate-coupling' calculation is performed. This involves calculating the matrix elements of the two terms separately, usually applying LS coupling, and combining them in J state energy matrices. These are diagonalised to solve for the relative energies of the multiplets, labeled here as '$^{2S+1}L_J$', and their wavefunctions. The wavefunctions are linear combinations of pure LS coupled wavefunctions. Intermediate-coupling does not introduce any J state mixing. Typically the Coulomb interaction splits the ^{2S+1}L levels of a configuration by 10000cm^{-1} and the spin-orbit interaction further splits the $^{2S+1}L_J$ levels by 1000cm^{-1}.

In practice it is helpful to parameterise the matrix elements of both the Coulomb and spin-orbit interactions before performing the intermediate coupling calculation. This involves separating the angular and radial contributions of each element. These are labeled f_k and F^k respectively for the Coulomb interaction. For the spin-orbit interaction they are the $l_i \cdot s_i$ and $\zeta(r_i)$ components, respectively, of H_{SO}. Since the Slater F^k and spin-orbit $\zeta(r_i)$ integrals are purely radial they can be either calculated explicitly or treated as empirical parameters (as in this study). The energy levels of the free ion can be expressed in terms of these parameters. The triangular rule for the addition of angular momenta produces the constraint $k \leq 6$ on $4f$-electron parameters. Furthermore only even values of k will be associated with non-zero matrix elements, because of parity considerations. Terms with $k = 0$ have spherically symmetry and have already been eliminated from this calculation.

Additional interactions can be included as corrections to the intermediate-coupling calculation. Two more Coulomb terms will be considered, which arise from correlation interactions and three body interactions between the $4f$-electrons. The

former are formulated with three parameters α, β and γ. The latter arise when there are three or more $4f$-electrons and are parameterised with a rank six tensor T^k. Four other magnetic interactions are included in the calculations reported in this study. There is a correlated spin-orbit correction with parameters P^k. Spin-spin, orbit-orbit and spin-other-orbit interactions are parameterised by the Marvin integrals M^k.

2.1.2 The Crystal-Field Perturbation

The crystal-field perturbation V_{CF} may be conveniently expanded in terms of spherical harmonics, as the wave functions of the free ion are spherically symmetric. The expanded potential has the form:

$$V_{CF} = \sum_{k,q,i} B_q^k C_q^k(i)\,, \tag{2.4}$$

where B_q^k are the crystal-field parameters and C_q^k are the Racah tensor operators. As for the free-ion calculation, the values of k are constrained to $k = 0$, 2, 4 or 6. Again the $k = 0$ term produces a uniform shift in all the levels of a configuration and will not be included in these calculations. The tensor operators are derived from spherical harmonics Y_{kq} through the relation:

$$C_q^k = \sqrt{\frac{4\pi}{2k+1}}\, Y_{kq}\,.$$

The matrix elements of the crystal-field interaction have the form:

$$< \alpha SLJM|V_{CF}|\alpha' SL'J'M' > = \sum_{k,q} B_q^k < \alpha SLJM|U_q^k|\alpha' SL'J'M' >< f\|C^k\|f >\,,$$

where

$$< l\|C^k\|l' > = (-1)^l \sqrt{(2l+1)(2l'+1)} \begin{pmatrix} l & k & l' \\ 0 & 0 & 0 \end{pmatrix}$$

and α represents all the other quantum numbers which have been included in this calculation. The matrix elements of C^k can be evaluated without difficulty. All the single-electron tensor operators $C_q^k(i)$ are included additively in U_q^k. The matrix elements of the tensor operator U_q^k are diagonal in S and may be doubly reduced by applying the Wigner-Eckart theorem:

$$\begin{aligned} < \alpha SLJM|U_q^k|\alpha' SL'J'M' > &= (-1)^{J-M} \begin{pmatrix} J & k & M' \\ -M & q & M' \end{pmatrix} < \alpha SLJ|U^k|\alpha' SL'J' > \\ < \alpha SLJ|U^k|\alpha' SL'J' > &= (-1)^{S+L+M+k} \sqrt{(2J+1)(2J'+1)} \begin{Bmatrix} J & J' & k \\ L' & L & S \end{Bmatrix} \\ &\quad \times < \alpha SL|U^k|\alpha' SL' > \,. \end{aligned}$$

The numerical values of the 3j and 6j symbols have been tabulated in references such as Butler [18] and the doubly reduced matrix elements have been tabulated by Neilson and Koster [63]. The matrix for V_{CF} can now be assembled and diagonalised, yielding the energies of the crystal-field levels and their wavefunctions.

Within a $^{2S+1}L_J$ multiplet these levels will typically be split by 10-100cm^{-1}. In those ions with an odd number of $4f$-electrons, Kramers' ions, all the crystal-field levels will retain at least two-fold degeneracy. Crystal-field wavefunctions are linear combinations of $^{2S+1}L_J(M)$ states. The crystal-field introduces significant M mixing, breaking the JM degeneracy of the free-ion levels. Thus J and M are no longer good quantum numbers. In Chapter 4 it will be shown that the irreps of appropriate point-symmetry group are good labels for the crystal-field levels and that their interactions with external fields are naturally formulated in the parlance of group theory.

For a RE^{3+} centre the non-zero values of k and q are limited by the point symmetry of the crystal field. Several centres with C_{4v} symmetry will be investigated in this study. The symmetry operations of the C_{4v} group constrain q to just three values, $q = 0$ or ± 4. Equation 2.4 is applied to expand and parameterise the C_{4v} symmetry crystal-field potential:

$$V_{CF} = B_0^2 C_0^2 + B_0^4 C_0^4 + B_4^4 (C_4^4 + C_{-4}^4) + B_0^6 C_0^6 + B_4^6 (C_4^6 + C_{-4}^6) . \qquad (2.5)$$

In this study an alternate parameterisation will be used, one which separates the cubic and axial contributions to the C_{4v} symmetry crystal field. This distinction is physically significant when considering the $C_{4v}F^-$ RE^{3+} centres, where the axial component of the crystal field is generally smaller. The expansion of the crystal field potential becomes:

$$\begin{aligned} V_{CF} &= B_C^4 \left[C_0^4 + \sqrt{\frac{5}{14}}(C_4^4 + C_{-4}^4)\right] \\ &+ B_C^6 \left[C_0^6 - \sqrt{\frac{7}{2}}(C_4^6 + C_{-4}^6)\right] \\ &+ B_A^2 \, C_0^2 \\ &+ B_A^4 \left[C_0^4 - \sqrt{\frac{7}{10}}(C_4^4 + C_{-4}^4)\right] \\ &+ B_A^6 \left[C_0^6 + \sqrt{\frac{1}{14}}(C_4^6 + C_{-4}^6)\right] , \end{aligned} \qquad (2.6)$$

where B_C^k and B_A^k are the cubic and axial parameters respectively. Several crystal-field calculations were also performed on C_{3v} symmetry Tb^{3+} centres. The parameterisation of the C_{3v} symmetry crystal-field potential defined by Cockroft et al [25] was applied in these cases.

2.1.3 Transition Intensity Calculations

Parity conservation forbids electric-dipole transitions between states of the $4f^N$-configuration. Such transitions are observed spectroscopically however because of inter-configurational interactions, which introduce opposite-parity contributions to the states of the $4f^N$-configuration. Since the free-ion has spherically symmetric wave functions, there will be no inter-configurational interactions and consequently no electric-dipole transitions. However, a non-spherically symmetric crystal field can produce the required mixing, via the odd terms in the potential expansion in Equation 2.4. If a pure state $|4f\,\psi_a>$ of the $4f^N$-configuration interacts weakly with the states $|nl\,\psi_\kappa>$ of an opposite-parity configuration, a mixed state $|\phi_a>$ arises:

$$<\phi_a| = <4f\,\psi_a| + \sum_\kappa \frac{<4f\,\psi_a|V_{CF}|nl\,\psi_\kappa><nl\,\psi_\kappa|}{E(nl\,\psi_\kappa) - E(4f\,\psi_a)}. \tag{2.7}$$

The electric-dipole operator P^1_ρ can be expressed in terms of the Racah tensor operators C^1_ρ:

$$P^1_\rho = -\sum_i r_i C^1_\rho(i), \tag{2.8}$$

where $\rho = 0$ corresponds to the z component of the dipole moment and $\rho = \pm 1$ to the $x \pm iy$ components. The energy-matrix element for the transition between two mixed states $|\phi_a>$ and $|\phi_b>$ is:

$$\begin{aligned} <\phi_a|P^1_\rho|\phi_b> &= \sum_\kappa \frac{<4f\,\psi_a|V_{CF}|nl\,\psi_\kappa><nl\,\psi_\kappa|P^1_\rho|4f\,\psi_b>}{E(nl\,\psi_\kappa) - E(4f\,\psi_a)} \\ &+ \sum_\kappa \frac{<4f\,\psi_a|P^1_\rho|nl\,\psi_\kappa><nl\,\psi_\kappa|V_{CF}|4f\,\psi_b>}{E(nl\,\psi_\kappa) - E(4f\,\psi_b)}. \end{aligned} \tag{2.9}$$

Generally it is not possible to evaluate the matrix elements from this expression because both the odd-tensor operators C^k_q and the energies of other configurations $E(nl\,\psi_k)$ are unknown. To surmount these difficulties Judd and Ofelt have expressed the matrix elements in a revised form, introducing an intensity parameter $Y^\lambda_{q,\rho}$:

$$<\phi_a|P^1_\rho|\phi_b> = \sum_{\lambda,q} Y^\lambda_{q,\rho} < f^N \alpha_a S L_a J_a M_a | U^\lambda_{\rho+q} | f^N \alpha_b S L_b J_b M_b > . \tag{2.10}$$

This formulation assumes that each configuration has a small extent in comparison to the inter-configurational energy separations. Thus average energies E_{av} can be used in the denominators of Equation 2.9 and in the expression for $Y^\lambda_{q,\rho}$. These intensity parameters are functions of $\frac{1}{E_{av}}$, a radial integral, a crystal-field parameter, 3j symbols and $<f\|C^1\|l><l\|C^k\|f>$. As before $k = 2$, 4 or 6. The configurations which contribute to the perturbation are limited by the triangular condition for the 3j symbols $\Delta l = \pm 1$.

Selection rules for S, L and J arise from the triangular conditions of the appropriate coupling scheme. For both E1 and M1 transitions the rules $\Delta J = 0, \pm 1$

and $J+J' \geq 1$ apply. The selection rules for strict LS coupling are $\Delta S = 0$ and $\Delta L = 0, \pm 1$. With intermediate coupling these are broken by the spin-orbit interaction. However, in most cases the relative intensities of inter-multiplet transitions will still reflect these rules.

Transition intensities are proportional to the squares of the energy-matrix elements. Fermi's Golden Rule states that the absorption or spontaneous emission probability of each transition is proportional to the transition intensity. The radiative decay rate of a particular excited state is then the sum of the probabilities for all possible fluorescence pathways. Non-radiative relaxation processes will also contribute to the decay rate of the excited state. The fluorescence lifetime observed in an experiment is the reciprocal of this total decay rate, which includes both radiative and non-radiative contributions.

2.2 Local Vibrational Modes

Three types of hydrogen ion site were observed spectroscopically in this study: the interstitial and substitutional sites of RE^{3+} ion centres and the tetrahedral T_d symmetry lattice site. All of these centres exhibit a local vibrational mode which is optically active. This mode arises as the charged hydrogenic ion is free to move in the electric field produced by the ligand ions. A detailed description of hydrogen ion local modes appears in a review by Newman [64].

The isotopes of hydrogen are much lighter than the lattice ions, so the static-well approximation may be applied, in which the ligand ions are stationary in their equilibrium positions. The hydrogenic ion moves in a static potential and each site can be treated as a three-dimensional single-particle anharmonic oscillator. This is a reasonable approximation at low crystal temperatures and may be applied to the experiments reported here.

The vibrational energy levels of hydrogenic ions in the T_d symmetry site of CaF_2 were measured by Elliott et al [33]. The fundamental H^- and D^- ion levels are $965cm^{-1}$ and $689cm^{-1}$ respectively. These vibrational energies are higher than the phonon cut-off energy $463cm^{-1}$, which confirms that this is a local mode and cannot propagate through the crystal. The ratio of the hydrogen to deuterium energies is 1.40, close to the $\sqrt{2}$ value which arises from the $m^{-\frac{1}{2}}$ mass dependence for the energy of a harmonic oscillator. This result justifies the application of the static-well approximation.

The oscillator potential can be expanded in terms of the displacement x, y and z of the light ion from its equilibrium position. This potential must be invariant under the operations of the appropriate point-symmetry group, which is that associated with the site symmetry of the hydrogenic ion. Elliott et al [33] have shown that the potential of the T_d symmetry oscillator is:

$$\begin{aligned} V &= A(x^2+y^2+z^2) + B(xyz) \\ &\quad + C_1(x^4+y^4+z^4) + C_2(y^2z^2+x^2z^2+x^2y^2) + \ldots \end{aligned} \tag{2.11}$$

The first term is harmonic and it is also the dominant term in this Taylor series expansion. To solve for the energy levels, the anharmonic B and C terms are treated as second and first order perturbations of the harmonic oscillator respectively. These energies were expressed as:

$$E = N\hbar\omega + (\mu_1 C_1 + \mu_2 C_2)\left(\frac{\hbar}{2m\omega^2}\right)^2 - \frac{\lambda B^2\hbar^2}{24m^3\omega^4} + ... \qquad (2.12)$$

Here m is the mass of the oscillator, ω its fundamental vibration frequency and N the phonon number state ($N = N_x + N_y + N_z$). Integers μ_1, μ_2 and λ arise from the perturbation calculation and have been tabulated by Elliott et al for each state of the anharmonic oscillator.

These states are linear combinations of the $|N_xN_yN_z>$ occupation-number states and are labeled as the irreps of the relevant symmetry group (T_d). In particular the lowest level (N=0) is a γ_1 state, the first excited level (N=1) is a γ_5 state and the second excited levels (N=2) are γ_1, γ_3 and γ_5 states. Electric-dipole absorption transitions to N=2 and N=3 levels are possible because the number states are mixed by the anharmonic terms in equation 2.11. The E1-transition operator transforms like a γ_5 irrep in this symmetry. From the T_d group multiplication table in Koster ([50] Table 82) it is found that infrared absorption is allowed to the excited γ_5 states.

Infrared absorption spectra of the C_{4v} symmetry interstitial hydrogenic ion site were measured by Jones et al [47] [94] for most of the RE^{3+} ions. As for the T_d symmetry site, the energy levels exhibited the expected $m^{-\frac{1}{2}}$ mass dependence for the different hydrogen isotopes. Maradudin and Peretti [55] have shown that the Taylor expansion of the C_{4v} symmetry potential is:

$$\begin{aligned} V &= A(x^2+y^2) + A_2z^2 + B_1z^3 + B_2z(x^2+y^2) \\ &\quad + C_1z^4 + C_2(x^4+y^4) + C_3z^2(x^2+y^2) + C_4x^2y^2 + ... \end{aligned} \qquad (2.13)$$

They have performed the energy calculation by considering the B and C terms as perturbations, as for the T_d symmetry case. Expressions for the N=1 and N=2 energy levels appear in their paper. These have been recalculated by Reeves [77], who reports some corrections to their energies. There is now an axial component of the electric field, so states corresponding to oscillations in the z and x or y axes alone are no longer degenerate. The first excited levels (N=1) are γ_1 and γ_5 states and the second excited levels (N=2) are $2\gamma_1$, γ_3, γ_4 and γ_5 states. In this symmetry the E1-transition operator can transform like a γ_1 or γ_5 irrep (Table 4.7). Thus infrared absorption is allowed to excited γ_1 and γ_5 states.

Substitutional hydrogenic ion sites in RE^{3+} centres have lower symmetries than the interstitial site. In most cases they have C_1 symmetry, so there are no degenerate energy levels and all transitions are allowed.

2.3 The Electron-Phonon Interaction

The electron-phonon interaction is responsible for a number of physical effects, including the appearance of vibronic transitions in the optical spectra of the hydrogenic RE^{3+} centres. It arises from coupling between the $4f$-electrons and the local vibrational modes of the hydrogenic ions. The charge on a neighbouring hydrogenic ion contributes to the total crystal field experienced by the RE^{3+} ion. If the hydrogenic ion is vibrationally excited there will be a corresponding modulation of this crystal field. Since the other ligand ions are not static and can move to accommodate the motion of the hydrogenic ion, this modulation can be quite complex.

The electron-phonon interaction produces an 'isotope shift' in the RE^{3+} ion electronic transitions, for different isotopes of hydrogen. It will also shift the local-mode energies slightly and in some cases split degenerate vibrational levels [44]. To calculate the energy levels of the coupled system, the interaction potential $V_{EP}(t)$ is taken as the difference between the static and instantaneous crystal-field potentials:

$$V_{EP}(t) = V_{CF}(t) - \bar{V}_{CF} \,. \tag{2.14}$$

This potential is small and treated as a perturbation of the RE^{3+} Hamiltonian H. The wavefunctions $|\Psi_a N_x N_y N_z>$ of the combined system are products of the wavefunctions for the $4f$-electronic states and the local mode states:

$$|\Psi_a N_x N_y N_z> = |4f\,\psi_a> |N_x N_y N_z> \,. \tag{2.15}$$

It has already been shown that both sets of states are labeled by the irreps of point-symmetry groups. The states of the combined system also transform like irreps and the label appropriate for a particular state may be obtained from the multiplication tables of Koster et al [50].

2.4 Inter-Ion Energy Transfer and Upconversion

Energy transfer is observed spectroscopically as either cross relaxation or energy upconversion and is most apparent when the donor and acceptor ions are different species. Energy-transfer processes arise from physical interactions which couple the two ions involved. Multipole interactions arise from multipole coupling between the two electron clouds. Electric dipole-dipole interactions are dominant, but other electric and magnetic multipole interactions can also contribute to the overall coupling. The strength of that coupling depends upon the magnitude of the transition moments involved. Exchange interactions arise from electron exchanges between the ions and require a spatial overlap of the $4f$-electronic wavefunctions. This requirement results in strong angular and radial dependencies. Exchange interactions are only important when there are small inter-ionic separations and in RE^{3+} ion salts this is often a superexchange interaction, involving the intervening anions. Exchange interactions between RE^{3+} ions are usually weak because of the shielding and localisation of $4f$-electrons.

A theoretical description of energy-transfer can be developed by considering the Hamiltonian $H_{1,2}$ of the coupled ions:

$$H_{1,2} = H_1 + H_2 + H_{Int}\,. \tag{2.16}$$

H_{Int} is the interaction Hamiltonian, while H_1 and H_2 are the single-ion Hamiltonians. Both multipole and exchange interactions are included in H_{Int}, which is treated as a perturbation. Tensor operator techniques can be used to find the energy matrix elements of the coupled ions. The diagonal elements of the multipole interaction produce small shifts in the single-ion energy levels. Physically these originate from small changes in the crystal field due to the presence of the other ion and are usually included during the single-ion crystal-field calculation. The diagonal elements of the exchange interaction are associated with the splitting of degenerate crystal-field levels, particularly Kramers doublets. Energy transfer is represented by the off-diagonal elements.

Energy transfer via the multipole interation is a resonant process and requires spectral overlap of the homogeneously broadened transitions of the donor and acceptor ions. Such accidental overlaps are highly unlikely. In general energy transfer is a non-resonant phonon-assisted process and requires instead the spectral overlap of the donor and acceptor phonon side-bands. Ion-phonon coupling is weaker than ion-ion coupling and will be treated as a perturbation to $H_{1,2}$:

$$\begin{aligned} H &= H_{1,2} + V_P + H_{IP} \\ &= H_1 + H_2 + H_{Int} + V_P + H_{IP}\,. \end{aligned} \tag{2.17}$$

V_P is a potential representing the accessible phonon states and H_{IP} is the Hamiltonian for the electron-phonon interaction. Successively higher orders of perturbation correspond to higher order multi-phonon processes. An explicit temperature dependence arises in the term V_p, as the phonon spectrum is determined by the phonon density of states and their thermal occupancy.

The efficiency of energy-transfer processes will be affected by the relative number and distribution of donor and acceptor ions. Energy transfers are also possible between homogeneous pairs of donor or acceptor ions. Excitation migration or dispersion will affect the efficiency of processes such as upconversion. If the concentration of acceptor ions is small, then resonant donor-donor transfers can enhance efficient upconversion processes by exciting the donor ions in donor-acceptor pairs. In other systems such excitation migration is a loss mechanism, donor-donor cross relaxation for example. In highly ordered systems near-resonant energy transfer and back transfer is possible. Disordered systems are usually associated with larger energy mismatches and small migration probabilities. However larger energy mismatches and second-order processes can sometimes utilise regions of the phonon distribution where there is a higher phonon density of states.

Figure 2.1 shows the main energy transfer and upconversion processes which will be considered in this study. Excitation migration or dispersion involves just one

species of ion. Cross relaxation and co-operative upconversion can occur in either homogeneous or heterogeneous ion pairs. Co-operative upconversion is often called 'addition de photons pas transfert d'energie' (APTE). In homogeneous pairs where both ions have been excited by the laser beam, only one energy transfer (that labeled 'b') would be required to achieve upconversion.

All energy transfer processes depend upon the distance between the donor and acceptor ions. In most systems the inter-ionic separations are not fixed and this spatial dependence must be included in the rate equations for these processes. Usually an ensemble of pairs, which includes all possible pair separations, is averaged for each process. $CsCdBr_3:RE^{3+}$ crystals are highly ordered and the spatial relationship between the RE^{3+} ions of the main pair centre is fixed, so at low RE^{3+} ion concentrations the rate equations do not have to include inter-ion separations explicitly. At high RE^{3+} ion concentrations there may be an appreciable number of interacting pairs and energy transfer processes involving more than two ions may be observed.

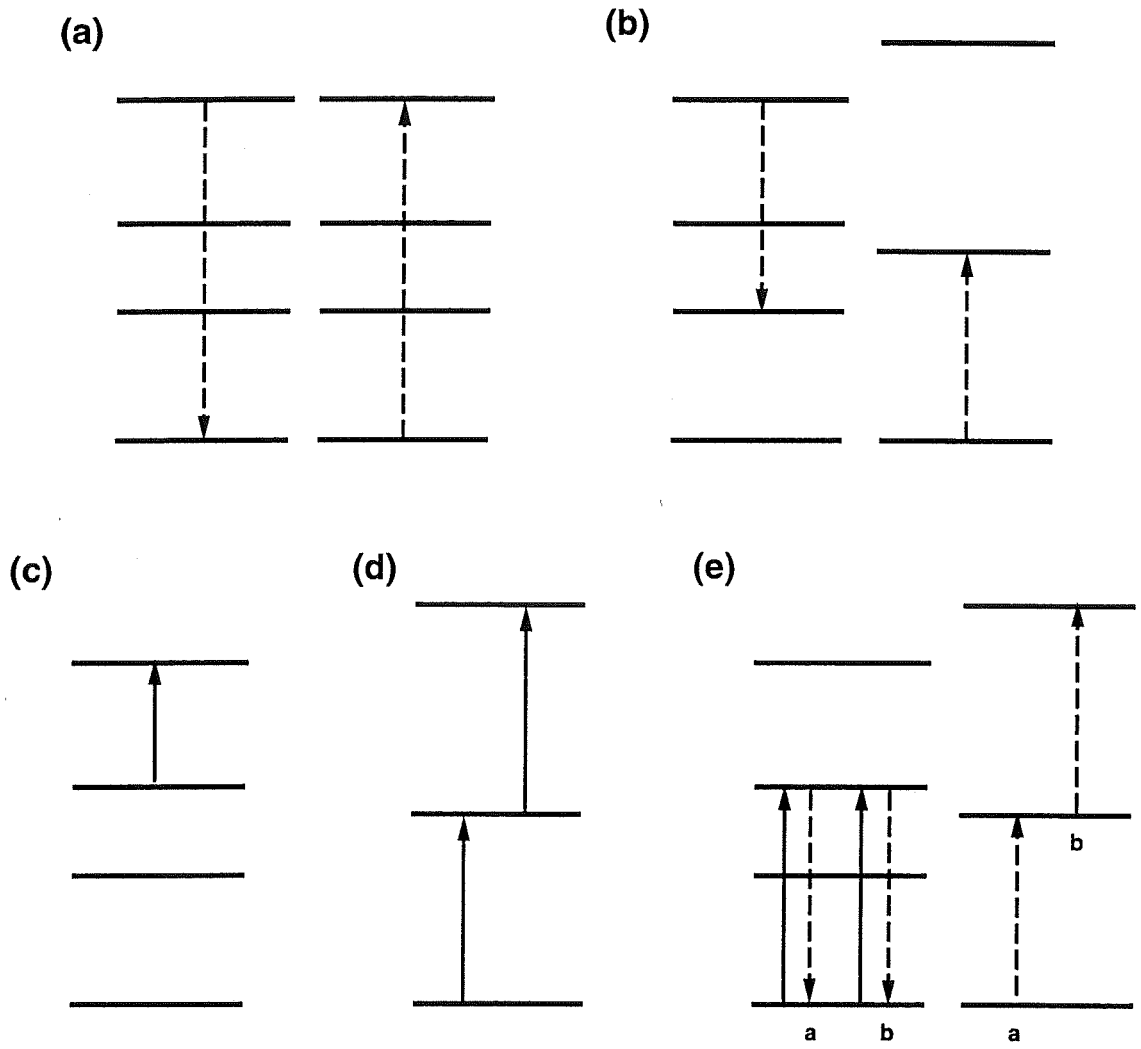

Figure 2.1: Energy transfer and upconversion processes: (a) resonant excitation migration (b) cross relaxation (c) excited state absorption (d) sequential absorption upconversion and (e) co-operative absorption upconversion.

Chapter 3

Experimental Considerations

3.1 Crystal Preparation

3.1.1 SrF_2 and CaF_2 Crystals

SrF_2:RE^{3+} and CaF_2:RE^{3+} crystal boles are grown from a melt by the Bridgman-Stockbarger technique. The alkaline-earth fluoride starting material was supplied as fragments by Optovac Inc. This is crushed into a fine powder, to which a measured amount of rare-earth fluoride is added. PrF_3 powder (99.9% pure) was supplied by Alfa Inorganics. TbF_3 powder (99.9% pure) was supplied by Johnson Matthey RE Products. The mixture is placed in a closed carbon crucible, which is lowered through the field produced by the work coil of a 38kW Arthur D. Little radio frequency induction furnace. A low power setting is held for several hours prior to lowering, to expurgate water and other contaminants. Lowering rates are typically $7mmh^{-1}$, for a period of 18h. The crystals are then annealed over 6h. Vacuum pressures, of less than 10^{-4}torr, are maintained in the furnace over this growth period. No PbF_3 or other oxygen scavenging materials were added to the mixture prior to melting.

The crystal boles grown in these crucibles are 10mm in diameter and 25-30mm long. Three or four crystals can be cut from each bole using a diamond saw. In most cases orientated crystals were required for polarisation spectroscopy. The orientation of a particular crystal bole can be obtained from its (111) cleavage planes. The orientated bole is glued to a customised jig for cutting. Two (111) planes, intersecting at an angle of 109.7° along a <110> axis, are used to locate the bole on the jig. These crystal planes are illustrated in the thesis of Khong ([53] Figure 3.1). Each crystal is produced with four faces, two in (100) planes and two in (010) planes, to enable the transmission of the excitation beam and to view fluorescence. Some <111> orientated crystals were also produced for infrared Zeeman spectroscopy.

The crystal faces are polished flat using successively higher grades of sand paper and abrasive powder. The final finished is produced with 800 grade silicon

carbide, lubricated with water to produce a smooth paste. The optical quality of a crystal was deemed sufficient when the steeple of the Christchurch Cathedral, approximately 5km away, could be viewed through the polished faces.

3.1.2 Hydrogenated and Deuterated Fluoride Crystals

Hydrogen and deuterium ions are introduced into fluoride crystals by diffusion, using the technique described by Hall and Schumacher [38]. Molten aluminium metal is used to remove F^- ions from the crystal lattice, which are in turn replaced by H^- or D^- ions. This reaction occurs in an atmosphere of H_2 or D_2 gas. Aluminum wire is cleaned with acetone and wrapped around a clean crystal, which is placed in an alumina crucible. A rotary vacuum pump is used to evacuate the furnace, as the crucible is heated to 150°C and left overnight to allow outgassing. In the morning the apparatus is flushed with H_2 gas, flushed again with H_2 or D_2 gas, and finally filled to produce the required H_2 or D_2 atmosphere. A mercury diffusion pump is used when flushing to minimise contaminant gases.

Two different sets of apparatus may be used to hydrogenate crystals. A low-pressure furnace, which is filled to 20mmHg below ambient pressure, produced both hydrogenated and deuterated crystals. A sketch of this furnace appears in the thesis of Khong ([53] Figure 3.2). After filling the temperature is raised to approximately 850°C and maintained for 60h typically. The crystal is then annealed over 3h by switching off the furnace and leaving all the thermal insulation in place. Slower annealing can be achieved by gradually lowering the thermostat setting through the first 100-200°C. All of the crystals used in this study were annealed to promote the formation of multi-hydrogenic ion RE^{3+} centres. Hydrogen ion concentrations in excess of $10^{19}cm^{-3}$ were reported by Hall and Schumacher, who used a similar low-pressure furnace.

German [37] and Shamu et al [83] have demonstrated that higher H_2 gas pressures will produce significantly higher H^- ion concentrations for shorter hydrogenation times. The same high-pressure furnace described by German was used to produce some of the hydrogenated crystals used in this study. The temperature in this furnace is raised to 900°C for approximately 1.25h. During hydrogenation the H_2 gas typically has an overpressure of 250psi. Again the crystal is annealed by simply switching off the furnace.

Most of the melted aluminium can be brushed off the surface of the crystal. However, there is often a surface layer which must be removed by etching in a solution of hydrochloric acid. The crystal faces can then be polished, as described.

3.1.3 $CsCdBr_3$ Crystals

Two very different techniques were used to grow $CsCdBr_3$:RE^{3+} crystals. Two crystals were prepared from a molten solution of the starting material, using a method developed by Mr Ross Ritchie (of the Department of Physics and Astronomy,

University of Canterbury). The starting material was CsBr (99.9% pure) supplied by the Aldrich Chemical Company, $CdBr_2$ (99% pure) supplied by Hopkins and Williams, and Tm_2O_3 and/or Pr_2O_3 (99.9% pure) supplied by Semi Elements Inc. Rare-earth oxides were used because their bromides were not available.

Before the growing apparatus is assembled, the chemicals and glass ware are dried for several days in an oven. Stoichiometric quantities of the starting material are placed in a Y-shaped glass vessel, which has been custom blown for this purpose from 8mm(i.d.) Pyrex tubing. A quartz sieve holds the mixture in the U-part of the vessel initially. Then a flow of HBr gas is established through the chemicals, creating a bromide atmosphere and converting the rare-earth compounds into their bromide form. This gas is dried by passing it through a concentrated sulphuric acid solution. The furnace can then be switched on and the temperature gradually increased to 560°C over 2.5h. The slow heating ensures that the chemicals are thoroughly dry when they melt. After reaching 560°C, this temperature and the gas flow are maintained for another 30 minutes. The direction of the gas flow is then reversed and the lower-stem of the vessel, which protrudes from the bottom of the furnace, heated with a gas torch. The molten material is extruded through the sieve and trickles down to the closed bottom of the stem. This is sealed off with the torch, just above the solidified melt, to make an ampoule.

The ampoule contains amorphous $CsCdBr_3$:RE^{3+} in an HBr atmosphere. The final crystal is grown in a Bridgman furnace by lowering the ampoule through a temperature gradient, at a rate of $0.85mmh^{-1}$. The hot zone is maintained at 520°C and the cool zone at 330°C. After the 8-10 days required to drop through the gradient, the crystal is annealed over 14h. The bottom of the ampoule has a small tapered bulb to allow the propagation of just one crystallite. In the best crystals obtained by this method, most of the bole is of sufficient quality for spectroscopy.

One of the $CsCdBr_3$ crystals used in this study was prepared from a solution, at Tulane University, Louisiana. Equal molar quantities of CsBr and $CdBr_2$ are mixed in water. $CsCdBr_3$ precipitates out of this solution almost immediately and is dried in a rapid draft of air. Rare-earth bromide is produced by mixing the metallic rare-earth with a concentrated HBr solution. The $REBr_3$ precipitate is dried on a watch glass in an oven and is very hydroscopic. Both precipitates are put together in the tube in which the crystal will be grown. A vacuum is maintained in this tube to avoid contamination. The mixture is melted using a gas torch to remove any water or excess Br_2 gas. When the melt stops boiling the tube is sealed and placed in a Bridgman furnace as before.

Some of the $CsCdBr_3$ crystal samples were orientated for polarisation studies of RE^{3+} centres. Every cleavage plane in a $CsCdBr_3$ crystal will include the crystallographic c-axis. An edge formed by two intersecting planes identifies the orientation of a sample. All the $CsCdBr_3$ crystals prepared for laser excitation spectroscopy were orientated, with at least three good faces to enable the transmission of the excitation beam and to view fluorescence.

$CsCdBr_3$ crystals are hygroscopic and rather delicate compared to other crys-

talline solids, such as the alkaline-earth fluorides. It was found that the condition of the crystals did not deteriorate appreciably in the dry atmosphere of Los Alamos. However repeated cycling of the samples between room temperature and 10K did cause them to become cloudy and crack. To minimise this deterioration in crystal quality they were attached to the cold finger of the refrigerator using a thermally conductive putty. During the upconversion experiments the pulsed laser beams were tightly focused inside the sample. Sometimes at high excitation powers material was sputtered from the crystal causing a small amount of surface damage.

3.2 Cryostats and Refrigerators

All of the experiments described in this thesis were performed at cryogenic temperatures. During infrared Zeeman spectroscopy a liquid helium dewar contained the superconducting magnet and samples. In this apparatus crystals are not actually immersed in helium; instead, thermal contact is made through a copper sample holder. Crystal temperatures were approximately 10K. Barium fluoride windows have replaced the cesium bromide windows used by Freeth [36]. Closed-cycle helium refrigerators were used in all other experiments.

The refrigerator units were two-stage CTI-Cryogenics Cryodyne Cryocoolers. The unit employed for infrared transmission spectroscopy produced sample temperatures of approximately 8K. The units employed for visible spectroscopy produced minimum sample temperatures of 10-14K. Copper crystal holders were screwed onto the cold head before each run. A number of crystal holders were available to accommodate for various crystal sizes and experimental geometries. Thermal contact was improved by placing a single layer of indium foil between the crystal holder and the cold head.

Fluoride crystals were attached to sample holders by copper plates, which were held in place by four tension screws. A layer of foil was sandwiched between the crystal and the holder. A thermally conductive putty, containing copper, was used to attach the more fragile $CsCdBr_3$ crystals to their sample holder.

Temperatures up to 120K were required during laser excitation experiments. These higher temperatures were generated by a small coil of resistive wire which is wound around the shaft of the cold head. Palm Beach Cryophysics Inc. Model 4025 Cryogenic Thermometer/Controllers were used to control the temperature of the cold head. The temperature of the sample was measured through a silicon diode attached to the base of the cold head.

3.3 Absorption Spectroscopy

Infrared transmission spectra were recorded with a Digilab model FTS-40 Fourier Transform Spectrometer, which has a spectral range from $400cm^{-1}$ to $4500cm^{-1}$. This is a single-beam fourier transform interferometer, with an optimum spectral

resolution of 0.1cm^{-1}. Infrared Zeeman spectroscopy was also performed using this instrument. A persistent superconducting magnet was used to produce magnetic fields of up to 4T. This apparatus is described by Freeth in his thesis ([36] 3.4.2).

Visible transmission spectra were produced using a 100W tungsten halogen lamp, with a 12V regulated power supply. Glass lenses were used to focus this light into the sample and then to project the image onto the entrance slits of a Spex Industries Inc Model 1700 single monochrometer. This is a 0.75m monochrometer with a 1180mm^{-1} grating. Most of the spectra recorded were obtained from the second-order reflection of this grating, to circumvent an anomaly in the 495nm region. The slitwidths were typically set in the 10-25μm range. Corning Glass colour filters were used to filter out the first-order spectrum. Photo-detection was provided by an EMI 9558 S20 (Na_2KSb-Cs cathode) photomultiplier tube, which was thermoelectrically cooled by a Products for Research Inc TE-104 refrigerated chamber. The output signal was processed by a Keithley Instruments Model 610B electrometer and a custom made active filter and variable-offset amplifier. Spectra were plotted on a Sekonic chart recorder.

3.4 CW Laser Selective Excitation Spectroscopy

The LSE spectroscopy reported in Chapters 5, 6, and 7 was performed using a Spectra Physics Inc Model 375 dye laser, with a Model 376 dye circulator. This laser was optically pumped by a Spectra Physics Inc argon ion laser; either a 15W Model 170 or a 15W Model 2045E. The latter provided the ultraviolet beam energy necessary to pump the blue Coumarin dyes. A Spectra Physics Model 573 three-plate birefringent filter was the only tuning element used in the dye laser. This produced beams with a spectral width of approximately 0.5cm^{-1} (FWHM). A stepper motor and drive unit controlled the tuning mechanism, which could be stepped in increments of 0.5cm^{-1}. The linear polarisation of the excitation beam could be selected with a Spectra Physics Model 310A polarisation rotator. Circularly-polarised beams were produced using PTI quarter wave plates. Linearly-polarising films were used to analyse fluorescence.

Several dyes were used to produce the required excitation beams. Rhodamine 590 perchlorate or 590 chloride, in an ethylene glycol solution, were used to pump the $^1D_2$ multiplet of praseodymium. The 514nm line of the argon laser was selected to pump these dyes. The perchlorate form produces yellow fluorescence and the chloride form (Rhodamine 6G) red fluorescence. The former was used to pump the higher $^1D_2$ levels of the $C_{4v}F^-$ centre, while the latter was ideal for pumping the Cs centres of praseodymium. Coumarin 480, in an 80% ethylene glycol 20% benzyl alcohol solution, was used to pump the $^3P_0$ and $^1I_6$ multiplets of praseodymium and the $^5D_4$ multiplet of terbium. Coumarin 460, in the same solvent, was used to pump the $^3P_1$ multiplet of praseodymium. These blue dyes were pumped with the 335-360nm multiline output of the argon-ion laser.

Two spectrometers were used in these experiments. Broadband excitation spectra were produced with a 0.25m Bausch and Lomb Inc single monochrometer. This is a low-resolution spectrometer with a 1350mm^{-1} grating, which was used to monitor simultaneously all the lines of an inter-multiplet fluorescence transition. These broadband spectra are not site selective and will comprise absorption features from all of the RE^{3+} ion centres. If necessary, the spectrometer could be placed just 300mm from the crystal, with an appropriate focusing lens, to monitor very weak fluorescence. Corning Glass colour filters were placed immediately in front of the entrance slit to eliminate any scattered laser light. Neutral density filters were often required to attenuate very strong fluorescence.

A thermoelectrically cooled EMI 9558 S20 or EMI 6255 S13 (Cs_3Sb-O cathode) photomultiplier tube was used as a photodetector with this spectrometer. The latter is a blue-sensitive tube, which was used when the S20 tube was operating on the Spex 1700 monochrometer. The output signal was then processed by either a voltage to frequency converter or a photon-counting system. The former was custom made and couples to the Keithley Instruments electrometer. The latter comprises a Princeton Applied Research Corp Model 1121A amplifier/discriminator and Model 1112 photon counter/processor. All of the broadband excitation spectra appearing in this thesis were recorded with the photon-counting system.

A Spex Industries Inc Model 1403 double monochrometer was used to record high-resolution fluorescence spectra and site selective excitation spectra. This is a 0.85m spectrometer with two 1800mm^{-1} holographic gratings, producing an optimal spectra resolution of 0.15cm^{-1}. The slitwidths were usually set in the 20-100μm range. A Spex Industries Inc Model CD2A 'Compudrive' was used to scan this spectrometer, under either manual or computer control. The photodetector was an RCA C31034 photomultiplier tube, which was thermoelectrically cooled to a temperature of -25°C. The signal was then processed by a Princeton Applied Research Corp Model 1121 amplifier/discriminator and the second channel of the photon counter/processor. A remote display was available to view the photon count in real time. This was necessary when performing some of the polarisation ratio measurements. Both the Spex monochrometers were equipped with Hanle quartz polarisation scramblers to remove the polarising effect of their gratings.

Data acquisition was controlled by an Apple IIe personal computer. This could be programmed to scan either the dye laser, for excitation spectroscopy, or the double monochrometer, for fluorescence spectroscopy. Simultaneously the digitised fluorescence signal was received from either the photon counter or the electrometer (through an analogue to digital converter) and recorded onto a floppy disc. A Hewlett Packard plotter was used to display the spectra in real time. The spectra appearing in this thesis were transfered subsequently to a Vax mainframe computer and plotted using Matlab.

3.5 Pulsed Laser Selective Excitation Spectroscopy

The LSE spectroscopy reported in Chapter 8 was conducted in the Upconversion Laser Laboratory of the Laser and Chemical Sciences Division of the Los Alamos National Laboratory. Two tunable laser beams were provided by Quanta Ray Model PDL1 and PDL3 pulsed dye lasers. These were pumped by Quanta Ray Model DCR3 and DCR2A Nd:YAG pulsed lasers, which generated 1064nm pulses at a repetition rate of 10Hz. The pump beams were upconverted by two Quanta Ray Model HG2 'harmonic generators'. The IR beams could be either doubled or tripled in frequency, as was appropriate for the particular dyes being pumped. Both Nd:YAG lasers were Q-switched, under instruction from a Stanford Research Systems Inc Model DG535 multichannel signal generator. A linear polarisation rotator was used to set the polarisation of one or both excitation beams.

Two laser dyes were used in these experiments. Coumarin 480, in a methanol solution, was used to pump the ^3P_J multiplets of praseodymium and the $^1G_4$ multiplet of thulium. LDS 798, in a methanol solution, was used to pump the $^3H_4$ multiplet of thulium. These dyes were pumped with 532nm and 355nm excitation beams respectively.

A Spex Industries Inc Model 1704 single monochrometer was employed in all of these experiments. This was used with thermoelectrically cooled Hamamatsu Model R995 or 7102 photomultiplier tubes. The former is suitable for detecting visible fluorescence, while the latter was used to detect infrared emission from the $^3H_4$ multiplet of thulium and the $^1G_4$ multiplet of praseodymium. The spectrometer slitwidths were typically set in the 100-500μm range and Corning Glass colour filters were required to separate the different spectral orders. The fluorescence signal was amplified by a 30MHz SRA440 amplifier and analysed with a Stanford Research Systems Inc Model SR250 Gated Integrator and Boxcar Averager. The SR250 unit was triggered by the same signal pulse as the Nd:YAG lasers. The cable termination was usually 50ohms, but larger terminations were used on occasions to enhance weak fluorescence signals with long transients.

Single fluorescence transients could be viewed on a Tektronix Model 11420 digitising oscilloscope. Multiple transients could be integrated and stored on this scope for later analysis. A clone IBM PC computer was used to control the data acquisition and to record the spectra produced. This was programmed to scan either one of the dye lasers or the spectrometer. The spectra and transients were later transfered to either an Apple Macintosh 11x computer or the Vax mainframe computer, where they were plotted using Igor or Matlab. The Igor programme was also used to fit these transients to theoretical temporal-functions, thereby obtaining experimental fluorescence lifetimes and inter-ion energy-transfer rates.

3.6 Time Domain Spectroscopy

The fluorescence lifetime measurements reported in Chapters 5, 6 and 7 were made using a Photochemical Research Associates Inc Model LN107 amplified pulsed dye laser, pumped by a PRA Model LN1000 nitrogen laser. This nitrogen laser produces 3371Å 1mJ pulses, of 600ps (FWHM) duration. The dye laser is tuned by a 1800mm^{-1} holographic grating, in a near-grazing incidence configuration. 500ps (FWHM) duration pulses of up to 100μJ can be produced by this single-pass dye laser. A repetition rate of approximately 2Hz was typical for these experiments.

The Spex Model 1700 spectrometer, with the thermoelectrically cooled EMI 9558 photomultiplier tube, was used to analyse the resulting fluorescence. The signal was processed by a Hitachi Model VC-6275 digital-storage oscilloscope. It has 4000 8-bit channels and up to 256 individual transients can be integrated, taking approximately 5 minutes. A pyro-electric detector attached to the dye laser, which monitors scattered light from the nitrogen laser, triggers this scope.

The stored transients and their parameters were transfered to an IBM PC computer via an IEEE (GPIB) interface. A GW-BASIC programme was written to control this interface. This programme could also fit single-exponential functions to whole transients or to a smaller range selected by the user. The fitted functions were of the form:

$$Y(t) = S + A_0 e^{-\lambda t}.$$

The programme initially calculates the displacement S, using the whole transient. Three equally space data points (at t, $t+\delta t$ and $t+2\delta t$) are required to obtain each value for S:

$$S = \frac{Y(t)\cdot Y(t+2\delta t) - Y(t+\delta t)^2}{Y(t) + Y(t+2\delta t) - 2Y(t+\delta t)}.$$

Exactly 256 discrete values of S are calculated, with δt=1330 channels, to establish an average value $\bar{S}$. A 1x4000 working array, called $HOLD(I)$, is created and initially $HOLD(I) = Y(I) - \bar{S}$. The Napierian logarithm of each element is calculated, $HOLD(I) = LOG(HOLD(I))$, and the logarithmic transient is plotted to check for linearity. A least-squares fitting algorithm is used to find the decay rate, which is scaled to give λ in units of s^{-1}. If fitting to the whole experimental transient, the programme will then recalculate λ using just the channels in the range $0 \rightarrow \frac{2}{\lambda}$s. An example of such a fitted transient appears in Figure 3.1.

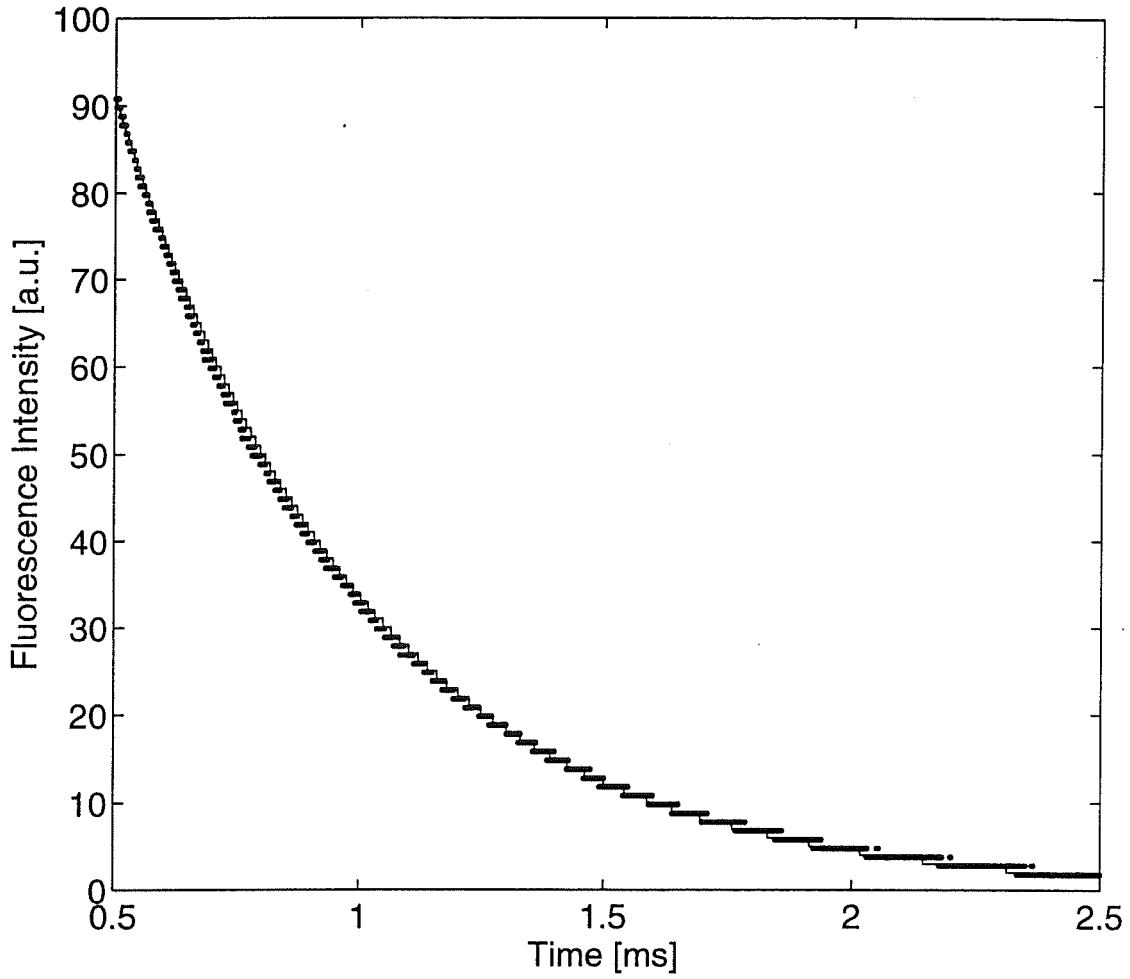

Figure 3.1: An experimental transient obtained using the PRA pulsed dye laser and the Hitachi digital-storage oscilloscope. This is the transient of the broad-band $^1D_2 \rightarrow {}^3H_4$ fluorescence from the $C_{4v}F^-$ centre in the $CaF_2:Pr^{3+}:D^-$ crystal, after pulsed excitation of praseodymium to the $^1D_2$ multiplet. The GW-BASIC programme fitted this transient to a single-exponential function, obtaining a fluorescence lifetime of $504\mu s$ for the $^1D_2$ state. The fitted function is shown here as a connected decay curve. Displacement $\bar{S}$ was calculated by the programme and has been subtracted from both the experimental and fitted decay curves.

Chapter 4

Polarisation Behaviour of RE^{3+} Transitions in Crystalline Centres

4.1 Introduction

An optically-active ion in a crystalline centre will experience an electric field, the 'crystal field', due to the charges on the ligand ions. The symmetry of this crystal field, at the location of this ion, will be one of the 32 possible crystallographic-point symmetries. Thus the optically-active centre can be associated with a point-symmetry group. The crystal field removes the directional degeneracy of the free ion, with the consequences that the $^{2S+1}L_J$ electronic states of the lowest-energy configuration ($4f^N$ in the case of the lanthanide ions) become non-degenerate and the transitions between these states are no longer forbidden.

The interaction of the crystal field with a RE^{3+} ion can be included in the Schrödinger equation for the centre as a perturbation, by the addition of a potential term V_{CF} to the free-ion Hamiltonian H_{FI}. This potential, and so too the embellished Hamiltonian H, must be invariant under the coordinate transformations of the appropriate point-symmetry group. An equivalent statement is that the Hamiltonian commutes with the operators of the symmetry group.

Given this condition it can be demonstrated that the eigenfunctions of any given eigenstate of the Hamiltonian always remain eigenfunctions of that state under the operations of this symmetry group. For any complete set of independent degenerate wavefunctions this can only occur if these wavefunctions are also basis functions for a representation of the symmetry group. For example, the eigenstate could be an energy state of the $4f^N$-configuration of a RE^{3+} ion. Thus each energy level of the rare-earth centre can be associated with a representation of the pertinent symmetry group. A rigorous presentation of this argument is given by Weissbluth ([90] Section 8.1).

By assuming that these representations are irreducible it is thus possible to label each energy level by an irreducible representation (irrep) of the symmetry group. The associated wavefunctions can be given the same irrep label and the degeneracy

is equal to the dimensionality of the irrep. A physical interpretation of this is that the energy-wavefunctions transform under the operations of the symmetry group in the same way as basis functions of the irrep do. Irreps are good quantum 'labels' for the energy levels of a RE^{3+} ion in a crystal field, of well defined point symmetry, as crystal-field interactions can only occur between those states associated with the same irrep [93].

When considering electromagnetic interactions between this electronic system and a quantized radiation field it is often useful to write the interaction matrix elements in Dirac notation. An interaction between an initial electronic state, $|i>$, and a final electronic state, $|f>$, would be expressed as:

$$< f| \boldsymbol{P}^n_\rho |i> ,$$

where $\boldsymbol{P}^n_\rho$ is the multipole-interaction operator. These interaction operators can also be labelled by the irreps of the symmetry group. The basis functions of these irreps indicate the polarisation of the radiation field with respect to the symmetry axes of the centre.

When considering the polarisation behaviour of RE^{3+} transitions, these interactions can be naturally formulated in the notation of group theory. The Wigner-Eckart theorem of quantum physics justifies this, as it allows the separation of those aspects of the interaction which depend on the symmetry properties of the system from those aspects which are concerned with the fundamental physical processes. The theorem permits a factorisation of the interaction matrix elements into a symmetry dependent factor, which can be considered using group theory, and a reduced matrix element. Using the notation of group theory an interaction between two electronic states, γ_i and γ_f, would be dependant on the condition:

$$\gamma_i \times \gamma_{em} \supset \gamma_f , \tag{4.1}$$

where γ_{em} is the irrep label of the multipole-interaction operator.

The relationships between the symmetry groups and the relationships between the irreps within each symmetry group are well established and have been published in tabulated form. Koster et al [50] have produced such a tabulation in their treatise on the properties of the 32 crystallographic-point groups. Those tables which are relevant to the work reported in this thesis are reproduced in the following section.

4.2 Properties of the Point-Symmetry Groups

4.2.1 Descriptions of the Symmetry Groups

The following descriptions may be considered definitions of these point symmetries for the purposes of this thesis. The cartesian-axis conventions adopted by Koster et al [50], for those symmetries generated by the symmetry-breaking effect of an applied

electric field, are also given. In Figure 4.1 some of these symmetries are illustrated by example, using specific crystalline centres. The relevant point symmetries are:

$\mathbf{O}_h$ This symmetry consists of all the operations which send a cube onto itself; these being the identity, rotations, reflections, improper rotations, and inversion.

$\mathbf{C}_{4v}$ This symmetry consists of the identity, a four-fold rotation axis **Z**, and four reflection planes which include this axis. Two of these reflections are taken in the orthogonal planes **XZ** and **YZ**, which bisect the other two reflection planes.

$\mathbf{C}_{2v}$ This symmetry consists of the identity, a two-fold rotation axis **z**, and two mutually orthogonal reflection planes, **xz** and **yz**.

$\mathbf{C}_{3v}$ This symmetry consists of the identity, a three-fold rotation axis **z**, and three reflection planes which include this axis. These reflection planes have mutual angular separations of 120^o.

$\mathbf{C}_s$ This symmetry consists of the identity and a single reflection plane, **xy**. When considering $\mathbf{C}_s$ as a derivative of $\mathbf{C}_{4v}$, the **Z** axis of $\mathbf{C}_{4v}$ is equivalent to the **y** axis of $\mathbf{C}_s$.

$\mathbf{C}_1$ This symmetry consists of the identity alone.

The symmetry operations given are sufficient to generate the single groups associated with each symmetry. If 2πn rotations with n even are distinguished from 2πn rotations with n odd, then the double-symmetry groups can be generated. The double groups will include the additional operation of rotation through an angle of 2πn.

4.2.2 Irreducible Representations and their Basis Functions

Each symmetry group will have a unique set of irreps, each of which can be generated from a set of linearly-independent basis functions. These basis functions are not unique, so when considering a physical system it is prudent to choose the basis set which produces the simplest formulation of the physical processes of interest.

The electronic wavefunctions of an even-electron ion can be labeled by the irreps of the appropriate single group. Odd-electron systems have half-integer spin and are not invariant under coordinate rotations of 2π. Thus the wavefunctions of an odd-electron atom or ion must be labeled by those irreps which belong to the double group only. The electric-dipole interaction (E1) matrices have the form:

$$\hat{e} \cdot < f | \boldsymbol{R} | i >,$$

where $\boldsymbol{R}$ represents the electric dipole, produced here by the charges on the nucleus and its attendant electron cloud, and $\hat{e}$ represents the linear polarisation of the

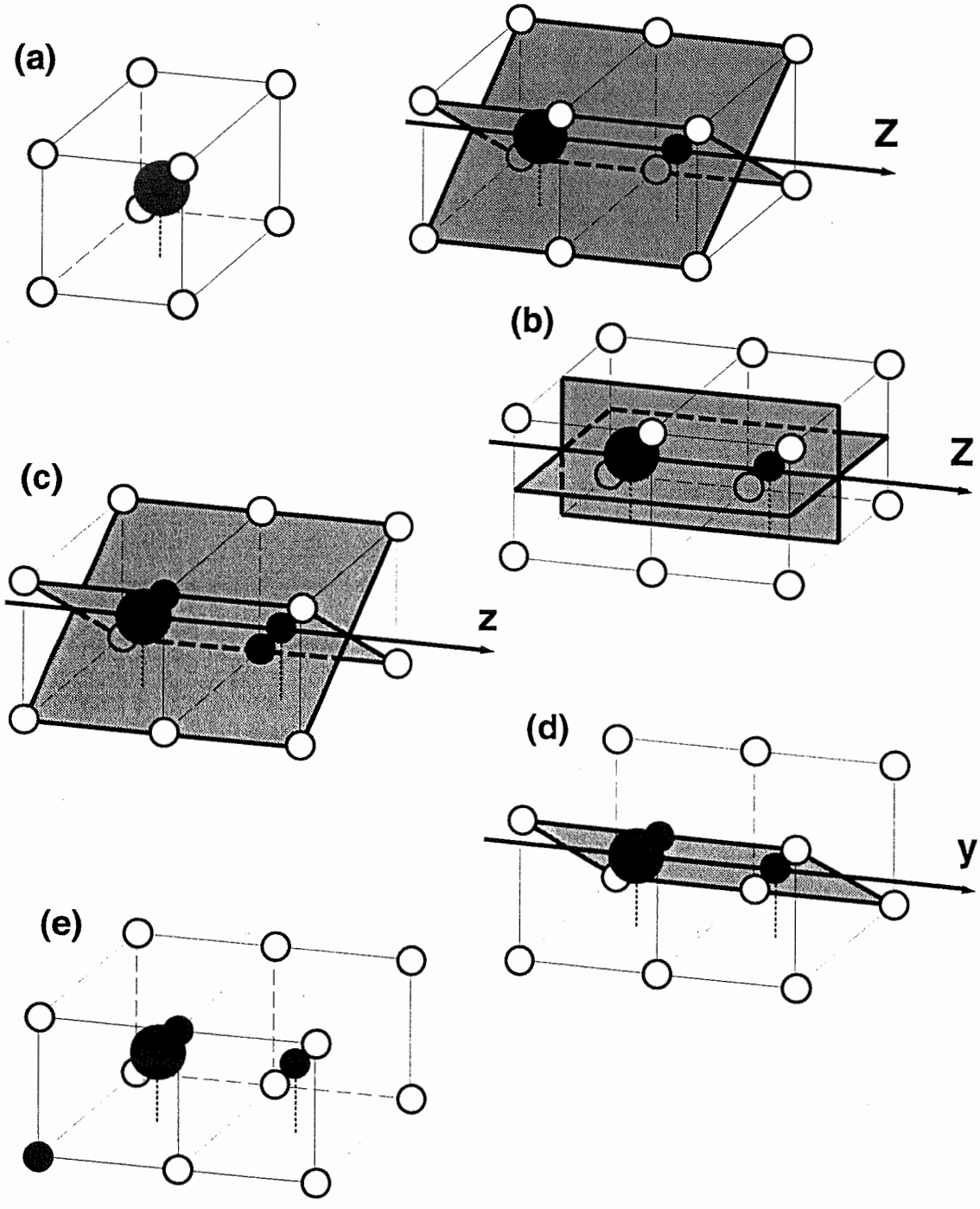

Figure 4.1: Examples of crystallographic symmetry centres: (**a**) the O_h symmetry Ca^{2+} site in CaF_2, (**b**) the $C_{4v}H^-$ centre, (**c**) the C_{2v} symmetry Cs(4) centre, (**d**) the C_s symmetry Cs(1) centre and (**e**) the C_1 symmetry Cs(4)* centre. The planes of reflection and axes of rotational symmetry are shown, except for (**a**). These are Pr^{3+} centres which will be investigated in this thesis.

Table 4.1: The irreps and basis functions of the single-symmetry groups. Reproduced from Koster et al.

Group	Irrep	Basis Functions
C_{4v}	γ_1	Z
	γ_2	S_Z
	γ_3	(X^2-Y^2)
	γ_4	XY
	γ_5	(S_X,S_Y) or (X,Y)
C_{2v}	γ_1	z
	γ_2	S_y or x
	γ_3	S_z or xy
	γ_4	S_x or y
C_{3v}	γ_1	z
	γ_2	S_z
	γ_3	(S_x,S_y) or (x,y)
C_s	γ_1	S_z or x or y
	γ_2	S_x or S_y or z
C_1	γ_1	arbitrary

radiation field [90]. Thus for an E1-electronic transition the irreps of the radiation field are restricted to those whose basis functions transform like the linear functions x, y, z. The magnetic-dipole interaction (M1) matrices have the form:

$$\hat{\boldsymbol{k}} \times \hat{\boldsymbol{e}} \cdot < f| \sum_j \boldsymbol{\mu_j} |i >$$

where $\boldsymbol{k}$ is the propagation vector of the electromagnetic field and $\boldsymbol{\mu_j}$ is the magnetic moment of the jth electron. Thus the irreps of M1-electronic transitions have basis functions which transform like the functions S_x, S_y and S_z. These are defined as even parity-functions which, in all other respects, transform like x, y and z.

Table 4.1 lists the irreps of the single groups and their basis functions, for the symmetries which are relevant to this thesis.

4.2.3 Compatibility Between the Symmetry Groups

The highly-degenerate $^{2S+1}L_J$ electronic energy levels of a free ion are invariant under the operations of R_3, the symmetry group of all possible rotations in three-dimensional space. A crystal field with cubic symmetry, O_h, will break these degen-

Table 4.2: Compatibility between the relevant single-symmetry groups and their subgroups. Reproduced from Koster et al.

Group	**Group Irrep**	**Subgroup**	**Subgroup Irreps**
C_{4v}	γ_1	C_{2v}	γ_1
	γ_2		γ_3
	γ_3		γ_1
	γ_4		γ_3
	γ_5		$\gamma_2 + \gamma_4$
	γ_1	C_s	γ_1
	γ_2		γ_2
	γ_3		γ_1
	γ_4		γ_2
	γ_5		$\gamma_1 + \gamma_2$
C_{2v}	γ_1	C_s	γ_1
	γ_2		γ_2
	γ_3		γ_2
	γ_4		γ_1

eracies and the new energy levels can be labeled by the irreps of the O_h symmetry group, with the denotation Γ_i. In a crystal field of lower symmetry the system will have an even greater number of energy levels and these may be labeled as the irreps of the appropriate symmetry group, denoted γ_i. In spectroscopic studies it is often useful to keep the cubic labels for centres of lower symmetry, as the wavefunctions will still retain their essential cubic character. This may be lost as the non-cubic components of the crystal field become more significant.

Such a notion of descending symmetries can be applied to an ion in any crystal field. The decomposition of the various point-symmetry groups into their respective subgroups is well established. The relationships between the point groups are shown schematically by Koster et al ([50] Figure 5). Each point symmetry can be derived from O_h through sequential symmetry breaking. This concept is useful when identifying the energy levels of a ion in a centre of known symmetry. The appropriate point-symmetry group will have a lineage of supergroups and the wavefunctions of the optically-active ion may exhibit characteristics of these supergroups.

Table 4.2 shows the relationships between the irreps of the single groups relevant to this study and their subgroups. The subgroup irreps listed in column four are those obtained by symmetry breaking through the application of an electric field.

The number of sublevels in each $^{2S+1}L_J$ multiplet and their possible irrep

labels is determined entirely by the symmetry of the crystal field and can be calculated group theoretically. Each set of J-states of the free ion is associated with a $(2J+1)$-fold degenerate representation γ_r of R_3. The group associated with the symmetry of the crystal field will be a subgroup of R_3. The number of sublevels is determined by the number of times the irreducible representations of the subgroup γ_s occur in the reduction of γ_r under the appropriate subgroup operations. These values n_s can be easily calculated as group theory shows that they are related to the characters of the subgroup χ_s and the character of the reducible representation χ_r. This relationship is expressed as:

$$n_s = \frac{1}{h} \sum_R \chi_s(R) \cdot \chi_r(R) \,,$$

where h is the order of the subgroup and R identifies the operations of the subgroup ([90] Section 3.3).

An example of such a reduction is presented in Wybourne ([93] Section 6.3), where the J-state splittings of all the point symmetries are also tabulated. Koster et al [50] lists the characters of all the point-symmetry groups.

4.2.4 Irrep Multiplication Tables

The irreps of a symmetry group will transform among themselves multiplicatively. Equation 4.1 demonstrates that this property can be usefully applied in physical situations, where the irreps are associated with quantum states. For an ion in a crystal field these tables can be used to distinguish the symmetry allowed E1 and M1 electronic transitions and to determine their polarisation behaviour.

Tables 4.3, 4.4, 4.5 and 4.6 are the irrep-multiplication tables for the relevant single groups. The group C_1 has only one irrep, γ_1, and its product with itself is necessarily γ_1.

When considering electronic transitions, it is often convenient to have these relationships tabulated in a form such that the polarisation (π or σ) of any transition of interest can be readily obtained. Table 4.7 gives the irrep labels and the polarisations of all the symmetry allowed E1 transitions between electronic states. In a π-polarised E1 transition the transition moment is parallel to the **z** axis of the symmetry centre. Table 4.8 gives the irrep labels and polarisations of all the allowed M1 transitions in a C_{4v} symmetry crystal field. The magnetic transition moment is parallel to the **z** axis in a π-polarised M1 transition.

Table 4.3: Multiplication table for the single group C_{4v}. Reproduced from Koster et al.

	γ_1	γ_2	γ_3	γ_4	γ_5
γ_1	γ_1	γ_2	γ_3	γ_4	γ_5
γ_2		γ_1	γ_4	γ_3	γ_5
γ_3			γ_1	γ_2	γ_5
γ_4				γ_1	γ_5
γ_5					$\gamma_1 + \gamma_2$ $+\gamma_3 + \gamma_4$

Table 4.4: Multiplication table for the single group C_{2v}. Reproduced from Koster et al.

	γ_1	γ_2	γ_3	γ_4
γ_1	γ_1	γ_2	γ_3	γ_4
γ_2		γ_1	γ_4	γ_3
γ_3			γ_1	γ_2
γ_4				γ_1

Table 4.5: Multiplication table for the single group C_{3v}. Reproduced from Koster et al.

	γ_1	γ_2	γ_3
γ_1	γ_1	γ_2	γ_3
γ_2		γ_1	γ_3
γ_3			$\gamma_1 + \gamma_2$ $+\gamma_3$

Table 4.6: Multiplication table for the single group C_s. Reproduced from Koster et al.

	γ_1	γ_2
γ_1	γ_1	γ_2
γ_2		γ_1

Table 4.7: Polarisation selection rules for E1-electronic transitions in crystal fields of different symmetries.

Symmetry	State $\longleftrightarrow$ State	Transition	Polarisation	Comment
C_{4v}	$\gamma_a \leftrightarrow \gamma_a$	$\gamma_1(Z)$	π	a = 1, 2, 3, 4, 5
	$\gamma_5 \leftrightarrow \gamma_b$	$\gamma_5(X,Y)$	σ	b = 1, 2, 3, 4
C_{2v}	$\gamma_b \leftrightarrow \gamma_b$	$\gamma_1(z)$	π	b = 1, 2, 3, 4
	$\gamma_1 \leftrightarrow \gamma_2$	$\gamma_2(x)$	σ	
	$\gamma_1 \leftrightarrow \gamma_4$	$\gamma_4(y)$	σ	
	$\gamma_2 \leftrightarrow \gamma_3$	$\gamma_4(y)$	σ	
	$\gamma_3 \leftrightarrow \gamma_4$	$\gamma_2(x)$	σ	
C_{3v}	$\gamma_c \leftrightarrow \gamma_c$	$\gamma_1(z)$	π	c = 1, 2
	$\gamma_3 \leftrightarrow \gamma_c$	$\gamma_3(x,y)$	σ	c = 1, 2
	$\gamma_3 \leftrightarrow \gamma_3$	$\gamma_1(z) + \gamma_3(x,y)$	$\pi+\sigma$	
C_s	$\gamma_1 \leftrightarrow \gamma_2$	$\gamma_2(z)$	π	
	$\gamma_c \leftrightarrow \gamma_c$	$\gamma_1(x \text{ or } y)$	σ	c = 1, 2
C_1	$\gamma_1 \leftrightarrow \gamma_1$	$\gamma_1(x, y \text{ or } z)$	$\pi+\sigma$	

Table 4.8: Polarisation selection rules for M1-electronic transitions in a C_{4v} symmetry crystal field.

State $\longleftrightarrow$ State	Transition	Polarisation	Comment
$\gamma_1 \leftrightarrow \gamma_2$	$\gamma_2(S_Z)$	π	
$\gamma_3 \leftrightarrow \gamma_4$	$\gamma_2(S_Z)$	π	
$\gamma_5 \leftrightarrow \gamma_5$	$\gamma_2(S_Z)$	π	
$\gamma_5 \leftrightarrow \gamma_b$	$\gamma_5(S_X, S_Y)$	σ	b = 1, 2, 3, 4

4.3 Calculation of the Symmetry Dependent Polarisation Ratios for RE^{3+} Centres in Alkaline-Earth Fluoride Crystals

In the previous section it was demonstrated that the point symmetry of the local crystal field determines the polarisation behaviour of the electronic transitions of an optically-active ion. Conversely it is also possible to determine experimentally the symmetry of a crystalline centre from the polarisation behaviour of its electronic transitions.

Each electric-dipole transition of a centre will have a transition moment which can be resolved into three cartesian components. These components of the transition moment (CTMs) are identified by their relationship to the symmetry axes of the centre. In this thesis the CTMs of absorption transitions will be labeled 'a', 'b', and 'c' while the CTMs of emission transitions will be labeled 'd', 'e', and 'f'. They are the CTMs orientated parallel to the **x**, **y**, and **z** symmetry axes respectively. Components of M1-transition moments will be distinguished by a prime.

When considering polarisation experiments a frame of reference must be defined. The geometry which will be used when conducting polarisation experiments is shown in Figure 4.2. The axes X, Y, Z will henceforth be called the 'crystal axes'. The excitation beam propagates in the X direction while the fluorescence propagating in the Z direction is selected for detection. This fluorescence can be analysed with a linearly-polarising film while the linear polarisation of the excitation beam can be selected using a polarisation rotator. A particular configuration of the experimental geometry will be given by the notational convention X(i,j)Z, where i and j refer to the linear polarisation of the excitation beam and fluorescence respectively. When i is given as 'C' the excitation beam is circularly polarised. When i is given as 'YZ' or 'ZY' the beam is linearly polarised with the electric vector bisecting the X and Y crystal axes. In the coordinate frame defined by the crystal axes the former has the electric vector in the (+Y,+Z) domain, while the latter has the electric vector in the (+Y,-Z) domain.

The polarisation behaviour of each symmetry will be characterised by a set of polarisation ratios. These polarisation ratios are defined as the ratio of the fluorescence intensities obtained in the geometries X(Y,X)Z and X(Y,Y)Z. The same ratio will be obtained in the geometries X(Z,Y)Z and X(Y,Y)Z, for the symetries considered in this study. The former will be called fluorescence ratios and the latter excitation ratios. A distinct polarisation ratio can be calculated for each possible pair of absorption and emission transitions, as defined by their irrep labels.

The group theoretical symmetry considerations discussed in the previous section are sufficient to determine the polarisation of a transition with respect to the axis system of a symmetry centre. Polarisation ratios represent the integrated polarisation behaviour due all possible orientations of the symmetry centre with respect to the crystal axes. The orientations that a particular centre can adopt will be de-

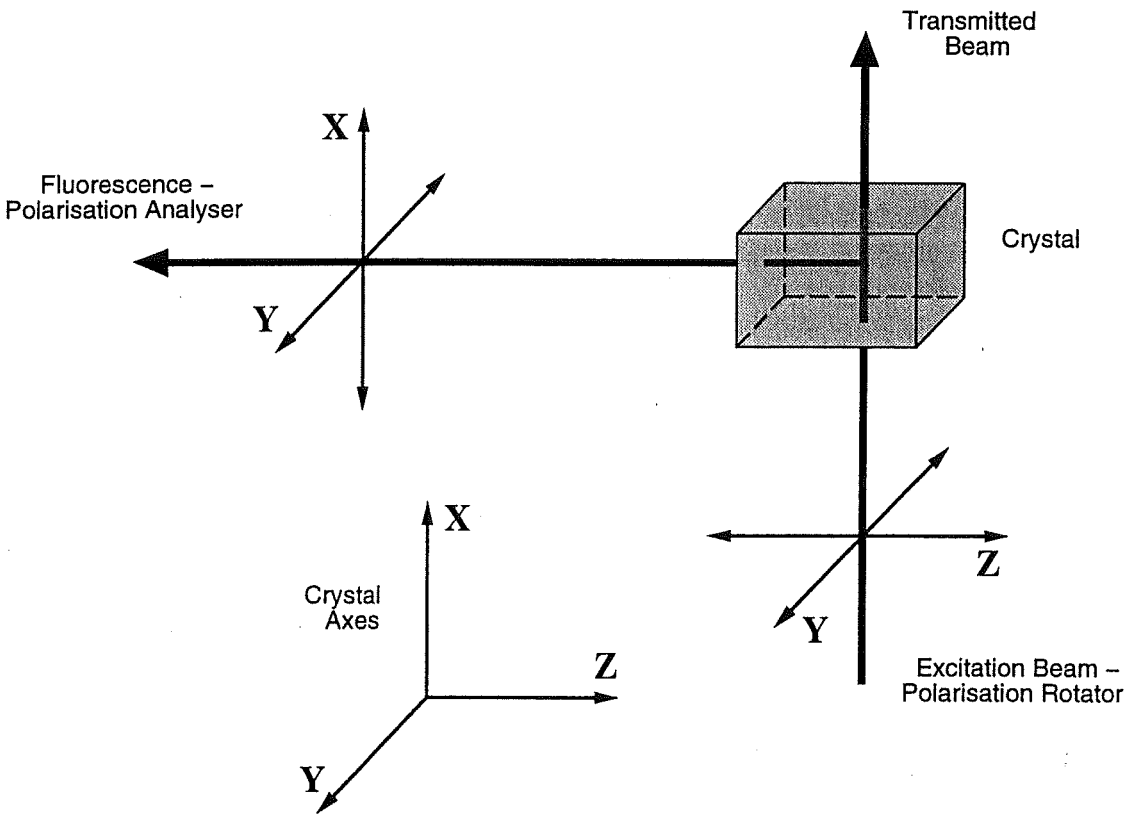

Figure 4.2: The experimental geometry used in the polarisation studies of RE^{3+} centres in alkaline-earth fluoride crystals. $CsCdBr_3$ crystals were orientated with the c-axis parallel to the Y crystal axis.

termined by the ionic configuration which comprises that centre and the space-group symmetry of the host lattice.

Polarisation ratios have been presented previously for the main symmetries adopted by trivalent RE^{3+} ion centres in alkaline-earth fluoride crystals, notably in the theses of Nigel Cockroft [27], Khong Yoon Loong [53] and Roger Reeves [77]. However the polarisation ratios obtained by Khong do not correctly take into account the physical effect of Malus' Law. In addition their derivation implicitly assumes, incorrectly, that the CTMs of the absorption and emission transitions are equal valued. Fortunately these factors only affect those polarisation ratios which are explicitly functions of the CTMs ('a','b', ... 'f').

4.3.1 Symmetry Centre Orientations

There are three possible ways of orientating a C_{4v} symmetry RE^{3+} centre in an alkaline-earth fluoride lattice. These are illustrated in Figure 4.3 using the $C_{4v}H^-$ centre as an example. Each orientation has been labeled with an arbitrarily assigned number. The orientation labels will always be denoted in this thesis by enclosing them in brackets.

Similarly there are six possible ways of orientating C_{2v} symmetry centres in such a lattice. In addition two distinct C_{2v} configurations can be obtained from a C_{4v} symmetry centre by symmetry breaking. Each of these configurations retains two of the four C_{4v} reflection planes. Khong [53] notes that two distinct C_{2v} configurations can be derived from a parent C_{4v} centre by substituting two of the cations in the nearest-neighbour cation sphere. These he labeled '(a)' and '(b)'. This labeling convention will be generalised here and used when discussing any C_{2v} symmetry RE^{3+} centre.

The six possible orientations of a C_{2v} symmetry centre are illustrated by example in Figures 4.4 and 4.5. Note that the word 'orientation' refers to the spatial relationship between the symmetry axes of a centre and the crystal axes without regard to axial direction (which is indicated by the arrowheads). In fact a C_{2v} symmetry centre can be orientated in two different ways, with regard to axial direction, while still having the same 'orientation'. These two sub-orientations will not be distinguished here as they exhibit the same optical behavior.

C_s symmetry centres again occur in two distinct configurations, each of which can be orientated in six ways. The possible orientations of C_s(a) and C_s(b) symmetry centres are illustrated in Figures 4.6 and 4.7. Here each orientation can be decomposed into four sub-orientations by considering axial direction.

A C_1 symmetry centre can have one of six possible orientations in the lattice and each orientation is composed of four sub-orientations. C_1 centres do not have reflection symmetry so there is a distinct left and right-handed configuration of each centre. If these configurations are distinguished then eight sub-orientations, four left-handed and four right-handed, will constitute each orientation. The six possible orientations of a right-handed C_1 centre are shown in Figure 4.8.

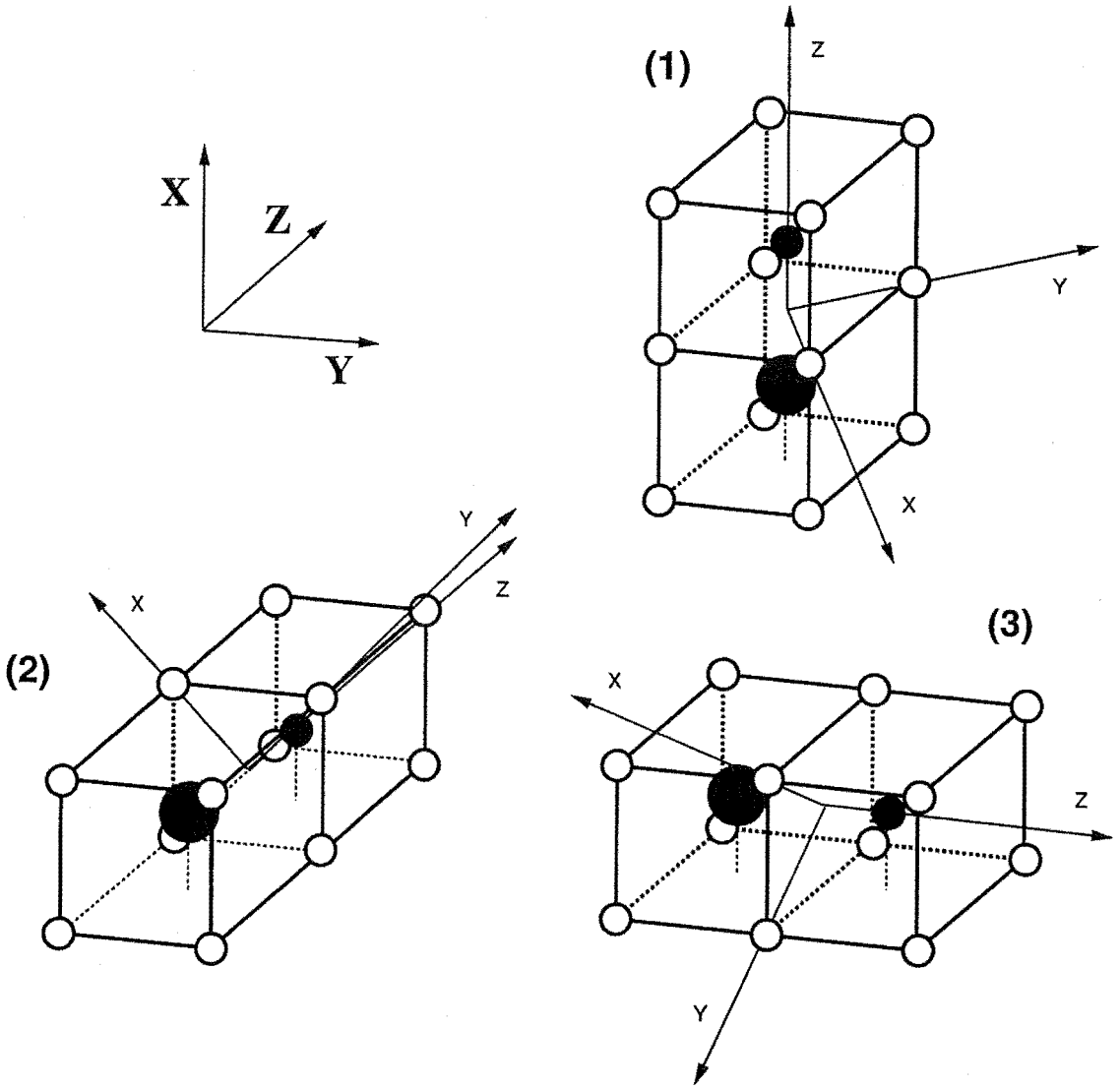

Figure 4.3: The three possible orientations of a C_{4v} symmetry RE^{3+} centre in the alkaline-earth fluoride lattice. This is illustrated by example using the $C_{4v}H^{-}$ centre. The crystal axes are also shown.

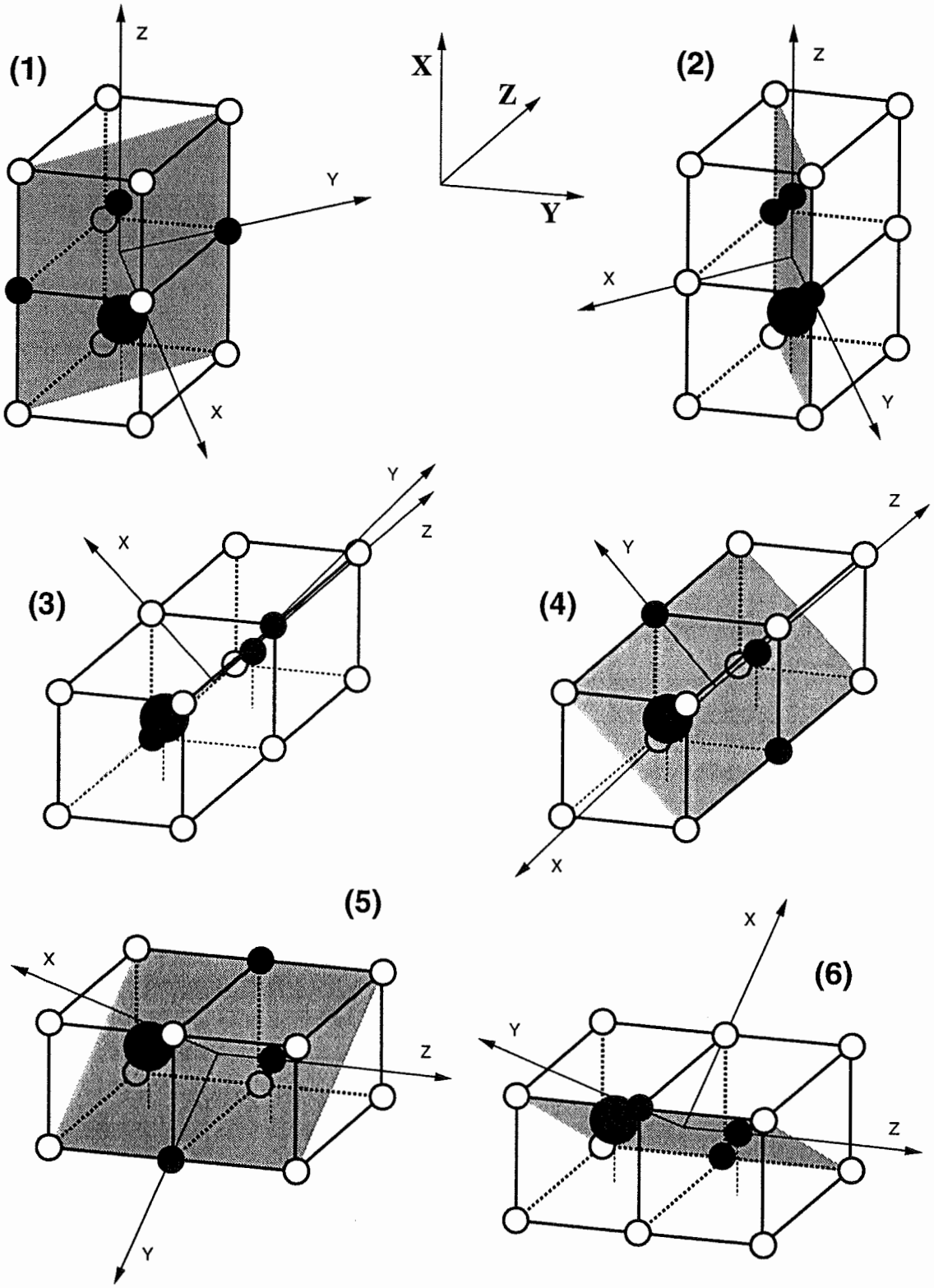

Figure 4.4: The six possible orientations of a C_{2v}(a) symmetry RE^{3+} centre in the alkaline-earth fluoride lattice. This is illustrated by example using the Cs(4) centre.

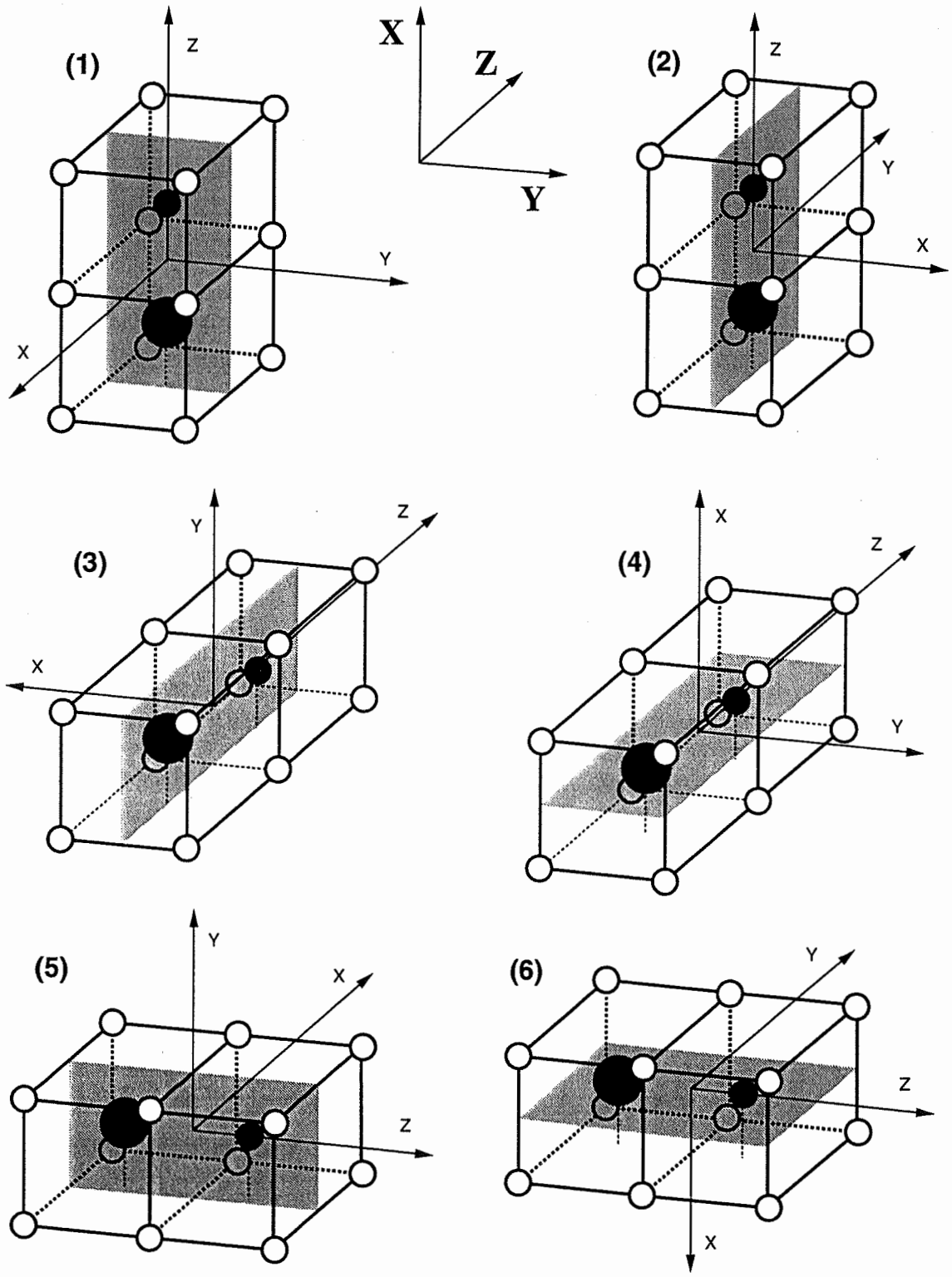

Figure 4.5: The six possible orientations of a C_{2v}(b) symmetry RE^{3+} centre in the alkaline-earth fluoride lattice. None of the hydrogenic centres identified so far exhibit this symmetry.

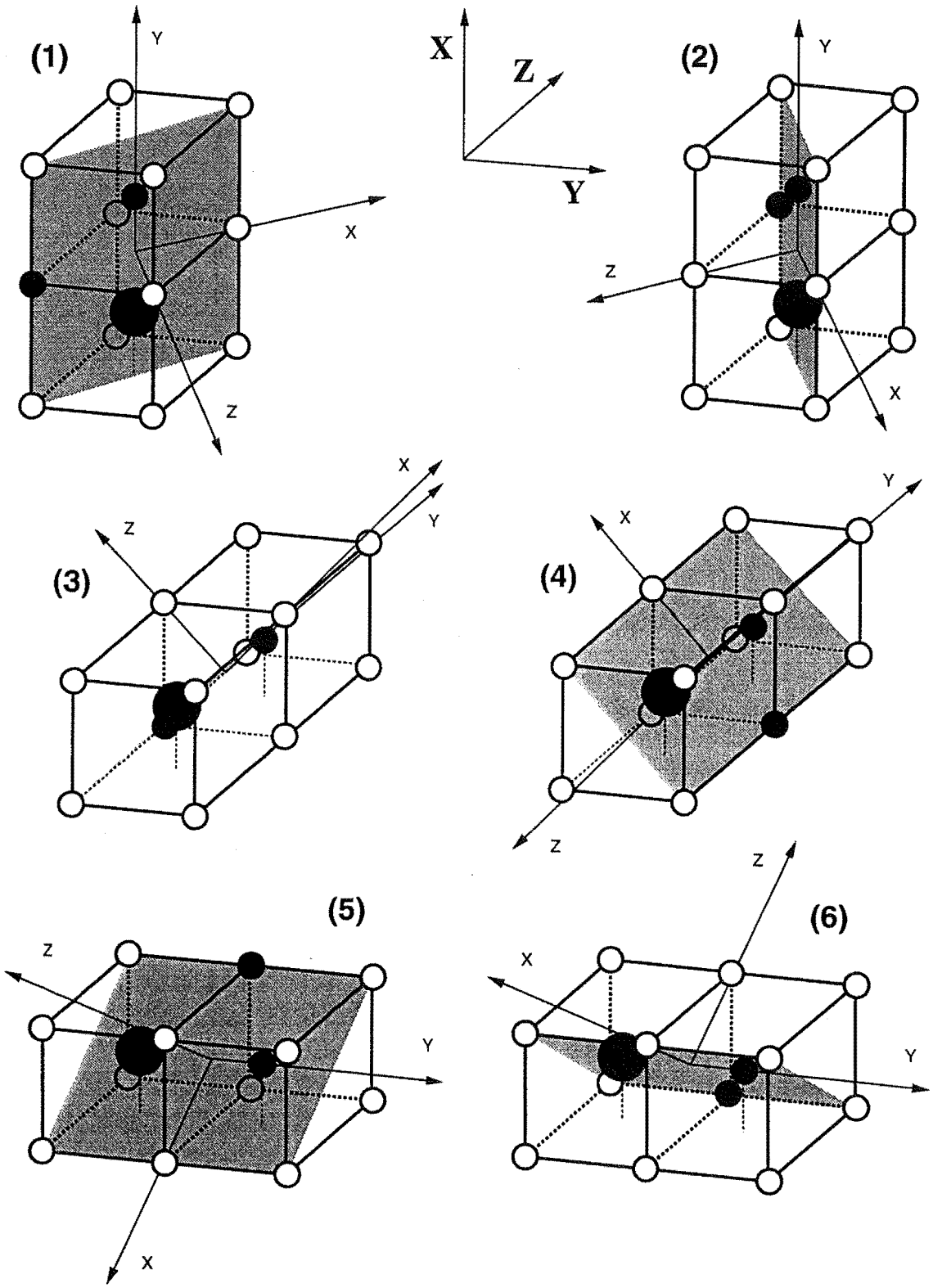

Figure 4.6: The six possible orientations of a C_s(a) symmetry RE^{3+} centre in the alkaline-earth fluoride lattice. This is illustrated by example using the Cs(1) centre.

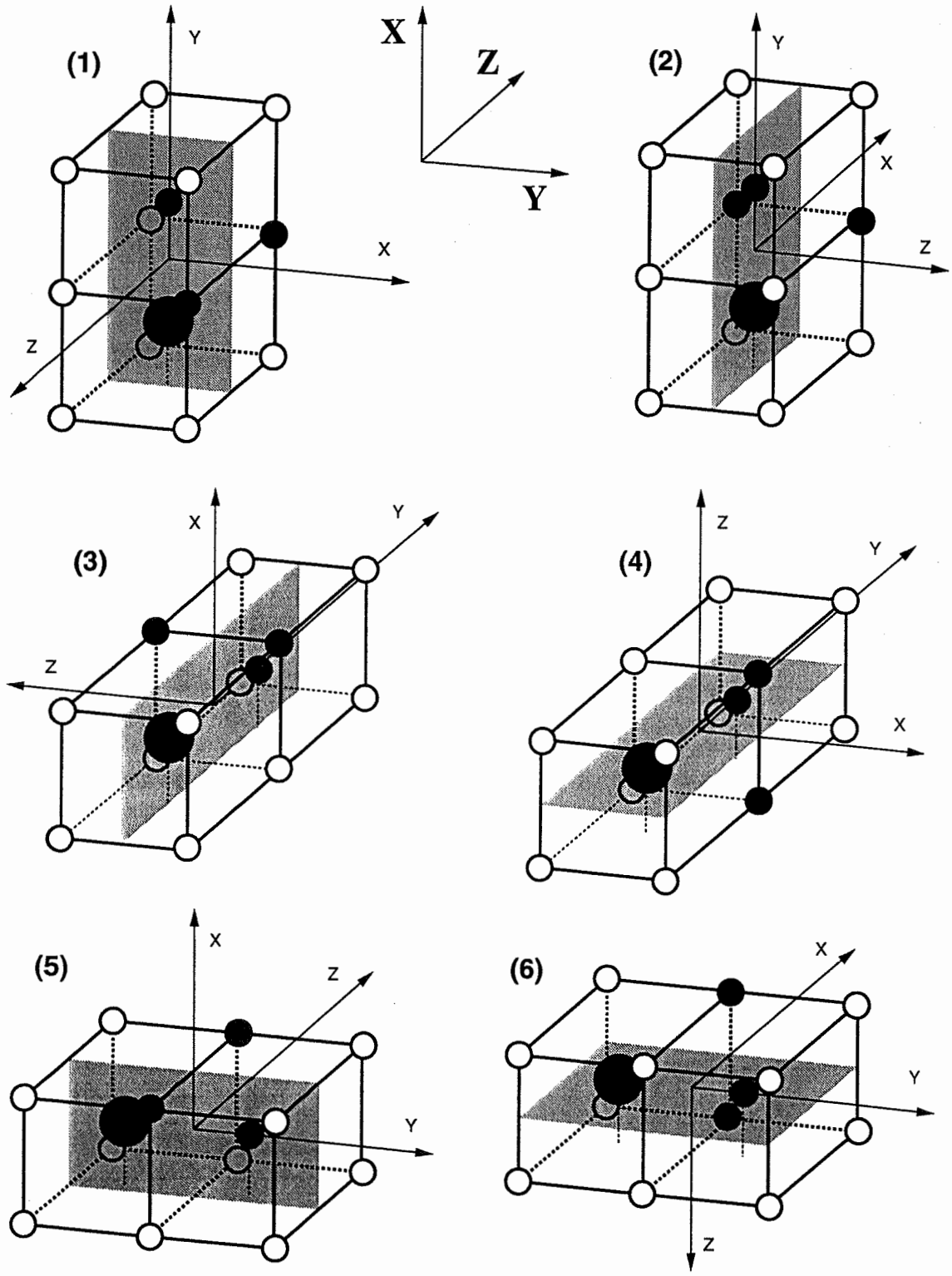

Figure 4.7: The six possible orientations of a C_s(b) symmetry RE^{3+} centre in the alkaline-earth fluoride lattice. This is illustrated by example using the Cs(2) centre.

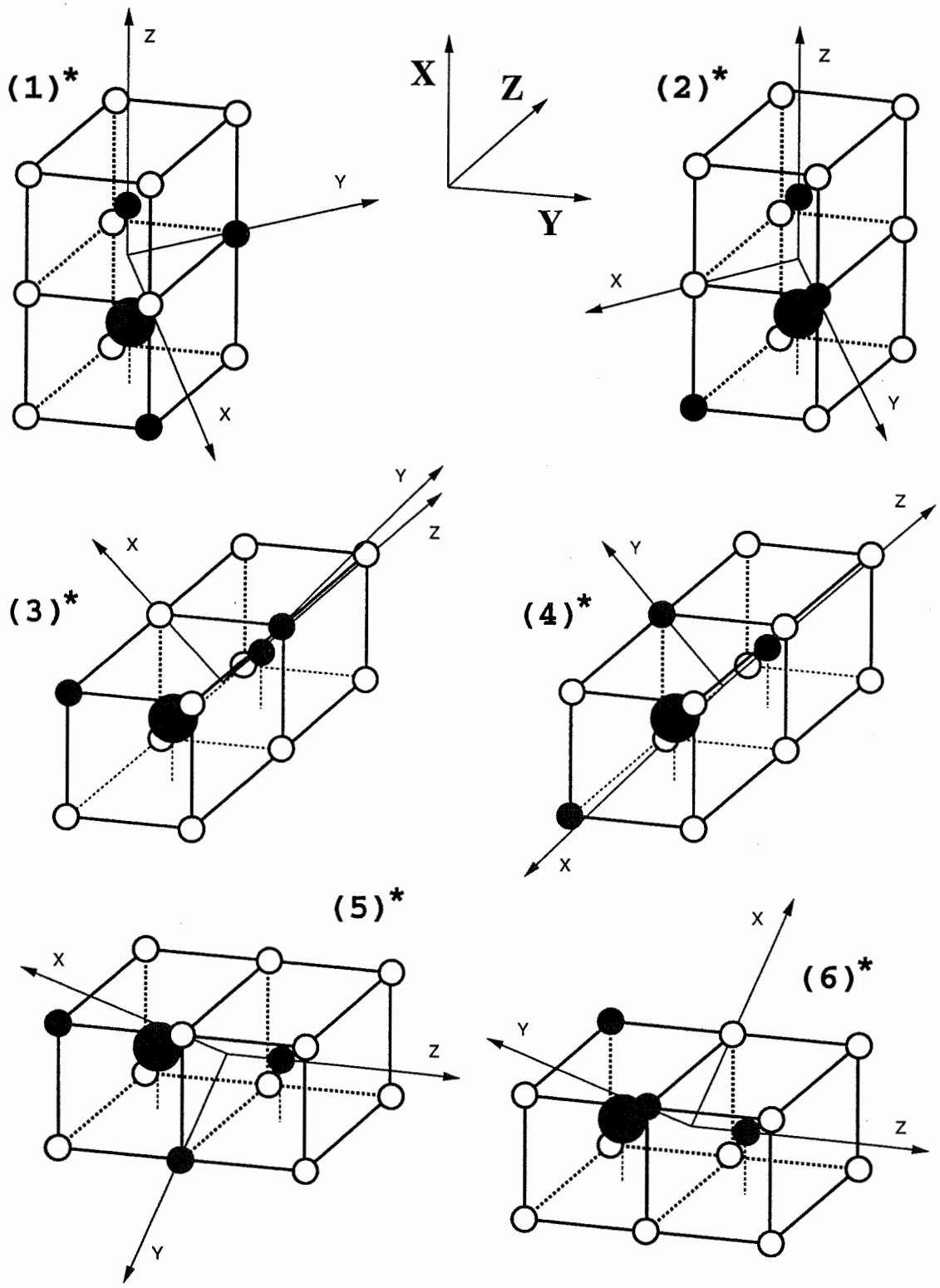

Figure 4.8: The six possible orientations of a C_1 symmetry RE^{3+} centre in the alkaline-earth fluoride lattice. This is illustrated by example using the Cs(4)* centre.

4.3.2 The Polarisation Ratios

Fluorescence polarisation ratios for all the relevant point symmetries adopted by trivalent RE^{3+} ion centres are tabulated in this subsection. The format of these tables is very similar to that used by Khong [53]. It has been adopted as the contribution of each orientation to the integrated fluorescence intensity is very apparent.

The irreps labelling the excitation and fluorescence transitions are given in the first and third column respectively. The linear polarisation of the excitation beam and the linear polarisation of the analysed fluorescence are given in the second and fourth columns. The last column contains the fluorescence polarisation ratios which would be obtained under these excitation and fluorescence conditions. Each of the other columns is associated with one of the possible orientations of a RE^{3+} centre.

Rows are divided into sections. Each section is associated with an excitation transition irrep and an excitation polarisation. The first row of each section indicates the relative probabilities of excitation for the different orientations under these excitation conditions. These relative probabilities are calculated using Malus' Law and will often depend upon the relative magnitudes of the non-zero CTMs of the particular excitation transition. The remaining rows of a section contain the relative contributions of the different orientations to the observed fluorescence. These will depend upon Malus' Law as it applies to the fluorescence, the CTMs of the fluorescence transitions, as well the relative excitation probabilities already tabulated. When the excitation beam is Z polarised the fluorescence polarisation ratios will always be 1:1. This occurs as the fluorescence polarisation is analysed in the XY plane, which is symmetrical with respect to the Z axis.

Excitation polarisation ratios can be easily derived from these tables. To do this it is necessary in every instance to substitute X for Z and Z for X. Old column two then becomes new column four and vice versa. The polarisation ratios in the last column become the Z:Y excitation ratios.

Several of the C_s symmetry polarisation ratios can only be expressed in terms of the CTMs and not as simple numerical ratios. The ratio for γ_1 excitation and γ_1 fluorescence of both C_s(a) and C_s(b) is unrestricted between the limits 1:0 and 0:1. However the ratios $\frac{1}{2}$a+c:a and $\frac{1}{2}$d+e:d of $C_s(a)$ are constrained to a smaller range, which can be easily calculated. Consider the former ratio expressed as a fraction:

$$k = \frac{\frac{1}{2}a + c}{a}.$$

This expression can be rearranged and written as:

$$c = a(k - \tfrac{1}{2}).$$

The requirement that the CTMs are real and positive will constrain k to the range:

$$k > \tfrac{1}{2}.$$

Thus the observed polarisation ratio will always be between the limits 1:0 and 1:2. The ratio $\frac{1}{2}$d+e:d will be constrained within the same limits.

Table 4.9: E1-transition polarisation ratios for the symmetry C_{4v}.

Absorption		**Emission**		**Centre**			**Ratio X : Y**
				(1)	**(2)**	**(3)**	
γ_5	Y			$\frac{1}{2}$(a+b)	$\frac{1}{2}$(a+b)	0	
		γ_5	X	0	$\frac{1}{4}$(a+b)(d+e)	0	
			Y	$\frac{1}{4}$(a+b)(d+e)	$\frac{1}{4}$(a+b)(d+e)	0	1 : 2
		γ_1	X	$\frac{1}{2}$(a+b)f	0	0	
			Y	0	0	0	1 : 0
	Z			$\frac{1}{2}$(a+b)	0	$\frac{1}{2}$(a+b)	
		γ_5	X	0	0	$\frac{1}{4}$(a+b)(d+e)	
			Y	$\frac{1}{4}$(a+b)(d+e)	0	0	1 : 1
		γ_1	X	$\frac{1}{2}$(a+b)f	0	0	
			Y	0	0	$\frac{1}{2}$(a+b)f	1 : 1
γ_1	Y			0	0	c	
		γ_5	X	0	0	$\frac{1}{2}$c(d+e)	
			Y	0	0	0	1 : 0
		γ_1	X	0	0	0	
			Y	0	0	cf	0 : 1
	Z			0	c	0	
		γ_5	X	0	$\frac{1}{2}$c(d+e)	0	
			Y	0	$\frac{1}{2}$c(d+e)	0	1 : 1
		γ_1	X	0	0	0	
			Y	0	0	0	0 : 0

Table 4.10: E1-excitation M1-fluorescence transition polarisation ratios for the symmetry C_{4v}.

Absorption		**Emission**		**Center** (1)	**Center** (2)	**Center** (3)	**Ratio X : Y**
γ_5	Y			$\frac{1}{2}$(a+b)	$\frac{1}{2}$(a+b)	0	
		γ_5	X	$\frac{1}{4}$(a+b)(d′+e′)	$\frac{1}{4}$(a+b)(d′+e′)	0	
			Y	0	$\frac{1}{4}$(a+b)(d′+e′)	0	2 : 1
		γ_2	X	0	0	0	
			Y	$\frac{1}{2}$(a+b)f′	0	0	0 : 1
	Z			$\frac{1}{2}$(a+b)	0	$\frac{1}{2}$(a+b)	
		γ_5	X	$\frac{1}{4}$(a+b)(d′+e′)	0	0	
			Y	0	0	$\frac{1}{4}$(a+b)(d′+e′)	1 : 1
		γ_2	X	0	0	$\frac{1}{2}$(a+b)f′	
			Y	$\frac{1}{2}$(a+b)f′	0	0	1 : 1
γ_1	Y			0	0	c	
		γ_5	X	0	0	0	
			Y	0	0	$\frac{1}{2}$c(d′+e′)	0 : 1
		γ_2	X	0	0	cf′	
			Y	0	0	0	1 : 0
	Z			0	c	0	
		γ_5	X	0	$\frac{1}{2}$c(d′+e′)	0	
			Y	0	$\frac{1}{2}$c(d′+e′)	0	1 : 1
		γ_2	X	0	0	0	
			Y	0	0	0	0 : 0

Table 4.11: E1-transition polarisation ratios for the symmetry C_{2v}(a).

Absorption		**Emission**		**Centre**						**Ratio X : Y**
				(1)	**(2)**	**(3)**	**(4)**	**(5)**	**(6)**	
γ_1	Y			0	0	0	0	c	c	
		γ_1	X	0	0	0	0	0	0	
			Y	0	0	0	0	cf	cf	0 : 1
		γ_2	X	0	0	0	0	$\frac{1}{2}$cd	$\frac{1}{2}$cd	
			Y	0	0	0	0	0	0	1 : 0
		γ_4	X	0	0	0	0	$\frac{1}{2}$ce	$\frac{1}{2}$ce	
			Y	0	0	0	0	0	0	1 : 0
	Z			0	0	c	c	0	0	
		γ_1	X	0	0	0	0	0	0	
			Y	0	0	0	0	0	0	0 : 0
		γ_2	X	0	0	$\frac{1}{2}$cd	$\frac{1}{2}$cd	0	0	
			Y	0	0	$\frac{1}{2}$cd	$\frac{1}{2}$cd	0	0	1 : 1
		γ_4	X	0	0	$\frac{1}{2}$ce	$\frac{1}{2}$ce	0	0	
			Y	0	0	$\frac{1}{2}$ce	$\frac{1}{2}$ce	0	0	1 : 1
γ_2	Y			$\frac{1}{2}$a	$\frac{1}{2}$a	$\frac{1}{2}$a	$\frac{1}{2}$a	0	0	
		γ_1	X	$\frac{1}{2}$af	$\frac{1}{2}$af	0	0	0	0	
			Y	0	0	0	0	0	0	1 : 0
		γ_2	X	0	0	$\frac{1}{4}$ad	$\frac{1}{4}$ad	0	0	
			Y	$\frac{1}{4}$ad	$\frac{1}{4}$ad	$\frac{1}{4}$ad	$\frac{1}{4}$ad	0	0	1 : 2
		γ_4	X	0	0	$\frac{1}{4}$ae	$\frac{1}{4}$ae	0	0	
			Y	$\frac{1}{4}$ae	$\frac{1}{4}$ae	$\frac{1}{4}$ae	$\frac{1}{4}$ae	0	0	1 : 2
	Z			$\frac{1}{2}$a	$\frac{1}{2}$a	0	0	$\frac{1}{2}$a	$\frac{1}{2}$a	
		γ_1	X	$\frac{1}{2}$af	$\frac{1}{2}$af	0	0	0	0	
			Y	0	0	0	0	$\frac{1}{2}$af	$\frac{1}{2}$af	1 : 1
		γ_2	X	0	0	0	0	$\frac{1}{4}$ad	$\frac{1}{4}$ad	
			Y	$\frac{1}{4}$ad	$\frac{1}{4}$ad	0	0	0	0	1 : 1
		γ_4	X	0	0	0	0	$\frac{1}{4}$ae	$\frac{1}{4}$ae	
			Y	$\frac{1}{4}$ae	$\frac{1}{4}$ae	0	0	0	0	1 : 1
γ_4	Y			$\frac{1}{2}$b	$\frac{1}{2}$b	$\frac{1}{2}$b	$\frac{1}{2}$b	0	0	
		γ_1	X	$\frac{1}{2}$bf	$\frac{1}{2}$bf	0	0	0	0	
			Y	0	0	0	0	0	0	1 : 0
		γ_2	X	0	0	$\frac{1}{4}$bd	$\frac{1}{4}$bd	0	0	
			Y	$\frac{1}{4}$bd	$\frac{1}{4}$bd	$\frac{1}{4}$bd	$\frac{1}{4}$bd	0	0	1 : 2
		γ_4	X	0	0	$\frac{1}{4}$be	$\frac{1}{4}$be	0	0	
			Y	$\frac{1}{4}$be	$\frac{1}{4}$be	$\frac{1}{4}$be	$\frac{1}{4}$be	0	0	1 : 2
	Z			$\frac{1}{2}$b	$\frac{1}{2}$b	0	0	$\frac{1}{2}$b	$\frac{1}{2}$b	
		γ_1	X	$\frac{1}{2}$bf	$\frac{1}{2}$bf	0	0	0	0	
			Y	0	0	0	0	$\frac{1}{2}$bf	$\frac{1}{2}$bf	1 : 1
		γ_2	X	0	0	0	0	$\frac{1}{4}$bd	$\frac{1}{4}$bd	
			Y	$\frac{1}{4}$bd	$\frac{1}{4}$bd	0	0	0	0	1 : 1
		γ_4	X	0	0	0	0	$\frac{1}{4}$be	$\frac{1}{4}$be	
			Y	$\frac{1}{4}$be	$\frac{1}{4}$be	0	0	0	0	1 : 1

Table 4.12: E1-transition polarisation ratios for the symmetry C_{2v}(b).

Absorption		**Emission**		**Centre**						**Ratio X : Y**
				(1)	**(2)**	**(3)**	**(4)**	**(5)**	**(6)**	
γ_1	Y			0	0	0	0	c	c	
		γ_1	X	0	0	0	0	0	0	
			Y	0	0	0	0	cf	cf	0 : 1
		γ_2	X	0	0	0	0	0	cd	
			Y	0	0	0	0	0	0	1 : 0
		γ_4	X	0	0	0	0	ce	0	
			Y	0	0	0	0	0	0	1 : 0
	Z			0	0	c	c	0	0	
		γ_1	X	0	0	0	0	0	0	
			Y	0	0	0	0	0	0	0 : 0
		γ_2	X	0	0	0	cd	0	0	
			Y	0	0	cd	0	0	0	1 : 1
		γ_4	X	0	0	ce	0	0	0	
			Y	0	0	0	ce	0	0	1 : 1
γ_2	Y			0	a	a	0	0	0	
		γ_1	X	0	af	0	0	0	0	
			Y	0	0	0	0	0	0	1 : 0
		γ_2	X	0	0	0	0	0	0	
			Y	0	ad	ad	0	0	0	0 : 1
		γ_4	X	0	0	ae	0	0	0	
			Y	0	0	0	0	0	0	1 : 0
	Z			a	0	0	0	a	0	
		γ_1	X	af	0	0	0	0	0	
			Y	0	0	0	0	af	0	1 : 1
		γ_2	X	0	0	0	0	0	0	
			Y	0	0	0	0	0	0	0 : 0
		γ_4	X	0	0	0	0	ae	0	
			Y	ae	0	0	0	0	0	1 : 1
γ_4	Y			b	0	0	b	0	0	
		γ_1	X	bf	0	0	0	0	0	
			Y	0	0	0	0	0	0	1: 0
		γ_2	X	0	0	0	bd	0	0	
			Y	0	0	0	0	0	0	1 : 0
		γ_4	X	0	0	0	0	0	0	
			Y	be	0	0	be	0	0	0 : 1
	Z			0	b	0	0	0	b	
		γ_1	X	0	bf	0	0	0	0	
			Y	0	0	0	0	0	bf	1 : 1
		γ_2	X	0	0	0	0	0	bd	
			Y	0	bd	0	0	0	0	1 : 1
		γ_4	X	0	0	0	0	0	0	
			Y	0	0	0	0	0	0	0 : 0

Table 4.13: E1-transition polarisation ratios for the symmetry C_s(a).

Absorption		**Emission**		**Centre**						**Ratio X : Y**
				(1)	**(2)**	**(3)**	**(4)**	**(5)**	**(6)**	
γ_1	Y			$\frac{1}{2}$a	$\frac{1}{2}$a	$\frac{1}{2}$a	$\frac{1}{2}$a	b	b	
		γ_1	X	$\frac{1}{2}$ae	$\frac{1}{2}$ae	$\frac{1}{4}$ad	$\frac{1}{4}$ad	$\frac{1}{2}$bd	$\frac{1}{2}$bd	
			Y	$\frac{1}{4}$ad	$\frac{1}{4}$ad	$\frac{1}{4}$ad	$\frac{1}{4}$ad	be	be	$\frac{1}{2}$ad+bd+ae : ad+2be
		γ_2	X	0	0	$\frac{1}{4}$af	$\frac{1}{4}$af	$\frac{1}{2}$bf	$\frac{1}{2}$bf	
			Y	$\frac{1}{4}$af	$\frac{1}{4}$af	$\frac{1}{4}$af	$\frac{1}{4}$af	0	0	$\frac{1}{2}$a+b : a
	Z			$\frac{1}{2}$a	$\frac{1}{2}$a	b	b	$\frac{1}{2}$a	$\frac{1}{2}$a	
		γ_1	X	$\frac{1}{2}$ae	$\frac{1}{2}$ae	$\frac{1}{2}$ bd	$\frac{1}{2}$bd	$\frac{1}{4}$ad	$\frac{1}{4}$ad	
			Y	$\frac{1}{4}$ad	$\frac{1}{4}$ad	$\frac{1}{2}$bd	$\frac{1}{2}$bd	$\frac{1}{2}$ae	$\frac{1}{2}$ae	1 : 1
		γ_2	X	0	0	$\frac{1}{2}$bf	$\frac{1}{2}$bf	$\frac{1}{4}$af	$\frac{1}{4}$af	
			Y	$\frac{1}{4}$af	$\frac{1}{4}$af	$\frac{1}{2}$bf	$\frac{1}{2}$bf	0	0	1 : 1
γ_2	Y			$\frac{1}{2}$c	$\frac{1}{2}$c	$\frac{1}{2}$c	$\frac{1}{2}$c	0	0	
		γ_1	X	$\frac{1}{2}$ce	$\frac{1}{2}$ce	$\frac{1}{4}$cd	$\frac{1}{4}$cd	0	0	
			Y	$\frac{1}{4}$cd	$\frac{1}{4}$cd	$\frac{1}{4}$cd	$\frac{1}{4}$cd	0	0	$\frac{1}{2}$d+e : d
		γ_2	X	0	0	$\frac{1}{4}$cf	$\frac{1}{4}$cf	0	0	
			Y	$\frac{1}{4}$cf	$\frac{1}{4}$cf	$\frac{1}{4}$cf	$\frac{1}{4}$cf	0	0	1 : 2
	Z			$\frac{1}{2}$c	$\frac{1}{2}$c	0	0	$\frac{1}{2}$c	$\frac{1}{2}$c	
		γ_1	X	$\frac{1}{2}$ce	$\frac{1}{2}$ce	0	0	$\frac{1}{4}$cd	$\frac{1}{4}$cd	
			Y	$\frac{1}{4}$cd	$\frac{1}{4}$cd	0	0	$\frac{1}{2}$ce	$\frac{1}{2}$ce	1 : 1
		γ_2	X	0	0	0	0	$\frac{1}{4}$cf	$\frac{1}{4}$cf	
			Y	$\frac{1}{4}$cf	$\frac{1}{4}$cf	0	0	0	0	1 : 1

Table 4.14: E1-transition polarisation ratios for the symmetry C_s(b).

Absorption		**Emission**		**Centre**						**Ratio X : Y**
				(1)	**(2)**	**(3)**	**(4)**	**(5)**	**(6)**	
γ_1	Y			a	0	0	a	b	b	
		γ_1	X	ae	0	0	0	bd	0	
			Y	ad	0	0	ad	be	be	ae+bd : 2ad+2be
		γ_2	X	0	0	0	af	0	bf	
			Y	0	0	0	0	0	0	1 : 0
	Z			0	a	b	b	0	a	
		γ_1	X	0	ae	bd	0	0	0	
			Y	0	0	0	bd	0	ae	1 : 1
		γ_2	X	0	0	0	bf	0	af	
			Y	0	af	bf	0	0	0	1 : 1
γ_2	Y			0	c	c	0	0	0	
		γ_1	X	0	ce	cd	0	0	0	
			Y	0	0	0	0	0	0	1 : 0
		γ_2	X	0	0	0	0	0	0	
			Y	0	cf	cf	0	0	0	0 : 1
	Z			c	0	0	0	c	0	
		γ_1	X	ce	0	0	0	cd	0	
			Y	cd	0	0	0	ce	0	1 : 1
		γ_2	X	0	0	0	0	0	0	
			Y	0	0	0	0	0	0	0 : 0

4.3.3 Higher-Symmetry Approximations of the Polarisation Ratios

In Section 2.3 the notion of descending symmetries was introduced and the compatibility between a number of single groups and their subgroups was tabulated. This information can be useful when using empirical polarisation ratios to assign irrep labels to the transitions and energy levels of a RE^{3+} centre.

The wavefunctions of a RE^{3+} ion located in a lattice site will not be significantly altered by very small changes in the local crystal field. The transition dipole moments will be similarly unaffected. Although an additional component to the crystal field may break the point symmetry of the original centre, the relative CTMs of each transition will not change significantly while this component remains small. If symmetry breaking does occur then this will split some degenerate energy levels into two or more sub-levels. As a consequence each observed transition from/to such a degenerate level will be split up into a number of distinct transitions. One of these transitions will originate from/terminate on each of these sub-levels. The sum of the dipole moments of these transitions will be approximately equal to the dipole moment of the original transition which was associated with the degenerate level.

This principle can be applied when investigating the low-symmetry hydrogenic centres in hydrogenated SrF_2:RE^{3+} and CaF_2:RE^{3+} crystals. These are modifications of the parent $C_{4v}H^-$ centre, obtained by substituting H^- ions for lattice F^- ions. The C_{4v} axial symmetry of the crystal field is broken in these centres due to the presence of the substitutional ions, however the non-axial component is relatively small. Thus the relative CTMs of each transition in the lower-symmetry field can be approximated by substituting the appropriate CTMs of the parent C_{4v} H^- centre. This will henceforth be called 'the C_{4v} approximation' or more generally the 'high-symmetry approximation'.

The fluorescence polarisation ratios obtained in the C_{4v} approximation for centres with C_{2v} or C_s symmetry are tabulated in this subsection. These tables have been generated from the more general polarisation ratio tables for these symmetries, Tables 4.11 to 4.14. The C_{4v} approximation is made by assigning the value zero to each CTM which is zero valued in the parent field.

The irrep labels of the excitation and fluorescence transitions of the parent C_{4v} centre are given in the first two columns of Tables 4.17, 4.18, 4.15 and 4.16. Those pairs of discrete transitions in the lower-symmetry centre which will produce fluorescence in the C_{4v} approximation are listed in the third and forth columns. The last two columns give their fluorescence polarisation ratios in the C_{4v} approximation. Only E1 transitions have been considered in these tables.

All the polarisation ratios obtained using the C_{4v} approximation can be expressed as simple numerical ratios. In those cases where the ratios were previously found to be either unrestricted or loosely constrained they are now exactly determined. For each pair of excitation and fluorescence transitions the approximate

numerical ratio will depend upon the polarisations of the two parent C_{4v} transitions. In those cases where the polarisation ratios are 0:1, 0:0 or 1:0 in the parent centre, the corresponding transitions in a lower-symmetry field must have the same ratio.

The C_{4v} approximation is also useful because it excludes a large number of transitions which are forbidden in the C_{4v} field, but are allowed in a lower-symmetry field. Although allowed, these will be necessarily very weak in intensity. This information is useful when interpreting spectra obtained from low-symmetry centres. For example: a $\gamma_5 \rightarrow \gamma_5$ excitation transition in a parent C_{4v} centre is a π-polarised γ_1 transition. If a C_s symmetry centre is created by breaking the axial symmetry this transition will split into 4 distinct transitions. However in the C_{4v} approximation only two of these transitions are likely to be intense enough to observed spectroscopically.

Table 4.15: C_{4v} symmetry approximations to the C_{2v}(a) polarisation ratios.

C_{4v}		C_{2v}(a)		Polarisation Ratio	
Absorption	**Emission**	**Absorption**	**Emission**	**X : Y**	**X : Y**
γ_5	γ_5	γ_2	γ_2	$\frac{1}{2}$ad : ad	1 : 2
			γ_4	$\frac{1}{2}$ae : ae	1 : 2
		γ_4	γ_2	$\frac{1}{2}$bd : bd	1 : 2
			γ_4	$\frac{1}{2}$be : be	1 : 2
	γ_1	γ_2	γ_1	af : 0	1 : 0
		γ_4	γ_1	bf : 0	1 : 0
γ_1	γ_5	γ_1	γ_2	cd : 0	1 : 0
			γ_4	ce : 0	1 : 0
	γ_1	γ_1	γ_1	0 : 2cf	0 : 1

Table 4.16: C_{4v} symmetry approximations to the C_{2v}(b) polarisation ratios.

C_{4v}		C_{2v}(b)		Polarisation Ratio	
Absorption	**Emission**	**Absorption**	**Emission**	**X : Y**	**X : Y**
γ_5	γ_5	γ_2	γ_2	0 : 2ad	0 : 1
			γ_4	ae : 0	1 : 0
		γ_4	γ_2	bd : 0	1 : 0
			γ_4	0 : 2be	0 : 1
	γ_1	γ_2	γ_1	af : 0	1 : 0
		γ_4	γ_1	bf : 0	1 : 0
γ_1	γ_5	γ_1	γ_2	cd : 0	1 : 0
			γ_4	ce : 0	1 : 0
	γ_1	γ_1	γ_1	0 : 2cf	0 : 1

Table 4.17: C_{4v} symmetry approximations to the C_s(a) polarisation ratios.

C_{4v}		C_s(a)		Polarisation Ratio	
Absorption	**Emission**	**Absorption**	**Emission**	**X : Y**	**X : Y**
γ_5	γ_5	γ_1	γ_1	$\frac{1}{2}$ad : ad	1 : 2
			γ_2	$\frac{1}{2}$af : af	1 : 2
		γ_2	γ_1	$\frac{1}{2}$cd : cd	1 : 2
			γ_2	$\frac{1}{2}$cf : cf	1 : 2
	γ_1	γ_1	γ_1	ae : 0	1 : 0
		γ_2	γ_1	e : 0	1 : 0
γ_1	γ_5	γ_1	γ_1	bd : 0	1 : 0
			γ_2	b : 0	1 : 0
	γ_1	γ_1	γ_1	0 : be	0 : 1

Table 4.18: C_{4v} symmetry approximations to the C_s(b) polarisation ratios.

C_{4v}		C_s(b)		Polarisation Ratio	
Absorption	**Emission**	**Absorption**	**Emission**	**X : Y**	**X : Y**
γ_5	γ_5	γ_1	γ_1	0 : 2ad	0 : 1
			γ_2	af : 0	1 : 0
		γ_2	γ_1	cd : 0	1 : 0
			γ_2	0 : 2cf	0 : 1
	γ_1	γ_1	γ_1	ae : 0	1 : 0
		γ_2	γ_1	ce : 0	1 : 0
γ_1	γ_5	γ_1	γ_1	bd : 0	1 : 0
			γ_2	bf : 0	1 : 0
	γ_1	γ_1	γ_1	0 : 2be	0 : 1

Chapter 5

Spectroscopy of Pr^{3+} Centres in Hydrogenated and Deuterated SrF_2 and CaF_2 Crystals

5.1 The Spectroscopy of Hydrogenated and Deuterated SrF_2:Pr^{3+} and CaF_2:Pr^{3+} Crystals

5.1.1 Absorption Spectra

Transmission spectra were obtained for pure, hydrogenated and deuterated SrF_2:Pr^{3+} and CaF_2:Pr^{3+} crystals by Roger Reeves. These are presented in his PhD Thesis ([77] Figures IV.2.1, IV.3.1, V.1.1 and V.2.1) and they show absorption transitions to the $^1D_2$, $^3P_0$ and $^3P_1$ multiplets of praseodymium at 10K. Jacobs [45] and latter Reeves [77] have identified many of the electronic transitions observed and these are associated with a number of specific Pr^{3+} centres. The absorption transitions to the ^3P_J multiplets are generally much stronger than those to the $^1D_2$ multiplet. The former are spin allowed and were expected to be very suitable for selective laser excitation of the various Pr^{3+} centres.

Reeves [75] [76] [77] and Khong [49] [53] have both conducted very thorough laser selective excitation studies of the Pr^{3+} centres in SrF_2 and CaF_2 crystals. In their experiments the $^3H_4 \rightarrow {}^1D_2$ inter-multiplet transitions were pumped selectively, using the Spectra Physics 375 dye laser with a Rhodamine 590 dye solution. In this study Coumarin 460 and 480 dyes have also been used to pump selectively the blue $^3H_4 \rightarrow {}^3P_0$ and $^3H_4 \rightarrow {}^3P_1$ inter-multiplet transitions. Pumping the strongest absorption transitions produces orange coloured fluorescence from the $C_{4v}F^-$ centres and red fluorescence from the hydrogenic centres.

Several SrF_2:Pr^{3+}(0.05mole%) and CaF_2:Pr^{3+}(0.05mole%) crystal boles were grown for this study. Hydrogenated crystals were treated in the high-pressure furnace, while deuterated crystals were treated in the low-pressure furnace. Broadband

excitation spectra were recorded for all the crystals included in this study. These broadband spectra show the same absorption features as transmission spectra, although the hydrogenic centre transitions appear much weaker in the former due to the efficient non-radiative relaxation processes which occur in these centres. Broadband excitation spectra of the deuterated crystals are presented in this section. The deuterated crystals contain all of the centre configurations observed in the other crystals and these spectra are representative of all the absorption spectra obtained.

Broadband excitation spectra showing the $^3H_4 \rightarrow {}^1D_2$ absorption transitions were obtained by monitoring the $^1D_2 \rightarrow {}^3H_4$ emission at 625nm, Figure 5.1. These transitions have already been assigned by Reeves and Khong. The spectra are included here for reference. A complete set of excitation spectra, which also show the absorption transitions in hyrdrogenated and tritiated crystals, is presented in the thesis of Reeves.

Broadband excitation spectra showing the $^3H_4 \rightarrow {}^3P_0$ absorption transitions were obtained by monitoring the $^1D_2 \rightarrow {}^3H_4$ and $^3P_0 \rightarrow {}^3H_6$ emission at 610nm, Figure 5.2. As expected blue pumping of the $^3H_4 \rightarrow {}^3P_J$ transitions was more efficient than red pumping of the $^3H_4 \rightarrow {}^1D_2$ transitions and most of the spectroscopy in the blue region could be performed with laser powers of less than 15mW. These absorption spectra to the $^3P_0$ singlet state are like those to the $^1D_2$ multiplet, with the centres appearing in the same order and with similar relative intensities. Some additional weaker transitions also appear in the blue spectra and it will be shown that these are due to absorption to the $^1I_6$ multiplet of praseodymium.

Broadband excitation spectra showing the $^3H_4 \rightarrow {}^3P_1$ absorption transitions were also obtained by monitoring the emission at 610nm, Figure 5.3. A broad excitation band appears in these spectra and is attributed to the lattice phonon and hydrogen vibrational modes which couple to the $^3P_0$ electronic state. The phonon bands associated with these Pr^{3+} centres were studied by Reeves [77].

5.1.2 Selective Excitation Spectra

Site-selective excitation spectra showing absorption transitions to the $^3P_0$, $^3P_1$ and $^1I_6$ multiplets in the deuterated crystals are shown in Figures 5.4, 5.5 and 5.6. These were obtained by monitoring the $^1D_2(1) \rightarrow {}^3H_4(1)$ or $^1D_2(1) \rightarrow {}^3H_5(1)$ fluorescence transitions, which were identified by Reeves and Khong. The principle excitation transitions of each centre are listed in Tables 5.1 and 5.2. Reeves observed small isotopic shifts in the $^3H_4 \rightarrow {}^1D_2$ transition energies between the hydrogen and deuterium varieties of each centre, due to the electron-phonon interaction. Similar shifts are also exhibited by the $^3H_4 \rightarrow {}^3P_0$ transitions.

The $^3P_0$ levels of the $C_{4v}F^-$, $C_{4v}H^-$ and $C_{4v}D^-$ centres were identified by Jacobs and Reeves. $^3P_0$ is a γ_1 singlet state. In this study a second weaker absorption transition was found for each centre in the region of the $^3H_4(1) \rightarrow {}^3P_0$ transition, Figure 5.4. This was unexpected, although it might be a spin forbidden $^3H_4 \rightarrow {}^1I_6$ transition. These are usually very weak and are rarely observed in other hosts.

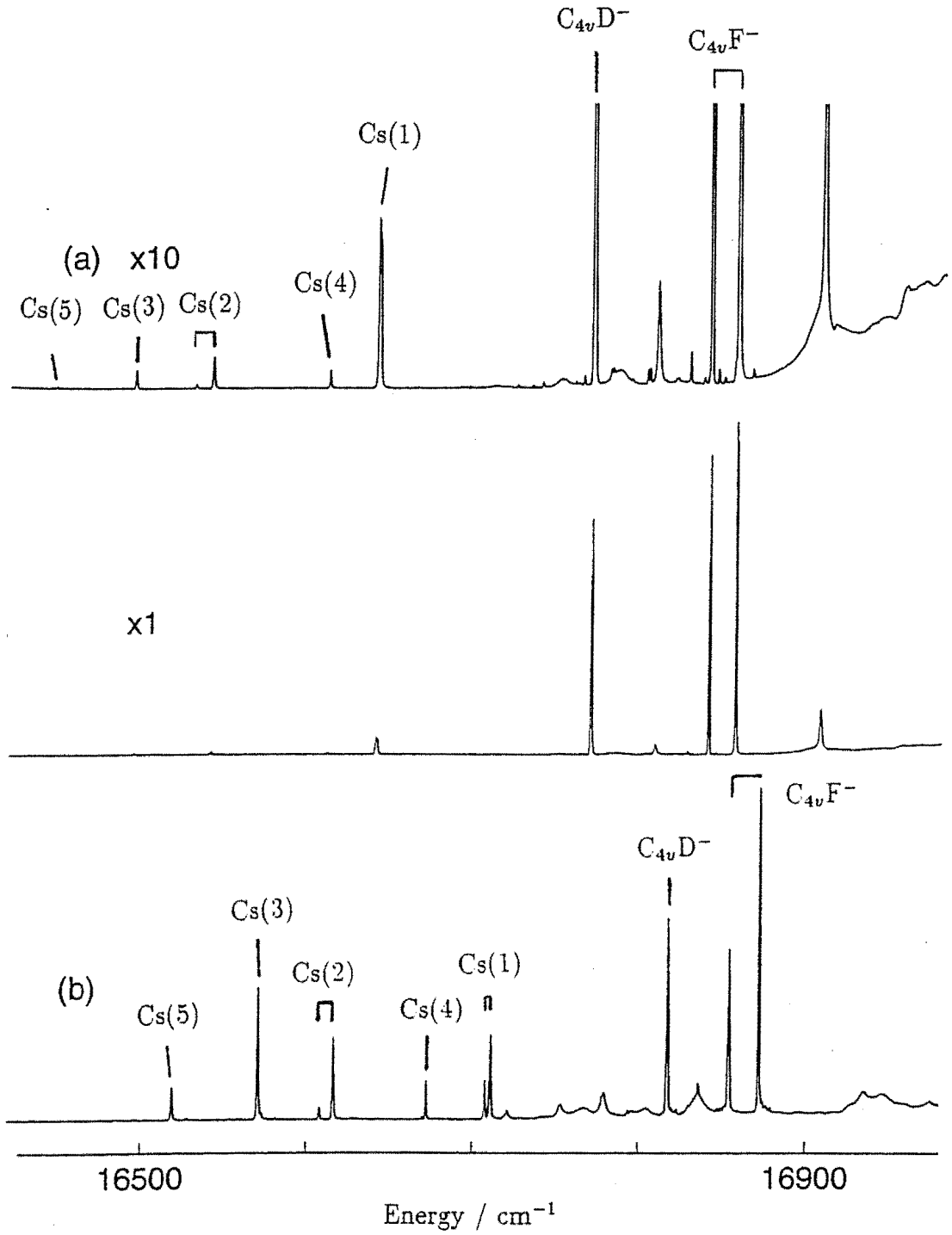

Figure 5.1: Broadband excitation spectra showing the $^3H_4 \rightarrow {}^1D_2$ transitions, while monitoring the fluorescence at 625nm in the (a) CaF_2:Pr^{3+}:D^- and (b) SrF_2:Pr^{3+}:D^- crystals.

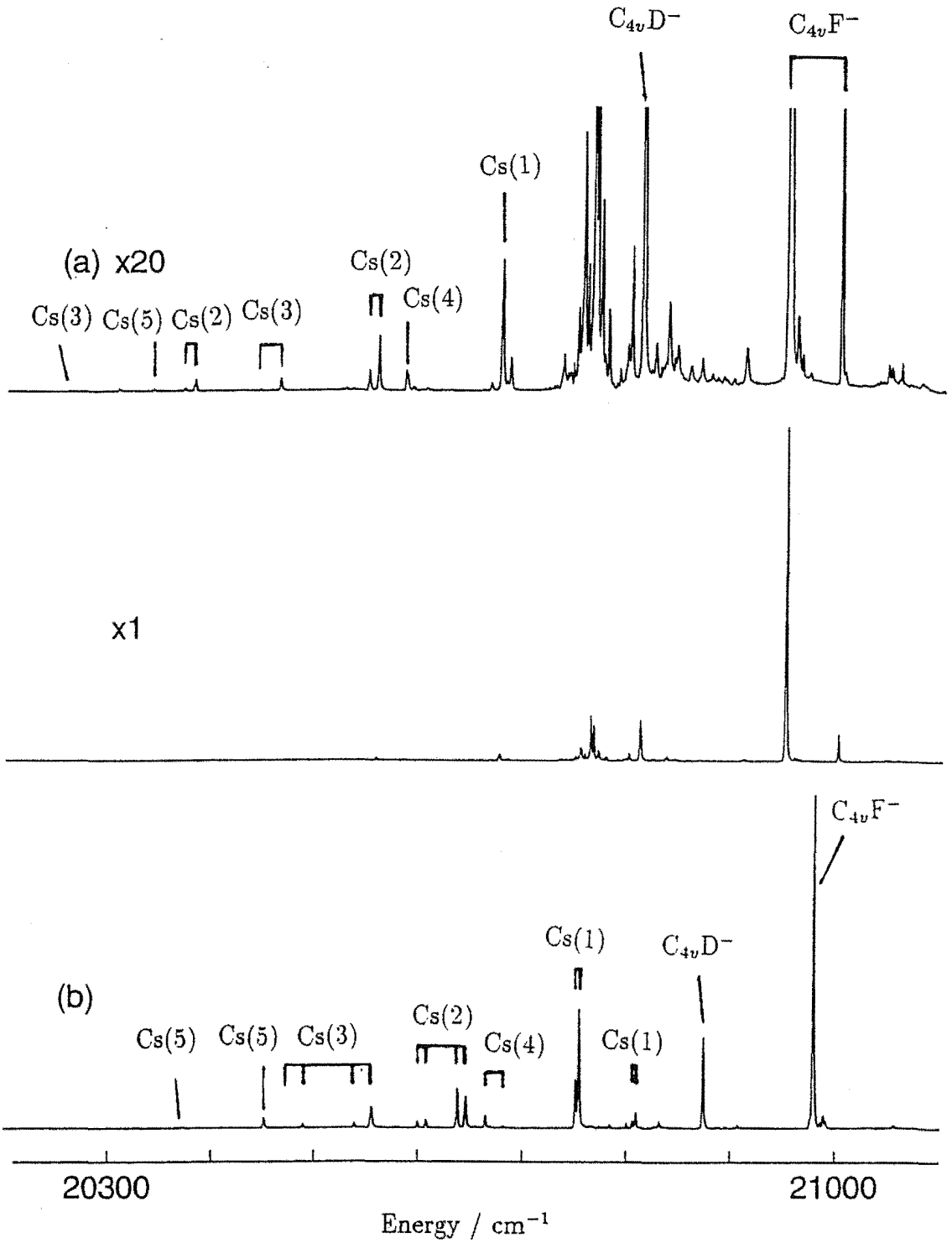

Figure 5.2: Broadband excitation spectra showing the $^3H_4 \rightarrow {}^3P_0$ transitions, while monitoring the fluorescence at 610nm in the (a) CaF_2:Pr^{3+}:D^- and (b) SrF_2:Pr^{3+}:D^- crystals.

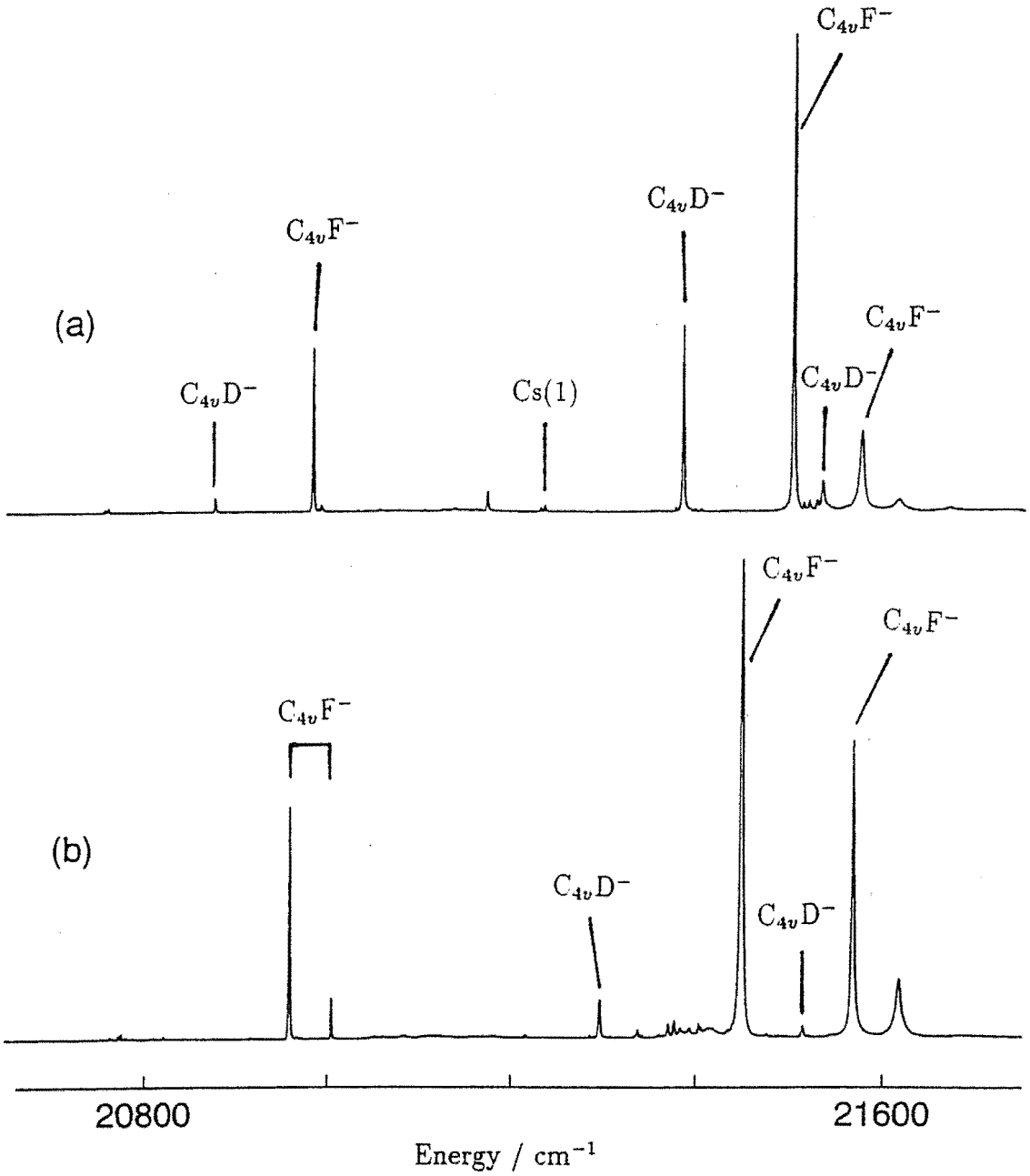

Figure 5.3: Broadband excitation spectra showing the $^3H_4 \rightarrow {}^3P_1$ transitions, while monitoring the fluorescence at 610nm in the (a) SrF_2:Pr^{3+}:D^- and (b) CaF_2:Pr^{3+}:D^- crystals.

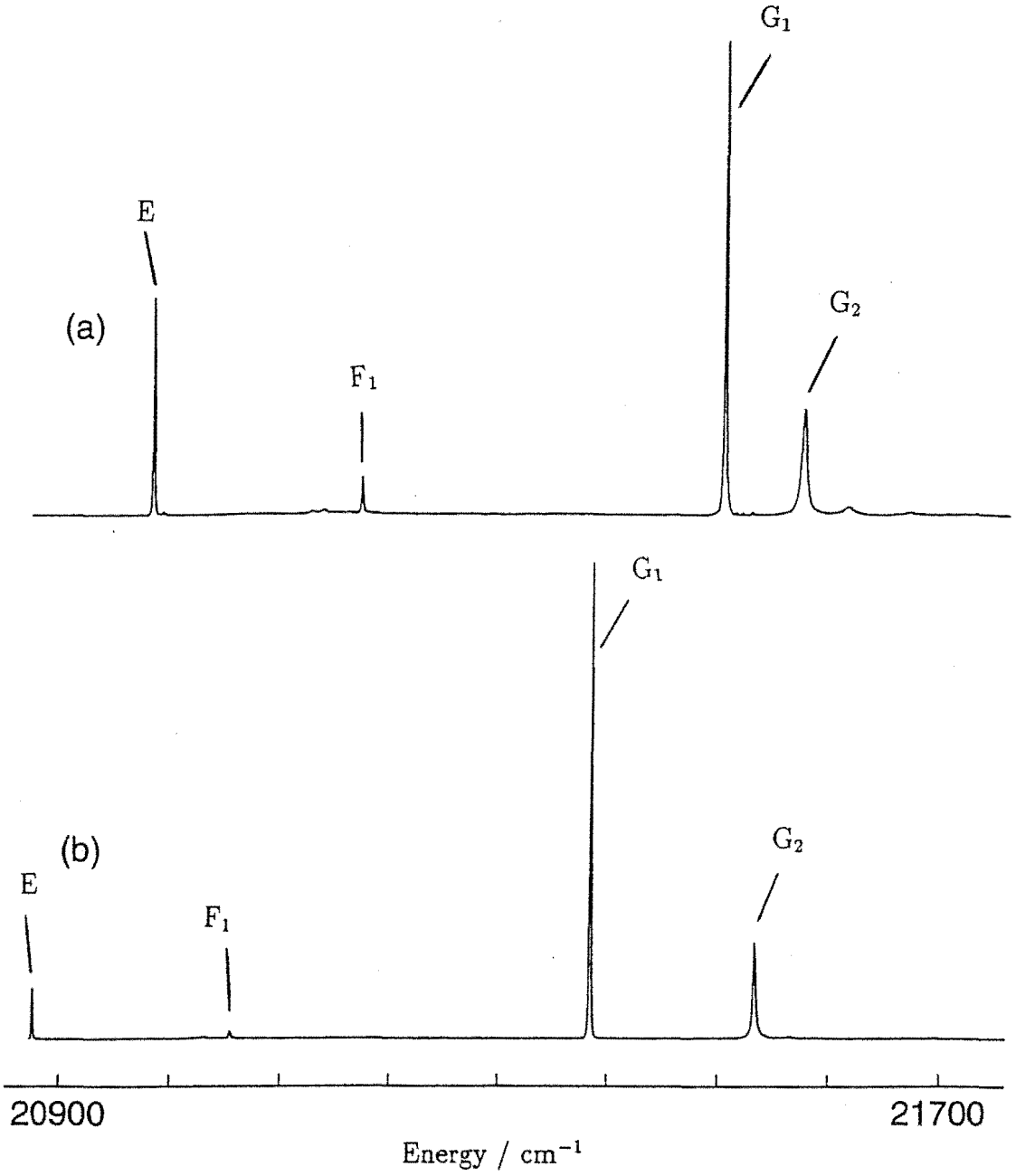

Figure 5.4: Selective excitation spectra of the SrF_2:Pr^{3+}:D^- crystal showing the $^3H_4 \rightarrow {}^3P_0$, $^3H_4 \rightarrow {}^1I_6$ and $^3H_4 \rightarrow {}^3P_1$ transitions of (a) the $C_{4v}F^-$ centre and (b) the $C_{4v}D^-$ centre.

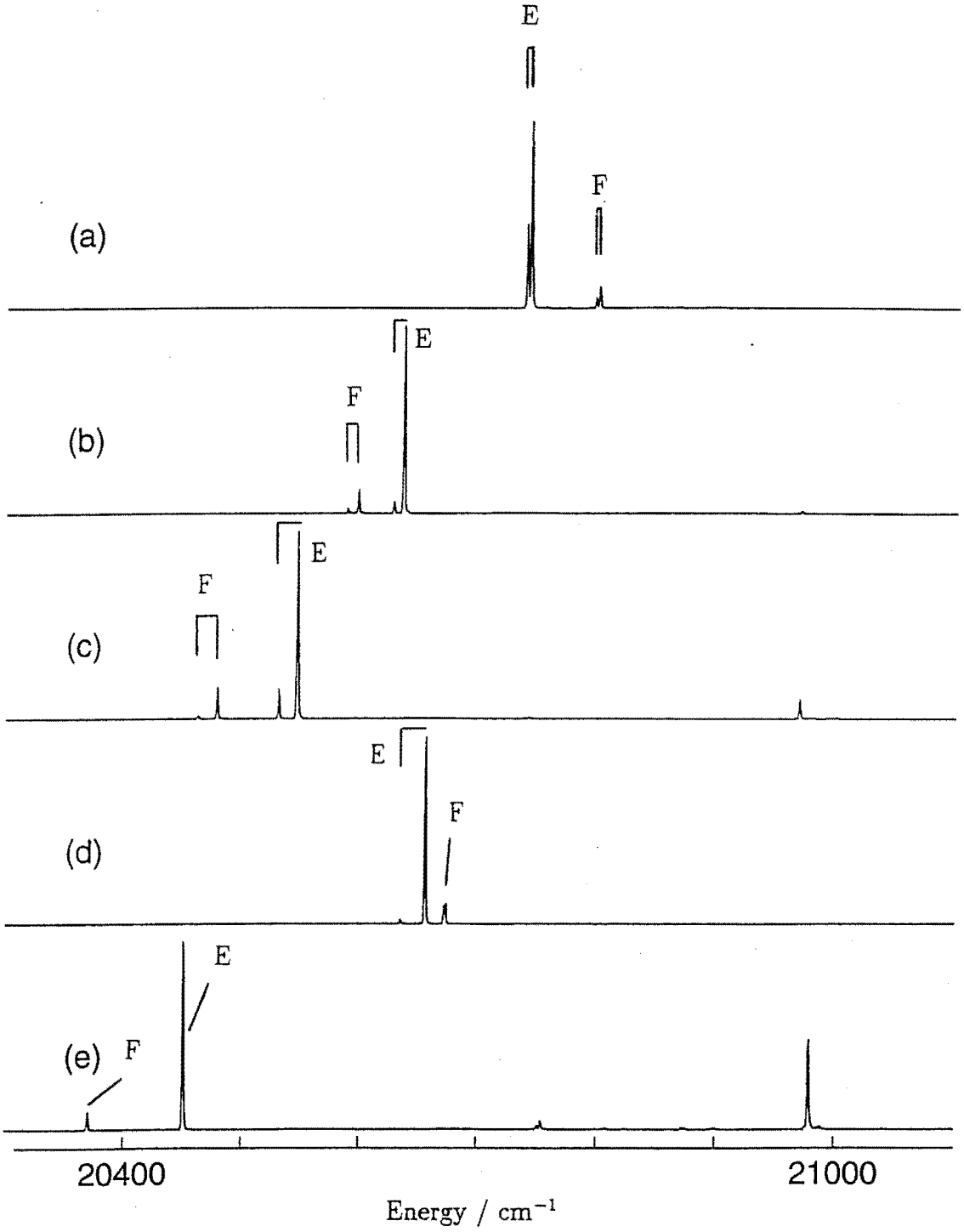

Figure 5.5: Selective excitation spectra of centres in the SrF_2:Pr^{3+}:D^- crystal showing the $^3H_4 \rightarrow {}^3P_0$ and $^3H_4 \rightarrow {}^1I_6$ transitions; (**a**) Cs(1) (**b**) Cs(2) (**c**) Cs(3) (**d**) Cs(4) and (**e**) Cs(5).

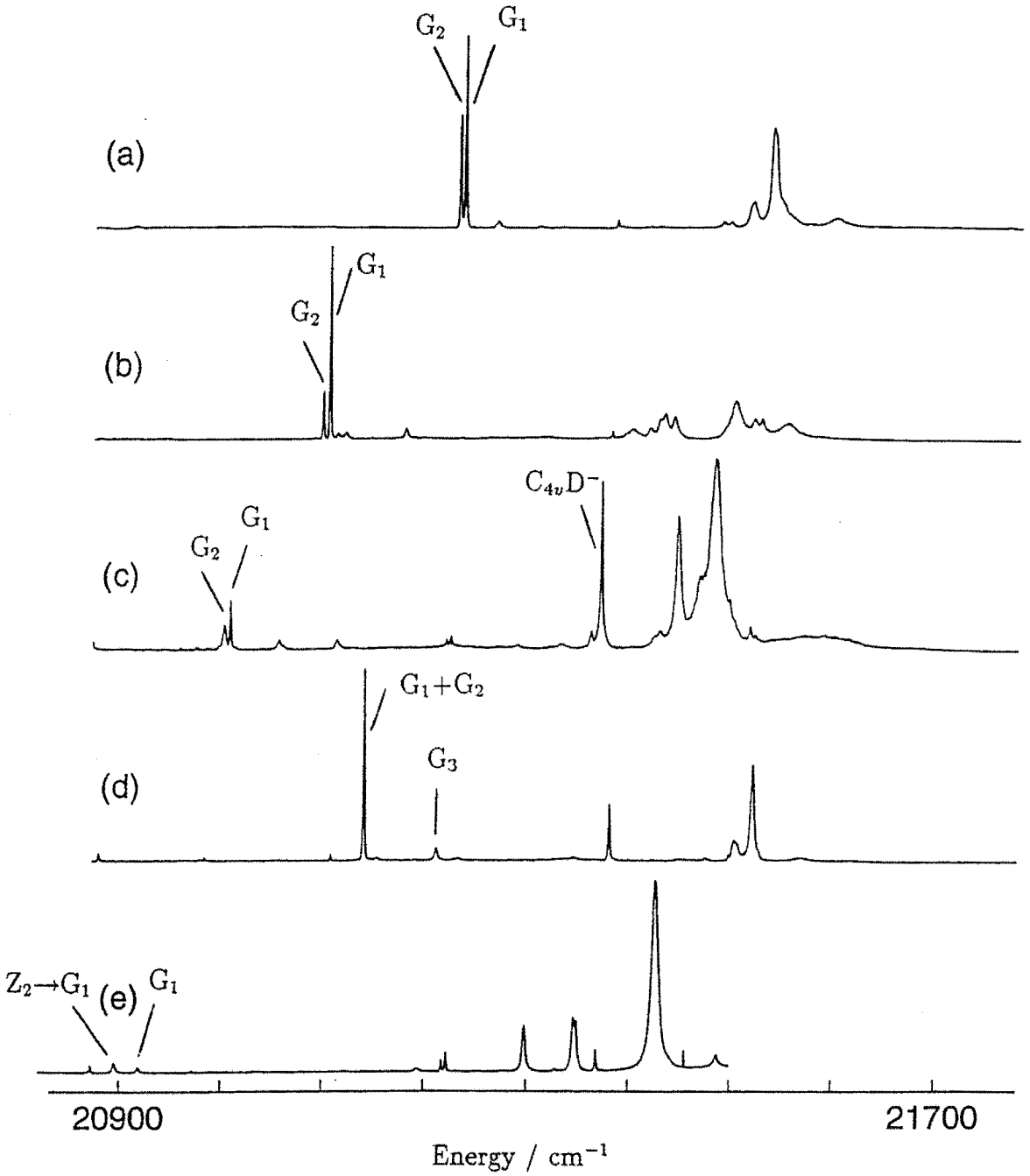

Figure 5.6: Selective excitation spectra of centres in the SrF_2:Pr^{3+}:D^- crystal showing the $^3H_4 \rightarrow {}^3P_1$ transitions; (a) Cs(1) (b) Cs(2) (c) Cs(3) (d) Cs(4) and (e) Cs(5).

Table 5.1: The energy levels of the hydrogenic centres in the SrF_2 host, in units of cm^{-1}. These energies have an uncertainty of $\pm 0.2 cm^{-1}$. *Level obtained by Reeves.

Centre	$^3H_4(Z_2)$		$^1D_2(\gamma_1)$		$^3P_0(\gamma_1)$		$^1I_6(\gamma_1)$	$^3P_1(\gamma_5)$	$^3P_1(\gamma_2)$
	H^-	D^-	H^-	D^-	H^-	D^-	D^-	D^-	D^-
C_{4v}	-	-	*16814.7	*16815.2	*20873.6	20871.1	21052.2	21386.4	21533.9
Cs(1)	3.3	3.4	16706.7	16706.5	20752.6	20750.9	20806.9	21236.5	-
Cs(2)	7.6	8.4	16611.2	16612.0	20643.1	20642.8	20605.7	21104.4	-
Cs(3)	16.1	16.4	16564.4	16566.6	20552.2	20554.0	20489.0	21011.9	-
Cs(4)	22.2	21.8	16665.8	16667.3	20663.3	20662.8	20680.3	21142.0	21212.4
Cs(5)	-	-	16514.0	16517.9	20446.5	20450.4	20372.1	20918.8	-

Table 5.2: The energy levels of the hydrogenic centres in the CaF_2 host, in units of cm^{-1}. These energies have an uncertainty of $\pm 0.2 cm^{-1}$. *Level obtained by Reeves.

Centre	$^3H_4(Z_2)$		$^1D_2(\gamma_1)$		$^3P_0(\gamma_1)$		$^1I_6(\gamma_1)$	$^3P_1(\gamma_5)$	$^3P_1(\gamma_2)$
	H^-	D^-	H^-	D^-	H^-	D^-	D^-	D^-	D^-
C_{4v}	-	-	*16754.8	*16754.5	*20815.4	*20811.9	-	21299.7	21513.6
Cs(1)	-	0.5	16627.3	16627.8	-	20676.9	20585.5	-	-
Cs(2)	-	9.6	16529.0	16530.3	-	20559.7	20383.2	-	-
Cs(3)	-	18.4	16483.9	16486.2	-	20463.9	20268.1	-	-
Cs(4)	-	19.9	16597.0	16598.5	-	20585.1	20462.8	-	-
Cs(5)	-	-	16436.4	16440.6	-	20345.0	20151.4	-	-

Polarisation-ratio measurements show that it is a singlet state in all of these centres. It is possible to mix states of the same irrep through higher order crystal-field interactions. For this reason the stronger line is attributed to the $^3P_0$ state and the weaker line to a γ_1 state of the $^1I_6$ multiplet, which gains intensity due to its proximity to the $^3P_0$ level. There are two γ_1 levels in the $^1I_6$ multiplet. This transition to the $^1I_6$ multiplet has also been reported by Boonyarith et al [14] and by Tissue and Wright [88], who have observed it in the $C_{4v}F^-$ centre of CaF_2. In both cases they confirmed its assignment through Zeeman spectroscopy.

The multi-hydrogenic ion Cs centres also exhibit this transition to the $^1I_6$ multiplet, Figure 5.5. In the Cs(1), Cs(2), Cs(3) and Cs(4) centres the $^3H_4(1) \rightarrow {}^3P_0$ and $^3H_4(1) \rightarrow {}^1I_6(1)$ absorption transitions exhibit a common splitting. This splitting arises from the doublet γ_5 ground state of the parent C_{4v} symmetry centre. In lower-symmetry crystal fields this degeneracy is broken. The two resulting levels are both populated at 10K and the ground-state splitting is seen in absorption to singlet excited states. The Cs(5) centre does not exhibit such splittings in excitation to the $^1D_2(1)$, $^3P_0$ or $^1I_6(1)$ states. However both the Cs(3) and Cs(5) centres have another low lying excited state which is populated at 10K. The $^3H_4(3)$ level of Cs(3) is located at 37.3cm^{-1} and the $^3H_4(2)$ level of Cs(5) at 22.9cm^{-1}, in the SrF_2:Pr^{3+}:D^- crystal.

The γ_5 ground-state splitting in the low-symmetry centres will grow as the off-axis component of the crystal field increases. From the $^3H_4(2)$ levels in Table 5.1 the Cs centres can be placed in the following order of decreasing axial symmetry: Cs(5), Cs(1), Cs(2), Cs(3) and Cs(4).

Two absorption transitions to the $^3P_1$ multiplet were observed for the $C_{4v}F^-$ centre, Figure 5.4. The $^3P_1$ multiplet will comprise a singlet γ_2 state and a doublet γ_5 state in a crystal field of C_{4v} symmetry. Polarisation-ratio measurements established that the singlet state is the higher of the two energy levels, confirming the assignment of Jacobs, Table 5.5.

In comparison to the $^3H_4 \rightarrow {}^3P_1$ absorption transitions of the C_{4v} symmetry parent centres, the transitions of the Cs centres are quite weak, Figure 5.6. The singlet γ_2 state appears very weakly in the selective excitation spectra of the multi-hydrogenic centres. The $^3H_4(1)(\gamma_5) \rightarrow {}^3P_1(1)(\gamma_5)$ transition of the parent centre is clearly split into two transitions in the Cs(1), Cs(2) and Cs(3) centres. This splitting is different from the ground-state splitting which was observed in the other excitation spectra.

Tables 4.15 to 4.18 show that two distinct γ_1 transitions should become apparent on breaking the C_{4v} symmetry. The observed splitting will thus correspond to the energy difference between the two γ_1 transitions. Two weaker transitions should also arise in C_s symmetry centres from the breaking of the γ_5 degeneracies. These were not identified in any of these spectra. No splitting was observed in the absorption transitions to the $^3P_1(1)$ level of the Cs(4) and Cs(5) centres. Since a ground-state splitting has been observed for the Cs(4) centre, this suggests that the two γ_1 transitions overlap. The $^3H_4(2) \rightarrow {}^3P_1(1)$ transition is stronger than the

$^3H_4(1) \rightarrow {}^3P_1(1)$ transition in the excitation spectrum of the Cs(5) centre.

Since the ground-state splittings of the Cs centres are known, it should be possible to deduce the $^3P_1$ doublet splitting of each centre from these spectra. The energy difference between the two γ_1 transitions is either the sum of or the difference between the $^3H_4(1)$ and $^3P_1(1)$ doublet splittings. The former will be true if the doublets have split in the same sense, the latter if they split in the opposite sense. The observed splittings in the SrF_2:Pr^{3+}:D^- crystal are: Cs(1) $(5.3\pm0.2)cm^{-1}$, Cs(2) $7.9cm^{-1}$, Cs(3) $5.4cm^{-1}$ and Cs(4) $0.0cm^{-1}$. These correspond to $^3P_1$ doublet splittings of: Cs(1) $(-1.9\pm0.4)cm^{-1}$, Cs(2) $+0.5cm^{-1}$, Cs(3) $+11.0cm^{-1}$ and Cs(4) $+21.8cm^{-1}$. A positive sign indicates splitting in the same sense. The $^3P_1$ doublet splitting follows the same trend observed for the ground state splitting, which was attributed to changes in the axial symmetry of the crystal field.

Non of the multi-hydrogenic ion centres exhibit strong absorption to the higher levels of the $^3P_1$ and $^1D_2$ multiplets. This could be due to the additional non-radiative decay channels accessible through coupling to the vibrational modes of the substitutional hydrogenic ions. Additional relaxation pathways shorten the excitation lifetime of the higher Stark levels, broadening the absorption transitions until they can no longer be distinguished. Such broadening is already apparent in the transitions to the $^3P_1(2)$ level in the $C_{4v}F^-$ and $C_{4v}D^-$ centres, Figure 5.4. The lifetime of the $^3P_1(1)$ state will also be affected by non-radiative relaxation to the $^3P_0$ state. This may account for the apparent reduction in absorption to the $^3P_1(1)$ level in the hydrogenic centres.

A distinct absorption band appears in the excitation spectrum of each of the hydrogenic centres. Most of these excitation features have energies 500 to $800cm^{-1}$ greater the $^3H_4(1) \rightarrow {}^3P_0$ zero-phonon transition. This suggests that they are due to the local vibrational modes of the deuterium ions, which are coupled to the $^3P_0$ electronic state. However, the spectral distribution of these levels is quite different from that observed by Reeves when he studied the vibrational modes of these centres. These levels also have energies which are higher than those of the lattice phonon modes, which terminate at approximately $600cm^{-1}$. The origin of these excitation features was not established in this study and they warrant further investigation.

5.1.3 Fluorescence Spectra

The dominant relaxation pathways of the $C_{4v}F^-$ centre are radiative for both red and blue excitation. Exciting the Pr^{3+} ions to the $^3P_0$, $^1I_6$ or $^3P_1$ multiplets produces fluorescence from the $^3P_0$ multiplet and also a small amount of $^1D_2$ fluorescence. Blue pumping of the $C_{4v}D^-$ centre produces a significantly higher fraction of $^1D_2$ fluorescence and blue pumping of the $C_{4v}H^-$ centre even more. Most of the fluorescence obtained when exciting the Cs centres to the $^3P_0$ or $^3P_1$ multiplets emanates from the $^1D_2$ multiplet. Reeves [77] demonstrated that non-radiative relaxation, via coupling to the vibrational modes of the hydrogenic ions, accounted for the observed feeding of the $^3P_0$ population to the $^1D_2$ multiplet.

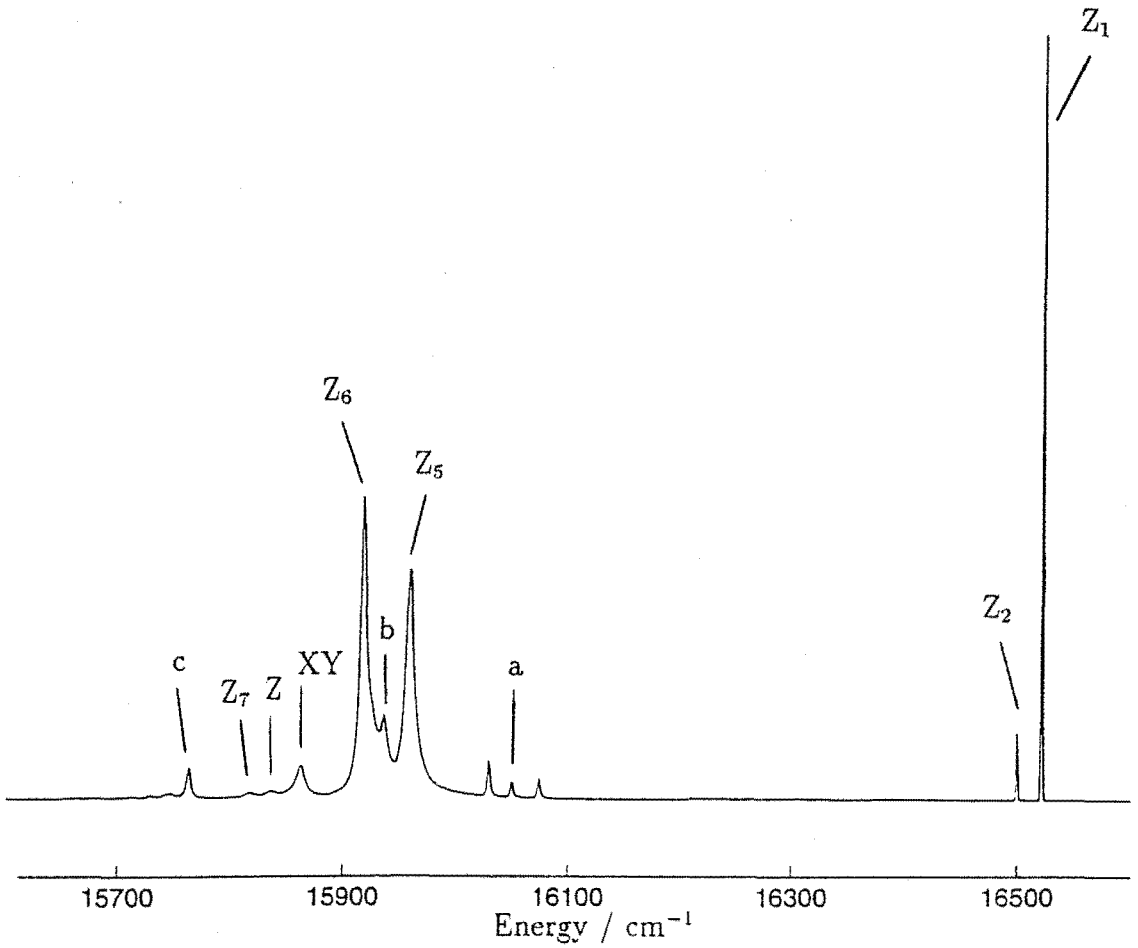

Figure 5.7: A fluorescence spectrum showing the $^1D_2 \rightarrow {}^3H_4$ transitions of the Cs(5) centre in the SrF_2:Pr^{3+}:D^- crystal.

Reeves [77] has produced fluorescence spectra showing the $^1D_2 \rightarrow {}^3H_4$ emission from the Cs(1), Cs(2), Cs(3) and Cs(4) centres. Figure 5.7 is the equivalent fluorescence spectrum of the Cs(5) centre. This clearly shows weak emission to the $^3H_4(2)$ level at 22.9cm^{-1}. Reeves observed multiple local-mode vibronic lines in the spectra of the Cs centres. From the number of lines observed he concluded that the Cs(1), Cs(2) and Cs(4) centres each comprise just one substitutional hydrogenic ion site, while the Cs(3) centre comprises at least two. The Cs(5) centre exhibits only five vibronic lines, which suggests that it also contains one substitutional hydrogenic ion site. The electronic levels of the $^3H_4$ multiplet and the deuterium ion local mode energies are listed in Table 5.3 for the Cs(5) centre.

Fluorescence spectra showing the $^1D_2 \rightarrow {}^3H_5$ inter-multiplet transitions were obtained for each Cs centre, Figure 5.8. The vibronic side-bands of the zero-phonon

Table 5.3: The energy levels observed in the $^1D_2 \rightarrow {}^3H_4$ fluorescence spectrum of the Cs(5) centre in the SrF_2:Pr^{3+}:D^- crystal, in units of cm^{-1}. These energies have experimental uncertainties of $\pm 2cm^{-1}$.

Site	State	Energy
Pr^{3+} Electronic Levels	$Z_1(\gamma_5)$	0
	$Z_2(\gamma_1)$	22.9
	$Z_5(\gamma_1)$	562
	$Z_6(\gamma_5)$	604
	$Z_7(\gamma_3)$	705
Interstitial D^- Local Mode	xy	659
	z	686
Substitutional D^- Local Mode	a	471
	b	585
	c	759

electronic transitions are much weaker in these spectra, as they are affected by a pseudo-quadrupole selection rule which favours $\Delta J=2$ vibronic transitions [48]. As a consequence these spectra are dominated by the electronic transitions to the lowest levels of the $^3H_5$ multiplet. The $^1D_2 \rightarrow {}^3H_6$ transitions of the hydrogenic centres are shown in Figure 5.9. These spectra show how the Stark levels of the $^3H_5$ and $^3H_6$ multiplets respond to the changes in the crystal-field, caused by the successive substitution of F^- ions by D^- ions. Polarisation ratios were obtained for several of the centres.

In the low-symmetry centres the $^1D_2(1)(\gamma_1) \rightarrow {}^3H_6(1)(\gamma_5)$ transition of the parent centre has clearly split into two distinct transitions, which have quite different intensities. It is easy to show, using the C_{4v} approximation, that these distinct transitions should instead exhibit similar intensities. A high-resolution infrared absorption scan of the $^3H_4(1)(\gamma_5) \rightarrow {}^3H_6(1)(\gamma_5)$ transition in the $C_{4v}F^-$ centre revealed a $(0.53\pm0.10)cm^{-1}$ splitting in the $^3H_6(1)$ level. This suggests that there is some, as yet unidentified, interaction between the two states of the doublet, which might also account for the asymmetric splitting observed in the Cs centres.

Transitions terminating on γ_1 and γ_5 states of the parent centre dominate these spectra. The $^1D_2(1)$ level has thus been assigned as a γ_1 state. Reeves observed that this level exhibits the characteristics of both a γ_1 and a γ_3 state. The results obtained in this study indicate that the former is dominant and the $^1D_2(1)$ level will henceforth be treated as a γ_1 state.

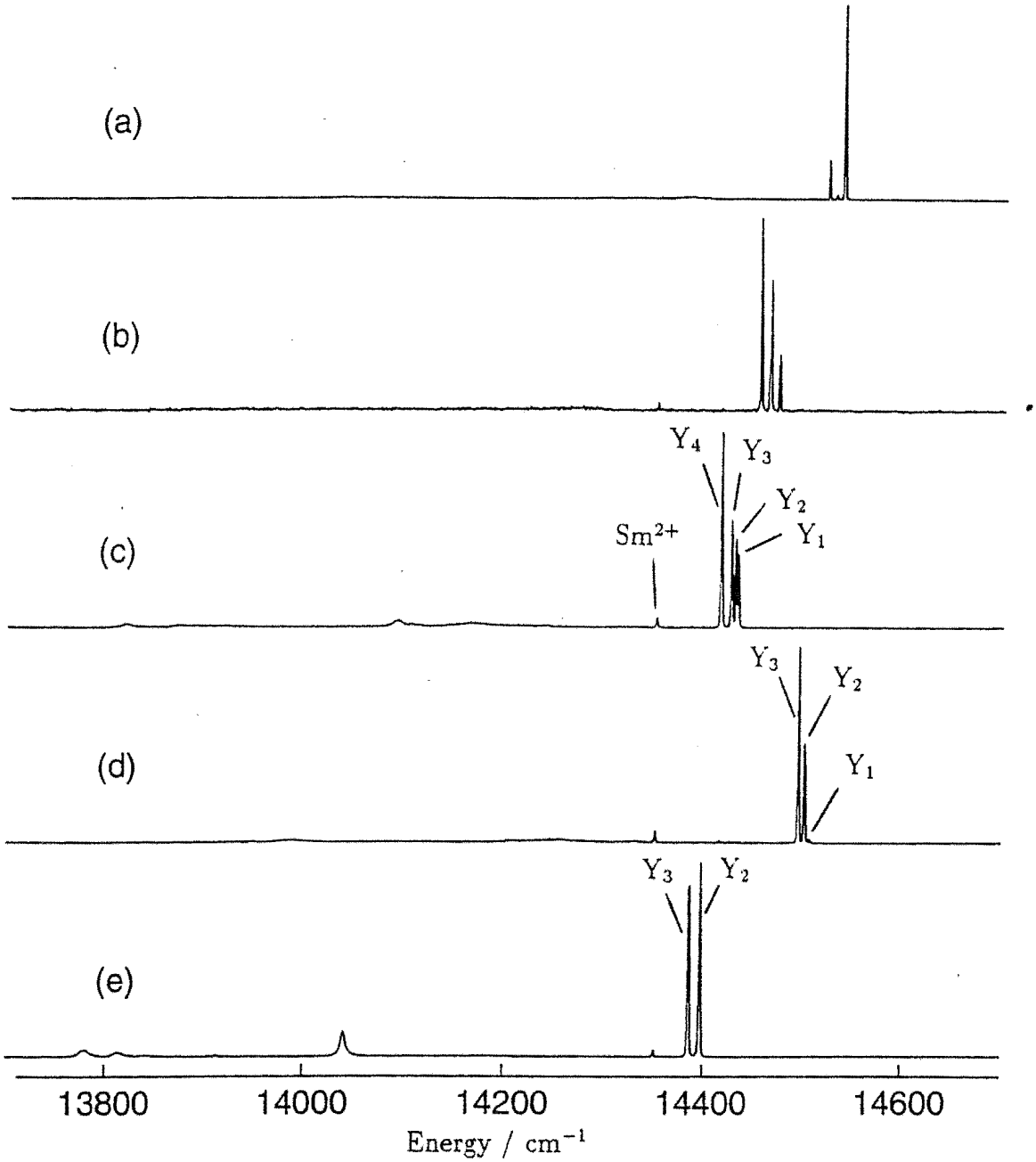

Figure 5.8: Fluorescence spectra of centres in the SrF_2:Pr^{3+}:D^- crystal showing the $^1D_2 \rightarrow {}^3H_5$ transitions of: (a) Cs(1) (b) Cs(2) (c) Cs(3) (d) Cs(4) and (e) Cs(5).

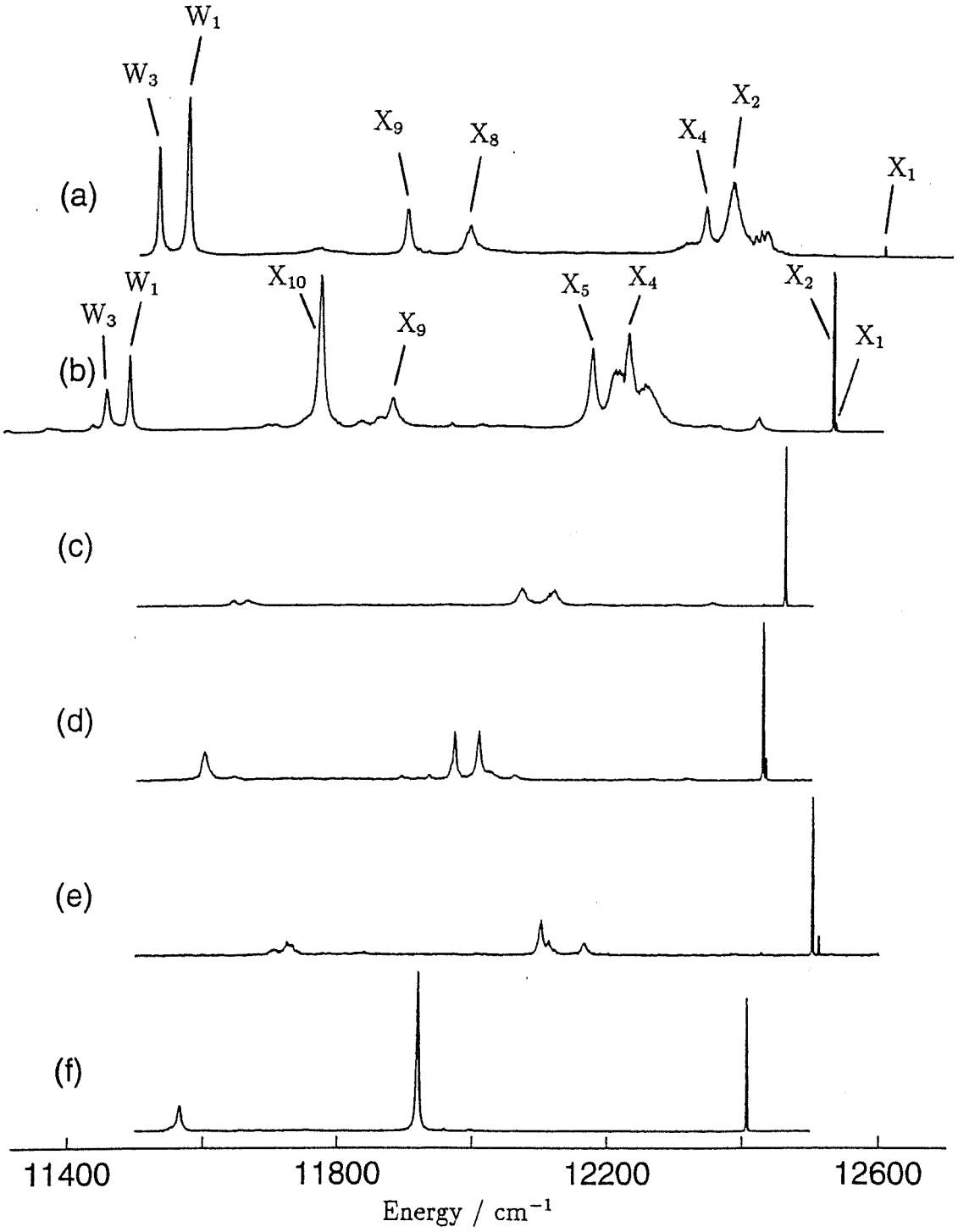

Figure 5.9: Fluorescence spectra of centres in the SrF_2:Pr^{3+}:D^- crystal showing the $^1D_2 \rightarrow {}^3H_6$ transitions of: (a) $C_{4v}D^-$ (b) Cs(1) (c) Cs(2) (d) Cs(3) (e) Cs(4) and (f) Cs(5).

Table 5.4: The energy levels of the hydrogenic photoproduct centres observed in excitation, in units of cm^{-1}. These energies have an uncertainty of $\pm 0.2 cm^{-1}$.

Host	Centre	$^3H_4(Z_2)$		$^1D_2(\gamma_1)$		$^3P_0(\gamma_1)$
		H^-	D^-	H^-	D^-	D^-
SrF_2	Cs(2)*	17.3	17.2	16664.2	16664.7	20682.0
	Cs(3)*	13.0	13.4	16566.9	16568.7	20574.6
	Cs(4)*	11.2	11.8	16675.4	16676.7	20690.7
	Cs(5)*	-	-	16501.5	16504.2	20483.1
CaF_2	Cs(2)*	-	15.2	-	16578.0	20607.9
	Cs(3)*	-	15.9	-	16480.6	20486.0
	Cs(4)*	-	18.6	-	16597.3	20619.4
	Cs(5)*	-	-	-	-	20380.1

5.1.4 Photoproduct Centres

Photoproduct centres are obtained by bleaching the multi-hydrogenic ion Cs centres. The Cs(2), Cs(3), Cs(4) and Cs(5) centres were all found to have one discrete photoproduct each. These are shown spectroscopically in Figure 5.10. The principle excitation transitions of each photoproduct centre are listed in Table 5.4. All of these Cs* centres exhibit splittings in the doublet γ_5 ground state of the parent centre, suggesting that none of them are C_{4v} symmetry configurations. Like its Cs(3) parent centre, the Cs(3)* centre has a low lying Z_3 level, which is populated at 10K. This is located at $27.9 cm^{-1}$ in the SrF_2:Pr^{3+}:D^- crystal. Two weaker excitation transtions, shorter in wavelength than the dominant $Z_1 \rightarrow E$ transition of the Cs*(5) centre, appear after bleaching the Cs(5) centre, Figure 5.10(d). They seem to be associated with the Cs*(5) centre and are erased when it is bleached. These are tentatively assigned as absorption transitions to the $^1I_6$ multiplet of the Cs*(5) centre.

Polarisation ratios were not obtained for the Cs* centres in this study. Instead, their model configurations and symmetries will be deduced from the bleaching behaviour of the Cs centres. The irrep labels given in Table 5.4 have been assigned through spectroscopic comparison with the Cs centres.

Reeves observed two new $^3H_4 \rightarrow {}^1D_2$ transitions after bleaching the Cs(4) centre, which he labeled P_1 and P_2. Bleaching experiments, which will be reported in the next chapter, confirmed that these are the $Z_1 \rightarrow D_1$ and $Z_2 \rightarrow D_1$ transitions of the Cs(4)* photoproduct centre.

5.2 Polarisation Behaviour

5.2.1 Experimental Polarisation Ratios

Polarisation ratios were measured for each of the Cs centres to establish their crystal-field symmetries and to assign irrep labels to the experimentally determined energy levels. It is difficult to perform such polarisation measurements on bleachable centres, as exposure to the laser beam depopulates those orientations which are being selectively excited. Thus the assumption that all orientations are equally populated, which is used in the calculation of these ratios, is no longer valid.

Khong [53] obtained some polarisation ratios by producing polarised fluorescence spectra for all of the Cs centres. It is difficult to obtain the relative intensities of different transitions from spectra, as bleaching occurs during the time taken to scan the monochrometer. To overcome this problem Khong pre-bleached the centres before beginning each scan. This method can produce errors in the measured ratios for several reasons. Two polarisation spectra are required to obtain each ratio. If these are to be comparable it is important that the centre receives the same pre-bleaching treatment before each scan. During pre-bleaching different orientations of the centre may be excited via different CTMs of the excitation transition (Section 4.3). These orientations will bleach at the different rates and so the assumption that all orientations of the centre are equally populated will be invalid. In some cases this will affect the measured polarisation ratios. To interpret such ratios the ionic configuration of the centre, the bleaching mechanisms and the irrep labels of the two transitions must already be known.

In these experiments a quite different method was used to measure polarisation ratios of unbleached centres. The crystal is attached to the cold head of the helium refrigerator which is mounted onto a XY table. This enables the crystal to be manœuvred through the path of the excitation beam, which propagates in the Z direction. A beam block is used as a shutter and this is placed between the laser and the crystal.

After tuning the dye laser and the monochrometer to the excitation and fluorescence transitions of interest the shutter is closed. The table is then moved very slightly so that a virgin piece of unexposed crystal lies in the path of the excitation beam. The intensity of the analysed fluorescence can then be measured by opening the shutter for a period of less than 2s. This is the time required to obtain a single reading from the photon counter, for which the set integration time is 1s. Without moving the crystal, the intensity of the alternate polarisation is measured to obtain a ratio. The crystal is then translated and the measurement repeated, but this time the order in which the two polarisations are sampled is reversed. This procedure is repeated several times, with each ratio obtained from a piece of virgin crystal. The final experimental ratio is the average of all of these ratios. Recording transposed pairs of ratios cancels out the error caused by bleaching, which will occur during the brief time the shutter is open.

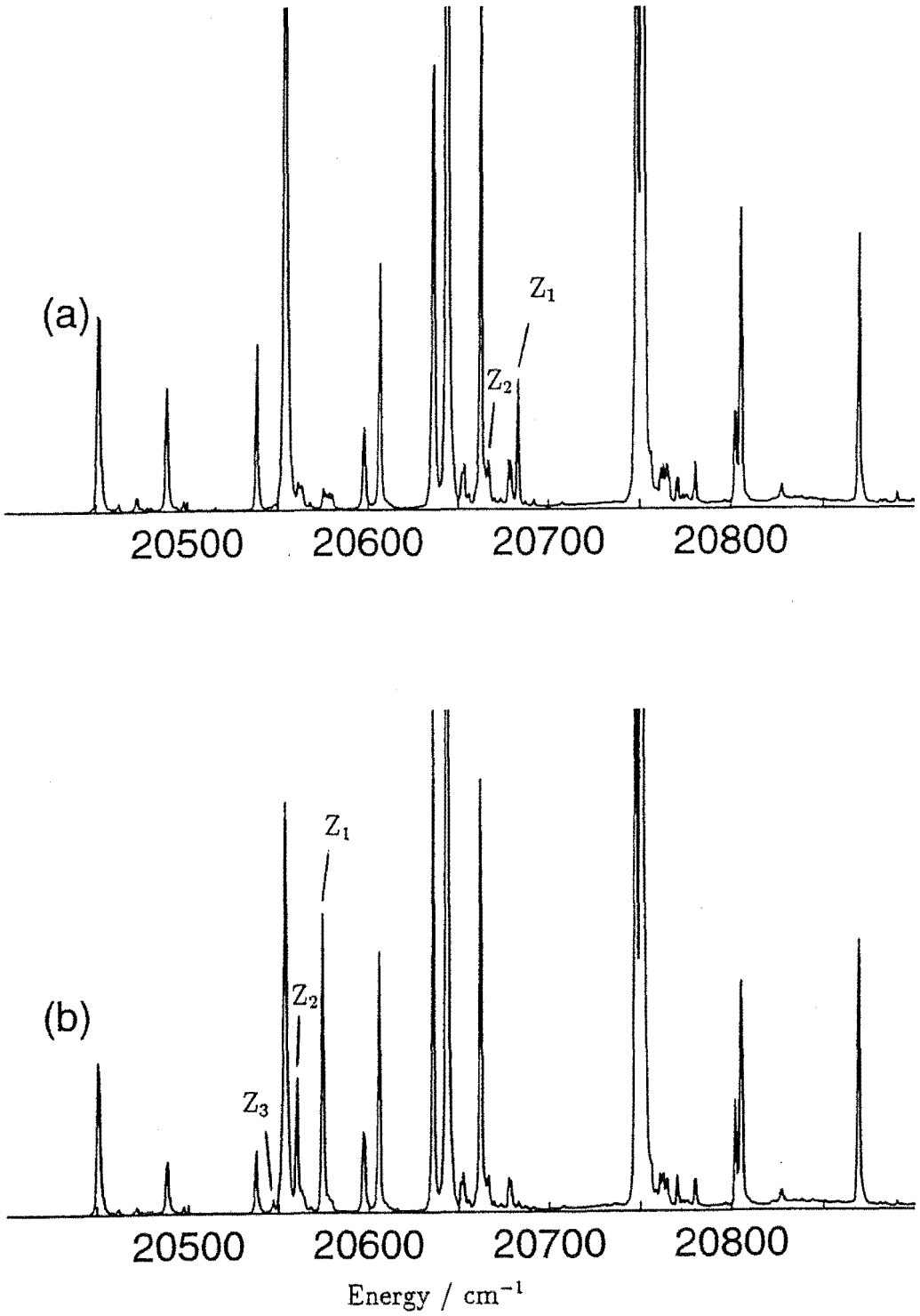
(a)
Z1
Z2
20500
20600
20700
20800
(b)
Z1
Z2
Z3
20500
20600
20700
20800
Energy / cm-1

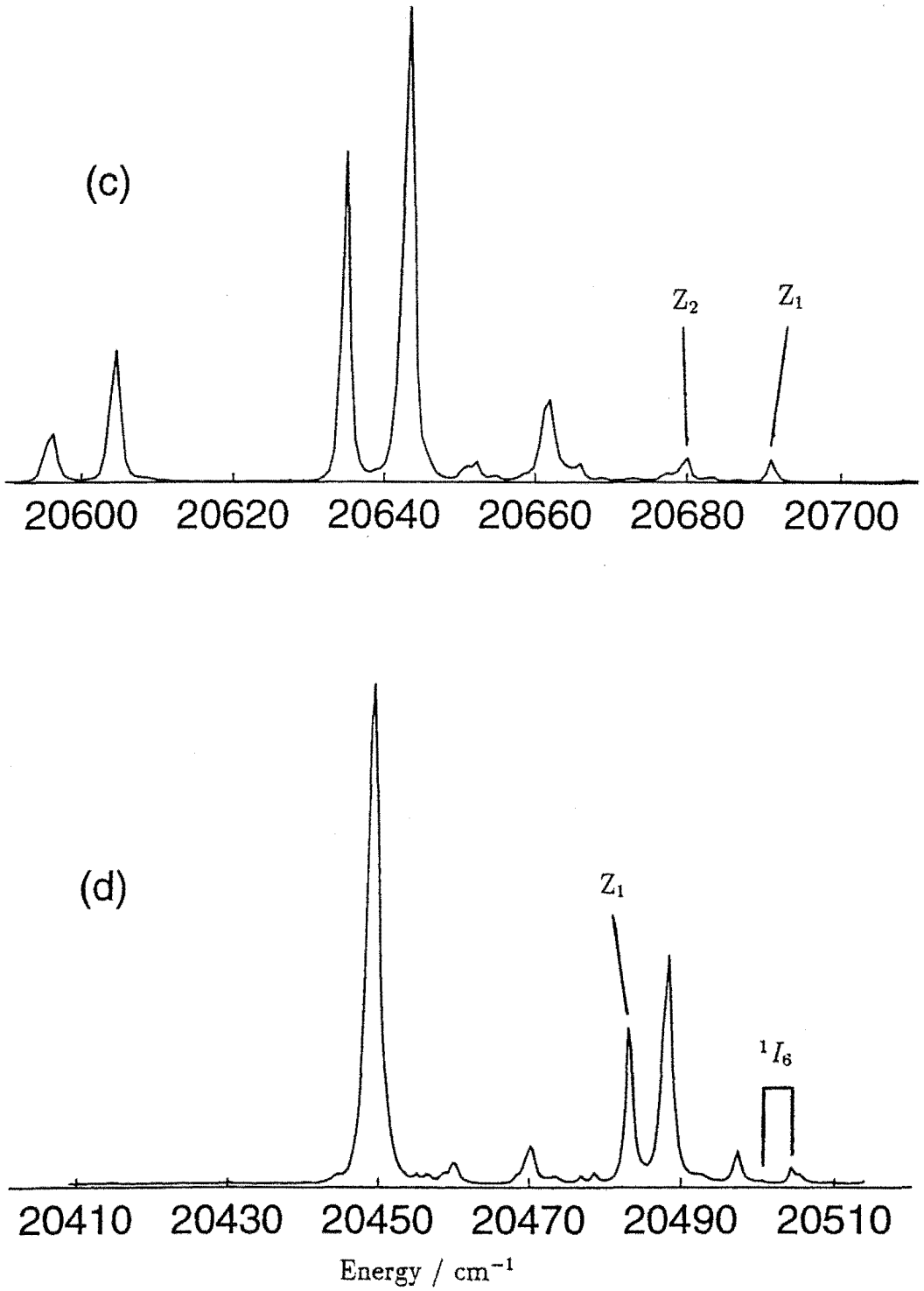

Figure 5.10: Broadband excitation spectra showing the $^3H_4 \rightarrow {}^3P_0$ transitions of (a) the $Cs(2)^*$ centre, (b) the $Cs(3)^*$ centre, (c) the $Cs(4)^*$ centre and (d) the $Cs(5)^*$ centre, while monitoring the fluorescence at 610nm in the $SrF_2:Pr^{3+}:D^-$.

As expected transposing the order in which the two polarisations are sampled makes a significant difference to the ratios obtained, often up to 50%, depending upon the laser power and the bleaching rate of the centre. However the averaged ratios are more consistent, typically varying by less than 5%. The largest source of error arises from the background count and the quantum noise of the detector/photon-counting system.

Experimental fluorescence polarisation ratios for each centre in the SrF_2:Pr^{3+}:D^- crystal are listed in the last column of Table 5.5. This is a representative sample of transitions. Through knowing the transition energies in the $C_{4v}D^-$ parent centre, and by careful observation of how the energy levels change from centre to centre, a small set of candidate parent transitions can be identified in each case. From this set the appropriate parent transitions were deduced using the Cs centre ratios listed and the level assignments of Reeves. The polarisation ratios expected in the C_{4v} approximation are listed in Tables 4.15 to 4.18 for the various possible sub-symmetries. These tables were used to assign irrep labels to the Cs centre levels and to establish the Pr^{3+} ion site symmetries. The irrep assignments of the Cs centre levels must be compatible with those of the parent centre levels, Table 4.2. The polarisation ratios expected in the C_{4v} approximation could then be obtained from the tables and these are listed in the fifth column.

In the following chapter some bleaching curves will be presented for the Cs(2) centre. These will be used to show unequivocally that its Z_1 and Z_2 levels are γ_1 and γ_2 states respectively. This result fixes the ground-state irrep labels for all the C_s and C_{2v} symmetry hydrogenic centres. The G_1 and G_2 levels follow as it has already been established, for each centre, whether the $^3P_1$ doublet splitting is in the same sense as the ground-state splitting.

5.2.2 Cs Centre Symmetries

It has already been established that the Cs(1) centre has a crystal field with symmetry less than C_{4v}, as the ground-state doublet of the parent centre is clearly split. The $Z_1 \rightarrow E/D_1 \rightarrow Z_1$ ratios are all close to the 1:2 ratios expected for C_{2v}(a) or C_s(a) symmetry ionic configurations. This is consistent with the C_s(a) symmetry configuration which Reeves deduced from the bleaching behaviour of the Cs(1) centre, Figure 5.12(a). Polarisation ratios have also been obtained for the fluorescence transitions observed to the $^3H_6$ multiplet. These have been used to assign irrep labels to the $^3H_6$ levels of the Cs(1) centre. The X_4 and X_9 doublet γ_5 states of the parent centre are broadened sufficiently to conceal any low-symmetry splittings which might be present. In such cases it is necessary to consider the contributions of both fluorescence transitions to the observed polarisation ratio. Figures 5.9(a) and (b) together show how the $^3H_6$ levels change as the C_{4v} symmetry of the parent centre is broken by the introduction of a single substitutional deuterium ion.

The $Z_1 \rightarrow E/D_1 \rightarrow Z_1$ and $Z_1 \rightarrow F_1/D_1 \rightarrow Z_1$ ratios of the Cs(2) centre establish that it has a C_s(b) symmetry configuration. No C_{2v}(b) symmetry configurations

are possible through anion substitutions in the neighbourhood the Pr^{3+} ion. This symmetry assignment is also consistent with the ionic configuration proposed for the Cs(2) centre by Reeves, Figure 5.12(b).

The $Z_1 \rightarrow E/D_1 \rightarrow Z_1$ ratios of the Cs(4) centre indicate that it has either a C_{2v}(a) or C_s(a) configuration. Reeves proposed a C_{2v}(a) symmetry configuration for this centre, Figure 5.12(c). Both the Cs(2) and Cs(4) centres comprise two substitutional hydrogenic ions.

The Cs(3) centre must also have either a C_{2v}(a) or C_s(a) ionic configuration. Although a model has not yet been proposed for this centre, Reeves has demonstrated that it consists of at least three hydrogenic ions. The bleaching behaviour and fluorescence lifetimes of the Cs(3) centre will be discussed in the following sections and used to show that it has a C_s(a) configuration. The γ_1 and γ_2 irrep labels of the C_s group have been assigned to the Cs(3) levels in Table 5.5.

Spectra obtained for the Cs(5) centre show that it does not exhibit the low-symmetry doublet-state splittings observed in the other Cs centres. This suggests that it has the C_{4v} symmetry of the parent centre. The polarisation data presented in Table 5.5 supports this thesis by showing conclusively that the Z_2 level of the Cs(5) centre can not be attributed to a splitting of the $Z_1(\gamma_5)$ ground-state of the parent centre. The $Z \rightarrow E/D \rightarrow Z$ ratios alone are inconclusive and only eliminate C_{2v}(a) and C_s(a) symmetry configurations. The other low-symmetry configurations are ruled out by the $Z_1 \rightarrow G_1/D_1 \rightarrow Z_2$ ratio. This would be 1:0 for a γ_5 parent fluorescence transition. The 0:1 ratio implied by the 0.42 experimental value is only possible if the terminating state of the parent transition is a singlet. A 0:1 ratio also suggests that this is an E1 transition to a γ_1 state rather than an M1 transition to a γ_2 state. The strength of the $Z_2 \rightarrow E(\gamma_1)$ transition in the Cs(5) centre also supports this assignment. $D \rightarrow Y$ ratios were also obtained, for all the Cs centres, but are listed in Table 5.5 only for the Cs(5) centre.

5.2.3 A Spectroscopic Analysis of Symmetry Breaking

Fluorescence spectra showing $^1D_2 \rightarrow {}^3H_5$ transitions from several centres appear in Figure 5.11 and demonstrate the changes in the Stark levels from centre to centre. In Figure IV.1.1(a) Reeves [77] shows how the $^3H_5$ multiplet should respond as the crystal field changes from cubic to purely axial symmetry. As the axial component increases in strength the $\Gamma_4{}^1\gamma_5$ and $\Gamma_3\gamma_1$ levels cross over to become Y_2 and Y_3 respectively. The D_1 and D_2 levels of the $C_{4v}F^-$ centre were assigned as γ_3 and γ_1 states respectively. The spectrum in Figure 5.11(a) shows the fluorescence to the $Y_1(\Gamma_4\gamma_2)$, $Y_2(\Gamma_3\gamma_1)$ and $Y_3(\Gamma_4\gamma_5)$ levels in this centre. These have mutual separations of $26cm^{-1}$ and $64cm^{-1}$ respectively. Substitution of the interstitial F^- ion by a D^- ion increases the axial component of the crystal field and has reduced these separations to $23cm^{-1}$ and $43cm^{-1}$ respectively, Figure 5.11(b).

The Cs(4) centre has two substitutional D^- ions and a C_{2v}(a) symmetry ionic configuration. The off-axis component of the crystal field has not produced a

Table 5.5: Polarisation ratios for specific excitation and fluorescence transitions of the Pr^{3+} centres in SrF_2:Pr^{3+}:D^-. The Cs centre transitions are given alongside the appropriate parent transitions of the $C_{4v}D^-$ centre. The calculated ratios are those obtained in the C_{4v} approximation.

Centre	$C_{4v}D^-$ Transitions		Cs Transitions		Ratio X:Y	
	Excitation	Fluorescence	Excitation	Fluorescence	Calc'	Exp't
$C_{4v}F^-$	$Z_1(\gamma_5)\rightarrow F_1(\gamma_1)$	$E(\gamma_1)\rightarrow Z_1(\gamma_5)$			1:2	0.64
	$Z_1(\gamma_5)\rightarrow G_1(\gamma_5)$				1:0	14.0
	$Z_1(\gamma_5)\rightarrow G_2(\gamma_2)$				1:2	0.61
Cs(1)	$Z_1(\gamma_5)\rightarrow E(\gamma_1)$	$D_1(\gamma_1)\rightarrow Z_1(\gamma_5)$	$Z_1(\gamma_1)\rightarrow E(\gamma_1)$	$D_1(\gamma_1)\rightarrow Z_1(\gamma_1)$	1:2	0.65
				$D_1(\gamma_1)\rightarrow Z_2(\gamma_2)$	1:2	0.62
			$Z_2(\gamma_2)\rightarrow E(\gamma_1)$	$D_1(\gamma_1)\rightarrow Z_1(\gamma_1)$	1:2	0.65
				$D_1(\gamma_1)\rightarrow Z_2(\gamma_2)$	1:2	0.59
	$Z_1(\gamma_5)\rightarrow G_1(\gamma_5)$	$D_1(\gamma_1)\rightarrow Z_1(\gamma_5)$	$Z_1(\gamma_1)\rightarrow G_1(\gamma_1)$	$D_1(\gamma_1)\rightarrow Z_1(\gamma_1)$	1:0	3.94
				$D_1(\gamma_1)\rightarrow Z_2(\gamma_2)$	1:0	6.88
			$Z_2(\gamma_2)\rightarrow G_2(\gamma_2)$	$D_1(\gamma_1)\rightarrow Z_1(\gamma_1)$	1:0	3.09
				$D_1(\gamma_1)\rightarrow Z_2(\gamma_2)$	1:0	4.20
	$Z_1(\gamma_5)\rightarrow D_1(\gamma_1)$	$D_1(\gamma_1)\rightarrow X_1(\gamma_5)$	$Z_1(\gamma_1)\rightarrow D_1(\gamma_1)$	$D_1(\gamma_1)\rightarrow X_1(\gamma_{1/2})$	1:2	0.62
			$Z_2(\gamma_2)\rightarrow D_1(\gamma_1)$		1:2	0.55
			$Z_1(\gamma_1)\rightarrow D_1(\gamma_1)$	$D_1(\gamma_1)\rightarrow X_2(\gamma_{2/1})$	1:2	0.66
			$Z_2(\gamma_2)\rightarrow D_1(\gamma_1)$		1:2	0.59
	$Z_1(\gamma_5)\rightarrow D_1(\gamma_1)$	$D_1(\gamma_1)\rightarrow X_4(\gamma_5)$	$Z_1(\gamma_1)\rightarrow D_1(\gamma_1)$	$D_1\rightarrow X_5$	1:2	0.67
			$Z_2(\gamma_2)\rightarrow D_1(\gamma_1)$	$(\gamma_1\rightarrow\gamma_1+\gamma_2)$	1:2	0.63
	$Z_1(\gamma_5)\rightarrow D_1(\gamma_1)$	$D_1(\gamma_1)\rightarrow X_8(\gamma_1)$	$Z_1(\gamma_1)\rightarrow D_1(\gamma_1)$	$D_1(\gamma_1)\rightarrow X_9(\gamma_1)$	1:0	1.81
			$Z_2(\gamma_2)\rightarrow D_1(\gamma_1)$		1:0	2.00
	$Z_1(\gamma_5)\rightarrow D_1(\gamma_1)$	$D_1(\gamma_1)\rightarrow X_9(\gamma_5)$	$Z_1(\gamma_1)\rightarrow D_1(\gamma_1)$	$D_1\rightarrow X_{10}$	1:2	0.78
			$Z_2(\gamma_2)\rightarrow D_1(\gamma_1)$	$(\gamma_1\rightarrow\gamma_1+\gamma_2)$	1:2	0.77
Cs(2)	$Z_1(\gamma_5)\rightarrow E(\gamma_1)$	$D_1(\gamma_1)\rightarrow Z_1(\gamma_5)$	$Z_1(\gamma_1)\rightarrow E(\gamma_1)$	$D_1(\gamma_1)\rightarrow Z_1(\gamma_1)$	0:1	0.14
				$D_1(\gamma_1)\rightarrow Z_2(\gamma_2)$	1:0	9.82
			$Z_2(\gamma_2)\rightarrow E(\gamma_1)$	$D_1(\gamma_1)\rightarrow Z_1(\gamma_1)$	1:0	8.34
				$D_1(\gamma_1)\rightarrow Z_2(\gamma_2)$	0:1	0.12
	$Z_1(\gamma_5)\rightarrow F_1(\gamma_1)$	$D_1(\gamma_1)\rightarrow Z_1(\gamma_5)$	$Z_1(\gamma_1)\rightarrow F_1(\gamma_1)$	$D_1(\gamma_1)\rightarrow Z_1(\gamma_1)$	0:1	0.23
				$D_1(\gamma_1)\rightarrow Z_2(\gamma_2)$	1:0	3.08
			$Z_2(\gamma_2)\rightarrow F_1(\gamma_1)$	$D_1(\gamma_1)\rightarrow Z_1(\gamma_1)$	1:0	2.22
				$D_1(\gamma_1)\rightarrow Z_2(\gamma_2)$	0:1	0.22
	$Z_1(\gamma_5)\rightarrow G_1(\gamma_5)$	$D_1(\gamma_1)\rightarrow Z_1(\gamma_5)$	$Z_1(\gamma_1)\rightarrow G_1(\gamma_1)$	$D_1(\gamma_1)\rightarrow Z_1(\gamma_1)$	1:0	3.99
				$D_1(\gamma_1)\rightarrow Z_2(\gamma_2)$	1:0	4.52
			$Z_2(\gamma_2)\rightarrow G_2(\gamma_2)$	$D_1(\gamma_1)\rightarrow Z_1(\gamma_1)$	1:0	1.81
				$D_1(\gamma_1)\rightarrow Z_2(\gamma_2)$	1:0	2.85

Centre	$C_{4v}D^-$ Transitions		Cs Transitions		Ratio X:Y	
	Excitation	Fluorescence	Excitation	Fluorescence	Calc'	Exp't
Cs(3)	$Z_1(\gamma_5)\rightarrow E(\gamma_1)$	$D_1(\gamma_1)\rightarrow Z_1(\gamma_5)$	$Z_1(\gamma_1)\rightarrow E(\gamma_1)$	$D_1(\gamma_1)\rightarrow Z_1(\gamma_1)$	1:2	0.60
				$D_1(\gamma_1)\rightarrow Z_2(\gamma_2)$	1:2	0.59
			$Z_2(\gamma_2)\rightarrow E(\gamma_1)$	$D_1(\gamma_1)\rightarrow Z_1(\gamma_1)$	1:2	0.58
				$D_1(\gamma_1)\rightarrow Z_2(\gamma_2)$	1:2	0.61
	$Z_1(\gamma_5)\rightarrow F_1(\gamma_1)$	$D_1(\gamma_1)\rightarrow Z_1(\gamma_5)$	$Z_1(\gamma_1)\rightarrow F_1(\gamma_1)$	$D_1(\gamma_1)\rightarrow Z_1(\gamma_1)$	1:2	0.62
				$D_1(\gamma_1)\rightarrow Z_2(\gamma_2)$	1:2	0.65
			$Z_2(\gamma_2)\rightarrow F_1(\gamma_1)$	$D_1(\gamma_1)\rightarrow Z_1(\gamma_1)$	1:2	0.59
				$D_1(\gamma_1)\rightarrow Z_2(\gamma_2)$	1:2	0.48
	$Z_1(\gamma_5)\rightarrow G_1(\gamma_5)$	$D_1(\gamma_1)\rightarrow Z_1(\gamma_5)$	$Z_1(\gamma_1)\rightarrow G_1(\gamma_1)$	$D_1(\gamma_1)\rightarrow Z_1(\gamma_1)$	1:0	1.39
				$D_1(\gamma_1)\rightarrow Z_2(\gamma_2)$	1:0	1.24
			$Z_2(\gamma_2)\rightarrow G_2(\gamma_2)$	$D_1(\gamma_1)\rightarrow Z_1(\gamma_1)$	1:0	1.69
				$D_1(\gamma_1)\rightarrow Z_2(\gamma_2)$	1:0	1.39
Cs(4)	$Z_1(\gamma_5)\rightarrow E(\gamma_1)$	$D_1(\gamma_1)\rightarrow Z_1(\gamma_5)$	$Z_1(\gamma_4)\rightarrow E(\gamma_1)$	$D_1(\gamma_1)\rightarrow Z_1(\gamma_4)$	1:2	0.58
				$D_1(\gamma_1)\rightarrow Z_2(\gamma_2)$	1:2	0.61
			$Z_2(\gamma_2)\rightarrow E(\gamma_1)$	$D_1(\gamma_1)\rightarrow Z_1(\gamma_4)$	1:2	0.58
				$D_1(\gamma_1)\rightarrow Z_2(\gamma_2)$	1:2	0.57
	$Z_1(\gamma_5)\rightarrow G_1(\gamma_5)$	$D_1(\gamma_1)\rightarrow Z_1(\gamma_5)$	$Z_1\rightarrow G_1 + Z_2\rightarrow G_2$	$D_1(\gamma_1)\rightarrow Z_1(\gamma_4)$	1:0	5.32
			$(\gamma_4\rightarrow\gamma_4) + (\gamma_2\rightarrow\gamma_2)$	$D_1(\gamma_1)\rightarrow Z_2(\gamma_2)$	1:0	4.21
	$Z_1(\gamma_5)\rightarrow G_2(\gamma_2)$	$D_1(\gamma_1)\rightarrow Z_1(\gamma_5)$	$Z_1(\gamma_4)\rightarrow G_3(\gamma_3)$	$D_1(\gamma_1)\rightarrow Z_1(\gamma_4)$	1:2	0.64
				$D_1(\gamma_1)\rightarrow Z_2(\gamma_2)$	1:2	0.73
Cs(5)	$Z_1(\gamma_5)\rightarrow E(\gamma_1)$	$D_1(\gamma_1)\rightarrow Z_1(\gamma_5)$	$Z_1(\gamma_5)\rightarrow E(\gamma_1)$	$D_1(\gamma_1)\rightarrow Z_1(\gamma_5)$	1:2	0.58
		$D_1(\gamma_1)\rightarrow Z_3(\gamma_1)$		$D_1(\gamma_1)\rightarrow Z_2(\gamma_1)$	1:0	8.02
	$Z_3(\gamma_1)\rightarrow E(\gamma_1)$	$D_1(\gamma_1)\rightarrow Z_1(\gamma_5)$	$Z_2(\gamma_1)\rightarrow E(\gamma_1)$	$D_1(\gamma_1)\rightarrow Z_1(\gamma_5)$	1:0	4.30
		$D_1(\gamma_1)\rightarrow Z_3(\gamma_1)$		$D_1(\gamma_1)\rightarrow Z_2(\gamma_1)$	0:1	0.24
	$Z_1(\gamma_5)\rightarrow F_1(\gamma_1)$	$D_1(\gamma_1)\rightarrow Z_1(\gamma_5)$	$Z_1(\gamma_5)\rightarrow F_1(\gamma_1)$	$D_1(\gamma_1)\rightarrow Z_1(\gamma_5)$	1:2	0.59
		$D_1(\gamma_1)\rightarrow Z_3(\gamma_1)$		$D_1(\gamma_1)\rightarrow Z_2(\gamma_1)$	1:0	7.8
	$Z_1(\gamma_5)\rightarrow G_1(\gamma_5)$	$D_1(\gamma_1)\rightarrow Z_1(\gamma_5)$	$Z_1(\gamma_5)\rightarrow G_1(\gamma_5)$	$D_1(\gamma_1)\rightarrow Z_1(\gamma_5)$	1:0	5.14
		$D_1(\gamma_1)\rightarrow Z_3(\gamma_1)$		$D_1(\gamma_1)\rightarrow Z_2(\gamma_1)$	0:1	0.42
	$Z_3(\gamma_1)\rightarrow G_1(\gamma_5)$	$D_1(\gamma_1)\rightarrow Z_1(\gamma_5)$	$Z_2(\gamma_1)\rightarrow G_1(\gamma_5)$	$D_1(\gamma_1)\rightarrow Z_1(\gamma_5)$	1:2	1.02
		$D_1(\gamma_1)\rightarrow Z_3(\gamma_1)$		$D_1(\gamma_1)\rightarrow Z_2(\gamma_1)$	1:0	1.07
	$Z_1(\gamma_5)\rightarrow E(\gamma_1)$	$D_1(\gamma_1)\rightarrow Y_2(\gamma_1)$	$Z_1(\gamma_5)\rightarrow E(\gamma_1)$	$D_1(\gamma_1)\rightarrow Y_3(\gamma_1)$	1:0	7.9
		$D_1(\gamma_1)\rightarrow Y_3(\gamma_5)$		$D_1(\gamma_1)\rightarrow Y_2(\gamma_5)$	1:2	0.55
		$D_1(\gamma_1)\rightarrow Y_7(\gamma_5)$		$D_1(\gamma_1)\rightarrow Y_7(\gamma_5)$	1:2	0.58
	$Z_3(\gamma_1)\rightarrow E(\gamma_1)$	$D_1(\gamma_1)\rightarrow Y_2(\gamma_1)$	$Z_2(\gamma_1)\rightarrow E(\gamma_1)$	$D_1(\gamma_1)\rightarrow Y_3(\gamma_1)$	0:1	0.28
		$D_1(\gamma_1)\rightarrow Y_3(\gamma_5)$		$D_1(\gamma_1)\rightarrow Y_2(\gamma_5)$	1:0	3.94

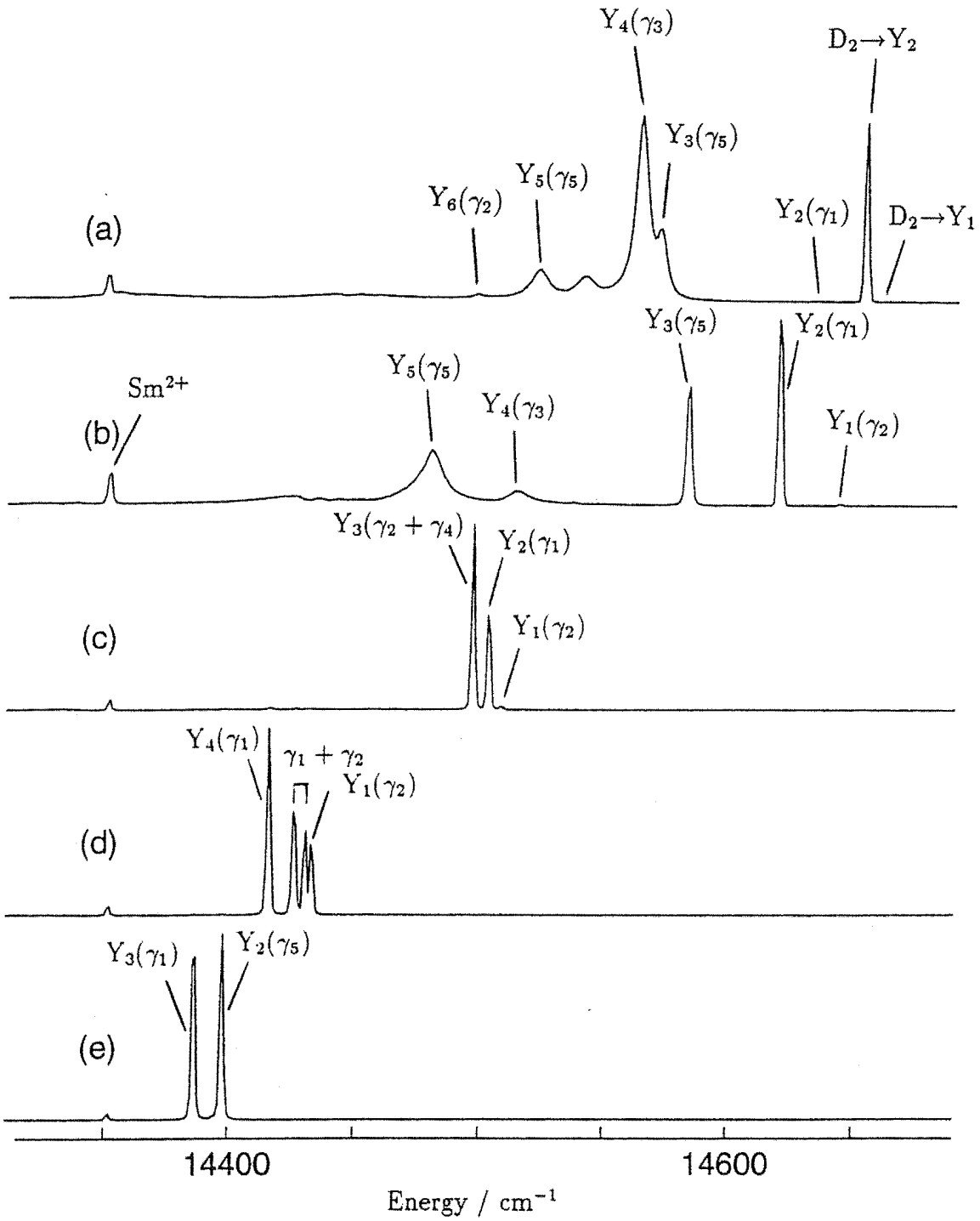

Figure 5.11: Fluorescence spectra of centres in the SrF_2:Pr^{3+}:D^- crystal showing the $^1D_2 \rightarrow {}^3H_5$ transitions of: (a) $C_{4v}F^-$ (b) $C_{4v}D^-$ (c) Cs(4) (d) Cs(3) and (e) Cs(5).

significant splitting in the γ_5 doublet of the parent centre, however the separation between the γ_1 and γ_5 states of the parent centre is now only $5cm^{-1}$. A doublet splitting of $4.3cm^{-1}$ is apparent in the C_s(a) symmetry Cs(3) centre and the γ_1 and γ_5 states have now crossed over. The $D_1(\gamma_1)\rightarrow Y_1(\gamma_2)$ transition of the parent centre has greatly increased in intensity in the Cs(3) centre. This is an allowed transition in a lower symmetry crystal field. It may also have gained some intensity due to the proximity of the $Y_1(\gamma_2)$ level to the γ_2 level of the split doublet.

As the Cs(5) centre has C_{4v} symmetry its spectra can readily be compared with those of the $C_{4v}F^-$ and $C_{4v}D^-$ centres. Clearly the crossing over of the $\Gamma_3\gamma_1$ and $\Gamma_4\gamma_5$ states is attributable to a stronger axial crystal field in the multi-hydrogenic ion centres. The magnetic-dipole $D_1(\gamma_1)\rightarrow Y_1(\gamma_2)$ transition does not appear in the Cs(5) spectrum, however it might be obscured by one of the stronger transitions.

5.2.4 Calculation of Relative CTMs from Experimental Polarisation Ratios

Three of the four C_s(a) symmetry polarisation ratios can only be expressed in terms of the CTMs and not as simple numerical ratios, Table 4.13. When experimental polarisation ratios are known for transitions in a centre of C_s(a) symmetry, it should be possible to calculate the relative CTMs of those transitions. This is demonstrated in Tables 5.6 and 5.7 for the Cs(1) and Cs(3) centres. The calculated values are very approximate because of subtraction errors produced in these calculations.

In all cases the values obtained for the relative CTMs are consistent with the polarisations of the parent transitions. The definitions of the symmetry groups in Section 4.2 describe how the symmetry axes of a centre transform when the symmetry is reduced from C_{4v} to C_s. The $D_1\leftrightarrow Z_1$ transition is σ-polarised in the $C_{4v}D^-$ centre, with c or f = 0. Thus the b or e CTM should be relatively small in the C_s(a) symmetry centres. This is also true of the $Z_1\rightarrow E$ and $Z_1\rightarrow F_1$ transitions. All the other transitions considered were π-polarised in the C_{4v} symmetry field, with a = b = 0 or d = e = 0. In these cases the a and c or d and f CTMs should be small in the C_s(a) symmetry centres.

5.3 Fluorescence Lifetimes

The pulsed dye laser and the digital oscilloscope were used to measure the $^1D_2$ multiplet fluorescence lifetimes of all the Pr^{3+} centres studied. The 10K experimental lifetimes of the $^1D_2$ multiplet are given in Table 5.8.

Reeves et al [76] have already reported fluorescence lifetimes for the C_{4v} symmetry centres. Their measurements were also made on crystals with Pr^{3+} ion concentrations of 0.05%. However the $C_{4v}F^-$ centre lifetimes obtained in this study are quite different, by 34% for SrF_2 and 18% for CaF_2. This suggests that there are non-radiative contributions to the $^1D_2$ multiplet lifetime, probably due to inter-ionic

Table 5.6: Examples showing how the relative CTMs of E1 transitions can be calculated from experimental polarisation ratios. These ratios were obtained from the Cs(1) centre.

$C_{4v}D^-$ Excitation / Fluorescence	Cs(1) Excitation / Fluorescence	Experimental Ratio X:Y	Relative CTMs
$Z_1(\gamma_5)\rightarrow E(\gamma_1)$ / $D_1(\gamma_1)\rightarrow Z_1(\gamma_5)$	$Z_2(\gamma_2)\rightarrow E(\gamma_1)$ / $D_1(\gamma_1)\rightarrow Z_1(\gamma_1)$	$\frac{\frac{1}{2}d+e}{d} = 0.65$	d=6.7e
$Z_1(\gamma_5)\rightarrow D_1(\gamma_1)$ / $D_1(\gamma_1)\rightarrow Z_1(\gamma_5)$	$Z_1(\gamma_1)\rightarrow D_1(\gamma_1)$ / $D_1(\gamma_1)\rightarrow X_2(\gamma_2)$	$\frac{\frac{1}{2}a+b}{a} = 0.66$	a=6.3b
$Z_1(\gamma_5)\rightarrow G_1(\gamma_5)$ / $D_1(\gamma_1)\rightarrow Z_1(\gamma_5)$	$Z_1(\gamma_1)\rightarrow G_1(\gamma_1)$ / $D_1(\gamma_1)\rightarrow Z_2(\gamma_2)$	$\frac{\frac{1}{2}a+b}{a} = 6.88$	b=6.4a
$Z_1(\gamma_5)\rightarrow G_1(\gamma_5)$ / $D_1(\gamma_1)\rightarrow Z_1(\gamma_5)$	$Z_2(\gamma_2)\rightarrow G_2(\gamma_2)$ / $D_1(\gamma_1)\rightarrow Z_2(\gamma_2)$	$\frac{\frac{1}{2}a+b}{a} = 4.20$	b=3.7a
$Z_1(\gamma_5)\rightarrow D_1(\gamma_1)$ / $D_1(\gamma_1)\rightarrow X_8(\gamma_1)$	$Z_2(\gamma_2)\rightarrow D_1(\gamma_1)$ / $D_1(\gamma_1)\rightarrow X_9(\gamma_1)$	$\frac{\frac{1}{2}d+e}{d} = 2.00$	e=1.50d

Table 5.7: Examples showing how the relative CTMs of E1 transitions can be calculated from experimental polarisation ratios. These ratios were obtained from the Cs(3) centre.

$C_{4v}D^-$ Excitation / Fluorescence	Cs(3) Excitation / Fluorescence	Experimental Ratio X:Y	Relative CTMs
$Z_1(\gamma_5)\rightarrow E(\gamma_1)$ / $D_1(\gamma_1)\rightarrow Z_1(\gamma_5)$	$Z_2(\gamma_2)\rightarrow E(\gamma_1)$ / $D_1(\gamma_1)\rightarrow Z_1(\gamma_1)$	$\frac{\frac{1}{2}d+e}{d} = 0.58$	d=12.5e
$Z_1(\gamma_5)\rightarrow F_1(\gamma_1)$ / $D_1(\gamma_1)\rightarrow Z_1(\gamma_5)$	$Z_2(\gamma_2)\rightarrow F_1(\gamma_1)$ / $D_1(\gamma_1)\rightarrow Z_1(\gamma_1)$	$\frac{\frac{1}{2}d+e}{d} = 0.59$	d=11.1e
$Z_1(\gamma_5)\rightarrow E(\gamma_1)$ / $D_1(\gamma_1)\rightarrow Z_1(\gamma_5)$	$Z_1(\gamma_1)\rightarrow E(\gamma_1)$ / $D_1(\gamma_1)\rightarrow Z_1(\gamma_1)$	$\frac{\frac{1}{2}a+b}{a} = 0.59$	a=11.1b
$Z_1(\gamma_5)\rightarrow F_1(\gamma_1)$ / $D_1(\gamma_1)\rightarrow Z_1(\gamma_5)$	$Z_1(\gamma_1)\rightarrow F_1(\gamma_1)$ / $D_1(\gamma_1)\rightarrow Z_2(\gamma_2)$	$\frac{\frac{1}{2}a+b}{a} = 0.65$	a=6.7b
$Z_1(\gamma_5)\rightarrow E(\gamma_1)$ / $D_1(\gamma_1)\rightarrow Y_2(\gamma_1)$	$Z_2(\gamma_2)\rightarrow E(\gamma_1)$ / $D_1(\gamma_1)\rightarrow Y_4(\gamma_1)$	$\frac{\frac{1}{2}d+e}{d} = 2.35$	e=1.85d

Table 5.8: The $^1D_2$ multiplet fluorescence lifetimes of the Pr^{3+} centres in the deuterated crystals, in units of μs.

Centre	SrF_2 Crystal	CaF_2 Crystal
$C_{4v}F^-$	1330±70	510±10
$C_{4v}D^-$	350±7	90±2
Cs(1)	62±2	9.4±0.2
Cs(2)	23.0±0.5	4.2±0.1
Cs(3)	15.7±0.8	3.2±0.2
Cs(4)	26.6±0.5	6.2±0.3
Cs(5)	10.5±0.2	-

energy-transfer processes such as cross relaxation and upconversion. Upconversion fluorescence, from the $^3P_0$ state, has been observed in both hosts while exciting Pr^{3+} ions to the $^1D_2$ multiplet [52] [76]. The efficiency of these processes will be highly dependent on the Pr^{3+} ion concentration and may also be affected by crystal growing conditions. For example, annealing is known to enhance the formation of cluster centres in this material [22].

In both studies the CaF_2 lifetime was shorter than the SrF_2 lifetime for the $C_{4v}F^-$ centre. The CaF_2 crystal has a smaller lattice parameter, which will result in higher energy-transfer efficiencies and a stronger crystal field in this host. The fluorescence transition probabilities, and therefore the relaxation rates, will depend upon the strength of the crystal-field. Crystal-field parameters were available for the C_{4v} centre in both hosts (Jon Wells, Private Communication), but these alone were not sufficient to account for the relative $^1D_2$ lifetimes found experimentally.

Reeves et al observed that the fluorescence lifetimes of the hydrogenic C_{4v} centres are shorter than those of the fluorine C_{4v} centres. This was attributed to the additional non-radiative decay channels accessible through coupling to the vibrational modes of the hydrogenic interstitial ion. The $C_{4v}D^-$ centre lifetimes reported here are similar to those of Reeves et al. Much better agreement would be expected for the hydrogenic centres, as the dominant relaxation pathway is via energy transfer to the attendant hydrogenic ions.

The Cs centre fluorescence lifetimes are much shorter than those of the parent centres and vary significantly from centre to centre. Each successive substitutional hydrogenic ion will provide additional non-radiative relaxation pathways and so reduce the $^1D_2$ lifetime. From the experimental lifetimes in Table 5.8 these centres can be placed in the following order of decreasing fluorescence lifetime: Cs(1), Cs(4), Cs(2), Cs(3) and Cs(5).

Table 5.9: The $^1D_2$ multiplet fluorescence lifetimes of the deuterium Cs centres analysed in terms of sequential D^- ion substitutions. The 'discrete' decay rates have been calculated by considering the Cs(2) and Cs(4) centres independently. The 'averaged' decay rates were calculated using the mean of the Cs(2) and Cs(4) fluorescence decay rates. All are given in units of 1000s$^-$1.

Crystal	Centre	Fluorescence Decay Rate	Parent Centre	Fluorescence Decay Rate	D^- Ion Decay Rates Discrete	Averaged
SrF_2	Cs(1)	16.1±0.5	$C_{4v}D^-$	2.86±0.06	13.2±0.6	13.2±0.6
	Cs(4)	37.6±0.7	Cs(1)	16.1±0.5	21.5±1.2	
	Cs(2)	43.5±0.9	Cs(1)	16.1±0.5	27.4±1.4	24.5±1.3
	Cs(3)	63.7±3.2	Cs(4)	37.6±0.7	26.1±3.9	
	Cs(3)	63.7±3.2	Cs(2)	43.5±0.9	20.2±4.1	23.2±4.0
	Cs(5)	95.2±1.8	Cs(3)	63.7±3.2	31.5±5.0	31.5±5.0
CaF_2	Cs(1)	106±3	$C_{4v}D^-$	11.1±0.3	95±4	95±4
	Cs(4)	161±8	Cs(1)	106±3	55±11	
	Cs(2)	238±6	Cs(1)	106±3	132±9	94±10
	Cs(3)	312±20	Cs(4)	161±8	151±28	
	Cs(3)	312±20	Cs(2)	238±6	74±26	112±27

If it is assumed that all the substitutional hydrogenic ions are located in the nearest-neighbour coordination sphere of the Pr^{3+} ion, then these experimental lifetimes can be analysed in terms of successive D^- ion substitutions. If the substitutional D^- ions are equidistant from the Pr^{3+} ion, then they will all contribute equally to the non-radiative relaxation of the centre. The analysis is most easily formulated by considering fluorescence decay rates, which are the numerical reciprocals of fluorescence lifetimes. Each Cs centre will have a faster fluorescence decay rate than its 'parent centre', which has one less substitutional D^- ion. This fluorescence decay rate is the sum of the parental decay rate and the decay rate attributable to non-radiative relaxation via the additional D^- ion. These successive D^- ion contributions to the experimental fluorescence decay rate are given in the sixth column of Table 5.9.

As expected non-radiative decay via the substitutional D^- ions is more efficient in the CaF_2 crystal than in the SrF_2 crystal, with average D^- ion decay rates of 101000s^{-1} and 23300s^{-1} respectively. The most consistent decay rates were obtained when the Cs(3) centre was assigned three substitutional hydrogenic ions and the Cs(5) centre four. Even with these assignments Table 5.9 shows that there is still a significant variation in the decay rates obtained for each host. This anal-

ysis was simplified by an implicit assumption that each substitution can be made without displacing any of the other ions in the Pr^{3+} centre. In fact all the ions will be displaced slightly to absorb the strain caused by the inclusion of an additional defect. Thus each of the hydrogenic ions already present in the parent centre will move with respect to the Pr^{3+} ion and their total contribution to the fluorescence decay rate will change. This may explain the variations in the D^- decay rates found experimentally.

Both the Cs(2) and Cs(4) centres contain two substitutional hydrogenic ions. If the D^- ion decay rates are re-calculated, using the average fluorescence decay rates of the Cs(2) and Cs(4) centres, much more consistent values are obtained. These are listed in the last column of Table 5.9. Indeed all of the CaF_2 values are in agreement, within experimental uncertainty.

5.4 Model Configurations for the Cs Centres

The Cs(1), Cs(2) and Cs(4) centre configurations proposed by Reeves et al [75] have been tested and confirmed in this chapter, Figure 5.12(a), (b) and (c). Model configurations can now be presented for the Cs(3) and Cs(5) centres.

The spectroscopy and polarisation behaviour of the Cs(5) centre indicates that it has C_{4v} symmetry. It comprises four substitutional hydrogenic ions, all of these located in equivalent sites in the nearest-neighbour coordination sphere of the Pr^{3+} ion. The Cs(5) centre bleaches producing a single discrete photoproduct. There are only two possible C_{4v} symmetry configurations which can be obtained by substitution of four anions in a Pr^{3+} centre. However only the configuration of Figure 5.12 (d) is conducive to bleaching. This is the configuration proposed for the Cs(5) centre and it exhibits all the features required to account for these experimental observations.

The Cs(3) centre has either a C_s(a) or C_{2v}(a) configuration, with three substitutional hydrogenic ions. These are located in at least two inequivalent sites in the nearest-neighbour coordination sphere of the Pr^{3+} ion. The Cs(3) centre bleaches producing a single discrete photoproduct. No C_{2v}(a) symmetry configurations with three substitutional hydrogenic ions are possible, so the Cs(3) centre must have C_s symmetry. There are three possible C_s(a) configurations for the Cs(3) centre, Figure 5.13. Although all of these would be bleachable by the interstitialcy-noncolinear mechanism, only the configuration of Figure 5.13(c) is necessarily constrained to a single discrete photo-product.

In the Cs(1), Cs(2), Cs(4) and Cs(5) centres the substitutional hydrogenic ions are always located in the (100) anion plane between the Pr^{3+} ion and the interstitial hydrogenic ion. This trait always produces the minimum possible spatial separations between the hydrogenic ions of a centre and suggests that there is an affinity between these ions. There is no reason why the Cs(3) centre should be different from the other Cs centres in this respect. For this reason the ionic configuration

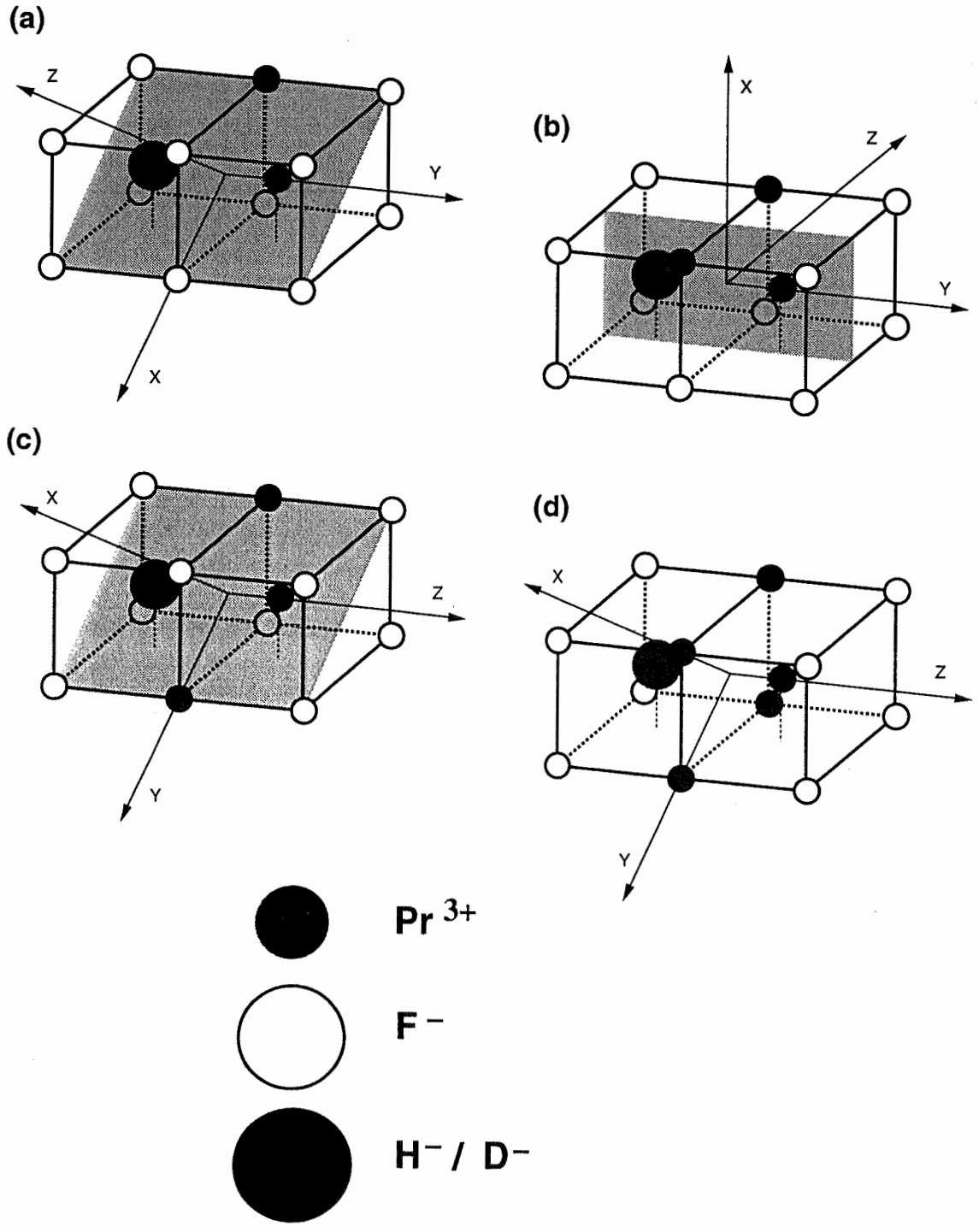

Figure 5.12: The proposed ionic configurations for the **(a)** Cs(1) **(b)** Cs(2) **(c)** Cs(4) and **(d)** Cs(5) centres. The ions in the key are drawn to the same scale as the CaF_2 lattice cages.

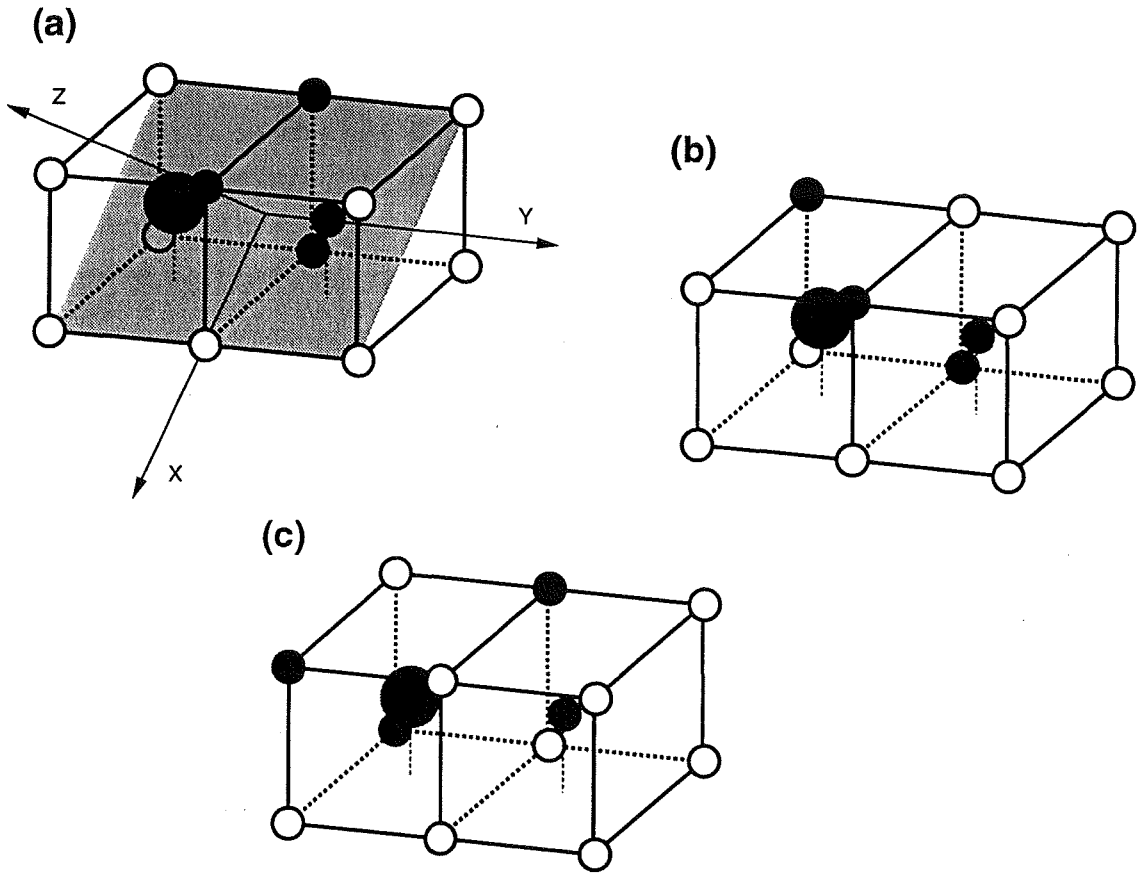

Figure 5.13: Possible ionic configurations for the Cs(3) centre, which are consistent with the experimental observations. The configuration in (a) is proposed for this centre.

in Figure 5.13(a) is tentatively assigned to the Cs(3) centre.

Such an affinity between hydrogenic ions would also explain why Cs(2) centres form preferentially to Cs(4) centres. However, it is very difficult to conceive of a physical process which produces a significant attractive force between the hydrogenic ions. The H^- ion, unlike the hydrogen atom, has a particularly low polarisability and so Van der Waals forces are unlikely to be culpable. A more significant determinant of ionic configurations in crystals is the polarising effect of a local crystal field [56]. However the axial component of the crystal field in a Pr^{3+} centre would tend to place the more polarisable F^- ions in the (100) plane where the substitutional hydrogenic ions are instead located.

A more reasonable explanation for the observed clustering of the hydrogenic ions is that it minimises the lattice strain produced by the Pr^{3+} centre. This appears to be the case in both hosts. Significant strain already exists in the $C_{4v}F^-$ centres due to the trivalent cation substitution and the presence of an additional monovalent interstitial ion. In the anion substitutions which produce the hydrogenic centres F^- ions (with atomic radii of 1.33Å) are replaced by larger hydrogenic ions (with atomic radii of 1.54Å), producing additional strain.

Chapter 6

Bleaching of the Praseodymium Cs Centres

6.1 The Bleaching Behaviour of the Cs Centres

All of the Cs centres are bleachable. The bleaching behaviour of the Cs(1), Cs(2), Cs(3) and Cs(4) centres has been studied by Reeves [75] [77]. A preliminary investigation of the Cs(5) centre was made by Khong [49] [53], who also investigated bleaching in mixed alkaline-earth centres of praseodymium.

Reeves observed two types of bleaching, which are distinguished by the nature of the photoproduct centres produced. In reorientational bleaching, the excited centres are reorientated to produce equivalent photoproduct centres. These photoproduct centres will still have absorption transitions which lie within the inhomogeneously-broadened excitation transition of the Cs centre. However bleaching of the fluorescence is observed as those orientations which are resonant with the polarised excitation beam will gradually become depopulated. The fluorescence can be recovered by switching the laser polarisation to excite those orientations of the Cs centre which were preferentially populated by the bleaching process. Further irradiation in the new laser polarisation will often repopulate those orientations which were initially depleted and in this way the bleaching is reversible. The Cs centres can be shepherded between orthogonal orientations by the appropriate choices of excitation polarisation.

The second type of bleaching produces discrete-photoproduct centres with absorption transitions that lie outside the inhomogeneously-broadened excitation transition of the parent Cs centre. These photoproduct centres are orthogonal to their original orientations, as defined by the relative position of the interstitial ion. They also have inequivalent ionic configurations to the parent Cs centres. All of the Cs* centres are bleachable and their photoproducts have the original Cs centre configuration. Thus discrete-photoproduct formation bleaching is also reversible. Like reorientational bleaching, the various orientations of these centres are preferentially populated and depopulated in accordance with the chosen excitation polarisation.

Reeves found that Cs centres which contain the lighter hydrogen isotopes (H^- or D^-) bleach much more quickly than their counterparts containing the heavier hydrogen isotopes (D^- or T^-). This trend was attributed to the isotopic dependence of the vibrational local-mode energies, which is a direct consequence of the different masses of these isotopes.

Reeves and Khong observed the following bleaching behaviour in the Cs centres when pumping the $Z_1/Z_2 \rightarrow D_1$ absorption transitions:

Cs(1) The Cs(1) centre exhibits reorientational bleaching only, when exciting from either the Z_1 or Z_2 level. In <100> orientated crystals the bleached fluorescence is almost fully recoverable in alternating sequences of X and Y polarised excitation. The fluorescence decay curves are non-exponential, although the initial decay fits to a single-exponential function. The observed bleaching rates are inversely proportional to the excitation-beam intensity.

Cs(2) The Cs(2) centre exhibits both reorientational bleaching and bleaching producing a discrete photoproduct, Cs(2)*. As a result of the latter, bleached fluorescence was only partially recoverable by switching the excitation polarisation. However, the fluorescence becomes almost fully recoverable after many cycles between orthogonal excitation polarisations. No recovery was ever observed when pumping the $Z_2 \rightarrow D_1$ transition. The intensity of this transition is not changed significantly by pumping the $Z_1 \rightarrow D_1$ transition. Irradiation of the Cs(2)* photoproduct centre restores almost all of the bleached Cs(2) centre fluorescence.

Cs(3) The Cs(3) centre exhibits only discrete-photoproduct formation bleaching. Bleaching of the Cs(3)* centre restores most of the lost fluorescence intensity. The $Z_1 \rightarrow D_1$ and $Z_2 \rightarrow D_1$ transitions of the photoproduct do not bleach independently. More complete recovery of the Cs(3) fluorescence is achieved if both these transitions are pumped, in turn.

Cs(4) The Cs(4) centre exhibits only discrete-photoproduct formation bleaching. The $Z_1 \rightarrow D_1$ and $Z_2 \rightarrow D_1$ transitions of the Cs(4)* photoproduct centre do not bleach independently. Pumping both these transitions only partially restores the bleached Cs(4) fluorescence. No new photoproduct centres are observed after excitation of the Cs(4)* centre.

Cs(5) The Cs(5) centre exhibits only discrete-photoproduct formation bleaching. Bleaching of the Cs(5)* centre partially restores the lost fluorescence intensity.

6.2 Bleaching Mechanisms and Model Configurations for the Cs* Centres

Cockroft et al [26] concluded from their studies of a number of hydrogenated and deuterated CaF_2:RE^{3+} and SrF_2:RE^{3+} crystals that bleaching is due to light-induced migration of H^-/D^- ions about the RE^{3+} ion. Reorientation of the $C_{4v}F^-$ centre has been observed at higher temperatures, of the order of 200K, by Edgar and Welsh [32]. This is due to thermally-induced migration of the interstitial F^- ion between equivalent sites adjacent to the RE^{3+} ion. They used EPR and dielectric loss measurements to obtain an activation energy of 0.395±0.005eV for this relaxation in the Gd^{3+} centre. However light-induced F^- ion migration is not observed in the $C_{4v}F^-$ RE^{3+} centres.

Corish et al [28] have observed that there are two possible mechanisms for the reorientation of a $C_{4v}F^-$ centre. In the interstitialcy-noncolinear mechanism the interstitial F^- ion substitutes for a nearest-neighbour lattice F^- ion, while the latter moves to a new interstitial site. In the second mechanism the interstitial F^- ion makes a direct jump through one of the edges of the F^- ion cube. This is assisted by a (111) relaxation of the two F^- ions nearest to the mobile interstitial. Corish et al calculated the activation energies of both mechanisms and found that former is favoured, having a lower energy for all the lanthanides.

Edgar and Welsh observed a similar reorientation of the $C_{4v}H^-$ and $C_{4v}D^-$ centres of the Gd^{3+} ion through EPR. The activation energies measured for these hydrogenic centres were very similar to those of the fluoride centre; being 0.38±0.03eV and 0.43±0.02eV respectively. Non of these C_{4v} symmetry centres exhibit light-induced anion migration, which suggests that the presence of at least one substitutional hydrogenic ion is a crucial prerequisite to bleaching.

Reeves [75] [77] concluded that the interstitialcy-noncolinear mechanism is responsible for the bleaching observed in the multi-hydrogenic ion Cs centres, Figure 6.1. The interstitial hydrogenic ion replaces a substitutional hydrogenic ion, while the latter moves to a new interstitial site. This accounts for the main features of the bleaching behaviour observed in the Cs(1), Cs(2) and Cs(4) centres [75]. It is also consistent with the result of Corish et al and helps to explain why no bleaching of the $C_{4v}H^-$ centre is observed. Clearly the activation energy of the direct jump mechanism is prohibitively high in these Pr^{3+} centres.

The Cs* centre configurations can be deduced from the bleaching behaviour of the parent Cs centres. It has been shown that the low-mass hydrogenic ions are the only species which participate in the bleaching process. This presents a considerable constraint when predicting the possible migration pathways of the hydrogenic ions and the ionic configurations of the photoproduct centres. Model configurations have already been proposed for the Cs(2)* and Cs(4)* centres by Reeves. These are shown in Figure 6.2(a) and (c).

Only one photoproduct can be produced by the interstitialcy mechanism from each of the Cs(1), Cs(4) and Cs(5) centres, Figure 6.1(a), (d) and (e). The Cs(1)

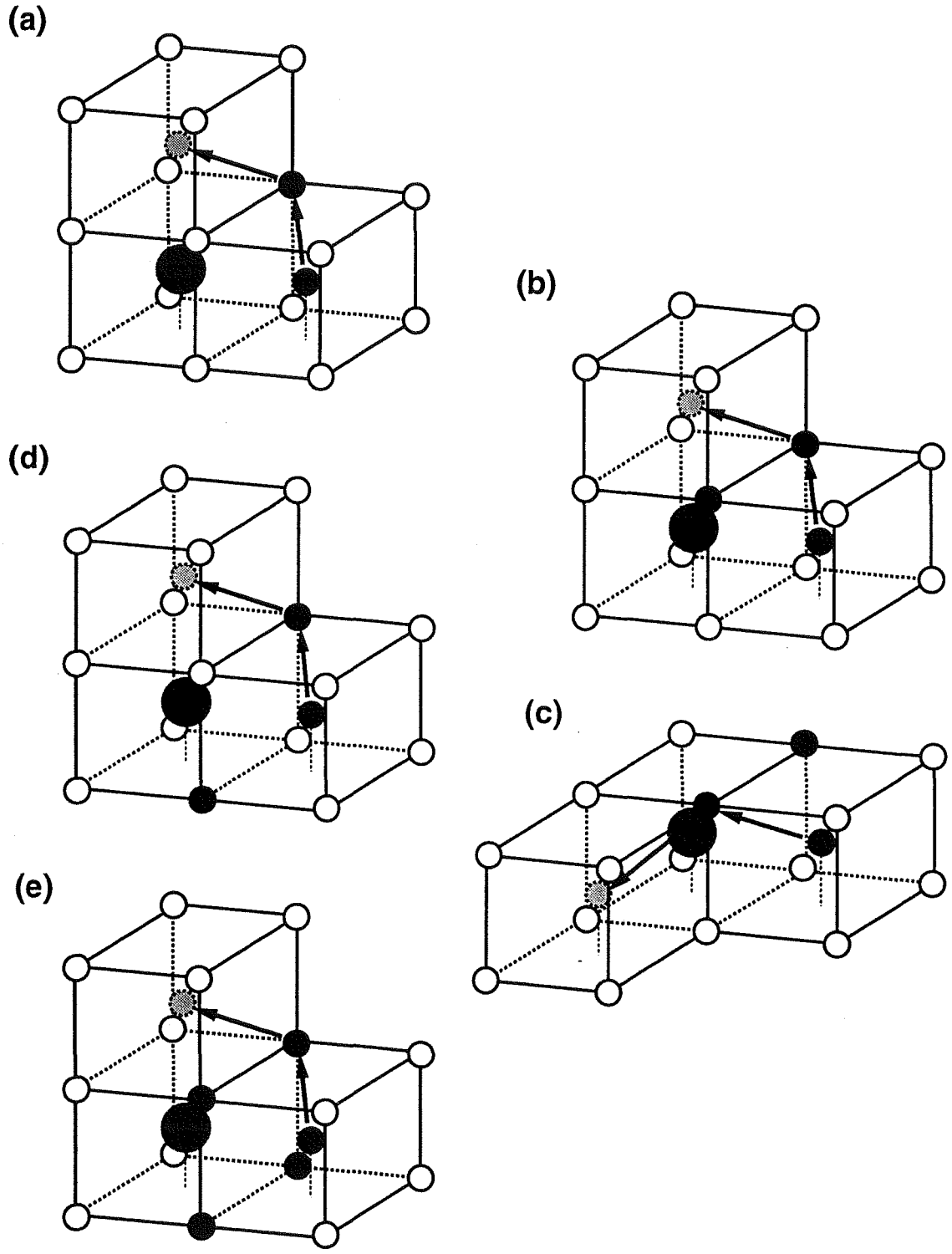

Figure 6.1: The proposed mechanisms for reorientational bleaching of the (**a**) Cs(1) and (**b**) Cs(2) centres and discrete-photoproduct formation bleaching of the (**c**) Cs(2) (**d**) Cs(4) and (**e**) Cs(5) centres. The mechanisms shown for the Cs(1), Cs(2) and Cs(4) centres were first proposed by Reeves.

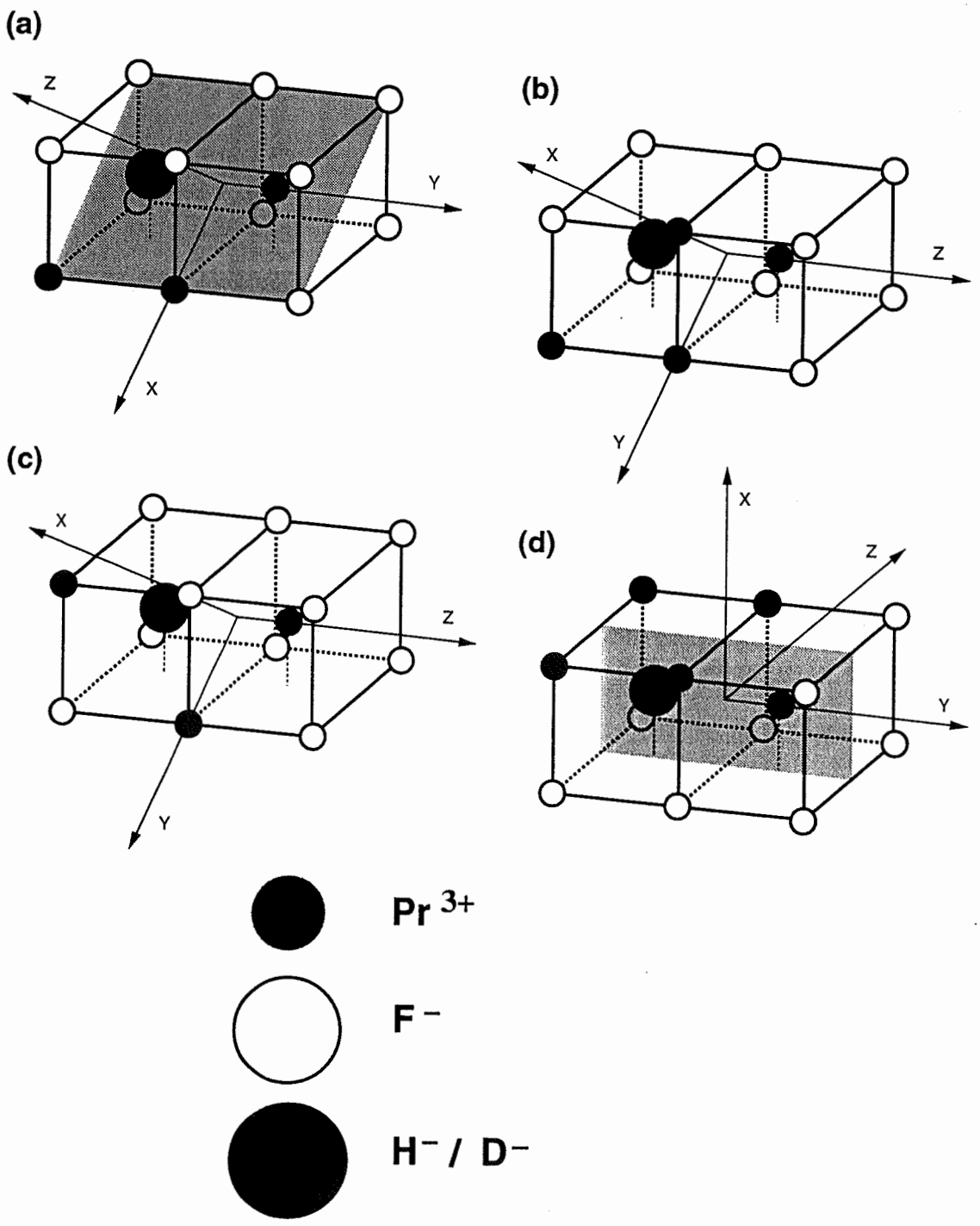

Figure 6.2: The proposed ionic configurations of the (a) Cs(2)* (b) Cs(3)* (c) Cs(4)* and (d) Cs(5)* centres. The ions in the key are drawn to the same scale as the CaF_2 lattice cages.

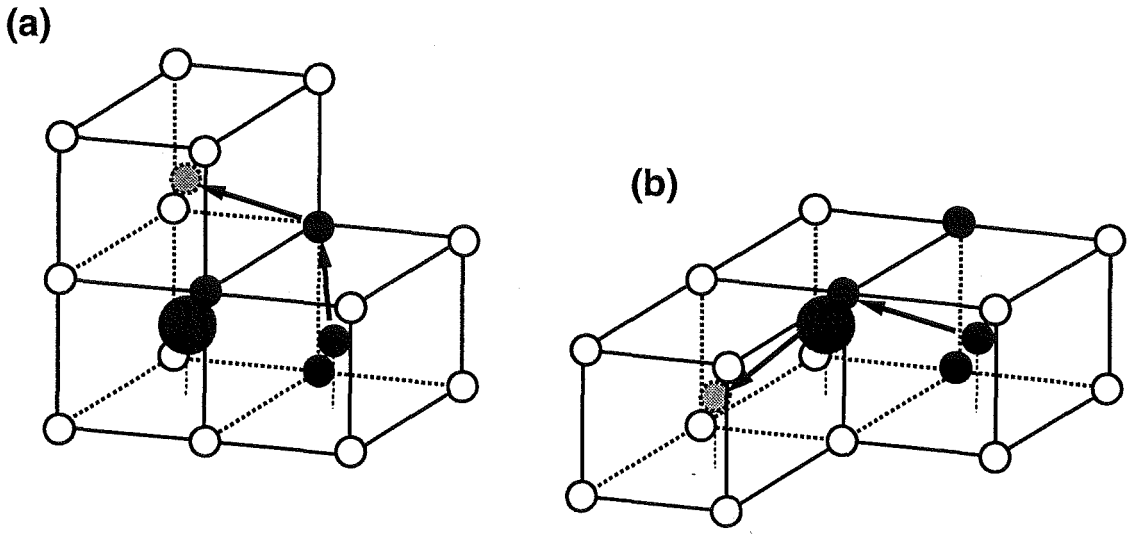

Figure 6.3: The proposed mechanisms for discrete-photoproduct formation bleaching in the Cs(3) centre. The mechanism in (a) is tentatively assigned as that producing the experimentally observed photoproduct Cs(3)*.

centre is simply reorientated. The Cs(4) and Cs(5) centres have discrete photoproducts, the Cs(4)* and Cs(5)* centres respectively. The Cs(5)* centre is shown in Figure 6.2(d). Two photoproducts can be produced by the interstitialcy mechanism from the Cs(2) centre, Figure 6.1(b) and (c). The Cs(2) centre can either be reorientated or adopt a discrete-photoproduct configuration, Cs(2)*. It is interesting to note that the hydrogenic ions are more closely clustered in the Cs(2) centre than in the Cs(2)* centre. If an affinity does exist between the hydrogenic ions, then reorientational bleaching of the Cs(2) centres may be preferred.

Two discrete photoproducts can be produced by the interstitialcy mechanism from the Cs(3) centre, Figure 6.3. However, only one photoproduct centre is observed experimentally. The formation of a single discrete photoproduct may be preferred due to the tendency for the hydrogenic ions to cluster together. This would favour the bleaching pathway shown in Figure 6.3(a). Thus the ionic configuration in Figure 6.2 is tentatively assigned to the Cs(3)* centre. It is also possible that the Cs(3) centre has one of the other ionic configurations illustrated in Figure 5.12.

The symmetry axes of the Cs* centres are shown in Figure 6.2. The Cs(2)* centre has a C_s(a) symmetry configuration and the Cs(5)* centre has a C_s(b) symmetry configuration. The Cs(3)* and Cs(4)* centres both have C_1 symmetry configurations. Figures 4.3 to 4.8 define the labeling of the different orientations adopted by these Pr^{3+} centres.

6.3 Bleaching Pathways

Having proposed model configurations and bleaching mechanisms for all of the Cs and Cs* centres, it is now possible to determine the specific bleaching pathways which are accessible when any particular orientation of a centre is bleached. These bleaching pathways have been identified and are given in Tables 6.1 to 6.5. The first column lists the orientations of the parent centre. The other columns list the orientations of the photoproduct centre which are produced when each orientation of the parent centre is selectively irradiated.

When an absorption transition of a centre is pumped by the polarised excitation beam, a particular subset of orientations will be excited, Tables 4.9 to 4.14. These orientations are selectively depopulated when irradiated, as other orientations of the photoproduct centre become more populated. In Tables 6.6 to 6.16 the bleaching pathways have been re-tabulated for each centre in terms of the excitation transition irreps appropriate for that symmetry. Each section of each table is associated with an excitation transition irrep and an excitation polarisation. The third column gives the relative excitation probabilities for the different orientations, in terms of the CTMs of the pump transition. The fourth column lists the orientations of the centre which are resonant with the excitation beam. The remaining columns list the orientations of the photoproduct centre which are produced during bleaching. These tables will be used to interpret polarised bleaching experiments.

The Cs(3)* and Cs(4)* centres both have C_1 symmetry, so it is not possible to determine from symmetry considerations alone which orientations of these centres will be resonant with a polarised excitation beam. However, for these particular centres, the C_{4v} approximation may be applied to predict the rudimentary polarised bleaching behaviour. Three pairs of Cs(3)* and Cs(4)* centre orientations can be distinguished by their different bleaching pathways, Tables 6.3 and 6.4. These pairs of orientations are: (1)*+(2)*, (3)*+(4)* and (5)*+(6)*. Fortunately these are the same pairs which are obtained from orientations (1), (2) and (3) of the parent C_{4v} centre through symmetry breaking, Figures 4.3 and 4.8. Thus the bleaching pathways of these C_1 symmetry centres can be retabulated in terms of the excitation transition irrep labels of the parent C_{4v} centre. The C_{4v} approximation could equally be applied to the Cs(1), Cs(2)*, Cs(3) and Cs(4) centres, Tables 6.6, 6.10, 6.11 and 6.13. This is easily demonstrated by pairing the appropriate orientations in these tables and then assigning the value zero to each CTM which is zero valued in the parent C_{4v} symmetry field.

Rate equations can now be written to describe the bleaching processes which occur during the polarised irradiation of a centre. Each set of equations can be solved to obtain the transient fluorescence intensity during bleaching. These theoretical functions can be compared to experimental bleaching curves. Discrete-photoproduct formation bleaching will produce exponential decay. This decay could have one or more terms; the number of terms being determined by the non zero CTMs of the excitation transition. Reorientational bleaching will produce more complicated

Table 6.1: The bleaching pathways of the Cs(1) centre.

Cs(1)	→	**Cs(1)**			
(1)	→	(3)	(4)	(5)	(6)
(2)	→	(3)	(4)	(5)	(6)
(3)	→	(1)	(2)	(5)	(6)
(4)	→	(1)	(2)	(5)	(6)
(5)	→	(1)	(2)	(3)	(4)
(6)	→	(1)	(2)	(3)	(4)

Table 6.2: The bleaching pathways of the Cs(2) and Cs(2)* centres.

Cs(2)	→	**Cs(2)**
(1)	→	(5)
(2)	→	(3)
(3)	→	(2)
(4)	→	(6)
(5)	→	(1)
(6)	→	(4)

Cs(2)	→	**Cs(2)***	
(1)	→	(3)*	(4)*
(2)	→	(5)*	(6)*
(3)	→	(5)*	(6)*
(4)	→	(1)*	(2)*
(5)	→	(3)*	(4)*
(6)	→	(1)*	(2)*

Cs(2)*	→	**Cs(2)**	
(1)*	→	(4)	(6)
(2)*	→	(4)	(6)
(3)*	→	(1)	(5)
(4)*	→	(1)	(5)
(5)*	→	(2)	(3)
(6)*	→	(2)	(3)

Table 6.3: The bleaching pathways of the Cs(3) and Cs(3)* centres.

Cs(3)	→	**Cs(3)***			
(1)	→	(3)*	(4)*	(5)*	(6)*
(2)	→	(3)*	(4)*	(5)*	(6)*
(3)	→	(1)*	(2)*	(5)*	(6)*
(4)	→	(1)*	(2)*	(5)*	(6)*
(5)	→	(1)*	(2)*	(3)*	(4)*
(6)	→	(1)*	(2)*	(3)*	(4)*

Cs(3)*	→	**Cs(3)**			
(1)*	→	(3)	(4)	(5)	(6)
(2)*	→	(3)	(4)	(5)	(6)
(3)*	→	(1)	(2)	(5)	(6)
(4)*	→	(1)	(2)	(5)	(6)
(5)*	→	(1)	(2)	(3)	(4)
(6)*	→	(1)	(2)	(3)	(4)

Table 6.4: The bleaching pathways of the Cs(4) and Cs(4)* centres.

Cs(4)	→	**Cs(4)***			
(1)	→	(3)*	(4)*	(5)*	(6)*
(2)	→	(3)*	(4)*	(5)*	(6)*
(3)	→	(1)*	(2)*	(5)*	(6)*
(4)	→	(1)*	(2)*	(5)*	(6)*
(5)	→	(1)*	(2)*	(3)*	(4)*
(6)	→	(1)*	(2)*	(3)*	(4)*

Cs(4)*	→	**Cs(4)**			
(1)*	→	(3)	(4)	(5)	(6)
(2)*	→	(3)	(4)	(5)	(6)
(3)*	→	(1)	(2)	(5)	(6)
(4)*	→	(1)	(2)	(5)	(6)
(5)*	→	(1)	(2)	(3)	(4)
(6)*	→	(1)	(2)	(3)	(4)

Table 6.5: The bleaching pathways of the Cs(5) and Cs(5)* centres.

Cs(5)	→	**Cs(5)***	
(1)	→	(3)*	(5)*
(2)	→	(2)*	(6)*
(3)	→	(1)*	(4)*

Cs(5)*	→	**Cs(5)**
(1)*	→	(3)
(2)*	→	(2)
(3)*	→	(1)
(4)*	→	(3)
(5)*	→	(1)
(6)*	→	(2)

decay curves, as the different orientations do not bleach independently.

The tables show that the different orientations of a centre can be selectively bleached, producing either reorientated centres or discrete-photoproduct centres. If the photoproduct centres are then irradiated with a polarised beam some of the bleached centres will be restored to their original configurations. If a Cs(3), Cs(4) or Cs(5) centre undergoes such a bleaching sequence, then that centre will always be restored to its original orientation. This is also true for the reorientational bleaching of a Cs(2) centre. However, the reorientational bleaching of a Cs(1) centre or the discrete-photoproduct formation bleaching of a Cs(2) centre will not always restore a particular centre to its original orientation. This irreversible aspect should be taken into account when analysing bleaching sequences.

6.4 Polarisation Bleaching Experiments

6.4.1 The Cs(1) Centre

A number of experiments were performed to test the bleaching mechanism proposed for the Cs(1) centre. Table 6.6 shows that it will exhibit the same bleaching behaviour when pumping the γ_1 $Z_1 \rightarrow D_1/E$ transitions as it does when pumping the γ_2 $Z_2 \rightarrow D_1/E$ transitions. If the Cs(1) centre is irradiated with either an Y or Z polarised beam, then the fluorescence intensity which is lost through bleaching should always be recovered by switching to the orthogonal excitation polarisation. Indeed the fluorescence intensity observed immediately after switching the polarisation should be greater than the initial fluorescence intensity of the unbleached crystal.

Table 6.6: Bleaching pathways of the Cs(1) centre.

Absorption		**CTM**	**Cs(1)**	→	**Cs(1)**			
γ_1	Y	$\frac{1}{2}$a	(1)	→	(3)	(4)	(5)	(6)
			(2)	→	(3)	(4)	(5)	(6)
			(3)	→	(1)	(2)	(5)	(6)
			(4)	→	(1)	(2)	(5)	(6)
		b	(5)	→	(1)	(2)	(3)	(4)
			(6)	→	(1)	(2)	(3)	(4)
	Z	$\frac{1}{2}$a	(1)	→	(3)	(4)	(5)	(6)
			(2)	→	(3)	(4)	(5)	(6)
			(5)	→	(1)	(2)	(3)	(4)
			(6)	→	(1)	(2)	(3)	(4)
		b	(3)	→	(1)	(2)	(5)	(6)
			(4)	→	(1)	(2)	(5)	(6)
γ_2	Y	$\frac{1}{2}$c	(1)	→	(3)	(4)	(5)	(6)
			(2)	→	(3)	(4)	(5)	(6)
			(3)	→	(1)	(2)	(5)	(6)
			(4)	→	(1)	(2)	(5)	(6)
	Z	$\frac{1}{2}$c	(1)	→	(3)	(4)	(5)	(6)
			(2)	→	(3)	(4)	(5)	(6)
			(5)	→	(1)	(2)	(3)	(4)
			(6)	→	(1)	(2)	(3)	(4)

Table 6.7: Bleaching pathways of the Cs(1) centre, for diagonal excitation

Absorption		**CTM**	**Cs(1)**	→	**Cs(1)**			
γ_1	YZ	a	(1)	→	(3)	(4)	(5)	(6)
		$\frac{1}{4}$a + $\frac{1}{2}$b	(3)	→	(1)	(2)	(5)	(6)
			(4)	→	(1)	(2)	(5)	(6)
			(5)	→	(1)	(2)	(3)	(4)
			(6)	→	(1)	(2)	(3)	(4)
	ZY	a	(2)	→	(3)	(4)	(5)	(6)
		$\frac{1}{4}$a + $\frac{1}{2}$b	(3)	→	(1)	(2)	(5)	(6)
			(4)	→	(1)	(2)	(5)	(6)
			(5)	→	(1)	(2)	(3)	(4)
			(6)	→	(1)	(2)	(3)	(4)
γ_2	YZ	c	(2)	→	(3)	(4)	(5)	(6)
		$\frac{1}{4}$c	(3)	→	(1)	(2)	(5)	(6)
			(4)	→	(1)	(2)	(5)	(6)
			(5)	→	(1)	(2)	(3)	(4)
			(6)	→	(1)	(2)	(3)	(4)
	ZY	c	(1)	→	(3)	(4)	(5)	(6)
		$\frac{1}{4}$c	(3)	→	(1)	(2)	(5)	(6)
			(4)	→	(1)	(2)	(5)	(6)
			(5)	→	(1)	(2)	(3)	(4)
			(6)	→	(1)	(2)	(3)	(4)

Table 6.8: Reorientational bleaching pathways of the Cs(2) centre.

Absorption		**CTM**	**Cs(2)**		**Cs(2)**
γ_1	Y	a	(1)	→	(5)
			(4)	→	(6)
		b	(5)	→	(1)
			(6)	→	(4)
	Z	a	(2)	→	(3)
			(6)	→	(4)
		b	(3)	→	(2)
			(4)	→	(6)
γ_2	Y	c	(2)	→	(3)
			(3)	→	(2)
	Z	c	(1)	→	(5)
			(5)	→	(1)

Table 6.9: Bleaching pathways of the Cs(2) centre, which produce the discrete-photoproduct centre Cs(2)*.

Absorption		**CTM**	**Cs(2)**		**Cs(2)***	
γ_1	Y	a	(1)	→	(3)*	(4)*
			(4)	→	(1)*	(2)*
		b	(5)	→	(3)*	(4)*
			(6)	→	(1)*	(2)*
	Z	a	(2)	→	(5)*	(6)*
			(6)	→	(1)*	(2)*
		b	(3)	→	(5)*	(6)*
			(4)	→	(1)*	(2)*
γ_2	Y	c	(2)	→	(5)*	(6)*
			(3)	→	(5)*	(6)*
	Z	c	(1)	→	(3)*	(4)*
			(5)	→	(3)*	(4)*

Table 6.10: Bleaching pathways of the Cs(2)* centre.

Absorption		**CTM**	**Cs(2)***		**Cs(2)**	
γ_1	Y	$\frac{1}{2}$a	(1)*	→	(4)	(6)
			(2)*	→	(4)	(6)
			(3)*	→	(1)	(5)
			(4)*	→	(1)	(5)
		b	(5)*	→	(2)	(3)
			(6)*	→	(2)	(3)
	Z	$\frac{1}{2}$a	(1)*	→	(4)	(6)
			(2)*	→	(4)	(6)
			(5)*	→	(2)	(3)
			(6)*	→	(2)	(3)
		b	(3)*	→	(1)	(5)
			(4)*	→	(1)	(5)
γ_2	Y	$\frac{1}{2}$c	(1)*	→	(4)	(6)
			(2)*	→	(4)	(6)
			(3)*	→	(1)	(5)
			(4)*	→	(1)	(5)
	Z	$\frac{1}{2}$c	(1)*	→	(4)	(6)
			(2)*	→	(4)	(6)
			(5)*	→	(2)	(3)
			(6)*	→	(2)	(3)

Table 6.11: Bleaching pathways of the Cs(3) centre.

Absorption		**CTM**	**Cs(3)**	→	**Cs(3)***			
γ_1	Y	$\frac{1}{2}$a	(1)	→	(3)*	(4)*	(5)*	(6)*
			(2)	→	(3)*	(4)*	(5)*	(6)*
			(3)	→	(1)*	(2)*	(5)*	(6)*
			(4)	→	(1)*	(2)*	(5)*	(6)*
		b	(5)	→	(1)*	(2)*	(3)*	(4)*
			(6)	→	(1)*	(2)*	(3)*	(4)*
	Z	$\frac{1}{2}$a	(1)	→	(3)*	(4)*	(5)*	(6)*
			(2)	→	(3)*	(4)*	(5)*	(6)*
			(5)	→	(1)*	(2)*	(3)*	(4)*
			(6)	→	(1)*	(2)*	(3)*	(4)*
		b	(3)	→	(1)*	(2)*	(5)*	(6)*
			(4)	→	(1)*	(2)*	(5)*	(6)*
γ_2	Y	$\frac{1}{2}$c	(1)	→	(3)*	(4)*	(5)*	(6)*
			(2)	→	(3)*	(4)*	(5)*	(6)*
			(3)	→	(1)*	(2)*	(5)*	(6)*
			(4)	→	(1)*	(2)*	(5)*	(6)*
	Z	$\frac{1}{2}$c	(1)	→	(3)*	(4)*	(5)*	(6)*
			(2)	→	(3)*	(4)*	(5)*	(6)*
			(5)	→	(1)*	(2)*	(3)*	(4)*
			(6)	→	(1)*	(2)*	(3)*	(4)*

Table 6.12: Bleaching pathways of the Cs(3)* centre, using the C_{4v} approximation

C_{4v} **Absorption**		**CTM**	**Cs(3)***	→	**Cs(3)**			
γ_5	Y	$\frac{1}{2}$(a+b)	(1)*+(2)*	→	(3)	(4)	(5)	(6)
			(3)*+(4)*	→	(1)	(2)	(5)	(6)
	Z	$\frac{1}{2}$(a+b)	(1)*+(2)*	→	(3)	(4)	(5)	(6)
			(5)*+(6)*	→	(1)	(2)	(3)	(4)
γ_1	Y	c	(5)*+(6)*	→	(1)	(2)	(3)	(4)
	Z	c	(3)*+(4)*	→	(1)	(2)	(5)	(6)

Table 6.13: Bleaching pathways of the Cs(4) centre.

Absorption		CTM	Cs(4)	→	Cs(4)*			
γ_1	Y	c	(5)	→	(1)*	(2)*	(3)*	(4)*
			(6)	→	(1)*	(2)*	(3)*	(4)*
	Z	c	(3)	→	(1)*	(2)*	(3)*	(4)*
			(4)	→	(1)*	(2)*	(3)*	(4)*
γ_2	Y	$\frac{1}{2}$a	(1)	→	(3)*	(4)*	(5)*	(6)*
			(2)	→	(3)*	(4)*	(5)*	(6)*
			(3)	→	(1)*	(2)*	(5)*	(6)*
			(4)	→	(1)*	(2)*	(5)*	(6)*
	Z	$\frac{1}{2}$a	(1)	→	(3)*	(4)*	(5)*	(6)*
			(2)	→	(3)*	(4)*	(5)*	(6)*
			(5)	→	(1)*	(2)*	(3)*	(4)*
			(6)	→	(1)*	(2)*	(3)*	(4)*
γ_4	Y	$\frac{1}{2}$b	(1)	→	(3)*	(4)*	(5)*	(6)*
			(2)	→	(3)*	(4)*	(5)*	(6)*
			(3)	→	(1)*	(2)*	(5)*	(6)*
			(4)	→	(1)*	(2)*	(5)*	(6)*
	Z	$\frac{1}{2}$b	(1)	→	(3)*	(4)*	(5)*	(6)*
			(2)	→	(3)*	(4)*	(5)*	(6)*
			(5)	→	(1)*	(2)*	(3)*	(4)*
			(6)	→	(1)*	(2)*	(3)*	(4)*

Table 6.14: Bleaching pathways of the Cs(4)* centre, using the C_{4v} approximation.

C_{4v}	Absorption	CTM	Cs(4)*	→	Cs(4)			
γ_5	Y	$\frac{1}{2}$(a+b)	(1)*+(2)*	→	(3)	(4)	(5)	(6)
			(3)*+(4)*	→	(1)	(2)	(5)	(6)
	Z	$\frac{1}{2}$(a+b)	(1)*+(2)*	→	(3)	(4)	(5)	(6)
			(5)*+(6)*	→	(1)	(2)	(3)	(4)
γ_1	Y	c	(5)*+(6)*	→	(1)	(2)	(3)	(4)
	Z	c	(3)*+(4)*	→	(1)	(2)	(5)	(6)

Table 6.15: Bleaching pathways of the Cs(5) centre.

Absorption		**CTM**	**Cs(5)**		**Cs(5)***	
γ_5	Y	$\frac{1}{2}$(a+b)	(1)	→	(3)*	(5)*
			(2)	→	(2)*	(6)*
	Z	$\frac{1}{2}$(a+b)	(1)	→	(3)*	(5)*
			(3)	→	(1)*	(4)*
γ_1	Y	c	(3)	→	(1)*	(4)*
	Z	c	(2)	→	(2)*	(6)*

Table 6.16: Bleaching pathways of the Cs(5)* centre.

Absorption		**CTM**	**Cs(5)***		**Cs(5)**
γ_1	Y	a	(1)*	→	(3)
			(4)*	→	(3)
		b	(5)*	→	(1)
			(6)*	→	(2)
	Z	a	(2)*	→	(2)
			(6)*	→	(2)
		b	(3)*	→	(1)
			(4)*	→	(3)
γ_2	Y	c	(2)*	→	(2)
			(3)*	→	(1)
	Z	c	(1)*	→	(3)
			(5)*	→	(1)

This is demonstrated in the bleaching sequence of Figure 6.4, for the γ_2 $Z_2 \rightarrow E$ transition. Population is exchanged between two pairs of orientations, (3)+(4) and (5)+(6), while the other orientations, (1)+(2), are partially depleted. The X polarisation of the γ_2 $D_1 \rightarrow Z_2$ fluorescence was analysed so that only orientations (3), (4), (5) and (6) were seen in fluorescence. This should enhance the apparent reversible-polarisation bleaching as it is these orientations which are being alternately depleted and repopulated. The fluorescence is enhanced on first switching the excitation polarisation, but this is followed by a gradual decline during subsequent cycles. After about 5 minutes of alternately bleaching each polarisation, an equilibrium condition is reached in which full fluorescence recovery is achieved in the course of each cycle.

This decline is not predicted by the proposed bleaching model. This type of behaviour was also observed in the Cs(2) centre and was attributed to discrete-photoproduct formation bleaching. However, a careful search did not reveal any discrete photoproducts of the Cs(1) centre. Another mechanism which could produce such a gradual decline in fluorescence intensity has been observed in the Cs(2) centre by Attenberger et al [7]. They burned a 5GHz wide spectral hole in the $Z_1 \rightarrow E$ absorption transition of the Cs(2) centre, which has a spectral width of approximately 14GHz (FWHM) at 10K. A broad anti-hole feature was produced, enhancing the absorption over the rest of the inhomogeneously-broadened line. This was attributed to the reorientational-bleaching mechanism, which yields Cs(2) centres that are shifted within the inhomogeneously-broadened transition. When a centre has been reorientated it will experience a slightly different crystal field, in the reference frame defined by the reorientated symmetry axes, due to the apparent spatial redistribution of defects in the neighbourhood of that centre. Such a change in the crystal field will shift the Pr^{3+} ion energy levels slightly and so shift the transition energies. In some reorientated centres the homogeneously-broadened absorption transition will lie outside the laser line, but still within the inhomogeneously-broadened transition. These centres can no longer participate in the bleaching process and their fluorescence will not be recovered by switching the excitation polarisation. Other centres will still be resonant with the excitation beam after reorientation. It is these centres which are responsible for the long sequences of reversible-polarised bleaching which have been observed in the Cs(1) and Cs(2) centres.

This redistribution of centres within the inhomogeneously-broadened excitation transition will also occur during reorientational bleaching of the Cs(1) centre. Over successive bleaching cycles this will cause a decrease in the recoverable fluorescence until an equilibrium condition is reached and fully reversible bleaching becomes attainable. This describes the behaviour observed in Figure 6.4, where over 60% of the fluorescence can no longer be recovered after four cycles.

Almost identical bleaching sequences are obtained by pumping the γ_1 $Z_1 \rightarrow D_1$ and $Z_1 \rightarrow E$ excitation transitions. Both these transitions are derived from γ_5 parent transitions. Table 6.6 shows that reversible-polarisation bleaching will not be observed if the condition 2a=b applies to the CTMs. The C_{4v} approximation predicts that $a \gg b$ for both these transitions. In Table 5.6 this was confirmed for the $Z_1 \rightarrow D_1$

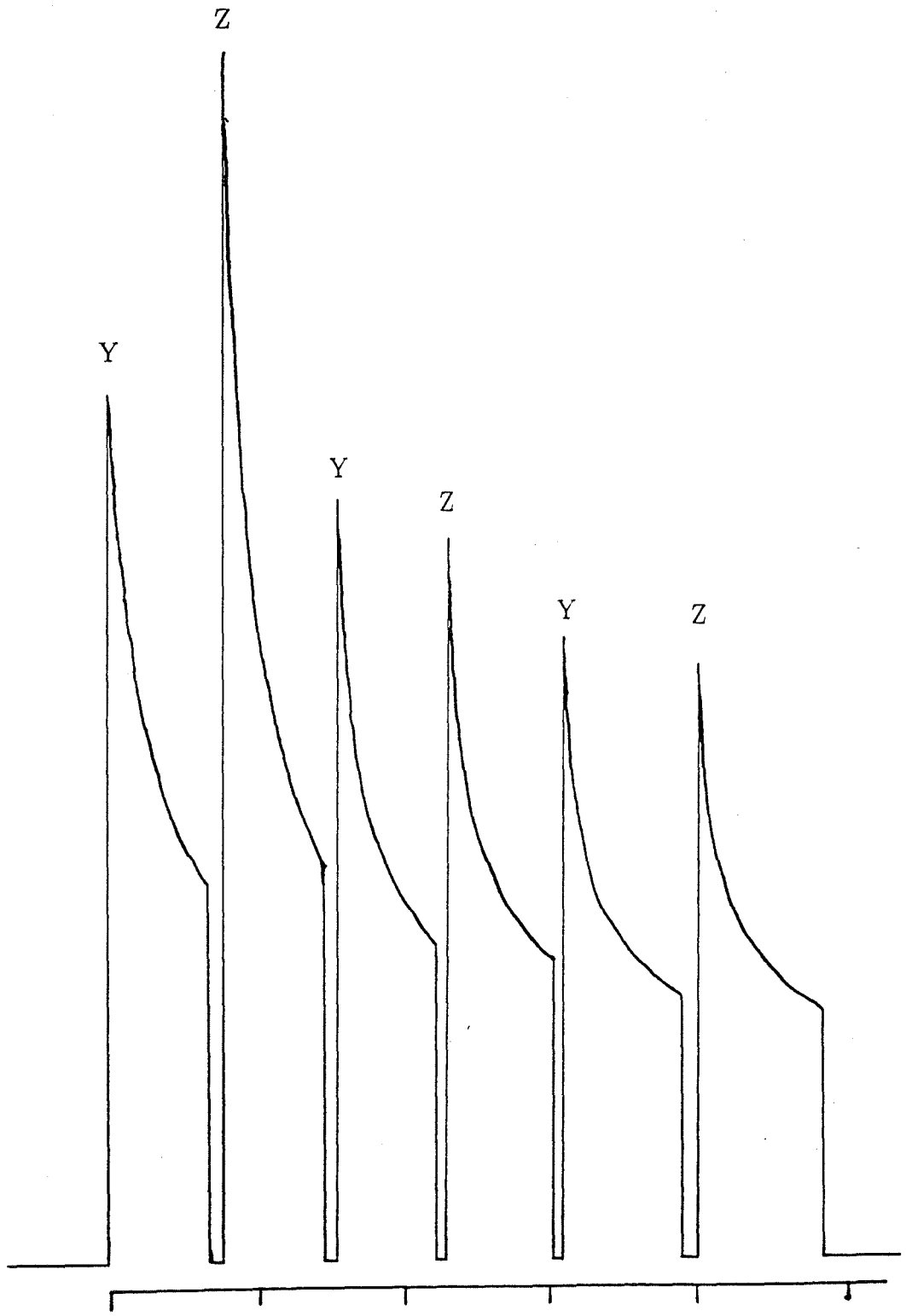

Figure 6.4: A polarisation-bleaching sequence for the Cs(1) centre in the SrF_2:Pr^{3+}:D^- crystal. The $Z_2 \rightarrow E$ transition was pumped, while monitoring the X polarised $D_1 \rightarrow Z_2$ fluorescence. The tick-marks are at 1 minute intervals.

transition when it was found that a≈6.3b.

As another test of the bleaching mechanism proposed for the Cs(1) centre a bleaching sequence was obtained for the YZ linear excitation polarisation. This is shown in Figure 6.5. Bleaching the γ_1 $Z_1 \rightarrow D_1$ transition enhances the fluorescence obtained when pumping the γ_2 $Z_2 \rightarrow D_1$ transition. Table 6.7 shows that YZ polarised excitation of a γ_1 transition will deplete orientation (1) and populate orientation (2). The bleached fluorescence can be recovered by pumping a γ_2 transition as orientation (2) will then be resonant with the excitation beam. This redistribution of the Cs(1) centre population can occur despite the fact that no single centre may be reorientated between orientations (1) and (2) .

The Cs(1) centre could also be bleached by a circularly-polarised excitation beam when pumping either the $Z_1 \rightarrow D_1$ or the $Z_2 \rightarrow D_1$ transition. Both the Y and Z polarisation components will be present in a C polarised beam, so it will be resonant with all six orientations of the Cs(1) centre, Table 6.6. Bleaching can occur because orientations (1)+(2) are more strongly coupled to the excitation beam than the other orientations. Orientations (1)+(2) will be depleted and the other orientations will become more populated until an equilibrium population distribution is attained.

Using Tables 6.6 and 6.7 rate equations can be derived which describe the changing populations of the Cs(1) centre orientations under the various bleaching conditions. These may be solved to determine the transient populations of these orientations and the time dependence of the fluorescence intensity during bleaching. Rate equations and their solutions will be considered here for Y, YZ and C polarised excitation of the Cs(1) centre. The following nomenclature will be used to denote the populations of different sets of orientations: $a_1 \equiv (1)$, $a_2 \equiv (2)$, $a \equiv (1)+(2)$, $b \equiv (3)+(4)$ and $c \equiv (5)+(6)$.

The rate equations for Y polarisation pumping of a γ_2 transition are:

$$\begin{aligned} \dot{a}(t) &= -2Wa(t) + Wb(t) \\ \dot{b}(t) &= Wa(t) - 2Wb(t) \\ \dot{c}(t) &= Wa(t) + Wb(t)\,, \end{aligned}$$

where W is the bleaching rate appropriate for the CTM $\frac{1}{2}$c. Solving these equations produces the following functions for the transient populations of the Cs(1) centre orientations:

$$\begin{aligned} a(t) &= \tfrac{1}{2}(a_0 + b_0)e^{-Wt} + \tfrac{1}{2}(a_0 - b_0)e^{-3Wt} \\ b(t) &= \tfrac{1}{2}(a_0 + b_0)e^{-Wt} - \tfrac{1}{2}(a_0 - b_0)e^{-3Wt} \\ c(t) &= a_0 + b_0 + c_0 - (a_0 + b_0)e^{-Wt}\,. \end{aligned}$$

a_0, b_0 and c_0 denote the initial populations of the orientations. Only orientations (1)+(2) and (3)+(4) will fluoresce under these excitation conditions, with an integrated fluorescence intensity of:

$$\begin{aligned} I(t) &= \beta W\,(a(t) + b(t)) \\ &\quad \beta W(a_0 + b_0)e^{-Wt}\,, \end{aligned} \tag{6.1}$$

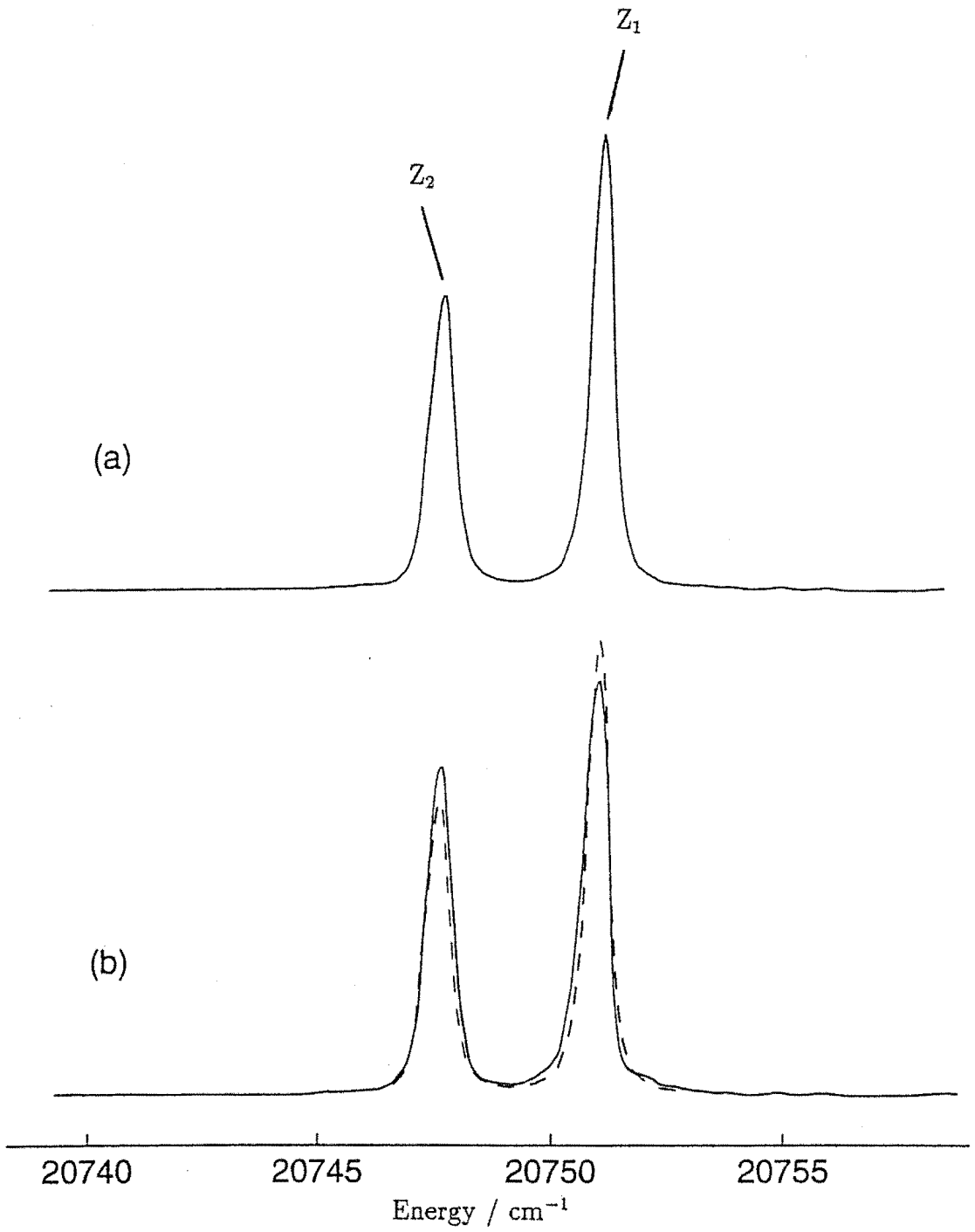

Figure 6.5: A bleaching sequence showing the $Z_1 \rightarrow D_1$ and $Z_2 \rightarrow D_1$ absorption transitions of the Cs(1) centre in the SrF_2:Pr^{3+}:D^- crystal. The excitation beam was YZ polarised throughout this experiment and the fluorescence was not analysed. Spectrum (**a**) shows these transitions prior to bleaching and (**b**) shows them after the $Z_1 \rightarrow D_1$ transition has been bleached. The spectrum of (**a**) has been reproduced in (**b**) for comparison.

where β is a constant. The predicted bleaching curve is exponential and the fluorescence intensity limits to zero under continuous irradiation.

Two sets of rate equations are required to describe YZ polarised bleaching. The Cs(1) centres present in a virgin piece of crystal can be divided into four equal groups, according to the orientations which are accessible to them through reorientational bleaching. For example, a quarter of the centres can only be reorientated between the orientations (1), (4) and (6). The other groups comprise the orientations (1)+(3)+(5), (2)+(5)+(4) and (2)+(3)+(6). For YZ polarised pumping of a γ_2 transition, orientation (2) is resonant with the excitation beam, but orientation (1) is not. Since population cannot be exchanged between orientations (1) and (2), they must also be included in separate sets of rate equations. Centres in the first two groups will be identified by the subscript '1', while centres in the other two groups will be labeled '2'.

The rate equations for YZ polarised pumping of a γ_2 transition are:

$$\begin{aligned}
\dot{a_1}(t) &= \tfrac{1}{2}Wb_1(t) + \tfrac{1}{2}Wc_1(t) \\
\dot{b_1}(t) &= -Wb_1(t) + \tfrac{1}{2}Wc_1(t) \\
\dot{c_1}(t) &= \tfrac{1}{2}Wb_1(t) - Wc_1(t)\,,
\end{aligned}$$

and

$$\begin{aligned}
\dot{a_2}(t) &= -4Wa_2(t) + \tfrac{1}{2}Wb_2(t) + \tfrac{1}{2}Wc_2(t) \\
\dot{b_2}(t) &= 2Wa_2(t) - Wb_2(t) + \tfrac{1}{2}Wc_2(t) \\
\dot{c_2}(t) &= 2Wa_2(t) + \tfrac{1}{2}Wb_2(t) - Wc_2(t)\,.
\end{aligned}$$

These equations can be solved for the transient populations of the orientations which are:

$$\begin{aligned}
a_1(t) &= \tfrac{1}{2}(2a_1 + b_0 + c_0) - \tfrac{1}{2}(b_0 + c_0)e^{-\frac{1}{2}Wt} \\
b_1(t) &= \tfrac{1}{4}(b_0 + c_0)e^{-\frac{1}{2}Wt} + \tfrac{1}{4}(b_0 - c_0)e^{-\frac{3}{2}Wt} \\
c_1(t) &= \tfrac{1}{4}(b_0 + c_0)e^{-\frac{1}{2}Wt} - \tfrac{1}{4}(b_0 - c_0)e^{-\frac{3}{2}Wt}\,,
\end{aligned}$$

and

$$\begin{aligned}
a_2(t) &= \tfrac{1}{18}(2a_2 + b_0 + c_0) + \tfrac{1}{18}(16a_2 - b_0 - c_0)e^{-\frac{9}{2}Wt} \\
b_2(t) &= \tfrac{2}{9}(2a_2 + b_0 + c_0) - \tfrac{1}{36}(16a_2 - b_0 - c_0)e^{-\frac{9}{2}Wt} + \tfrac{1}{4}(b_0 - c_0)e^{-\frac{3}{2}Wt} \\
c_2(t) &= \tfrac{2}{9}(2a_2 + b_0 + c_0) - \tfrac{1}{36}(16a_2 - b_0 - c_0)e^{-\frac{9}{2}Wt} - \tfrac{1}{4}(b_0 - c_0)e^{-\frac{3}{2}Wt}\,.
\end{aligned}$$

All centres, except those in orientation (1), will contribute to the fluorescence which has an intensity of:

$$\begin{aligned}
I(t) &= \beta W\left(2a_2(t) + \tfrac{1}{2}b(t) + \tfrac{1}{2}c(t)\right) \\
&= \beta W\left(\tfrac{3}{9}(2a_2 + b_0 + c_0) + \tfrac{1}{12}(16a_2 - b_0 - c_0)e^{-\frac{9}{2}Wt} + \tfrac{1}{4}(b_0 + c_0)e^{-\frac{1}{2}Wt}\right) \quad (6.2)
\end{aligned}$$

The integrated fluorescence intensity is a function of two exponential terms and a constant. The second term is associated with population transfer from orientation (2) to orientations (3)+(4) and (5)+(6). The third term is associated with transfer from orientations (3)+(4) and (5)+(6) to orientation (1). Under continuous irradiation the fluorescence intensity will limit to 50% of its value before bleaching, if all orientations were equally populated initially.

The rate equations for C polarised pumping of a γ_2 transition are:

$$\begin{aligned}
\dot{a}(t) &= -2Wa(t) + \tfrac{1}{2}Wb(t) + \tfrac{1}{2}Wc(t) \\
\dot{b}(t) &= Wa(t) - Wb(t) + \tfrac{1}{2}Wc(t) \\
\dot{c}(t) &= Wa(t) + \tfrac{1}{2}Wb(t) - Wc(t) .
\end{aligned}$$

The effect of Malus' law has been taken into account, so the bleaching rate W remains unchanged. The transient populations of the Cs(1) centre orientations are:

$$\begin{aligned}
a(t) &= \tfrac{1}{5}(a_0 + b_0 + c_0) + \tfrac{1}{5}(4a_0 - b_0 - c_0)e^{-\frac{5}{2}Wt} \\
b(t) &= \tfrac{2}{5}(a_0 + b_0 + c_0) - \tfrac{1}{10}(4a_0 - b_0 - c_0)e^{-\frac{5}{2}Wt} + \tfrac{1}{2}(b_0 - c_0)e^{-\frac{3}{2}Wt} \\
c(t) &= \tfrac{2}{5}(a_0 + b_0 + c_0) - \tfrac{1}{10}(4a_0 - b_0 - c_0)e^{-\frac{5}{2}Wt} - \tfrac{1}{2}(b_0 - c_0)e^{-\frac{3}{2}Wt} .
\end{aligned}$$

The integrated fluorescence intensity is thus:

$$\begin{aligned}
I(t) &= \beta\tfrac{W}{2}\,(2a(t) + b(t) + c(t)) \\
&\quad \beta\tfrac{W}{2}\left(\tfrac{6}{5}(a_0 + b_0 + c_0) + \tfrac{1}{5}(4a_0 - b_0 - c_0)e^{-\frac{5}{2}Wt}\right) ,
\end{aligned} \tag{6.3}$$

where the factor of $\frac{1}{2}$ common to all terms is due to Malus' law. Again the predicted bleaching curve is exponential, but in this case the fluorescence intensity will limit to 90% of its value before bleaching.

Bleaching curves have been obtained under all three of the excitation conditions considered above. The same initial fluorescence intensity is predicted in each case ($I_0 = 2\beta W a_0$ where $a_0 = b_0 = c_0$) and this was observed experimentally. When the Cs(1) centre was irradiated with a C polarised beam the fluorescence could be bleached to less than 56% of its initial intensity, much lower than the 90% predicted. This discrepancy may also be attributed to the redistribution of Cs(1) centres within the inhomogeneously-broadened absorption transition, which takes some of the centres out of resonance with the excitation beam. The models presented above do not take this into account, so the $I(t)$ functions predicted cannot be fitted to the experimental bleaching curves. However it is still possible to make some crude comparisons between them.

Differentiation of $I(t)$ yields the bleaching rate. During irradiation the population distribution will become increasingly affected by the redistribution of centres within the inhomogeneously-broadened laser line. For this reason the different bleaching rates are best compared at $t = 0$. However, the measured bleaching rates

will still contain an additional contribution due to this mechanism. At $t = 0$ the predicted relative bleaching rates for the different excitation polarisations are: $\frac{C}{Y} = 0.5$ and $\frac{YZ}{Y} = 1.25$. The experimental rates were: $\frac{C}{Y} = 0.75 \pm 0.22$ and $\frac{YZ}{Y} = 1.07 \pm 0.28$. Both results indicate that YZ polarised bleaching is more efficient than Y polarised bleaching, at $t = 0$. Similarly C polarised bleaching is the least efficient.

The rate equations for Y polarisation pumping of a γ_1 transition are:

$$\begin{aligned}
\dot{a}(t) &= -2W_1 a(t) + W_1 b(t) + W_2 c(t) \\
\dot{b}(t) &= W_1 a(t) - 2W_1 b(t) + W_2 c(t) \\
\dot{c}(t) &= W_1 a(t) + W_1 b(t) - 2W_2 c(t)\,,
\end{aligned}$$

where W_1 and W_2 are the bleaching rates appropriate for the CTMs $\frac{1}{2}$a and b respectively. The following functions are obtained for the transient populations of the Cs(1) orientations:

$$\begin{aligned}
a(t) &= \frac{W_1}{W_1 + 2W_2}(a_0 + b_0 + c_0) + \frac{1}{2W_1 + 4W_2}(W_1 a_0 + W_1 b_0 - 2W_2 c_0) e^{-(W_1 + 2W_2)t} \\
&\quad + \tfrac{1}{2}(a_0 - b_0) e^{-3Wt} \\
b(t) &= \frac{W_2}{W_1 + 2W_2}(a_0 + b_0 + c_0) + \frac{1}{2W_1 + 4W_2}(W_1 a_0 + W_1 b_0 - 2W_2 c_0) e^{-(W_1 + 2W_2)t} \\
&\quad - \tfrac{1}{2}(a_0 - b_0) e^{-3Wt} \\
c(t) &= \frac{W_1}{W_1 + 2W_2}(a_0 + b_0 + c_0) - \frac{1}{W_1 + W_2}(W_1 a_0 + W_1 b_0 - 2W_2 c_0) e^{-(W_1 + 2W_2)t}\,.
\end{aligned}$$

The integrated fluorescence intensity is thus:

$$\begin{aligned}
I(t) &= \beta\,(W_1 a(t) + W_1 b(t) + W_2 c(t)) \\
&\quad \beta \left(\frac{3W_1 W_2}{W_1 + 2W_2}(a_0 + b_0 + c_0) + \frac{W_1 - W_2}{W_1 + 2W_2}(W_1 a_0 + W_1 b_0 - 2W_2 c_0) e^{-(W_1 + 2W_2)t} \right) \quad (6.4)
\end{aligned}$$

Once again the bleaching curve is exponential and the fluorescence intensity generally has a non-zero limit under continuous irradiation. In the special case where $W_2 = 0$, Equation 6.4 becomes Equation 6.1, with $W = W_1$.

None of the bleaching curves obtained while pumping γ_1 transitions of the Cs(1) centre fitted well to single-exponential functions. Cockroft [27] observed that the equivalent centre of Er^{3+} exhibits a reciprocal time dependence. The bleaching curves of the Cs(1) centre also fit very well to the function $I(t) = A + B\frac{1}{t}$. This result alone would suggest that bleaching is a cooperative process, as the reciprocal function $N(t) \propto \frac{1}{N}$ is the solution to the rate equation $\dot{N}(t) \propto N^2$. Thus each reorientation would require the excitation of two centres. However, there is no other evidence for this conclusion. The most likely explanation for the observed time dependence is that it is artifact of the redistribution of Cs(1) centres within the inhomogeneously-broadened excitation transition. This process will introduce at least one more term into the expression for $I(t)$, which might be sufficient to produce the observed time dependence.

6.4.2 The Cs(2) Centre

The Cs(2) centre exhibits both reorientational bleaching and discrete-photoproduct formation bleaching. Figure 6.6 shows two bleaching sequences for the Cs(2) centre, which will be analysed using Tables 6.8 and 6.9. In sequence (a) the γ_2 $Z_2 \rightarrow E$ transition is pumped. The X polarised fluorescence of the γ_1 $D_1 \rightarrow Z_1$ transition is analysed, so that only orientations (1), (2), (3) and (5) are seen in fluorescence. Although reorientational bleaching occurs during either Y or Z polarised excitation, this alone will not push these centres out of resonance with the excitation beam. Thus the observed fluorescence bleaching must be due to discrete-photoproduct formation and the redistribution of centres within the inhomogeneously-broadened absorption transition. Both polarisations bleach independently, with orientations (2)+(3) depopulated during Y polarised excitation and orientations (1)+(5) depopulated during Z polarised excitation.

Figure 6.6(b) is a bleaching sequence obtained when pumping the γ_1 $Z_1 \rightarrow E$ transition of the Cs(2) centre. The X polarised fluorescence of the γ_2 $D_1 \rightarrow Z_2$ transition is analysed, so that only orientations (4) and (6) are seen in fluorescence. Bleaching is possible because of the inequality of the CTMs a and b ($a \gg b$ for the $Z_1 \rightarrow E$ transition). Table 6.8 shows that during Y polarised excitation orientations (1) and (4) are depopulated, while orientations (5) and (6) become more populated. The lost fluorescence is recovered on switching to the Z polarisation, as orientation (6) is now resonant with the excitation beam. This produces a fluorescence enhancement during the first cycle. Orientations (2) and (6) are then depopulated and orientations (3) and (4) become more populated. Population is thus exchanged between orientations (4) and (6) and reversible-polarised bleaching is observed.

Discrete-photoproduct formation bleaching and the redistribution of centres within the inhomogeneously-broadened transition should produce a decrease in the recovered fluorescence over successive cycles. In the first two cycles this is observed, however in subsequent cycles the bleached fluorescence is almost fully recoverable. This result suggests that discrete-photoproduct formation bleaching is much less efficient than reorientational bleaching of the Cs(2) centre.

Reeves obtained a similar bleaching sequence while pumping the $Z_1 \rightarrow D_1$ transition and monitoring the unanalysed broadband fluorescence. Although reversible-polarised bleaching was observed, there was a gradual decline in the fluorescence recovered after each cycle. Over successive cycles this decline was arrested and after 30 minutes full recovery could be achieved in the course of each cycle. Table 6.8 shows that orientations (1) and (2) are progressively depopulated while pumping the $Z_1 \rightarrow D_1$ transition and that the lost fluorescence cannot be recovered. Fully reversible polarisation bleaching will be observed when orientations (1), (2), (3) and (5) attain an equilibrium population distribution, due to population exchange between orientations (4) and (6).

The models predict that quite distinctive bleaching behaviour should be observed for γ_1 and γ_2 excitation. Figure 6.6 shows that two very different bleaching

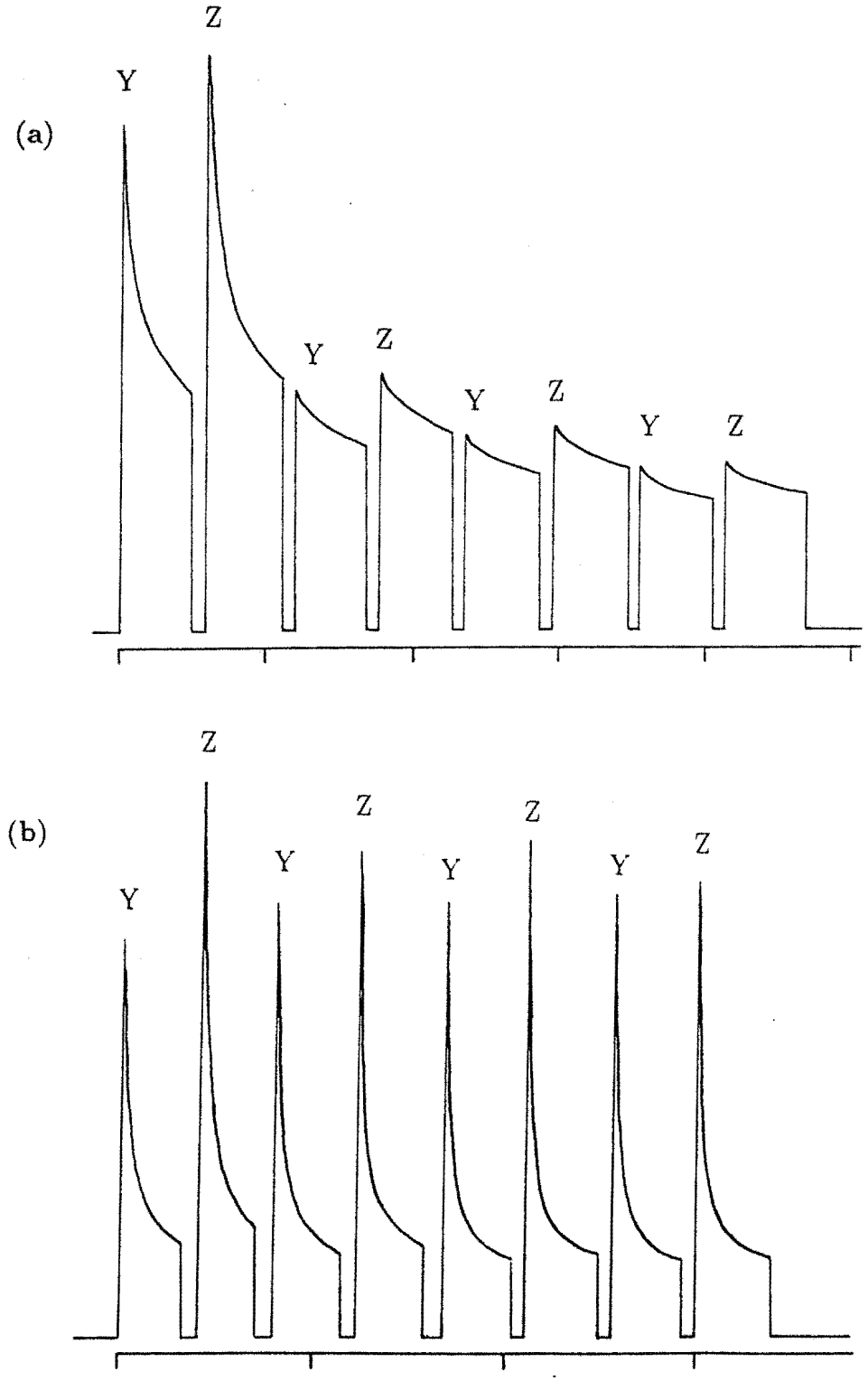

Figure 6.6: Polarisation-bleaching sequences for the Cs(2) centre in the SrF_2:Pr^{3+}:D^- crystal. **(a)** pumping the $Z_2 \rightarrow E$ transition while monitoring the X polarised $D_1 \rightarrow Z_1$ fluorescence. **(b)** pumping the $Z_1 \rightarrow E$ transition while monitoring the X polarised $D_1 \rightarrow Z_2$ fluorescence. The tick-marks are at 1 minute intervals.

sequences are obtained when pumping the $Z_1 \rightarrow D_1$ and $Z_2 \rightarrow D_1$ transitions of the Cs(2) centre. Thus it is possible to make definitive irrep assignments for these transitions and for the Z_1 and Z_2 states. They are identified as γ_1 and γ_2 states respectively. The models predict that reversible-polarised bleaching occurs when pumping the $Z_1 \rightarrow D_1$ transition, but not while pumping the $Z_2 \rightarrow D_1$ transition. This is the same as the behaviour observed by Reeves.

The photoproduct Cs(2)* centre will be produced during the bleaching sequence of Figure 6.6 (a). Table 6.9 shows that orientations (5)*+(6)* and orientations (3)*+(4)* of the Cs(2)* centre will be populated in turn. This selective population of the Cs(2)* centre is demonstrated in Figure 6.7. After the $Z_2 \rightarrow D_1$ transition of the Cs(2) centre is pumped with a Y polarised beam, the transitions of the Cs(2)* centre appear in the Z polarised excitation spectrum (c), but not in the Y polarised spectrum (b). This is consistent with the model, which predicts that orientations (5)*+(6)* will be resonant with a Z polarised beam, but not with a Y polarised beam. The γ_1 $Z_1 \rightarrow D_1$ transition of the Cs(2)* centre appears weakly in the Y polarised scan, as the CTM b is non-zero in the C_s symmetry crystal field. Similarly after Z polarised irradiation of the Cs(2) centre, the absorption transitions of the Cs(2)* centre appear in the Y polarised excitation spectrum (e), but not in the Z polarised spectrum (d).

Pumping the $Z_2 \rightarrow D_1$ transition will also affect the fluorescence obtained when the excitation beam is resonant with the $Z_1 \rightarrow D_1$ transition. After bleaching with a Y polarised beam this fluorescence has been reduced to 55% of its initial intensity in the Z polarised excitation spectrum (c), however it remains unchanged in the Y polarised spectrum (b). Table 6.8 shows that orientations (2) and (3), which are depopulated during the Y polarised pumping of the $Z_2 \rightarrow E$ transition, can only be excited by a Z polarised beam. The populations of other orientations, which fluoresce during Y polarised excitation, are unchanged by this bleaching.

6.4.3 The Cs(3) Centre

A bleaching sequence was obtained for discrete-photoproduct formation bleaching of the Cs(3) centre, Figure 6.8. This will be analysed using Tables 6.11 and 6.12. Pumping the γ_2 $Z_2 \rightarrow E$ transition with a Y polarised beam depopulates orientations (1), (2), (3) and (4) of the Cs(3) centre. Table 6.11 shows that half of the fluorescence observed during Z polarised pumping of the $Z_2 \rightarrow E$ transition is emitted by orientations (5) and (6). This explains why this transition still appears in Figure 6.8(d), with approximately half of its initial intensity.

All six orientations of the Cs(3)* centre become populated through Y polarised bleaching of the Cs(3) centre, Table 6.11. Half the centres will occupy orientations (5)* and (6)*, with the remainder distributed among the other four orientations. Thus the γ_5 $Z_1/Z_2 \rightarrow E$ excitation transitions of the Cs(3)* centre appear stronger by approximately 50% in the Z polarisation scan, Figures 6.8(c) and (d).

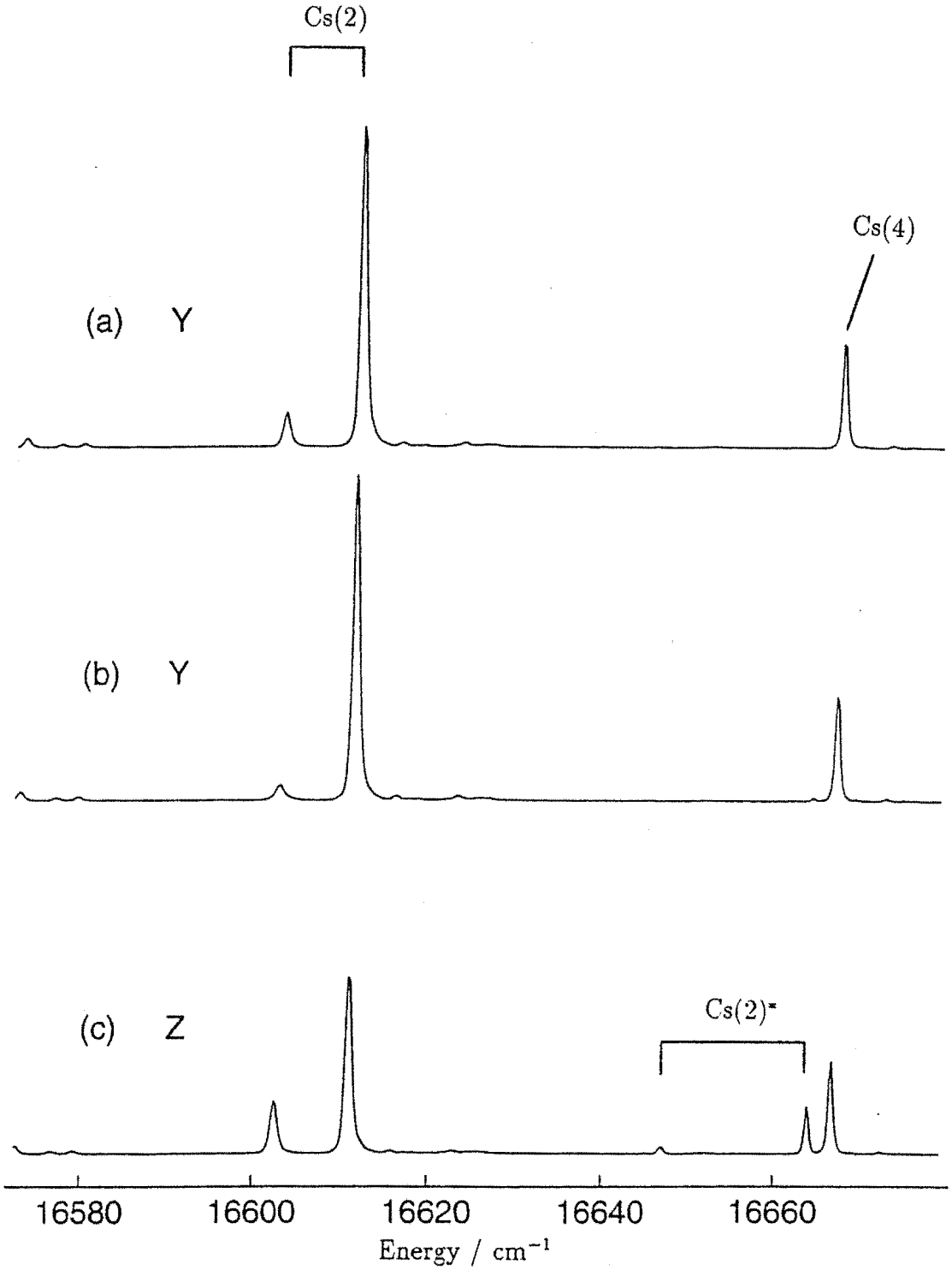
Cs(2)
Cs(4)
(a) Y
(b) Y
(c) Z
Cs(2)*
16580
16600
16620
16640
16660
Energy / cm^{-1}

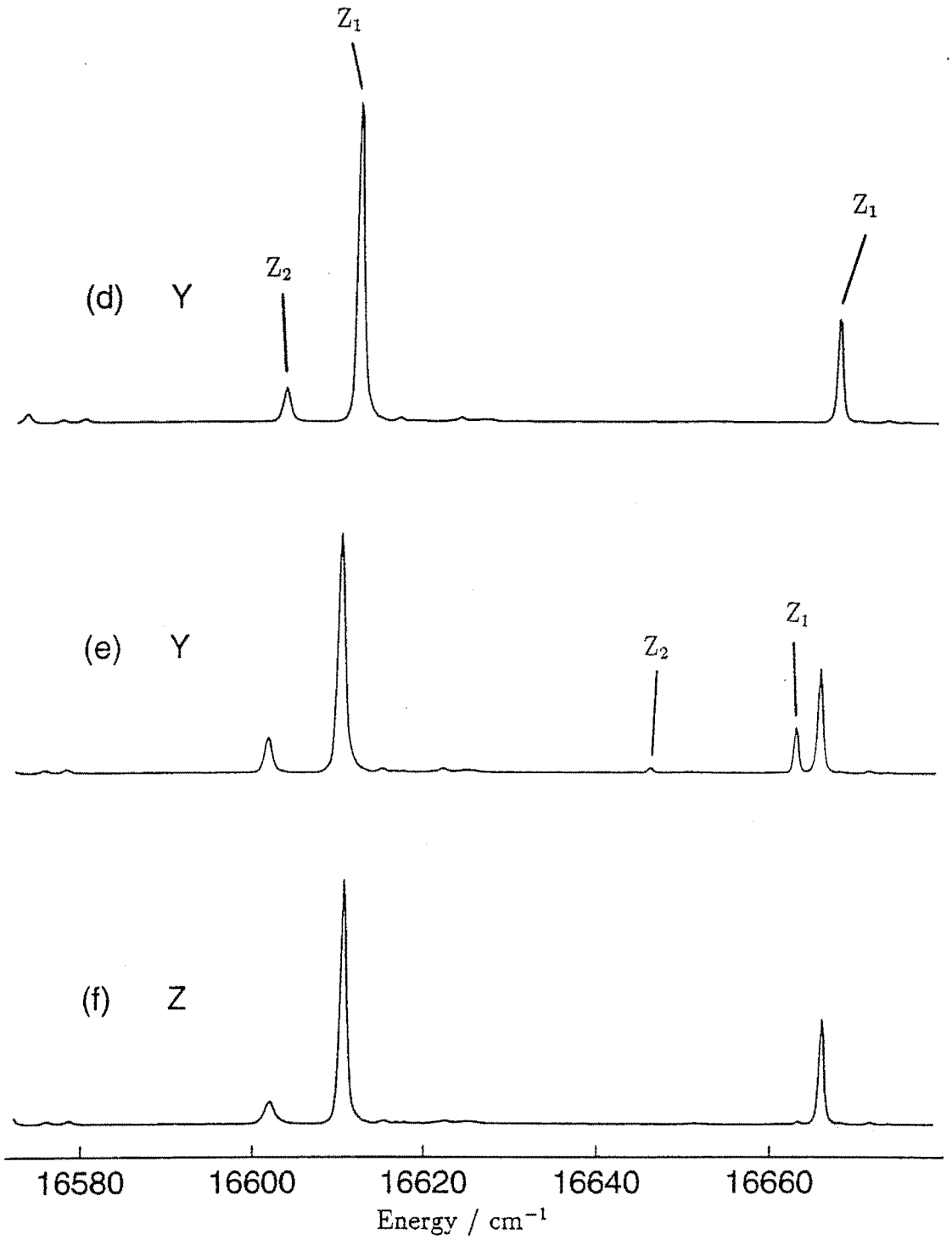

Figure 6.7: A polarisation-bleaching sequence showing the $Z_1 \rightarrow D_1$ and $Z_2 \rightarrow D_1$ absorption transitions of the Cs(2) and Cs(2)* centres. Excitation spectra (a) and (d) show these transitions prior to bleaching the Cs(2) centre. Spectra (b) and (c) were produced after Y polarised irradiation of the $Z_2 \rightarrow D_1$ transition. Spectra (e) and (f) were produced after Z polarised irradiation, in a virgin piece of crystal. (a), (b), (d), (e) are Y polarised and (c) and (f) are Z polarised excitation scans.

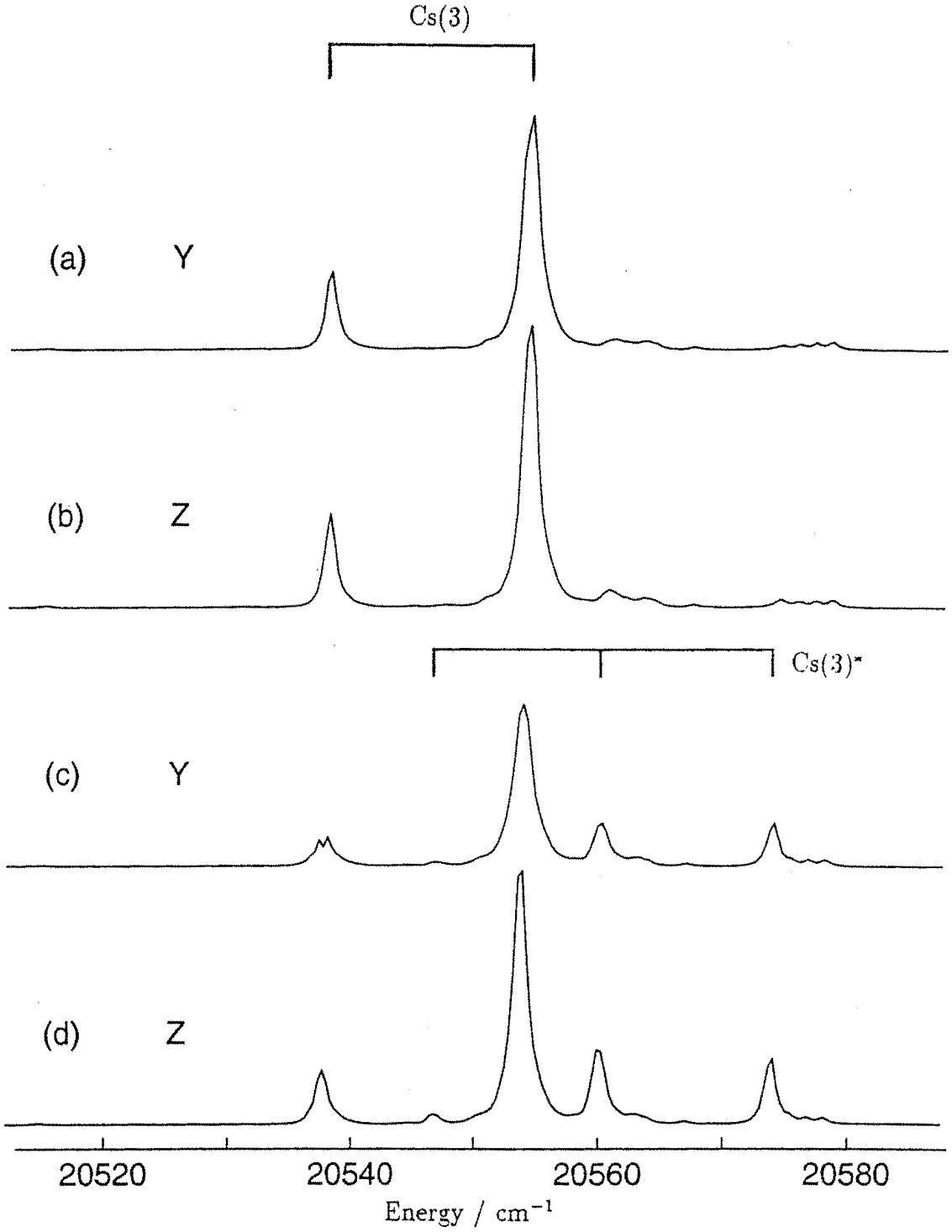
Cs(3)
(a) Y
(b) Z
Cs(3)*
(c) Y
(d) Z
20520
20540
20560
20580
Energy / cm^{-1}

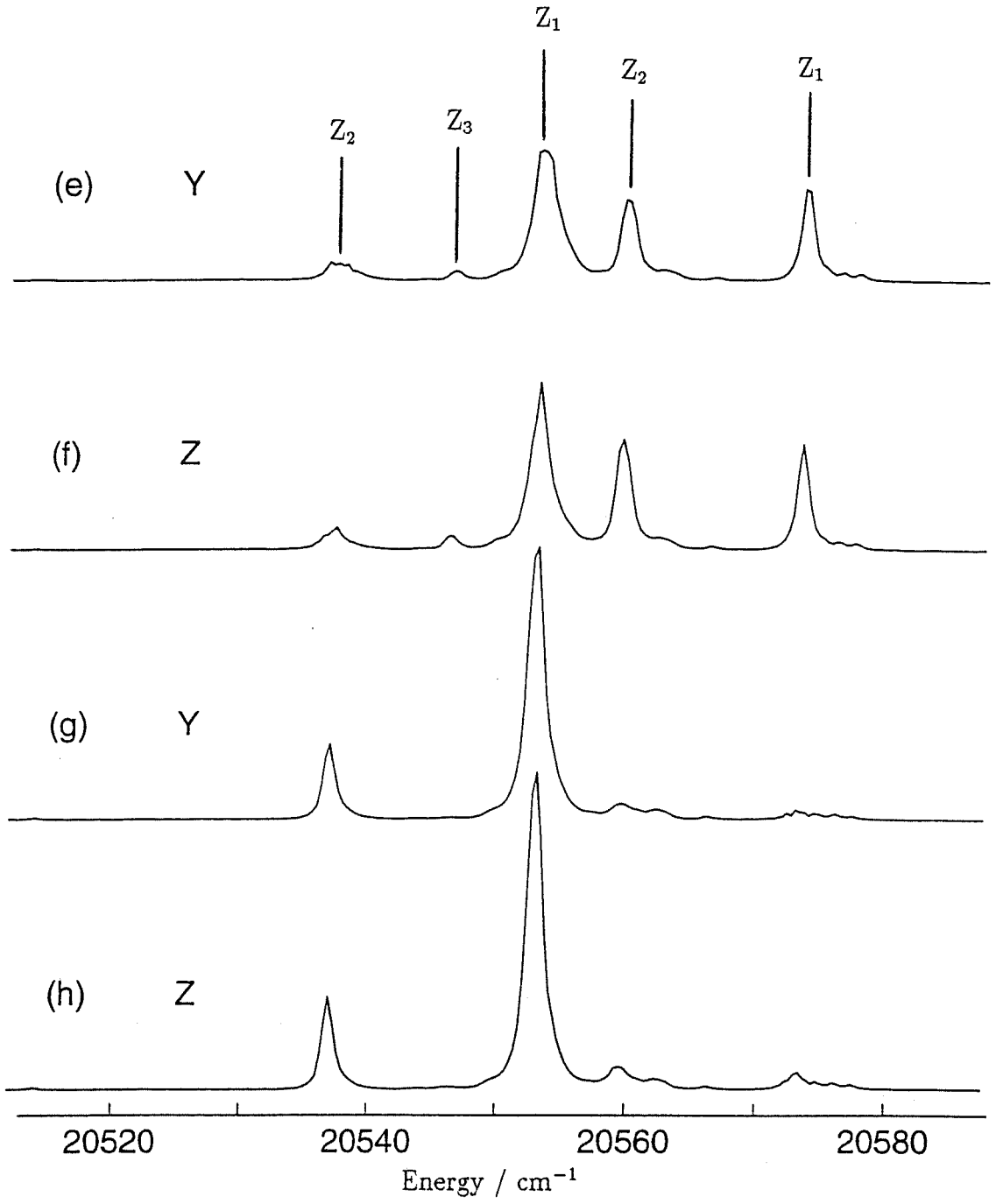

Figure 6.8: A polarisation-bleaching sequence showing the $Z_1 \rightarrow E$ and $Z_2 \rightarrow E$ absorption transitions of the Cs(3) and Cs(3)* centres in the $SrF_2:Pr^{3+}:D^-$ crystal. Excitation spectra (a) and (b) show these transitions prior to bleaching the Cs(2) centre. Spectra (c) and (d) were produced after Y polarised irradiation of the $Z_2 \rightarrow E$ transition, at a fixed excitation energy. Spectra (e) and (f) were produced after further Y and Z polarised irradiation, during which the excitation beam was scanned through the excitation transition. The Cs(3)* centre was then bleached by Y polarised pumping of the $Z_1 \rightarrow E$ transition and spectra (g) and (h) were obtained. (a), (c), (e) and (g) are Y polarised excitation scans and (b), (d), (f) and (h) are Z polarised excitation scans.

Selective irradiation has produced a spectral hole in the $Z_2 \rightarrow E$ transition of the Cs(3) centre, instead of bleaching it completely, Figure 6.8(c). Clearly the excitation beam is narrower than the inhomogeneously-broadened excitation transition. To completely bleach the Cs(3) centre some modulation of the excitation beam is required, so that the whole spectral line is irradiated, Figures 6.8(e) and (f).

Pumping the $Z_1 \rightarrow E$ transition of the Cs(3)* centre with a Y polarised beam repopulates orientations (5) and (6) more rapidly than the other orientations of the Cs(3) centre, Table 6.12. Thus the $Z_2 \rightarrow E$ transition of the Cs(3) centre appears stronger during Z polarised excitation, Figures 6.8(g) and (h). Additional pumping of the Cs(3)* transition with a Z polarised beam completely restores the Cs(3) centre fluorescence (not shown).

6.4.4 The Cs(4) Centre

A bleaching sequence was obtained for discrete-photoproduct formation bleaching of the Cs(4) centre, Figure 6.9. This will be analysed using Tables 6.13 and 6.14. Pumping the γ_4 $Z_1 \rightarrow D_1$ transition with a Y polarised excitation beam depopulates orientations (1), (2), (3) and (4) of the Cs(4) centre. Table 6.13 shows that orientations (5) and (6), which are unaffected by this bleaching, contribute half of the fluorescence observed during Z polarised pumping of the $Z_1 \rightarrow E$ transition. This is demonstrated in Figure 6.9(c), where this transition appears with approximately half its initial intensity.

Table 6.14 shows that Y polarised pumping of the Cs(4)* centre γ_5 $Z_1 \rightarrow D_1$ transition will restore orientations (1), (2), (3) and (4) to half their initial occupancy. Meanwhile the other half of that origional population remains bound in orientations (5)* and (6)*. Thus half of the intensity lost by the $Z_1 \rightarrow D_1$ transition of the Cs(4) centre during the initial bleaching is recovered, Figure 6.9(d). This fluorescence is restored further by additional Z polarised pumping of the Cs(4)* transition, Figure 6.9(e).

Using Tables 6.11 to 6.16 rate equations can be derived which describe the depopulation of the Cs centre orientations during discrete-photoproduct formation bleaching. This will be demonstrated by considering the bleaching of the Cs(4) centre in the SrF_2:Pr^{3+}:D^- crystal. The rate equations for discrete-photoproduct formation bleaching are much simpler than those for reorientational bleaching as there is no transfer of population between the orientations of the centre being irradiated. For all excitation polarisations it should be possible to bleach completely the observed fluorescence. The same nomenclature will be used to denote the populations of the centre orientations: $a_1 \equiv (1)$, $a_2 \equiv (2)$, $a \equiv (1)+(2)$, $b \equiv (3)+(4)$ and $c \equiv (5)+(6)$.

The rate equations for Y polarisation pumping of a γ_4 transition are:

$$\begin{aligned} \dot{a}(t) &= -2Wa(t) \\ \dot{b}(t) &= -2Wb(t), \end{aligned}$$

where W is the bleaching rate appropriate for the $\frac{1}{2}$b CTM. Solving these equations gives the following functions for the populations of the Cs(4) centre orientations:

$$\begin{aligned} a(t) &= a_0 e^{-2Wt} \\ b(t) &= b_0 e^{-2Wt} \\ c(t) &= c_0 . \end{aligned}$$

Only orientations (1)+(2) and (3)+(4) will fluoresce under these excitation conditions, with an integrated fluorescence intensity of:

$$\begin{aligned} I(t) &= \beta W (a(t) + b(t)) \\ &\quad \beta W (a_0 + b_0) e^{-2Wt} , \end{aligned} \tag{6.5}$$

where β is a constant. The predicted bleaching curve is exponential and the fluorescence intensity limits to zero under continuous irradiation.

The rate equations for YZ polarised pumping of a γ_4 transition are obtained by considering the possible orientations of the Cs(4) centre with respect to the crystal axes, Figure 4.4. Orientation (2) is not resonant with the excitation beam. The excitation probability of orientation (1) is four times that of orientations (3), (4), (5) and (6), hence:

$$\begin{aligned} \dot{a_1}(t) &= -4W a_1(t) \\ \dot{b}(t) &= -W b(t) \\ \dot{c}(t) &= -W c(t) . \end{aligned}$$

These equations can be solved for the transient populations of the orientations which are:

$$\begin{aligned} a_1(t) &= a_1 e^{-4Wt} \\ b(t) &= b_0 e^{-Wt} \\ c(t) &= c_0 e^{-Wt} . \end{aligned}$$

All centres, except those in orientation (2), will contribute to the fluorescence which has an intensity of:

$$\begin{aligned} I(t) &= \beta W \left(2a(t) + \tfrac{1}{2} b(t) + \tfrac{1}{2} c(t) \right) \\ &= \beta W \left(2a_1 e^{-4Wt} + \tfrac{1}{2} (b_0 + c_0) e^{-Wt} \right) . \end{aligned} \tag{6.6}$$

The predicted bleaching curve has two exponential terms and the fluorescence intensity will limit to zero under continuous irradiation.

The rate equations for C polarised pumping of a γ_4 transition are:

$$\begin{aligned} \dot{a}(t) &= -2W a(t) \\ \dot{b}(t) &= -W b(t) \\ \dot{c}(t) &= -W c(t) . \end{aligned}$$

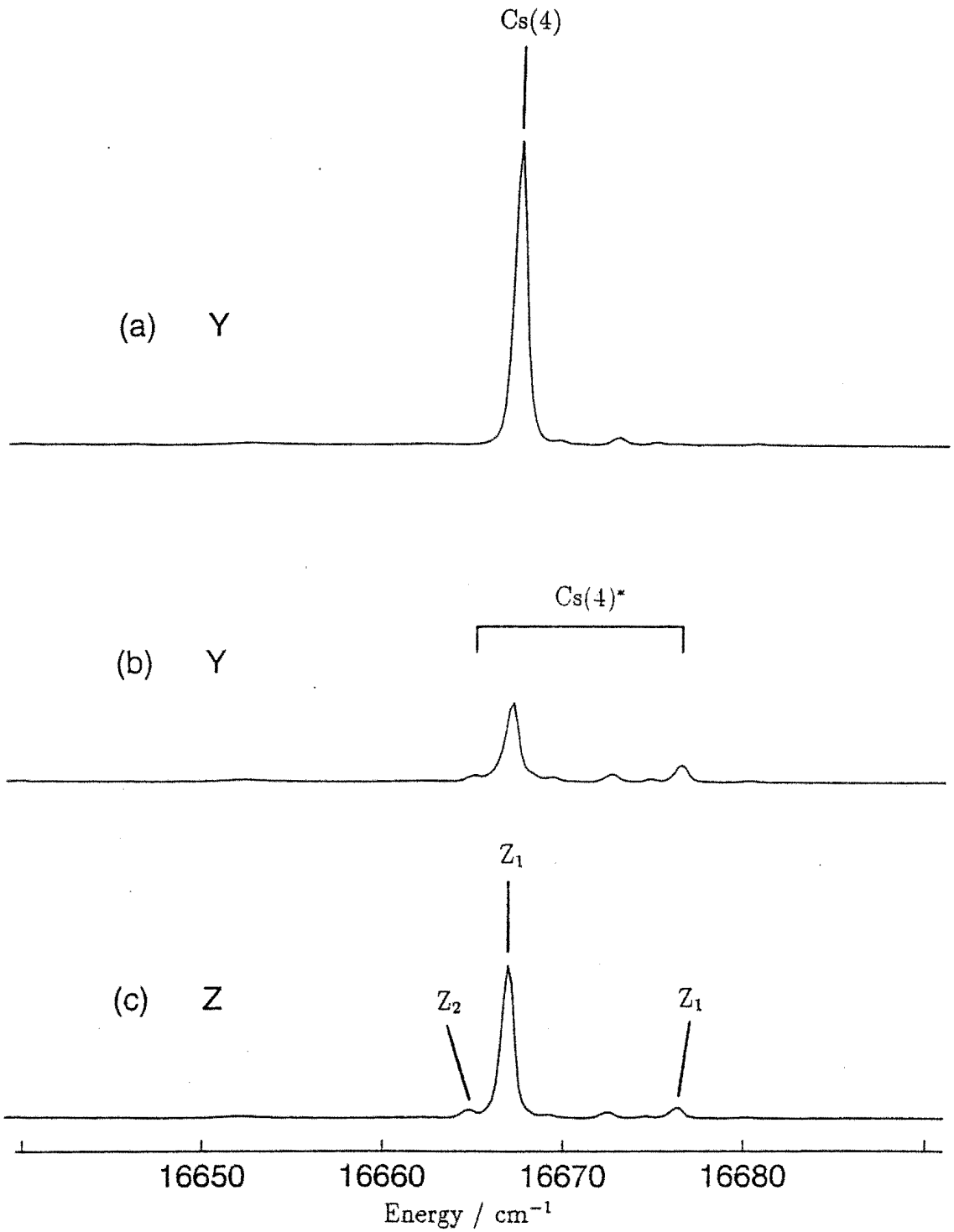
Cs(4)
(a) Y
Cs(4)*
(b) Y
Z1
(c) Z
Z2
Z1
16650
16660
16670
16680
Energy / cm-1

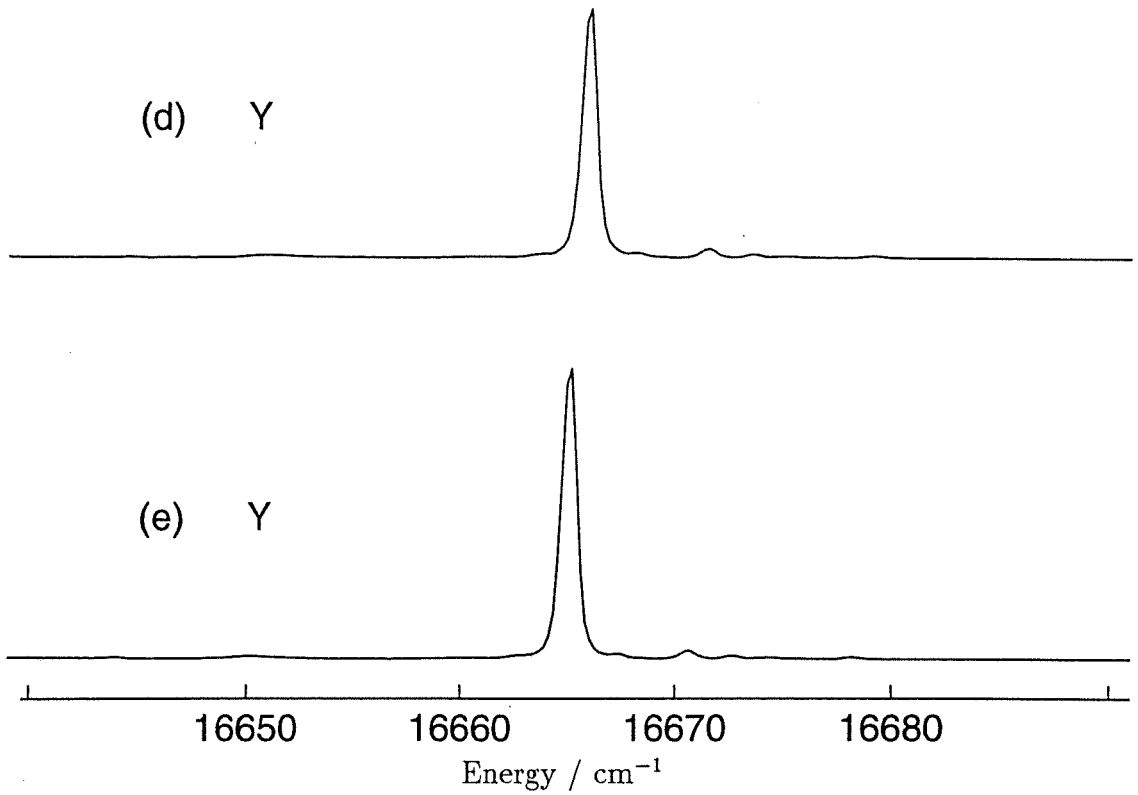

Figure 6.9: A polarisation-bleaching sequence showing the absorption transitions of the Cs(4) and Cs(4)* centres in the SrF_2:$Pr^{3+}D^-$ crystal. The excitation spectrum (**a**) shows the Cs(4) $Z_1 \rightarrow D_1$ transition prior to bleaching. Spectra (**b**) and (**c**) were produced after Y polarised irradiation of this transition. The Cs(4)* centre was then bleached by Y polarised pumping of the $Z_1 \rightarrow D_1$ transition (**d**) and then Z polarised pumping (**e**). (**a**), (**b**), (**d**) and (**e**) are Y polarised excitation scans and (**c**) is a Z polarised excitation scan.

The transient populations of the Cs(4) centre orientations are:

$$\begin{aligned} a(t) &= a_0 e^{-2Wt} \\ b(t) &= b_0 e^{-Wt} \\ c(t) &= c_0 e^{-Wt}. \end{aligned}$$

The integrated fluorescence intensity is thus:

$$\begin{aligned} I(t) &= \beta\tfrac{W}{2}\left(2a(t) + b(t) + c(t)\right) \\ &\quad \beta\tfrac{W}{2}\left(2a_0 e^{-2Wt} + (b_0 + c_0)e^{-Wt}\right). \end{aligned} \tag{6.7}$$

Again the predicted bleaching curve has two exponential terms.

Bleaching curves have been obtained under all three of the excitation conditions considered above. The same initial fluorescence intensity is predicted in each case ($I_0 = 2\beta W a_0$ where $a_0 = b_0 = c_0$) and this was observed experimentally. Differentiation of $I(t)$ yields the bleaching rate. At $t = 0$ the relative bleaching rates predicted for the different excitation polarisations are: $\frac{C}{Y} = 0.75$ and $\frac{YZ}{Y} = 1.25$. The experimental rates are: $\frac{C}{Y} = 0.57\pm0.19$ and $\frac{YZ}{Y} = 1.32\pm0.43$. Both results indicate that YZ polarised bleaching is more efficient than Y polarised bleaching, at $t = 0$. Similarly C polarised bleaching is the least efficient.

The bleaching curves produced during Y polarised irradiation of the $Z_1 \rightarrow D_1$ transition fitted very well to single-exponential functions. The experimental bleaching rates for 30mW pumping were: $1.54\text{x}10^{-2}\text{s}^{-1}$ in the $SrF_2:Pr^{3+}:D^-$ crystal and $1.24\text{x}10^{-2}\text{s}^{-1}$ in the $CaF_2:Pr^{3+}:D^-$ crystal.

Almost complete restoration of the Cs(4) centre fluorescence is achieved when both polarisations of the Cs(4)* transition are bleached. This suggests that the Cs(4)* centre is the only photoproduct of the Cs(4) centre. These centres will have similar crystal-fields, as demonstrated by their spectral proximity, and so similar transition intensities. It is therefore surprising that the integrated line strength of the Cs(4)* centre after bleaching, in Figure 6.9(b) and (c), is much less than that of the Cs(4) centre prior to bleaching, Figure 6.9(a). The non-radiative relaxation processes must be more efficient in the Cs(4)* centre, so making it appear weaker in excitation.

6.4.5 The Cs(5) Centre

A bleaching sequence was obtained for discrete-photoproduct formation bleaching of the Cs(5) centre, Figure 6.10. This will be analysed using Tables 6.15 and 6.16. Pumping the γ_5 $Z_1 \rightarrow E$ transition with a Y polarised beam depopulates orientations (1) and (2) of the Cs(5) centre. Table 6.15 shows that orientation (1) contributes half of the fluorescence observed during Z polarised pumping of the $Z_1 \rightarrow E$ transition. This is demonstrated in Figures 6.10(c) and (d), where this transition appears weakly in the Y polarisation and with approximately half its initial intensity in the Z polarisation.

Orientations (2)*, (3)*, (5)* and (6)* of the Cs(5)* centre are populated after bleaching. Table 6.16 shows that the γ_1 $Z_1 \rightarrow E$ transition should exhibit stronger fluorescence during Z polarised excitation than it does during Y polarised excitation, as a$\gg$b in the C_{4v} approximation. The Cs(5)* transition does have the predicted relative intensities in Figures 6.10(c) and (d). The two weaker excitation transitions which appear after bleaching the Cs(5) centre are tentatively assigned as absorption transitions to the $^1I_6$ multiplet of the Cs*(5) centre.

Figures 6.10(e) and (f) show that further Z polarised pumping of the γ_5 $Z_1 \rightarrow E$ transition has bleached almost all of the fluorescence from the Cs(5) centre. All six orientations of the Cs(5)* centre should now be populated. The γ_1 $Z_1 \rightarrow E$ transition of the Cs(5)* centre was then bleached with a Y polarised excitation beam, Figures 6.10 (g) and (h). Table 6.16 shows that orientations (1)*, (4)*, (5)* and (6)* should be depopulated. Orientations (2)* and (3)* will be excited during Z polarised excitation, so not all of the Cs(5)* centre fluorescence has been bleached in Figure 6.10(h). Y polarised bleaching the Cs(5)* centre will repopulate orientation (3) and partially repopulate orientations (1) and (2). Thus the Cs(5) centre fluorescence is stronger during Z polarised pumping of the $Z_1 \rightarrow E$ transition than it is during Y polarised pumping.

6.5 Thermal Restoration of Bleached Fluorescence

6.5.1 Introduction

The bleaching processes of the Cs centres are reversible; either selectively by irradiating the photoproduct centres or collectively by heating the whole crystal. In both these reverting processes phonon induced motion of the hydrogenic ions restores the origional Cs centre. During irradiation phonons are generated by the phonon-assisted relaxation of excited Pr^{3+} ions. Lattice phonons are also produced when the crystal is heated and this will henceforth be called thermal restoration of fluorescence (TRF).

If the hydrogenic ions in a centre are excited sufficiently, through phonon absorption, they may be able to overcome the potential barriers which confine them in their present sites. The excited hydrogenic ions subsequently relax by emitting phonons. A centre will bleach if two hydrogenic ions migrate to produce a new stable ionic configuration before this relaxation occurs. Thus bleaching is a phonon-scattering process. The Cs* centres are never observed in virgin crystal which has been cooled from room temperature. This suggests that the Cs centre configurations are lower in energy than their respective Cs* photoproduct centres. Centres become trapped in their lowest-energy configurations as the crystal is cooled.

Bleaching will create a non-thermal distribution of centres. During TRF the hydrogenic ions have sufficient energy to overcome the potential barriers which divide the accessible configurations. As the crystal is cooled again, the higher energy configurations will be depleted and an equilibrium population distribution is re-

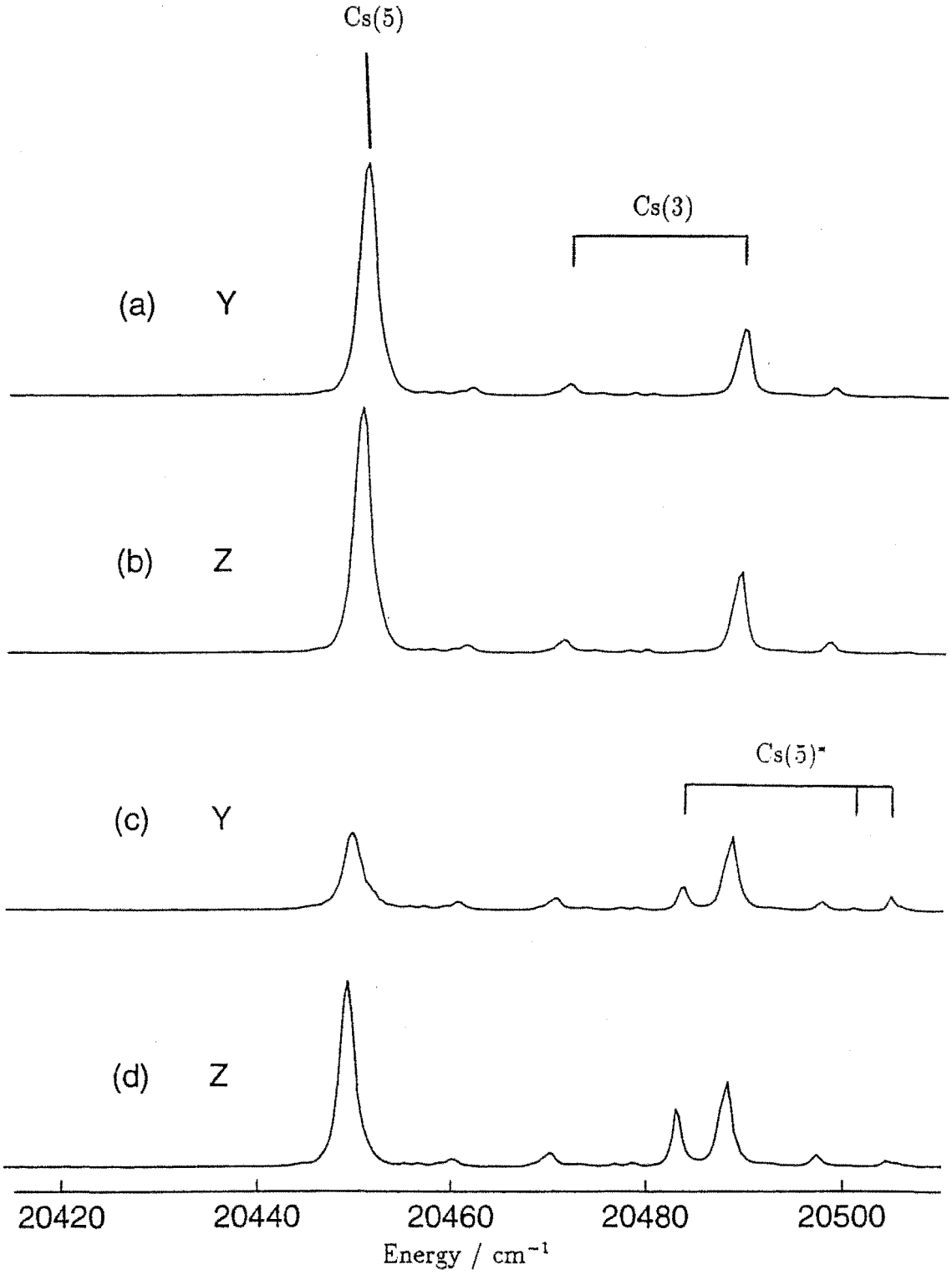
Cs(5)
Cs(3)
(a) Y
(b) Z
Cs(5)*
(c) Y
(d) Z
20420
20440
20460
20480
20500
Energy / cm⁻¹

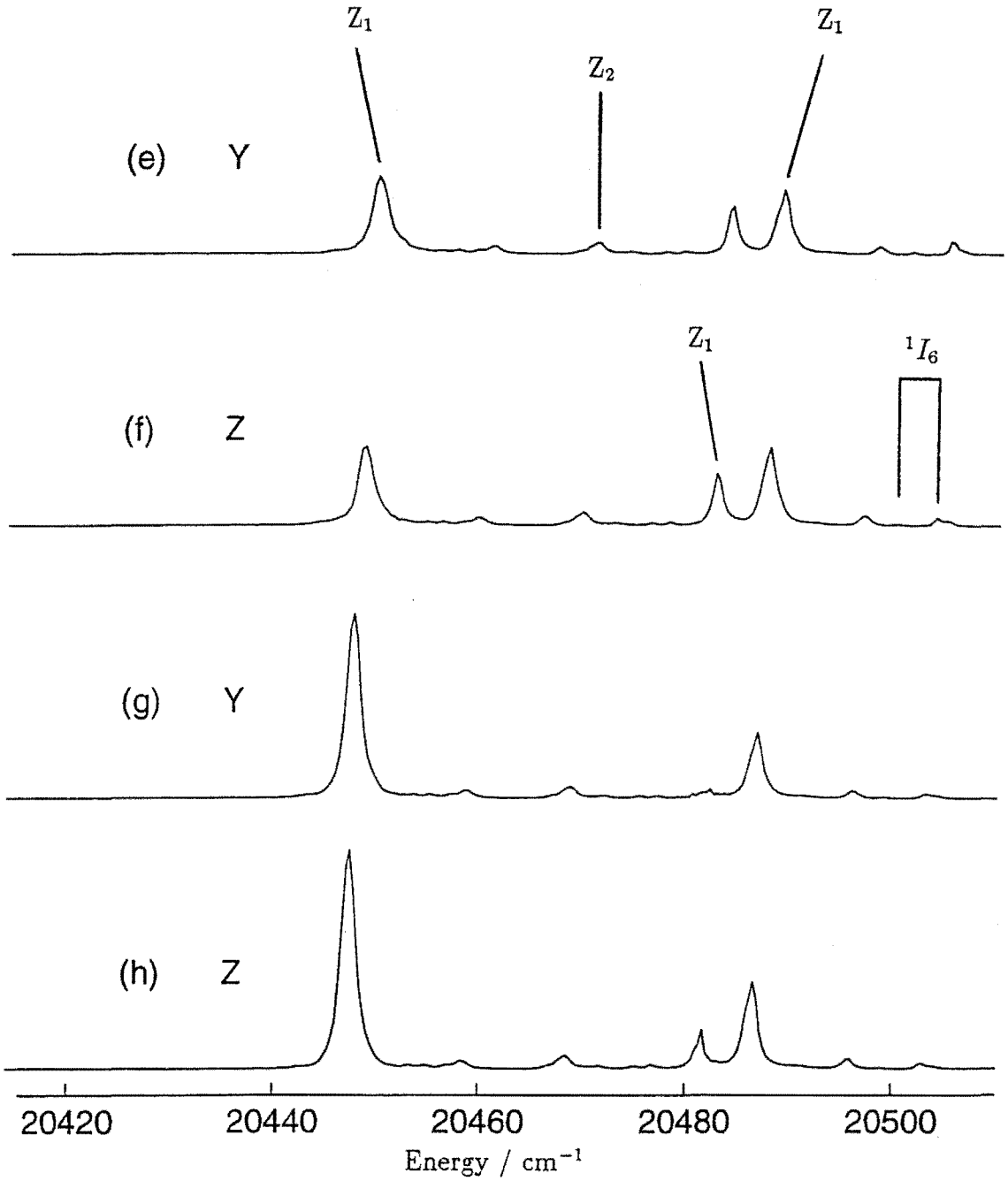

Figure 6.10: A polarisation-bleaching sequence showing the $Z_1 \rightarrow E$ and $Z_2 \rightarrow E$ absorption transitions of the Cs(5) and Cs(5)* centres in the SrF_2:$Pr^{3+}D^-$ crystal. Excitation spectra (a) and (b) show these transitions prior to bleaching the Cs(2) centre. Spectra (c) and (d) were produced after Y polarised irradiation of the $Z_1 \rightarrow E$ transition. Spectra (e) and (f) were produced after further Z polarised irradiation. The Cs(5)* centre was then bleached through Y polarised pumping of the $Z_1 \rightarrow E$ transition and spectra (g) and (h) were obtained. (a), (c), (e) and (g) are Y polarised excitation scans and (b), (d), (f) and (h) are Z polarised excitation scans.

established among the lower-energy configurations. Those centres which undergo discrete-photoproduct formation bleaching will revert to their Cs configurations. The Cs centres which undergo reorientational bleaching are restored, so that all orientations are equally populated.

The stable configurations which are accessible to a centre can be represented in energy space by potential wells. Bleaching is a transition between two of those configurations, so it is useful to consider the appropriate double-well potential (DWP). These DWPs can be parameterised by the position coordinates of the two mobile hydrogenic ions. A description of the DWPs involved in the reorientational bleaching and discrete-photoproduct formation bleaching of the Cs(2) centre has been given by Attenberger [9]. TRF can provide information about the barrier energies of these DWPs. The following experiments were performed to establish the reverting temperatures of the Cs centres. These temperatures will be used to establish the relative barrier heights of the DWPs, and so the activation energies for these bleaching processes.

6.5.2 Thermal-Reverting Temperatures

Three types of experiment were performed to find the restoration temperatures. The first experiment was used to find the approximate reverting temperatures. Initially the Cs centre is bleached thoroughly at 10K by selective irradiation. Then, with the laser tuned to the same excitation transition, the temperature of the crystal is slowly increased. The broadband fluorescence is monitored and its intensity is recorded at intervals of 5K. Increasing the temperature broadens the excitation transition, so initially the fluorescence intensity will decrease. However, above a critical temperature TRF will occur and the fluorescence intensity will start to increase again as the Cs centres are restored. This experimental procedure will henceforth be called 'thermal annealing'.

Figure 6.11 is a thermal-reverting profile for the Cs(2) centre. This is a particularly interesting example because TRF occurs twice during thermal annealing, at 65K and 90K. Subsequent experiments will show that this restoration is due to discrete-photoproduct formation bleaching and reorientational bleaching respectively. The temperatures obtained by thermal annealing are listed in the third column of Table 6.17. For each centre this is the lowest temperature for which a recovery in the fluorescence could clearly be discerned. Approximate reverting temperatures can be obtained quickly by this method, however more accurate temperatures are required to compare the barrier heights of DWPs.

The second experiment is used to find the temperature at which a discrete-photoproduct Cs^* centre reverts to the origional Cs centre. Initially the Cs centre is selectively irradiated at 10K, producing the Cs^* centres. The laser is then tuned to match an absorption transition of the Cs^* centre and a shutter is used to establish quickly the initial fluorescence intensity of this photoproduct centre. Then the crystal is heated to a set temperature, which is maintained for 5 minutes, before it

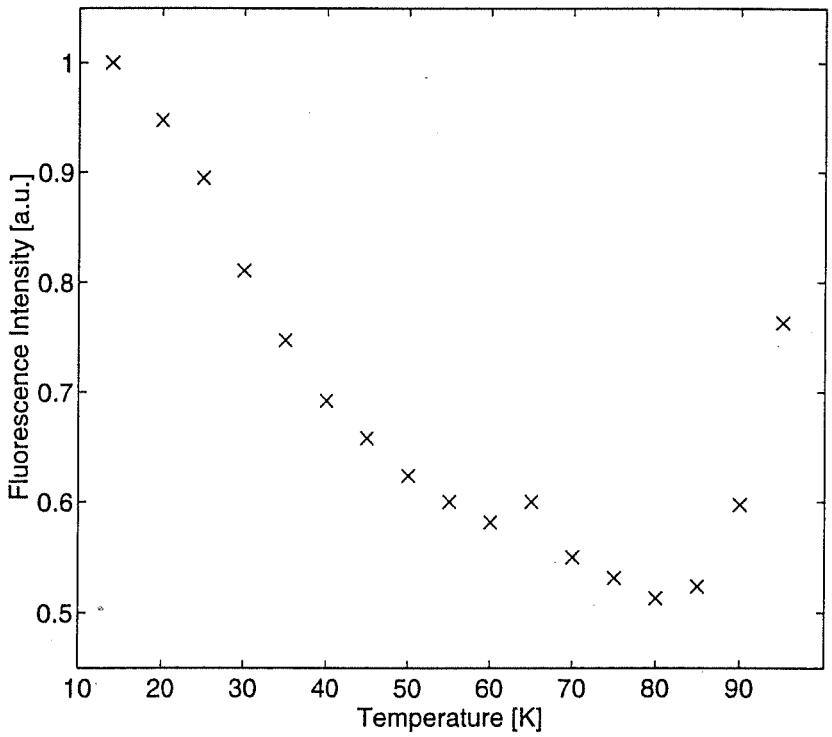

Figure 6.11: Thermal restoration of bleached Cs(2) centre fluorescence in the CaF_2:Pr^{3+}:D^- crystal, due to thermal annealing.

Table 6.17: The thermal reverting temperatures of the Cs centres, in units of K. The 'Cs(2)' values are associated with reorientational bleaching and the 'Cs(2)*' values are associated with discrete photoproduct formation bleaching of the Cs(2) centre. The temperatures in the last column were obtained by observing the thermal depletion of the Cs(2)* centre fluorescence.

Host	**Centre**	**Thermal Annealing**	**Thermal Cycling**		
		D^-	**H^-**	**D^-**	
SrF_2	Cs(1)	100±5	101±3	99±3	
	Cs(2)	95±5	99±3	100±2	
	Cs(2)*	85±5	-	-	82±3
	Cs(3)	75±5	79±5	80±3	
	Cs(4)	90±5	102±3	101±3	
	Cs(5)	75±5	79±5	81±3	
CaF_2	Cs(1)	85±5	-	-	
	Cs(2)	90±5	-	90±3	
	Cs(2)*	65±5	66±5	62±5	56±7
	Cs(3)	65±5	63±5	65±3	
	Cs(4)	65±5	-	77±2	
	Cs(5)	60±5	-	66±3	

is cooled down again to 10K. The final fluorescence intensity of the Cs* centre is measured and the difference between the initial and final values is then the TRF. This thermal cycling can be repeated for a range of set temperatures to obtain a profile of the TRF and so the rate of thermally induced barrier crossing. Before each cycle the Cs centre is bleached to repopulate the Cs* centre. This method, henceforth called 'thermal cycling', implicitly assumes that all of the Cs centres revert to the origional Cs centre. The assumption is reasonable for the Cs centres of praseodymium, as no new photoproduct centres have been found after bleaching any of the Cs* centres.

The thermal depletion of the Cs(2)* centre fluorescence, caused by thermal cycling of the SrF_2:Pr^{3+}:D^- crystal, is plotted in Figure 6.12(a). The quantity shown is the final fluorescence intensity as a fraction of the initial fluorescence intensity. Even at low temperatures the Cs(2)* centre is consistently depopulated by approximately one third. This is attributed to the unavoidable bleaching caused by selective irradiation during the brief time the fluorescence intensity is being measured.

A thermal-reverting profile for the Cs(2) centre has been produced from the same data, Figure 6.12(b), and this can be compared with other reverting profiles. A 100% thermal restoration of the Cs(2) centre fluorescence corresponds to a total depopulation of the Cs(2)* centre. The regions above and below the reverting temperature are clearly seen in Figure 6.12 and the temperature at which the fluorescence of the Cs(2) centre is partially restored to $1 - \frac{1}{e}$ of its initial intensity is determined to be (82±3)K. The thermal-restoration temperatures obtained by this method are given in the last column of Table 6.17. This result clearly identifies discrete photoproduct formation bleaching with the lower of the two Cs(2) centre reverting temperatures found in the thermal-annealing experiment.

A similar method of thermal cycling is used to measure the reverting temperatures associated with the bleaching mechanisms of other centres, including reorientational bleaching. Again the Cs centre is selectively irradiated at 10K, producing the photoproduct centres. When the centre has been bleached the residual fluorescence intensity is recorded and the shutter is closed. Then the crystal is heated to a set temperature, which is maintained for 5 minutes, before it is cooled to 10K. The final fluorescence intensity of the Cs centre is measured and the restored fluorescence is the difference between the final and initial fluorescence intensities.

Reverting profiles for the thermal reorientation of preferentially orientated Cs(2) centres are plotted in Figure 6.13 for (a) the SrF_2:Pr^{3+}:H^- crystal and (b) the SrF_2:Pr^{3+}:D^- crystal. Initially the Cs(2) centres will be distributed equally between all equivalent orientations. Bleaching selectively depopulates those orientations resonant with the excitation beam, producing a new population distribution. On heating the crystal, thermally-induced barrier crossing will tend to restore the initial population distribution, and so some of the 10K fluorescence is recovered. A TRF of 100% corresponds to a total repopulation of the depleted orientations.

At low temperatures the recovery of the Cs(2) centre is less than the 33% recovery found in Figure 6.12(b). This is partially attributable to the bleaching rate

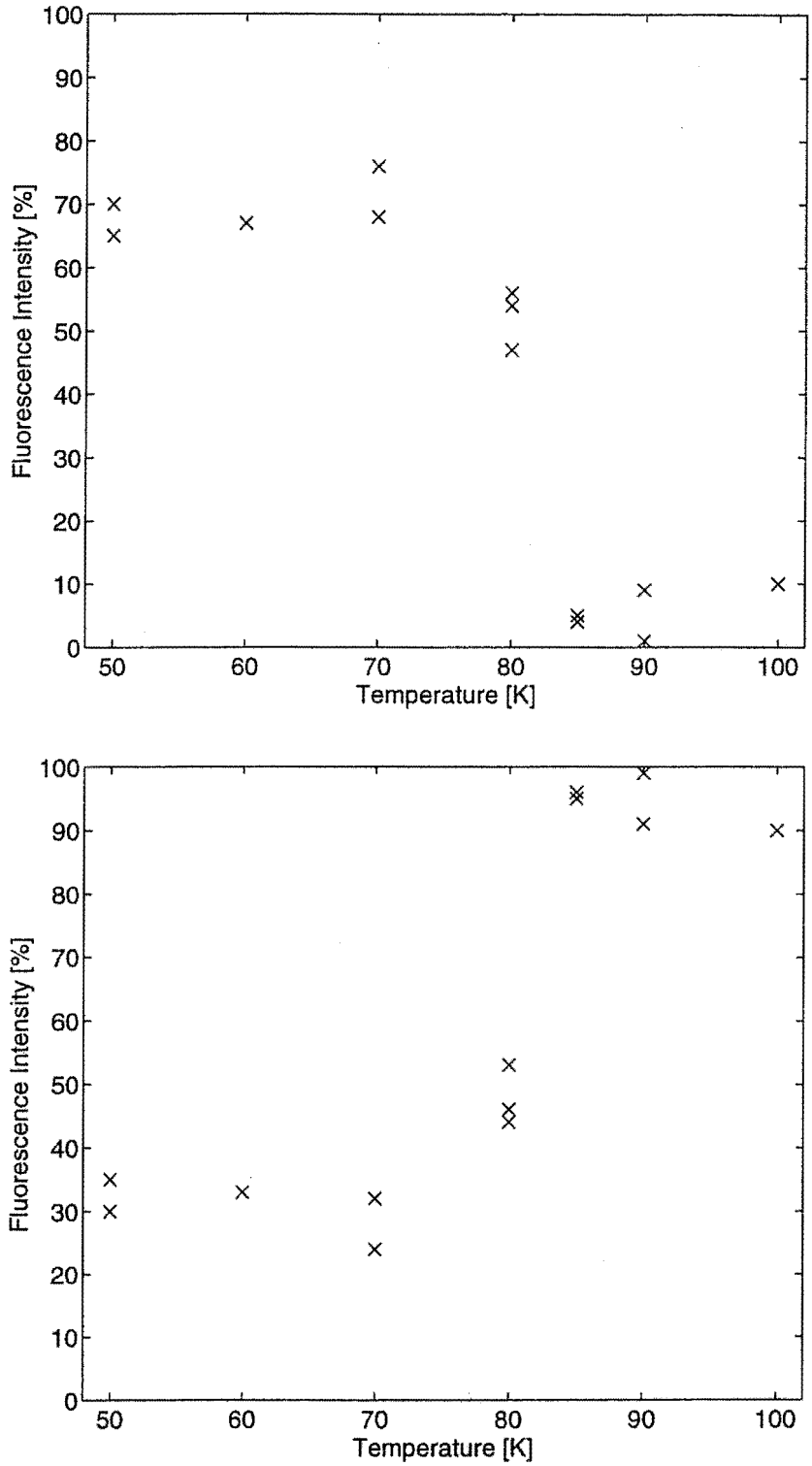

Figure 6.12: **(a)** Thermal depletion of the Cs(2)* centre fluorescence in the SrF_2:Pr^{3+}:D^- crystal, due to thermal cycling. In **(b)** these data have been replotted to illustrate the thermal restoration of the Cs(2) centre fluorescence.

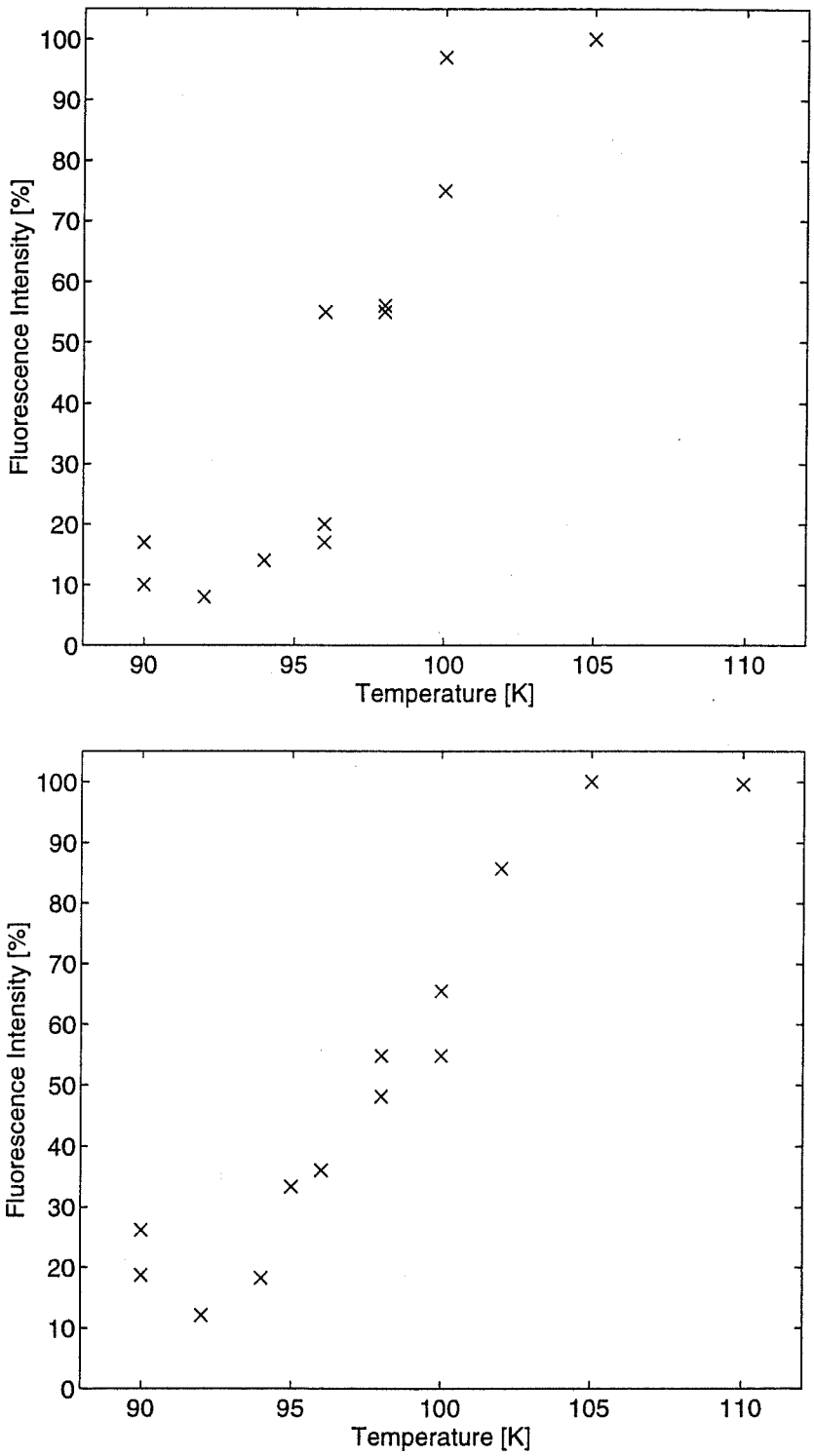

Figure 6.13: Thermal restoration of the bleached Cs(2) centre fluorescence in the (**a**) SrF_2:Pr^{3+}:H^- crystal and (**b**) SrF_2:Pr^{3+}:D^- crystal, due to thermal cycling.

of the Cs(2) centre, which is slower than that of the Cs(2)* centre. In this case there is an additional contribution to the observed repopulation from the thermal reverting of the Cs(2)* centres created during the initial bleaching. As the observed repopulation is approximately 20%, it is concluded that less than a fifth of all of the Cs(2) centres converted to the Cs(2)* photoproduct centre during bleaching. The temperature at which the fluorescence is restored to $1 - \frac{1}{e}$ of its initial intensity is determined to be (100±3)K in the SrF_2:Pr^{3+}:H^- crystal and (99±2)K in the SrF_2:Pr^{3+}:D^- crystal.

The thermal-reverting temperatures obtained by this second thermal cycling method are given in the fourth and fifth columns of Table 6.17. No result could be obtained for the Cs(1) centre in the CaF_2:Pr^{3+} host because of the near degeneracy of the Z_1 and Z_2 levels. For all the Cs centres the reverting temperatures are the same, within uncertainties, in both the hydrogen and deuterium varieties of the centre. Hence the reverting process which occurs during thermal restoration is independent of the mass of the mobile ions. This eliminates tunnelling processes, which have a $\sqrt{m}$ mass dependence, but is consistent with the model of barrier crossing in a DWP which will be presented here.

6.5.3 Estimating the Barrier Potentials

Consider an ensemble of DWPs in a material at temperature T. A barrier potential, W_m, can be crossed if this ensemble interacts for a time t with the phonons at the high frequency part of the Planck spectrum. W_m is given to good approximation by [8]:

$$W_m = kTln(\tfrac{t}{\tau_0}), \tag{6.8}$$

which is the classical Arrehenius relation for transitions between two configurations. τ_0 is the characteristic time between successive barrier crossing attempts and k is Boltzman's constant. In a spectral hole burning experiment, where the absorption transition is irradiated for a set time t, the temperature T is that required to give a $1 - \frac{1}{e}$ refilling of the spectral hole.

A Cs bleaching centre will have a narrow distribution of barrier heights, arising from the small inhomogeneous variations in the local crystal-field between the different sites in the crystal. Equation 6.8 is used to calculate the barrier heights of the hydrogenic centre DWPs from the experimental reverting temperatures, T. This type of calculation has been performed in other studies of spectral hole burning systems; for example Spitzer et al [86] have successfully applied this analysis to CN^- in KBr.

A value for the constant τ_0 is required to perform this calculation. During light-induced bleaching the hydrogenic ions are excited through the absorption of phonons which are emitted by the optically-active Pr^{3+} ion. If the hydrogenic ions must be excited into a local-vibrational mode to enable bleaching, then the $(\tau_0)^{-1}$ value is simply taken as the fundamental vibronic frequency. However, if bleaching is a non-resonant phonon-scattering process then another value for τ_0 will be

Table 6.18: The DWP barrier heights calculated from the experimental thermal reverting temperatures, in units of cm^{-1}.

Host	Centre	Reverting T	Resonant W_m	Non-Resonant W_m
SrF_2	Cs(1)	100±3	2540±80	2270±70
	Cs(2)	99±3	2510±80	2250±70
	Cs(2)*	82±3	2080±80	1860±70
	Cs(3)	80±3	2030±80	1810±70
	Cs(4)	102±3	2590±80	2310±70
	Cs(5)	81±3	2060±80	1840±70
CaF_2	Cs(2)	90±3	2280±80	2040±70
	Cs(2)*	63±5	1600±130	1430±110
	Cs(3)	65±3	1650±80	1470±70
	Cs(4)	77±2	1950±50	1750±50
	Cs(5)	66±3	1670±80	1500±70

appropriate. It has not yet been established whether the local-vibrational mode is involved in the bleaching process, however the results obtained from other spectral hole burning systems suggest that such phonon scattering is generally non-resonant (A. J. Sievers, private communication).

Equation 6.8 shows that W_m is not particularly sensitive to the value of τ_0. This is useful for it allows two approximations to be made in the calculation of τ_0 for the resonant case. The hydrogenic ion local-vibrational mode frequencies for the cubic lattice site have been used instead of those for the particular interstitial and substitutional sites of each Cs centre. The vibrational modes of the cubic sites were first studied by Elliott et al [33], who obtained the following values for the first excited level (N=1): SrF_2:H^- 893.2cm^{-1}, SrF_2:D^- 640.4cm^{-1}, CaF_2:H^- 965.6cm^{-1} and CaF_2:D^- 694.3cm^{-1}. These have been averaged to obtain a single energy value E_0=798.4cm^{-1}=1.59x10^{-20}J, which is related to τ_0 by the expression $E_0 = \frac{h}{\tau_0}$. A single τ_0 value of 4.2x10^{-12}s will be used for all the Cs centres studied.

The τ_0 value used for the non-resonant calculation was 2x10^{-12}s. It was derived by extrapolation from the τ_0 values measured in Langmuir-Blodgett films. A description of this derivation is given by Attenberger et al [7]. Estimates of the DWP barrier heights, calculated from the experimental reverting temperatures, are given in Table 6.18. Both resonant and non-resonant phonon scattering has been considered.

6.5.4 The Double-Well Potentials of the Cs(2) Centre

The Cs(2) centre is unique in that it exhibits both reorientational bleaching and photoproduct-formation bleaching. The TRF experiments have revealed that the potential barrier W_r^1 crossed when the Cs(2)* centre reverts to the Cs(2) centre is smaller than the barrier W_r^2 crossed during reorientation of the Cs(2) centre:

$$W_r^1 < W_r^2 .$$

It has already been noted, in the discussion of the Cs(2) centre bleaching sequences and thermal reverting profiles, that bleaching produces reorientated Cs(2) centres in preference to Cs(2)* centres. Hence the barrier potential W_b^1 crossed during the formation of Cs(2)* photoproduct centres is necessarily greater than the barrier potential W_b^2 crossed during reorientational bleaching:

$$W_b^1 > W_b^2 .$$

However the mechanism for reorientational bleaching of the Cs(2) centre is the same as that for thermal restoration of the Cs(2) centre fluorescence, Figure 6.1(b). Thus the DWP associated with the reorientation process can be assumed to be fairly symmetric:

$$W_b^2 \approx W_r^2 .$$

A slight inequality arises as there will be a modification to the arrangement of the neighbouring crystallographic defects in the reference frame of the reorientated centre. It is this asymmetry which causes the redistribution of centres within the inhomogeneously-broadened excitation transition observed during reorientational bleaching. The DWP for reorientational bleaching of the Cs(2) centre is sketched in Figure 6.14(a).

Combining the above equations yields the inequality:

$$W_r^1 < W_b^1 .$$

Thus the DWP associated with the formation of the discrete-photoproduct centre Cs(2)* is necessarily asymmetric, Figure 6.14(b).

6.5.5 Discussion

The experimental barrier heights of the Cs centres and the reorientational activation energies of the parent C_{4v} symmetry centres vary by less than an order of magnitude. The former are listed in Table 6.18, while the latter were measured by Edgar and Welsh [32] who obtained the following values in CaF_2:Gd^{3+} crystals: $C_{4v}F^-$ 3180±40cm^{-1}, $C_{4v}H^-$ 3060±240cm^{-1} and $C_{4v}D^-$ 3470±160cm^{-1}. Reorientational processes, exhibited by the $C_{4v}F^-$, $C_{4v}H^-$, $C_{4v}D^-$, Cs(1) and Cs(2) centres, are associated with symmetric DWPs. The barrier heights in symmetric DWPs can be directly compared.

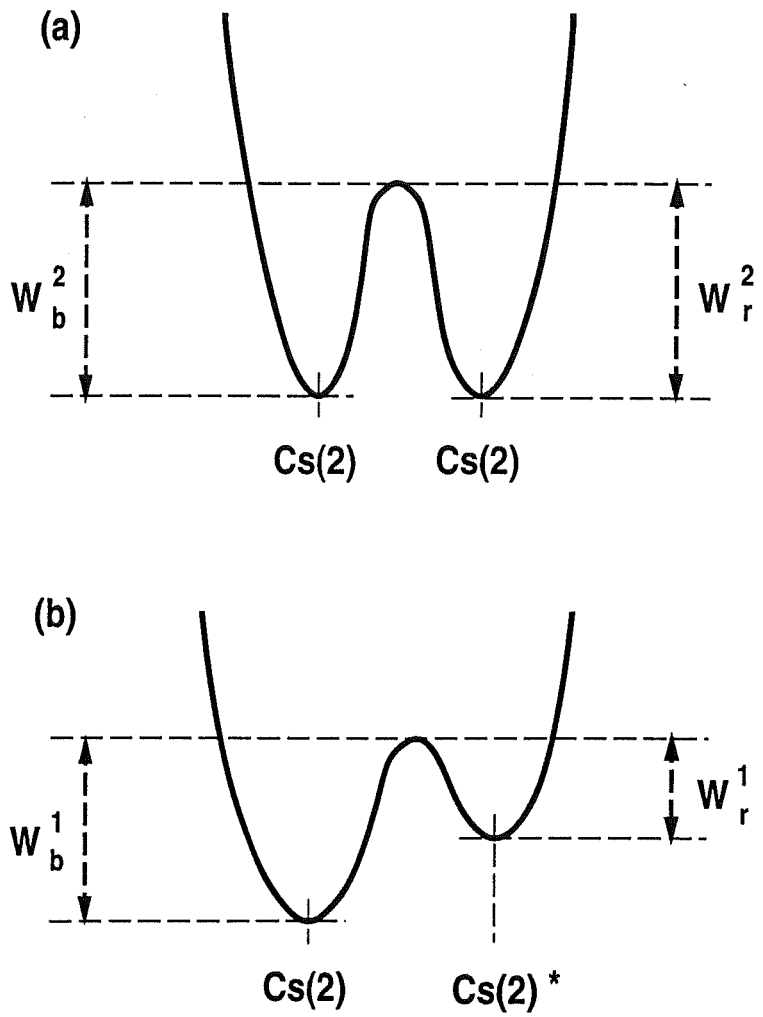

Figure 6.14: (a) The symmetric double-well potential for reorientational bleaching of the Cs(2) centre. (b) The asymmetric double-well potential for discrete-photoproduct formation bleaching of the Cs(2) centre.

It has been suggested that the interstitialcy-noncolinear mechanism might be assisted by multiple hydrogenic ion substitutions in the nearest-neighbour coordination sphere of the Pr^{3+} ion. During the bleaching process one of these substitutional hydrogenic ions will be mobile. The others would tend to relax away from the corner of the cube vacated by this mobile ion. The lighter spongy hydrogenic ions should be more affable than the harder fluoride ions. This relaxation would lower the energy of the saddle-point configuration. However, the Cs(1) and Cs(2) centres have almost identical barrier heights in the SrF_2 crystal. The presence of a second substitutional hydrogenic ion in the Cs(2) centre, which is located in the same cube edge, has not apparently aided the bleaching mechanism significantly.

Discrete-photoproduct formation bleaching processes are associated with asymmetric DWPs. The potential barrier measured in the thermal-reverting experiments is that which must be surmounted by a centre during its transition from a Cs* configuration to a Cs configuration. It seems likely that the most significant determinant of the barrier height is the energy difference between the two stable configurations. The barriers confronting the Cs(2)*, Cs(3)* and Cs(5)* configurations are all very similar. The Cs(4)* configuration has a much higher barrier and in SrF_2 it is almost identical to the reorientational barriers of the Cs(1) and Cs(2) configurations. No reason has been found to explain this result.

Reorientational bleaching has never been observed during irradiation of the $C_{4v}F^-$ and $C_{4v}H^-$ centres. Clearly the heavier F^- ions are not amenable to light-induced migration. This is consistent with the dramatic isotopic dependence of Cs centre bleaching efficiencies. It has already been established that the mass of the mobile ion species is not a determinant of the barrier potentials. However, this mass may affect the frequency at which the mobile ions will encounter those barriers ($\frac{1}{r_0}$).

If the mobile ions are excited, then they will move about their equilibrium sites. To first order this is simple-harmonic motion and the oscillation frequency will have a characteristic $m^{-\frac{1}{2}}$ mass-dependence. This is also the frequency at which the mobile ions will encounter the potential barrier which inhibits their migration. Thus lighter mobile ions will have more attempts at crossing this barrier during the short time that they are vibrationally excited.

Another important determinant of bleaching efficiency is the ability of the mobile ions to couple to the optically active ion, via the electron-phonon interaction. If bleaching is a non-resonant phonon-scattering process then no obvious mass dependence arises. In the resonant case barrier crossing can only occur when the mobile ions have been excited into a vibrational level which is higher than the barrier potential. These energy levels of the local vibrational mode have a $m^{-\frac{1}{2}}$ mass-dependence. Thus higher-order phonon-assisted relaxation processes are required to excite heavier ions above this barrier potential.

This would also explain the isotopic dependence of the bleaching efficiency. Reeves [77] has investigated the radiative and non-radiative relaxation pathways accessible to the Pr^{3+} ion in a Cs centre. He observed that the dominant non-radiative relaxation channel involves the vibrational excitation of the attendant hydrogenic

ions, as this is the lowest-order phonon-assisted relaxation mechanism. For a particular ionic configuration the non-radiative relaxation rate will be much higher in a hydrogen ion centre than it is in a deuterium ion centre. Thus the bleaching efficiency should be greater for those centres comprising the lighter hydrogen ions, as observed. This would also explain why the $C_{4v}F^-$ and $C_{4v}H^-$ centres do not exhibit reorientational bleaching, as the F^- ion mass is nineteen times that of the H^- ion. It has already been noted that the dominant relaxation channel from the $^3P_0$ and $^1D_2$ multiplets of the $C_{4v}F^-$ centre is radiative.

In both the resonant and non-resonant phonon scattering mechanisms, a necessary condition for bleaching to occur is that barrier potential must be less than the energy gap between the initial and final levels of the non-radiative RE^{3+} ion transition. If the potential is greater than this transition energy, then the mobile ions will not acquire sufficient energy to cross the barrier. The Pr^{3+} ion has many inter-multiplet transitions which satisfy this condition.

Chapter 7

Spectroscopy of Tb^{3+} Centres in SrF_2 and CaF_2 Crystals

7.1 Introduction

This chapter reports the first laser selective excitation study of terbium in CaF_2 and SrF_2 crystals. A fluorescence study of CaF_2:Tb^{3+} at liquid-nitrogen temperature was reported by Rabbiner in 1965 [69]. However his interpretation of the spectra he obtained assumed that there was only one significant Tb^{3+} centre in this host, having an O_h point symmetry. Rabbiner justified this assumption by observing that a lower-symmetry Tb^{3+} centre would exhibit many more dipole allowed transitions than he observed. In a later paper [70] he derived the theoretical energy levels for a Tb^{3+} ion in a cubic crystal field and observed close agreement with the empirical energy levels. He concluded that any charge compensating ion must be "too far away from these sites to cause any appreciable alteration in the original cubal symmetry". From the many subsequent LSE studies of CaF_2:RE^{3+} crystals it is known that trivalent lanthanide ions preferentially form centres of tetragonal or trigonal symmetry, in which the charge-compensating ions are located in nearest-neighbour or next-nearest-neighbour interstitial sites respectively.

A more recent study of fluorescence from CaF_2:Tb^{3+} was reported by Rao et al in 1980 [74]. Their study was also conducted at liquid-nitrogen temperature using an argon ion laser and a nitrogen laser to excite the $^5D_4$ and $^5D_3$ multiplets of the Tb^{3+} ion non selectively. The spectra they obtained show the presence of more than one Tb^{3+} site. The new site observed was much weaker spectroscopically than the dominant site observed by Rabbiner, with transitions appearing on the long wavelength side of the main site transitions.

Another study of CaF_2:Tb^{3+} in which the Tb^{3+} ions were excited by the blue lines of an argon ion laser was reported by Chrysochoos [21] in 1983. His room temperature and 125K fluorescence spectra also exhibit two main groups of emission lines, which Chrysochoos calls group I and II. These were tentatively assigned as C_{4v} and C_{3v} respectively, by comparison with the fluorescence spectra of Tb^{3+} ions

in other hosts of known symmetry.

An EPR study of CaF_2:Tb^{3+} by Forrester and Hempstead [35] provides a more definitive survey of the Tb^{3+} centres in this host. They observed EPR due to one type of tetragonal centre and one type of trigonal centre. The former was attributed to Tb^{3+} ions which have an F^- ion occupying the nearest-neighbour interstitial site. EPR alone could not distinguish whether the axial symmetry of the trigonal centres arises from an interstitial F^- ion or a lattice O^{2+} ion. The splitting of the two lowest electronic states of the tetragonal centre was measured to be 5.134±0.006GHz (0.17 cm^{-1}). They reported a $g_{||}$ value of 17.77±0.02.

Antipin et al [5] have studied SrF_2:Tb^{3+} by EPR. Two tetragonal centres were detected in their crystals grown by the Bridgman method in a fluorinating atmosphere. Terbium was introduced into the melt as Tb_2O_3. The transition between the two lowest states, γ_3 and γ_4 in a tetragonal crystal field, was pumped and found to have an energy of 14.4±0.2GHz (0.48cm^{-1}) in the dominant tetragonal centre. They report a $g_{||}$ value of 17.95±0.05 for this centre.

The Tb^{3+} ion has been investigated in a number of other materials. A particularly interesting series of studies was performed by Richardson et al [81] [82]. This work was primarily concerned with magnetic circularly-polarised excitation and fluorescence of Tb^{3+} ions.

7.2 The Spectroscopy of the Pure CaF_2:Tb^{3+} and SrF_2: Tb^{3+} Crystals

7.2.1 Absorption Spectra

Transmission spectra were obtained for both crystals. A number of absorption features were found in the two regions where the $^7F_6 \rightarrow {}^5D_4$ and the $^7F_6 \rightarrow {}^5D_3$ inter-multiplet transitions would be expected. These Tb^{3+} ion absorption features are very much weaker than the $^3H_4 \rightarrow {}^1D_2$ and the $^3H_4 \rightarrow {}^3P_0$ transitions of Pr^{3+} ions in the same hosts, and they could only be clearly discerned in uncut crystal boles which were longer than 3cm. Transitions for SrF_2 were much stronger in absorption than those of CaF_2.

Infrared transmission spectra were also obtained using the FTIR spectrometer. These show absorption transitions between the ground state and the $^7F_5$, $^7F_4$, and $^7F_3$ multiplets. A number of singlet levels which do not contribute to the visible fluorescence were found this way. Infrared Zeeman spectroscopy was used to distinguish doublet and singlet levels in these multiplets, which assisted in the assignment of irrep-labels to the states.

Only the $^7F_6 \rightarrow {}^5D_4$ absorption transitions of the Tb^{3+} ion are within the range of the Spectra Physics 375 dye laser, so all the LSE spectra which will be presented here were obtained by pumping these transitions. Pumping the strongest excitation features produced fluorescence which could easily be seen by eye and

without a colour filter. This fluorescence was always green in colour.

Broadband excitation spectra were obtained by monitoring the fluorescence at 545nm, where the maximum fluorescence intensity from both crystals was found, Figure 7.1. For each crystal studied these broadband excitation spectra were very similar to the transmission spectra. However the excitation spectra showed the absorption transitions much more clearly, with many less-intense electronic transitions and phonon features appearing.

One centre dominates the broadband excitation spectrum of SrF_2:Tb^{3+}. It will be shown that this is the same tetragonal $C_{4v}F^-$ centre which has been found in a number of lanthanide doped CaF_2-type crystals [27] [39] [62] [77]. Some minor centres are also evident; of these two are sufficiently strong in excitation to be seen in Figure 7.1(a) and their transitions are of comparable intensity. One of these is the trigonal $C_{3v}F^-$ centre which has also been observed in studies of other lanthanides [27] [62]. The absorption transitions belonging this centre are distinct from those of the $C_{4v}F^-$ centre and are lower in energy.

The other minor centre in SrF_2:Tb^{3+} is spectroscopically very close to the dominant $C_{4v}F^-$ centre and might be the second tetragonal centre found in the EPR experiments of Antipin et al [5]. It could be a mixed centre [53] due to small quantities of CaF_2 being present in the SrF_2 material from which this crystal was grown. Although this centre was identified only in this work, the possibility makes it an attractive candidate for further investigation.

Two centres of comparable intensity are prominent in the broadband excitation spectrum of CaF_2:Tb^{3+}. It will be shown that these are the CaF_2 counterparts of the tetragonal $C_{4v}F^-$ and trigonal $C_{3v}F^-$ centres found in the SrF_2:Tb^{3+} crystal. In various papers Brown et al [15] predicted that the $C_{3v}F^-$ centre never becomes dominant in the CaF_2 host. That so many $C_{3v}F^-$ centres are found in the CaF_2:Tb^{3+} crystals studied presents a challenge to this prediction.

7.2.2 Selective Excitation Spectra

Site-selective excitation spectra were obtained by monitoring specific $^5D_4 \rightarrow {}^7F_5$ fluorescence transitions in SrF_2:Tb^{3+} and CaF_2:Tb^{3+}, Figures 7.2 and 7.3 respectively. These selective spectra were used to distinguish the excitation transitions belonging to the different Tb^{3+} ion centres. The energies of the most prominent $^7F_6 \rightarrow {}^5D_4$ excitation transitions of each centre are given in Table 7.1.

Each centre also has a very broad excitation band, higher in energy than these electronic transitions. Such bands have been observed for other lanthanides, such as praseodymium [77], and have been identified as the phonon bands which are due to lattice-vibronic states coupling to the electronic states of the lanthanide ion. The phonon bands of the $C_{4v}F^-$ centres of the Pr^{3+} ion have well defined structure and were studied by Reeves. The phonon bands which are associated with these Tb^{3+} centres are comparatively featureless and will not be analysed here.

In excitation the minor tetragonal centre of SrF_2:Tb^{3+} appears almost iden-

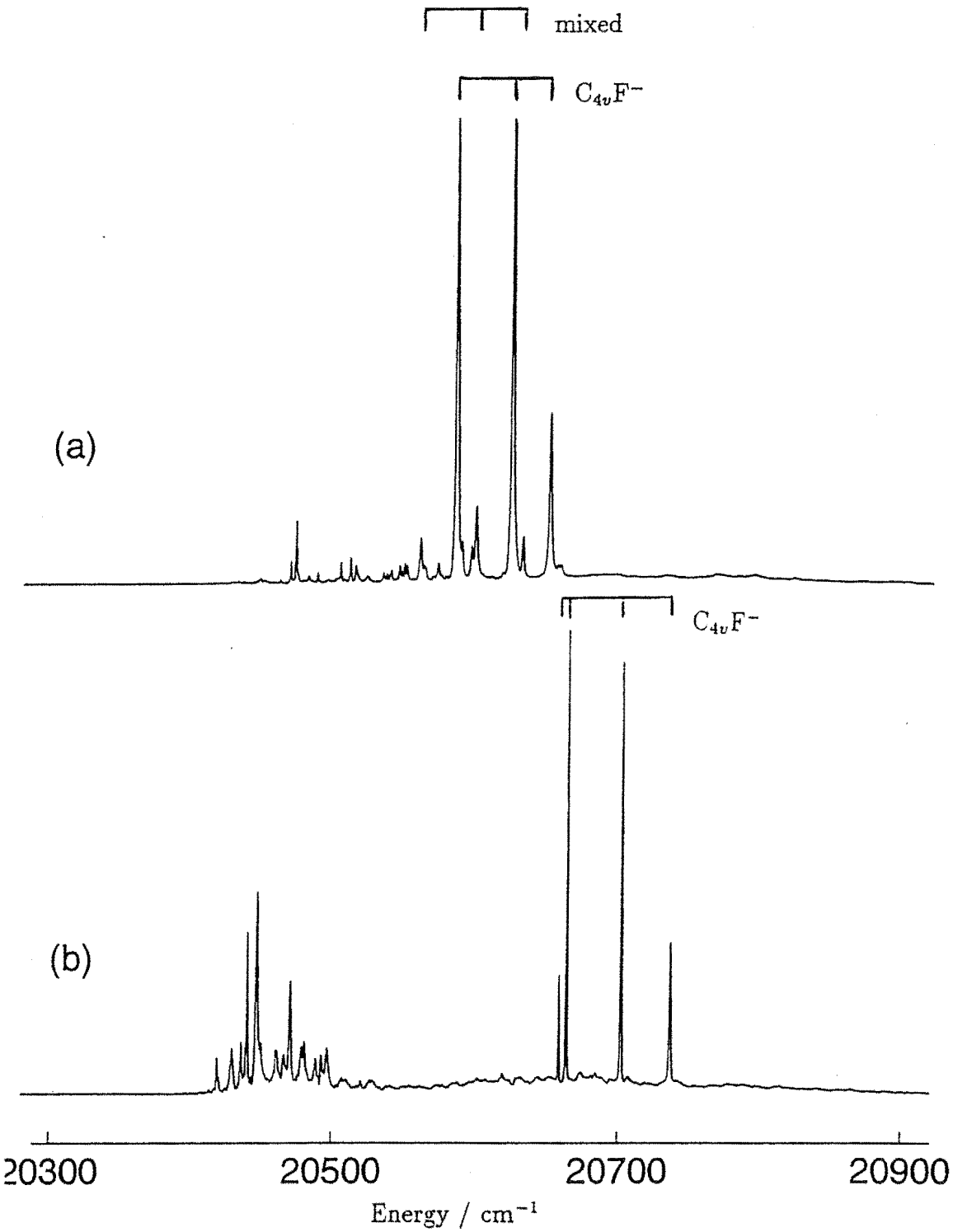

Figure 7.1: Broadband excitation spectra showing the $^7F_6 \rightarrow {}^5D_4$ absorption transitions, while monitoring the fluorescence at 545nm in (a) the SrF_2:Tb^{3+} and (b) the CaF_2:Tb^{3+} crystal.

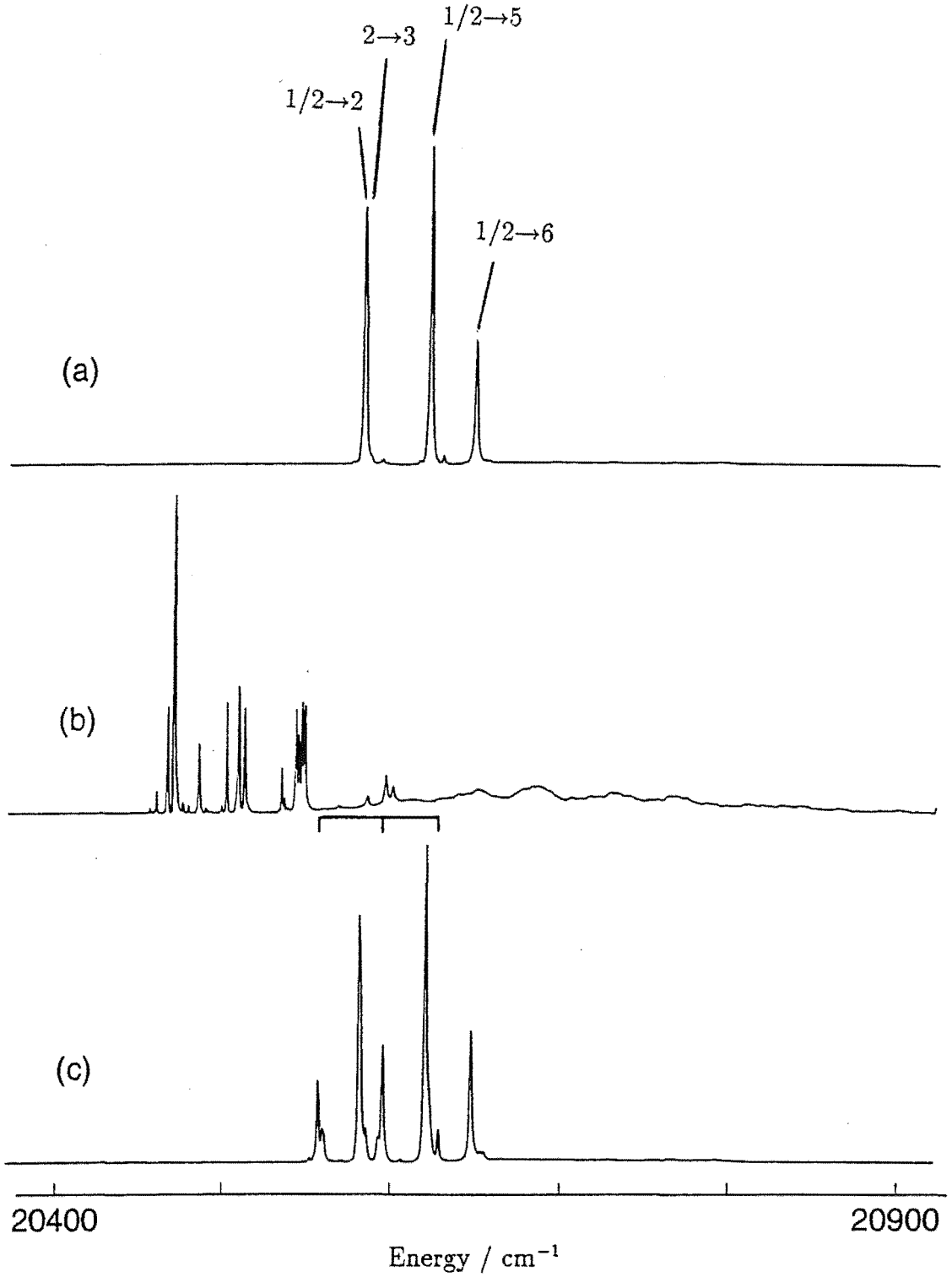

Figure 7.2: Excitation spectra of centres in the SrF_2:Tb^{3+} crystal showing the $^7F_6$ $\rightarrow$ $^5D_4$ transitions, while monitoring specific $^5D_4 \rightarrow {}^7F_5$ transitions of; (a) $C_{4v}F^-$, (b) $C_{3v}F^-$ and (c) the minor C_{4v} like centre

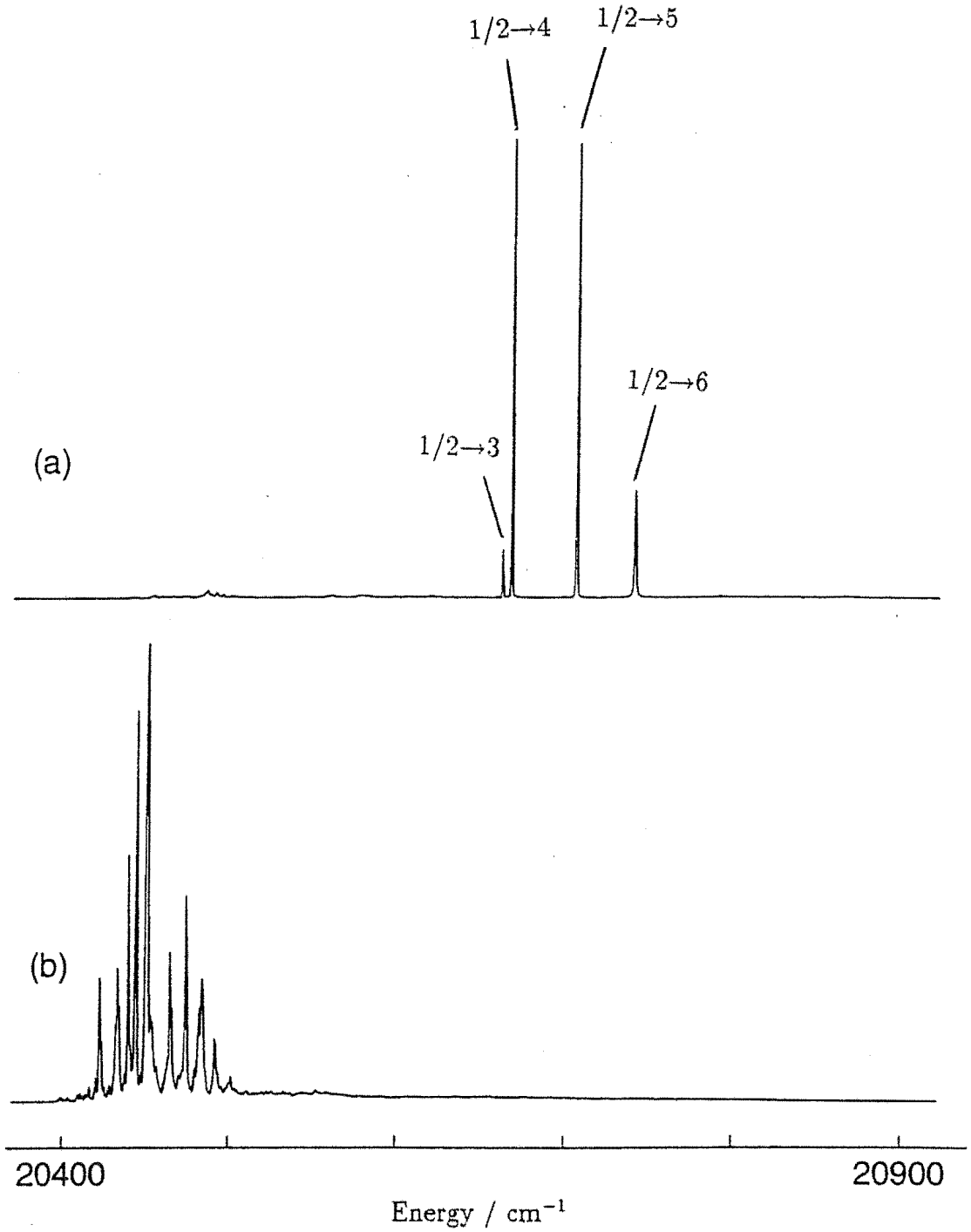

Figure 7.3: Excitation spectra of centres in the CaF_2:Tb^{3+} crystal showing the $^7F_6$ $\rightarrow$ $^5D_4$ transitions, while monitoring specific $^5D_4$ $\rightarrow$ $^7F_5$ transitions of; (a) $C_{4v}F^-$ and (b) $C_{3v}F^-$

Table 7.1: Some $^5D_4$ multiplet energy levels (vacuum) of the fluoride ion centres observed in excitation, in units of cm^{-1}. The energies have an uncertainty of $\pm 0.2 cm^{-1}$.

Centre	SrF_2	CaF_2
$C_{4v}F^-$	20603.0	20666.0
	20604.0	20672.0
	20640.2	20710.3
	20666.1	20743.5
$C_{3v}F^-$	20489.1	20451.6
	20493.0	20457.7
Mixed C_{4v}	20578.8	-
	20619.9	-
	20641.5	-

tical to the $C_{4v}F^-$ centre, which is consistent with its assignment as a mixed centre. Khong [53] observed that the excitation transitions of the mixed centres of Pr^{3+} appear as satelites of the parent $C_{4v}F^-$ transitions.

7.2.3 Fluorescence Spectra

The $^5D_4 \rightarrow {}^7F_5$ transitions of the Tb^{3+} ion dominate the fluorescence spectra of all the centres studied. This explains the green colour of the Tb^{3+} ion fluorescence and is consistent with the intensity measurements and calculations obtained in other studies [81] [82]. It is well documented that the $^5D_4 \rightarrow {}^7F_5$ fluorescence also has a significant magnetic-dipole component and exhibits strong chiroptical activity. These $\Delta J = 1$ transitions are magnetic dipole allowed. Indeed it is for these reasons that this emission is used extensively as a probe of lanthanide ion coordination behaviour in solutions and chiral systems [80]. A large magnetic-dipole component has also been found in the $^5D_4 \rightarrow {}^7F_3$ fluorescence. Intra-configurational electric-dipole transitions are forbidden in free ions, but become allowed when the ions are immersed in a crystal field, due to crystal-field mixing. These electric-dipole transitions become more prominant as the strength of the crystal field increases.

Fluorescence spectra of the $^5D_4 \rightarrow {}^7F_5$ transitions were obtained by LSE of each centre in SrF_2:Tb^{3+} and CaF_2:Tb^{3+}, Figures 7.4 and 7.5 respectively. The fluorescence spectrum of the minor tetragonal centre of SrF_2 is again very similar to that of the $C_{4v}F^-$ centre. The $^5D_4 \rightarrow {}^7F_J$ transitions of the $C_{4v}F^-$ centres appear in Figures 7.6 and 7.7

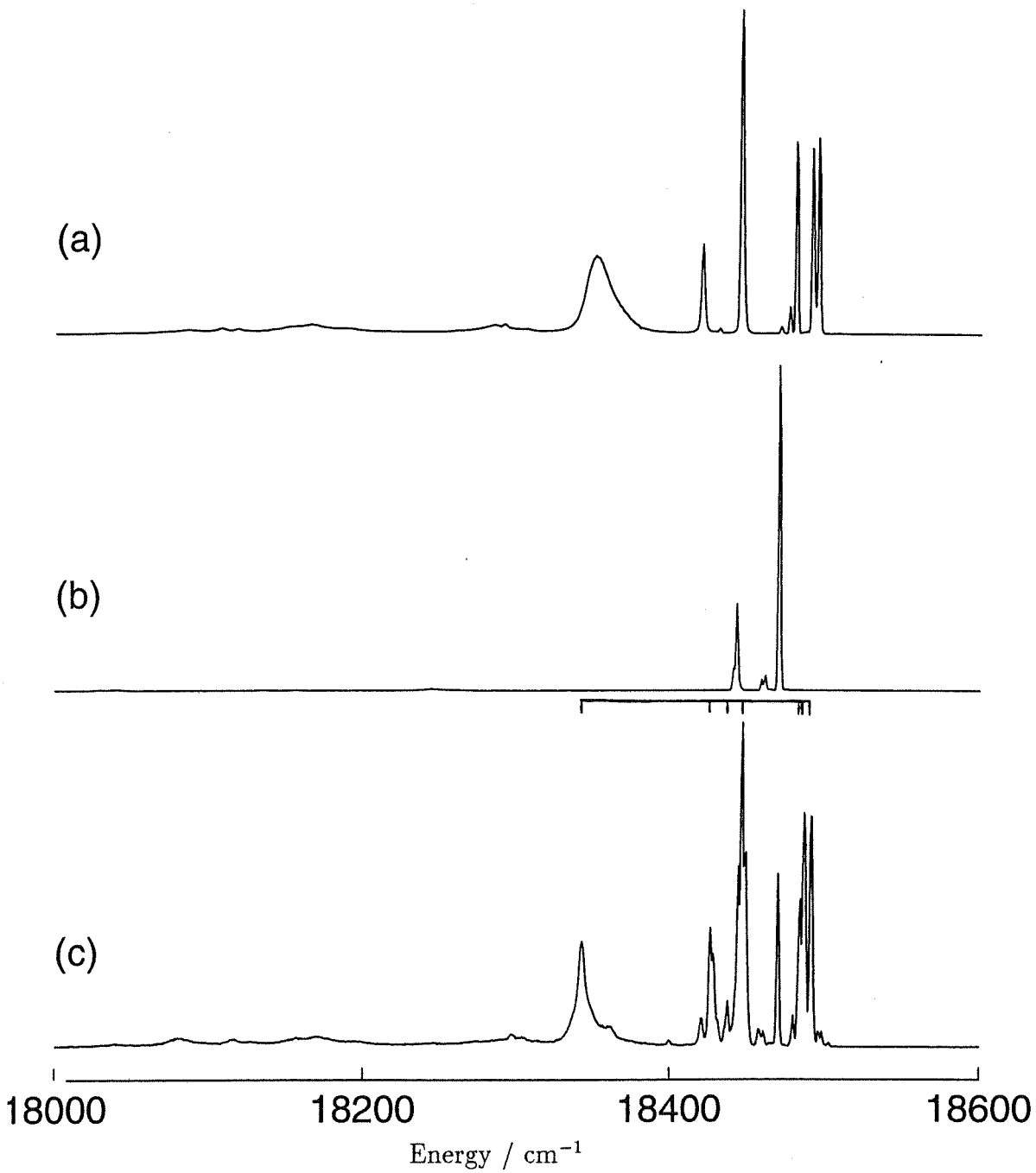

Figure 7.4: Fluorescence spectra of centres in the SrF_2:Tb^{3+} crystal showing the $^5D_4 \rightarrow {}^7F_5$ transitions of; (a) $C_{4v}F^-$ (b) $C_{3v}F^-$ and (c) the minor C_{4v} like centre.

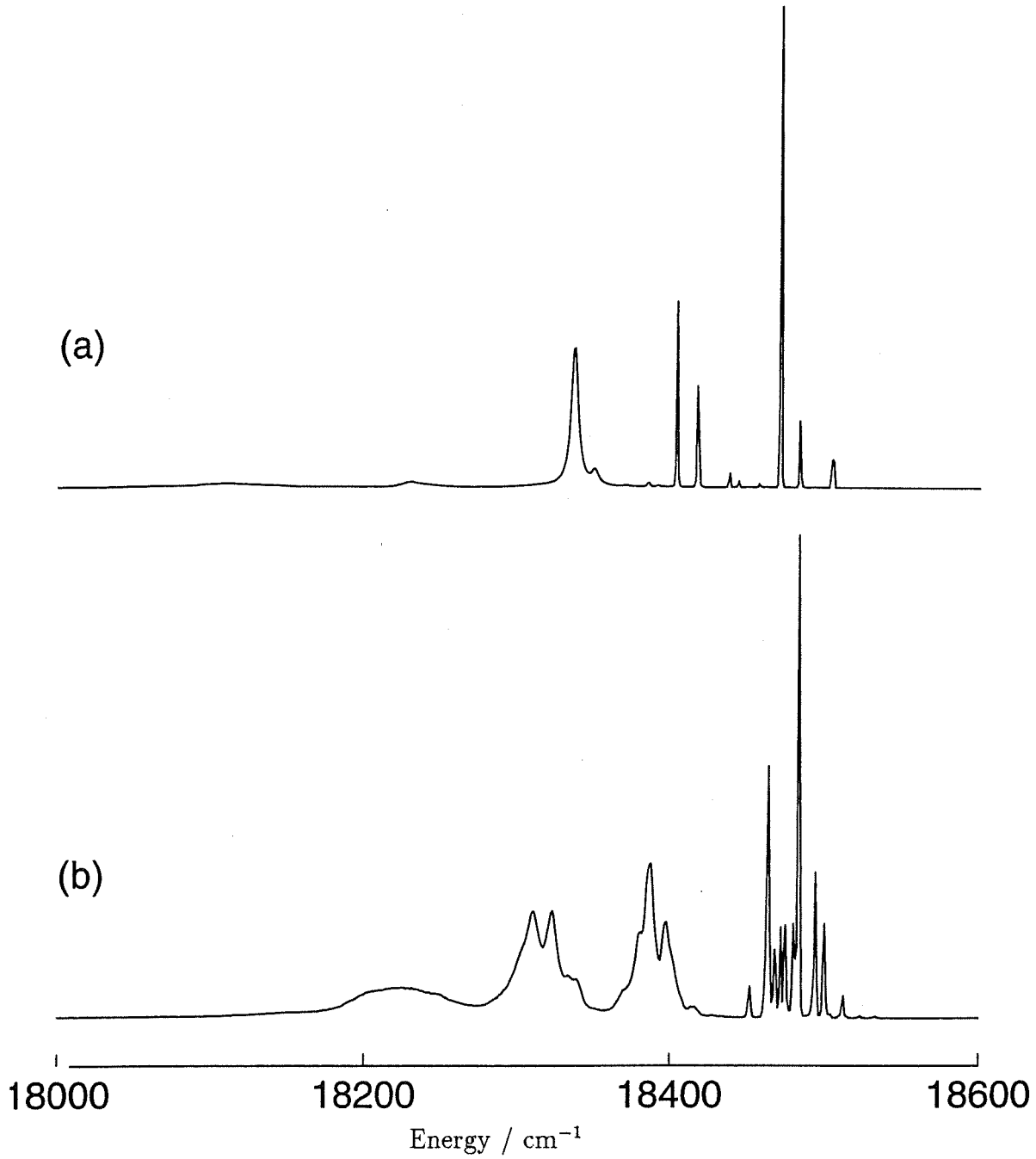

Figure 7.5: Fluorescence spectra of centres in the CaF_2 crystal showing the $^5D_4 \rightarrow {}^7F_5$ transitions of; (a) $C_{4v}F^-$ and (b) $C_{3v}F^-$.

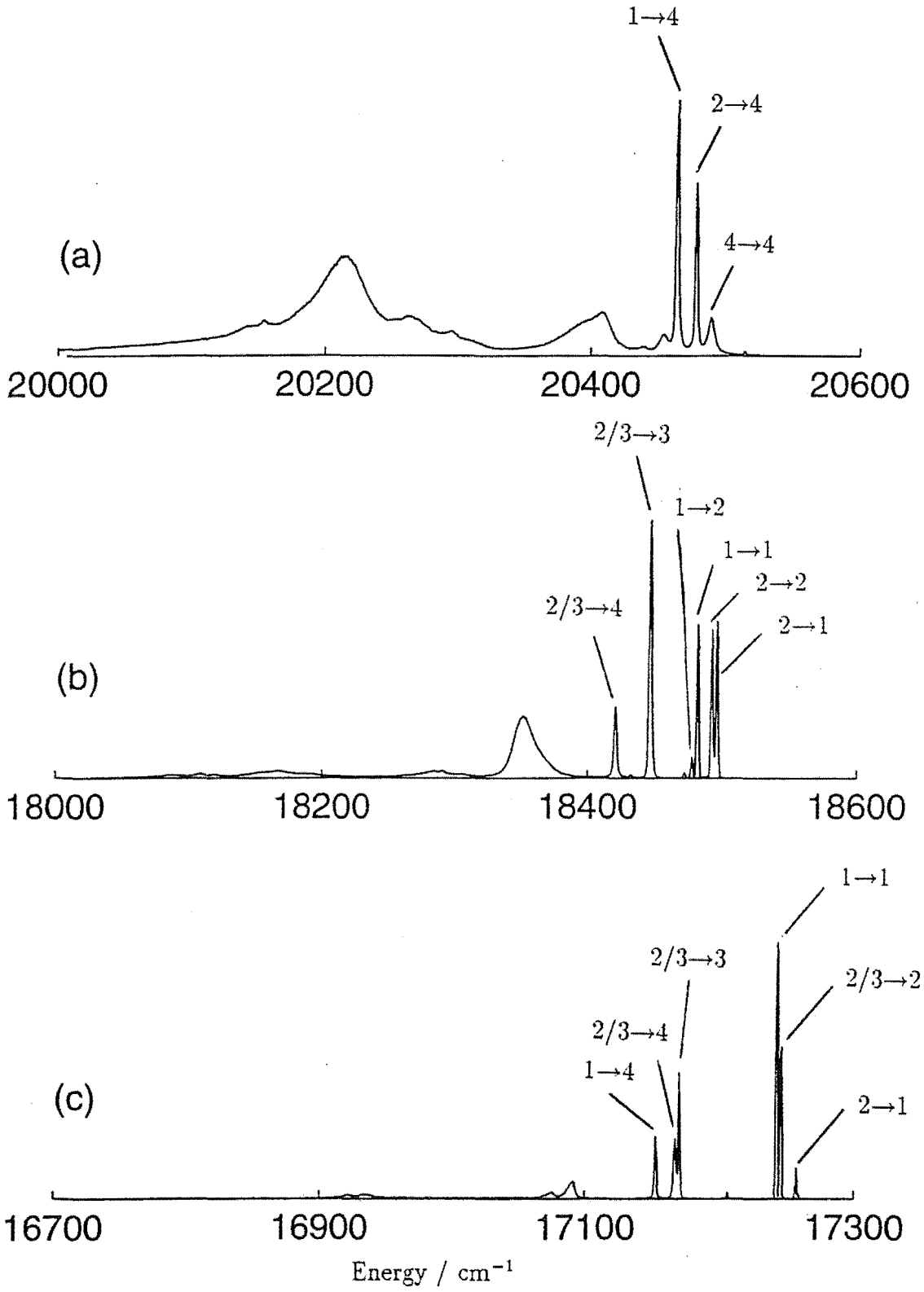
1→4
2→4
4→4
(a)
20000
20200
20400
20600
2/3→3
1→2
1→1
2→2
2/3→4
2→1
(b)
18000
18200
18400
18600
1→1
2/3→3
2/3→2
2/3→4
1→4
2→1
(c)
16700
16900
17100
17300
Energy / cm^{-1}

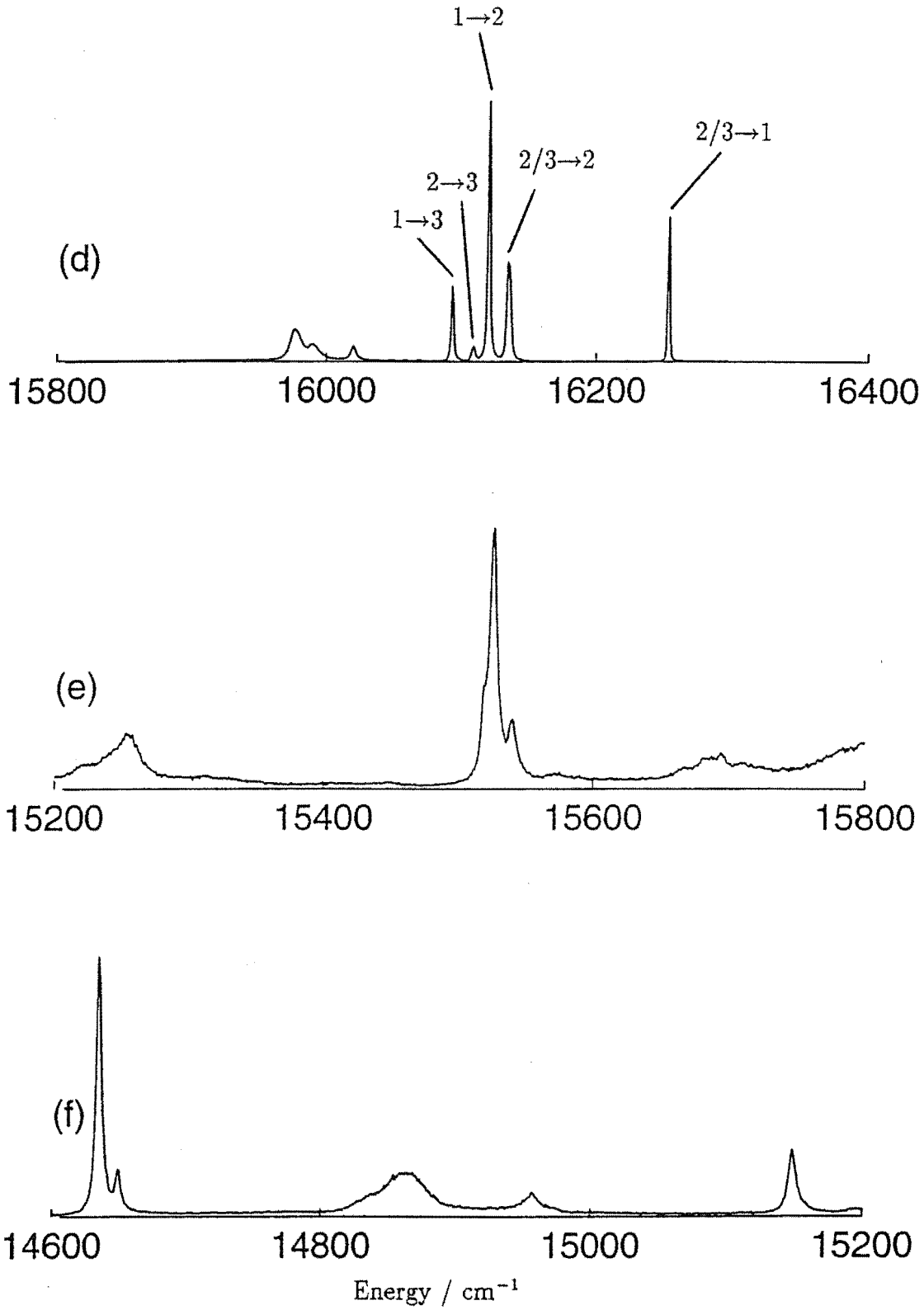

Figure 7.6: Fluorescence spectra of the $C_{4v}F^-$ centre in SrF_2, showing transitions to the (a) $^7F_6$ (b) $^7F_5$ (c) $^7F_4$ (d) $^7F_3$ (e) $^7F_2$ and (f) $^7F_1$ and $^7F_0$ multiplets.

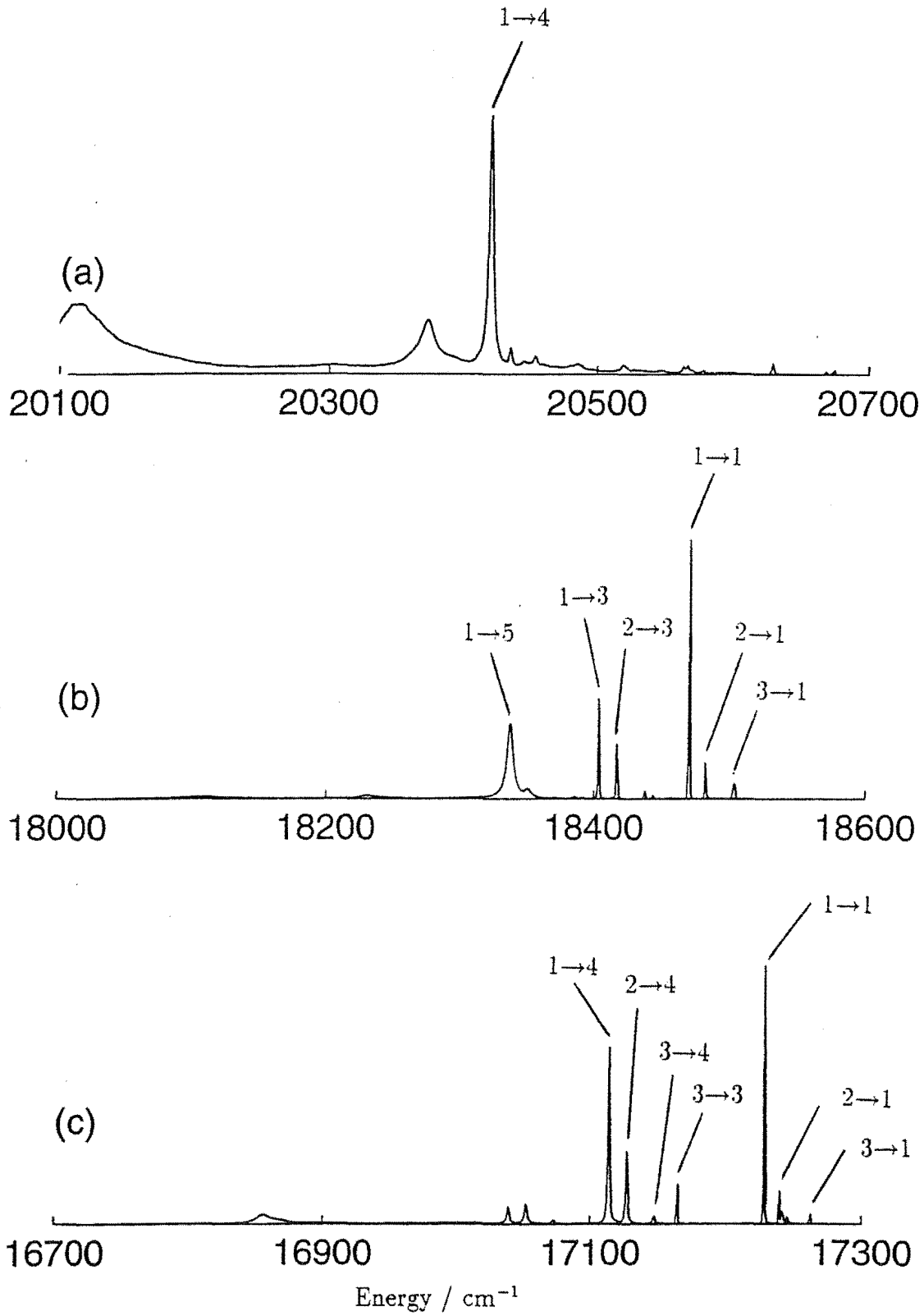
1→4
(a)
20100
20300
20500
20700
1→1
1→3
1→5
2→3
2→1
3→1
(b)
18000
18200
18400
18600
1→1
1→4
2→4
3→4
3→3
2→1
3→1
(c)
16700
16900
17100
17300
Energy / cm⁻¹

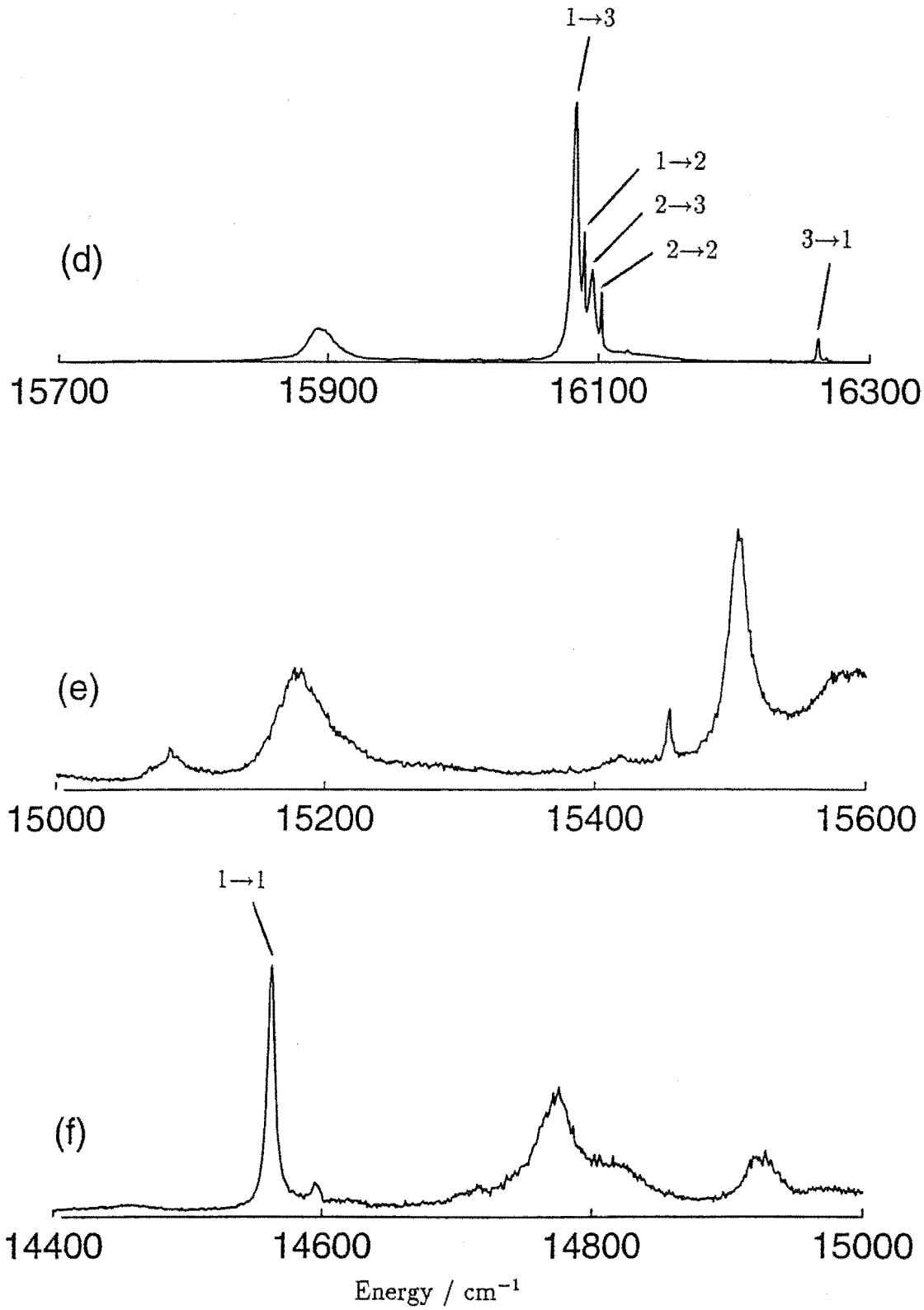

Figure 7.7: Fluorescence spectra of the $C_{4v}F^-$ centre in CaF_2, showing transitions to the (a) $^7F_6$ (b) $^7F_5$ (c) $^7F_4$ (d) $^7F_3$ (e) $^7F_2$ and (f) $^7F_1$ and $^7F_0$ multiplets.

7.3 The $C_{4v}F^-$ Centres in SrF_2:Tb^{3+} and CaF_2:Tb^{3+}

7.3.1 The Electronic Energy Levels and their Irrep Labels

Laser selective excitation of the $C_{4v}F^-$ centres produced fluorescence to most of the ^7F_J multiplets at 10K, Figures 7.6 and 7.7. In both hosts sharp electronic transitions were observed to the lower levels of the $^7F_6$, $^7F_5$, $^7F_4$ and $^7F_3$ multiplets. Other broader electronic transitions were observed to all of the ^7F_J multiplets. When the temperature of the crystals was increased many of the fluorescence transitions increased in intensity and some new transitions appeared. This suggests that there is more than one low lying level in the emitting $^5D_4$ multiplet.

From the spectra obtained by LSE and FTIR absorption 20 electronic energy levels of the SrF_2 centre and 22 levels of the CaF_2 centre were determined. These are listed in the fifth column of Tables 7.3 and 7.4 respectively. It is useful to associate the levels which have been identified with the electronic states of the Tb^{3+} ion. As in other studies this is done here by considering the dipole-selection rules of the electronic transitions.

In the SrF_2 centre the transition from the ground state to the lowest level of the $^5D_4$ multiplet is never observed. If both the electric and the magnetic-dipole transition are forbidden then both of these states must be singlets, one being γ_1 or γ_2 and the other γ_3 or γ_4. The fluorescence transition from the lowest level of the $^5D_4$ multiplet to the singlet γ_1 state of the $^7F_0$ multiplet is observed, which restricts the former to a γ_1 or γ_2 irrep assignment. In CaF_2 the transitions to the two lowest levels of the $^5D_4$ multiplet are never observed, thus both of these states are either γ_1 or γ_2. It follows that the ground states are either γ_3 or γ_4.

From these tentative irrep assignments information about the labels of the other levels can be deduced. If a level is seen in absorption from the ground state then it must be one of γ_3, γ_4 or γ_5. If a level is seen in emission from the lowest level of the $^5D_4$ multiplet the it will be γ_1, γ_2 or γ_5. Note that both absorption and emission transitions are allowed to a γ_5 state. Some of the γ_5 doublets were also distinguished by FTIR Zeeman spectroscopy. A transverse-magnetic field was applied to orientated crystals and the doublet g-splitting factors were measured and compared (J-P. R. Wells, private communication). A preliminary energy-level scheme was thus inferred.

Interpreting the polarisation ratios obtained from polarised emission spectra should provide the most definitive assignment of irrep labels to the experimentally determined energy levels. The $^5D_4 \rightarrow {}^7F_5$ polarised fluorescence spectra of Figures 7.8 and 7.9 are typical of those which were obtained by selective excitation of the $C_{4v}F^-$ centres. In Figure 7.8 a wide range of polarisation ratios is exhibited, more than the 1:2 and 1:0 ratios or the 0:1 and 1:0 ratios expected for pure electric-dipole coupling in a C_{4v} symmetry crystal field (Chapter 4). The same can be said of Figure 7.9 where a number of the weaker transitions exhibit ratios close to 1:1.

Any attempt to make irrep label assignments from the experimental polari-

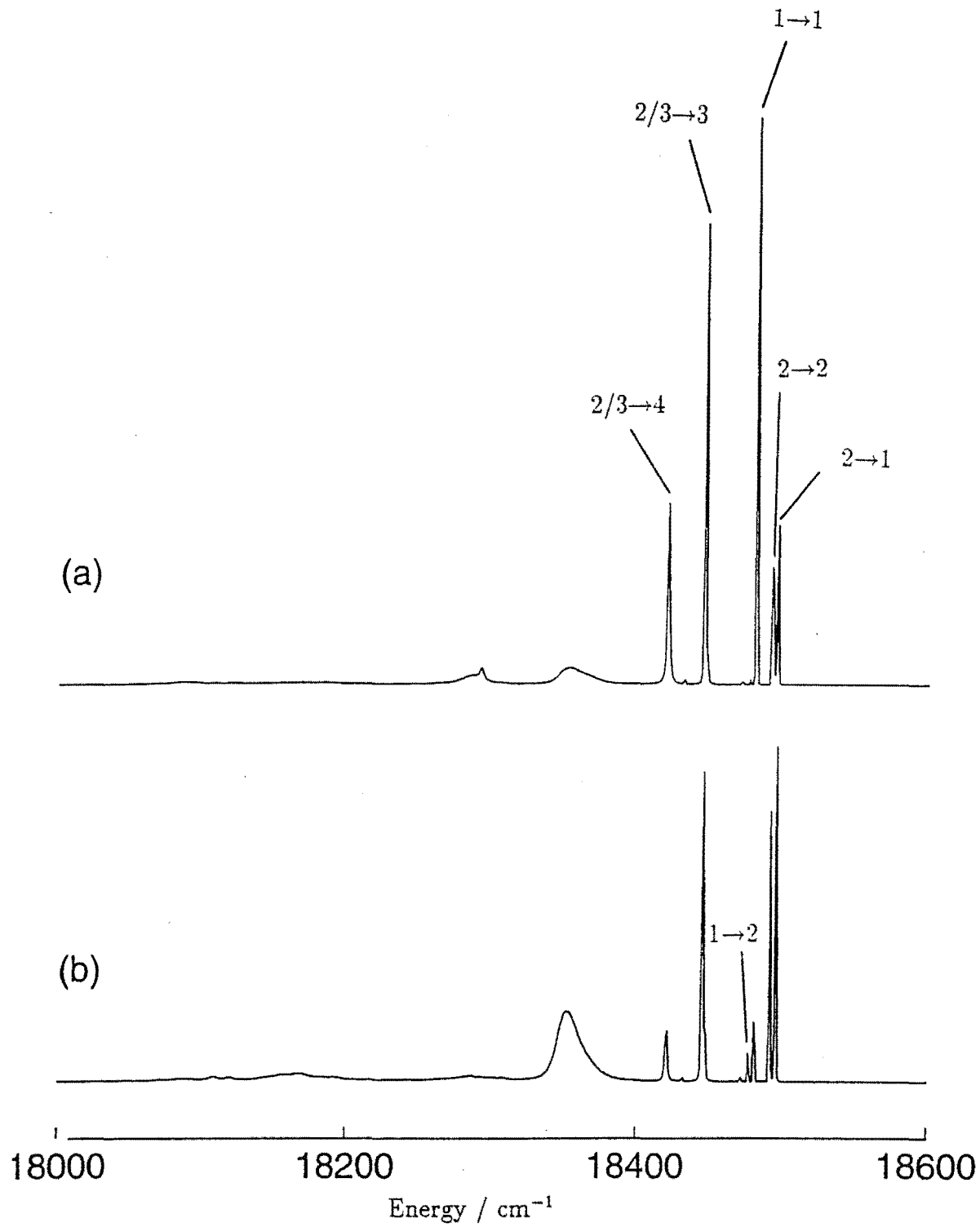

Figure 7.8: Polarised fluorescence spectra of the $C_{4v}F^-$ centre in the SrF_2:Tb^{3+} crystal while pumping the $Z_1 \rightarrow A_5$ transition; (a) x(yx)z and (b) x(yy)z.

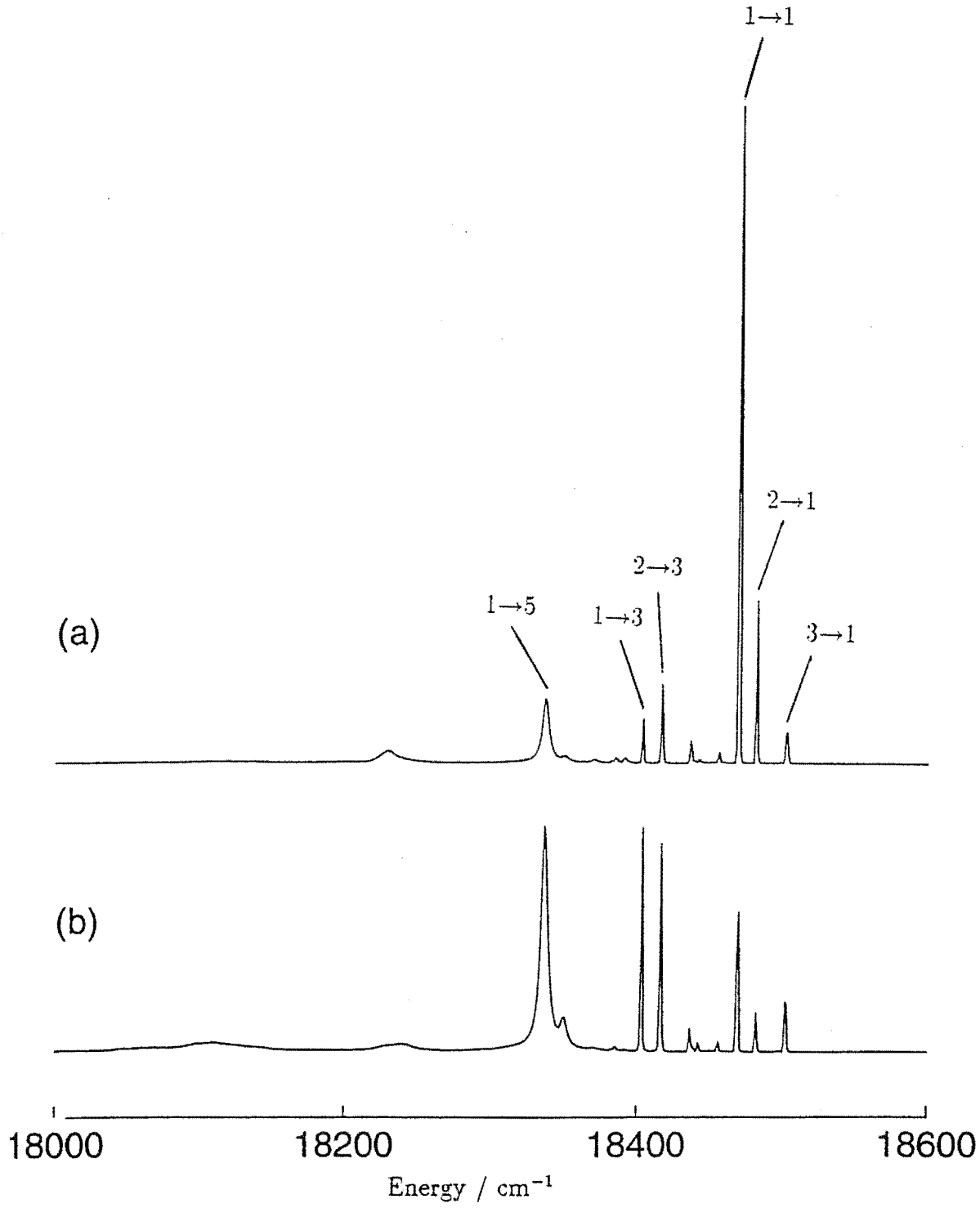

Figure 7.9: Polarised fluorescence spectra of the $C_{4v}F^-$ centre in the CaF_2:Tb^{3+} crystal while pumping the $Z_1 \rightarrow A_5$ transition; (a) x(yx)z and (b) x(yy)z.

sation ratios, while assuming electric-dipole transitions and a C_{4v} symmetry crystal field, was thwarted by apparent inconsistencies in the experimental results. It will be necessary to abandon one of these assumptions in order to interpret the complicated polarisation behaviour of this centre. This will be discussed in the following Section.

7.3.2 Crystal-Field and Transition-Intensity Calculations

Theoretical energy level calculations were performed using the Tb^{3+} free-ion parameters obtained by Carnall et al [19] and the F-Shell Empirical Programmes written by M. F. Reid (The Departent of Physics and Astronomy, University of Canterbury). $C_{4v}F^-$ centre crystal-field parameters were available for other lanthanides and the parameters used in this calculation were obtained by interpolation. These are listed in columns two and four of Table 7.2. The predicted energy levels were surprisingly close to the empirical levels, with an average difference of $13.4cm^{-1}$ for SrF_2 and $16.3cm^{-1}$ for CaF_2, Tables 7.3 and 7.4. There was sufficient agreement with the irrep labelling scheme already deduced to make some more definite irrep assignments. These results support the notion that this is the tetragonal $C_{4v}F^-$ centre.

A similar calculation was performed for the Tb^{3+} $C_{3v}F^-$ centre, using the Ho^{3+} ion crystal-field parameters obtained by Mujaji [62] and the fitted Tb^{3+} free-ion parameters obtained here. The levels calculated for the trigonal centre also exhibited striking agreement with the empirical levels ascribed to the C_{3v} centre in these Tb^{3+} doped crystals.

Crystal-field parameter fits were made to the empirical energy levels. The best fits were obtained by allowing the F^4 and ζ free-ion parameters as well as all the crystal-field parameters to vary. The parameter fits always converged uniquely and the final parameters which were obtained are listed in Table 7.2. These $C_{4v}F^-$ centre crystal-field parameters for Tb^{3+} are reasonable when compared with the parameters obtained in studies of other lanthanides. The fitted energy levels are presented in column four of Tables 7.3 and 7.4. The average absolute difference between the fitted energy levels and the empirical levels is $6.9cm^{-1}$ for SrF_2 and $7.5cm^{-1}$ for CaF_2. The calculated Z_3 level for SrF_2 of $125.6cm^{-1}$ is numerically very close to the $123cm^{-1}$ value measured by Antipin et al [5].

To understand the complicated polarisation behaviour of the $Tb^{3+}C_{4v}F^-$ centres transition-intensity calculations were performed to resolve the transition intensities into their electric and magnetic-dipole components. These calculations used the C_{4v} crystal-field wave functions calculated during the crystal-field parameter fit. A simple point-charge point-dipole calculation was preformed to estimate the A^{λ}_{tp} intensity parameters which were used in these transition-intensity calculations. This calculation is like those described by Reid et al [78] for other lanthanide complexes. The resulting parameters were: A^2_{10}=7.2x10^{-10}, A^2_{30}=-5.8x10^{-11}, A^4_{30}=4.8x10^{-11}, A^4_{50}=-2.3x10^{-11}, A^4_{54}=1.2x10^{-11}, A^6_{50}=2.6x10^{-10}, A^5_{54}=-1.4x10^{-10}, A^6_{70}=6.5x10^{-14}, and A^6_{74}=1.5x10^{-13}.

Table 7.2: The Tb^{3+} free-ion parameters and the $C_{4v}F^-$ centre crystal-field parameters.

	SrF_2		CaF_2	
Parameter	**Initial**	**Fitted**	**Initial**	**Fitted**
F^2	90426	90426	90426	90426
F^4	58964	58934±30	58964	58572±35
F^6	47252	47252	47252	47252
ζ	1699	1698±7	1699	1686±9
B_C^4	-1200	-1101±32	-1330	-1330±30
B_C^6	580	474±20	590	624±20
B_A^2	420	482±20	720	807±23
B_A^4	375	450±23	450	504±24
B_A^6	375	334±27	450	445±30
n		20		22
σ		11.0		12.4

7.3.3 Analysis of the $C_{4v}F^-$ Centre Polarisation Behaviour

The programme predicted that four absorption transitions to the $^5D_4$ multiplet are allowed, in agreement with the observed excitation spectra, Figures 7.2(a) and 7.3(a). The lowest γ_3 and γ_4 levels of the $^7F_6$ multiplet are considered degenerate for the purposes of this analysis. All four transitions are both electric and magnetic-dipole allowed, the electric-dipole components being at least two orders of magnitude greater than the magnetic-dipole components. This is a reasonable result given that the $^7F_6 \rightarrow {}^5D_4$ transition is neither electric nor magnetic-dipole allowed in the free ion.

Fluorescence transitions from the $^5D_4$ multiplet have a more significant magnetic-dipole character. In both SrF_2 and CaF_2 the A_1 level is a γ_1 singlet state. Some of the most intense fluorescence transitions from the A_1 level to the $^7F_1$, $^7F_3$, $^7F_4$, $^7F_5$ and $^7F_6$ multiplets are either purely magnetic-dipole or have a significant magnetic-dipole component. These are of comparable intensity to the electric-dipole transitions. The A_2 level of SrF_2 and the A_3 level of CaF_2 are both γ_5 doublet states. Transitions from these γ_5 states to the $^7F_3$, $^7F_4$ and $^7F_5$ multiplets also exhibit large magnetic-dipole components.

Generally the $^5D_4 \rightarrow {}^7F_3$, $^7F_4$ and $^7F_6$ inter-multiplet transitions, which are magnetic-dipole allowed in the free ion, are of mixed electric and magnetic-dipole character in the C_{4v} crystal-field. Fluorescence transitions to the other ^7F_J multiplets, which are forbidden in the free ion, are usually dominated by their electric-dipole components, unless this is specifically forbidden by the electric-dipole selec-

Table 7.3: The experimental and calculated electronic energy levels (vacuum) of the Tb^{3+} $C_{4v}F^-$ centre in SrF_2, in units of cm^{-1}. The difference between the fitted and the experimental levels is given in the last column. The experimental energies have an uncertainty of $\pm 0.2 cm^{-1}$.

Multiplet	State	Calculated	Fitted	Empirical	Difference
$^7F_6$	$Z_1(\gamma_3)$	0.0	2.2	0.0	-2.2
	$Z_2(\gamma_4)$	0.2	2.6	0.0	-2.6
	$Z_3(\gamma_5)$	126.8	125.6		
	$Z_4(\gamma_1)$	137.1	134.7	128.7	-6.0
	$Z_5(\gamma_3)$	126.3	139.6		
	$Z_6(\gamma_5)$	183.6	183.3		
	$Z_7(\gamma_2)$	223.9	221.4		
	$Z_8(\gamma_1)$	359.7	383.8		
	$Z_9(\gamma_5)$	363.3	388.6		
	$Z_{10}(\gamma_4)$	369.2	394.3		
$^7F_5$	$Y_1(\gamma_2)$	2081.0	2103.9	2109.5	+5.6
	$Y_2(\gamma_1)$	2081.6	2106.6	2113.2	+6.6
	$Y_3(\gamma_5)$	2127.9	2151.0	2160.0	+9.0
	$Y_4(\gamma_3)$	2162.3	2183.6	2185.7	+2.1
	$Y_5(\gamma_5)$	2215.1	2212.5		
	$Y_6(\gamma_2)$	2256.4	2284.5		
	$Y_7(\gamma_5)$	2384.3	2383.6		
	$Y_8(\gamma_4)$	2458.6	2453.6		
$^7F_4$	$X_1(\gamma_1)$	3326.1	3348.0	3348.8	+0.8
	$X_2(\gamma_4)$	3358.0	3367.7	3361.6	-6.1
	$X_3(\gamma_3)$	3390.5	3441.5	3437.8	-3.7
	$X_4(\gamma_5)$	3435.8	3438.2	3441.2	+3.0
	$X_5(\gamma_2)$	3505.9	3502.3		
	$X_6(\gamma_5)$	3630.9	3639.4		
	$X_7(\gamma_1)$	3886.4	3838.4		
$^7F_3$	$W_1(\gamma_3)$	4355.3	4368.7	4353.4	-15.3
	$W_2(\gamma_5)$	4479.4	4475.8	4472.2	-3.6
	$W_3(\gamma_2)$	4492.3	4486.5	4497.1	+10.6
	$W_4(\gamma_4)$	4573.6	4580.7		
	$W_5(\gamma_5)$	4593.8	4591.3		
$^7F_2$	$V_1(\gamma_1)$	5076.7	5090.0		
	$V_2(\gamma_3)$	5120.4	5142.2		
	$V_3(\gamma_5)$	5328.5	5304.4		
	$V_4(\gamma_4)$	5415.1	5413.4		
$^7F_1$	$U_1(\gamma_2)$	5647.3	5631.5		
	$U_2(\gamma_5)$	5749.5	5754.1		
$^7F_0$	$T_1(\gamma_1)$	5937.8	5939.5		
$^5D_4$	$A_1(\gamma_1)$	20590.0	20590.2	20587.2	-3.0
	$A_2(\gamma_5)$	20584.3	20591.1	20603.0	+11.9
	$A_3(\gamma_4)$	20579.5	20587.5	20604.1	+16.6
	$A_4(\gamma_2)$	20617.2	20613.9	20616.6	+2.7
	$A_5(\gamma_3)$	20644.4	20656.3	20640.2	-16.1
	$A_6(\gamma_5)$	20672.5	20678.0	20666.1	-11.9
	$A_7(\gamma_1)$	20703.9			

Table 7.4: The experimental and calculated electronic energy levels (vacuum) of the Tb^{3+} $C_{4v}F^-$ centre in CaF_2, in units of cm^{-1}. The difference between the fitted and the experimental levels is given in the last column. The experimental energies have an uncertainty of $\pm 0.2 cm^{-1}$.

Multiplet	State	Calculated	Fitted	Empirical	Difference
$^7F_6$	$Z_1(\gamma_3)$	0.0	1.8	0.0	-1.8
	$Z_2(\gamma_4)$	0.2	1.9	0.0	-1.9
	$Z_3(\gamma_5)$	205.5	193.9		
	$Z_4(\gamma_1)$	237.5	227.6	215.0	-12.6
	$Z_5(\gamma_3)$	252.7	250.8		
	$Z_6(\gamma_5)$	271.0	292.0		
	$Z_7(\gamma_2)$	312.5	323.5		
	$Z_8(\gamma_1)$	516.8	558.7		
	$Z_9(\gamma_5)$	526.3	569.5		
	$Z_{10}(\gamma_4)$	535.5	579.7		
$^7F_5$	$Y_1(\gamma_2)$	2154.9	2158.1	2164.2	+6.1
	$Y_2(\gamma_1)$	2155.3	2158.1		
	$Y_3(\gamma_5)$	2228.8	2223.1	2231.3	+8.2
	$Y_4(\gamma_3)$	2283.4	2291.7	2283.2	-8.5
	$Y_5(\gamma_5)$	2293.5	2291.2	2298.7	+7.5
	$Y_6(\gamma_2)$	2398.2	2408.2		
	$Y_7(\gamma_5)$	2502.2	2514.5		
	$Y_8(\gamma_4)$	2580.5	2595.9		
$^7F_4$	$X_1(\gamma_1)$	3425.0	3406.6	3407.1	+0.5
	$X_2(\gamma_4)$	3433.5	3436.6	3429.5	-7.1
	$X_3(\gamma_3)$	3506.2	3506.8	3505.7	-0.8
	$X_4(\gamma_5)$	3526.5	3525.2	3522.4	-2.8
	$X_5(\gamma_2)$	3605.5	3598.2	3597.0	-1.2
	$X_6(\gamma_5)$	3758.1	3767.3		
	$X_7(\gamma_1)$	4006.7	4016.5		
$^7F_3$	$W_1(\gamma_3)$	4435.0	4417.2	4407.9	-9.3
	$W_2(\gamma_2)$	4559.4	4543.3	4548.2	+4.9
	$W_3(\gamma_5)$	4566.4	4558.9	4555.1	-3.8
	$W_4(\gamma_4)$	4712.7	4722.8		
	$W_5(\gamma_5)$	4734.9	4740.6		
$^7F_2$	$V_1(\gamma_1)$	5143.2	5127.8		
	$V_2(\gamma_3)$	5263.1	5269.1		
	$V_3(\gamma_5)$	5453.7	5443.2		
	$V_4(\gamma_4)$	5570.5	5574.3		
$^7F_1$	$U_1(\gamma_2)$	5731.0	5709.4		
	$U_2(\gamma_5)$	5897.8	5896.8		
$^7F_0$	$T_1(\gamma_1)$	6069.5	6062.9	6070.5	+7.6
$^5D_4$	$A_1(\gamma_1)$	20681.4	20635.9	20632.4	-3.5
	$A_2(\gamma_2)$	20704.5	20659.4	20645.7	-13.7
	$A_3(\gamma_5)$	20683.6	20645.7	20666.0	+20.3
	$A_4(\gamma_4)$	20682.9	20646.5	20672.0	+25.5
	$A_5(\gamma_3)$	20760.4	20725.9	20710.3	-15.6
	$A_6(\gamma_5)$	20791.1	20756.2	20743.5	-12.7
	$A_7(\gamma_1)$	20821.5	20785.0		

tion rules.

The fluorescence polarisation ratios of specific excitation and fluorescence transitions have been calculated, using the results of the transition-intensity calculations and the elementary polarisation ratios listed in Tables 4.9 and 4.10. These calculated ratios are compared to the empirical ratios, for a representative sample of SrF_2 C_{4v} centre transitions, in Table 7.5. Where there are near degeneracies which could not be resolved by the monochrometer, the calculated transition intensities have been used to determine the contribution of each transition to the observed polarisation ratio. This approach is demonstrated for the unresolved fluorescence transitions from the A_2 and A_3 levels. Many of the observed fluorescence transitions will have both electric and magnetic-dipole components, and these are associated with numerically different polarisation ratios. Both of these contributions must be taken into account when calculating the observed polarisation ratios, as shown in Table 7.5.

For pure electric or magnetic-dipole transitions there is very good agreement between the calculated and empirical polarisation ratios. The quality of the experimental ratios obtained here is similar to that obtained in other studies of the RE^{3+} C_{4v} centre in SrF_2 [27] [62] [77]. For mixed-dipole transitions there is also good agreement between the calculated and experimental ratios. When comparing the two ratios it is important to note that the 'Inten' programme only provides estimates of the relative electric and magnetic-dipole strengths, which are generated using the intensity parameters supplied as input. The polarisation ratios which are associated with a mixed transition are particularly sensitive to this partitioning of the observed transition, as the ratio of the electric part is necessarily the numerical inverse of the ratio of the magnetic part. Thus these calculated ratios can be considered only estimates when the observed fluorescence transition contains both an electric and a magnetic moment.

Although the polarisation behaviour of this Tb^{3+} centre is very complicated it is still possible to use the empirical polarisation ratios to assign irrep labels to electronic energy levels (Y_1 and Y_2 for example) and also to test the symmetry of the centre. The success of the crystal-field fit to the experimental energy levels and of the interpretation of the empirical polarisation ratios confirms that this is indeed the $C_{4v}F^-$ centre.

7.4 The Spectroscopy of the Hydrogenated and Deuterated SrF_2:Tb^{3+} and CaF_2:Tb^{3+} Crystals

7.4.1 Absorption Spectra

Hydrogenated and deuterated crystals were prepared for each Tb^{3+} doped fluoride host. The former were hydrogenated in the high-pressure furnace while the later were

Table 7.5: Polarisation ratios for specific excitation and emission transitions of the $C_{4v}F^-$ centre in the SrF_2:Tb^{3+} crystal. Since the A_2 and A_3 levels could not be resolved by the monochrometer the observed polarisation ratios of the transitions from these levels are determined by the contributions from both fluorescence transitions.

Transitions		**E-Dipole**		**M-Dipole**		**Ratios**	
Excitation	**Emission**	**%**	**Ratio**	**%**	**Ratio**	**Calc'**	**Exp't**
$Z_1(\gamma_3)\rightarrow A_5(\gamma_3)$	$A_1(\gamma_1)\rightarrow Z_4(\gamma_1)$	100	0:1	-	-	0:1	0.14
	$A_2(\gamma_5)\rightarrow Z_4(\gamma_1)$	99	1:0	1	0:1	99	5.4
$Z_{1/2}(\gamma_{3/4})\rightarrow A_6(\gamma_5)$	$A_1(\gamma_1)\rightarrow Z_4(\gamma_1)$	100	1:0	-	-	1:0	7.9
	$A_2(\gamma_5)\rightarrow Z_4(\gamma_1)$	99	1:2	1	2:1	0.51	0.58
$Z_1(\gamma_3)\rightarrow A_5(\gamma_3)$	$A_1(\gamma_1)\rightarrow Y_1(\gamma_2)$	-	-	100	1:0	1:0	9.6
	$A_2(\gamma_5)\rightarrow Y_1(\gamma_2)$	54	1:0	46	0:1	1.17	0.48
$Z_{1/2}(\gamma_{3/4})\rightarrow A_6(\gamma_5)$	$A_1(\gamma_1)\rightarrow Y_1(\gamma_2)$	-	-	100	0:1	0:1	0.15
	$A_2(\gamma_5)\rightarrow Y_1(\gamma_2)$	54	1:2	46	2:1	0.96	0.90
$Z_1(\gamma_3)\rightarrow A_5(\gamma_3)$	$A_1(\gamma_1)\rightarrow Y_2(\gamma_1)$	100	0:1	-	-	0:1	0.17
	$A_2(\gamma_5)\rightarrow Y_2(\gamma_1)$	61	1:0	39	0:1	1.56	0.44
$Z_{1/2}(\gamma_{3/4})\rightarrow A_6(\gamma_5)$	$A_1(\gamma_1)\rightarrow Y_2(\gamma_1)$	100	1:0	-	-	1:0	7.8
	$A_2(\gamma_5)\rightarrow Y_2(\gamma_1)$	61	1:2	39	2:1	0.86	0.86
$Z_1(\gamma_3)\rightarrow A_5(\gamma_3)$	$A_2(\gamma_5)\rightarrow Y_4(\gamma_3)$	90	1:0	10	0:1	9.0	
	$A_3(\gamma_4)\rightarrow Y_4(\gamma_3)$	-	-	100	1:0	1:0	
						10.5	3.7
$Z_{1/2}(\gamma_{3/4})\rightarrow A_6(\gamma_5)$	$A_2(\gamma_5)\rightarrow Y_4(\gamma_3)$	90	1:2	10	2:1	0.58	
	$A_3(\gamma_4)\rightarrow Y_4(\gamma_3)$	-	-	100	0:1	0:1	
						0.47	0.61
$Z_1(\gamma_3)\rightarrow A_5(\gamma_3)$	$A_1(\gamma_1)\rightarrow X_1(\gamma_1)$	100	0:1	-	-	0:1	0.14
$Z_{1/2}(\gamma_{3/4})\rightarrow A_6(\gamma_5)$		100	0:1	-	-	1:0	7.5
$Z_1(\gamma_3)\rightarrow A_5(\gamma_3)$	$A_2(\gamma_5)\rightarrow X_3(\gamma_3)$	99	1:0	1	0:1	99	
	$A_3(\gamma_4)\rightarrow X_3(\gamma_3)$	-	-	100	1:0	1:0	
						99	6.9
$Z_{1/2}(\gamma_{3/4})\rightarrow A_6(\gamma_5)$	$A_2(\gamma_5)\rightarrow X_3(\gamma_3)$	99	1:2	1	2:1	0.51	
	$A_3(\gamma_4)\rightarrow X_3(\gamma_3)$	-	-	100	0:1	0:1	
						0.50	0.45
$Z_1(\gamma_3)\rightarrow A_5(\gamma_3)$	$A_1(\gamma_3)\rightarrow X_4(\gamma_5)$	100	1:0	0	0:1	1:0	6.18
$Z_{1/2}(\gamma_{3/4})\rightarrow A_6(\gamma_5)$		100	1:2	0	2:1	1:2	0.60
$Z_{1/2}(\gamma_{3/4})\rightarrow A_6(\gamma_5)$	$A_2(\gamma_5)\rightarrow W_1(\gamma_3)$	0	1:2	100	2:1	2:1	
	$A_3(\gamma_4)\rightarrow W_1(\gamma_3)$	-	-	100	0:1	0:1	
						0.84	1.21

deuterated in the low-pressure furnace. The nominal H^- and D^- ion concentrations of these crystals were obtained using the line strength of the second-harmonic absorption transition of the tetrahedral hydrogenic site local-vibrational mode. This provides a relative measure of hydrogenic ion concentration. The proceedure to derive this quantity has been described in detail by German [37]. The results obtained for the crystals studied were: $171cm^{-2}$ for SrF_2:Tb^{3+}:H^-, $19cm^{-2}$ for SrF_2:Tb^{3+}:D^-, $163cm^{-2}$ for CaF_2:Tb^{3+}:H^- and $16cm^{-2}$ for CaF_2:Tb^{3+}:D^-. These measured line strengths have uncertainties of only a few percent. However, these values can only be considered as indicative of the number of hydrogenic ions located in Tb^{3+} centres. The hydrogenation/deuteration times for these crystals were 1.25h, 34.5h, 1.25h and 55h respectively.

Transmission spectra were obtained for both types of hydrogenated crystal. The dominant absorption features in these hydrogenated crystals were different from those observed in the parent crystals and generally they exhibited stronger absorption. As in the parent crystals, transitions were observed to both the $^5D_4$ and the $^5D_3$ multiplets.

Broadband excitation spectra of the hydrogenated and deuterated crystals were obtained, again by monitoring the $^5D_4 \rightarrow {}^7F_5$ inter-multiplet fluorescence at 545nm. As in the parent crystals these broadband excitation spectra were almost identical spectroscopically to their respective transmission spectra, so only the former are presented here, Figures 7.10 and 7.11.

The weakly-deuterated SrF_2:Tb^{3+}:D^- crystal is dominated in excitation by the Tb^{3+} $C_{4v}F^-$ centre. Some new excitation transitions appear in the same energy region as the $C_{4v}F^-$ transitions. These may be $Tb^{3+}C_{4v}F^-$ centres, modified by D^- ion substitutions.

The SrF_2:Tb^{3+}:H^- crystal has been heavily hydrogenated and has a very different excitation spectrum from its weakly-deuterated counterpart. The most significant difference is that the excitation transitions of the $C_{4v}F^-$ centre are barely discernible among the many more intense transitions which were not present in the parent crystal. There are broadly two groups of excitation transitions. One of these contains transitions which are generally higher in energy than those of the $C_{4v}F^-$ centre. These might be hydrogenic centres associated with this tetragonal parent centre. The lower-energy group is located in the same region as the trigonal $C_{3v}F^-$ centre found in the SrF_2:Tb^{3+} parent crystal.

Many new trigonal centres and their hydrogenic modifications might have been produced during the thermal stress of the hydrogenation process, when this crystal was heated to over 1000°C in a 1.72MPa (overpressure) atmosphere of hydrogen. The deuterated crystal was treated in a low-pressure furnace, where it was only heated to 850°C.

When comparing the excitation spectra of the two deuterated crystals, Figure 7.10(b) and Figure 7.11(b), it is evident that there has been much more gettering of D^- ions by the Tb^{3+} centres in the CaF_2 crystal than in the SrF_2 crystal. This may be due, in part, to the diffusion of the light D^- ions at ambient temperatures

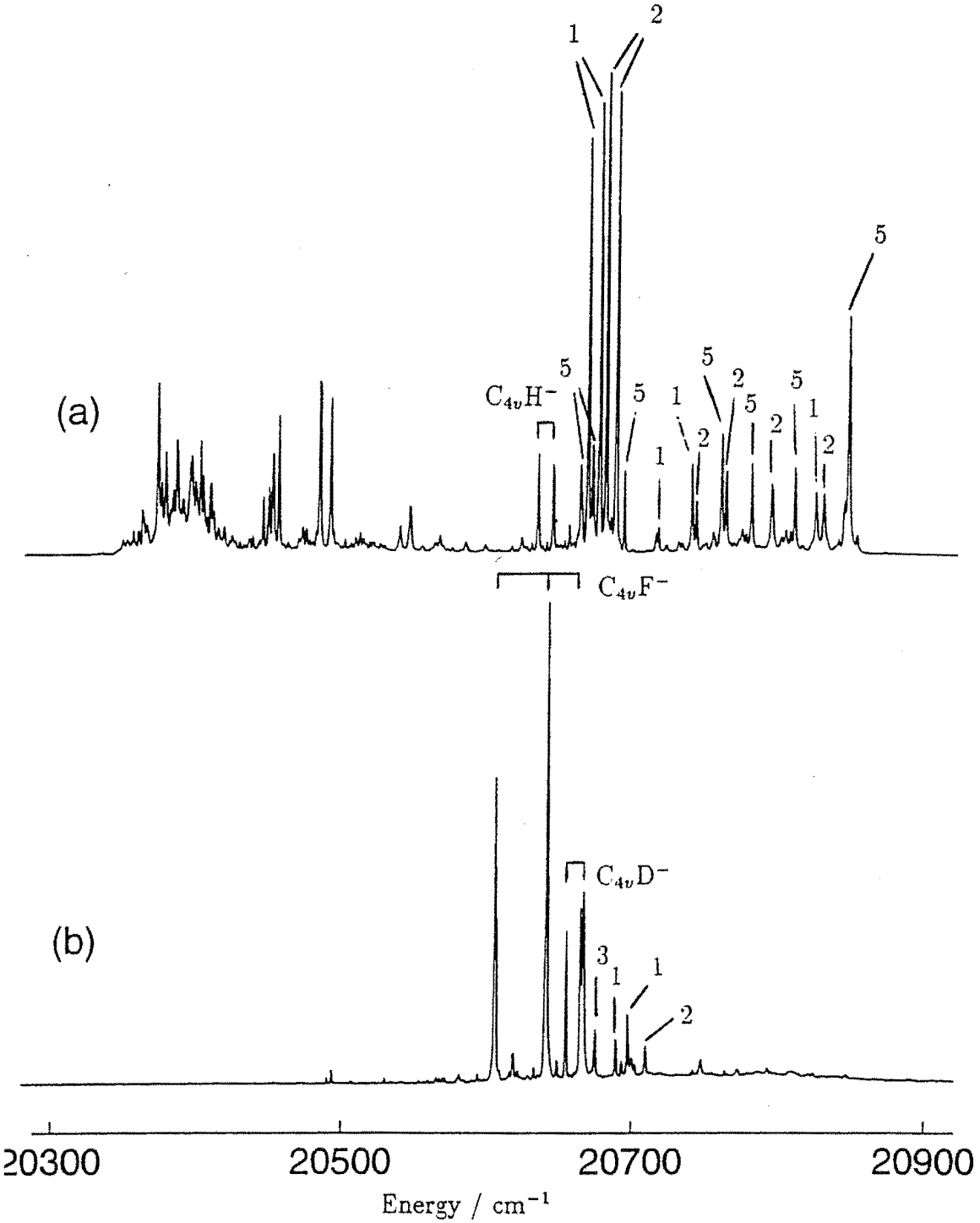

Figure 7.10: Broadband excitation spectra of (a) the hydrogenated and (b) the deuterated SrF_2:Tb^{3+} crystals, while monitoring the fluorescence at 545nm.

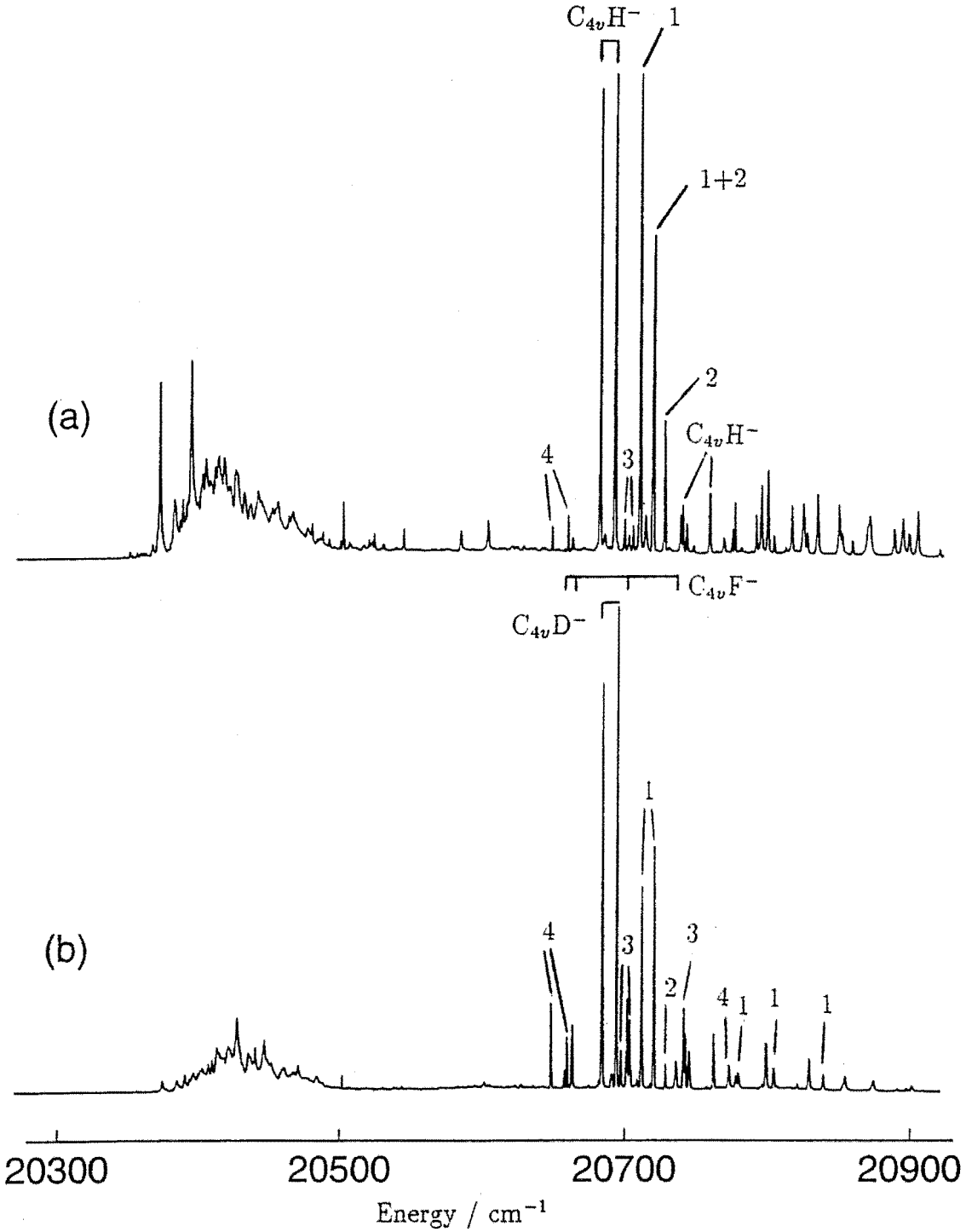

Figure 7.11: Broadband excitation spectra of (a) the hydrogenated and (b) the deuterated CaF_2:Tb^{3+} crystals, while monitoring the fluorescence at 545nm.

as the crystals age. There is some anecdotal evidence of this occurring in the Pr^{3+} doped crystals as well. When these spectra were recorded the CaF_2 crystal was two years old and so much older than the SrF_2 crystal, which had been deuterated just 10 days before.

The excitation spectrum of the CaF_2:Tb^{3+}:D^- crystal is much more like that of the SrF_2:Tb^{3+}:H^- crystal, with the transitions of the Tb^{3+} C_{4v} centre being comparatively minor compared to the new transitions which appear after deuteration. Again two groups of excitation transitions occur, with energies that suggest that these are associated with the $C_{3v}F^-$ centre and the $C_{4v}F^-$ centre.

The hydrogenated CaF_2 crystal is also dominated by transitions which are absent in the parent crystal. It has an excitation spectrum which is very similar to that of the CaF_2:Tb^{3+}:D^- crystal; indeed so much so that many of the transitions can clearly be identified as being common to both crystals.

7.4.2 Selective Excitation Spectra

Site-selective excitation spectra, for each crystal, were obtained by monitoring specific $^5D_4 \rightarrow {}^7F_5$ fluorescence transitions; Figures 7.12, 7.13, 7.14, and 7.15. By judicious choice of the transitions being monitored, good selectivity between the different centres was achieved. Only those centres with excitation features in the region of the Tb^{3+} $C_{4v}F^-$ transitions were studied here, although there are other centres present in these crystals. The centres derived from the tetragonal parent are of most interest as their spectroscopy and bleaching behaviour can be compared with that of the Cs centres of Pr^{3+}.

The principle $^7F_6 \rightarrow {}^5D_4$ excitation transitions of each centre investigated here are given in Table 7.6. Small isotropic shifts in the transition energies, of a few cm^{-1} in most cases, are observed between the hydrogen and deuterium varieties of each centre; Figures 7.12 and 7.13. These shifts confirm the hydrogenic nature of these centres. Such isotopic energy shifts are also exhibited by the hydrogenic centres of the Pr^{3+} ion; these are generally smaller, being approximately $1cm^{-1}$ for most centres.

The dominant centre in both the deuterated crystals has been labeled $C_{4v}D^-$, and it will be shown that this is most likely to be the $C_{4v}F^-$ centre modified by D^- ion substitution of the interstitial F^- ion. The H^- tetragonal centre is much less prominent in the hydrogenated crystals, for which the hydrogenation process is more efficient. This trend is expected as multiple-hydrogenic ion centres will form as the hydrogenic ion concentration is increased [37].

The $C_{4v}D^-$ and $C_{4v}H^-$ centres of SrF_2 and CaF_2 all have very similar excitation spectra. Each is dominated by the two lowest energy transitions, which are accompanied by five other transitions which are all an order of magnitude weaker. This comprises all seven of the $^5D_4$ levels expected in a tetragonal crystal field. The third level is also clearly split into two components. Such splittings are unexpected in the C_{4v} field. That so many transitions are observed to the $^5D_4$ multiplet in this

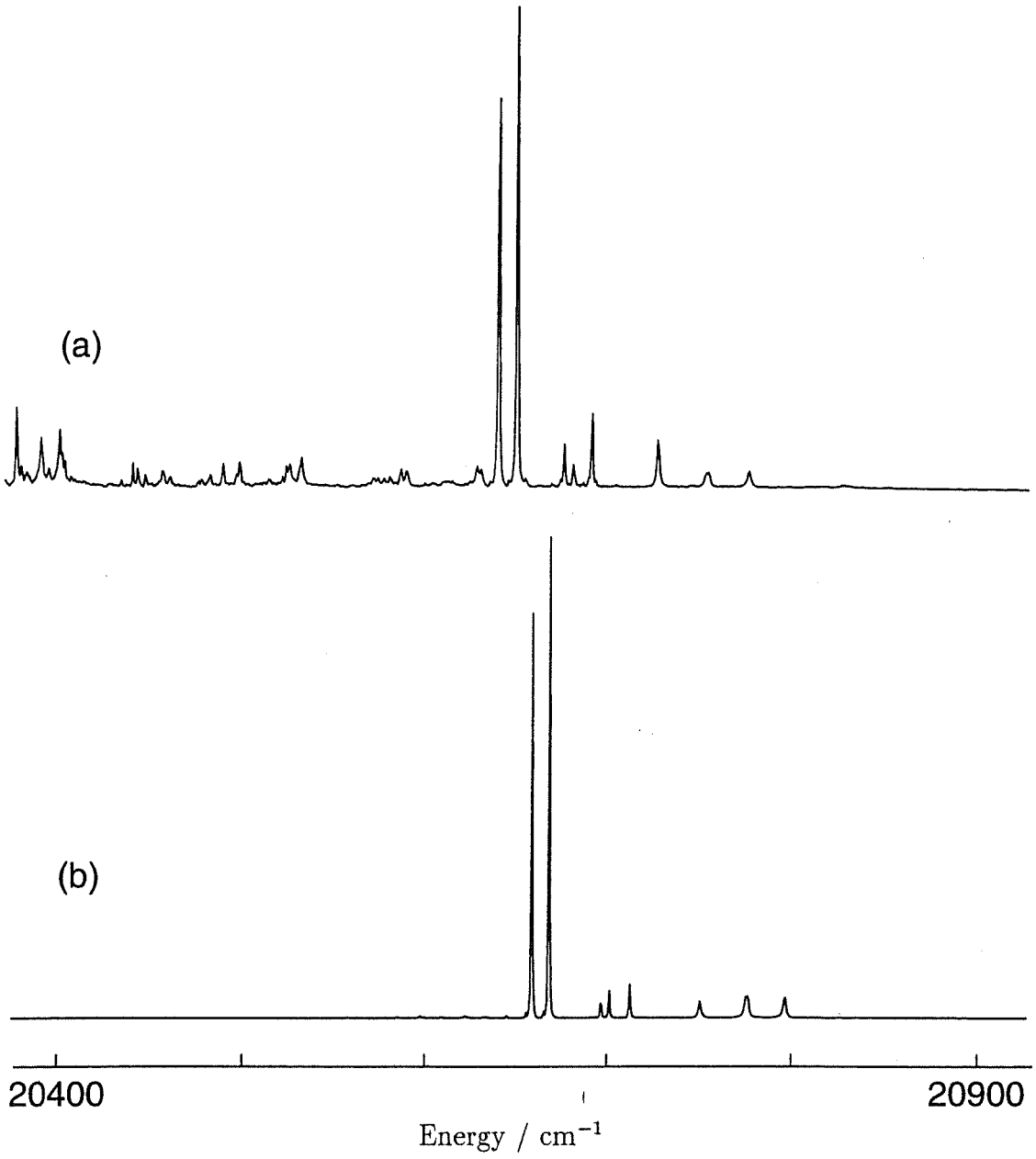

Figure 7.12: Selective excitation spectra of the hydrogenated SrF_2:Tb^{3+} crystals showing the $^7F_6 \rightarrow {}^5D_4$ transitions of **(a)** the $C_{4v}H^-$ centre and **(b)** the $C_{4v}D^-$ centre.

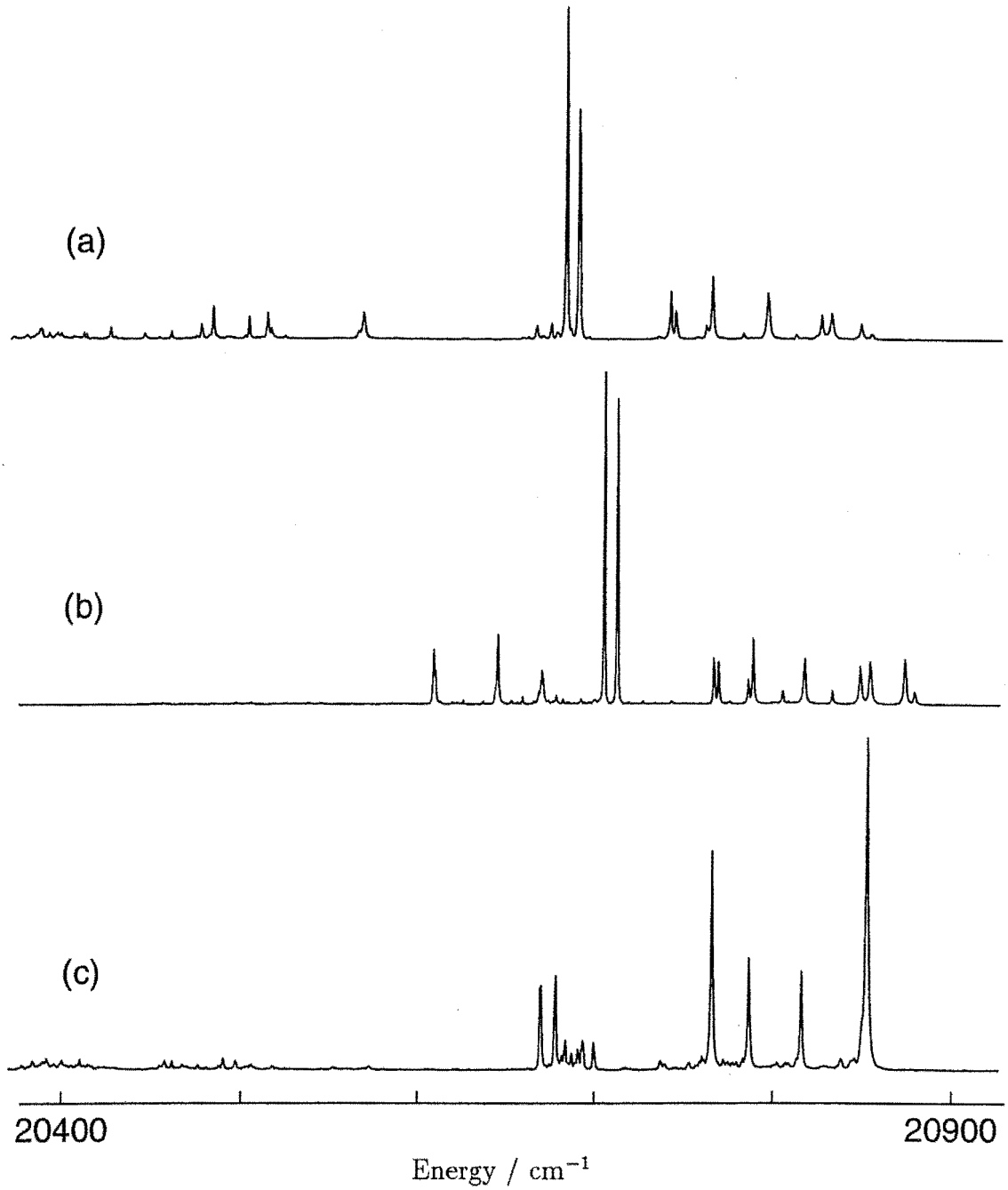

Figure 7.13: Selective excitation spectra of the hydrogenated SrF_2:Tb^{3+} crystals showing the $^7F_6 \rightarrow {}^5D_4$ transitions of the (**a**) hydrogen and (**b**) deuterium Ls(2) centre. (**c**) Selective excitation spectrum of the Ls(5) centre in the SrF_2:Tb^{3+}:H^- crystal, showing the $^7F_6 \rightarrow {}^5D_4$ transitions.

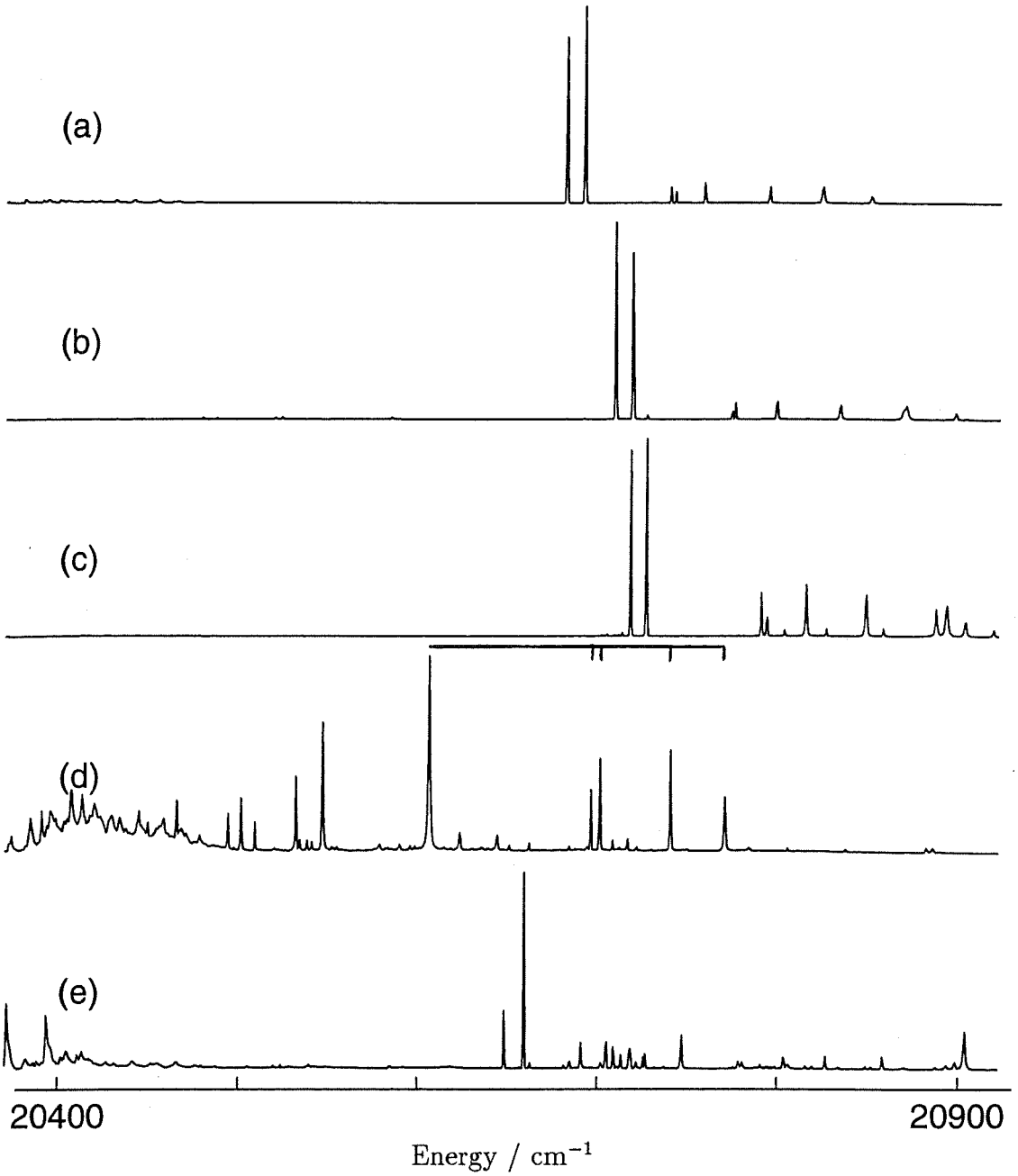

Figure 7.14: Selective excitation spectra of centres in the CaF_2:Tb^{3+}:H^- crystal, showing the $^7F_6 \rightarrow {}^5D_4$ transitions; **(a)** $C_{4v}H^-$ **(b)** Ls(1) **(c)** Ls(2) **(d)** Ls(3) and **(e)** Ls(4).

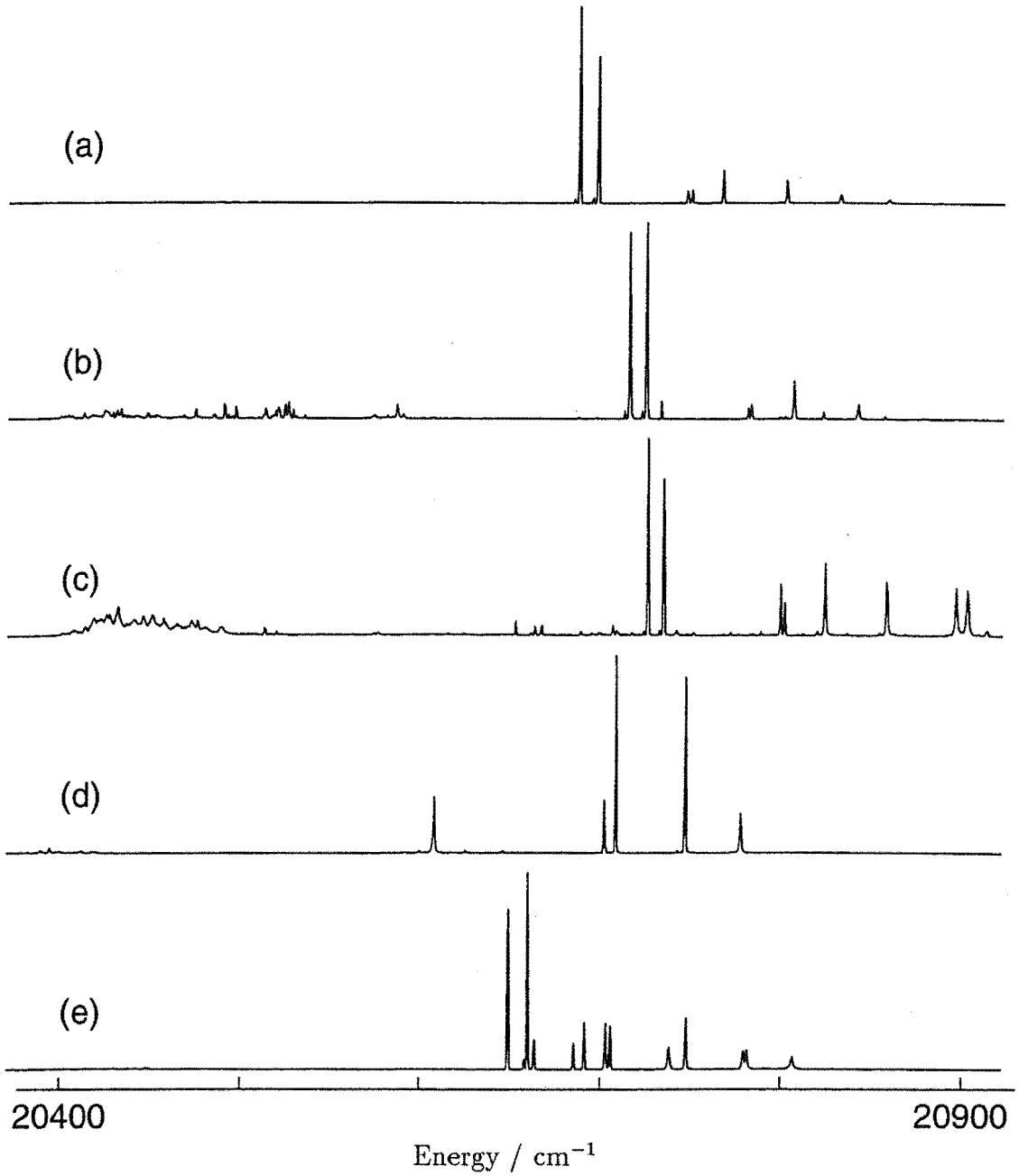

Figure 7.15: Selective excitation spectra of centres in the CaF_2:Tb^{3+}:D^- crystal, showing the $^7F_6 \rightarrow {}^5D_4$ transitions; **(a)** $C_{4v}D^-$ **(b)** Ls(1) **(c)** Ls(2) **(d)** Ls(3) and **(e)** Ls(4).

Table 7.6: Some $^5D_4$ multiplet energy levels (vacuum) of the hydrogenic centres observed in excitation, in units of cm^{-1}. The energies have an uncertainty of $\pm 0.2 cm^{-1}$.

Centre	SrF_2:Tb^{3+} Hydrogen	SrF_2:Tb^{3+} Deuterium	CaF_2:Tb^{3+} Hydrogen	CaF_2:Tb^{3+} Deuterium
$C_{4v}H^-/D^-$	20651.4	20656.6	20690.7	20693.1
	20661.5	20668.1	20700.7	20702.8
Ls(1)	20685.1	20688.3	20717.9	20720.3
	20693.3	20696.2	20726.6	20728.8
Ls(2)	20697.3	20700.5	20725.4	20728.6
	20704.9	20707.5	20733.6	20736.5
Ls(3)	-	20674.9	20701.8	20710.1
	-	20688.6	20706.9	20712.5
Ls(4)	-	-	20657.4	20656.7
	-	-	20668.6	20668.1
Ls(5)	20860.1	-	-	-

centre challenges its assignment as the hydrogenic tetragonal centre.

Four other centres were observed in the hydrogenated and deuterated CaF_2 crystals. In recognition that these centres are likely to be low-symmetry modifications of the $C_{4v}H^-$ and $C_{4v}D^-$ centres they have been labeled as Ls(1)..Ls(4), in order of decreasing excitation intensity. The excitation spectra of the $C_{4v}H^-$, Ls(1), Ls(2) and Ls(4) centres are all very similar, with the strongest excitation to the two lowest levels of $^5D_4$; Figures 7.14 and 7.15. This resemblance is suggestive of structural similarities between these centres. The spectrum of the Ls(3) centre is quite different, with four of its five transitions forming a pattern like that found in the $C_{4v}F^-$ spectrum.

Three of these low-symmetry centres were also found in the SrF_2 crystals. They were identified from their selective excitation and fluorescence spectra and by the relative order of their excitation transitions. The Ls(4) centre was not observed directly in the SrF_2 crystals. An additional centre, Ls(5), was found in the heavily-hydrogenated SrF_2:Tb^{3+}:H^- crystal, Figure 7.13(c). It is very different in excitation from the other hydrogenic centres studied.

The broadband excitation spectra indicate the relative populations of the different hydrogenic centres in the crystals, Figures 7.10 and 7.11. As H^- or D^- ions are absorbed by the crystal the hydrogenic C_{4v} centre displaces the $C_{4v}F^-$ centre as the dominant Tb^{3+} centre. At higher H^-/D^- ion concentrations the Ls(1) centre becomes more dominant. At still higher hydrogen ion loadings the population of the Ls(2) centre increases relative to that of the Ls(1) centre. The Ls(5) centre

was only observed in the crystal with the highest hydrogen concentration. The Ls(3) and Ls(4) centres never dominate the broadband excitation and their relative populations peak at lower concentrations of the hydrogenic ion.

For the Cs centres of the Pr^{3+} ion, such changes in the relative populations of the hydrogenic centres with hydrogen ion concentration were found to be a good indicator of the number of hydrogenic ions in each type of centre. These results suggest that the Ls centres of Tb^{3+} can be placed in the following order of increasing hydrogenic-ion composition: $C_{4v}H^-/D^-$, Ls(1), Ls(2), and Ls(5).

7.4.3 Fluorescence Spectra

Fluorescence Spectra of the $^5D_4 \rightarrow {}^7F_5$ transitions were obtained by LSE of each centre: Figures 7.16 to 7.20. All the fluorescence spectra are very alike, which suggests a likeness in the crystal-fields of these centres due to a common structure. The hydrogenic C_{4v} centre and the Ls(4) centre, in particular, are strikingly similar.

Some of the fluorescence transitions of the Ls(1) and Ls(2) centres are split. This may be low-symmetry splitting similar to that found in the hydrogenic Cs centres of Pr^{3+}. The centres labeled $C_{4v}H^-$ and $C_{4v}D^-$ do not show such splittings, which is in keeping with their symmetry assignment. The Ls(3) centre displays fewer fluorescence transitions than the other centres; a result which is also true for its excitation spectrum.

7.5 Bleaching of the Hydrogenic Ls Centres

7.5.1 Ls(1), Ls(2) and Ls(3) Centre Fluorescence Bleaching

Bleaching behaviour was observed in four of the hydrogenic centres of Tb^{3+}; in the Ls(1), Ls(2), Ls(3) and Ls(4) centres. The bleaching of the Ls(5) centre was not investigated. The bleaching rates observed while pumping $^7F_6 \rightarrow {}^5D_4$ absorption transitions of the Tb^{3+} Ls centres are generally much less than those observed during $^3H_4 \rightarrow {}^3P_0$ pumping of the Cs centres of Pr^{3+}. However these absorption transitions of Tb^{3+} ion are much weaker than those of the Pr^{3+} ion. No bleaching was found for the hydrogenic C_{4v} centres, which is consistent the absence of bleaching in the C_{4v} centres of the Pr^{3+} ion.

The bleaching rates of the H^- and D^- species of the Ls(1) and Ls(2) centres are compared in Figures 7.21 and 7.22. Clearly the H^- centres bleach more quickly than their equivalent D^- centres. This was also the case for the Cs centres of Pr^{3+} [75] and was attributed to the higher energies of the H^- ion local mode.

Figure 7.23(a) is a polarised-bleaching sequence for the Ls(1) centre. Both laser polarisations produce bleaching and after the first cycle there is a small recovery in the polarised fluorescence intensity on changing the excitation polarisation. The Ls(2) centre, Figure 7.23(b), bleaches much more quickly than the Ls(1) centre. In the first cycle both polarisations are bleached simultaneously. In subsequent

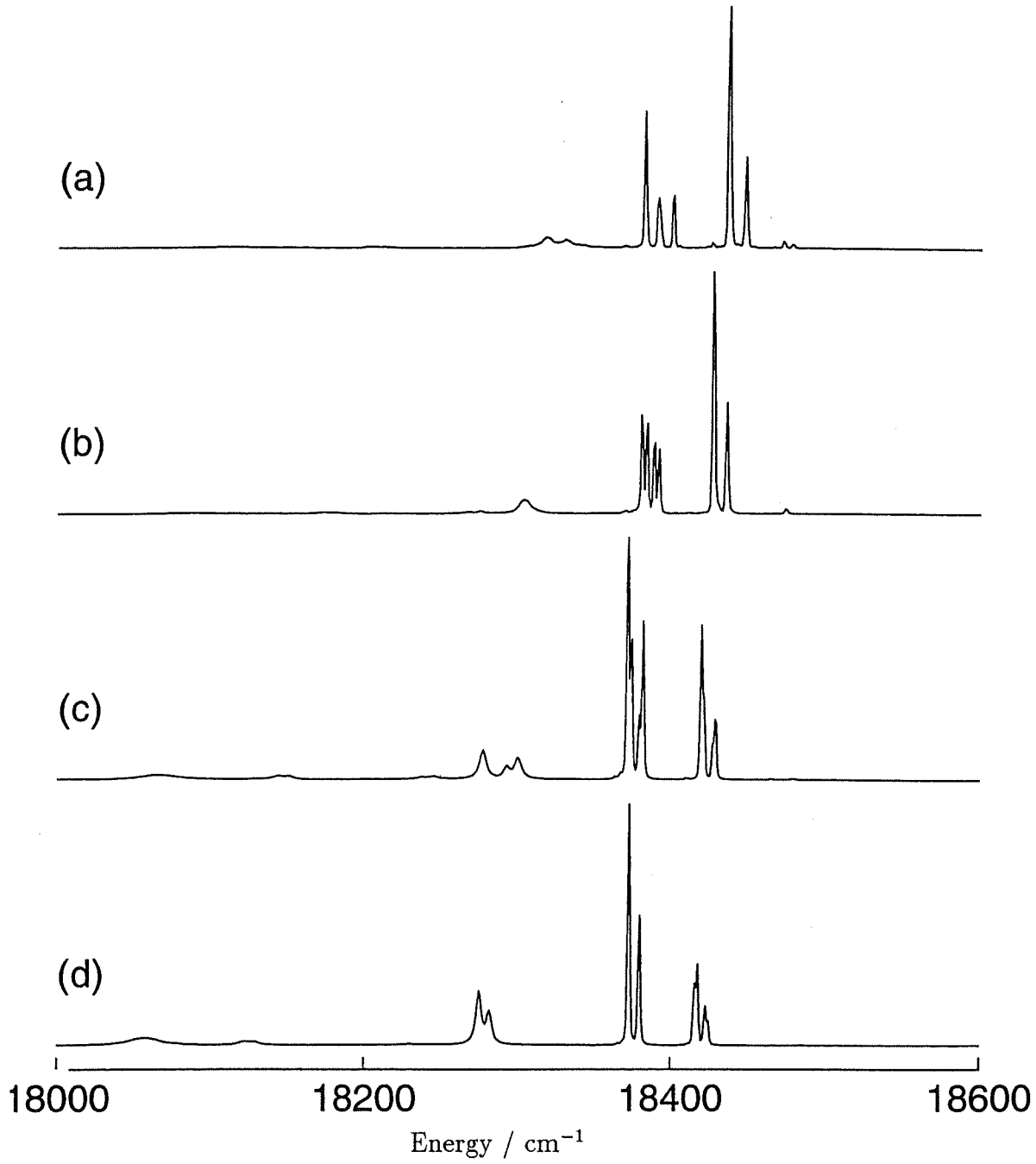

Figure 7.16: Fluorescence spectra of centres in the SrF_2:Tb^{3+}:H^- crystal showing the $^5D_4 \rightarrow {}^7F_5$ transitions of; **(a)** $C_{4v}H^-$, **(b)** Ls(1), **(c)** Ls(2) and **(d)** Ls(5).

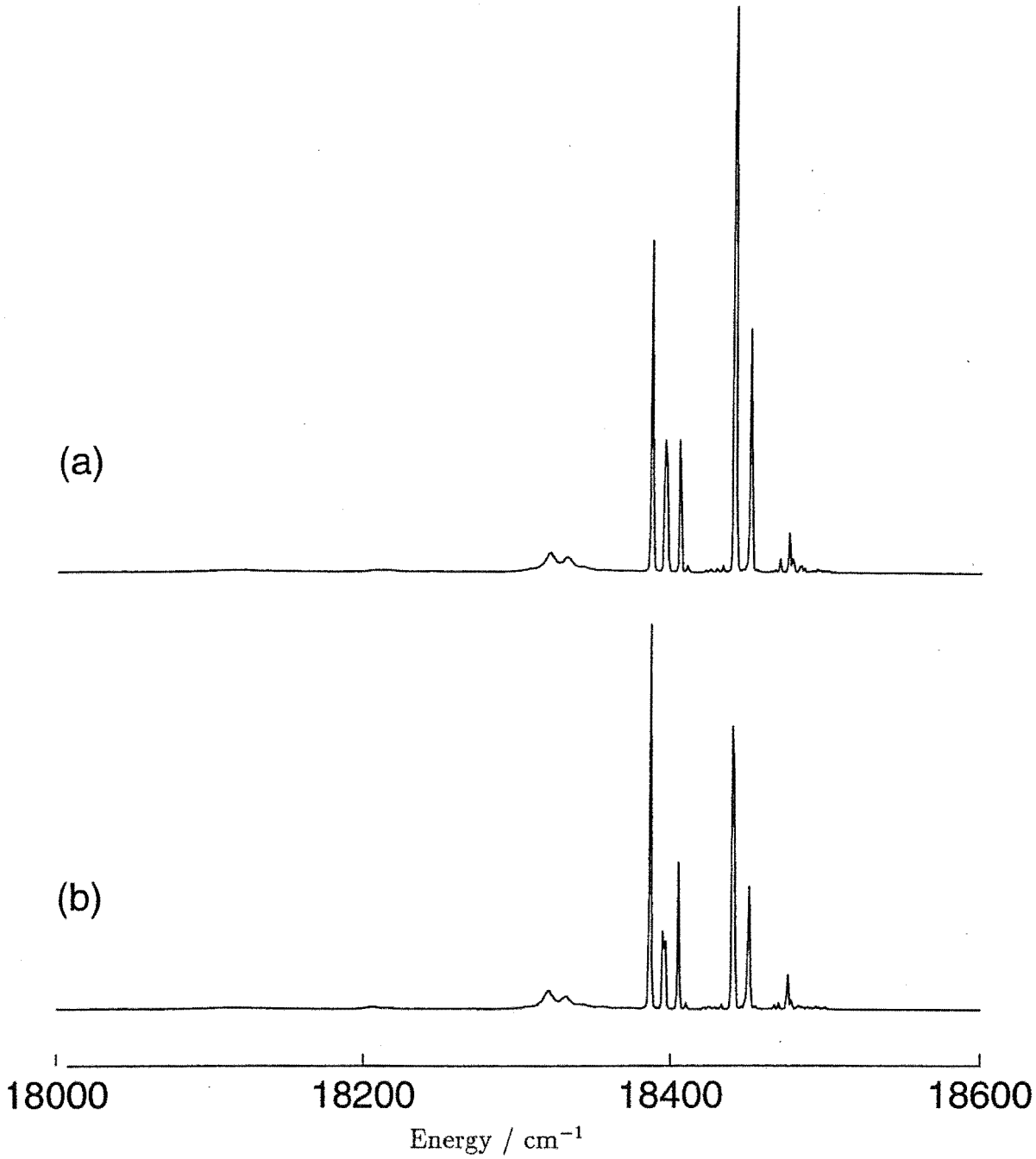

Figure 7.17: Polarised-fluorescence spectra of the $C_{4v}D^-$ centre in the SrF_2:Tb^{3+}:D^- crystal, while pumping the 20657cm^{-1} absorption transition; **(a)** x(yx)z and **(b)** x(yy)z.

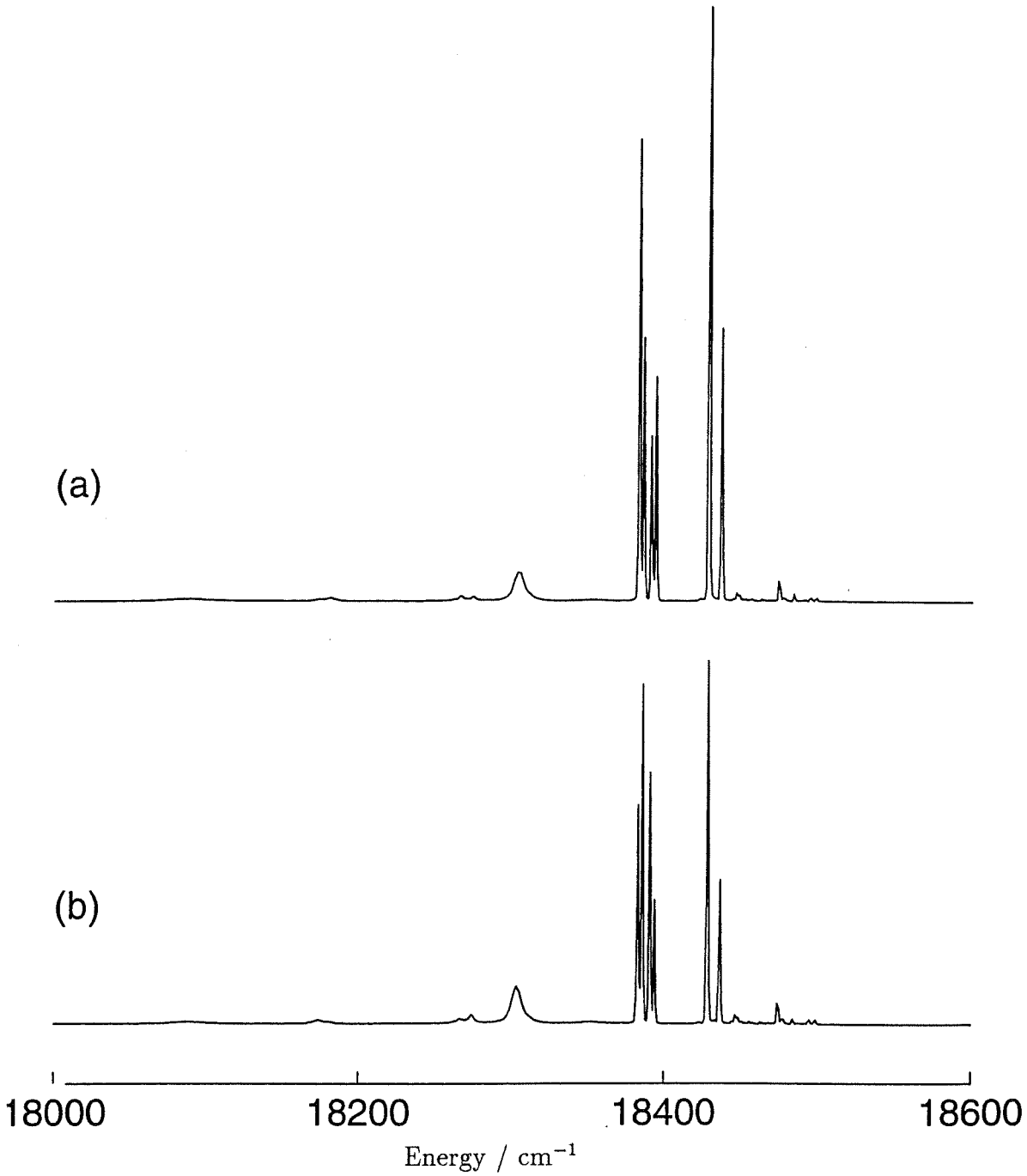

Figure 7.18: Polarised-fluorescence spectra of the Ls(1) centre in the SrF_2:Tb^{3+}:D^- crystal, while pumping the 20688cm^{-1} absorption transition; **(a)** x(yx)z and **(b)** x(yy)z.

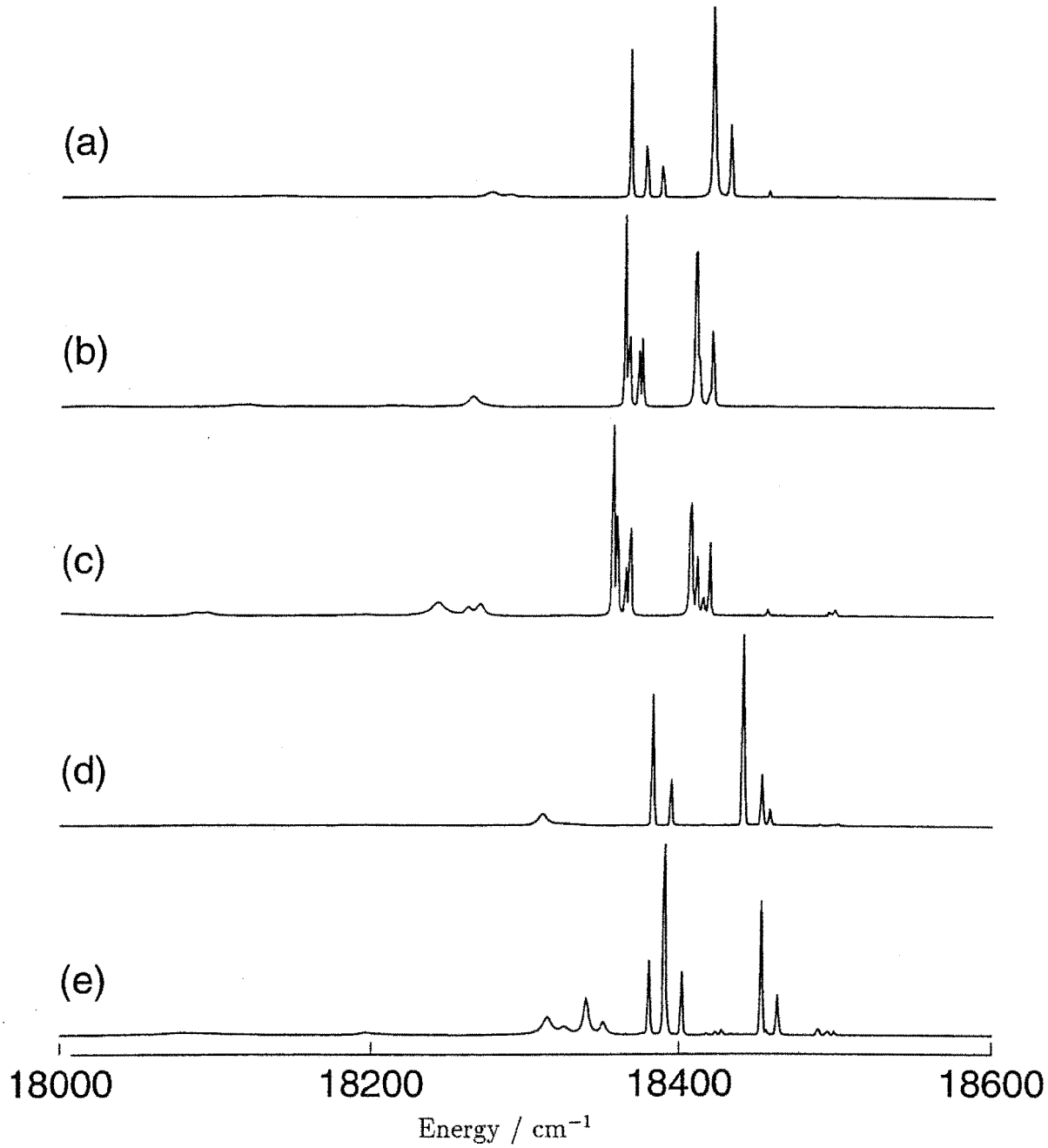

Figure 7.19: Fluorescence spectra of centres in the CaF_2:Tb^{3+}:H^- crystal showing the $^5D_4 \rightarrow {}^7F_5$ transitions of; **(a)** $C_{4v}H^-$, **(b)** Ls(1), **(c)** Ls(2), **(d)** Ls(3) and **(e)** Ls(4).

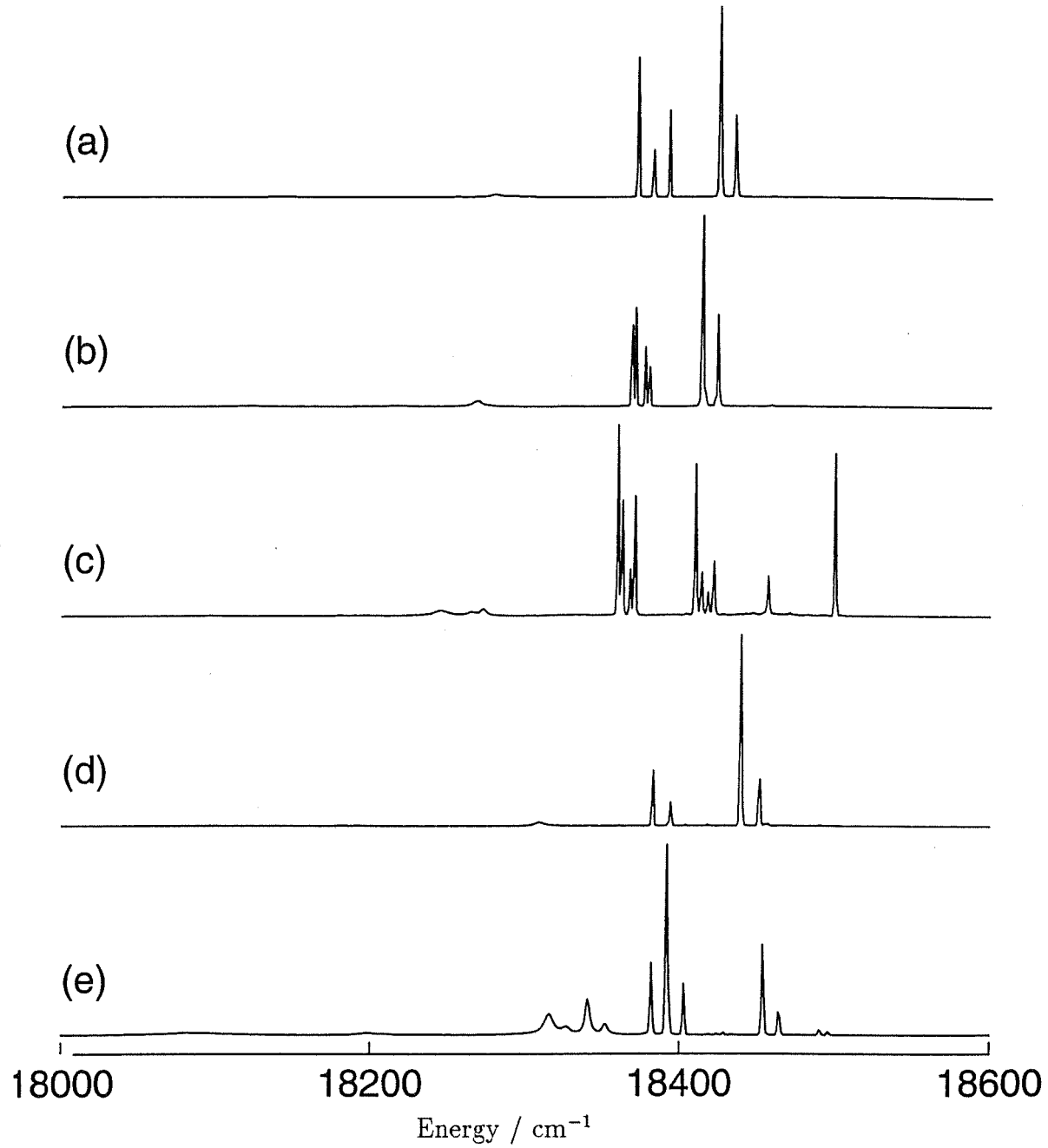

Figure 7.20: Fluorescence spectra of centres in the CaF_2:Tb^{3+}:D^- crystal showing the $^5D_4 \rightarrow {}^7F_5$ transitions of; **(a)** $C_{4v}D^-$, **(b)** Ls(1), **(c)** Ls(2), **(d)** Ls(3) and **(e)** Ls(4).

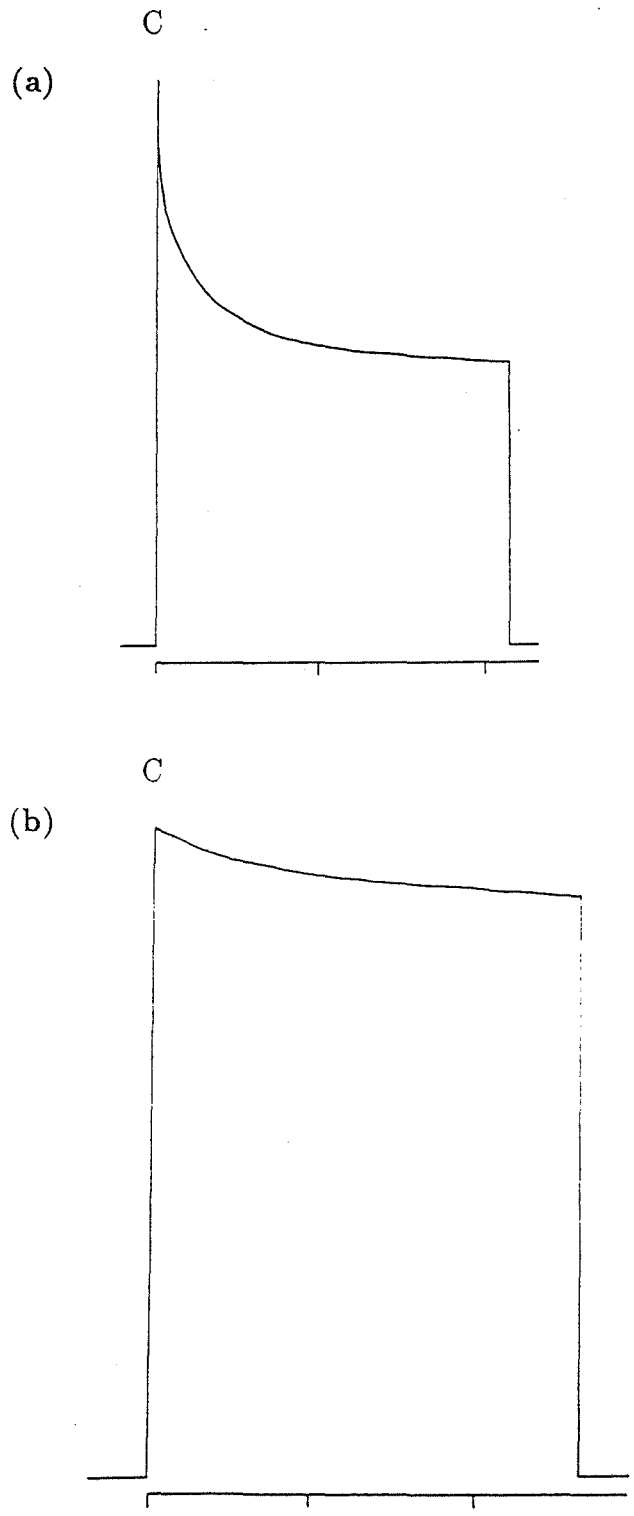

Figure 7.21: Bleaching curves for 15mW excitation of (a) the H^- and (b) the D^- species of Ls(1) centre in the CaF_2:Tb^{3+} crystal. The tick-marks are at 1 minute intervals.

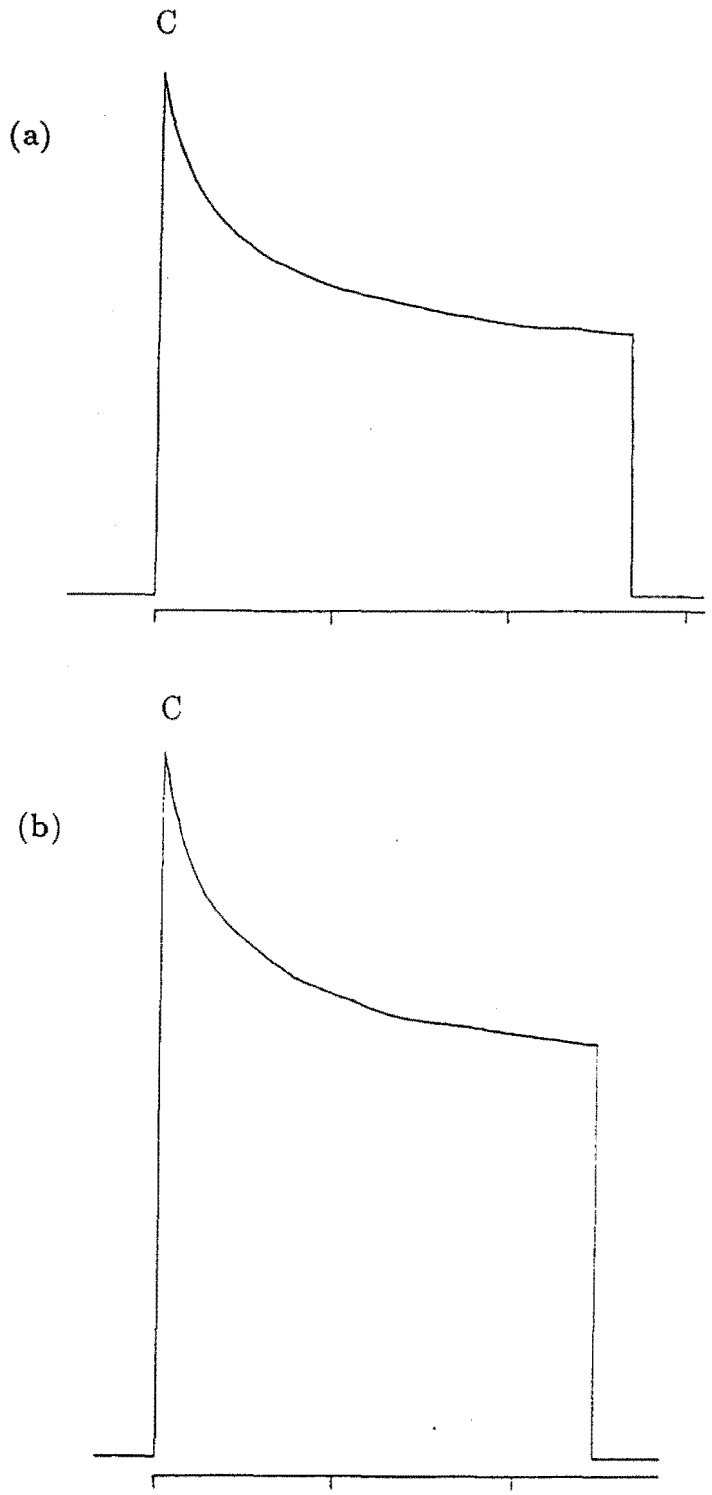

Figure 7.22: Bleaching curves for 15mW excitation of (a) the H^- and (b) the D^- species of Ls(2) centre in the CaF_2:Tb^{3+} crystal. The tick-marks are at 1 minute intervals.

cycles the bleaching becomes polarisation reversible. The Pr^{3+} centre bleaching work reported in Chapter 6 demonstrated that the polarisation of the excitation transition being pumped must be known in order to correctly interpret a bleaching sequence. Even so, it is apparent that the bleaching behaviour exhibited by the Ls(1) and Ls(2) centres in these sequences is very similar to that reported by Reeves [75] for the Cs(1) and Cs(2) centres.

The Ls(3) and Ls(4) centres exhibit a bleaching behaviour which is very different from any observed in the Cs centres of Pr^{3+}. The bleaching sequence of the Ls(3) centre, Figure 7.24(a), appears to be quite 'normal' with the two polarisations bleaching semi-independently and without any recovery in the polarised fluorescence on changing the excitation polarisation. Unlike the Ls(1) or Ls(2) centre bleaching, nearly all of the fluorescence from the Ls(3) centre can be bleached with long exposures to the excitation beam. This bleaching sequence is like that of the Cs(4) centre presented by Reeves.

7.5.2 Ls(4) Centre Fluorescence Enhancement

The 'bleaching' curves obtained for the Ls(4) centre, Figure 7.24(b), are very strange indeed. On pumping the absorption transitions of the Ls(4) centre the fluorescence intensity actually increases with exposure to the excitation beam. This is the first time that such an enhancement in fluorescence has been observed upon selective excitation of a hydrogenic centre. All the RE^{3+} 'bleachable' centres studied previously have exhibited fluorescence bleaching [27] [39] [53] [77]. As was the case for the photoproducts of the Cs centres of the Pr^{3+} ion, the Ls(4) centre could always be erased by heating the crystal to temperatures above 100K.

In a deuterated CaF_2 crystal, which has not been irradiated by the excitation beam, no fluorescence from the Ls(4) centre is observed when the shutter is first opened. This suggests that the Ls(4) centre is not present in the virgin deuterated crystal which has been cooled from room temperature. However, the hydrogenated CaF_2 crystal does appear to contain some Ls(4) centres prior to laser irradiation.

It was observed by eye that the line of green fluorescence caused by selectively exciting the Ls(4) centre increases in intensity while the laser is on. If the excitation beam is moved, so that a new region of the crystal is exposed, almost all of the fluorescence is extinguished. The intensity of the transmitted beam is not noticeably affected if the incident beam is quickly translated backwards and forwards through an exposed region of the crystal. This last result eliminates the possibility that the fluorescence enhancement is due to saturated absorption of the excitation beam and subsequent bleaching.

While trying to record this behaviour, by running broadband excitation scans, it was found that the laser does not have to be resonant with any of the Ls(4) excitation transitions to achieve an enhancement in the population of the Ls(4) centre. Indeed, the Ls(4) centre enhancement proceeded at a slower rate when pumping the absorption transitions of the Ls(4) centre. Enhancement could even be achieved by

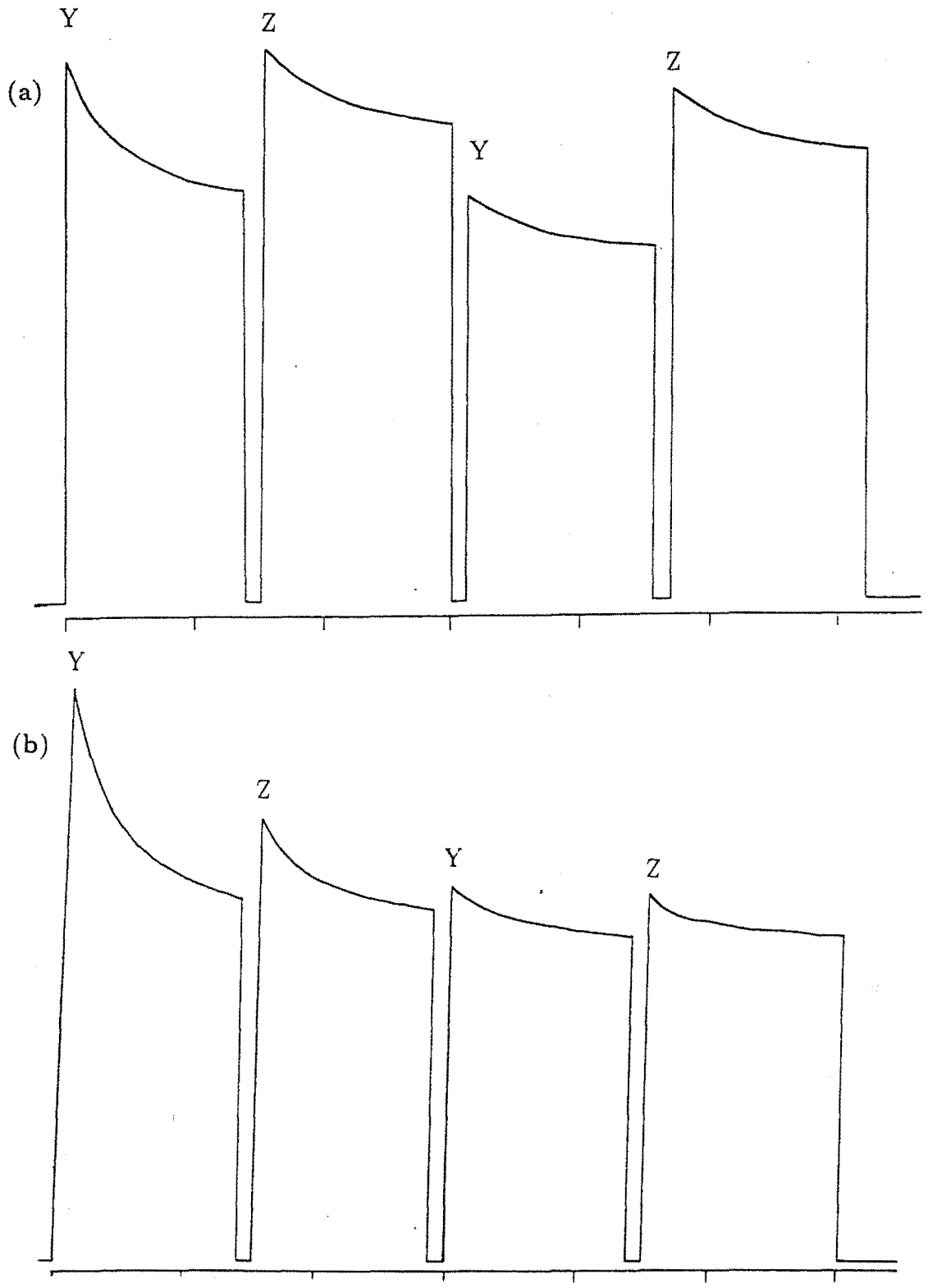

Figure 7.23: Polarisation-Bleaching Sequences for **(a)** the Ls(1) Centre and **(b)** the Ls(2) centre in the CaF_2:Tb^{3+}:D^- crystal. The excitation power is 15mW and the tick-marks are at 1 minute intervals.

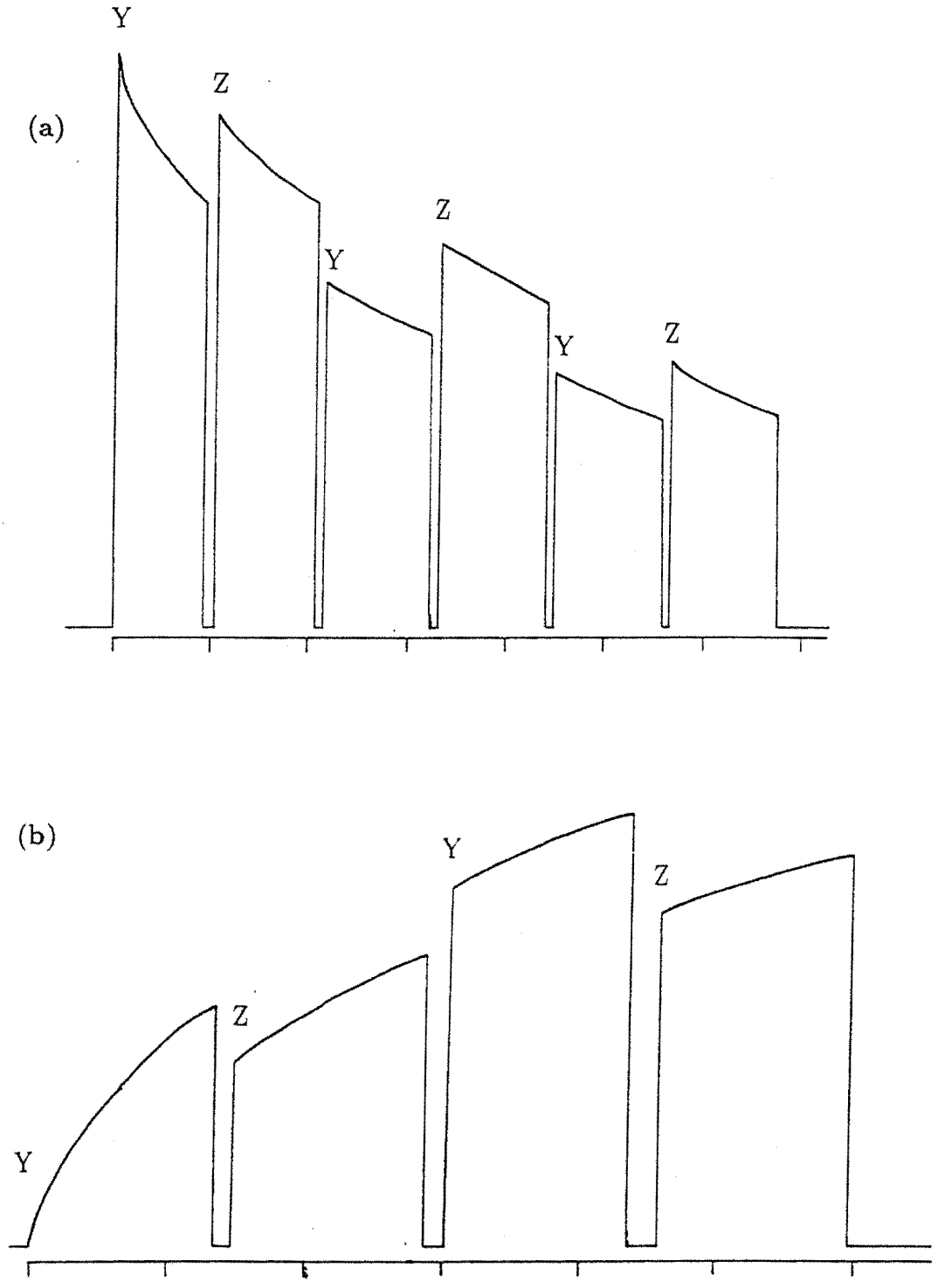

Figure 7.24: Polarisation-bleaching sequences for (a) the Ls(3) Centre and (b) the Ls(4) Centre in the CaF_2:Tb^{3+}:D^- Crystal. The excitation power is 15mW and the tick-marks are at 1 minute intervals.

tuning the laser to energies which are much lower than those of the Ls(4) centre transitions. For example: 5 minutes of exposure to a 15mW beam at 20567cm^{-1} increased the broadband fluorescence of Ls(4) from 5000 counts per second (just above the background-count) to 119000 counts per second. No particular absorption features can be found at 20567cm^{-1} in the broadband excitation spectra.

Broadband excitation spectra were produced by scanning the laser from lower to higher energies in an attempt to observe any changes in the crystal's spectrum which might accompany this fluorescence enhancement, Figure 7.25. It was found that even exposure to a weak 5mW beam, for the few minutes required to produce a spectrum, was enough to generate a significant number of Ls(4) centres, Figure 7.25(a). Another excitation scan was made, immediately following the first, and this revealed further enhancement of the Ls(4) centre and a notable bleaching of the Ls(3) centre fluorescence, Figure 7.25(b). The Ls(1) and Ls(2) centres are unchanged between the first and second scan. This result suggests that the Ls(3) and Ls(4) centres may be related by a common 'bleaching' mechanism.

It was found that the Ls(3) centre could also be bleached when the laser is detuned from any electronic excitation transitions. As in the previous example for Ls(4), the Ls(3) centre could be bleached when the laser is tuned to the unremarkable energy of 20567cm^{-1}. Since population of the Ls(4) centre is simultaneous with depopulation of the Ls(3) centre, the Ls(4) centre may be a photoproduct of the Ls(3) centre.

It has already been demonstrated, in the case of the Pr^{3+} ion bleachable centres, that bleaching is a phonon-scattering process in which the bleachable centre crosses the potential barrier between two possible configurational states. If the Ls(4) centre is indeed a photoproduct of the Ls(3) centre, then the barrier potential associated with thermal restoration of the Ls(3) centre will be the same as that associated with thermal depletion of the Ls(4) centre. The thermal cycling method, described in Chapter 6, was used to obtain the thermal-restoration profile of the Ls(3) centre and the thermal-depletion profile of the Ls(4) centre. Before each cycle to measure thermal restoration, the Ls(3) centre was re-bleached. During this bleaching and for the fluorescence measurements the laser was tuned to the 20712cm^{-1} excitation transition. Similarly, before each cycle to measure thermal depletion of the Ls(4) centre, the Ls(4) population was prepared by tuning the laser to the 20657cm^{-1} excitation transition and irradiating the crystal.

The thermal-restoration profile of the Ls(3) centre is identical to the thermal-depletion profile of the Ls(4) centre, Figure 7.26. This is very strong evidence that the Ls(4) centre is indeed a photoproduct of the Ls(3) centre. The 1-$\frac{1}{e}$ reverting temperature is (91$\pm$3)K, which corresponds to a barrier height of 2280$\pm$80cm^{-1} for resonant bleaching. This barrier height is of the same order as those found for the Cs centres of Pr^{3+}.

Energy must be supplied to a centre before barrier crossing, and so bleaching, can occur. It is clear that the fluorescence bleaching/enhancement process of the Ls(3) and Ls(4) centres requires energy which is supplied by the laser. However,

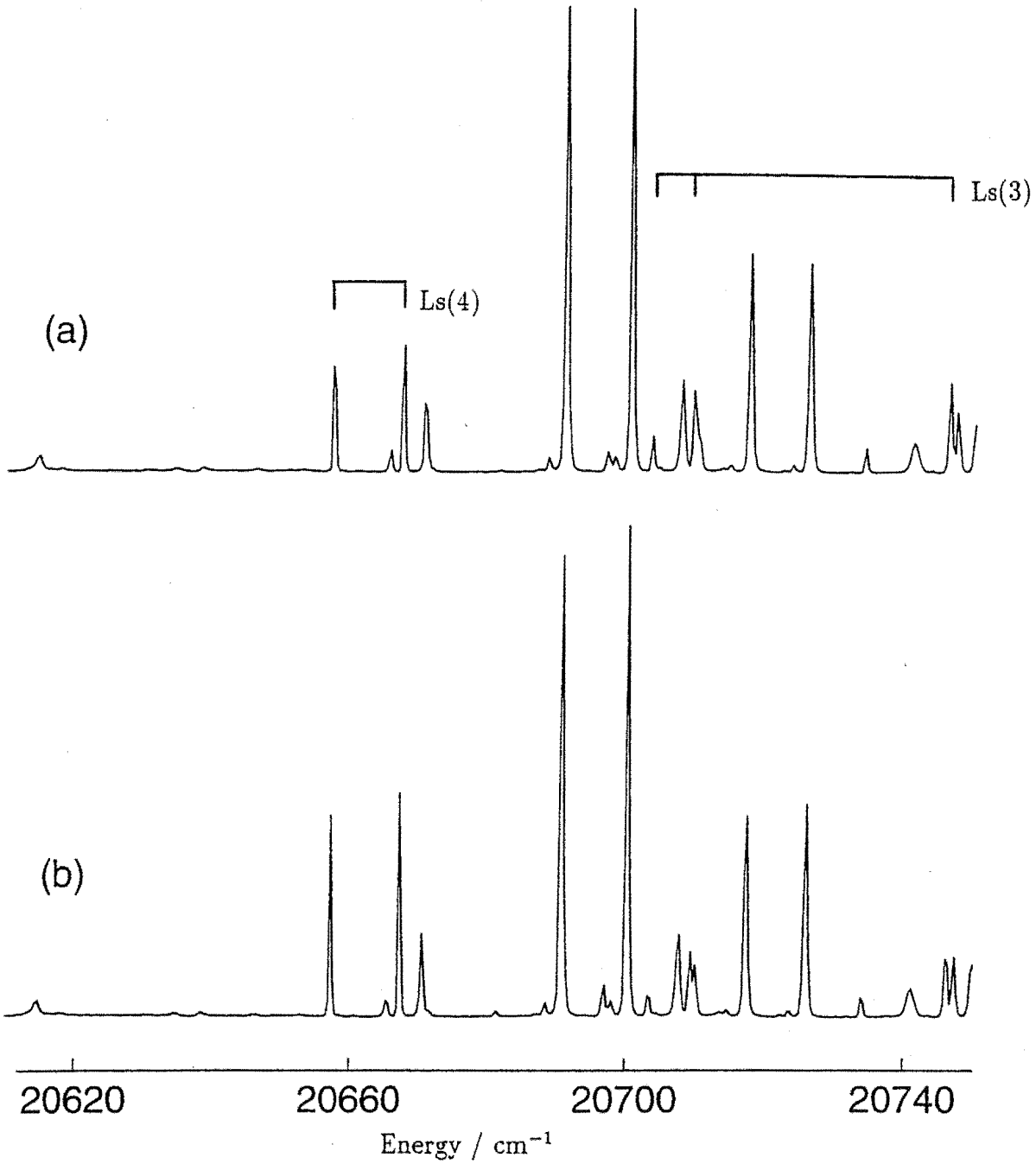

Figure 7.25: Broadband excitation spectra over the region of the Ls(3) and Ls(4) absorption transitions in the CaF_2:$Tb^{3+}D^-$ crystal; (a) the first scan and (b) the second scan. Each scan took 10 minutes and the laser power was 5mW.

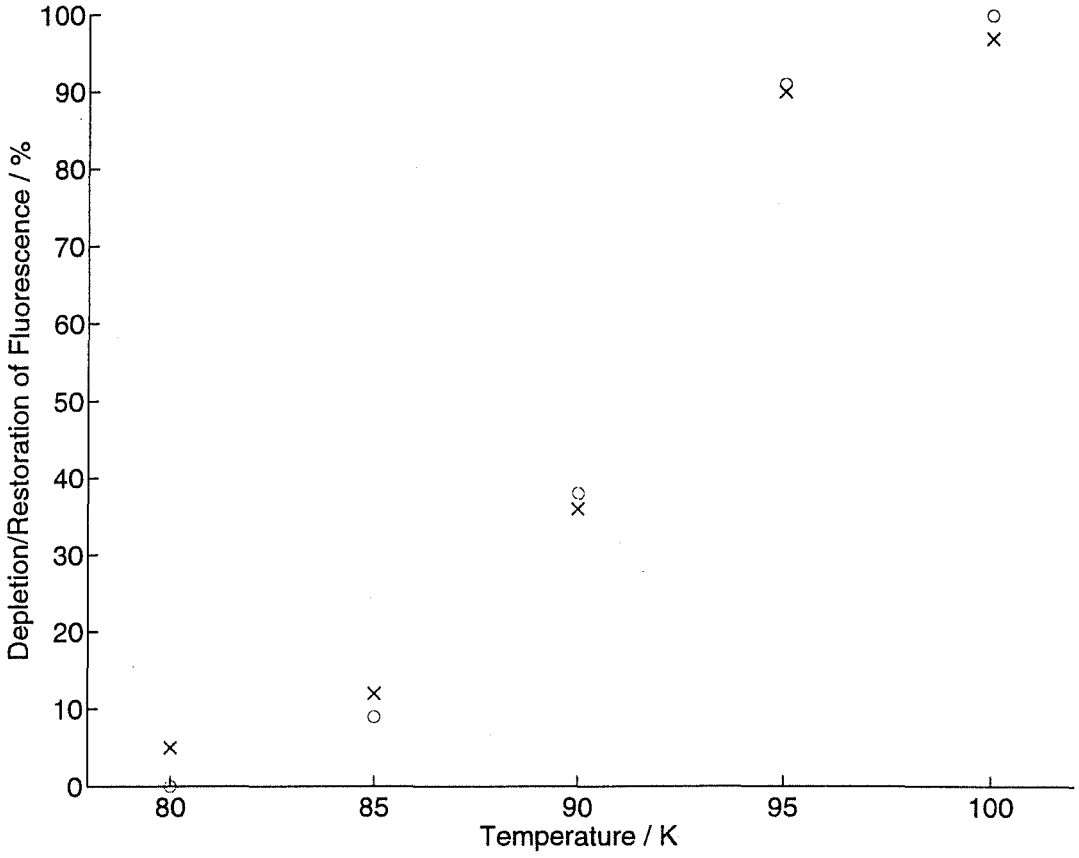

Figure 7.26: The thermal depletion of the Ls(4) centre (circles) and the thermal recovery of the Ls(3) centre (crosses) due to thermal cycling of the CaF_2:Tb^{3+}:D^- crystal.

how the laser beam can couple with these Tb^{3+} centres, when it is not tuned to pump an electronic transition, has not been established.

One possibility is that the fluorescence enhancement of the Ls(4) centre is due to the localised heating of the crystal caused by the laser beam itself. To test for this, a piece of virgin CaF_2:Tb^{3+}:D^- crystal was heated to a number of different set temperatures between 10K and 90K. During each thermal cycle the set temperature was held for 5 minutes before the crystal was cooled and then tested for the presence of Ls(4) centres. No enhancement in the Ls(4) population was achieved for any of the set temperatures. This result is not very surprising given the thermal-reverting behaviour which has already been observed and the two results are consistant.

It is interesting to note that the Ls(3) centre has the most extended $^5D_4$ multiplet of any of the Tb^{3+} centres. It is also the only hydrogenic centre, of those which have been studied so far, to have a photoproduct with strong excitation transitions higher in energy than the lowest level of its own excited multiplet. The Ls(3) centre may perhaps be excited via phonons which couple to its electronic states. Such a phonon band is observed in the selective excitation spectrum of the Ls(3) centre, Figure 7.27, having of the order of 1% the intensity of the main excitation transitions. If the Ls(3) centre has a sufficiently high bleaching efficiency then this may account for the bleaching behaviour which has been observed. That the enhancement of the Ls(4) centre occurs more slowely when the laser is resonant with the Ls(4) centre excitation transitions suggests that the Ls(4) centre itself is also bleachable. This bleaching is apparently much less efficient that the Ls(3) centre bleaching.

Such a difference between bleaching efficiencies of these two centres might arise if the hydrogenic ions of the Ls(4) centre are more remote from the Tb^{3+} ion than those of the Ls(3) centre. The bleaching efficiency of a centre is highly dependent apon the proximity of the hydrogenic ions to the optically-active rare-earth ion. However, this will not be a particularly important determinant of the barrier potentials which separate the configurational states and are measured in the thermal-cycling experiment.

If this is a correct interpretation of the Ls(3) centre bleaching mechanism then there will be a minimum excitation energy for which bleaching can be achieved, corresponding to the lowest level of the Ls(3) centre $^5D_4$ multiplet. This could easily be tested, but due to the failure of the argon laser this experiment could not be conducted in this study. It would also be interesting to investigate whether the Ls(4) centre bleaches, as the bleaching rates observed here suggest. If it does, then for each laser excitation energy and power there should be an equilibrium distribution of centres between the Ls(3) and the Ls(4) configurations, which is determined by their relative bleaching rates. Another important test of this model arises from the expectation that a centre in which the hydrogenic ions are more remote from the rare-earth ion should exhibit longer radiative lifetimes. This has already been demonstrated by comparing the $^1D_2$ multiplet fluorescence lifetimes of the different Pr^{3+} ion Cs centres in Chapter 5.

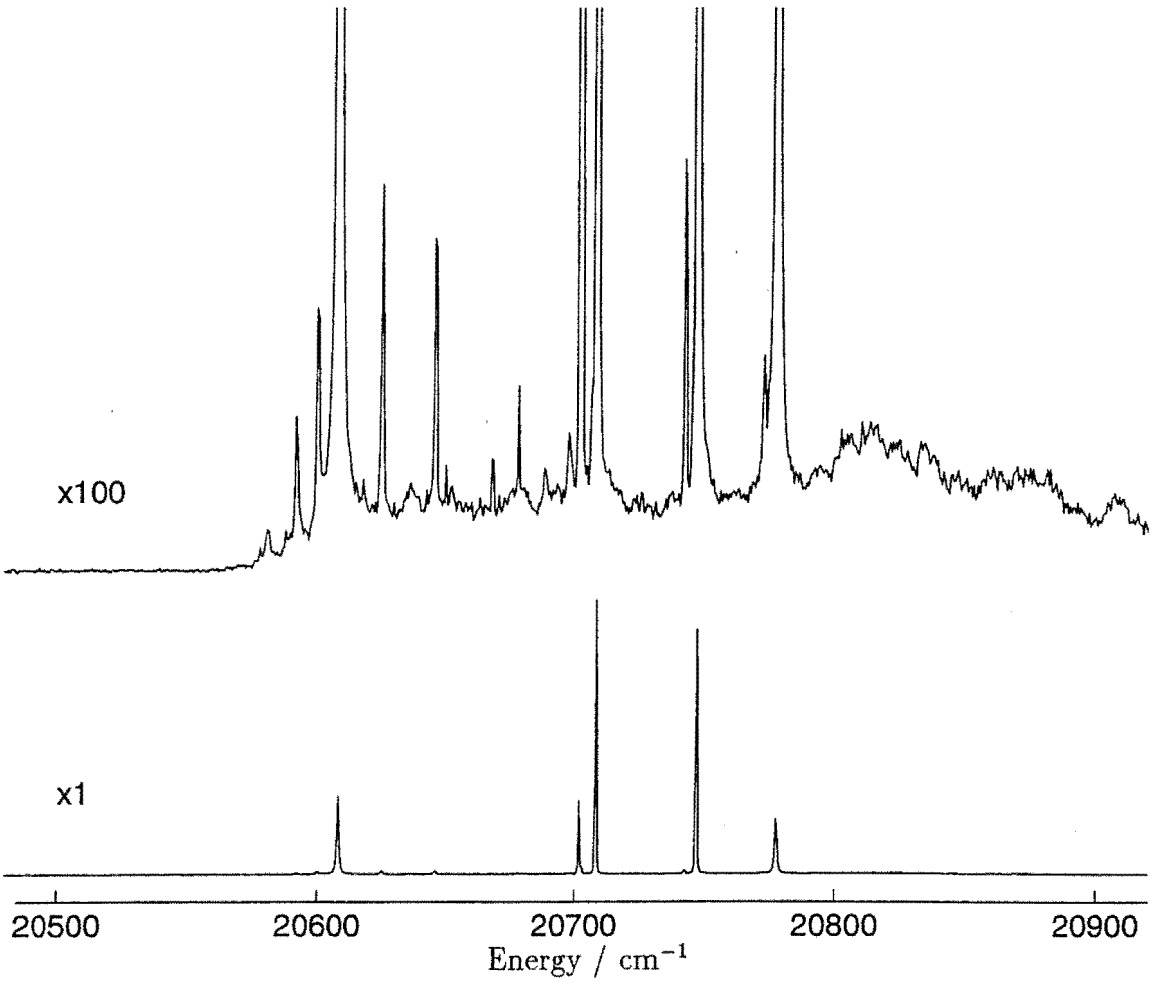

Figure 7.27: A selective excitation spectrum of the Ls(3) centre in the CaF_2:Tb^{3+}:D^- crystal showing the phonon bands which couple to the $^7F_6 \rightarrow {}^5D_4$ electronic transitions.

Table 7.7: The $^5D_4$ multiplet fluorescence lifetimes of the Tb^{3+} centres studied, in units of ms.

Centre	SrF_2		CaF_2	
$C_{3v}F^-$	-		5.9±0.3	
$C_{4v}F^-$	14.2±0.7		11.6±0.6	
	H^-	D^-	H^-	D^-
$C_{4v}H^-/D^-$	3.90±0.20	4.30±0.22	3.65±0.18	3.96±0.20
$Ls(1)$	3.77±0.19	-	3.71±0.19	4.19±0.21
$Ls(2)$	3.62±0.19	-	3.40±0.17	3.56±0.18
$Ls(3)$	-	-	3.37±0.17	3.62±0.18
$Ls(4)$	-	-	3.92±0.20	-
$Ls(5)$	3.91±0.20	-	-	-

In the CaF_2:Tb^{3+}:H^- crystal both the Ls(3) centre and the Ls(4) centre are present when the crystal is cooled to 10K from room temperature. This suggests that the double-well potential associated with these two hydrogen centre configurations is nearly symmetric. This is still consistent with the proposed model in which their unusual bleaching behaviour is ascribed to differences in their bleaching efficiencies, as distinct from differences in the respective barrier potentials which must be surmounted.

7.6 Fluorescence Lifetimes

7.6.1 The Fluoride Tb^{3+} Centres

The pulsed dye laser and the digital oscilloscope were used to measure the $^5D_4$ multiplet fluorescence lifetimes of many of the Tb^{3+} centres studied. The experimental lifetimes are given in Table 7.7. Not all the hydrogenic centres were amenable to selective excitation by the broad laser line of this pulsed system, which accounts for the many gaps in the table.

As was the case for the Pr^{3+} centres, the CaF_2 centre lifetimes were shorter than the SrF_2 centre lifetimes, reflecting the smaller inter-ionic spacings of the CaF_2 crystal lattice. The 14000cm^{-1} energy gap between the emitting $^5D_4$ multiplet and the next lowest $^7F_0$ multiplet is very large compared to the phonon cut-off energies of these materials, so it is likely that this observed relaxation is entirely radiative in the $C_{4v}F^-$ centres. If the assumption is made that most of this radiative relaxation is by electric-dipole transitions then it is clear that the transition probabilities,

and therefore the relaxation rates, will depend upon the strength of the crystal field. The crystal field is responsible for the configurational mixing which facilitates electric-dipole transitions within the $4f^N$-configuration. Such mixing is due to the coupling of opposite-parity states by the odd terms in the expansion of the crystal-field Hamiltonian. In Chapter 2 it was established that the electric-dipole transition probability between two states is the sum of expansion terms which vary as the square of the odd-parity crystal-field parameters.

The crystal-field model, used here to calculate the energy levels of the $4f^N$-configuration, includes only the even-parity terms as the odd-parity terms do not contribute to the first order determination of these energies. As a consequence only the even-parity terms have been fitted and are known. By making the reasonable assumption that the crystal-field parameters of the odd and even terms are related by simple scale factors, it is possible to make the approximation that the transition probabilities are proportional to the square of the dominant even-parity crystal-field parameter. In this instance the dominant component of the crystal field is the one which is responsible for the greatest perturbation of the rare-earth ion states. This approach was used very successfully by Mujaji [62] and Reeves [77] to account for fluorescence lifetimes in the Ho^{3+} and Pr^{3+} ion $C_{4v}F^-$ centres.

For the Tb^{3+} ion $C_{4v}F^-$ centres the (SrF_2/CaF_2) ratio of the $^5D_4$ multiplet lifetimes is found to be 1.22±0.12. The ratios of the squares of the fitted crystal-field parameters, $(CaF_2/SrF_2)^2$, are: (1.46±0.15) for B_C^4, (1.73±0.26) for B_C^6, (2.80±0.40) for B_A^2, (1.25±0.23) for B_A^4 and (1.78±0.52) for B_A^6. Thus the fourth-order parameters best account for the experimental fluorescence lifetimes of the $^5D_4$ multiplet of Tb^{3+}, as was the case for the E multiplet of the Ho^{3+} $C_{4v}F^-$ centres.

The $C_{4v}F^-$ centre and $C_{3v}F^-$ centre fluorescence lifetimes were found to be quite different for CaF_2, reflecting the very different crystal fields experienced by the Tb^{3+} ions in each centre.

7.6.2 The Hydrogenic Tb^{3+} Centres

The lifetimes of the Tb^{3+} hydrogenic C_{4v} centres are shorter than those of the fluorine C_{4v} centres. Reeves [76] found this to be the case for the Pr^{3+} C_{4v} centres, where the reduced fluorescence lifetimes were ascribed to the additional non-radiative decay channels accessible through coupling to the vibrational modes of the hydrogenic interstitial ion.

Reeves [76] also found that the $C_{4v}H^-$ centres of the Pr^{3+} ion have fluorescence lifetimes which are much shorter than those of the $C_{4v}D^-$ centres; shorter by a factor of 150 in SrF_2 and by 250 in CaF_2. This is a consequence of the very different C_{4v} site local-mode energies of the H^- and D^- ions, which necessitate higher order multi-phonon relaxation processes in the deuterated centres. However, there is very little difference between the lifetimes of the H^- and D^- species of Tb^{3+} centres; the former being shorter by a factor of 1.1 in each host. This suggests that non-radiative relaxation involving vibronic excitation of the hydrogenic interstitial is not

significant in these Tb^{3+} centres; not at all surprising given the 14000cm^{-1} inter-multiplet energy gap already noted.

That the hydrogenic C_{4v} centres of the Tb^{3+} ion do in fact exhibit shorter fluorescence lifetimes than the fluorine C_{4v} centres becomes an interesting question. This effect may just be a consequence of the change in the crystal field brought about by the anion substitution. Or this effect is may be due to the additional phonon-assisted radiative-relaxation channels which arise from the coupling of the electronic states of the Tb^{3+} ion to the vibrational states of the hydrogenic ion via the electron-phonon interaction.

If vibronic transitions are providing a significant relaxation pathway, then they should be observed in fluorescence as side-bands to the zero-phonon electronic transitions. Judd [48] has shown that there is a pseudo-quadrupole selection rule affecting the electronic components of such vibronic transitions. As a consequence $\Delta J = 2$ vibronic transitions will be the most prominent. Thus the fluorescence transitions to the ground multiplet of the Tb^{3+} ion should exhibit the strongest vibronic sidebands, as was the case for the $^1D_2$ multiplet emission of the Pr^{3+} ion.

No significant vibronic side bands were observed in the emission spectra of any of the Tb^{3+} hydrogenic centres and certainly nothing with the relative intensity required to account for a halving of the fluorescence lifetimes. It is important to note that the strength of the $4f^N$-electron-phonon coupling changes along the lanthanide series, being weakest for Gd^{3+} in the middle of the series [43]. It is concluded that the lifetimes of the hydrogenic C_{4v} centres are essentially radiative.

The Ls centre fluorescence lifetimes are not very different from those of the hydrogenic C_{4v} centres. Again this goes against the trends observed in the praseodymium system, where there were marked variations in the lifetimes of the different Cs centres, Chapter 5. That such a small distribution is observed in the lifetimes of the Tb^{3+} hydrogenic centres indicates that radiative relaxation is the dominant relaxation pathway for all of the Tb^{3+} centres. Thus it is not possible to make a meaningful analysis of these Ls centre lifetimes in terms of the effect of successive substitutions by hydrogenic ions.

One interesting result is that in the CaF_2:Tb^{3+}:H^- crystal it was found that the fluorescence lifetime of the Ls(4) centre is significantly greater than that of the Ls(3) centre. This is consistant with the model presented to explain their unusual bleaching behaviour.

Chapter 8

Energy-Transfer and Upconversion Processes of Pr^{3+} and Tm^{3+} Ions in $CsCdBr_3$ Crystals

8.1 Introduction

Three crystals were used in this study; a pure $CsCdBr_3$:Pr^{3+}(0.1mole%) crystal grown by Shawn Foo for his Honours III project, a pure $CsCdBr_3$:Tm^{3+}(1.0mole%) crystal provided by Nigel Cockroft, and a mixed $CsCdBr_3$:Tm^{3+}(0.5mole%):Pr^{3+}(0.1mole%) crystal grown for these experiments. The two crystals containing praseodymium ions were prepared from a melt. The pure thulium crystal was grown from a solution. These techniques for growing $CsCdBr_3$:RE^{3+} crystals are described in Chapter 3. All of the experiments described in this chapter were performed on samples at 10K.

Given that pair centre formation is preferred in the $CsCdBr_3$ lattice, it is important to establish the existance of the heterogeneous Tm^{3+}-Pr^{3+} pairs in the mixed-dopant crystal. If pair formation is random, without preference for homogeneous pairs, then most of the Pr^{3+} ions in the mixed crystal will be paired with Tm^{3+} ions. In a heterogeneous pair the prescence of the Pr^{3+} ion may assist the upconversion processes which excite the Tm^{3+} ion, and vice-versa. New upconversion mechanisms may also occur if there is sufficient coupling between the Tm^{3+} and Pr^{3+} ions. However upconversion in heterogeneous pairs after single-pulse selective excitation requires energy transfer from neighbouring excited pairs. Inter-pair energy transfer will be less efficient than intra-pair transfer. The former has a spatial dependence which will affect the efficiency of the transfer and so the efficiency of any upconversion processes.

The multiplication table of the C_{3v} symmetry group is given in Chapter 4 and can be used to identify particular electronic transitions in the polarised spectra of the main pair centre. A π-polarised transition is one in which the electric vector is parallel to the three-fold symmetry axis of the RE^{3+} ion site. The polarisation

ratios for the main pair centre can be determined trivially as the $CsCdBr_3$ crystal is uniaxial and so all the RE^{3+} ion sites will have a common symmetry axis.

8.2 A Review of the Upconversion Mechanisms of the Pr^{3+} and the Tm^{3+} Ions and of Upconversion Spectroscopy in $CsCdBr_3$ Crystals

Energy transfer between the ions of a pair centre was first observed by Buisson and Vial [17] in LaF_3:Pr^{3+}. In this host trivalent dopant ions are randomly distributed. A narrow-band pulsed laser was used to excite selectively the Pr^{3+} ions in pair centres to the $^1D_2$ multiplet. Upconversion fluorescence from the $^3P_0$ multiplet was then observed from the acceptor ions of the pairs participating in the upconversion. The mechanism for this upconversion was determined by Vial et al [89]. The donor Pr^{3+} ion relaxes to the $^1G_4$ multiplet while the acceptor ion is excited to $^3P_2$ multiplet. This is a phonon-assisted transfer which requires the emission of phonons with a total energy of at least $430cm^{-1}$. The acceptor ion can quickly relax non-radiatively to the metastable $^3P_0$ level.

Pr^{3+} centres in $CsCdBr_3$:Pr^{3+} were studied by Foo [34] using laser selective excitation. He identified eight Pr^{3+} centres of which two were identified as pair centres by the observation of upconversion fluorescence. The principal A-centre was one of these, with some blue fluorescence being observed during selective excitation of the Pr^{3+} ions to the $^1D_2$ multiplet. This upconversion fluorescence is due to transitions originating from the $^3P_1$ and $^3P_0$ multiplets. Foo's spectroscopic data for the A-centre suggests that it is indeed the Pr^{3+}-Cd^{2+}vacancy-Pr^{3+} dimer centre.

A study of the high-resolution laser and Zeeman spectroscopy of $CsCdBr_3$:Pr^{3+} was conducted by Ramaz et al [71] [73]. They identified 42 energy levels of the Pr^{3+} A-centre and determined their C_{3v} symmetry irrep labels. These energy levels are reproduced in Table 8.2 and were used to develop a simple crystal-field model of the site occupied by the Pr^{3+} ions in the A-centre. The crystal-field Hamiltonian was composed of a cubic O_h part and a smaller trigonal distortion. Their Zeeman results confirm that the Pr^{3+} ions reside in a slightly distorted octahedral field. Chaminade et al [20] used spectral hole burning to observe the Davydov splitting in the $^3H_4(1) \rightarrow {}^1D_2(1)$ transition of Pr^{3+} ions in the A-centre.

Upconversion fluorescence in $YLiF_4$:Tm^{3+} was reported by Nguyen et al [65]. They applied this upconversion mechanism to develop a blue-green upconversion laser which operates at 75K. This process requires two pulsed lasers to excite sequentially Tm^{3+} ions to the $^1D_2$ multiplet. The first laser, at 780.8nm, is resonant with a $^3H_6 \rightarrow {}^3H_4$ transition. The second laser, at 648.8nm, further excites the Tm^{3+} ion to the $^1D_2$ multiplet. Blue emission, $^1D_2 \rightarrow {}^3F_4$, and green emission, $^1D_2 \rightarrow {}^3H_5$, is obtained at 450nm and 510nm respectively. When a $YLiF_4$:Tm^{3+} crystal was used as the gain medium inside a resonator, coherent blue light was emitted

with a maximum overall efficiency of 1.3%.

In a subsequent paper Dulick et al [30] present an almost complete set of experimental energy levels for Tm^{3+} ions in $YLiF_4$:Tm^{3+}. S_4 group irrep labels were assigned to these levels and most of them were used in a least-square analysis to determine the crystal-field parameters of the S_4 symmetry Tm^{3+} site. A cross relaxation was found which quenches the $^1D_2$ multiplet. However no mechanisms were suggested to explain this relaxation.

A laser, using a very similar upconversion mechanism in a Tm^{3+} doped fluorozirconate fibre, has been demonstrated by Allain et al [2]. This was the first reported upconversion fibre laser. The fluoride glasses have been prefered to vitreous oxide glasses in upconversion studies because they have lower vibrational energies [68].

The spectroscopy of double-doped $CsCdBr_3$:Ce^{3+}:Tm^{3+} was investigated by McPherson and McPherson [57]. They established the existence of heterogeneous Ce^{3+}-Tm^{3+} pair centres by observing efficient energy transfer from Ce^{3+} ions to Tm^{3+} ions. Ce^{3+} ions were excited by laser radiation which was resonant with the $4f \rightarrow 5d$ electronic absorption at 27800cm^{-1}. The resulting emission was due to the $^3F_3 \rightarrow {}^3H_6$ transitions of the Tm^{3+} ion at 14200cm^{-1} and the $^3H_4 \rightarrow {}^3H_6$ transitions at 12300cm^{-1}. These emission features produce selective excitation spectra which are very similar to the absorption spectrum of the Ce^{3+} ion.

A new class of rare-earth pair centres was found in $CsCdBr_3$:Nd^{3+} by Barthou and Barthem [13]. They observed transitions associated with two new sites, B_1 and B_2, although the A-site is still the dominant location for Nd^{3+} ions in $CsCdBr_3$. The population ratio of B-sites to A-sites increases with neodymium concentration. Using laser selective excitation they demonstrated that sites B_1 and B_2 are related by energy transfer. The transfer rates for the B-centre are much greater than those of the A-centre, indicating that there is a smaller distance between the Nd^{3+} ions in the B-centre. Thus Barthou and Barthem concluded that these were strongly-coupled Nd^{3+} pair centres of the form Nd^{3+}-Nd^{3+}-Cd^{2+}vacancy. The spectroscopic differences between the two sites B_1 and B_2 occur because each of the Nd^{3+} ions in the pair experiences a different crystal-field.

Energy transfer processes between Nd^{3+} ions in $CsCdBr_3$:Nd^{3+} have been studied in great detail by Barthem et al [11] [12] [13]. Upconversion fluorescence from Er^{3+} pairs in $CsCdBr_3$ was reported by Cockroft et al [24]. They also report pair splittings in the absorption lines of the A-centre. In a later paper [23] mechanisms are proposed for the Er^{3+} upconversion observed and rate equations for these mechanisms are discussed. A mechanism which produces ultra-violet upconversion fluorescence, at 245nm, in Er^{3+} doped $CsMgCl_3$ was reported by McPherson et al [61].

The first upconversion laser was demonstrated by Silversmith et al in 1987 [84]. They acheived CW laser action at 549.6nm in an Er^{3+}:$YAlO_3$ crystal which was cooled to temperatures below 77K. Laser output powers as high as 1mW were produced by a $^4S_{3/2} \rightarrow {}^4I_{15/2}$ transition after sequential excitation of Er^{3+} to the

$^4F_{5/2}$ multiplet.

In 1990 the first infrared-pumped blue laser was reported by Herbert et al [42]. This laser used an Er^{3+}:$YLiF_4$ crystal to produce 2mW of CW emission from the $^2P_{3/2}(1) \rightarrow {}^4I_{11/2}(4)$ transition of Er^{3+} at 469.7nm. A room-temperature tunable upconversion laser was produced by Allain et al [3], also in 1990, using a holmium doped fluorozirconate glass. Output powers greater than 10mW were acheived for emission between 540 and 553nm, via the $^5S_2 \rightarrow {}^5I_8$ fluorescence transitions of the Ho^{3+} ion.

Recently Smart et al [85] announced the development of a room-temperature CW upconversion laser using a praseodymium doped fluorozirconate fibre. It produced laser oscillation at 491nm, 520nm, 605nm, and 635nm with thresholds which should enable laser diode pumped operation. The Pr^{3+} ions are sequentially excited by two lasers. The first laser, at 1010nm, is resonant with the $^3H_4 \rightarrow {}^1G_4$ absorption. The second laser, at 835nm, further excites the Pr^{3+} ions to the $^3P_1$ multiplet. At room temperature the three multiplets $^3P_1$, $^1I_6$, and $^3P_0$ are thermally coupled. 635nm lasing is produced by a $^3P_0 \rightarrow {}^3F_2$ transition and has been acheived with a maximum output power of 185mW and an overall efficiency of 7%. The blue 491nm output is due to a $^3P_0 \rightarrow {}^3H_4$ transition. Using a fibre which was not optimised, lasing in the blue was acheived with an output power of approximately 1mW. This laser is described in a review by Roger Macfarlane [54]. Other room temperature upconversion lasers have been reported by Allain et al [4] and Whitley et al [91].

A number of excitation mechanisms for upconversion lasers are presented in a recent paper by Lenth and Macfarlane [51]. Excellent reveiws on upconversion and energy transfer in rare-earth doped materials have been written by Auzel [10], Wright [92] and Yen [96].

8.3 Absorption Spectra

Transmission spectra were produced of each of the three crystals studied, using uncut and uncleaved booles. Figure 8.1 shows the absorption transitions in the blue region of the visible spectrum. The piece of mixed-dopant crystal used for these transmission measurements was thicker than either of the pure-dopant samples. This explains why the mixed crystal displays more intense absorption for all of the transitions observed. The spectum of the crystal doped only with praseodymium clearly shows the $^3H_4 \rightarrow {}^3P_0$ and the $^3H_4 \rightarrow {}^3P_2$ absorption transitions. The spectrum of the crystal doped only with thulium shows the $^3H_6 \rightarrow {}^1G_4$ absorption transitions.

The spectrum of the mixed-dopant crystal shows that both Pr^{3+} and Tm^{3+} ions have been accepted into the crystal lattice, however transitions to the $^1G_4$ multiplet are significantly broader in the pure-thulium crystal. This could be due to OH^- ion and/or H^- ion induced disorder in the lattice. These ions may have entered the lattice at the time the $CsCdBr_3$ precipitated out of solution. No such broadening of the of the Tm^{3+} ion transitions was observed during laser excita-

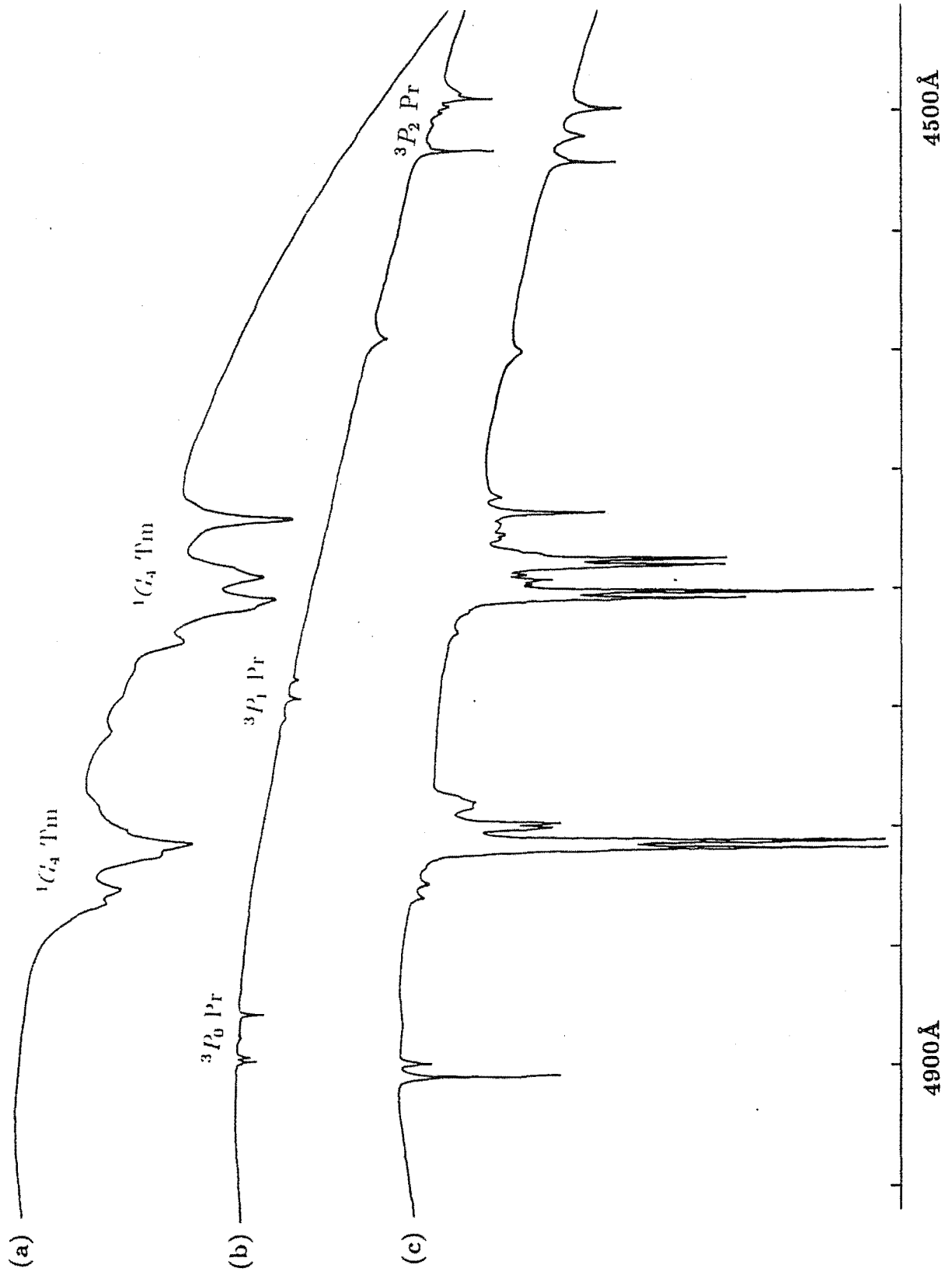

Figure 8.1: Transmission spectra of (a) the $CsCdBr_3:Tm^{3+}(1.0\%)$ crystal, (b) the $CsCdBr_3:Pr^{3+}(0.1\%)$ crystal and (c) the $CsCdBr_3:Tm^{3+}(0.5\%):Pr^{3+}(0.1\%)$ crystal.

tion, perhaps because the monochrometer was selecting a subset of sites within the inhomogeneously-broadened emission lines.

The OH^- ion has a vibrational-stretch mode transition at approximately $3500cm^{-1}$, an energy accessible to the FTIR spectrometer. A broad absorption feature, centred at approximately $3300cm^{-1}$, was found in the pure-thulium crystal, but not in the other crystals studied. A very similar transition, attributed to the OH^- ion, has been reported in $CdCl_2$ [46]. There is also an intense absorption feature at $1411cm^{-1}$, which is very much like the transition in $CdCl_2$ attributed to surface water [46]. This spectral region contains the transitions associated with the lowest free H_2O molecular rotational mode. However the transition in $CdCl_2$ is an absorption to the pure vibronic level at $1596cm^{-1}$. This is an allowed transition for an H_2O molecule which is located in the lattice such that it cannot rotate.

The ionic radii of the Pr^{3+} and Tm^{3+} ions are quite different, at 1.013Å and 0.869Å respectively [29]. Thus a Pr^{3+} ion in a Pr^{3+}-Pr^{3+} centre and the Pr^{3+} ion in a mixed Pr^{3+}-Tm^{3+} centre will experience slightly different crystal fields. This difference might be detected as a small discrepancy between the electronic energy levels of the two Pr^{3+} sites. Such a difference in transition energies should also be manifested by the different Tm^{3+} sites. However, these absorption spectra, with a resolution of 1Å (equivalent to $4.6cm^{-1}$ at 4750Å), do not show any obvious shifts in the transition energies. Careful comparison of the $^3H_4 \rightarrow {}^3P_2$ transition energies of the Pr^{3+} ion did reveal some small differences between the pure and mixed crystal.

8.4 The Spectroscopy of the $CsCdBr_3$:Tm^{3+} Crystal

8.4.1 The Electronic Energy Levels of the Pair Centre

No earlier studies of the spectroscopy of $CsCdBr_3$:Tm^{3+} were available when these experiments were performed. Only the major Tm^{3+} centre was investigated, although the transmission spectra do show some weak transitions due to minor centres. The most significant of these minor centres had $^{2S+1}L_J$ multiplets which were slightly lower in energy than those of the main centre. The transitions associated with the different Tm^{3+} centres were distinguised by laser selective excitation. Table 8.1 lists the energy levels of the main site which were derived from these empirical transition energies.

In Table 8.1 '$^3F_4$' and '$^3H_4$' have been chosen as the labels of the second and fourth multiplets respectively. This convention has been adopted by many authors, such as Dulick et al [30] and McPherson [57]. Other authors, such as Dieke [29] and Wright [92], label the second and fourth multipets as '$^3H_4$' and '$^3F_4$' respectively. The spin-orbit interaction, which is large compared to the Coulomb interaction for ions towards the end of the lanthanide series, is responsible for the reordering of the free-ion multiplets. A calculation of the eigenvector of the second multiplet will

Table 8.1: The experimental electronic energy levels (vacuum) of the Tm^{3+} A-centre in $CsCdBr_3$, in units of cm^{-1}. The energies have an uncertainty of $\pm 1 cm^{-1}$.

Multiplet	**Energy**	**Multiplet**	**Energy**
$^3H_6$	0.0	$^3F_3$	14331.4
	9.5		14334.8
	74.8		14357.3
	99.0		14369.4
	120.0		14395.3
	226.7	$^3F_2$	14892.8
	294.2		15022.4
	323.0	$^1G_4$	20796.3
$^3F_4$	5523.1		20833.6
	5544.1		21255.7
	5705.2		21314.2
	5737.0		21416.0
	5791.3	$^1D_2$	27337.0
$^3H_5$	8182.1		27380.0
$^3H_4$	12494.7		
	12515.9		
	12557.3		
	12633.9		
	12648.0		
	12772.9		

show that its $^3F_4$ component is much larger than its $^3H_4$ component [79].

8.4.2 Selective Excitation Spectra

An excitation spectrum Figure 8.2(a), while monitoring the $^3F_3 \rightarrow {}^3H_6$ fluorescence, reveals the energy levels of the $^1G_4$ multiplet. These transitions appear much narrower than they were in the transmission spectrum Figure 8.1(a). Fluorescence line narrowing may account for the smaller line-widths observed in excitation as the laser can selectively excite a subset of centres within the inhomogeneously-broadened spectral line. Here the monochrometer entrance slit has been set at 200μm, with a corresponding resolution of approximately 5cm^{-1}.

Figure 8.3(a) and (b) are σ and π-polarised excitation spectra showing the absorption transitions to the $^3H_4$ multiplet of the Tm^{3+} ion, while monitoring the $^3H_4 \rightarrow {}^3H_6$ fluorescence. The dramatic difference in the intensities of the spectral features observed for the two excitation polarisations demonstrates the symmetry dependent polarisation behaviour of the Tm^{3+} ion transitions in this material. There are far too many transitions in these excitation spectra for them all to be attributable to absorption from just the ground state in only one Tm^{3+} centre. If the Tm^{3+} ions are located in sites with C_{3v} symmetry, then the J=4 multiplets can have no more than 6 levels. The transmission spectra also show a greater than expected number of absorption transitions to the $^3F_2$, $^3F_3$, and $^1G_4$ multiplets. Some of the additional absorption transitions to the $^3H_4$ multiplet are due to excitation originating from the first excited state of the Tm^{3+} ions in the dominant pair centre. With an energy of 9.5cm^{-1}, this level will be thermally populated at 10K.

It is also possible that the monochrometer was unable to eliminate all of the emission from minor thulium centres. Some single-ion rare-earth centres and a minor pair centre have been observed in other studies of $CsCdBr_3$:RE^{3+} crystals [13] [20]. Indeed most of the additional transitions are no longer apparent in excitation when monitoring upconversion fluorescence and these must be associated with such minor centres. However, even when using upconversion to discern those transitions associated with multiple-ion centres, 13 transitions were still observed to the $^3H_4$ multiplet. Additional electronic energy levels may arise in the pair centres because of low-symmetry splitting of the γ_3 doublet states [62]. However, non of the $^3H_4$ multiplet states in Figure 8.3 appear to be split doublets.

Cockroft et al [23] observed six new upconverting centres in $CsCdBr_3$:Er^{3+}. In discussing their results they note that for upconversion to occur with pulsed excitation, two RE^{3+} ions must be present in the upconverting centre and these must have identical crystal fields and absorption energies. They conclude that the minor upconverting centres which they observed in $CsCdBr_3$:Er^{3+} were larger Er^{3+} ion clusters (N Cockroft, private communication). The presence of similar Tm^{3+} ion clusters may explain the other unidentified absorption transitions.

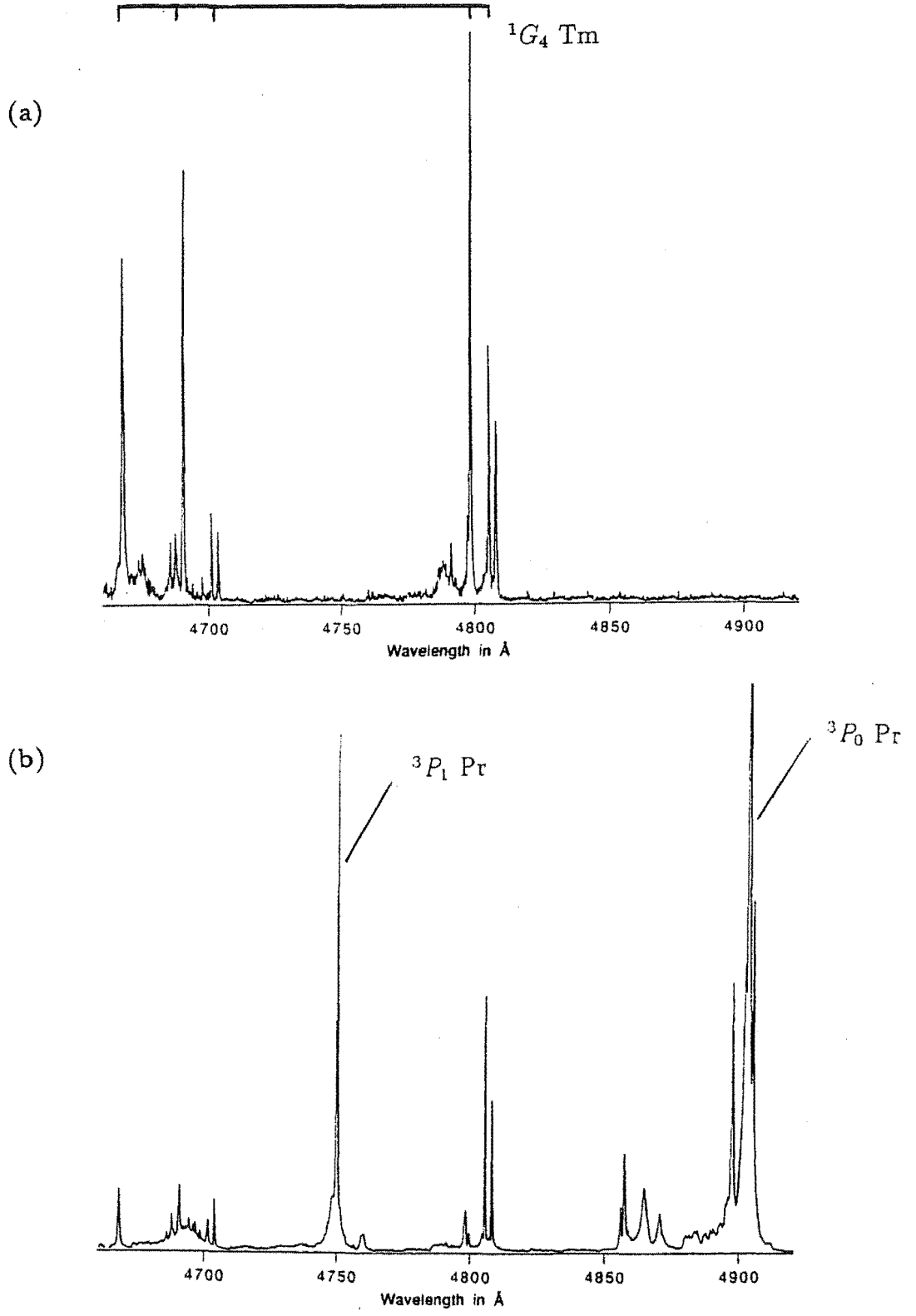

Figure 8.2: Excitation spectra showing the $^3H_6 \rightarrow {}^1G_4$ absorption transitions of thulium, while monitoring (a) the $^3F_3 \rightarrow {}^3H_6$ transition of thulium at 6971Å in the $CsCdBr_3$:Tm^{3+} crystal and (b) the $^3P_0 \rightarrow {}^3F_2$ transition of praseodymium at 6527Å in the $CsCdBr_3$:Tm^{3+}:Pr^{3+} crystal.

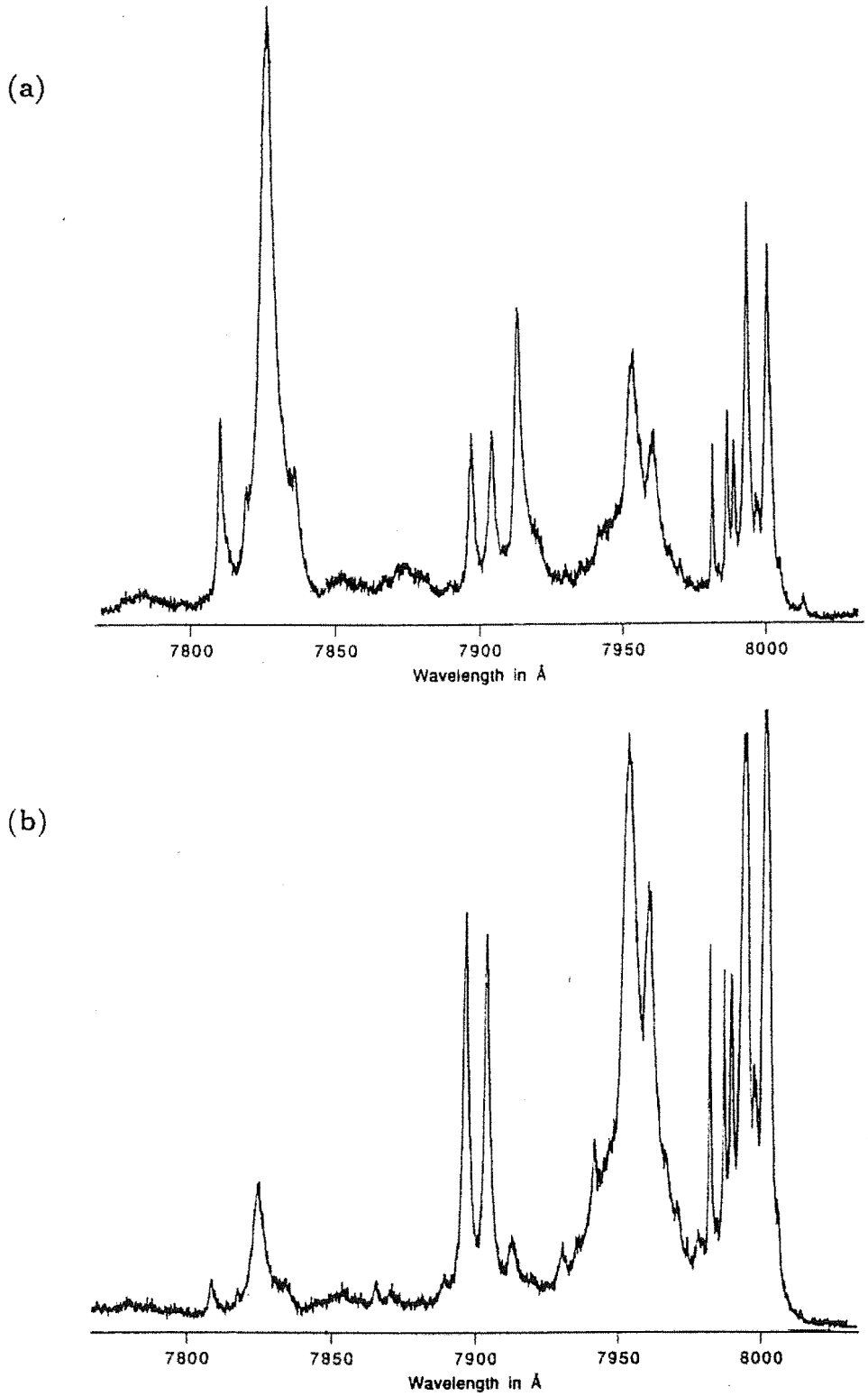

Figure 8.3: The (a) σ and (b) π-absorption transitions to the $^3H_4$ multiplet of thulium, while monitoring the $^3H_4 \rightarrow {}^3H_6$ transition at 8195Å in the $CsCdBr_3$:Tm^{3+} crystal.

8.4.3 Fluorescence Spectra

Laser selective excitation of the Tm^{3+} ions in the main pair centre to the $^1G_4$ multiplet produced fluorescence originating from both the $^1G_4$ and $^3F_3$ multiplets. Figure 8.4(a) is a fluorescence spectrum showing the $^3F_3 \rightarrow {}^3H_6$ emission. The process which populates the $^3F_3$ multiplet, and so produces this red fluorescence, was found to be the dominant relaxation pathway for Tm^{3+} ions excited to the $^1G_4$ multiplet. This is an interesting result as the branching ratio for the $^1G_4 \rightarrow {}^3F_2/{}^3F_3$ fluorescence has been found to be rather small for thulium in other hosts. The combined radiative-emission probablity to the $^3F_2$ and $^3F_3$ multiplets was calculated by Oomen [66] as 3% for thulium-doped fluorozirconate glasses and by Yeh et al [95] as 5% for thulium-doped barium-thorium fluoride glass. The $^3F_2$ multiplet levels are approximately $700cm^{-1}$ higher than the $^3F_3$ multiplet levels in these glasses, so the $^3F_2$ multiplet is readily depopulated by multi-phonon decay to the $^3F_3$ multiplet.

Figure 8.5(a) is a fluorescence spectrum showing the $^3H_4 \rightarrow {}^3H_6$ transitions during laser excition of the Tm^{3+} ions to the $^3H_4$ multiplet. The fluorescence lifetime of the $^3H_4$ multiplet of was measured and found to be $(960\pm10)\mu s$.

8.4.4 Fluorescence Transients

Figure 8.6(a) shows the transient of the $^1G_4 \rightarrow {}^3H_5$ fluorescence after pulsed excitation of the Tm^{3+} ions to the $^1G_4$ multiplet. A great deal of care was taken to exclude laser light from the detector during the recording of this transient. The radiative decay from the $^1G_4$ multiplet exhibits two distinct components, one being very much faster than the other. The slower contribution is exponential and its characteristic decay time was found to be $(285\pm30)\mu s$. The $^3F_3$ multiplet fluorescence, Figure 8.6(b), has a similar transient after the first $100\mu s$. There is a very fast rise in the fluorescence intensity. The complete decay curve does not fit well to a single-exponential function; although the tail does fit to an exponential function with $\tau=(270\pm50)\mu s$.

The fast rise in Figure 8.6(b) makes it unlikely that the $^3F_3$ multiplet is being populated radiatively. In those pair centres where both the Tm^{3+} ions are excited to the $^1G_4$ multiplet, an energy transfer which populates the $^3F_3$ and $^1D_2$ multiplets may account for the observed fluorescence from the $^3F_3$ multiplet. If the $^1D_2$ multiplet has been populated then the $^1D_2 \rightarrow {}^3F_4$ fluorescence should also be apparent. This emission has a rather large branching ratio for thulium in other hosts; 57% in $YLiF_4$:Tm^{3+} [30], 45% in Tm^{3+} doped barium-thorium fluoride glass [95], and 49% in Tm^{3+} doped fluorozirconate glasses [66]. No $^1D_2$ multiplet fluorescence could be found while exciting the Tm^{3+} ions to the $^1G_4$ multiplet. Indeed, no upconversion fluorescence was observed.

Another possible mechanism for populating the $^3F_3$ multiplet is shown in Figure 8.7. This cross relaxation, populating the $^3F_2$ and $^3F_4$ multiplets, can occur when just one of the Tm^{3+} ions in a pair is excited. When both ions are excited this relaxation pathway is available only after one of the Tm^{3+} ions has relaxed back

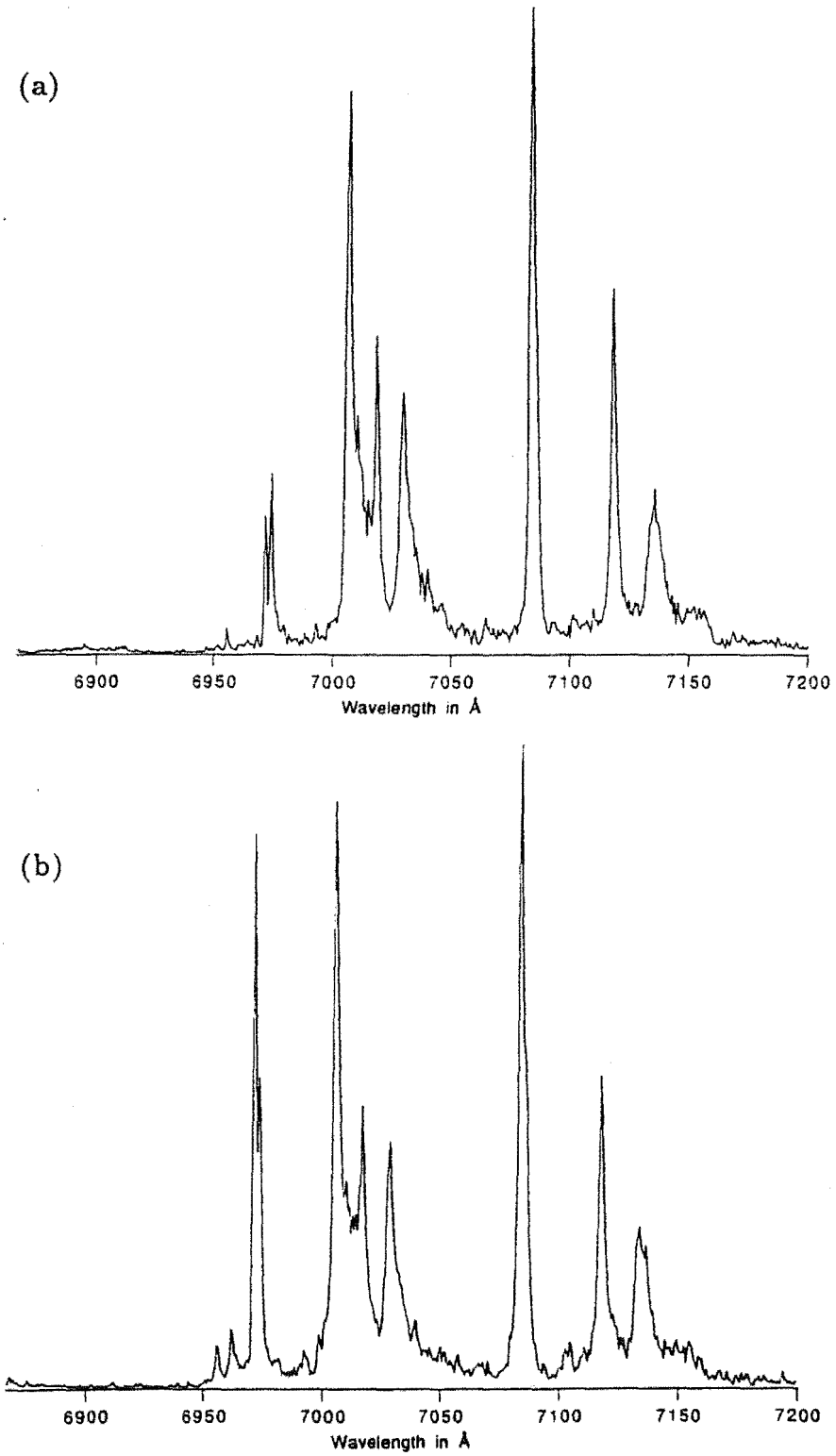

Figure 8.4: Fluorescence spectra showing the $^3F_3 \rightarrow {}^3H_6$ transitions, while exciting the Tm^{3+} ions to the $^1G_4$ multiplet, 4805Å, in (a) the $CsCdBr_3$:Tm^{3+} crystal and (b) the $CsCdBr_3$:Tm^{3+}:Pr^{3+} crystal.

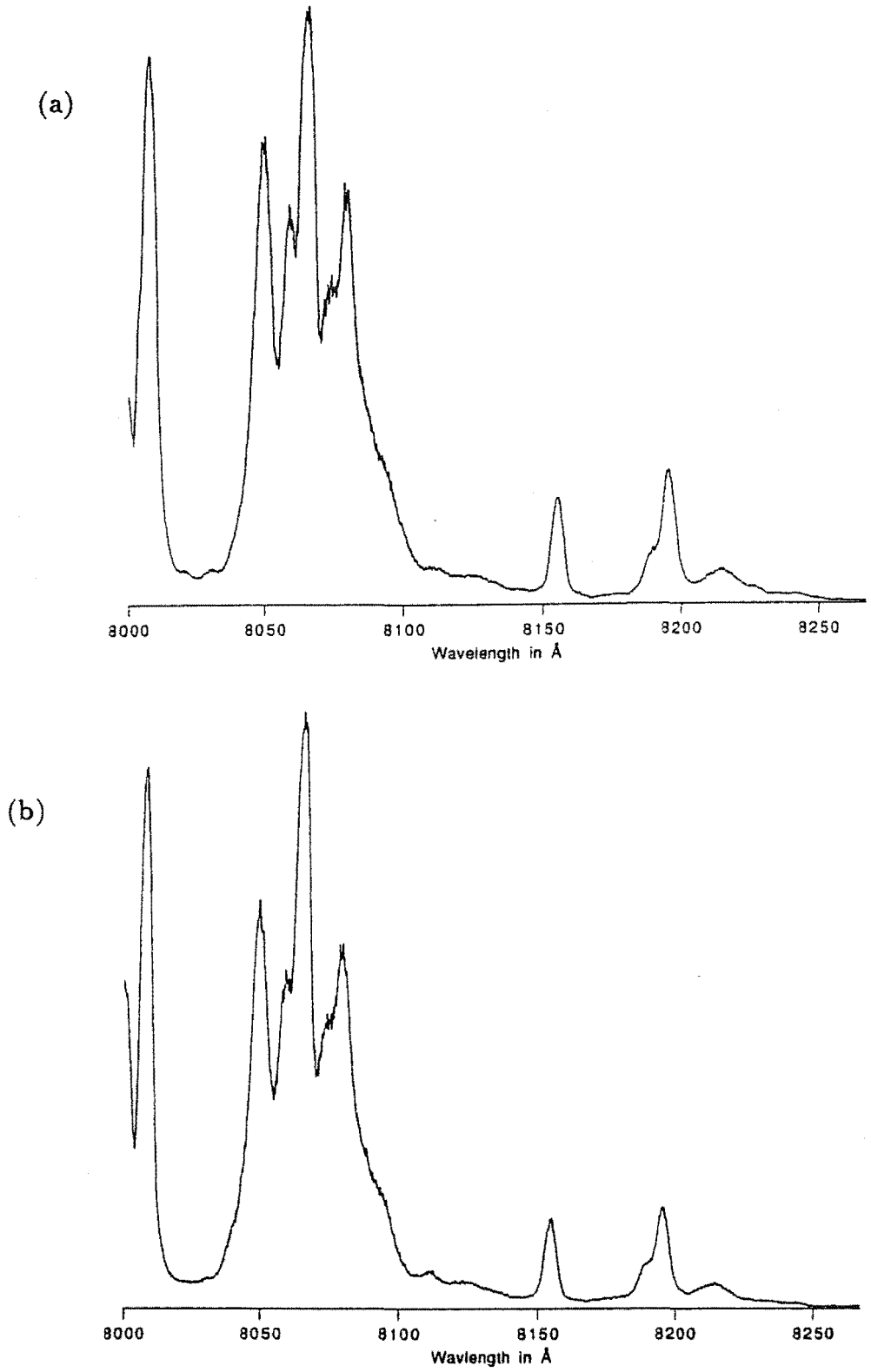

Figure 8.5: Fluorescence spectra showing the $^3H_4 \rightarrow {}^3H_6$ transitions, while exciting the Tm^{3+} ions to the $^3H_4$ multiplet, 7994Å, in (a) the $CsCdBr_3$:Tm^{3+} crystal and (b) the $CsCdBr_3$:Tm^{3+}:Pr^{3+} crystal.

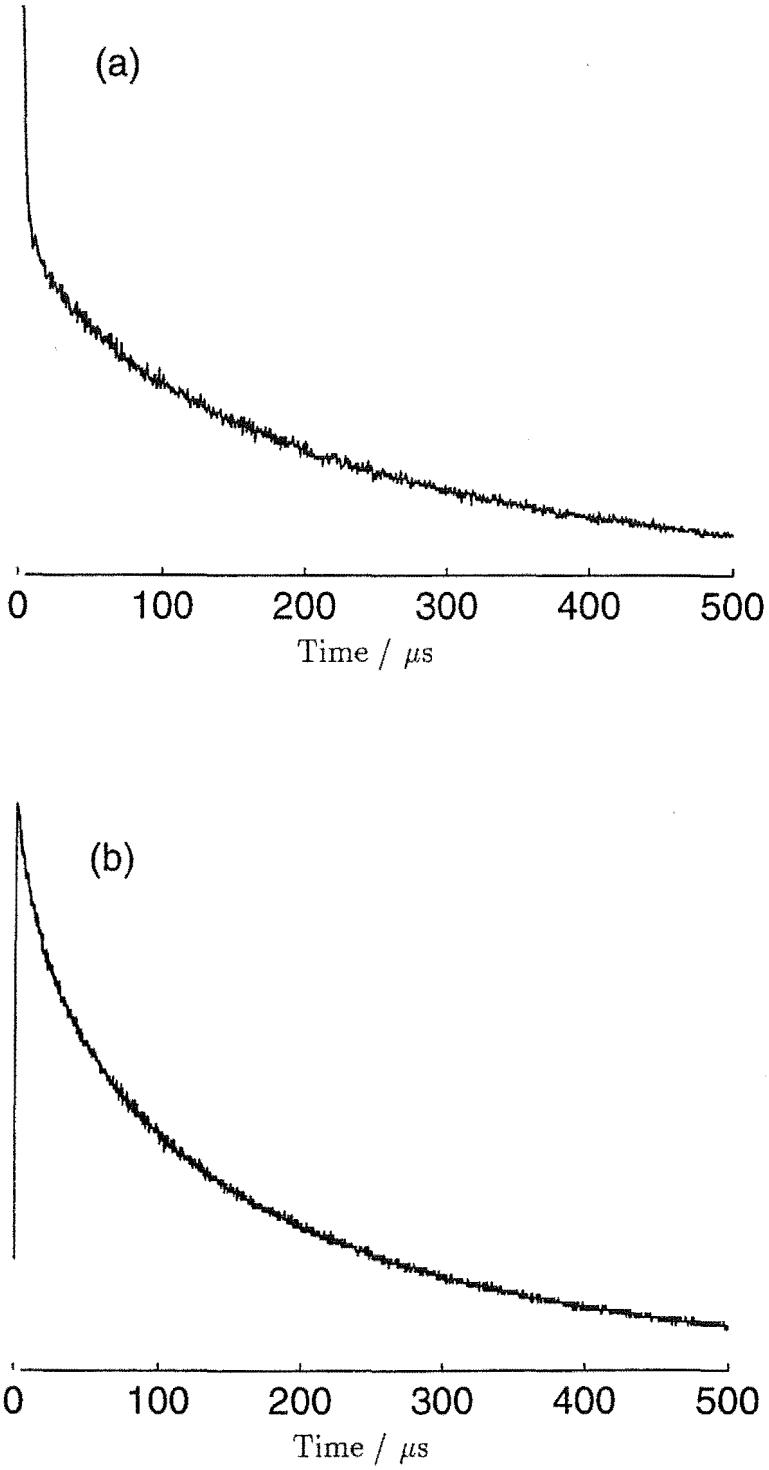

Figure 8.6: Transients of (**a**) the $^1G_4 \rightarrow {}^3H_6$ transition at 4825Å and (**b**) the $^3F_3 \rightarrow {}^3H_6$ transition at 7008Å after excitation of the Tm^{3+} ions to the $^1G_4$ multiplet, 4805Å, in the $CsCdBr_3$:Tm^{3+} crystal.

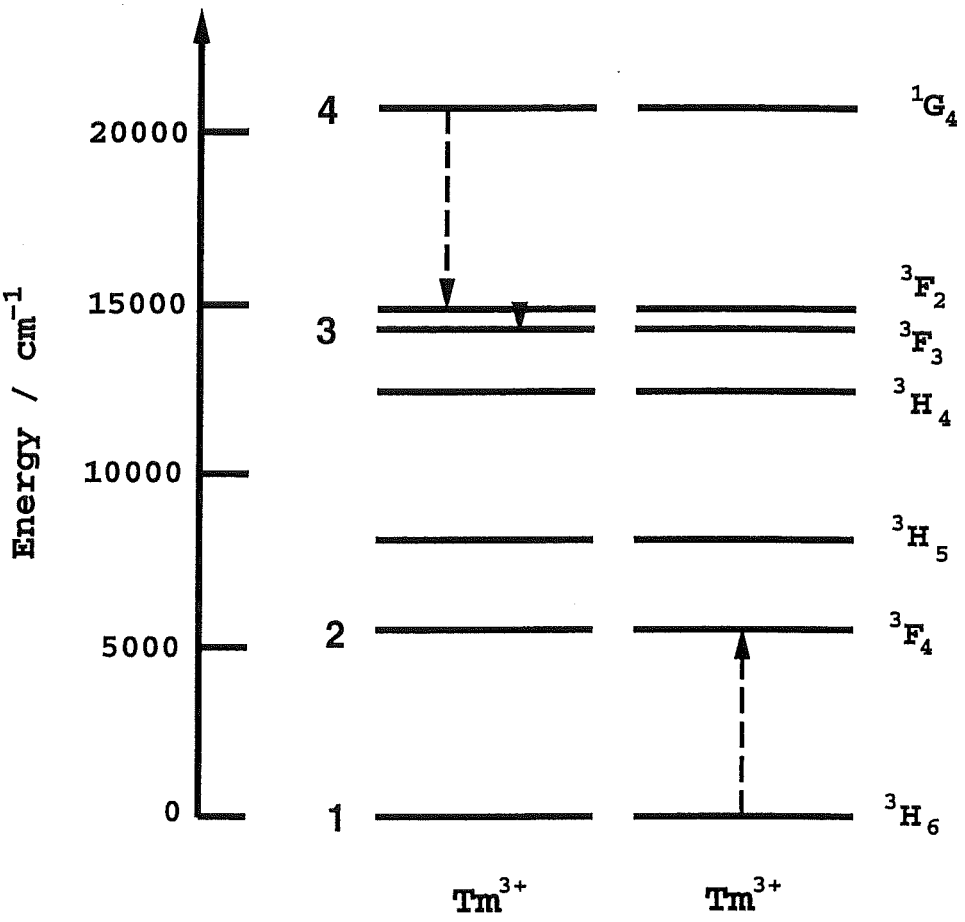

Figure 8.7: The proposed cross-relaxation mechanism which quenches the $^1G_4$ multiplet and populates the $^3F_3$ multiplet in the homogeneous Tm^{3+} pair centres.

to the ground state by some other process, perhaps radiatively. The difference in energy between the lowest level of the $^3F_2$ multiplet and the highest level of the $^3F_3$ multiplet is 497cm^{-1}. Since the phonon-cut-off energy in $CsCdBr_3$ is 163cm^{-1} [67], it seems likely that multi-phonon decay from the $^3F_2$ multiplet will populate the $^3F_3$ multiplet.

The energy mismatch associated with this energy transfer can be estimated using the empirical energy levels. The $^1G_4(1) \rightarrow {}^3F_2$ and $^3H_6(1) \rightarrow {}^3F_4$ transition energies are well matched, with the smallest difference between them being only 17cm^{-1}. However, a transfer exploiting this minimum energy mismatch would be endothermic. The minimum energy mismatch for an exothermic transfer is 37cm^{-1}. Such small differences in the electronic transition energies can easily be compensated for in a phonon-assisted transfer.

The transients of the fluorescence from the $^1G_4$ and $^3F_3$ multiplets can be

interpreted by considering the rate equations for various processes involved in this cross relaxation. N_d represents the number of pair centres where both ions have been excited by the laser pulse [$^1G_4$:$^1G_4$], N_s the number of singly-excited pairs [$^3H_6$:$^1G_4$], N_4/N_3 the total number of ions excited to the $^1G_4/^3F_3$ multiplet, W_t the energy-transfer rate, and W_i the fluorescence-decay rate of multiplet i in the abscence of energy transfer. The rate equations needed to describe this mechanism are:

$$\begin{aligned} \dot{N}_d &= -2W_4N_d \\ \dot{N}_s &= 2W_4N_d - (W_t + W_4)N_s \\ \dot{N}_3 &= W_tN_s - W_3N_3\,. \end{aligned}$$

The factor '2' appears in the expressions for $\dot{N}_d$ and $\dot{N}_s$ because the doubly-excited pairs are destroyed as soon as one of the two ions de-excites [17]. The multi-phonon decay of the $^3F_2$ multiplet is a very high-rate process and is treated as instantaneous in this model. The rate equations can be solved for the transient population of the $^1G_4$ multiplet:

$$\begin{aligned} N_4(t) &= 2N_d + N_s \\ &= 2N_d^0 e^{-2W_4t} + \frac{2W_4N_d^0}{W_t - W_4}\, e^{-2W_4t} + \left(\frac{-2W_4N_d^0}{W_t - W_4} + N_s^0\right) e^{-(W_t+W_4)t} \end{aligned} \quad (8.1)$$

In solving for $N_3(t)$ it has been assumed that the cross relaxation is quenching the $^1G_4$ multiplet in singly-excited pairs and so $W_t \gg W_4$. The solution has the form:

$$N_3(t) = Ae^{-2W_4t} + Be^{-W_tt} + Ce^{-W_3t}\,, \quad (8.2)$$

where A, B, and C are real valued functions of the various rate constants.

The cross relaxation mechanism proposed would account for the transients of the $^1G_4$ and $^3F_3$ multiplet fluorescence in the following way. When only one of the Tm^{3+} ions in a pair centre has been excited, this cross relaxation can proceed quenching the $^1G_4$ multiplet. This quenching corresponds to the initial fast component of the $^1G_4$ multiplet decay curve and the last exponential term of Equation 8.1. The slower part is associated with the fluorescence from Tm^{3+} ions in the doubly-excited pairs, where this cross-relaxation pathway is unavailable until one of the ions has returned to the ground state. Indeed the radiative relaxation producing this fluorescence would be the precursor to energy transfer in such pairs. Thus the doubly excited pairs are associated with the first two exponential terms of equation 8.1 and so the 285μs decay represents half the $^1G_4$ multiplet fluorescence lifetime (being (570$\pm$60)μs in the abscence of the cross-relaxation mechanism).

The $^3F_3$ multiplet is populated very quickly, as the cross relaxation and subsequent non-radiative decay of the $^3F_2$ multiplet are both high rate processes. After an initial quenching of the $^1G_4$ population, this mechanism will continue to populate the $^3F_3$ multiplet as Tm^{3+} ions in the 'doubly-excited pairs' return to the ground

state. The quenching corresponds to the second term in Equation 8.2 and the protracted process to the first term. This explains why the transients of the $^1G_4$ and $^3F_3$ multiplet fluorescence look so similar after the first $100\mu s$. However, they are not identical, since the latter contains an additional contribution due to radiative decay from the $^3F_3$ multiplet itself. This is represented by the third term of Equation 8.2. The radiative lifetime of the $^3F_3$ multiplet is apparently much less than $570\mu s$, since the initial part of its fluorescence transient is quite fast and the slow component of the decay is almost identical to that of the $^1G_4$ multiplet.

The mechanism proposed in Figure 8.7 could be tested by exciting the Tm^{3+} ions in a single-ion centre to the $^1G_4$ multiplet. If significant emission from the $^3F_3$ multiplet is still observed, then this cross relaxation is unlikely be the mechanism for populating the $^3F_3$ multiplet so efficiently in the pair centres. This might be a difficult experiment to perform because of the dominance of the major pair centre in the absorption spectrum of this material.

8.5 The Spectroscopy of the $CsCdBr_3$:Pr^{3+}:Tm^{3+} Crystal

8.5.1 The Electronic Energy Levels of the Pair Centre

Spectroscopic studies of $CsCdBr_3$:Pr^{3+} have already been reported by Foo [34] and Ramaz et al [72] [73]. In this work only the principal A-centre, in Foo's nomenclature, will be considered because it has the RE^{3+}-Cd^{2+}vacancy-RE^{3+} configuration conducive to energy transfer. The electronic energy levels found by Ramaz et al are listed in Table 8.2.

8.5.2 Selective Excitation Spectra

Figure 8.8 is an excitation spectrum showing the absorption transitions to the $^1G_4$ multiplet of thulium and to the $^3P_0$ and $^3P_1$ multiplets of praseodymium, while monitoring the $^3F_3 \rightarrow {}^3H_6$ fluorescence of thulium. The appearance of praseodymium transitions in this spectrum is the first evidence of energy transfer from Pr^{3+} ions to Tm^{3+} ions in this material.

Figure 8.2(b) shows the absorption transitions to the $^1G_4$ multiplet of thulium and to the $^3P_1$ and $^3P_0$ multiplets of praseodymium, while monitoring the $^3P_0 \rightarrow {}^3F_2$ fluorescence of praseodymium. The presence of thulium excitation transitions in this spectrum is evidence for a cross-relaxation process which depopulates the $^1G_4$ multiplet of the Tm^{3+} ion and excites the Pr^{3+} ions to the $^3P_0$ multiplet. Such energy transfers between the Tm^{3+} and Pr^{3+} ions provide strong evidence for the existence of heterogeneous pair centres.

Not all the transitions which appear in Figure 8.2(b) could be identified. Of particular interest are the excitation features with energies up to $200cm^{-1}$ higher

Table 8.2: The experimental electronic energy levels (vacuum) of the Pr^{3+} A-centre in $CsCdBr_3$ found by Ramaz, in units of cm^{-1}. An asterix denotes those levels first found in this study. The energies have an uncertainty of $\pm 1 cm^{-1}$.

Multiplet	Energy	Multiplet	Energy
$^3H_4$	0	$^3F_3$	6473
	166		6481
	196		6501
	323		6526
	551	$^3F_4$	6858
	575		6895
$^3H_5$	2230		6907
	2256		7050
	2310		7105
	2327		7111
	2523	$^1G_4$	*9777
	2544	$^1D_2$	16536
$^3H_6$	4364		16568
	4375		17005
	4416	$^3P_0$	20386
	4494	$^3P_1$	20956
	4701		*21048
	4725	$^1I_6$	*22085
	4761		*22117
	4782		*22187
	4843		*22226
$^3F_2$	5072	$^3P_2$	22106
	5148		22163
	5154		22216

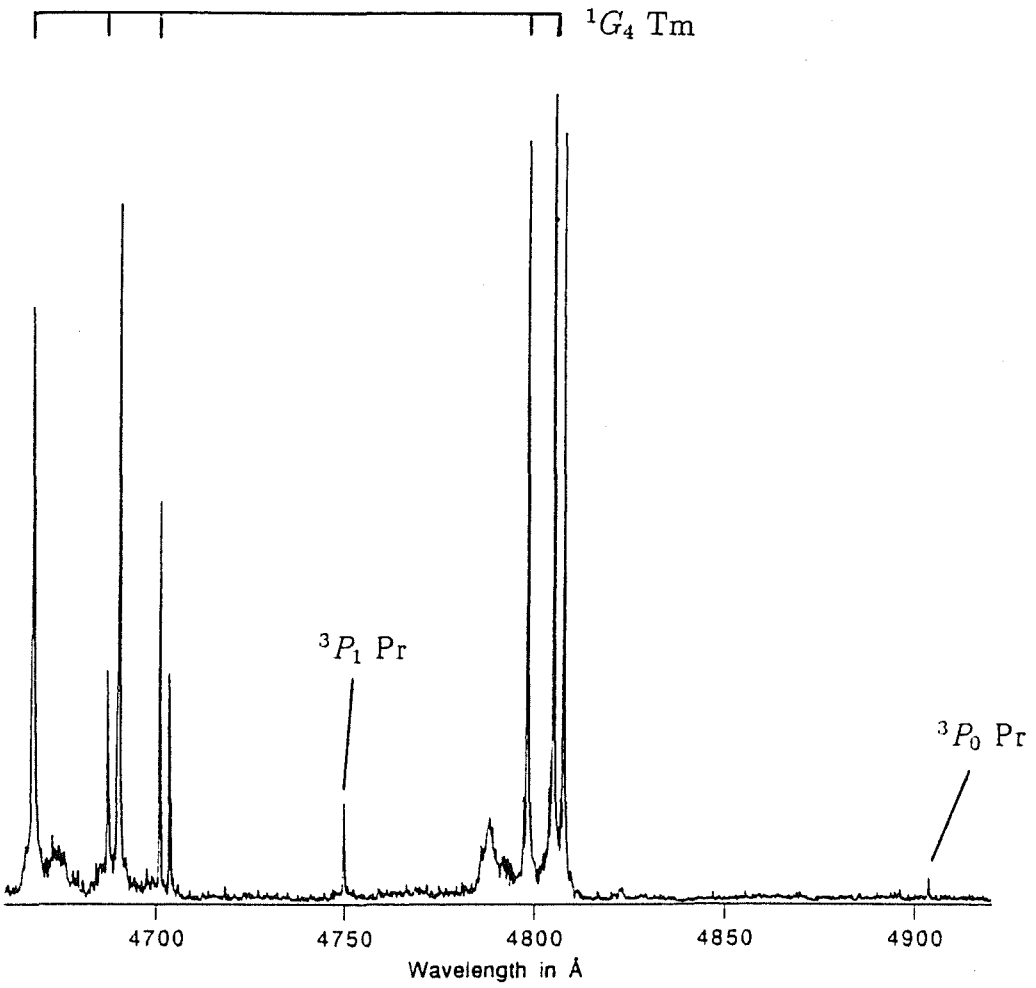

Figure 8.8: An excitation spectrum showing the $^3H_6 \rightarrow {}^1G_4$ absorption transitions of thulium and the $^3H_4 \rightarrow {}^3P_1$ and $^3H_4 \rightarrow {}^3P_0$ absorption transitions of praseodymium, while monitoring the $^3F_3 \rightarrow {}^3H_6$ transition of thulium at 6971Å in the $CsCdBr_3$:Tm^{3+}:Pr^{3+} crystal.

than the $^3H_6(1) \rightarrow {}^3P_0$ electronic transition of the Pr^{3+} pair centre. The transition at 20409cm^{-1} was found to be associated with a minor Pr^{3+} centre which was not related to the main pair centre. Some of the other unidentified transitions in this region may be associated with minor RE^{3+} ion centres. Such minor centres, with electronic energy levels higher those of the main pair centre, have been observed before in pure-dopant $CsCdBr_3$:Pr^{3+} crystals [34] and $CsCdBr_3$:Er^{3+} crystals (Nigel Cockroft, private communication).

An alternative explanation is that the unidentified transitions are due to a cooperative-absorption process, such as that observed by Buijs et al [16] in Eu^{3+} doped oxide crystals. However, the energy differences between these transitions and the $^3H_6(1) \rightarrow {}^3P_0$ transition do not match with any of the Tm^{3+} or Pr^{3+} ion electronic levels. Nor do they correspond to the lattice-phonon energies of $CsCdBr_3$ reported by Pilla et al [67]. Thus these unidentified transitions are attributed to minor centres.

Figure 8.9 shows the absorption transitions to the $^3P_0$ and $^3P_1$ multiplets of the Pr^{3+} ion, while monitoring the $^1D_2 \rightarrow {}^3H_4$ fluorescence of praseodymium. Comparison between this excitation spectrum and Figure 8.8 reveals that there is no emission from the $^1D_2$ multiplet of the Pr^{3+} ion after excitation of the Tm^{3+} ions to the $^1G_4$ multiplet. A mechanism for populating the $^1D_2$ multiplet, which involves cross relaxation from the $^3P_1$ or $^3P_0$ multiplets, can be deduced from the energy levels of Pr^{3+} ion and is shown in Figure 8.10.

This cross relaxation can occur in the homogeneous Pr^{3+} pair centres. The energy transfer which populates the $^1D_2$ and $^3H_6$ multiplets is exothermic, with an energy mismatch of 4cm^{-1}. The energy transfer which populates the $^1D_2$ and $^3H_5$ multiplets is also exothermic, with an energy mismatch of 837cm^{-1}. Similar cross relaxations in heterogeneous pair centres would have even larger energy mismatches and are therefore unlikely. For example, a cross relaxation from the $^1G_4$ multiplet of thulium to the $^1D_2$ multiplet of praseodymium would be endothermic, with an energy mismatch of 1263cm^{-1}. This explains why the $^3H_6 \rightarrow {}^1G_4$ absorption transitions of Tm^{3+} do not appear in Figure 8.9.

8.5.3 Fluorescence Spectra

The excitation spectra have shown a praseodymium energy level at 21048cm^{-1} which has not previously been reported. This level was ascribed to the $^3P_1$ multiplet. Figures 8.11(a), 8.12(a), 8.13(a), and 8.14 are fluorescence spectra obtained by exciting the Pr^{3+} ions to this level. The observation of $^1G_4 \rightarrow {}^3H_6$ fluorescence of thulium is another example of energy transfer within heterogeneous pairs; in this case a transfer from the $^3P_1$ multiplet of the Pr^{3+} ion to the $^1G_4$ multiplet of the Tm^{3+} ion. The occurrence of this transfer is not surprising as the energy range of the $^3P_1$ multiplet of praseodymium overlaps the energy range of the $^1G_4$ multiplet of thulium.

Figures 8.11(b), 8.12(b), and 8.13(b) are fluorescence spectra showing transitions from the $^3P_0$ multiplet of praseodymium and from the $^3F_3$ multiplet of thulium,

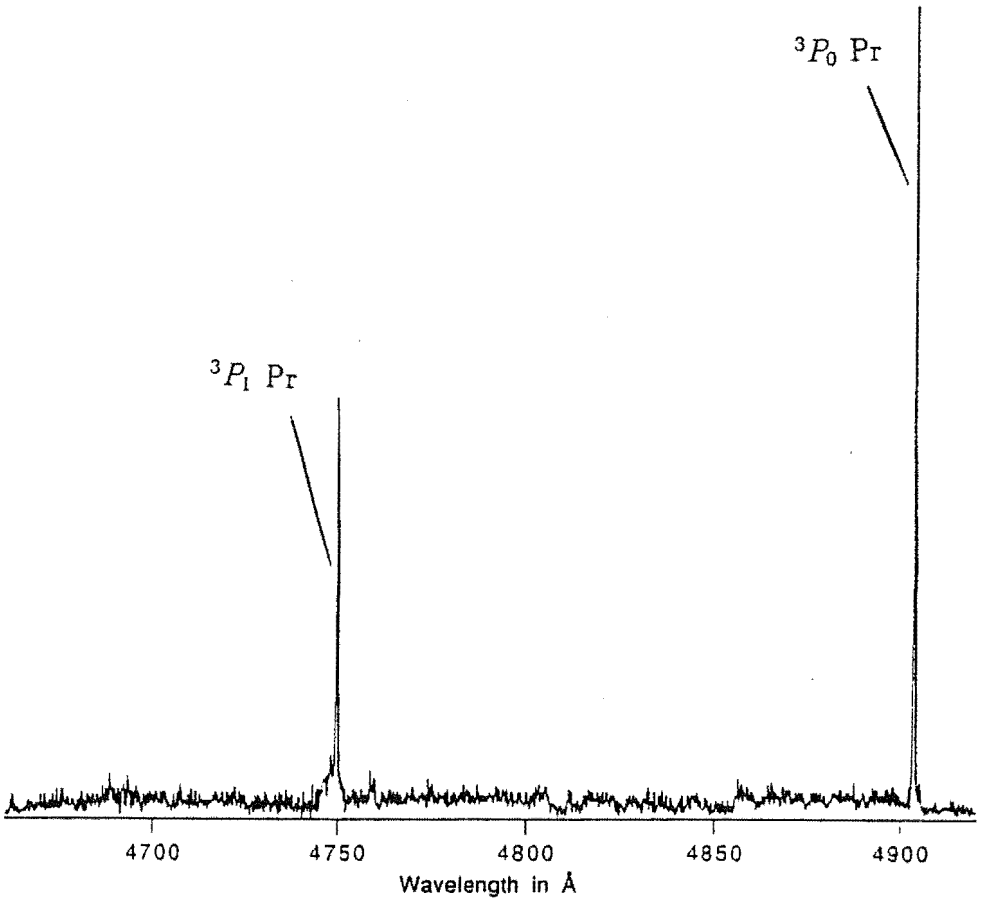

Figure 8.9: An excitation spectrum showing the $^3H_4 \rightarrow {}^3P_0$ and $^3H_4 \rightarrow {}^3P_1$ absorption transitions of praseodymium, while monitoring the $^1D_2 \rightarrow {}^3H_4$ transition of praseodymium at 6169Å in the $CsCdBr_3$:Pr^{3+}:Tm^{3+} crystal.

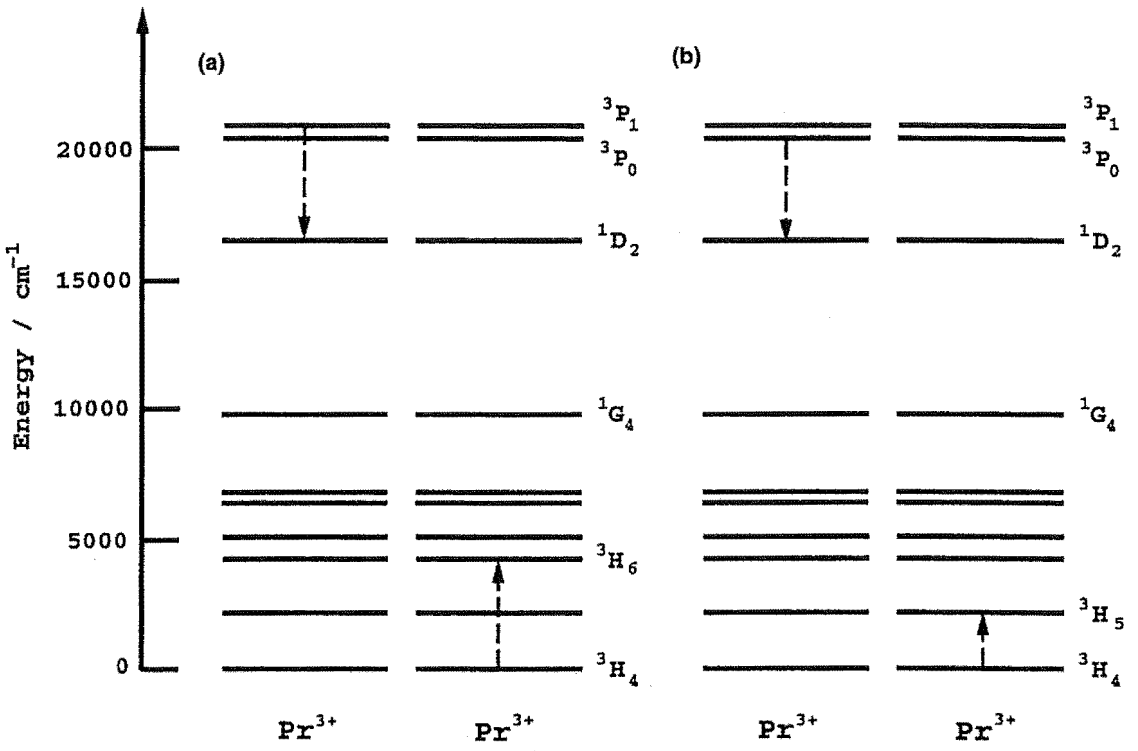

Figure 8.10: The proposed-cross relaxation mechanism which relaxes Pr^{3+} ions excited to (a) the $^3P_1$ or (b) the $^3P_0$ multiplet and populates the $^1D_2$ multiplet in homogeneous Pr^{3+} pair centres.

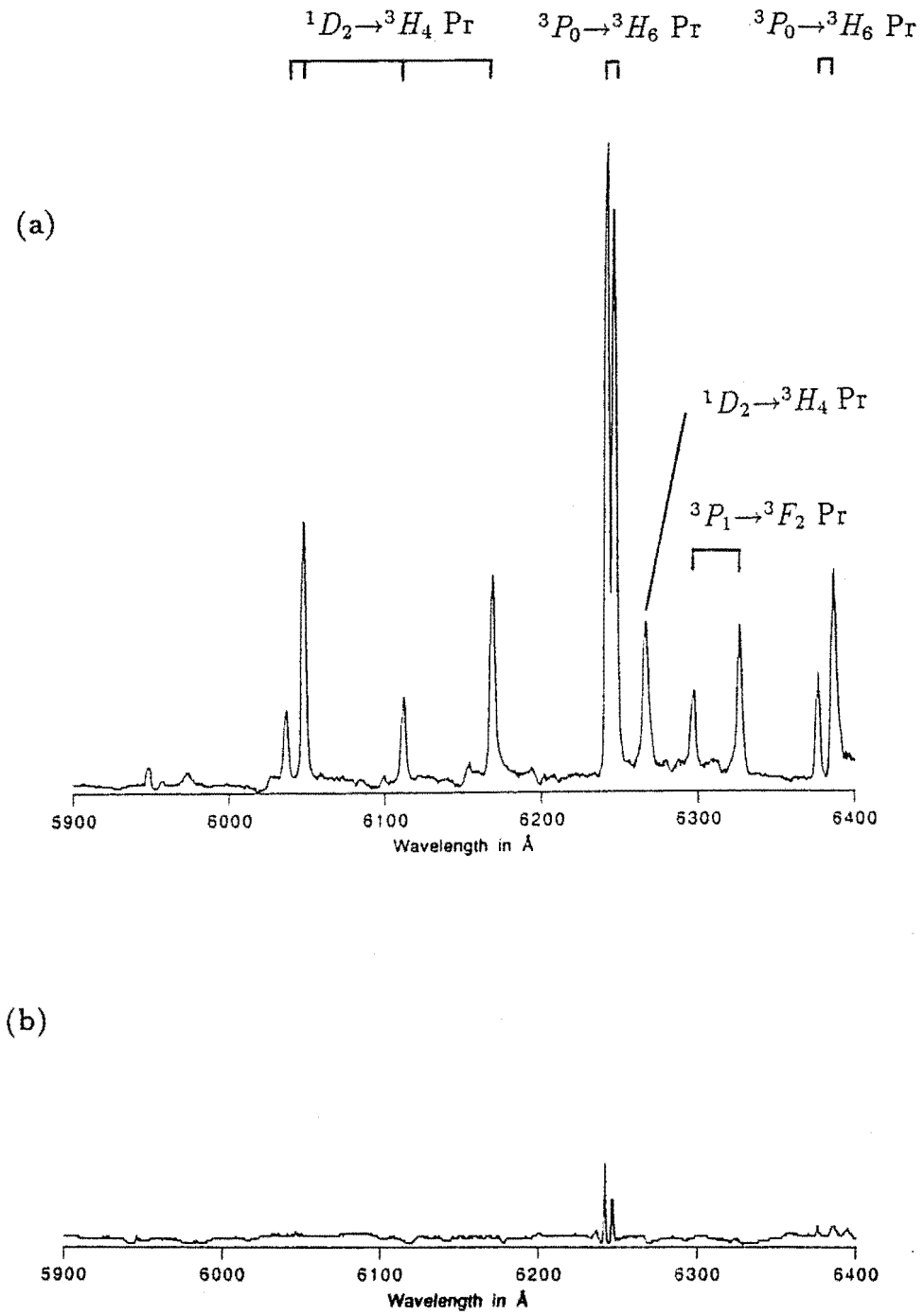

Figure 8.11: Fluorescence spectra showing the $^1D_2 \rightarrow {}^3H_4$, $^3P_0 \rightarrow {}^3H_6$ and $^3P_1 \rightarrow {}^3F_2$ transitions of praseodymium, while exciting (a) the Pr^{3+} ions to the $^3P_1$ multiplet, 4750Å, and (b) the Tm^{3+} ions to the $^1G_4$ multiplet, 4808Å, in the $CsCdBr_3$:Tm^{3+}:Pr^{3+} crystal.

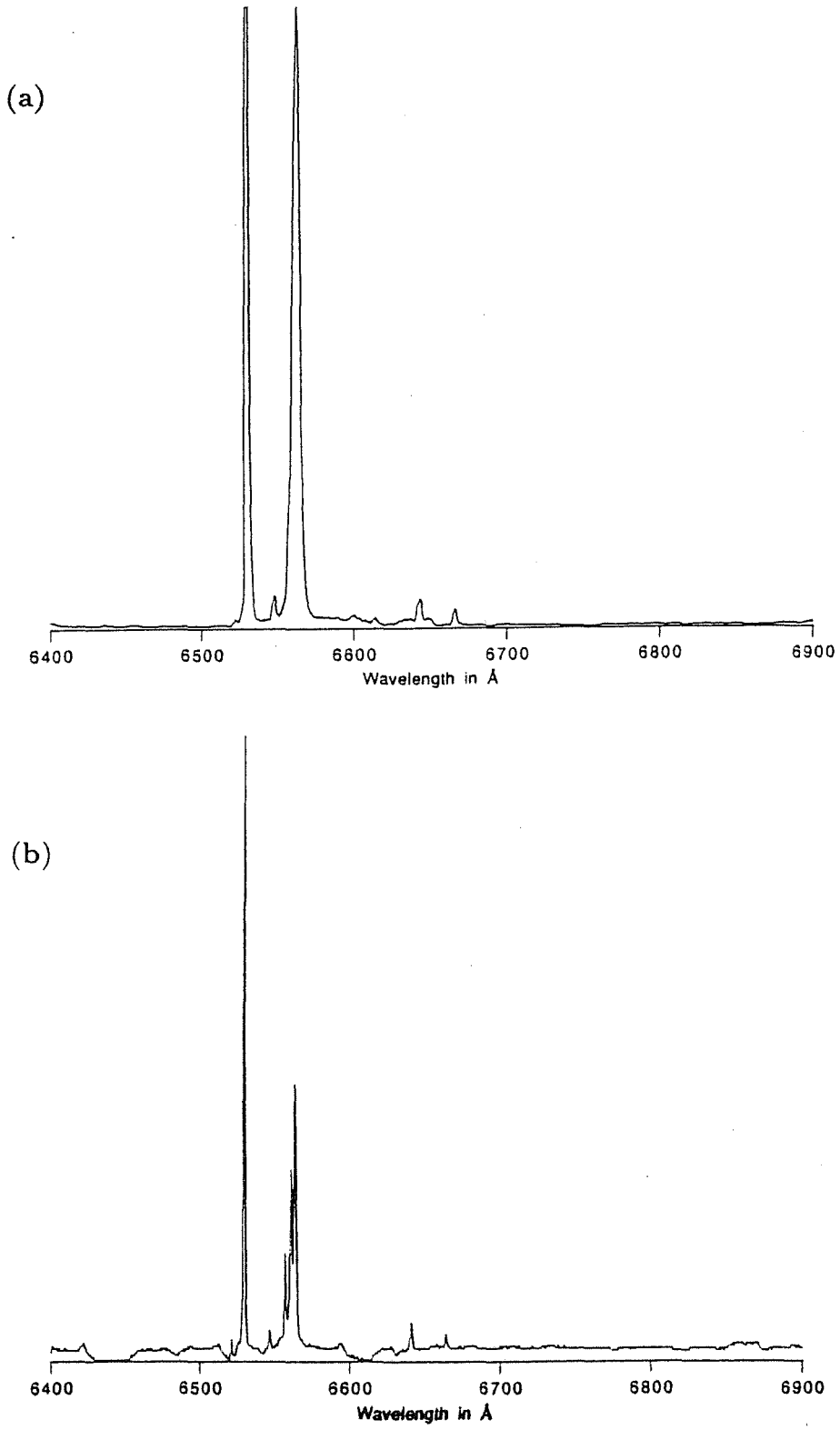

Figure 8.12: Fluorescence spectra showing the $^3P_0 \rightarrow {}^3F_2$ transitions of praseodymium, while exciting (a) the Pr^{3+} ions to the $^3P_1$ multiplet, 4750Å, and (b) the Tm^{3+} ions to the $^1G_4$ multiplet, 4808Å, in the $CsCdBr_3$:Tm^{3+}:Pr^{3+} crystal.

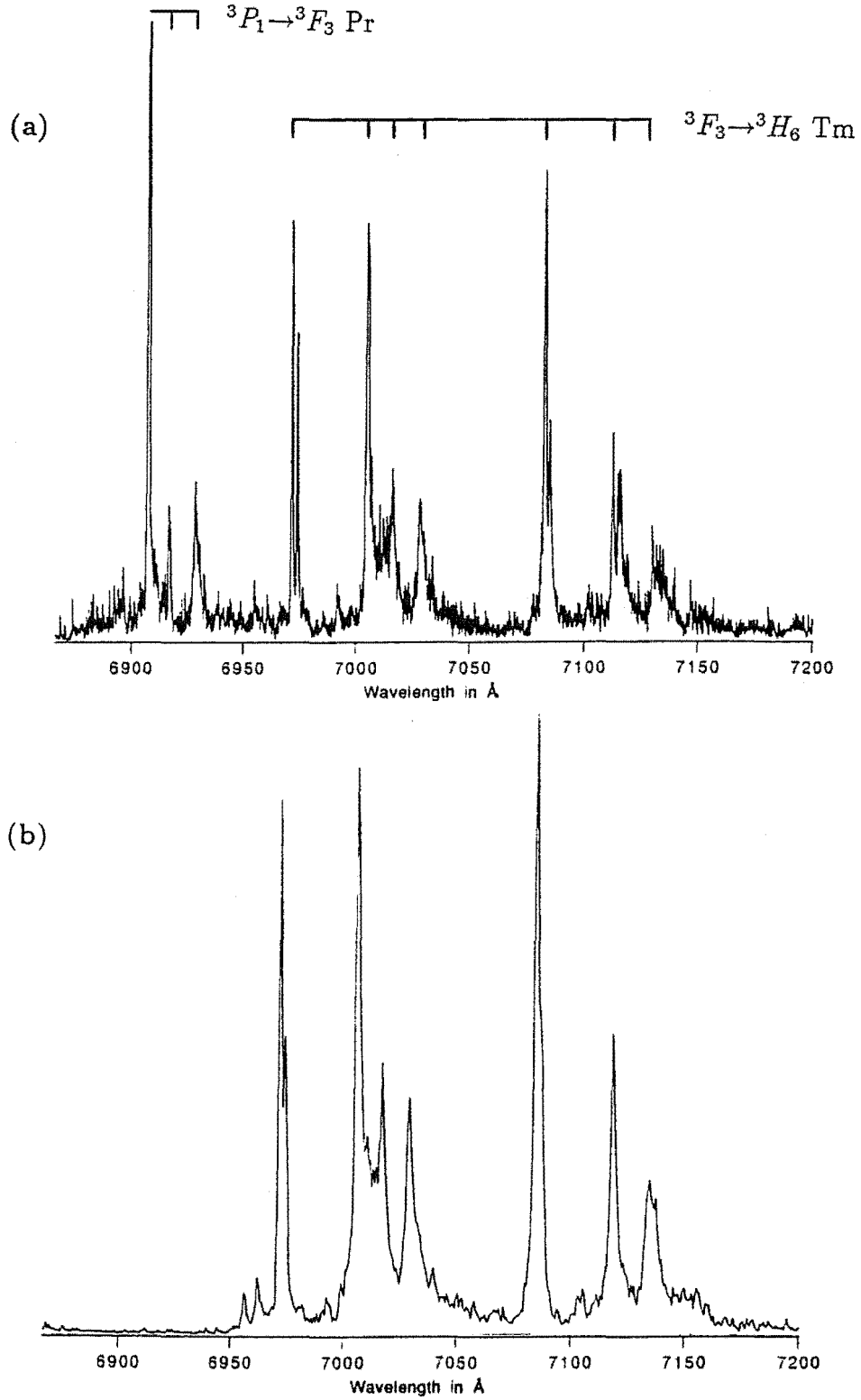

Figure 8.13: Fluorescence spectra showing the $^3F_3 \rightarrow {}^3H_6$ transtions of thulium and the $^3P_1 \rightarrow {}^3F_3$ transitions of praseodymium. while exciting (a) the Pr^{3+} ions to the $^3P_1$ multiplet, 4750Å. and (b) the Tm^{3+} ions to the $^1G_4$ multiplet, 4805Å, in the $CsCdBr_3:Tm^{3+}:Pr^{3+}$ crystal.

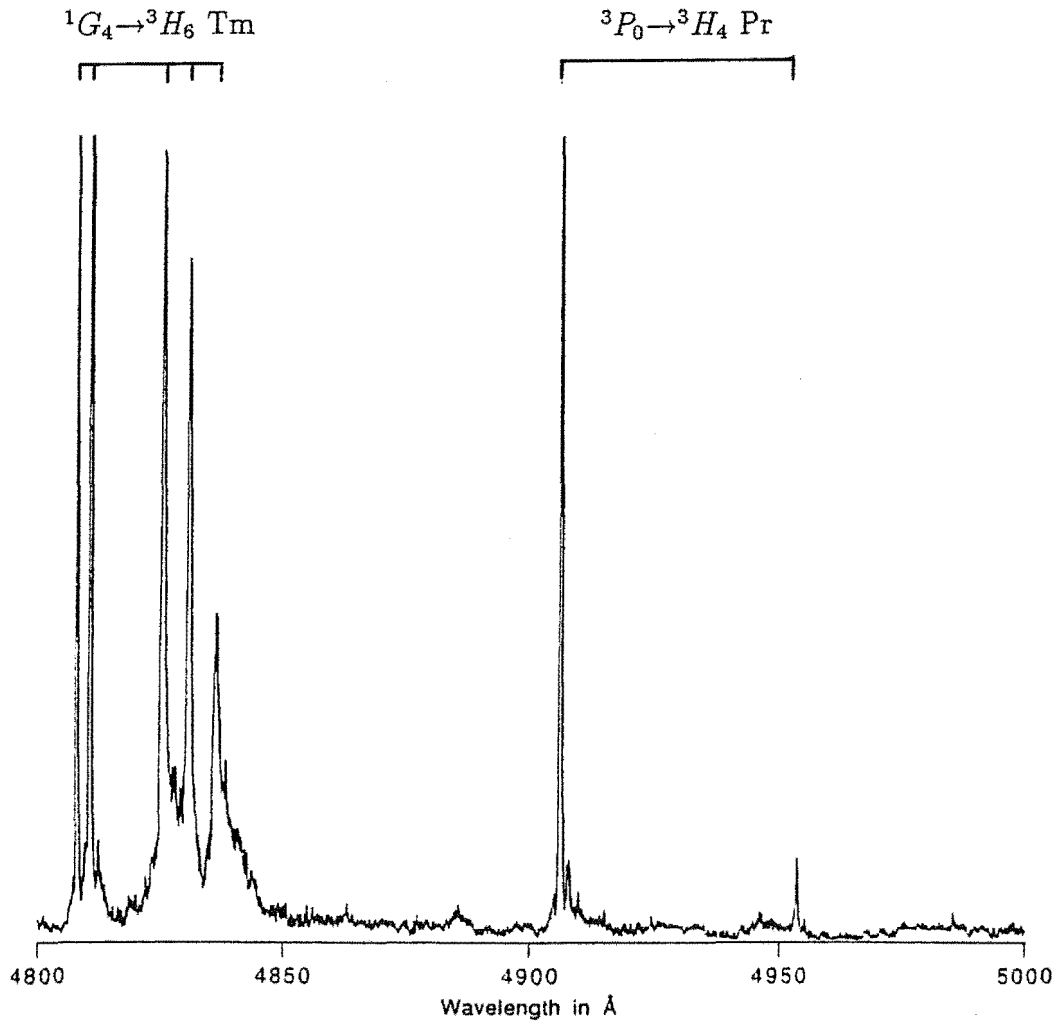

Figure 8.14: A fluorescence spectrum showing the $^1G_4 \rightarrow {}^3H_6$ transitions of thulium and the $^3P_0 \rightarrow {}^3H_4$ transitions of praseodymium, while exciting the Pr^{3+} ions to the $^3P_1$ multiplet, 4750Å, in the $CsCdBr_3$:Tm^{3+}:Pr^{3+} crystal.

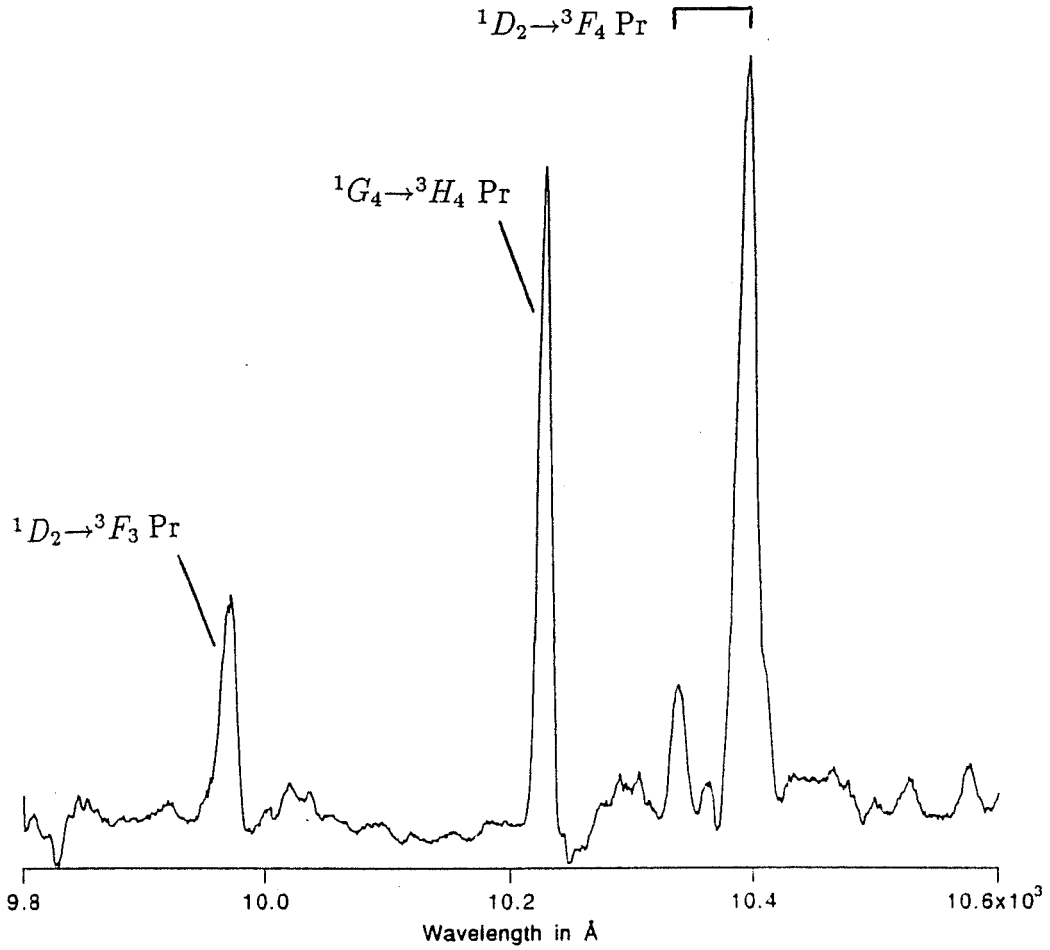

Figure 8.15: A fluorescence spectrum showing the $^1D_2 \rightarrow {}^3F_3$, $^1D_2 \rightarrow {}^3F_4$ and $^1G_4 \rightarrow {}^3H_4$ transitions of praseodymium, while exciting the Tm^{3+} ions to the $^3H_4$ multiplet, 7994Å, in the $CsCdBr_3$:Tm^{3+}:Pr^{3+} crystal.

while exciting the Tm^{3+} ions to the $^1G_4$ multiplet. The emission from praseodymium is a consequence of the cross relaxation from the $^1G_4$ multiplet of the Tm^{3+} ion to the $^3P_0$ multiplet of the Pr^{3+} ion, which has already been observed in excitation. This fluorescence is produced by the Pr^{3+} ions in heterogenous pairs. The fluorescence spectra obtained by selectively exciting the Pr^{3+} ions directly should also show emission from the homogeneous Pr^{3+} pairs, in which the Pr^{3+} ions are located in a slightly different crystal field. Careful comparison of the spectra obtained during blue selective excition of the Pr^{3+} and Tm^{3+} ions did not reveal any differences in the transition energies which could be attributed to these two distinct Pr^{3+} ion sites.

Figure 8.15 shows emission from the $^1G_4$ multiplet of praseodymium and the $^3H_4$ multiplet of thulium, while exciting the Tm^{3+} ions to the $^3H_4$ multiplet. This population of the $^1G_4$ multiplet of praseodymium is another example of cross relaxation in the heterogeneous pairs.

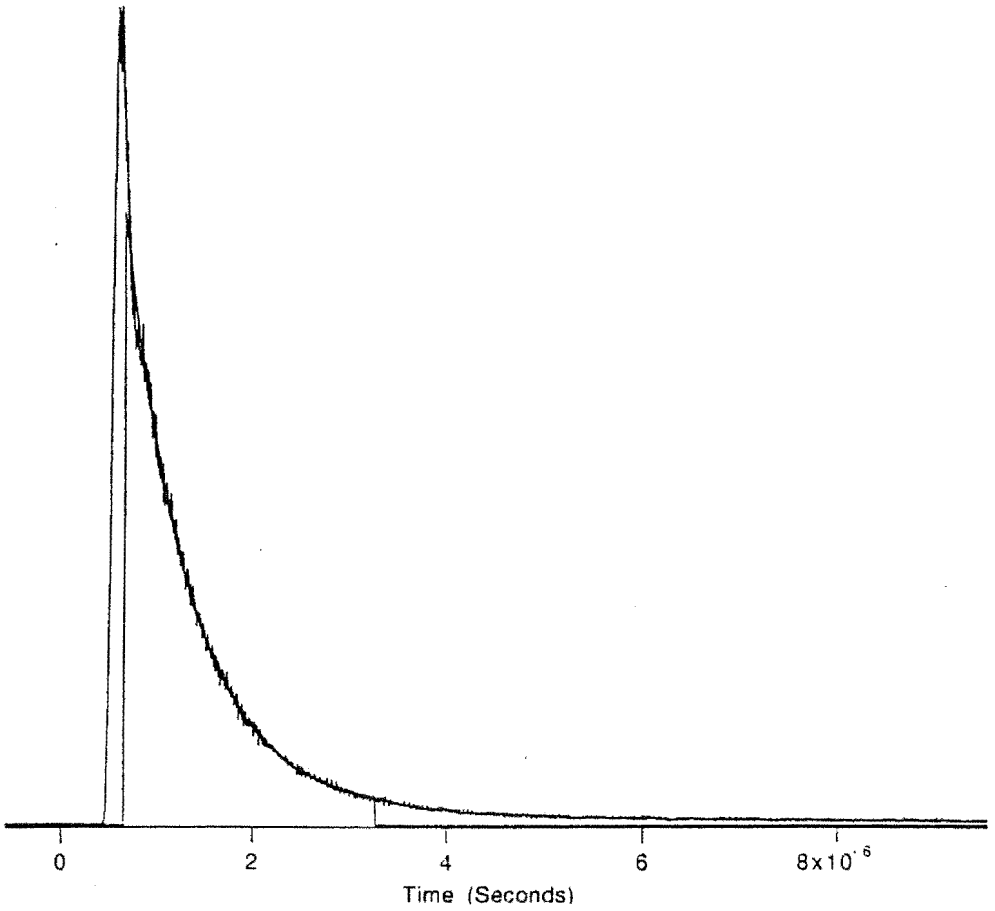

Figure 8.16: The transient of the $^3P_1 \rightarrow {}^3F_3$ transition of praseodymium at 6907Å, after excitation of the Pr^{3+} ions to the $^3P_1$ multiplet, 4750Å, in the $CsCdBr_3$:Pr^{3+}:Tm^{3+} crystal. This plot also shows a fit to a single-exponential decay function with τ = 680ns.

8.5.4 Fluoresence Transients

Figure 8.16 is the transient of the $^3P_1 \rightarrow {}^3F_3$ fluorescence of praseodymium after pulsed excitation of the Pr^{3+} ions to the $^3P_1$ multiplet. This multiplet has a very short fluorescence lifetime of (690±20)ns, which suggests that there is a quenching mechanism acting to relax the Pr^{3+} ions non-radiatively. The cross relaxation from the $^3P_1$ multiplet of praseodymium to the $^1G_4$ multiplet of thulium, which was observed spectroscopically, could well be responsible for this quenching.

Figure 8.17(a) is the transient of the $^3P_0 \rightarrow {}^3H_6$ fluorescence of praseodymium after excitation of the Pr^{3+} ions to the singlet $^3P_0$ state. The fluorescence lifetime of this state was found to be (15±1)μs. Figure 8.17(b) is the transient of the same transition while exciting the Pr^{3+} ions to the $^3P_1$ multiplet. Both the rise and decay curves fitted well to exponential functions, giving time-constants of (16±2)μs and (200±10)μs respectively. The former is clearly the radiative lifetime of the $^3P_0$ state

and the latter will be associated with some other excited state.

Figure 8.18(a) is the transient of the $^1G_4 \rightarrow {}^3H_4$ fluorescence of thulium after excitation of the Pr^{3+} ions to the $^3P_1$ multiplet. The decay curve fits well to a single-exponential function giving a time-constant of $(205\pm10)\mu$s. This suggests that the relaxation pathway which populates the $^3P_0$ multiplet consists of sequential cross relaxations, from the $^3P_1$ multiplet of praseodymium to the $^1G_4$ multiplet of thulium and then to the $^3P_0$ multiplet of praseodymium. This mechanism involves energy-transfer processes already identified from the spectroscopic observations and it accounts for the transient of the fluorescence from the $^3P_0$ state. The fluorescence lifetime of the $^1G_4$ multiplet of thulium in the heterogeneous centres can thus be identified with the 205μs decay. This is much less than the 570μs radiative decay time of the homogeneous Tm^{3+} pairs, as measured in the pure dopant crystal, due to the additional relaxation process involving Pr^{3+} ions.

The energy transfer from the $^3P_1$ multiplet of the Pr^{3+} ion to the $^1G_4$ multiplet of the Tm^{3+} ion has an energy mismatch of only $3cm^{-1}$. The energy transfer from the $^1G_4$ multiplet to the $^3P_0$ multiplet of the Pr^{3+} ion has an energy mismatch of $87cm^{-1}$. Both these transfer processes are exothermic. Figure 8.11(a) shows that the $^3P_0$ multiplet is populated very efficiently after excitation of the Pr^{3+} ions to the $^3P_1$ multiplet, which is good evidence for a high concentration of heterogeneous pair centres in this crystal.

Energy transfer from the $^3P_1$ multiplet to the $^3P_0$ multiplet should also occur in the homogeneous Pr^{3+} pair centres. This process would be exothermic, with an energy mismatch of only $5cm^{-1}$.

Figure 8.18(b) is the transient of the $^3F_3 \rightarrow {}^3H_6$ fluorescence of thulium after excitation of the Pr^{3+} ions to the $^3P_1$ multiplet. The rise time is very short. The decay curve, although rather like that of Figure 8.18(a), does not fit well to a single-exponential function. Figure 8.19(a) shows how the $^3F_3$ multiplet of the Tm^{3+} ion may be populated directly by cross relaxation from the $^3P_1$ multiplet of the Pr^{3+} ion. This mechanism would contribute to the quenching of the $^3P_1$ multiplet and may also explain the very short rise time of Figure 8.18(b). This energy transfer is exothermic, with an energy mismatch of $35cm^{-1}$.

Tm^{3+} ions which are excited to the $^1G_4$ multiplet, after energy transfer from the $^3P_1$ multiplet of praseodymium, could relax by populating the $^3F_3$ multiplet of thulium and the $^3F_3$ multiplet of praseodymium. This cross-relaxation mechanism is shown in Figure 8.19(b), and is rather like the mechanism which populates the $^3F_3$ multiplet in the $CsCdBr_3$:Tm^{3+} crystal, Figure 8.7. The energy transfer is endothermic, with an energy mismatch of $8cm^{-1}$. This mechanism accounts for the long-decay curve of Figure 8.18(b), which will be a function of both the changing population of the $^1G_4$ multiplet of thulium and the radiative lifetime of the $^3F_3$ multiplet of thulium. The cross-relaxation mechanisms shown in Figures 8.19(a) and (b) both populate the $^3F_3$ multiplet of thulium, after excitation of the Pr^{3+} ions to the $^3P_1$ multiplet.

Figure 8.8 shows that the $^3F_3$ multiplet of thulium is also populated after

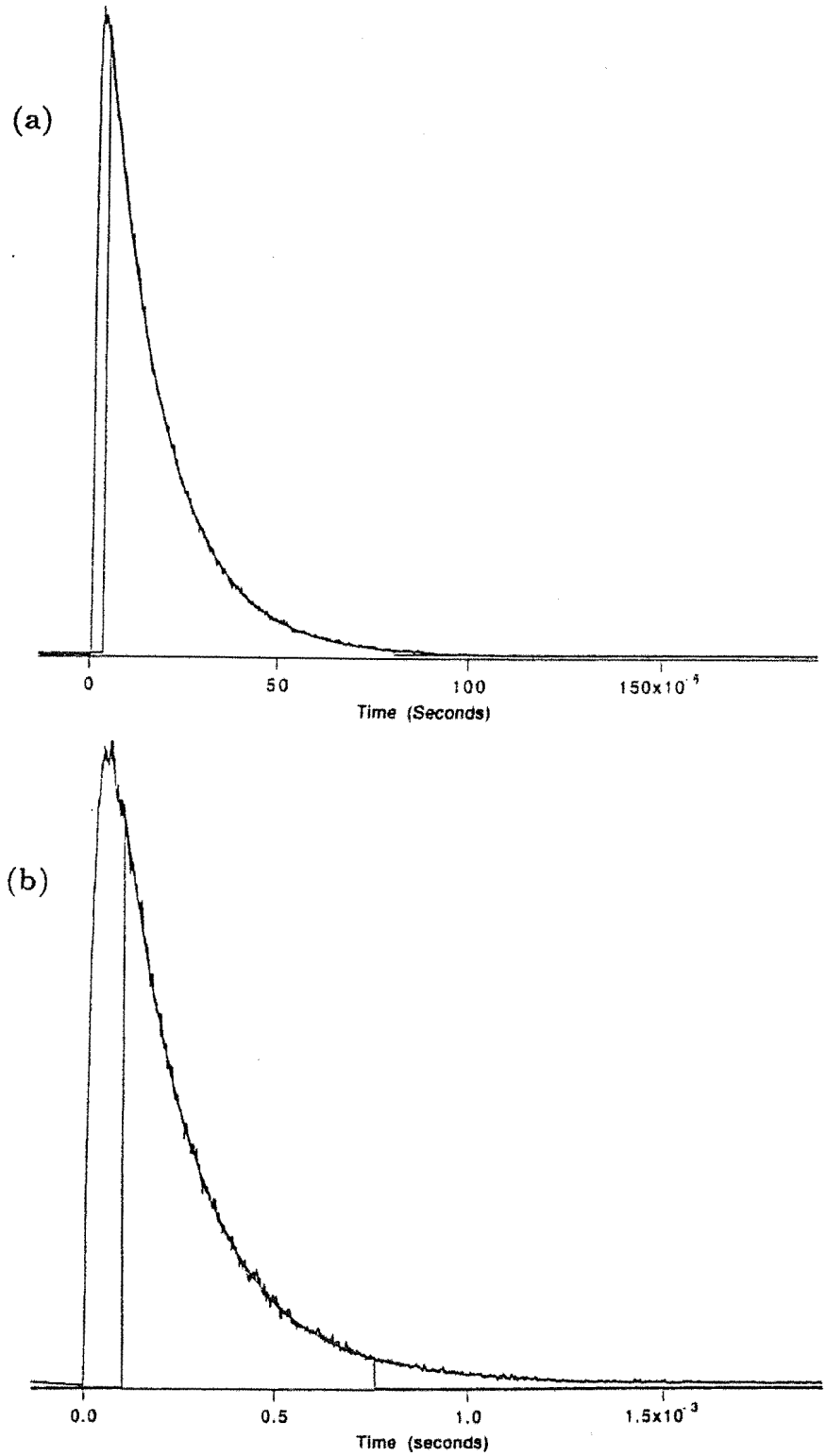

Figure 8.17: Transients of the $^3P_0 \rightarrow {}^3H_6$ transition of praseodymium at 6244Å, after excitation of the Pr^{3+} ions to (a) the $^3P_0$ multiplet, 4903Å, and (b) the $^3P_1$ multiplet, 4750Å, in the $CsCdBr_3$:Tm^{3+}:Pr^{3+} crystal. These plots also show fits to single exponential decay functions with (a) $\tau = 15.8\mu s$ and (b) $\tau = 201\mu s$.

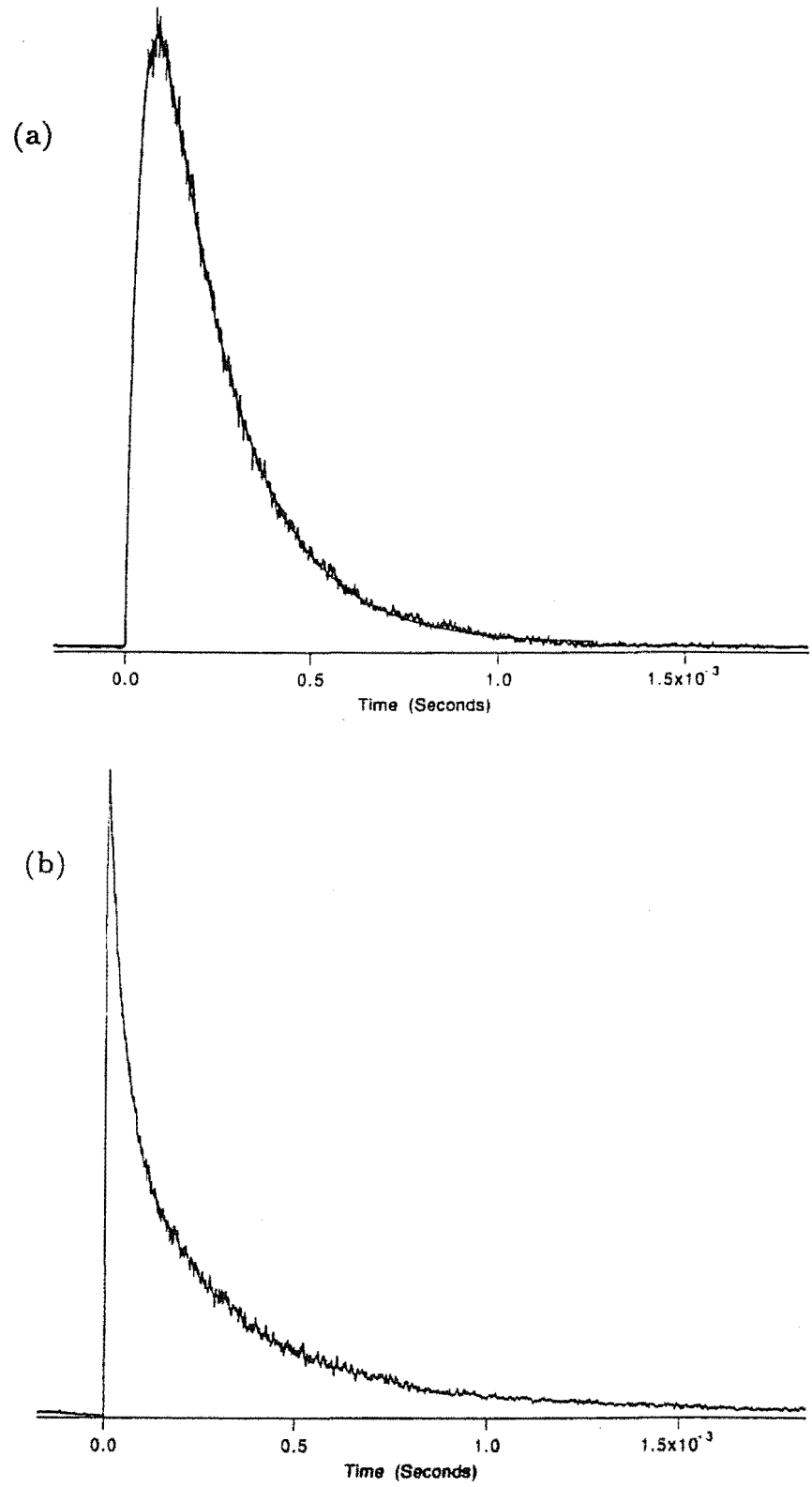

Figure 8.18: Transients of (a) the $^1G_4 \rightarrow {}^3H_6$ transition of thulium at 4825Å and (b) the $^3F_3 \rightarrow {}^3H_6$ transition of thulium at 6975Å, after excitation of the Pr^{3+} ions to the $^3P_1$ multiplet, 4750Å, in the $CsCdBr_3$:Tm^{3+}:Pr^{3+} crystal.

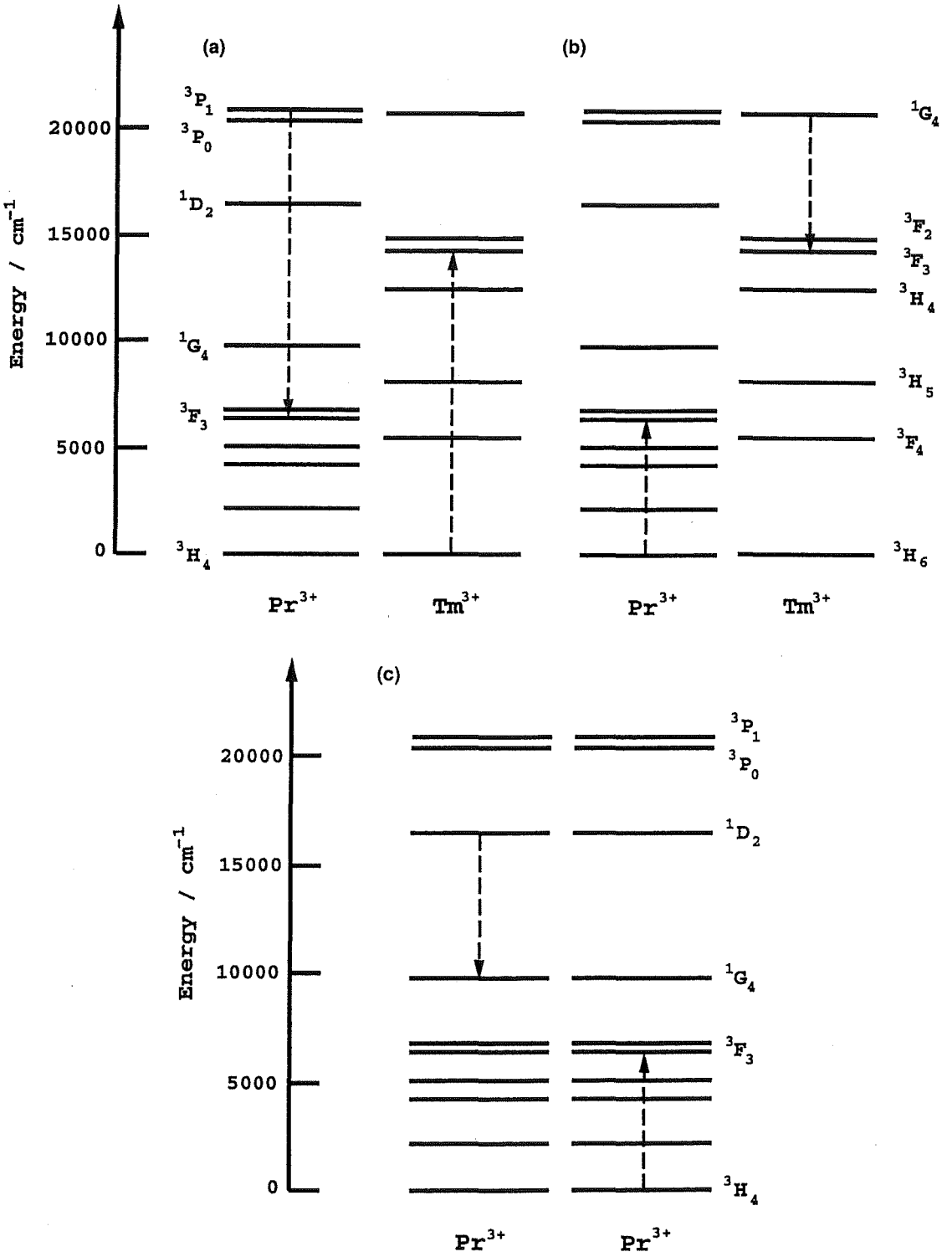

Figure 8.19: Proposed cross-relaxation mechanisms which relax (a) Pr^{3+} ions excited to the $^3P_1$ multiplet and (b) Tm^{3+} ions excited to the $^1G_4$ multiplet and populate the $^3F_3$ multiplet of thulium in the heterogeneous pair centres. (c) The proposed cross relaxation mechanism which relaxes Pr^{3+} ions excited to the $^1D_2$ multiplet and populates the $^1G_4$ and $^3F_3$ multiplets of praseodymium in homogeneous Pr^{3+} pair centres.

excitation of the $^3P_0$ multiplet of praseodymium. This observation too can be explained by a cross relaxation, from the $^3P_0$ multiplet of the Pr^{3+} ion to the $^3F_2$ multiplet of thulium and the $^3F_2$ multiplet of praseodymium. The energy transfer is exothermic, with an energy mismatch of 210cm^{-1}. The fluorescence lifetime of the $^3P_0$ multiplet of the Pr^{3+} ion has been measured, and was found to be (19±1)μs in the $CsCdBr_3$:Pr^{3+} crystal and (15±1)μs in the $CsCdBr_3$:Pr^{3+}:Tm^{3+} crystal. Ramaz has also reported the former as 20μs [73]. This reduction in the fluorescence lifetime of the $^3P_0$ multiplet, in the presence of the Tm^{3+} ions, may be attributable to this cross relaxation.

Figure 8.20 is the transient of the $^1D_2 \rightarrow {}^3H_4$ fluorescence after excitation of the Pr^{3+} ions to the $^3P_1$ multiplet. The rise time is very short. This is consistent with the efficient cross-relaxation mechanism proposed in Figure 8.10(a), where the $^1D_2$ multiplet is populated by cross relaxation from the $^3P_1$ multiplet. The decay curve does not fit well to a single-exponential function, although the tail of the decay has a time-constant of (450±50)μs. This is significantly longer than the 150μs fluorescence lifetime of the $^1D_2$ multiplet in the pure dopant crystal, determined by exciting the $^1D_2$ multiplet directly [73].

Cross-relaxation mechanisms might occur in homogeneous Pr^{3+} pair centres to depopulate the $^1D_2$ multiplet, Figure 8.19(c). This would reduce the $^1D_2$ multiplet fluorescence lifetime. The energy transfer which populates the $^1G_4$ and $^3F_3$ multiplets of praseodymium would be exothermic, with an energy mismatch of less than 233cm^{-1}. However, when the $^1D_2$ multiplet has been populated by cross relaxation from the $^3P_1$ multiplet, this relaxation pathway will not be available until the other Pr^{3+} ion has relaxed completely to the ground state. Since the cross relaxation excites the other ion to the $^3H_6$ multiplet, the decay time of the $^3H_6$ multiplet will affect the $^1D_2$ fluorescence lifetime. If the lifetime of the $^3H_6$ multiplet is at least the same order of magnitude as the 150μs lifetime of the $^1D_2$ multiplet, then the fluorescence lifetime of the $^1D_2$ multiplet will be longer for ^3P_J multiplet excitation than for direct excitation, as was observed.

When the radiative lifetimes of the $^3P_1$ and $^3P_0$ multiplets of praseodymium had been experimentally determined it was possible to establish the identity of the group of 'unidentified' transitions which were reported by Foo. Those at 18132cm^{-1} and 18075cm^{-1} (energies in air) are $^3P_0 \rightarrow {}^3H_5$ transitions and those at 18415cm^{-1} and 18700cm^{-1} are $^3P_1 \rightarrow {}^3H_5$ transitions. These assignments were confirmed using the energy levels of Ramaz [73].

8.6 Single-Laser Upconversion Spectroscopy

8.6.1 Infrared Excitation of Tm^{3+} Ions

The infrared $^3H_6 \rightarrow {}^3H_4$ absorption transitions of thulium are relatively strong and suitable for pumping with IR diode lasers [6]. The $^3H_4$ multiplet can also be populated efficiently by energy transfer from excited Cr^{3+} ions and there is much interest

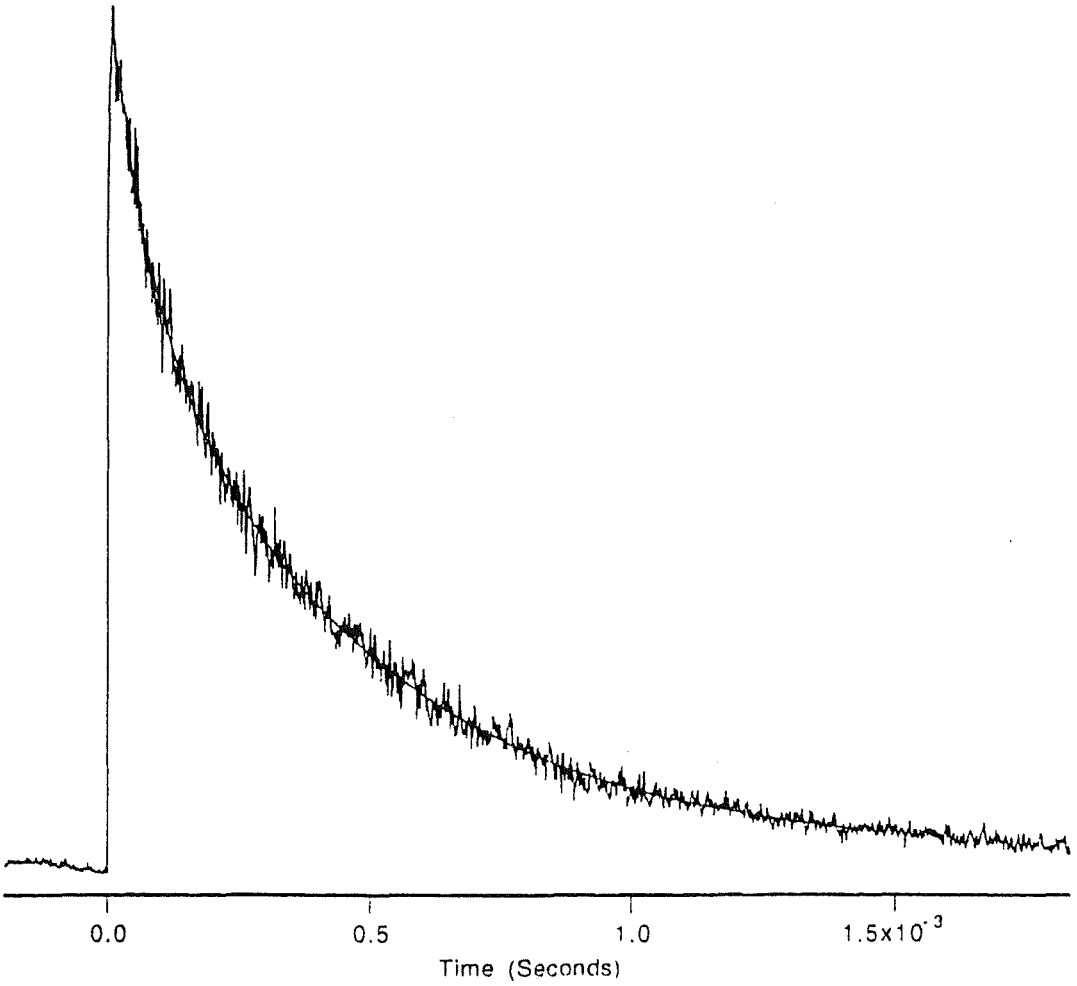

Figure 8.20: The transient of the $^1D_2 \rightarrow {}^3H_4$ transition of praseodymium at 6048Å, after excitation of the Pr^{3+} ions to the $^3P_1$ multiplet, 4750Å, in the $CsCdBr_3$:Pr^{3+}:Tm^{3+} crystal.

in finding efficient upconversion mechanisms which exploit this favourable excitation channel. In this study upconversion fluorescence has been observed from several excited states of thulium after excitation to the $^3H_4$ multiplet. These upconversion experiments will be described in this section.

Armagan et al [6] have studied the energy-transfer processes of IR pumped Tm^{3+} ions in YAG:Tm^{3+} crystals. They discovered that the $^3H_4$ multiplet is depopulated very efficiently by a cross-relaxation mechanism, which in turn populates the $^3F_4$ multiplet of both the ions involved in the transfer. This cross relaxation has also been observed in other thulium hosts. However, the energy transfer has a large energy mismatch ($900cm^{-1}$ in $CsCdBr_3$), so it is unlikely to be very efficient in $CsCdBr_3$ because of the low phonon cut-off energy ($163cm^{-1}$). No evidence was found for the occurence of this cross relaxation during these experiments.

8.6.2 Upconversion Spectroscopy of $CsCdBr_3$:Tm^{3+}

Figures 8.21(a) and 8.21(b) are polarised excitation spectra showing the absorption transitions to the $^3H_4$ multiplet, while monitoring the $^1G_4 \rightarrow {}^3H_6$ fluorescence. These upconversion excitation spectra can be compared with the excitation spectra of Figure 8.3, which were obtained by monitoring the emission from the $^3H_4$ multiplet itself. The laser pulse has a duration of 9ns and a repetition rate of 10Hz, so it is unlikely that the $^1G_4$ multiplet is being populated by sequential absorption. The $^1G_4$ multiplet has nearly twice the energy of the $^3H_4$ pump state. Thus an upconversion mechanism populating the $^1G_4$ multiplet by coperative absorption requires the excitation of at least two Tm^{3+} ions by the same laser pulse.

Figure 8.22 is an upconversion fluorescence spectrum showing the $^3F_3 \rightarrow {}^3H_6$ and the $^1D_2 \rightarrow {}^3F_4$ transitions, while exciting the Tm^{3+} ions to the $^3H_4$ multiplet. To populate the $^1D_2$ multiplet, at approximately $27500cm^{-1}$, by a coperative-upconversion mechanism requires that at least three Tm^{3+} ions are excited by the laser pulse. Thus the observation of this emission from the $^1D_2$ multiplet indicates that energy can also be transfered between the Tm^{3+} pairs. Inter-pair energy transfer producing upconversion has also reported by Cockroft et al [23] for $CsCdBr_3$:Er^{3+} crystals.

The transition energies in Figure 8.22(b) can be used to determine energy levels of the $^1D_2$ multiplet. The energy levels of the $^3F_4$ multiplet are listed in Table 8.1. Fluorescence from two of the $^1D_2$ multiplet levels is apparent in this spectrum, at $27337cm^{-1}$ and $27380cm^{-1}$. A multiplet with J=2 will have three levels in a site of C_{3v} symmetry.

Figure 8.23(a) is the transient of the $^3H_4 \rightarrow {}^3H_6$ fluorescence after excitation of the Tm^{3+} ions to the $^3H_4$ multiplet. The fluorescence lifetime of the $^3H_4$ multiplet, $(960\pm30)\mu s$, was found by fitting the transient to a single-exponential function. This can be compared with the transient of the $^3F_3 \rightarrow {}^3H_6$ upconversion fluorescence, Figure 8.23(b), also following excitation to the $^3H_4$ multiplet. The tail of the $^3F_3$ multiplet decay is somewhat faster than the $^3H_4$ multiplet decay. It was observed

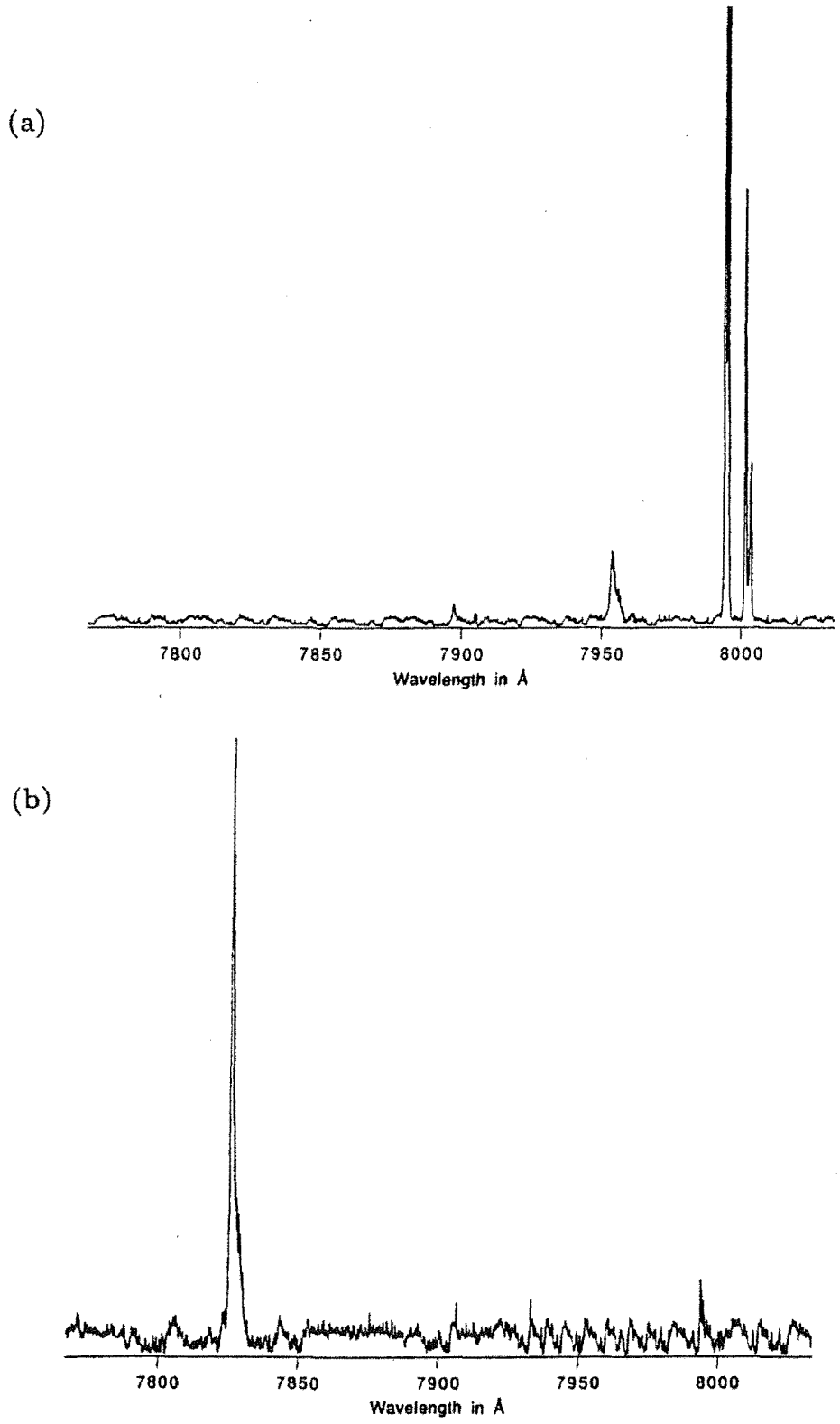

Figure 8.21: The (a) σ and (b) π-absorption transitions to the $^3H_4$ multiplet of thulium, while monitoring the $^1G_4 \rightarrow {}^3H_6$ transition at 4826Å in the $CsCdBr_3$:Tm^{3+} crystal.

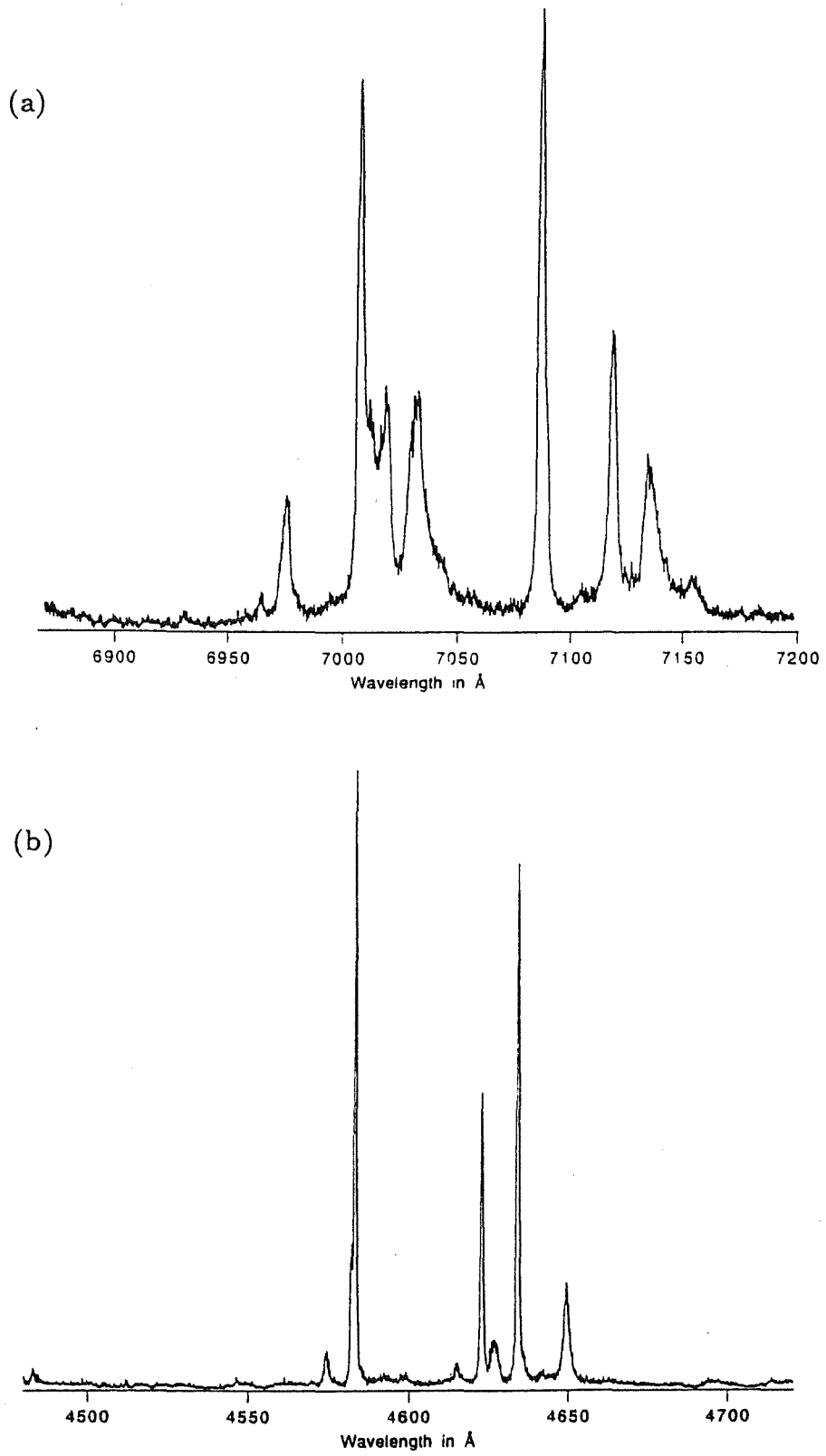

Figure 8.22: Upconversion fluorescence spectra showing (a) the $^3F_3 \rightarrow {}^3H_6$ and (b) the $^1D_2 \rightarrow {}^3F_4$ transitions, while exciting the Tm^{3+} ions to the $^3H_4$ multiplet in the $CsCdBr_3$:Tm^{3+} crystal.

that fluorescence transitions from the $^1G_4$ and $^3F_3$ multiplets have very similar transients, as was the case when the Tm^{3+} ions were excited to the $^1G_4$ multiplet directly. This suggests that the population of the $^3F_3$ multiplet is again being fed from the $^1G_4$ multiplet by cross relaxation.

A possible upconversion mechanism for populating the $^1G_4$ multiplet is given in Figure 8.24. This mechanism is favoured because it is consistent with the experimental observations already described, involves a small energy mismatch of $120cm^{-1}$, and only requires the excitation of two Tm^{3+} ions. Inter-pair energy transfer is not necessary to achieve upconversion.

Again rate equations can be used to interpret the transient of the upconversion fluorescence. N_d represents the number of pair centres in which both ions are excited by the laser pulse [$^3H_4$:$^3H_4$], N_p the number of [$^3H_4$:$^3H_5$] excited pairs, N_4 the $^1G_4$ multiplet population, W_t the energy transfer rate, W_{32} the $^3H_4 \rightarrow {}^3H_5$ transition rate, and W_i the fluorescence decay rate of multiplet i in the abscence of energy transfer. The rate equations needed to describe this mechanism are:

$$\begin{aligned} \dot{N}_d &= -2W_3N_d \\ \dot{N}_p &= 2W_{32}N_d - (W_2 + W_3)N_p - W_tN_p \\ \dot{N}_4 &= W_tN_p - W_4N_4 \,. \end{aligned}$$

These equations can be solve for the transient population of the $^1G_4$ multiplet, which has a solution of the form:

$$N_4(t) = Ae^{-2W_3t} + Be^{-(W_2+W_3+W_t)t} + Ce^{-W_4t}\,, \tag{8.3}$$

where A, B, and C are real valued functions of the various rate constants.

Figure 8.23(b) is dominated by a single rise and decay curve. This is the characteristic transient for energy-transfer processes where the various rate constants, represented in the three exponential terms of Equation 8.3, are of different orders of magnitude [87]. The time constant of the decay curve is determined by the 'slowest' exponetial term. A careful comparison with Figure 8.23 (a) shows that this is the first term of Equation 8.3, which is associated with the fluorescence lifetime of the $^3H_4$ multiplet.

Thus the rise curve of Figure 8.23 (b) corresponds to either the second or third term in Equation 8.3, whichever is smallest. The third term is associated with the fluorescence lifetime of $^1G_4$ multiplet. If the $^3F_3$ multiplet is being populated by cross relaxation from the $^1G_4$ multiplet, then the lifetime of the $^1G_4$ multiplet is less than $10\mu s$. This has already been demonstrated by exciting the $^1G_4$ multiplet directly. In this case the time constant of the rise curve will be determined by both the fluorescence lifetime of the $^3H_5$ multiplet and by the rate constant of the energy transfer which populates the $^1G_4$ multiplet.

The $^3H_4 \rightarrow {}^3H_5$ step in Figure 8.24 must be radiative since there are no cross relaxation or upconversion mechanisms which can populate the $^3H_5$ multiplet without a significant mismatch of energy. Thus the efficiency of this upconversion

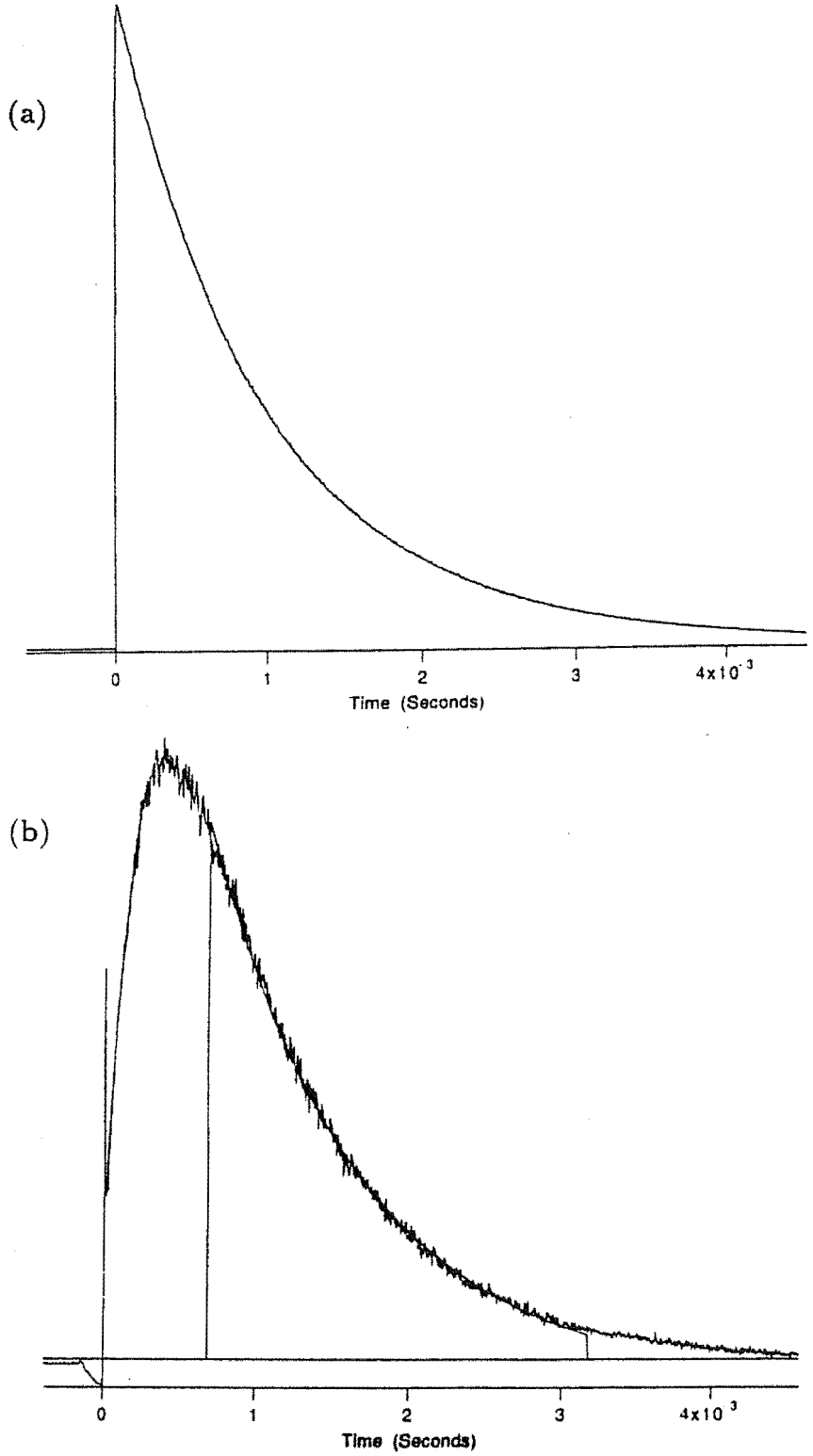

Figure 8.23: Transients of (a) the $^3H_4 \rightarrow {}^3H_6$ transition at 8027$\mathring{A}$ and (b) the $^3F_3 \rightarrow {}^3H_6$ transition at 7082$\mathring{A}$, after excitation of the Tm^{3+} ions to the $^3H_4$ mutiplet in the $CsCdBr_3$:Tm^{3+} crystal. This plot also shows the fit to a single exponential decay function with $\tau = 989\mu s$.

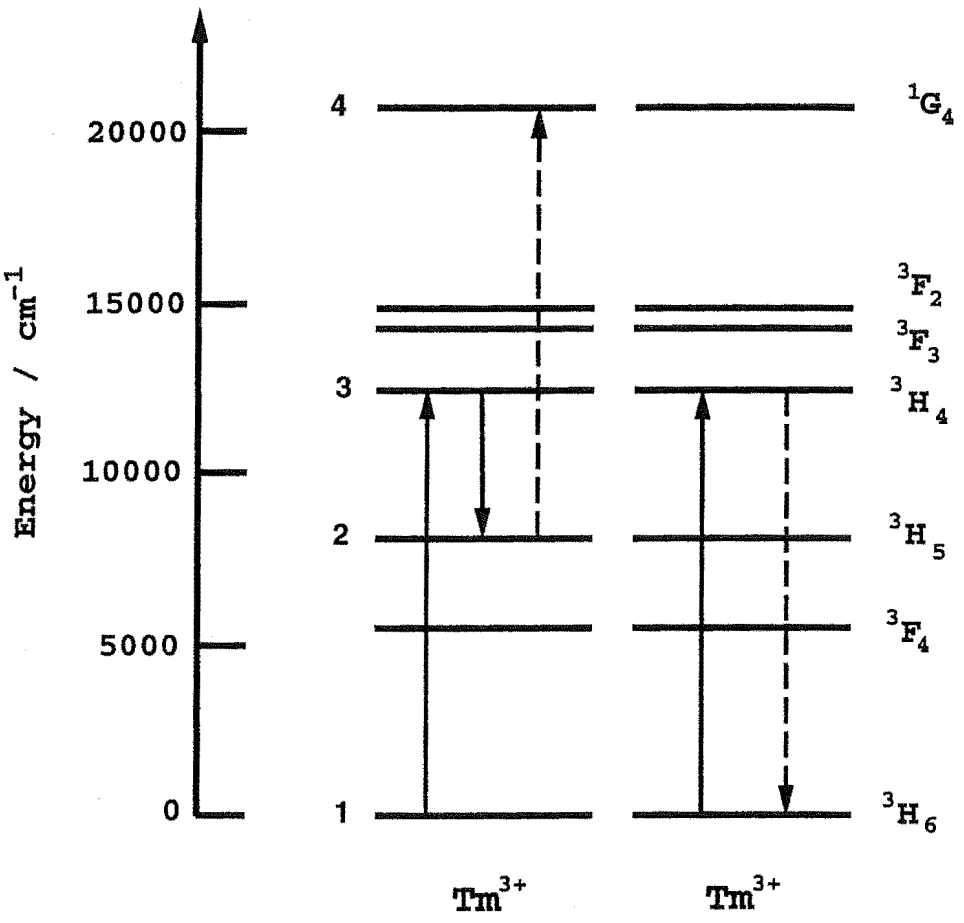

Figure 8.24: The proposed upconversion mechanism which populates the $^1G_4$ multiplet, after excitation of the Tm^{3+} ions to the $^3H_4$ multiplet in the homogeneous Tm^{3+} pair centres.

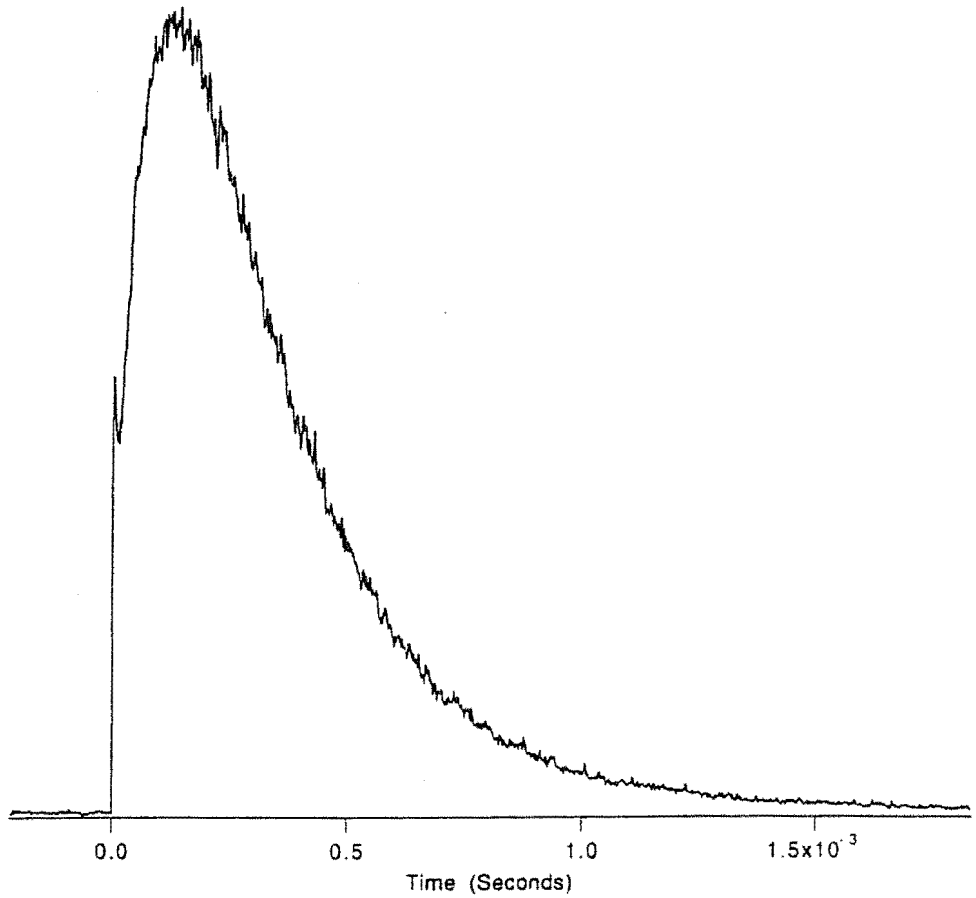

Figure 8.25: The transient of the $^1D_2 \rightarrow {}^3F_4$ transition at 4634Å, after excitation of the Tm^{3+} ions to the $^3H_4$ multiplet, 7995Å, in the $CsCdBr_3$:Tm^{3+} crystal.

process will be determined, in part, by the branching ratio for the $^3H_4 \rightarrow {}^3H_5$ fluorescence. This transition probability has been found to be quite low for thulium in other hosts; being 3% in both a fluorozironate glass [66] and a barium-thorium glass [95].

Figure 8.25 is the transient of the $^1D_2 \rightarrow {}^3F_4$ fluorescence after excitation of the Tm^{3+} ions to the $^3H_4$ multiplet. This transient has a faster decay curve than Figure 8.23 (b). A possible upconversion mechanism for populating the $^1D_2$ multiplet is given in Figure 8.26. The $^3F_2$ multiplet is populated by the cross relaxation of a Tm^{3+} ion. Figure 8.7, which has been excited to the $^1G_4$ multiplet by the upconversion mechanism already described. An energy transfer between two Tm^{3+} pairs is required to populate the $^1D_2$ multiplet. From the $^1D_2$ multiplet energy levels determined above, this energy transfer will be exothermic with an energy mismatch of only $8cm^{-1}$. However, an energy transfer between two pair centres will be less efficient than a transfer which occurs between the two ions of a pair.

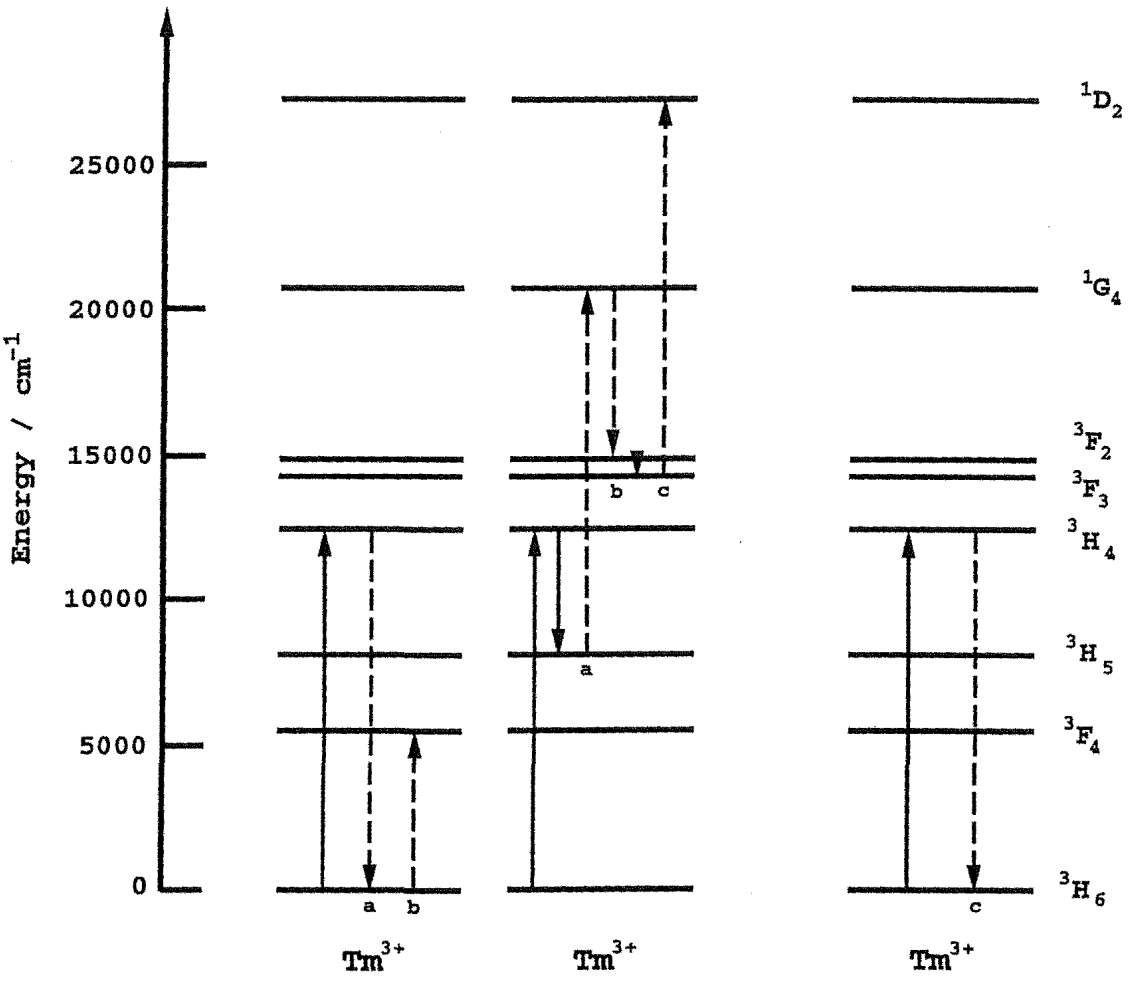

Figure 8.26: The proposed upconversion mechanism which populates the $^1D_2$ multiplet, after excitation of the Tm^{3+} ions to the $^3H_4$ multiplet in the $CsCdBr_3$:Tm^{3+} crystal.

Interpreting the transient of the $^1D_2$ multiplet fluorescence, Figure 8.25 (a), is very difficult since this is a complicated function of the rate constants for the upconversion mechanism populating the $^3F_3$ multiplet, the $^1D_2$ and $^3F_3$ multiplet fluorescence lifetimes, and the rate associated with the energy transfer which populates the $^1D_2$ multiplet. In addition the efficiency of this energy transfer is a function of the separation between the Tm^{3+} ion dimer pairs. It is difficult to account for this spatial dependance in a simple model as this distance is not a constant, although it may be reduced to a few discrete values since the inter-pair transfer processes will only be efficient for relatively small separations.

8.6.3 Upconversion spectroscopy of $CsCdBr_3$:Tm^{3+}:Pr^{3+}

The blue fluorescence from the $CsCdBr_3$:Tm^{3+}:Pr^{3+} crystal, which was observed during excitation of the Tm^{3+} ions to the $^3H_4$ multiplet, was visually much brighter than that from the $CsCdBr_3$:Tm^{3+} crystal, for the same excitation conditions of wavelength and power. This result was unexpected as the pure crystal has a higher thulium concentration and it suggests the occurrence of upconversion processes in the mixed crystal which either involve Pr^{3+} ions directly or are enhanced by the presence of Pr^{3+} ions.

Figure 8.27 is a pair of excitation spectra showing the absorption transitions to the $^3H_4$ multiplet of thulium, while monitoring (a) the $^3P_0 \rightarrow {}^3H_4$ fluorescence of praseodymium and (b) the $^1G_4 \rightarrow {}^3H_6$ fluorescence of thulium. The Tm^{3+} ions should reside in both homogeneous and heterogeneous pair centres. However, a careful comparison of these excitation spectra reveals no differences in the transition energies which can be ascribed to the two different Tm^{3+} ion sites. Fine excitation scans over just the 7825Å absorption transition while monitoring the fluorescence from the $^1G_4$ multiplet of thulium, in the pure and mixed-dopant crystals, and from the $^3P_0$ multiplet of praseodymium, in the mixed crystal, also failed to show any such shifts in the excitation energies. This result establishes an upper limit on any such shifts of $0.5cm^{-1}$.

Other experimenters have reported similar results from their studies of $CsCdBr_3$:RE^{3+} crystals. Mujaji [62] has studied the transitions of Ho^{3+} ions in homogeneous pair centres and in Ho^{3+}-Na^+ centres. She found that the transition energies of these two centres differed by less than the inhomogeneously-broadened linewidths. Barthem el al [12] studied centres in which Nd^{3+} ions are paired with the monovalent metals Li^+, Na^+ and Ag^+, which have ionic radii of 0.68Å, 0.97Å and 1.26Å respectively. They report that the Nd^{3+} ion transitions of these different centres display small shifts in their energies. The excitation spectra which appear in their paper show that these energy shifts are less than $0.1cm^{-1}$. Barthem et al also report that the spectral lines of pair and single Nd^{3+} ions associated with the same optical transition are separated by only a few cm^{-1} [12]. The same result was found for the transitions of Pr^{3+} ions in pair and single ion centres by Chaminade et al [20].

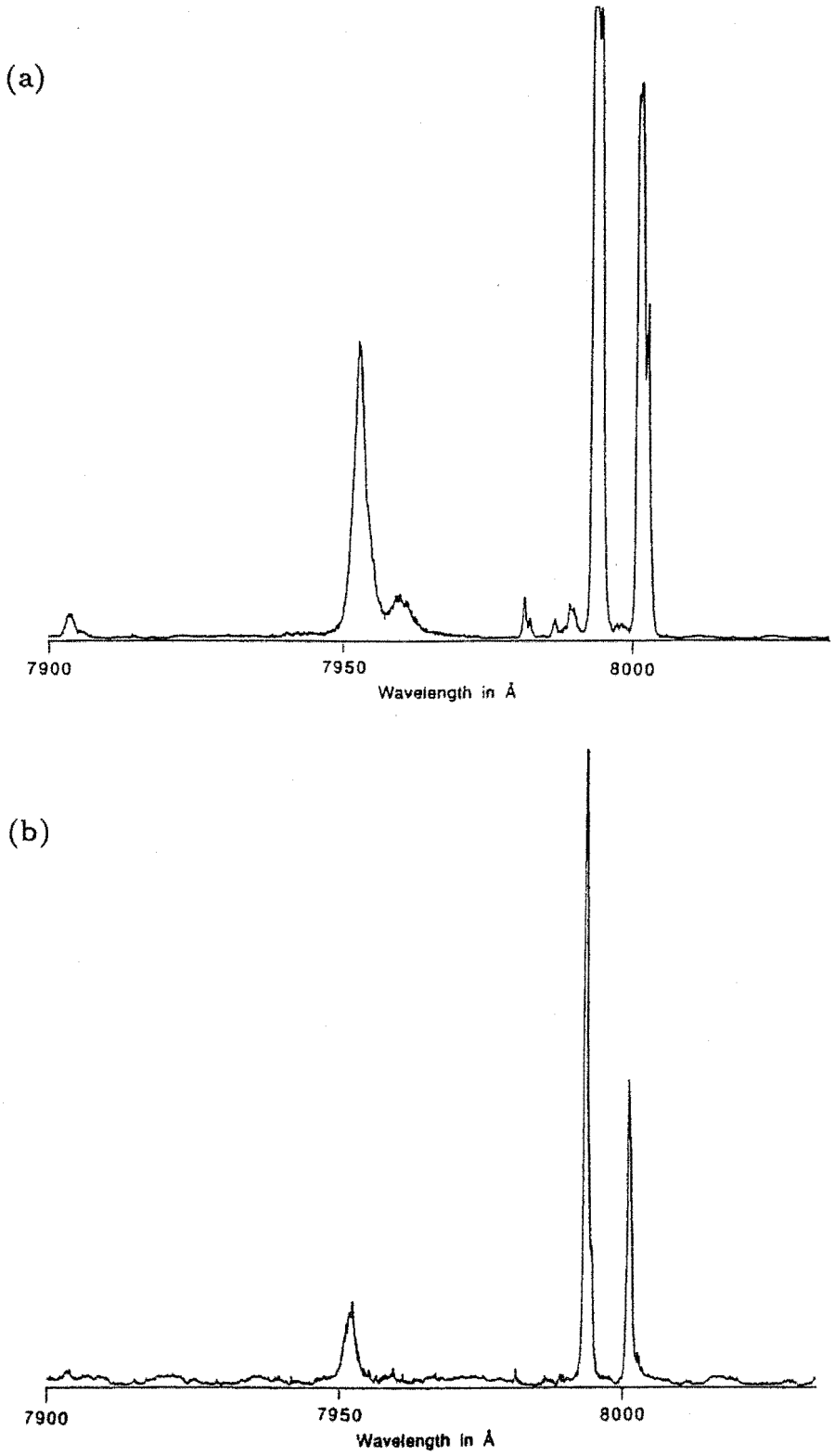

Figure 8.27: The absorption transitions to the $^3H_4$ multiplet of thulium, while monitoring (a) the $^3P_0 \rightarrow {}^3H_4$ transition of praseodymium at 4901Å and (b) the $^1G_4 \rightarrow {}^3H_6$ transition of thulium at 4826Å in the $CsCdBr_3$:Tm^{3+}:Pr^{3+} crystal.

From these observations it is apparent that the energy levels of rare-earth ions in $CsCdBr_3$ are not significantly affected by the size of neighbouring ions located on the C_{3v} axis of symmetry. In particular the nature of the ions providing the localised charge compensation do not appear to affect significantly the crystal field experienced by the trivalent rare-earth ions. This suggests that the axial perturbation of the crystal field is small compared to the total crystal field at the site of the trivalent impurity. This is consistant with the crystal-field fits of Barthem et al [11] and Ramaz [73] who used a crystal-field Hamiltonian which was composed of an O_h cubic part with only a small C_{3v} trigonal distortion.

Figure 8.28 shows upconversion fluorescence transitions from the $^1G_4$ multiplet of thulium and the $^3P_0$ multiplet of praseodymium while exciting the Tm^{3+} ions to the $^3H_4$ multiplet. This fluorescence spectrum can be compared with Figure 8.14, which was obtained by exciting the Pr^{3+} ions to the $^3P_1$ multiplet directly. Two additional spectral features occur in the upconversion fluorescence spectrum, only one of which could be identified. Upconversion fluorescence was also found from the $^1D_2$ multiplet of thulium and from the $^1D_2$ multiplet of praseodymium.

Figure 8.29 shows upconversion fluorescence from the $^3P_1$, $^3P_0$, and $^1D_2$ multiplets of praseodymium while exciting the Tm^{3+} ions to the $^3H_4$ multiplet. This can be compared to Figure 8.11(a), where the Pr^{3+} ions were excited to the $^3P_1$ multiplet directly. The integrated intensity of the upconversion fluorescence from the $^1D_2$ multiplet is much greater than that from the $^3P_1$ and $^3P_0$ multiplets, in Figure 8.29. This suggests that $^1D_2$ is being populated by a quite different upconversion mechanism to that which is populating the higher praseodymium multiplets.

Figure 8.30(a) is the transient of the $^1G_4 \rightarrow {}^3H_6$ fluorescence of thulium after excitation of the Tm^{3+} ions to the $^3H_4$ multiplet. It has a very similar decay curve to Figure 8.23(b), which is the transient observed in the $CsCdBr_3$:Tm^{3+} crystal, but the rise curve is much faster. This suggests that the main upconversion mechanism for populating the $^1G_4$ multiplet of thulium in the $CsCdBr_3$:Tm^{3+}:Pr^{3+} crystal involves the Pr^{3+} ions. The transients of the fluorescence from the $^1G_4$ and $^3F_3$ multiplets of thulium are very similar, as was the case for upconversion in the pure Tm^{3+} dopant crystal. This suggests that the $^3F_3$ multiplet is again being populated by the relaxation of Tm^{3+} ions from the $^1G_4$ multiplet. When this occurs in a heterogeneous pair centre the cross relaxation populates the $^3F_3$ multiplet of thulium and the $^3F_3$ multiplet of praseodymium, Figure 8.19.

Figure 8.30(b) is the transient of the $^3P_0 \rightarrow {}^3H_4$ fluorescence of praseodymium after excitation of the Tm^{3+} ions to the $^3H_4$ multiplet. The decay curve is faster than that for the $^1G_4$ multiplet fluorescence transient of thulium. This suggests that the $^3P_0$ multiplet is not being populated simply by the cross relaxation of thulium ions excited to the $^1G_4$ multiplet.

Figure 8.32(a) is the transient of the $^1G_4 \rightarrow {}^3H_4$ fluorescence of praseodymium after excitation of the Tm^{3+} ions to the $^3H_4$ multiplet. It has been included because the $^1G_4$ multiplet of praseodymium is a possible intermediate-storage state for the upconversion mechanisms which involve Pr^{3+} ions. The slow-decay curve shows that

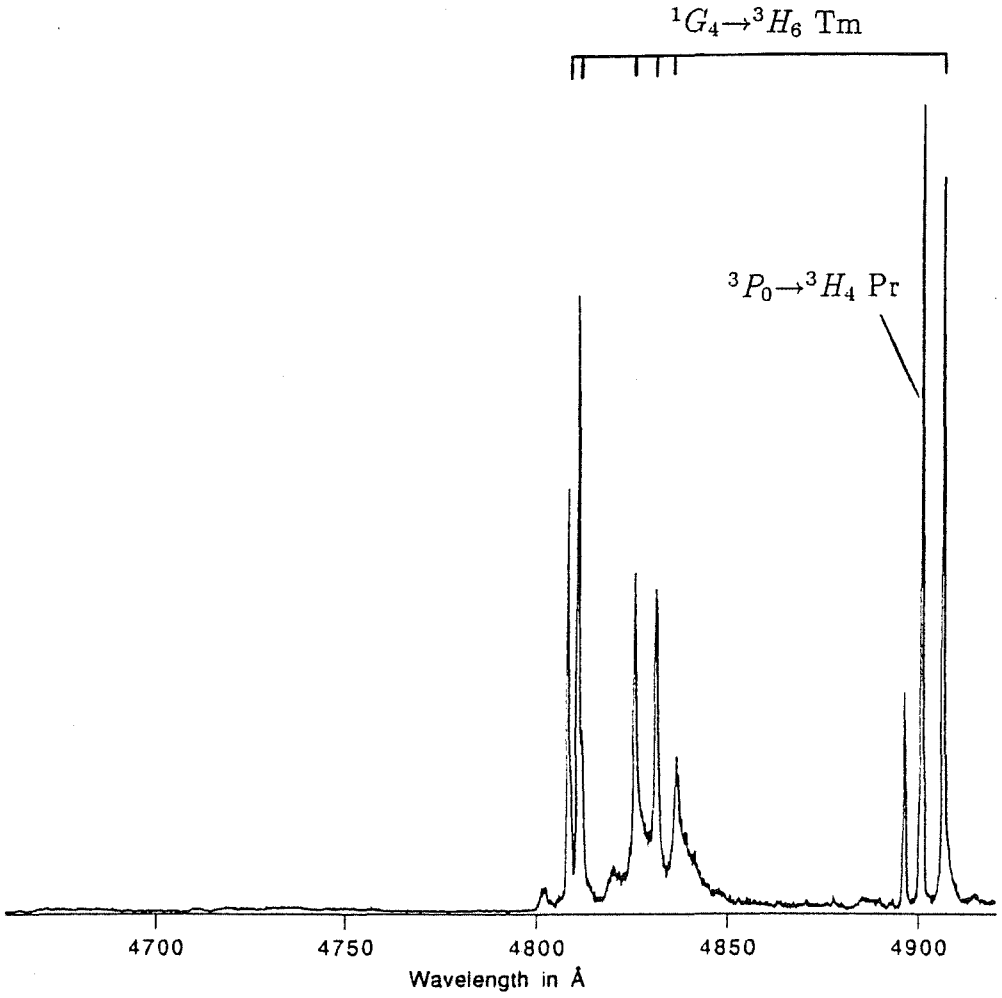

Figure 8.28: An upconversion fluorescence spectrum showing the $^1G_4 \rightarrow {}^3H_6$ transitions of thulium and the $^3P_0 \rightarrow {}^3H_4$ transitions of praseodymium, while exciting the Tm^{3+} ions to the $^3H_4$ multiplet, 7825Å, in the $CsCdBr_3$:Tm^{3+}:Pr^{3+} crystal.

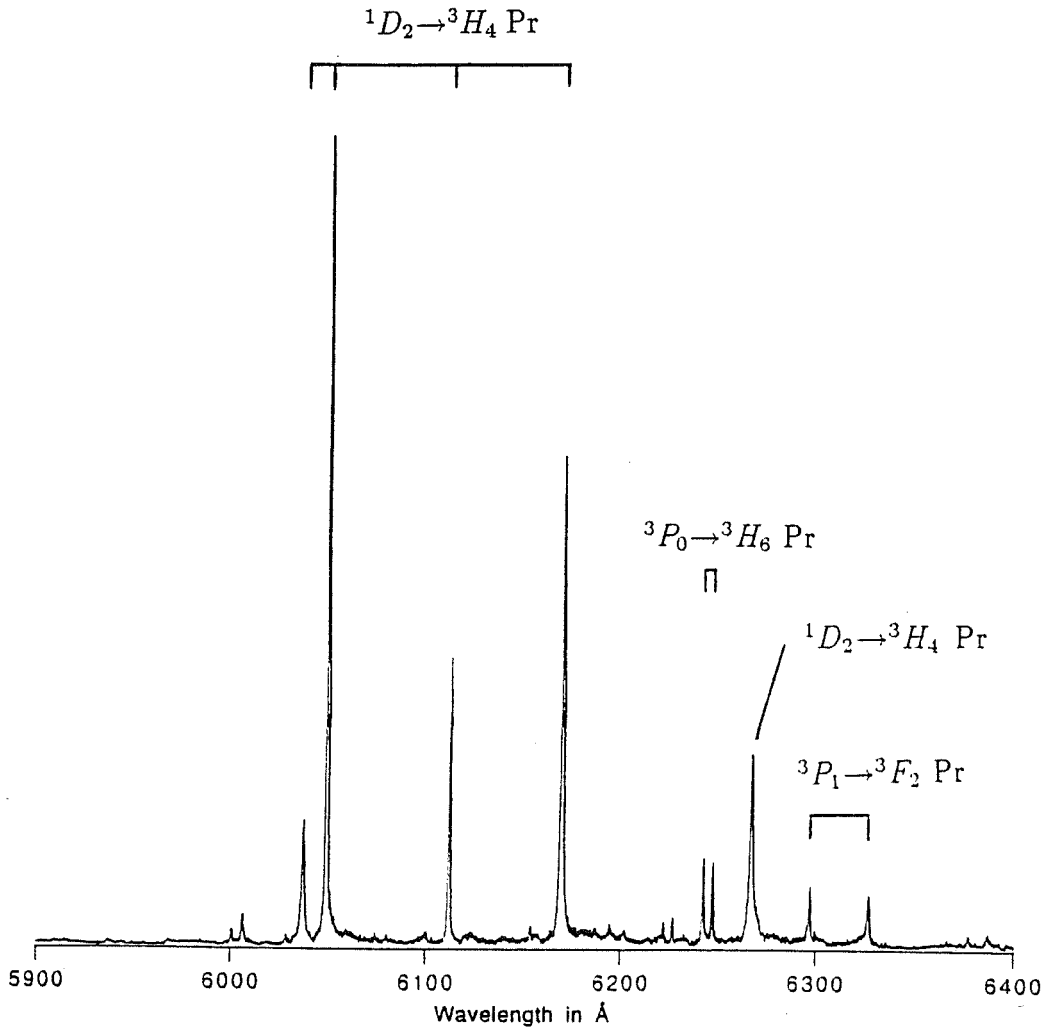

Figure 8.29: An upconversion fluorescence spectrum showing the $^1D_2 \rightarrow {}^3H_4$, $^3P_0 \rightarrow {}^3H_6$, and $^3P_1 \rightarrow {}^3F_2$ transitions of praseodymium, while exciting the Tm^{3+} ions to the $^3H_4$ multiplet, 7825Å, in the $CsCdBr_3$:Tm^{3+}:Pr^{3+} crystal.

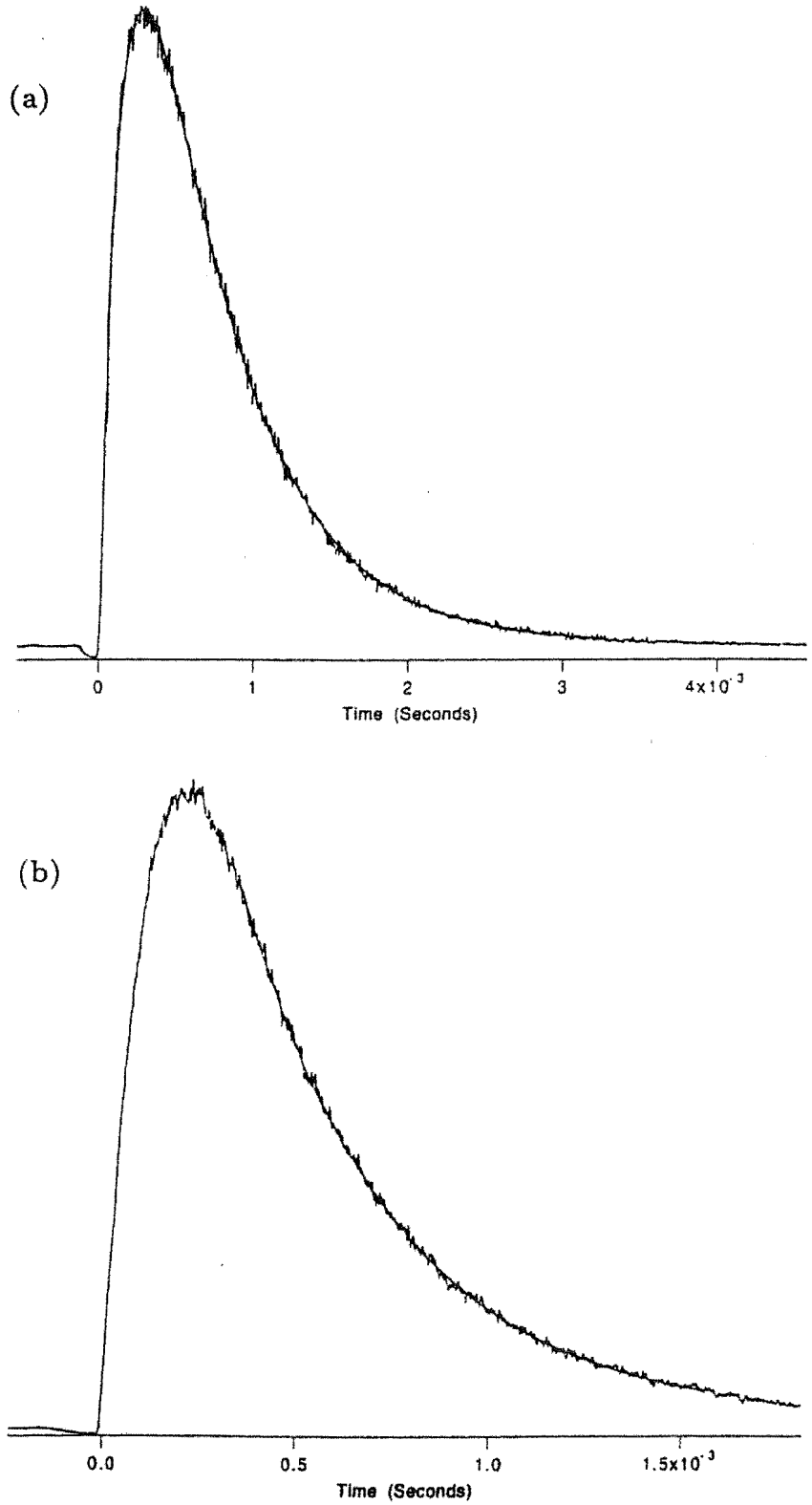

Figure 8.30: Transients of (a) the $^1G_4 \rightarrow {}^3H_6$ transition of thulium at 4808Å and (b) the $^3P_0 \rightarrow {}^3H_4$ transition of praseodymium at 4901Å, after excitation of the Tm^{3+} ions to the $^3H_4$ multiplet, 7825Å, in the $CsCdBr_3$:Tm^{3+}:Pr^{3+} crystal.

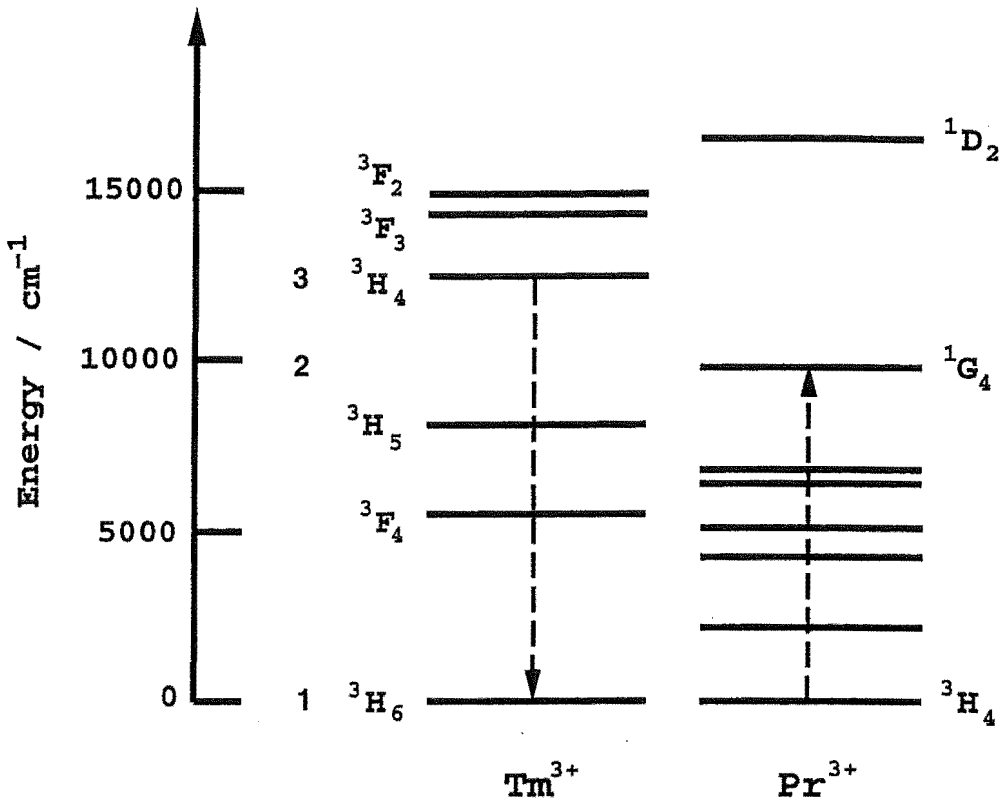

Figure 8.31: The proposed cross-relaxation mechanism which relaxes Tm^{3+} ions excited to the $^3H_4$ multiplet and populates the $^1G_4$ multiplet of praseodymium in the heterogeneous pair centres.

that the radiative lifetime of this multiplet is comparatively long, greater than 2ms, making it an ideal state for this energy-storage role. This fluorescence from the $^1G_4$ multiplet of praseodymium is evidence of yet another cross-relaxation process, this time from Tm^{3+} ions excited to the $^3H_4$ multiplet, Figure 8.31.

Rate equations can again be used to analyse the fluorescence transient of the $^1G_4$ multiplet of praseodymium. N_3 represents the number of heterogeneous pair centres in which the Tm^{3+} ion has been excited to the $^3H_4$ multiplet, N_2 the praseodymium $^1G_4$ multiplet population, W_t the rate constant for the energy transfer which populates the $^1G_4$ multiplet, W_T the sum of the rate constants for the upconversion processes which depopulate the $^1G_4$ multiplet, and W_2/W_3 the radiative lifetimes of the $^1G_4/^3H_4$ multiplets. The rate equations needed to describe this cross relaxation are:

$$\begin{aligned} \dot{N_3}(t) &= -(W_t + W_3)N_3(t)\,, \\ \dot{N_2}(t) &= W_t N_3(t) - (W_T + W_2)N_2(t)\,. \end{aligned}$$

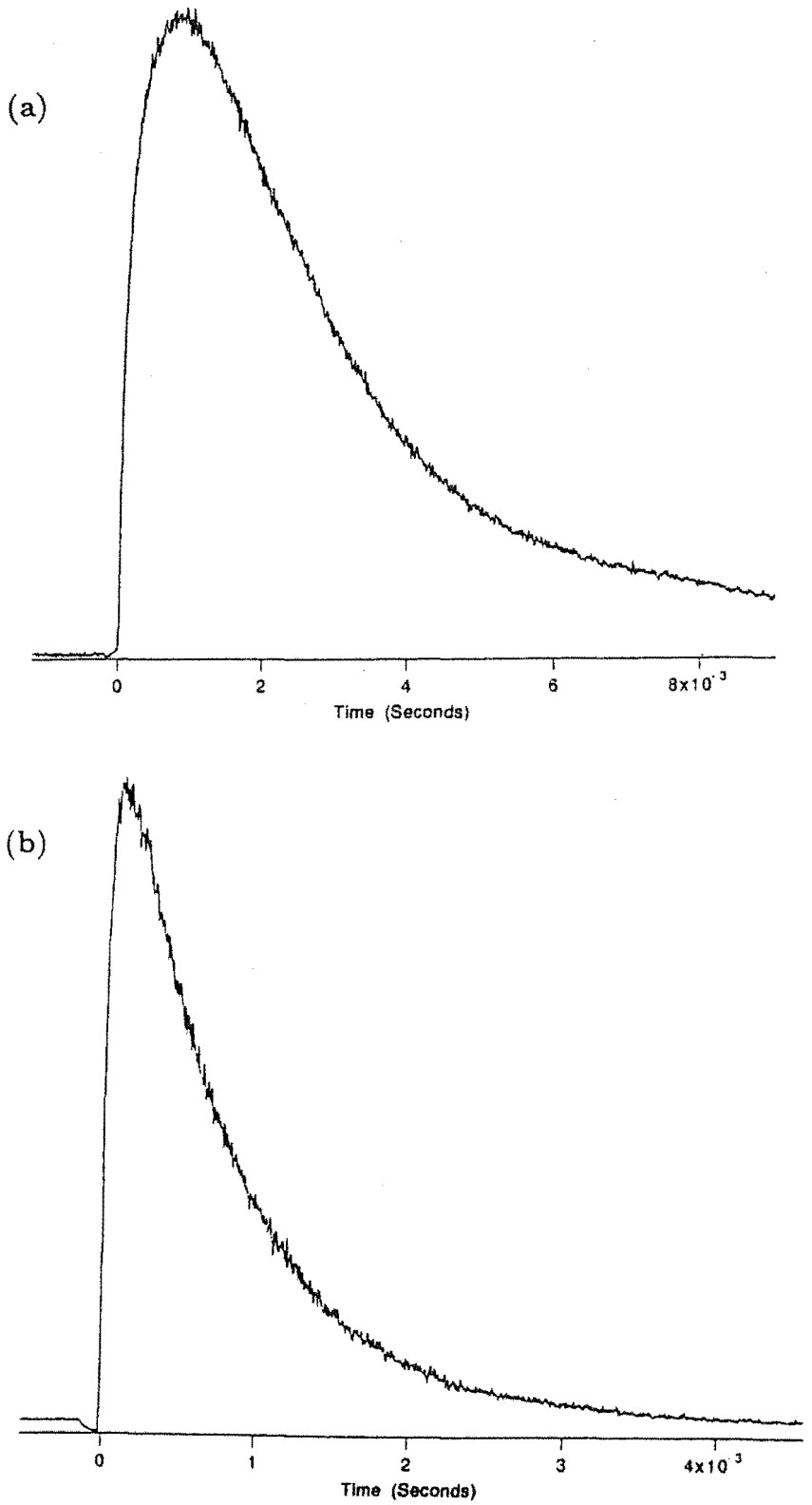

Figure 8.32: Transients of (a) the $^1G_4 \rightarrow {}^3H_4$ transition of praseodymium at 12220$\mathring{A}$ and (b) the $^1D_2 \rightarrow {}^3H_4$ transition of praseodymium at 6048$\mathring{A}$, after excitation of the Tm^{3+} ions to the $^3H_4$ multiplet in the $CsCdBr_3$:Tm^{3+}:Pr^{3+} crystal.

These equations can be solved for the transient population of the $^1G_4$ multiplet of praseodymium:

$$N_2(t) = \frac{N_3^0 W_t}{(W_T + W_2 - W_t - W_3)} \left(e^{-(W_t+W_3)t} - e^{-(W_T+W_2)t} \right) . \qquad (8.4)$$

The decay curve of Figure 8.32(a) is much slower than the W_3 radiative decay of the $^3H_4$ multiplet of thulium. Therefore it must be associated with the second term in Equation 8.4, which corresponds to the fluorescence lifetime of the $^1G_4$ multiplet of praseodymium. The rise curve is thus due to the first term, which corresponds to the fluorescence lifetime of the $^3H_4$ multiplet for Tm^{3+} ions in heterogeneous pair centres. This lifetime is much shorter than that of the $^3H_4$ multiplet for homogeneous Tm^{3+} pairs, because of the additional relaxation pathways which populate the Pr^{3+} ions.

Figure 8.32(b) is the transient of the $^1D_2 \rightarrow {}^3H_4$ fluorescence of praseodymium after excitation of the Tm^{3+} ions to the $^3H_4$ multiplet. The decay curve is very similar to that of Figure 8.30(a), which is the transient for fluorescence from the $^1G_4$ multiplet of thulium.

A possible mechanism for populating the $^1D_2$ multiplet of praseodymium is given in Figure 8.33. The $^1G_4$ multiplet of praseodymium is populated by cross relaxation from the $^3H_4$ multiplet of thulium. An inter-pair energy transfer is then required to excite further the Pr^{3+} ions to the $^1D_2$ multiplet. This transfer is exothermic with an energy mismatch of only $2cm^{-1}$.

Interpreting the transient of the fluorescence from the $^1D_2$ multipet of praseodymium is again very difficult. The transient will be a complicated function of the rate constants for the cross relaxation which populates the $^1G_4$ multiplet of praseodymium, the fluorescence lifetime of the $^1D_2$ multiplet in the heterogeneous pair centres, and the rate constant for the inter-pair energy transfer. The efficiency of this inter-pair energy transfer will have a spatial dependence which should be included in any model of this upconversion mechanism. However, it is interesting to note that the decay curve is similar to that observed for fluorescence from the $^3H_4$ multiplet in the homogeneous Tm^{3+} pair centres. This might be expected since this upconversion mechanism can continue only while the $^3H_4$ multiplet remains populated.

The transient of the $^1D_2 \rightarrow {}^3F_4$ fluorescence of thulium, after excitation of the Tm^{3+} ions to the $^3H_4$ multiplet in this crystal, is unchanged from that obtained for the $CsCdBr_3$:Tm^{3+} crystal, Figure 8.25. This suggests that the same upconversion mechanism, Figure 8.26, is populating the $^1D_2$ multiplet in both crystals. Only Tm^{3+} ions are involved in this upconversion.

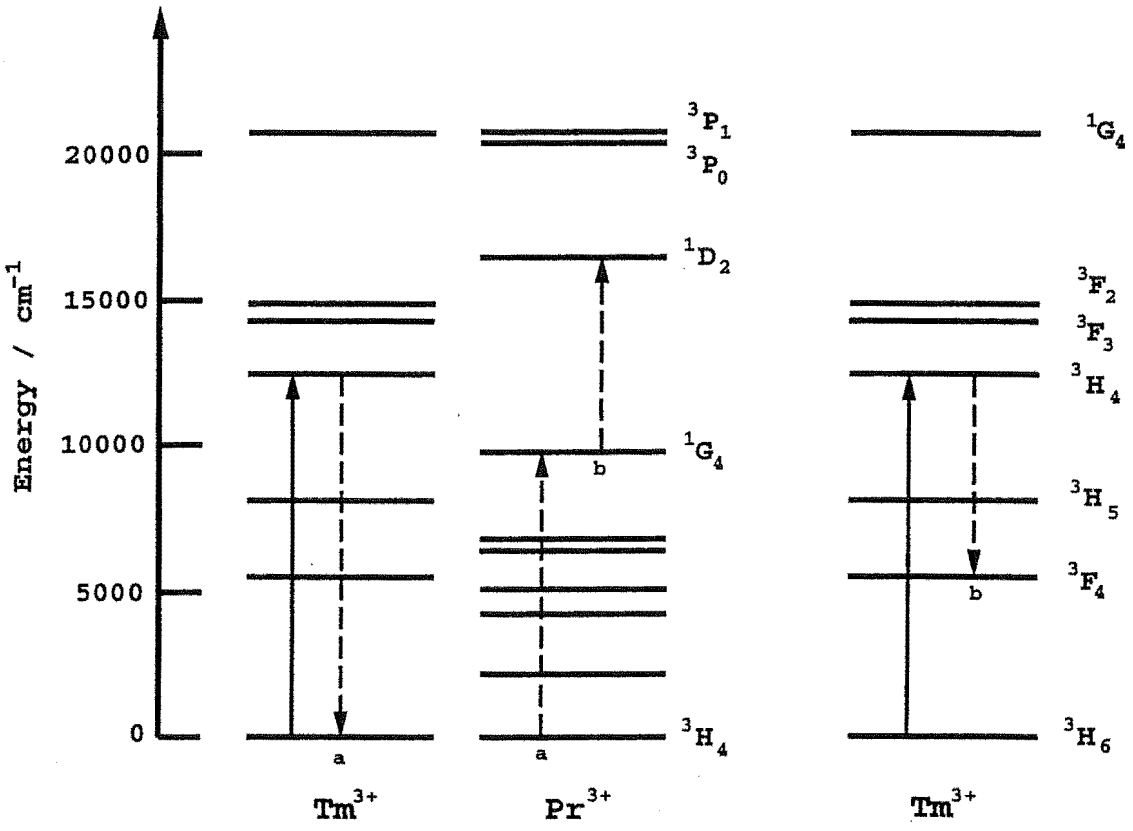

Figure 8.33: The proposed upconversion mechanism which populates the $^1D_2$ multiplet of praseodymium, after excitation of the Tm^{3+} ions to the $^3H_4$ multiplet in the $CsCdBr_3$:Tm^{3+}:Pr^{3+} crystal.

8.7 Two-Laser Upconversion Spectroscopy

8.7.1 Experimental Method

The upconversion experiments described so far were all conducted using a single pulsed laser. In the following experiments two pulsed dye lasers, their beams focused to the same point and along the same path through the crystal, were used to achieve upconversion. To obtain this focused geometry, mirrors were used to make the two laser beams parallel and then to direct them through a lens. This CaF_2 lens had a focal length of 50cm, which was many times the distance separating the two beams passing through it. Thus when the crystal is placed at the point where the two beams converge it will also be in the region where each beam is at its maximum intensity. The delay time between the first and second laser pulses was controlled by the Stanford Research Systems signal generator which triggered the Q-switched Nd:YAG lasers. These experiments were conducted with the lasers tuned to either the same wavelength, 'one-colour' experiments, or different wavelengths, 'two-colour' experiments.

One-colour experiments were useful to investigate the co-operative upconversion processes observed in the single-laser experiments, particularly the role of intermediate storage states in the upconversion mechanisms. When both lasers are tuned to an excitation wavelength which produces upconversion flourescence, there should be a delay time between the first and second pulse which is associated with the maximum upconversion fluorescence intensity. This delay time will usually coincide with the moment that an intermediate storage state is most populated, following the initial excitation of the centres by the first laser pulse.

Two-colour experiments can be used to find any excited state absorption (ESA) transitions which are accessible after the first excitation pulse. Again there will be an optimum delay time between the two lasers which will produce the maximum upconversion flourescence and this will also be determined by the population changes in intermediate storage states. Wright [92] suggests that such techniques are useful for probing the intermediate levels to see if their transient populations are consistent with the upconversion mechanism under consideration. New sequential upconversion processes might also be found by two-colour excitation spectroscopy.

8.7.2 Upconversion Spectroscopy of $CsCdBr_3$:Tm^{3+}:Pr^{3+}

Figure 8.34 is the transient of the $^3P_0 \rightarrow {}^3H_4$ fluorescence of praseodymium, with one-colour excitation of the Tm^{3+} ions to the $^3H_4$ multiplet. The first laser pulse produces upconversion fluorescence with the same transient as Figure 8.30(b). The second laser pulse, after a time delay of 600μs, produces an instantaneous enhancement in the upconversion fluorescence intensity. This enhanced fluorescence has a much shorter decay time than the single laser upconversion fluorescence, although after a few hundred micro-seconds the transients are similar. It was found that all

the upconversion fluorescence transitions in the $CsCdBr_3$:Tm^{3+}:Pr^{3+} crystal exhibited this fluorescence enhancement when two temporally separated lasers were used to excite the centres.

As expected, it was found that there was a time delay between the first and second laser pulse associated with the maximum upconversion fluorescence enhancement. If a number of these transients, with varying time delays, are plotted together then a picture emerges of the time varying population of the intermediate state in the upconversion mechanism. Such an envelope of transients is shown in Figure 8.35. These are the transients of the $^1G_4 \rightarrow {}^3H_6$ upconversion fluorescence of thulium, for two-laser excitation of the Tm^{3+} ions to the $^3H_4$ multiplet. The envelope is similar to the transient of the fluorescence from the $^1G_4$ multiplet of praseodymium, Figure 8.32(a), suggesting that this is the intermediate storage state for upconversion populating the $^1G_4$ multiplet of thulium.

To confirm the involvement of the $^1G_4$ multiplet of praseodymium in this upconversion mechanism, two-colour excitation scans were performed to search for any excited state absorption transitions from the $^1G_4$ multiplet. The first laser was tuned to excite the Tm^{3+} ions to the $^3H_4$ multiplet. Then, while monitoring upconversion fluorescence, the second laser was tuned through the wavelength region where these absorption transitions were expected. Figure 8.36(b) is the spectrum produced while monitoring the $^1G_4 \rightarrow {}^3H_6$ fluorescence of thulium. This can be compared with a single-laser excitation spectrum of the same region, Figure 8.36(a). It should be noted that while operating in this spectral range with this laser dye (LDS 798) the output power will decrease as the laser is tuned to longer wavelengths.

Four excited state absorption features appear in Figure 8.36(b). Three of these correspond to energy differences between the known levels of the $^3P_2$ multiplet of praseodymium and the lowest level of the $^1G_4$ multiplet of praseodymium. Transients of the most intense of these ESA transitions have been plotted to form an envelope, Figure 8.37(a). In Figure 8.37(b) the fluorescence due to the first laser pulse has been subtracted from each of the transients to produce an envelope which should more closely resemble the transient population of the $^1G_4$ multiplet of praseodymium. This was indeed the case as the envelope of Figure 8.37(b) is very much like the transient of the fluorescence from the $^1G_4$ multiplet of praseodymium, Figure 8.32(a).

A possible mechanism for populating the $^1G_4$ multiplet of thulium is given in Figure 8.38. The upconversion occurs in the mixed pair centres and uses the $^1G_4$ multiplet of praseodymium as an intermediate storage state. An inter-pair energy transfer excites the Pr^{3+} ions from the $^1G_4$ to the $^3P_2$ multiplet. This transfer has an energy mismatch of only $9cm^{-1}$. The $^1G_4$ multiplet of thulium is populated by cross relaxation from the $^3P_2$ multiplet of praseodymium. This second energy transfer has an energy mismatch of $115cm^{-1}$. Both of these transfer processes are exothermic. The $1058cm^{-1}$ energy gap separating the $^3P_2$ and $^3P_1$ multiplets of praseodymium makes it unlikely that the $^3P_1$ multiplet can be populated by multiphonon relaxation from the $^3P_2$ multiplet. The Pr^{3+} ions apparently prefer to relax

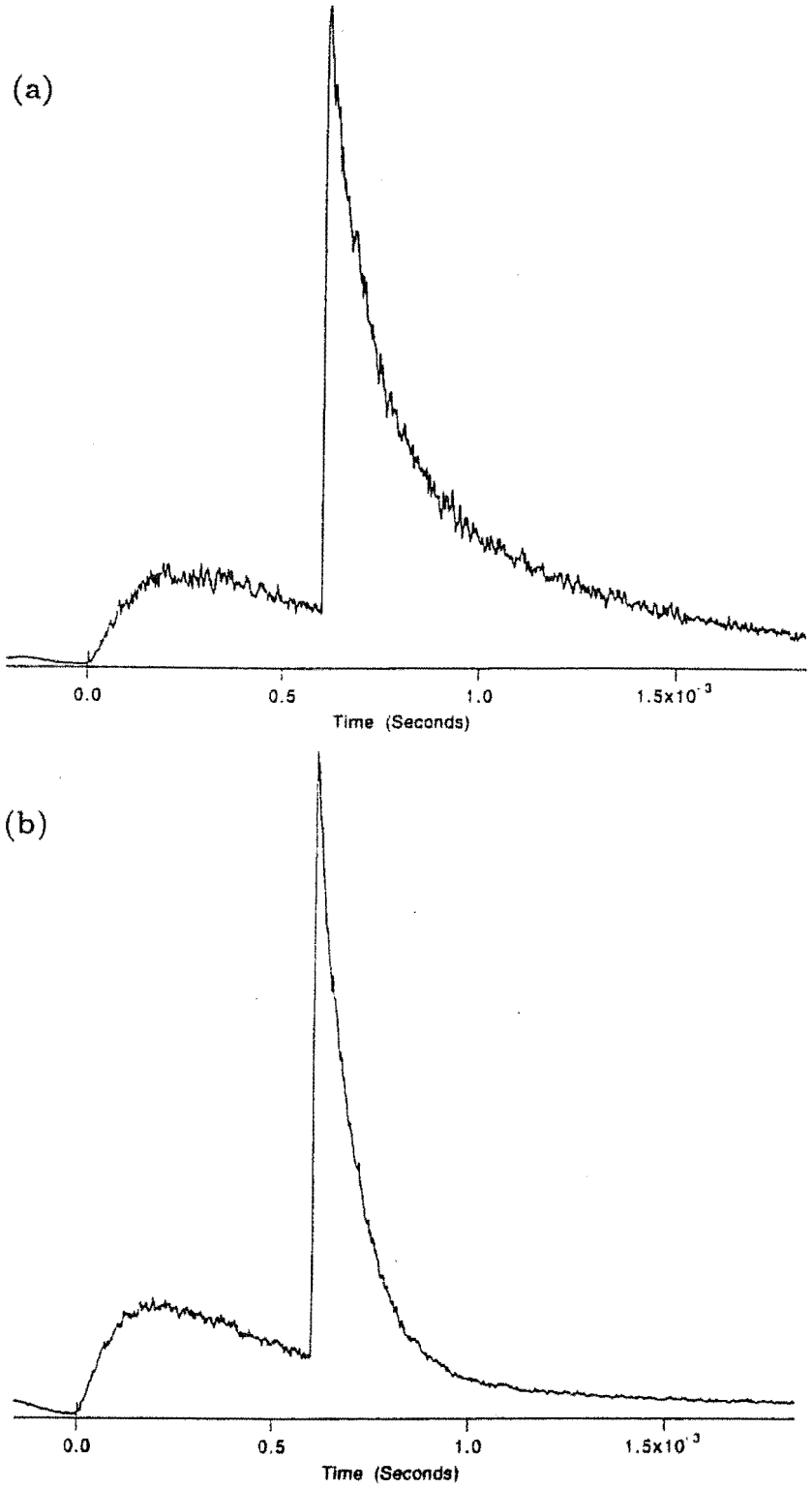

Figure 8.34: Transients of the $^3P_0 \rightarrow {}^3H_4$ transition of praseodymium at 4901Å, with (a) one-colour excitation of the Tm^{3+} ions to the $^3H_4$ multiplet, 7995Å, and (b) excitation of the Tm^{3+} ions to the $^3H_4$ multiplet, 7995Å, followed by an ESA, 8030Å, in the $CsCdBr_3$:Tm^{3+}:Pr^{3+} crystal. The time between the first and second laser pulses is 600μs.

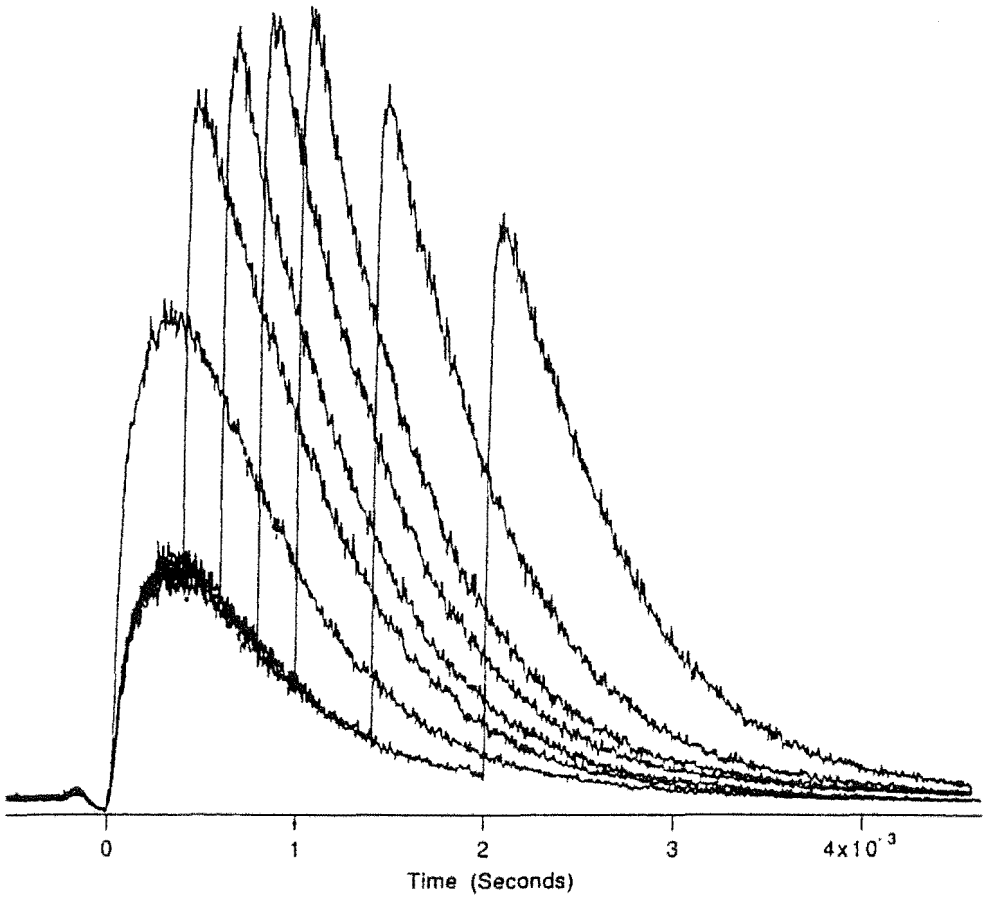

Figure 8.35: An envelope of transients for the $^1G_4 \rightarrow {}^3H_6$ transition of thulium at 4807Å, after one-colour excitation of the Tm^{3+} ions to the $^3H_4$ multiplet, 7995Å, in the $CsCdBr_3$:Tm^{3+}:Pr^{3+} crystal.

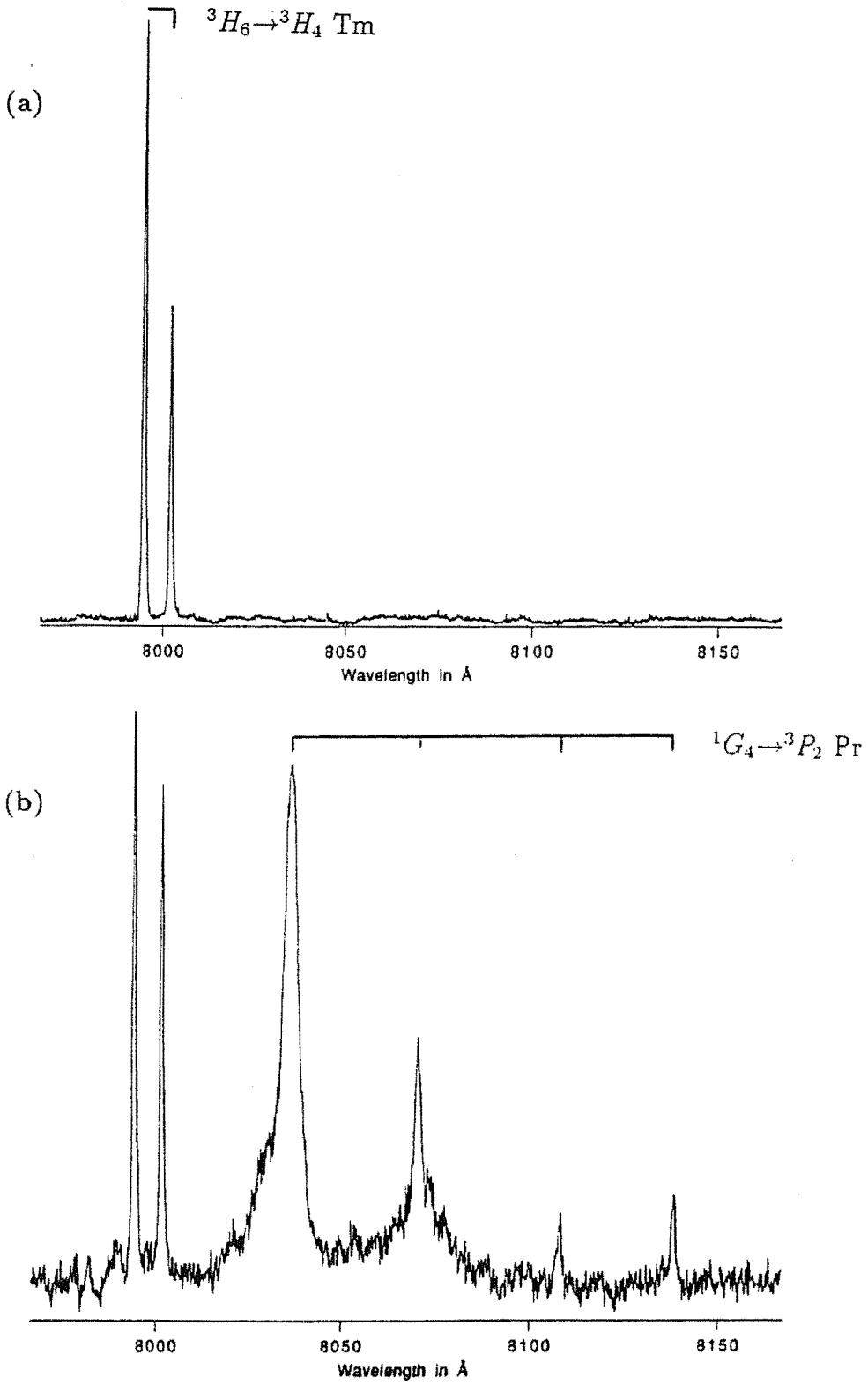

Figure 8.36: (a) Single-laser excitation and (b) two-laser excitation spectra showing the $^3H_6 \rightarrow {}^3H_4$ absorption transitions of thulium and the $^1G_4 \rightarrow {}^3P_2$ ESA transitions of praseodymium, while monitoring the $^1G_4 \rightarrow {}^3H_6$ transition of thulium at 4808Å in the $CsCdBr_3$:Tm^{3+}:Pr^{3+} crystal.

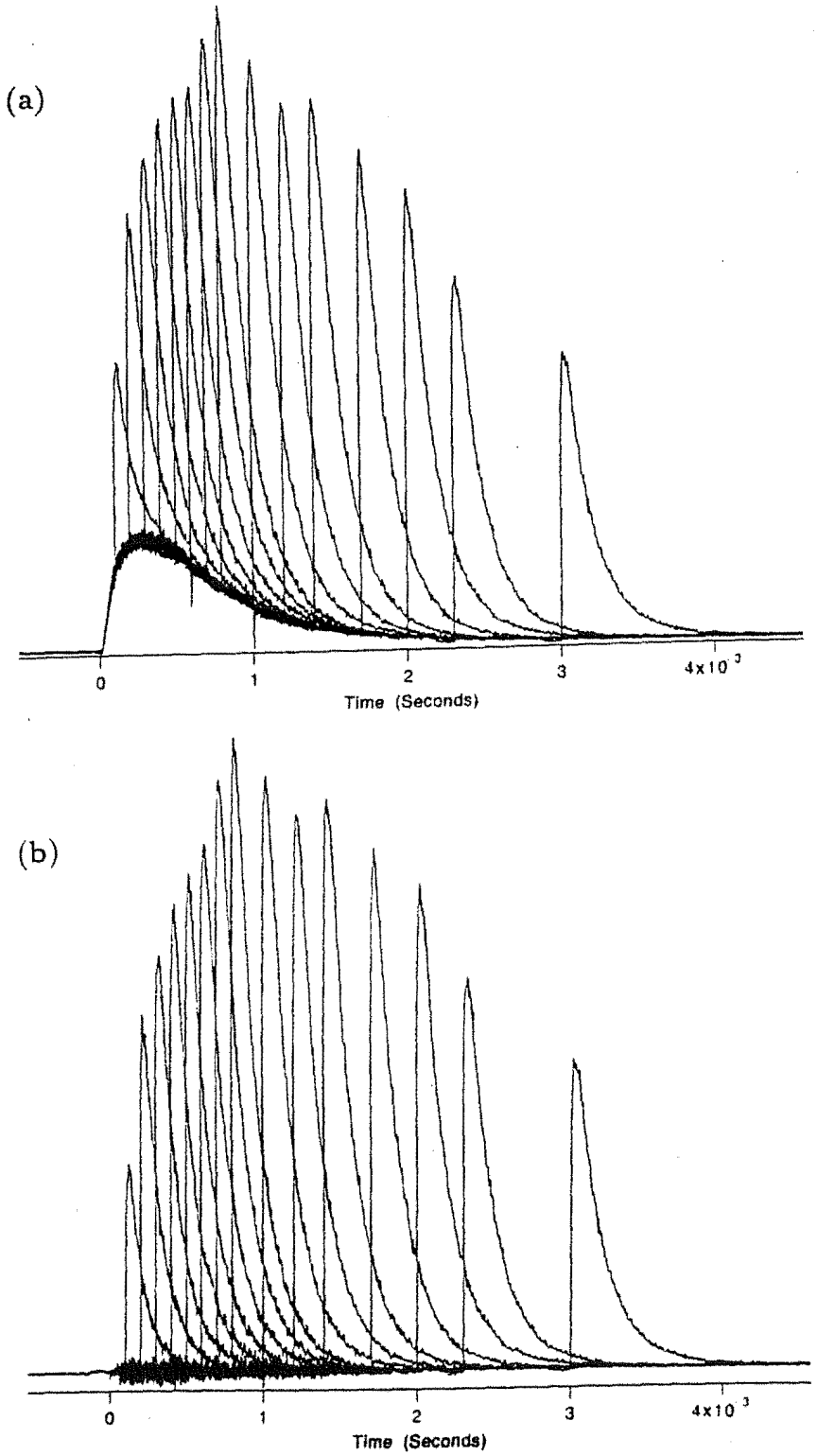

Figure 8.37: An envelope of transients for the $^1G_4 \rightarrow {}^3H_6$ fluorescence of thulium, with excitation of the Tm^{3+} ions to the $^3H_4$ multiplet, 7995Å, followed by an ESA, 8036Å, in the $CsCdBr_3$:Tm^{3+}:Pr^{3+} crystal. This envelope is shown (a) before and (b) after subtraction of the fluorescence due only to the first laser pulse.

via the energy transfer proposed.

The upconversion mechanism in Figure 8.38 is similar in many respects to that which populates the $^1D_2$ multiplet of praseodymium. This may explain why the transients of the upconversion fluorescence from these two multiplets are so alike. Once again the upconversion mechanism can only proceed while the $^3H_4$ multiplet of thulium remains populated. The fluorescence transient of the $^1G_4$ multiplet of thulium, Figure 8.30(a), is determined by three energy-transfer rates and the fluorescence lifetimes of five multiplets.

The upconversion mechanism in Figure 8.24, which populates the $^1G_4$ multiplet of thulium in the pure-dopant crystal, may also be operating in the mixed-dopant crystal. However it was not possible to distingush between the upconversion fluorescence produced by these two mechanisms. With higher resolution spectroscopy it should be possible to discriminate between the Tm^{3+} ion absorption transitions of the homogeneous and heterogeneous pair centres.

Figure 8.39(b) is a two-colour excitation spectrum produced while monitoring upconversion fluorescence from the $^3P_0$ multiplet of praseodymium. The first laser excited the Tm^{3+} ions to the $^3H_4$ multiplet while the second laser was tuned to find any ESA transitions. Figure 8.39(a) is a single-laser excitation spectrum of the same region and is included for comparison.

The ESA transitions found in Figure 8.36(b), while monitoring upconversion fluorescence from the $^1G_4$ multiplet of thulium, appear weakly in Figure 8.39(b). This is to be expected since it has already been established that energy transfer from the $^1G_4$ multiplet of thulium to the $^3P_0$ multiplet of praseodymium is possible in heterogeneous pairs. However the most intense ESA transitions which populate the $^3P_0$ multiplet of praseodymium were not observed while monitoring the fluorescence from the $^1G_4$ multiplet of thulim. This is additional evidence that main upconversion mechanism for populating the $^3P_0$ multiplet does not involve an energy transfer from the $^1G_4$ multiplet of thulium.

Figure 8.34(b) is the transient of the $^3P_0 \rightarrow {}^3H_4$ fluorescence of praseodymium, for two-colour sequential excitation. The first laser pulse excites the Tm^{3+} ions to the $^3H_4$ multiplet while the second laser pumps the ESA transition at 8030$\AA$. This enhanced upconversion fluorescence has a faster decay curve than Figure 8.34(a), which was due to one-colour excitation. In the case of one-colour excitation, both the laser pulses can independantly produce upconversion fluorescence, the second pulse also causing the enhanced upconversion fluorescence. In two-colour excitation, where the second laser is in resonance with an ESA, the second pulse will only excite those ions which are already in the metastable intermediate state. However, this second pulse will not by itself produce upconversion fluorescence. Thus the longer decay curve in Figure 8.34(a) is due to the additional component of the upconversion fluorescence which is attributable to co-operative upconversion initiated by the second laser pulse.

Figure 8.40 shows an envelope of transients for the $^3P_0 \rightarrow {}^3H_4$ upconversion fluorescence, with two-colour sequential excitation. The second laser is pumping

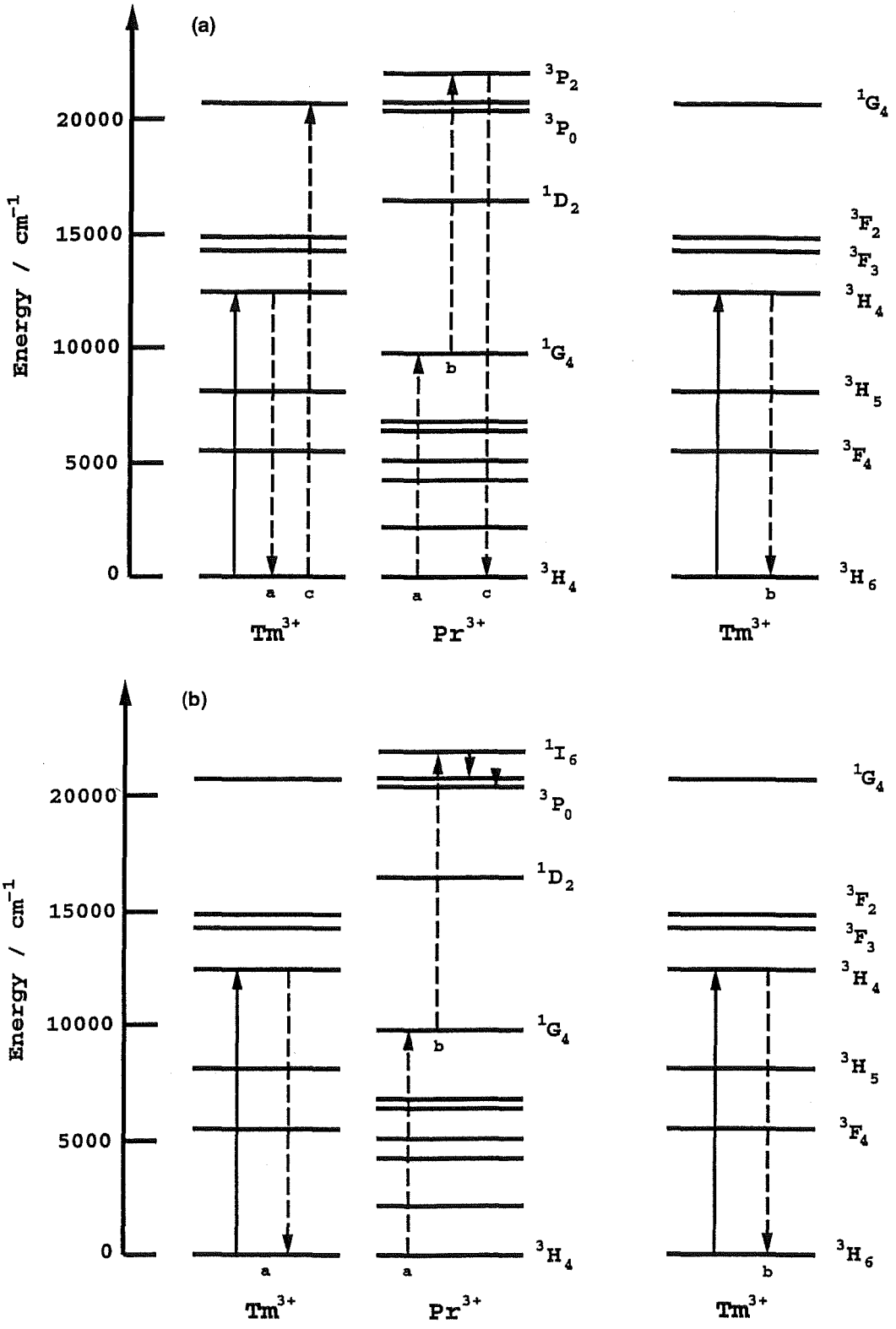

Figure 8.38: **(a)** The proposed upconversion mechanism for populating the $^1G_4$ multiplet of thulium, after excitation of the Tm^{3+} ions to the $^3H_4$ multiplet in the $CsCdBr_3$:Tm^{3+}:Pr^{3+} crystal. **(b)** The proposed mechanism for populating the $^3P_0$ multiplet of praseodymium, after excitation of the Tm^{3+} ions to the $^3H_4$ multiplet in the $CsCdBr_3$:Tm^{3+}:Pr^{3+} crystal.

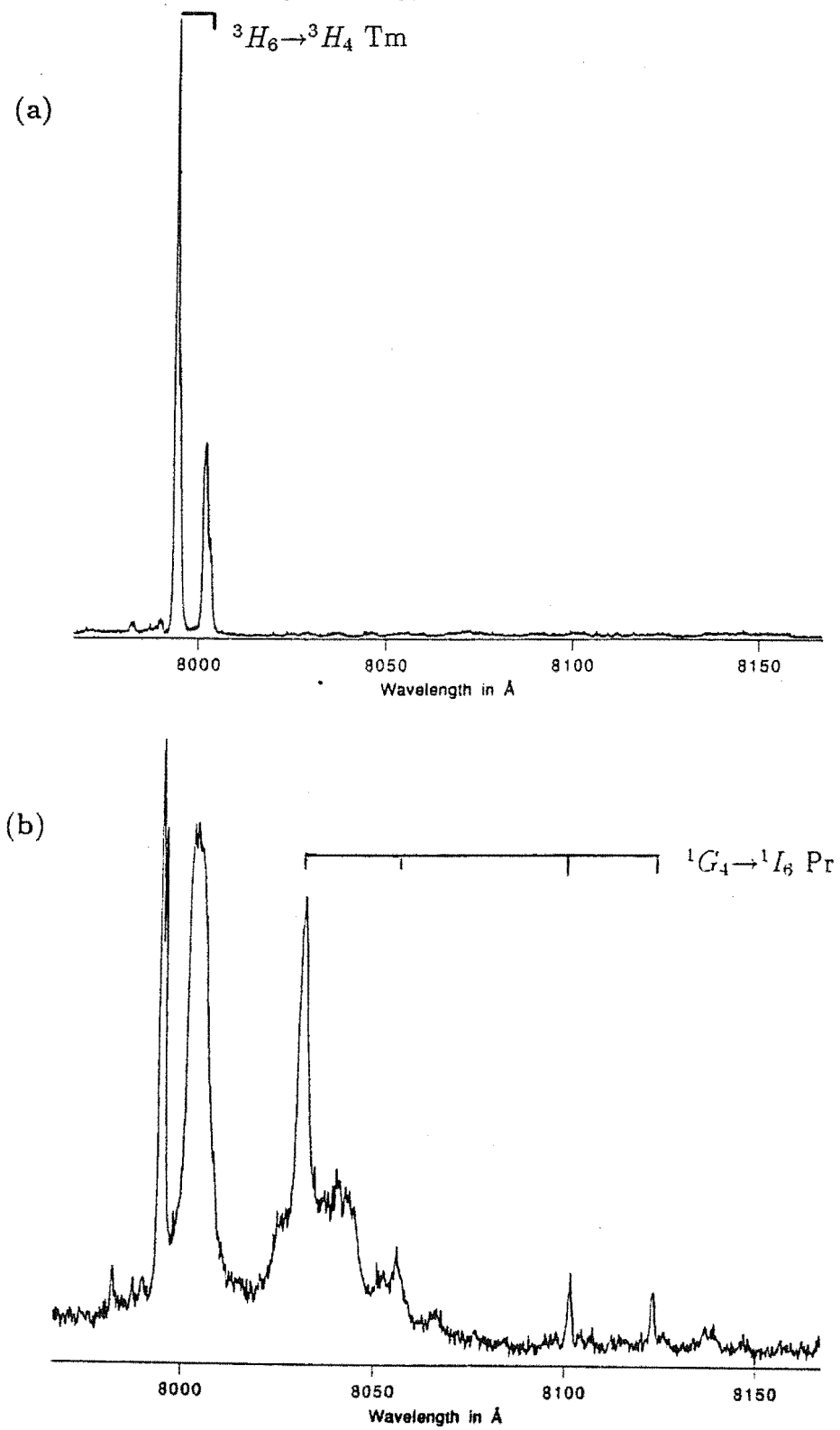

Figure 8.39: (a) Single-laser and (b) two-laser excitation spectra showing the $^3H_6 \rightarrow {}^3H_4$ absorption transitions of thulium and the $^1G_4 \rightarrow {}^1I_6$ ESA transitions of praseodymium, while monitoring the $^3P_0 \rightarrow {}^3H_4$ transition of praseodymium at 4901Å in the $CsCdBr_3$:Tm^{3+}:Pr^{3+} crystal.

the unidentified ESA transition at 8038Å. This envelope has faster decay than the transient of the $^1G_4$ multiplet of praseodymium, Figure 8.32(a). There are at least 6 ESA transitions in Figure 8.39(b) which populate the $^3P_0$ multiplet of praseodymium, but not the $^1G_4$ multiplet of thulium. Consultation of Table 8.1 shows that these are not transitions to the $^1G_4$ or $^1D_2$ multiplets of thulium. The only multiplet of praseodymium which could be higher in energy than the $^3P_0$ multiplet and has more than 5 levels is the $^1I_6$ multiplet. Thus these ESA transitions, which populate the $^3P_0$ multiplet, must be transitions between the $^1D_2$ and $^1I_6$ multiplets of praseodymium. Unlike the very weak $^3H_4 \rightarrow {}^1I_6$ absorption transitions of praseodymium, the $^1D_2 \rightarrow {}^1I_6$ transitions are spin allowed.

A possible mechanism for populating the $^3P_1$ and $^3P_0$ multiplets of praseodymium is given in Figure 8.38(b). It is similar to the mechanism in Figure 8.38(a) which populates the $^1G_4$ multiplet of thulium, with the $^1G_4$ multiplet of praseodymium again acting as an intermediate storage state. Using the energy levels of the $^1I_6$ multiplet, which have been calculated from the ESA transition energies of Figure 8.39(b), it can be established that the inter-pair energy transfer which excites the Pr^{3+} ions to the $^1I_6$ multiplet is exothermic, with an energy mismatch of less than $67cm^{-1}$. Less than $1036cm^{-1}$ of energy must be emitted in the non-radiative relaxation which populates the $^3P_1$ multiplet of praseodymium.

Figures 8.36 and 8.39 show that the $^1G_4$ multiplet of thulium is populated by cross relaxation from the $^3P_2$ multiplet of praseodymium, but is not populated from the $^1I_6$ multiplet of praseodymium. It has already been established that a Pr^{3+} ion excited to the $^3P_2$ multiplet will relax preferentially by the energy transfer which excites the Tm^{3+} ion to the $^1G_4$ multiplet. However there is no evidence for a similar cross-relaxation process depopulating the $^1I_6$ multiplet of praseodymium. This is not surprising since such an energy transfer would involve the $^1I_6 \rightarrow {}^3H_4$ transitions of praseodymium, which are spin forbidden and always very weak. A Pr^{3+} ion which has been excited to the $^1I_6$ multiplet may prefer to relax non-radiatively, populating the $^3P_1$ and $^3P_0$ multiplets.

If the $^1G_4$ multiplet of praseodymium is indeed an intermediate state for the upconversion mechanisms which populate the $^1G_4$ multiplet of thulium and the $^3P_0$ multiplet of praseodymium in the mixed-dopant crystal, then the second laser pulse should cause an immediate decrease in its population. This might be observable as a sudden decline in the intensity of the fluorescence from the $^1G_4$ multiplet of praseodymium. Figure 8.41 was produced by monitoring the fluoresence from the $^1G_4$ multiplet of praseodymium, while the first laser excited the Tm^{3+} ions to the $^3H_4$ multiplet and the second laser was tuned over a wavelength range which include the ESA transitions to the $^3P_2$ multiplet of praseodymium. It shows a definite decrease in this fluorescence as the second laser was scanned through 8036Å, where the strongest ESA was found in Figure 8.36(b). This transition has already been identified as that originating from the lowest level of the $^1G_4$ multiplet and terminating on the highest level of the $^3P_2$ multiplet of praseodymium.

Figure 8.42(a) is the transient of the fluorescence from the $^1G_4$ multiplet of

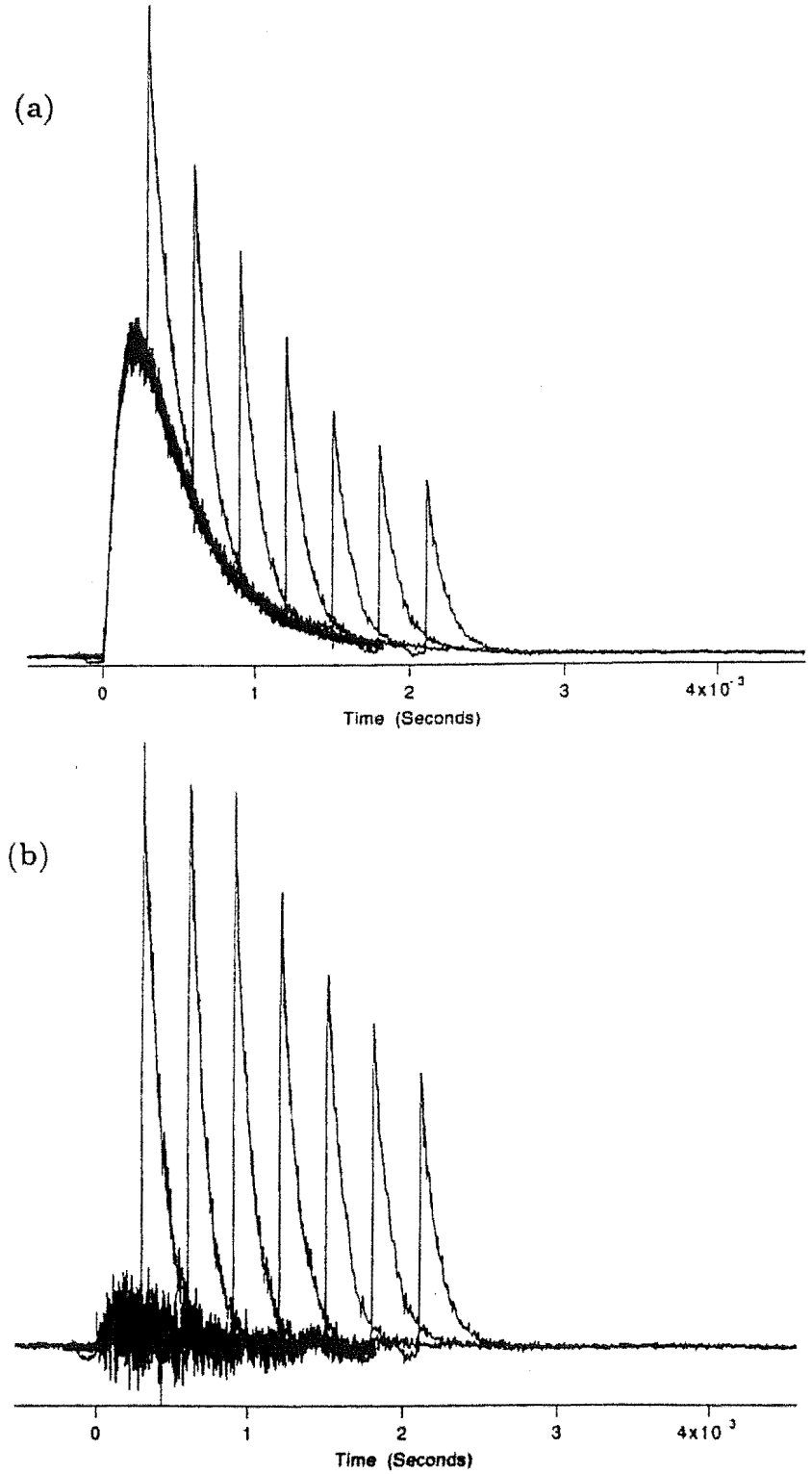

Figure 8.40: An envelope of transients for the $^3P_0 \rightarrow {}^3H_4$ fluorescence of praseodymium, with excitation of the Tm^{3+} ions to the $^3H_4$ multiplet, 7995Å, followed by an ESA, 8038Å, in the $CsCdBr_3$:Tm^{3+}:Pr^{3+} crystal. This envelope is shown (a) before and (b) after subtraction of the fluorescence due only to the first laser pulse.

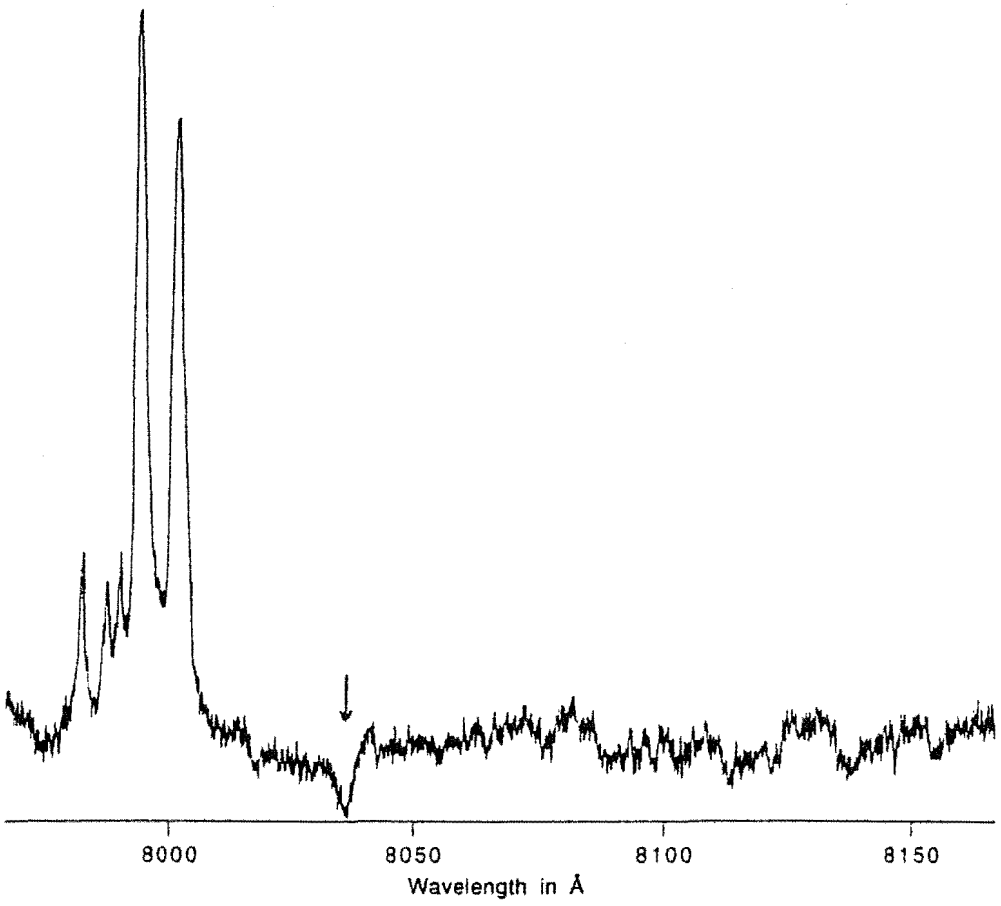

Figure 8.41: While monitoring the $^1G_4 \rightarrow {}^3H_4$ transition of praseodymium at 10227Å, the first laser excited the Tm^{3+} ions to the $^3H_4$ multiplet, 7995Å, as the second laser was scanned to produce this spectrum, in the $CsCdBr_3$:Tm^{3+}:Pr^{3+} crystal. The time delay between the first and second laser pulses was 1ms.

praseodymium, with the first laser exciting the Tm^{3+} ions to the $^3H_4$ multiplet and second laser in resonance with the ESA transition at 8036Å. The second laser pulse, after a 1ms delay, produces an immediate decrease in the fluorescence intensity, Figure 8.42(b). This confirms that the $^1G_4$ multiplet of praseodymium is the intermediate state in the upconversion process which populates the $^1G_4$ multiplet of thulium sequentially. It also confirms the assignment of the $^1G_4 \rightarrow {}^3P_2$ transitions in Figure 8.36(b).

It was expected that a similar decrease in the fluorescence from the $^1G_4$ multiplet of praseodymium would be found when the first and the second lasers were both exciting the Tm^{3+} ions to the $^3H_4$ multiplet. However no appreciable decrease in the fluorescence was observed after the second laser pulse. A positive result would have been very strong evidence supporting the upconversion mechanisms proposed in Figures 8.33 and 8.38.

The observation that the blue fluorescence from the mixed-dopant crystal was much more intense than that from the pure Tm^{3+} dopant crystal, during IR excitation of thulium, suggests that the upconversion mechanism proposed for the heterogeneous centres is more efficient than that proposed for the homogeneous Tm^{3+} centres. This may be attributable to the long radiative lifetime (greater than 2ms) of the $^1G_4$ multiplet of praseodymium. The efficiency of the cross-relaxation mechanism which populates this multiplet will also be an important determinant of the over-all efficiency of the upconversion mechanism.

Figure 8.43(a) shows the envelope of transients for the $^1D_2 \rightarrow {}^3F_4$ upconversion fluorescence of thulium, with one-colour excitation of the Tm^{3+} ions to the $^3H_4$ multiplet. The envelope has a faster decay curve than the transient of the $^1G_4$ multiplet fluorescence of praseodymium, Figure 8.32(a). This suggests that the upconversion mechanism populating the $^1D_2$ multiplet of thulium does not involve the $^1G_4$ multiplet of praseodymium as directly as the mechanism which populates the $^1G_4$ multiplet of thulium, shown in Figure 8.38(a).

Figure 8.44 is a two-colour excitation spectrum obtained while monitoring the upconversion fluorescence from the $^1D_2$ multiplet of thulium. The first laser excited the Tm^{3+} ions to the $^3H_4$ multiplet while the second laser was tuned to find any ESA. The weak ESA transitions that were found were the same as those which appeared in excitation while monitoring the upconversion fluorescence from the $^1G_4$ multiplet of thulium, Figure 8.36(b). These were identified as the $^1G_4 \rightarrow {}^3P_2$ transitions of praseodymium. Figure 8.44 demonstrates that excitation of the Pr^{3+} ions to the $^3P_2$ multiplet causes an increase in the population of the $^1D_2$ multiplet of thulium. Cross relaxation from the $^3P_2$ multiplet of praseodymium will populate the $^1G_4$ multiplet of thulium, Figure 8.38(a), and so the $^3F_3$ multiplet of thulium, Figure 8.19(a). This may assist the upconversion mechanism which populates the $^1D_2$ multiplet of thulium shown in Figure 8.26.

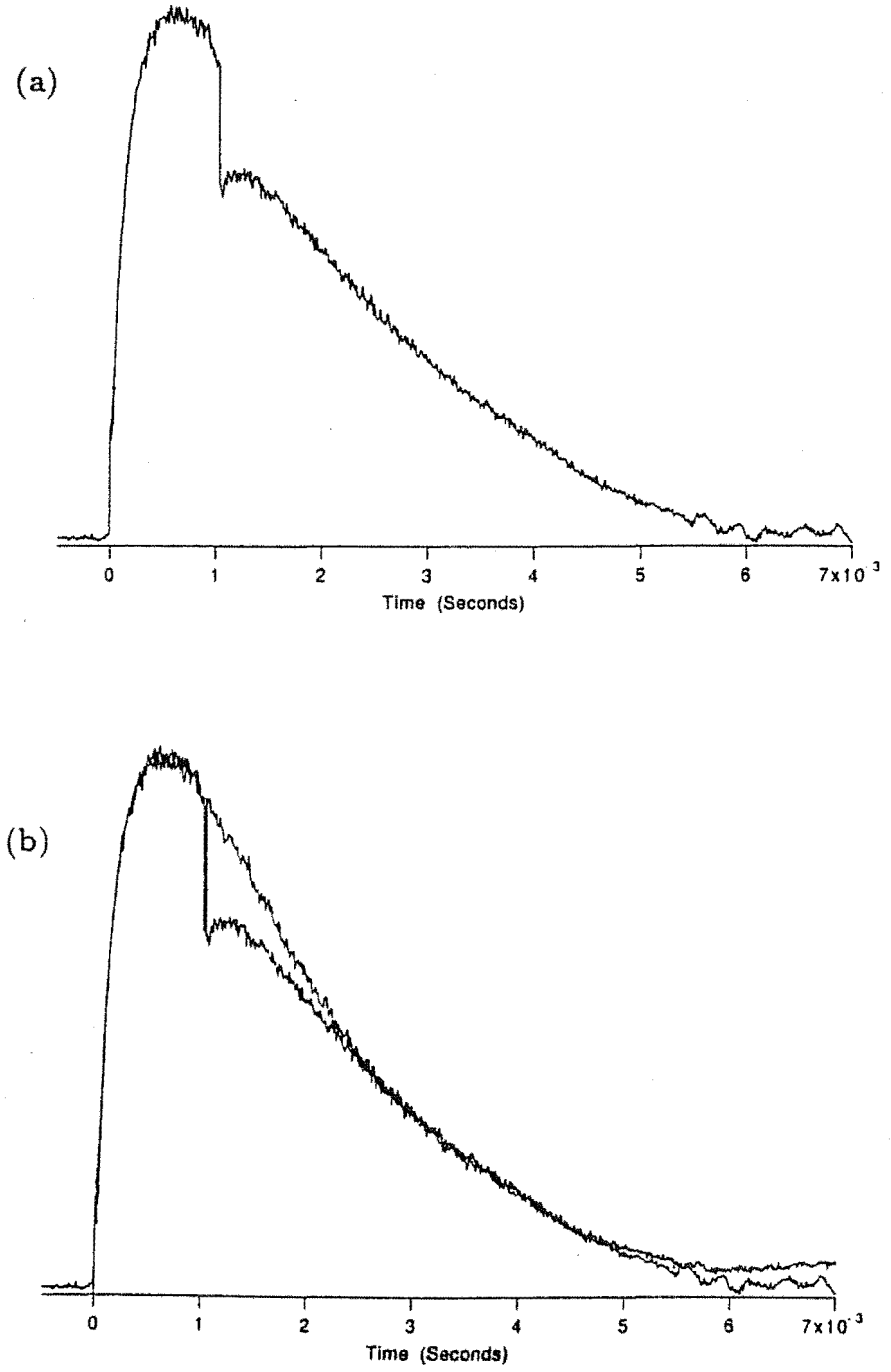

Figure 8.42: (a) The transient of the $^1G_4 \rightarrow {}^3H_4$ transition of praseodymium at 10227Å. The first laser excites the Tm^{3+} ions to the $^3H_4$ multiplet and the second laser is reasonant with the ESA at 8036Å in the $CsCdBr_3$:Tm^{3+}:Pr^{3+} crystal. (b) The transient as it appears both with and without the second laser pulse.

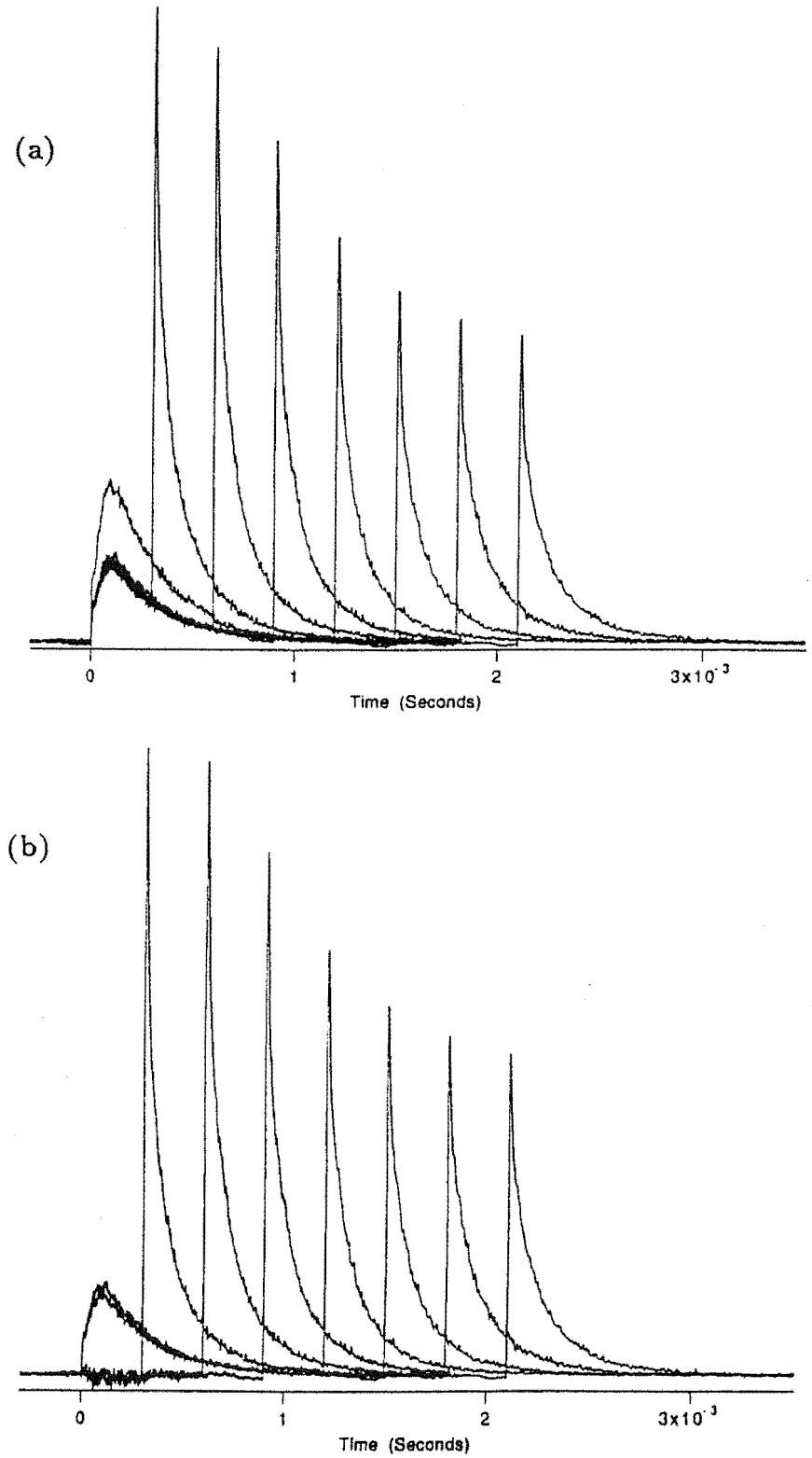

Figure 8.43: An envelope of transients for the $^1D_2 \rightarrow {}^3F_4$ fluorescence of thulium, with one-colour excitation of the Tm^{3+} ions to the $^3H_4$ multiplet in the $CsCdBr_3$:Tm^{3+}:Pr^{3+} crystal. This envelope is shown (a) before and (b) after subtraction of the fluorescence due only to the first laser pulse.

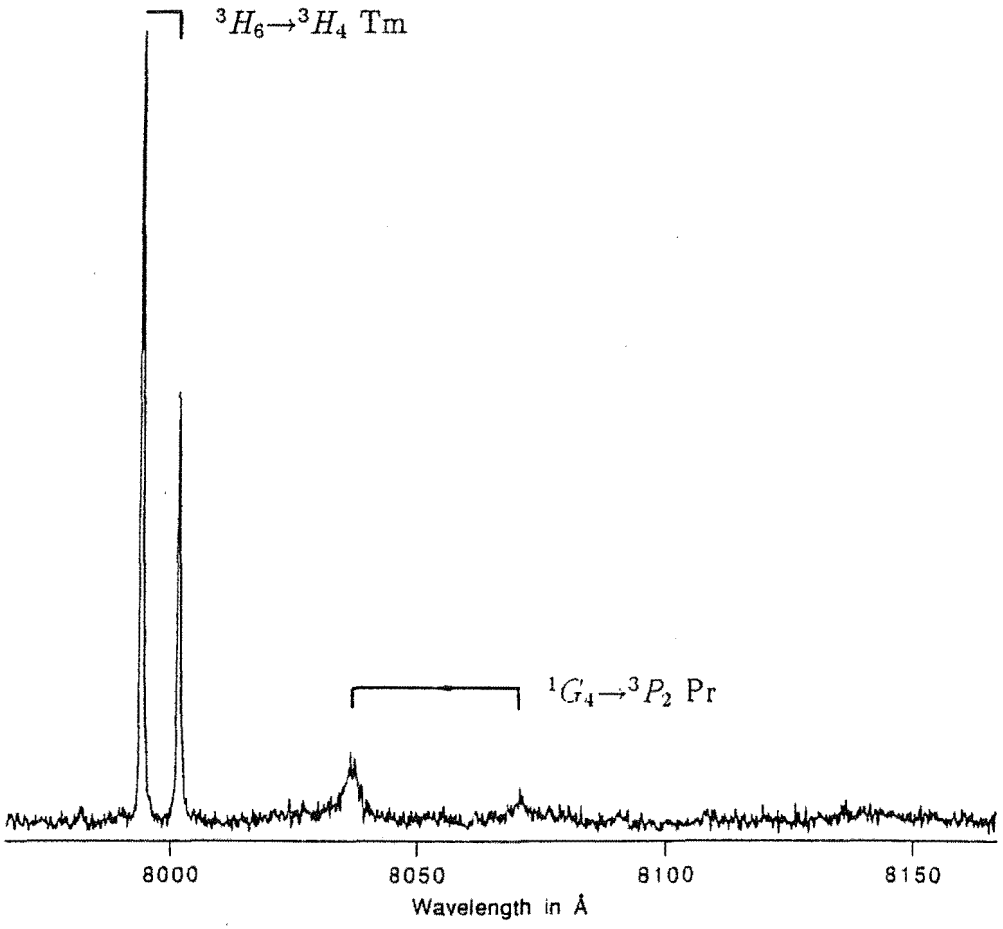

Figure 8.44: A two-laser excitation spectrum showing $^3H_6 \rightarrow {}^3H_4$ absorption transitions of thulium and the $^1G_4 \rightarrow {}^3P_2$ ESA transitions of praseodymium, while monitoring the $^1D_2 \rightarrow {}^3F_4$ transition of thulium at 4582Å in the $CsCdBr_3$:Tm^{3+}:Pr^{3+} crystal.

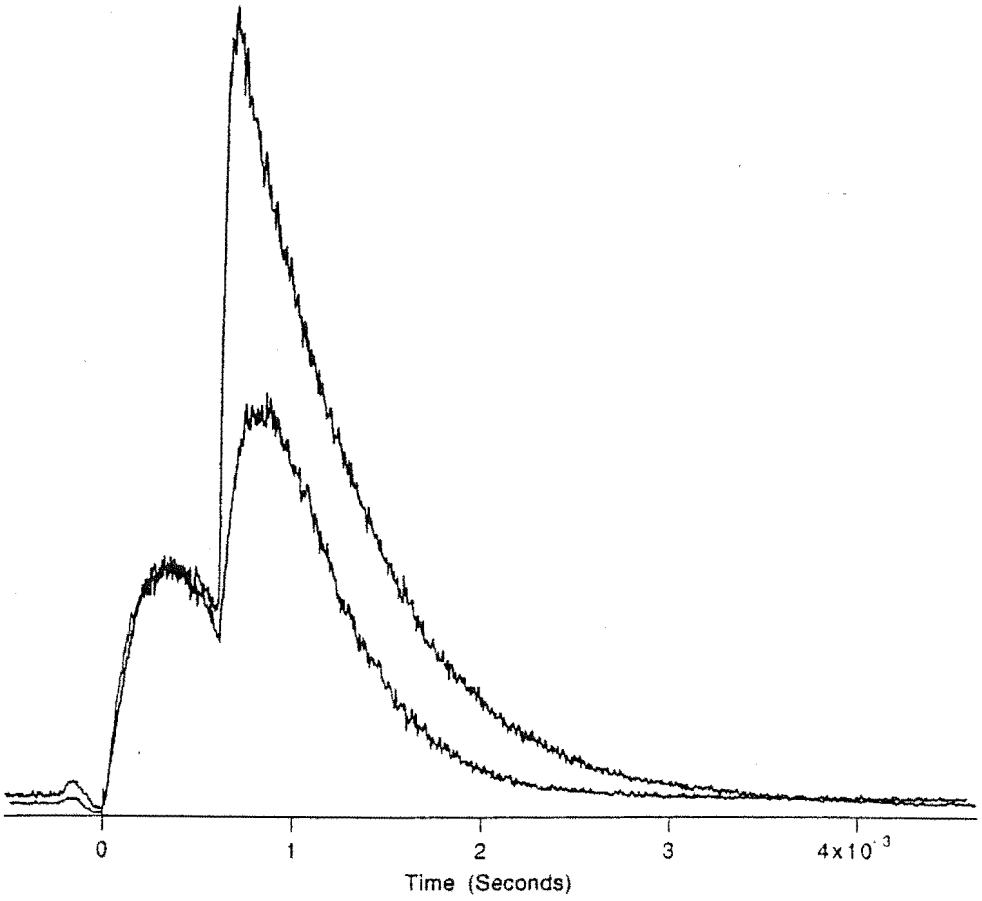

Figure 8.45: The transient of the $^1G_4 \rightarrow {}^3H_6$ transition at 4808.Å, after one-colour excitation of the Tm^{3+} ions to the $^3H_4$ multiplet, 7995.Å, in the $CsCdBr_3$:Tm^{3+} crystal. This plot also shows the transient obtained for the $CsCdBr_3$:Tm^{3+}:Pr^{3+} crystal, which exhibits upconversion fluorescence enhancement. The time between the first and the second laser pulses was 1ms.

8.7.3 Two-Laser Upconversion in $CsCdBr_3$:Tm^{3+}

Figure 8.45 is the transient of the $^1G_4 \rightarrow {}^3H_4$ upconversion fluorescence, with two-laser one-colour excitation of the Tm^{3+} ions to the $^3H_4$ multiplet. There is no instantaneous enhancement of the upconversion fluorescence due to the second laser pulse, as was the case in the mixed crystal. This suggests that the intermediate storage state in the upconversion mechanism, either the $^3H_4$ or the $^3H_5$ multiplet in the model proposed in Figure 8.24, does not remain populated for very long after the first laser pulse. The upconversion mechanism will be one process contributing to this depopulation. Figure 8.46 shows that as there is no enhancement of the upconversion fluorescence from the $^1G_4$ multiplet, no envelope of transients can be constructed.

No ESA transitions were found after excitation of the Tm^{3+} ions to the $^3H_4$

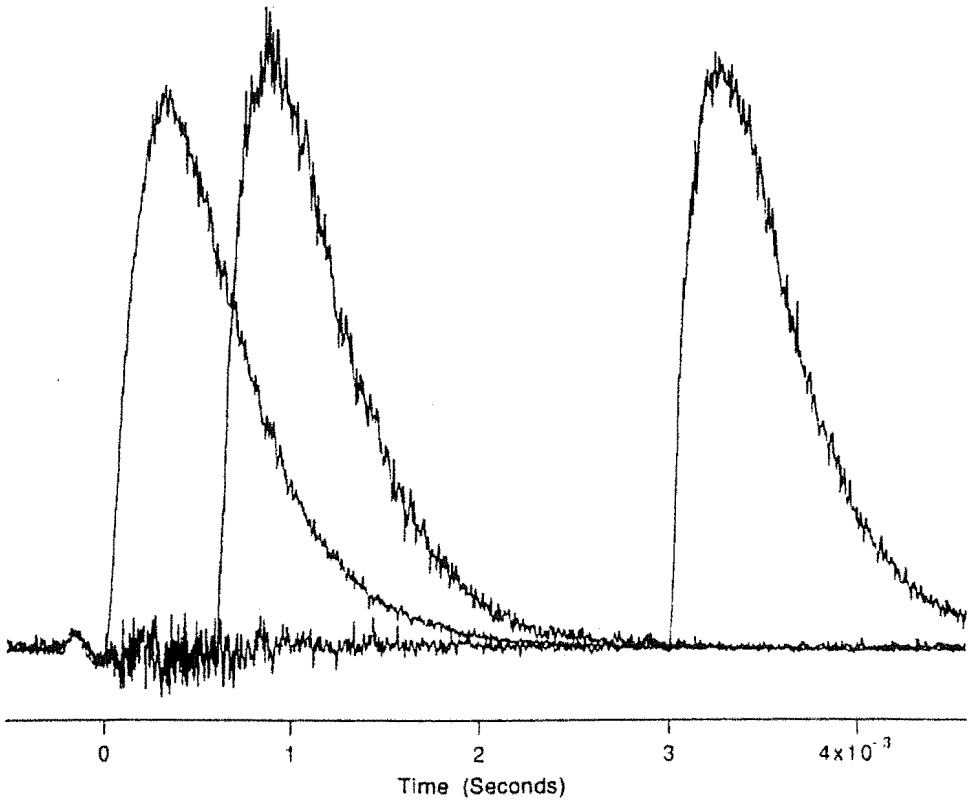

Figure 8.46: An envelope of transients for the $^1G_4 \rightarrow {}^3H_6$ fluorescence, with one-colour excitation of the Tm^{3+} ions to the $^3H_4$ multiplet in the $CsCdBr_3$:Tm^{3+} crystal. This envelope is shown after subtraction of the fluorescence due only to the first laser pulse.

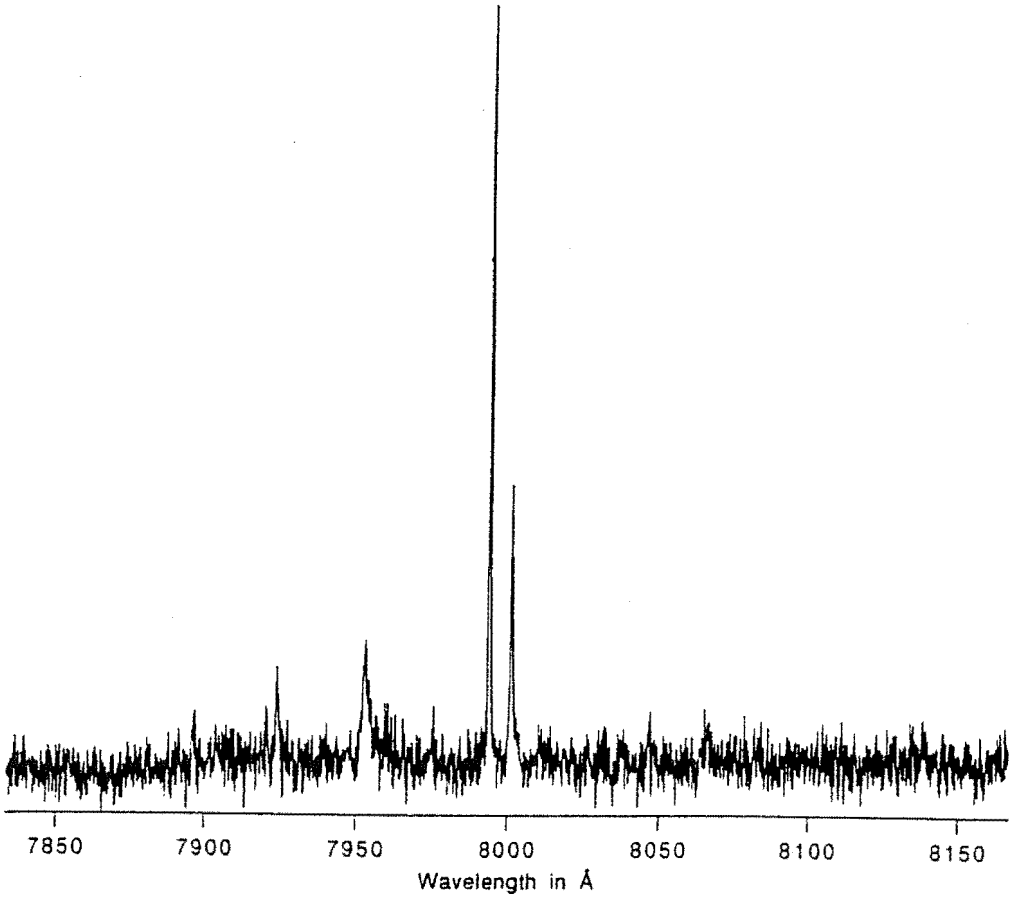

Figure 8.47: A two-laser excitation spectrum showing the $^3H_4 \rightarrow {}^3H_6$ absorption transitions, while monitoring the $^1G_4 \rightarrow {}^3H_6$ transition at 4808.Å in the $CsCdBr_3$:Tm^{3+} crystal.

multiplet, Figure 8.47. This was expected as the ESA transitions found in the mixed-dopant crystal were assigned to transitions of the Pr^{3+} ion.

Chapter 9

Conclusions

Laser selective excitation spectroscopy has been applied successfully to investigate electronic structure, excited-state relaxation, inter-ion energy transfer and fluorescence bleaching in several species of crystalline rare-earth centre.

Polarisation ratios have been determined for a number of possible RE^{3+} ion site symmetries in alkaline-earth fluoride crystals, with some corrections to ratios previously reported. Several of the C_s symmetry ratios cannot be expressed as simple numerical ratios. However they are constrained and for specific RE^{3+} centres, derived from higher symmetry parent centres, they can be estimated. In general the transition moments of RE^{3+} centres do not change dramatically when the site symmetry is broken by substitutional replacements of the ligand ions. This has been demonstrated in the case of the multi-hydrogenic ion Cs centres. Higher symmetry approximations could be applied in other studies of low-symmetry RE^{3+} systems.

Laser selective excitation spectroscopy was used to identify $^3P_0$, $^3P_1$ and $^1I_6$ multiplet crystal-field levels of the Pr^{3+} centres in hydrogenated SrF_2 and CaF_2 crystals. Good fluorescence polarisation ratios were obtained for the bleachable Cs centres, using a careful experimental procedure, and the Pr^{3+} site symmetries were deduced. Their $^1D_2$ fluorescence lifetimes were measured and analysed in terms of successive hydrogenic ion substitutions. Model configurations were proposed or confirmed for all of the known Cs centres.

Bleaching mechanisms were proposed for all of these bleachable centres, based on the general interstitialcy-noncolinear mechanism suggested by Reeves et al [75] [77]. Model configurations for the Cs^* centres and the bleaching pathways between the different centre orientations were thus deduced. These models were able to account for the observed polarised bleaching behaviour of each centre. It is hoped that this rigourous treatment, where the polarisation dependencies of the different centre orientations are included, will be applied to other crystalline hole-burning systems.

From all the investigations of fluorescence bleaching in these multi-hydrogenic ion RE^{3+} centres, a physical model emerges of bleaching as a phonon-scattering process, involving the migration of hydrogenic ions about the RE^{3+} ion. These phonons

are generated by the phonon-assisted relaxation of excited RE^{3+} ions. Heating the crystal generates lattice phonons and thermal-cycling experiments were used to establish the thermal-reverting temperatures of the different bleaching mechanisms. The results confirm that bleaching involves barrier crossing, in the double-well potential of two distinct configurations of a centre, and not quantum tunnelling. These experimental temperatures were sufficient to establish relative barrier potentials of the Cs centres.

Whether bleaching is a resonant process, involving the hydrogenic ion local vibrational mode, remains unknown. An important experimental test would be to look for bleaching in centres where the decay from an excited state to the ground state is purely radiative. The absence of efficient bleaching while populating such levels would be strong evidence for the resonant process. Both the gadolinium $^6P_{\frac{7}{2}}$ and ytterbium $^2F_{\frac{5}{2}}$ multiplets are good candidates for such an experiment.

The $C_{3v}F^-$ and $C_{4v}F^-$ centres of terbium in CaF_2 and SrF_2 crystals were identified spectroscopically. Irrep labels were assigned to the crystal-field levels of the $C_{4v}F^-$ centre and a crystal-field calculation yielded fitted values for the crystal-field parameters. Magnetic and electric-dipole transitions have comparable intensities in these Tb^{3+} centres, however polarisation ratio measurements are still useful when assigning irrep labels to transitions and crystal-field levels.

Six new Tb^{3+} centres were found in the hydrogenated CaF_2 and SrF_2 crystals. The Ls(1), Ls(2) and Ls(3) centres exhibit fluorescence bleaching, while the Ls(4) centre exhibits fluorescence enhancement. Hydrogen Ls centres bleach more rapidly than their deuterium counterparts, as observed for other multi-hydrogenic ion RE^{3+} centres. Bleaching experiments suggest that the Ls(4) centre is a photoproduct of the Ls(3) centre and that the fluorescence enhancement is also produced by light-induced anion migration.

Clearly this is an initial survey of the Tb^{3+} centres in these crystals. Many other hydrogenic centres, particularly those associated with the $C_{3v}F^-$ centre, were seen but are still to be identified selectively. The Ls centres produce strong fluorescence, unlike other multi-hydrogenic ion RE^{3+} centres, and a detailed study of their bleaching behaviour would be most illuminating. Most of our current understanding of bleaching has been gleaned from the Cs centres of praseodymium. The defect chemistry of the pure SrF_2:Tb^{3+} and CaF_2:Tb^{3+} crystals also deserves further study, as the Tb^{3+} centres are transitional between the predominance of tetragonal and trigonal RE^{3+} centres.

New cross-relaxation and upconversion mechanisms were identified in homogeneous and heterogeneous pairs of Pr^{3+} and Tm^{3+} ions. Upconversion fluorescence was observed from the $^1D_2$, $^3P_0$ and $^3P_1$ multiplets of praseodymium and the $^3F_3$, $^1G_4$ and $^1D_2$ multiplets of thulium after exciting the Tm^{3+} ions to the $^3H_4$ multiplet in a mixed-dopant $CsCdBr_3$ crystal. Some novel two-laser techniques were applied successfully to probe the transient populations of intermediate states in these upconversion processes. Further studies are now being conducted on mixed praseodymium and thulium doped fibres. Crystal-field levels have been obtained for the dominant

homogeneous Tm^{3+} centre in $CsCdBr_3$:Tm^{3+}. A more detailed spectroscopic study of this centre, which includes polarisation ratio measurements to identify the energy levels, would be a logical extension of this work.

Bibliography

[1] J. F. Ackerman, G. M. Cole, and S. L. Holt. The physical properties of some transition metal compounds of the ABX_3 type. *Inog. Chim. Acta*, 8:323–343, 1974.

[2] J. Y. Allain, M. Monerie, and H. Poignant. Blue upconversion fluorozirconate fibre laser. *Electron. Lett.*, 26(3):166–168, February 1990.

[3] J. Y. Allain, M. Monerie, and H. Poignant. Room temperature cw tunable green upconversion holmium fibre laser. *Electron. Lett.*, 26(4):261–262, February 1990.

[4] J. Y. Allain, M. Monerie, and H. Poignant. Tunable green upconversion erbium fibre laser. *Electron. Lett.*, 28(2):111–113, January 1992.

[5] A. A. Antipin, L. D. Livanova, and L. Y. Shekun. Paramagnetic resonance and spin-lattice relaxation of Tb^{3+} ions in SrF_2 single crystals. *Sov. Phys. - Solid State*, 10(5):1025–1029, November 1968.

[6] G. Armagan, A. M. Buoncristiani, and B. Di Bartolo. Excited state dynamics of thulium ions in yttrium aluminum garnets. *Optical Materials*, 1:11–20, 1992.

[7] T. Atenberger, U. Bogner, G. D. Jones, and K. M. Murdoch. Barrier crossing during holeburning of bleachable centres in SrF_2:Pr^{3+}:D^- crystals. For submission to Phys. Rev. B., 1993.

[8] T. Attenberger, I. Sildos, G. D. Jones, U. Bogner, and M. Maier. Persistent spectral hole-burning in electronic transitions of different types of lattice defects. *Radiation Effects and Defects in Solids*, 119:325–330, 1991.

[9] Thomas Attenberger. *Stabiles Spektrales Lochbrennen in Perylen/n-Heptan und Anderen Kristallinen Modellsystemen.* PhD thesis, Institut für Physik III, Universität Regensburg, 1992. Translation: Persistent Spectral Hole-Burning in Perylen/n-Heptane and Other Crystalline Model-Systems.

[10] F. Auzel. Upconversion processes in coupled ion systems. *J. Lumin.*, 45:341–345, 1990.

[11] R. B. Barthem, R. Buisson, and R. Cone. Spectroscopic analysis of Nd^{3+} pairs in $CsCdBr_3$. *J. Chem. Phys.*, 91(2):628, July 1989.

[12] R. B. Barthem, R. Buisson, F. Madèore, J. C. Vial, and J. P. Chaminade. De-excitation processes of optically excited Nd^{3+} pairs in $CsCdBr_3$. *J. Physique*, 48:379–387, 1987.

[13] C. Barthou and R. B. Barthem. Strongly coupled Nd^{3+} ion pairs in $CsCdBr_3$: Optical properties and energy transfer. *J. Lumin.*, 46:9–15, 1990.

[14] T. Boonyarith, J. P. D. Martin, B. Luo, and N. B. Manson. Zeeman measurements of Pr^{3+} centres in CaO and CaF_2. *J. Lumin.*, 51:149–156, 1992.

[15] M. R. Brown, K. G. Roots, J. M. Williams, W. A. Shand, C. Groter, and H. F. Kay. Experiments on Er^{3+} in SrF_2 II. concentration dependance of site symmetry. *J. Chem. Phys.*, 50:891, 1969.

[16] M. Buijs, A. Meyerink, and G. Blasse. Energy transfer between Eu^{3+} ions in a lattice with two different crystallographic sites: Y_2O_3:Eu^{3+}, Gd_2O_3:Eu^{3+} and Eu_2O_2. *J. Lumin.*, 37:9–20, 1987.

[17] R. Buisson and J.C. Vial. Transfer inside pairs of Pr^{3+} in LaF_4 studied by upconversion fluorescence. *J. Physique Lett.*, 42:115–118, 1981.

[18] P. H. Butler. *Point Group Symmetry Applications.* Plenum Press, New York, 1981.

[19] W. T. Carnall, G. L. Goodman, K. Rajnak, and R. S. Rana. A systematic analysis of the spectra of the lanthanides doped into single crystal LaF_3. *J. Chem. Phys.*, 90(7):3443–3457, April 1989.

[20] J. P. Chaminade, R. M. Macfarlane, F. Ramaz, and J. C. Vial. High resolution laser spectroscopy of rare earth doped $CsCdBr_3$. *J. Lumin.*, 48:531–535, 1991.

[21] J. Chrysochoos. Laser-induced emission of CaF_2-Tb^{3+} at room and low temperatures. *J. Less-Common Metals*, 93:73–80, 1983.

[22] C. D. Cleven, S. H. Lee, and J. C. Wright. Clustering and percolation of defects in Pr^{3+}:SrF_2 using site selective spectroscopy. *Phys. Rev. B*, 44(1):23–29, July 1991.

[23] N. J. Cockroft, G. D. Jones, and D. C. Nguyen. Dynamics and spectroscopy of infrared-to-visible upconversion in erbium doped cesium cadmium bromide. *Phys. Rev. B*, 45(10):5187–5198, March 1992.

[24] N. J. Cockroft, G. D. Jones, and R. W. Syme. Upconversion fluorescence spctroscopy of Er^{3+} pairs in $CsCdBr_3$. *J. Lumin.*, 43:275–281, 1989.

[25] N. J. Cockroft, G. D. Jones, and R. W. G. Syme. Site-selective laser spectroscopy of deuterated SrF_2:Er^{3+}. *J. Chem. Phys*, 94(4):2166–2177, February 1990.

[26] N. J. Cockroft, D. Thompson, G. D. Jones, and R. W. G. Syme. Site-selective spectroscopy of hydrogenic sites in CaF_2:Er^{3+} crystals. *J. Chem. Phys.*, 86(2):521–544, January 1987.

[27] Nigel J. Cockroft. *Laser Selective Excitation of Erbium Ions in Crystalline Solids.* PhD thesis, University of Canterbury, 1987.

[28] J Corish, C. R. A. Catlow, P. W. M. Jacobs, and S. N. Ong. Defect aggregation in anion-excess fluorites. Dopant monomers and dimers. *Phys. Rev. B*, 25(10):6425–6438, May 1982.

[29] G. H. Dieke. *Spectra and Energy Levels of Rare Earth Ions in Crystals.* Interscience of John Wiley & Sons, New York, 1968.

[30] M. Dulick, G. E. Faulkner, N. J. Cockroft, and D. C. Nguyen. Spectroscopy and dynamics of upconversion in Tm^{3+}:$YLiF_4$. *J. Lumin.*, 48:517–521, 1991.

[31] A. Edgar, C. A. Freeth, and G. D. Jones. Infrared and electron-paramagnetic-resonance spectra of trivalent rare-earth ions in hydrogenated strontium-fluoride crystals. *Phys. Rev. B*, 15(10):5023–5037, May 1977.

[32] A. Edgar and H. K. Welsh. Dielectric loss and EPR studies of CaF_2:Gd^{3+}. *J. Phys. C*, 8:L336–L340, 1975.

[33] R. J. Elliott, W. Hayes, G. D. Jones, H. F. Macdonald, and C. T. Sennett. Localised vibrations of H^- and D^- ions in the alkaline earth fluorides. *Proc. Roy. Soc.*, A289:1, 1965.

[34] S. P. Foo. Laser selective excitation of $CsCdBr_3$:Pr^{3+} crystals. Undergraduate Project Report 3, University of Canterbury, 1989.

[35] P. A. Forrester and C. F. Hempstead. Paramagnetic resonance of Tb^{3+} ions in $CaWO_4$ and CaF_2. *Phys. Rev.*, 126(3):923–929, May 1963.

[36] C. A. Freeth. *The Transverse Zeeman Effect in CaF_2:Er^{3+} Crystals.* PhD thesis, University of Canterbury, 1980.

[37] M. E. German. Hydrogenation treatment. Undergraduate Project Report 1, University of Canterbury, 1990.

[38] J. L. Hall and R. T. Schumacher. Electron spin resonance of hydrogen atoms in CaF_2. *Phys. Rev. B*, 127(6):1892–1912, September 1962.

[39] T. P. J. Han. *Laser Selective Excitation Studies of Neodymium.* PhD thesis, University of Canterbury, 1988.

[40] T. P. J. Han, G. D. Jones, and R. W. G. Syme. Site-selective spectroscopy of Nd^{3+} centers in CaF_2:Nd^{3+} and SrF_2:Nd^{3+}. *Phys. Rev. B*, 47(22):14706–14723, June 1993.

[41] L. H. Henling and G. L. McPherson. EPR spectra of magnetically coupled pairs of Gd^{3+} ions in crystals of $CsMgCl_3$, $CsMgBr_3$ and $CsCdBr_3$. *Phys. Rev. B*, 16(11):4756–4760, December 1977.

[42] T. Herbert, R. Wannemacher, W. Lenth, and R. M. Macfarlane. Blue and green cw upconversion lasing in Er^{3+}:$YLiF_4$. *Appl. Phys. Lett.*, 57(17):1727–1729, October 1990.

[43] S. Hüfner. *Optical Spectra of Transparent Rare Earth Compounds.* Academic Press, New York, 1978.

[44] I. T. Jacobs, G. D. Jones, K. Ždánský, and R. A. Satten. Electron-phonon interaction effects in the spectra of hydrogenated, deuterated, and tritiated crystals of calcium and strontium fluorides containing cerium. *Phys. Rev. B*, 3(9):2888–2910, May 1971.

[45] Ian T. Jacobs. *Rare Earth - Hydride Centres in the Alkaline Earth Fluorides.* PhD thesis, University of Canterbury, 1971.

[46] I. W. Johnstone. Impurity modes in $CdCl_2$ type crystals. Under Graduate Project Report 7, University of Canterbury, 1972.

[47] G. D. Jones, S. Peled, S. Rosenwake, and S. Yatsiv. Spectra of hydrogenated calcium fluoride containing rare-earth ions. *Phys. Rev.*, 183(2):353–369, July 1969.

[48] B. R. Judd. Vibronic contributions to ligand-induced pseudo-quadrupole absorption of rare-earth ions. *Phys. Scr.*, 21:543–548, June 1980.

[49] Y. L. Khong, G. D. Jones, and R. W. G. Syme. Laser-selective-excitation spectroscopy of Pr^{3+} centres in mixed alkaline-earth-fluoride crystals. *Phys. Rev. B*, 48(2):672–686, July 1993.

[50] G. F. Koster, J. D. Dimmock, R. G. Wheeler, and H. Statz. *Properties of the Thirty-Two Point Groups.* M.I.T. Press, Cambridge, 1963.

[51] W. Lenth and R. M. Macfarlane. Excitation mechanisms for upconversion lasers. *J. Lumin.*, 45:346–350, 1990.

[52] A. Lezama, M. Oria, and C. B. de Araujo. Site-selective spectroscopy via energy up-conversion in CaF_2:Pr^{3+}. *Phys. Rev. B*, 33(7):4493–4500, 1986.

[53] Khong Yoon Loong. *Laser Spectroscopy of Praseodymium Doped Mixed Alkaline Earth Fluorides.* PhD thesis, University of Canterbury, 1991.

[54] Roger Macfarlane. Fluoride fibres yield blue-green lasers. *Physics World*, page 18, October 1991.

[55] A. A. Maradudin and J. Peretti. Impurity-induced second-harmonic infrared absorption and raman scattering by u-centre localised modes in alkali-halide crystals. *Phys Rev.*, 161(3):852–860, September 1967.

[56] J. A. D. Mathew. Properties of small ions in ionic host lattices. *Solid State Comm.*, 3:365–367, 1965.

[57] A. M. McPherson and G. L. McPherson. Spectroscopic properties of a Ce^{3+}-Tm^{3+} center in $CsCdBr_3$ crystals: Absorption, emission, and energy transfer. *Solid State Commun.*, 37:501–505, 1981.

[58] G. L. McPherson and L. M. Henling. EPR spectrum of coupled pairs of Gd^{3+} ions in single crystals of $CsCdBr_3$. *Phys. Rev. B*, 16(5):1889–1892, September 1977.

[59] G. L. McPherson, W. Heung, and J. J. Barraza. Coupled pairs of chromium(III) ions in crystals of $CsMgCl_3$, $CsMgBr_3$, and $CsCdBr_3$. a case of charge compensation induced pair formation. *J. Am. Chem. Soc.*, 100:469–475, 1978.

[60] G. L. McPherson, A. M. McPherson, and J. L. Atwood. Structures of $CsMgBr_3$, $CsCdBr_3$, and $CsMgI_3$ - diamagnetic linear chain lattices. *J. Phys. Chem. Solids*, 41:495–499, 1980.

[61] G. L. McPherson and S. L. Meyerson. Intense up-converson luminescence resulting from the two-photon absorption of Er^{3+} ions in crystals of $CsMgCl_3$. *Chem. Phys. Lett.*, 179(4):325–328, April 1991.

[62] Marjorie Mujaji. *Solid State Spectroscopy: Laser Selective Exciation of Holmium Ions in Crystalline Solids.* PhD thesis, University of Canterbury, 1992.

[63] C. W. Neilson and G. F. Koster. *Spectroscopic Coefficients for the p^n, d^n and f^n Configurations.* M.I.T. Press, Cambridge, Massachusetts, 1963.

[64] R. C. Newman. *Infra-red Studies of Crystal Defects.* Taylor and Francis, London, 1973.

[65] D. C. Nguyen, G. E. Faulkner, and M. Dulick. Blue-green (450nm) upconversion Tm^{3+}:$YLiF_4$. *Appl. Optics*, 28(17):3553–3555, September 1989.

[66] E. W. J. L. Oomen. Up-conversion of red light into blue light in thulium doped fluorozirconate glasses. *J. Lumin.*, 50:317–332, 1992.

[67] O. Pilla, E. Cazzanelli, B. Blanzat, C. Andraud, and F. Pelle. Comparative raman study of phonon linewidths in pure and lead-doped $CsCdBr_3$. *Phys. Stat. Sol. B*, 144:845–851, 1987.

[68] R. S. Quimby, M. G. Drexhage, and M. J. Suscavage. Efficient frequency up-conversion via energy transfer in fluoride glasses. *Electron. Lett.*, 23(1):32–34, January 1987.

[69] N. Rabbiner. Fluorescence of Tb^{3+} in CaF_2. *J. Opt. Soc. Am.*, 55(4):436–438, April 1965.

[70] N. Rabbiner. Cubic crystal-field energy levels, Tb^{3+}:CaF_2 (I). *J. Opt. Soc. Am.*, 57(2):217–231, February 1967.

[71] F. Ramaz, R. M. Macfarlane, J. C. Vial, J. P. Chaminade, and F. Madéore. Laser and zeeman spectroscopy of Pr^{3+}:$CsCdBr_3$; a simplified crystal field model. *J. Lumin.*, 55:173–181, 1993.

[72] F. Ramaz, J. C. Vial, and R. M. Macfarlane. Measurement of the angular distribution of the crystallographic c-axis in a crystal of $CsCdBr_3$:Pr^{3+} using hole-burning stark spectroscopy. *Europhys. Lett.*, 22(3):217–222, April 1992.

[73] Francois Ramaz. *Etude et Caracterisation Optique de Cristaux Inorganiques Presentant le Phenomene de Formation de Tros Spectraux (Spectral Holeburning).* PhD thesis, Universite Joseph Fourier - Grenoble - France, 1991.

[74] D. Narayana Rao, P. Venkateswarlu, and D. Ramachandra Rao. Fluorescence spectrum of CaF_2:Tb^{3+} single crystal. *Indian J. Phys.*, 54B:305–310, 1980.

[75] R. J. Reeves, G. D. Jones, and R. W. G. Syme. Spectroscopy of reversible bleaching centers in hydrogenated SrF_2:Pr^{3+} and CaF_2:Pr^{3+} crystals. *Phys. Rev. B*, 40(10):6475–6484, October 1989.

[76] R. J. Reeves, G. D. Jones, and R. W. G. Syme. Site-selective laser spectroscopy of Pr^{3+} C_{4v} symmetry centres in hydrogenated CaF_2:Pr^{3+} and SrF_2:Pr^{3+} crystals. *Phys. Rev. B*, 46(10):5939–5958, September 1992.

[77] Roger J. Reeves. *Laser Selective Excitation of Praseodymium in Hydrated Fluorite Crystals.* PhD thesis, University of Canterbury, 1987.

[78] M. F. Reid, J. J. Dallara, and F. S. Richardson. Comparison of calculated and experimental $4f \rightarrow 4f$ intensity parameters for lanthanide complexes with isotropic ligands. *J. Chem. Phys.*, 79(12):5743–5751, December 1983.

[79] Reisfeld and Jorgensen. *Lasers and Excited States of Rare-Earths.* Springer-Verlag, New York, 1977.

[80] J. D. Saxe, T. R. Faulkner, and F. S. Richardson. Optical activity of the f-f transitions in trigonal dihedral D_3 lanthanide (111) complexes. *J. Chem. Phys.*, 76(4):1595–1623, 1982.

[81] J. D. Saxe, J. P. Morley, and F. S. Richardson. Polarised luminescence spectra of Tb^{3+} in trigonal Na_3 Tb(oxydiacetate)$_2$. $2NaClO_4$. $6H_2O$. *Molec. Phys.*, 47(2):407–429, 1982.

[82] R. W. Schwartz, H. G. Brittain, J. P. Riehl, W. Yeakel, and F. S. Richardson. Magnetic circularly polarised emission and magnetic circular dichroism study of the $^7F_J \leftrightarrow {}^5D_4$ transitions in crystalline $Cs_2NaTbCl_6$. *Molec. Phys.*, 34(2):361–379, 1977.

[83] R. E. Shamu, W. M. Hartmann, and E. L. Yasaitis. Localised vibrations of atomic hydrogen in CaF_2. *Phys. Rev. B*, 170(3):822–824, June 1968.

[84] A. J. Silversmith, W. Lenth, and R. M. Macfarlane. Green infrared-pumped erbium upconversion laser. *Appl. Phys. Lett.*, 51(24):1977–1979, December 1987.

[85] R. G. Smart, D. C. Hanna, A. C. Tropper, S. T. Davey, S. F. Carter, and D. Szebesta. CW room temperature upconversion lasing at blue, green, and red wavelengths in infrared-pumped Pr^{3+}-doped fluoride fibre. *Electron. Lett.*, 27(14):1307–1309, July 1991.

[86] R. C. Spitzer, W. P. Ambrose, and A. J. Sievers. Observation of persistent IR hole burning in the vibrational spectrum of CN^- in KBr. *Phys. Rev. B*, 34(10):7307–7317, November 1986.

[87] D. R. Tallant, M. P. Miller, and J. C. Wright. Energy transfer and relaxation phenomena in CaF_2:Er^{3+}. *J. Chem. Phys.*, 65(2):510–521, July 1976.

[88] B. M. Tissue and J. C. Wright. Site-selective laser spectroscopy of CaF_2:Pr^{3+} and CaF_2:Pr^{3+}, R^{3+} (R^{3+} = Y^{3+}, Gd^{3+}, Nd^{3+}). *Phys. Rev. B*, 36(18):9781–9789, December 1987.

[89] J. C. Vial, R. Buisson, F. Madeore, and M. Poirier. Upconversion studied by selective time resolved excitation techniques in Pr^{3+}:LaF_3. *J. Physique*, 40:913–920, September 1979.

[90] Mitchel Weissbluth. *Atoms and Molecules.* Academic Press, New York, 1978.

[91] T. Whitley, C. Millar, R. Wyatt. M. Brierley, and D. Szebesta. Upconversion pumped green lasing in erbium doped fluorozirconate fibre. *Electron. Lett.*, 27(20):1785–1786, September 1991.

[92] J. C. Wright. Upconversion and excited state energy transfer in rare-earth doped materials. In *Radiationless Processes in Molecules and Condensed Phases*, volume 15 of *Topics in Applied Physics.* Springer-Verlag, 1976.

[93] B. G. Wybourne. *Spectroscopic Properties of Rare-Earths.* John Wiley, New York, 1965.

[94] S. Yatsiv, S. Peled, and S. Rosenwaks. Spectra of H^- in CaF_2 containing trivalent rare earth ions. In H. M. Crosswhite and H. W. Moos, editors, *Optical Properties of Ions in Crystals*, pages 409–421. Interscience, New York, 1967.

[95] D. C. Yeh, W. A. Sibley, and M. J. Suscavage. Efficient frequency upconversion of Tm^{3+} ions in Yb^{3+} doped barium-thorium fluoride glass. *J. Appl. Phys.*, 63(9):4644–4650, May 1988.

[96] W. Yen. Experimental studies of energy transfer in rare earth ions in crystals. In *Spectroscopy of Solids Containing Rare Earths*, volume 21 of *Modern Problems in Condensed Matter Sciences*, pages 185–249. North Holland, 1987.